Pertanika Journal of

SCIENCE & TECHNOLOGY

JST

VOL. 31 (3) APR. 2023

PERTANIKA JOURNALS

A scientific journal published by Universiti Putra Malaysia Press

Pertanika Journal of Science & Technology
Pertanika Journal of Science & Technology

PERTANIKA JOURNAL OF SCIENCE & TECHNOLOGY

About the Journal

Overview

Pertanika Journal of Science & Technology is an official journal of Universiti Putra Malaysia. It is an open-access online scientific journal. It publishes original scientific outputs. It neither accepts nor commissions third party content.

Recognised internationally as the leading peer-reviewed interdisciplinary journal devoted to the publication of original papers, it serves as a forum for practical approaches to improve quality on issues pertaining to science and engineering and its related fields.

Pertanika Journal of Science & Technology currently publishes 6 issues a year (*January, March, April*, *July, August,* and *October*). It is considered for publication of original articles as per its scope. The journal publishes in **English** and it is open for submission by authors from all over the world.

The journal is available world-wide.

Aims and scope

Pertanika Journal of Science & Technology aims to provide a forum for high quality research related to science and engineering research. Areas relevant to the scope of the journal include: bioinformatics, bioscience, biotechnology and bio-molecular sciences, chemistry, computer science, ecology, engineering, engineering design, environmental control and management, mathematics and statistics, medicine and health sciences, nanotechnology, physics, safety and emergency management, and related fields of study.

History

Pertanika Journal of Science & Technology was founded in 1993 and focuses on research in science and engineering and its related fields.

Vision

To publish a journal of international repute.

Mission

Our goal is to bring the highest quality research to the widest possible audience.

Quality

We aim for excellence, sustained by a responsible and professional approach to journal publishing. Submissions can expect to receive a decision within 90 days. The elapsed time from submission to publication for the articles averages 180 days. We are working towards decreasing the processing time with the help of our editors and the reviewers.

Abstracting and indexing of Pertanika

Pertanika Journal of Science & Technology is now over 27 years old; this accumulated knowledge and experience has resulted the journal being abstracted and indexed in SCOPUS (Elsevier), Clarivate Web of Science (ESCI), EBSCO, ASEAN CITATION INDEX, Microsoft Academic, Google Scholar, and MyCite.

Citing journal articles

The abbreviation for Pertanika Journal of Science & Technology is *Pertanika J. Sci. & Technol.*

Publication policy

Pertanika policy prohibits an author from submitting the same manuscript for concurrent consideration by two or more publications. It prohibits as well publication of any manuscript that has already been published either in whole or substantial part elsewhere. It also does not permit publication of manuscript that has been published in full in proceedings.

Code of Ethics

The *Pertanika* journals and Universiti Putra Malaysia take seriously the responsibility of all of its journal publications to reflect the highest in publication ethics. Thus, all journals and journal editors are expected to abide by the journal's codes of ethics. Refer to *Pertanika*'s **Code of Ethics** for full details, or visit the journal's web link at http://www.pertanika.upm.edu.my/code_of_ethics.php

Originality

The author must ensure that when a manuscript is submitted to *Pertanika*, the manuscript must be an original work. The author should check the manuscript for any possible plagiarism using any program such as Turn-It-In or any other software before submitting the manuscripts to the *Pertanika* Editorial Office, Journal Division.

All submitted manuscripts must be in the journal's acceptable similarity index range:

≤ 20% – PASS; > 20% – REJECT.

International Standard Serial Number (ISSN)

An ISSN is an 8-digit code used to identify periodicals such as journals of all kinds and on all media–print and electronic.

Pertanika Journal of Science & Technology: e-ISSN 2231-8526 (Online).

Lag time

A decision on acceptance or rejection of a manuscript is reached in 90 days (average). The elapsed time from submission to publication for the articles averages 180 days.

Authorship

Authors are not permitted to add or remove any names from the authorship provided at the time of initial submission without the consent of the journal's Chief Executive Editor.

Manuscript preparation

For manuscript preparation, authors may refer to Pertanika's **INSTRUCTION TO AUTHORS**, available on the official website of *Pertanika*.

Editorial process

Authors who complete any submission are notified with an acknowledgement containing a manuscript ID on receipt of a manuscript, and upon the editorial decision regarding publication.

Pertanika follows a **double-blind peer-review** process. Manuscripts deemed suitable for publication are sent to reviewers. Authors are encouraged to suggest names of at least 3 potential reviewers at the time of submission of their manuscripts to *Pertanika*, but the editors will make the final selection and are not, however, bound by these suggestions.

Notification of the editorial decision is usually provided within 90 days from the receipt of manuscript. Publication of solicited manuscripts is not guaranteed. In most cases, manuscripts are accepted conditionally, pending an author's revision of the material.

The journal's peer review

In the peer-review process, 2 to 3 referees independently evaluate the scientific quality of the submitted manuscripts. At least 2 referee reports are required to help make a decision.

Peer reviewers are experts chosen by journal editors to provide written assessment of the **strengths** and **weaknesses** of written research, with the aim of improving the reporting of research and identifying the most appropriate and highest quality material for the journal.

Operating and review process

What happens to a manuscript once it is submitted to *Pertanika*? Typically, there are 7 steps to the editorial review process:

1. The journal's Chief Executive Editor and the Editor-in-Chief examine the paper to determine whether it is relevance to journal needs in terms of novelty, impact, design, procedure, language as well as presentation and allow it to proceed to the reviewing process. If not appropriate, the manuscript is rejected outright and the author is informed.

2. The Chief Executive Editor sends the article-identifying information having been removed, to 2 to 3 reviewers. They are specialists in the subject matter of the article. The Chief Executive Editor requests that they complete the review within 3 weeks.

   Comments to authors are about the appropriateness and adequacy of the theoretical or conceptual framework, literature review, method, results and discussion, and conclusions. Reviewers often include suggestions for strengthening of the manuscript. Comments to the editor are in the nature of the significance of the work and its potential contribution to the research field.

Pertanika Journal of Science & Technology
Pertanika Journal of Science & Technology

Pertanika Journal of Science & Technology
Pertanika Journal of Science & Technology
Pertanika Journal of Science & Technology

3. The Editor-in-Chief examines the review reports and decides whether to accept or reject the manuscript, invite the authors to revise and resubmit the manuscript, or seek additional review reports. In rare instances, the manuscript is accepted with almost no revision. Almost without exception, reviewers' comments (to the authors) are forwarded to the authors. If a revision is indicated, the editor provides guidelines for attending to the reviewers' suggestions and perhaps additional advice about revising the manuscript.

4. The authors decide whether and how to address the reviewers' comments and criticisms and the editor's concerns. The authors return a revised version of the paper to the Chief Executive Editor along with specific information describing how they have addressed' the concerns of the reviewers and the editor, usually in a tabular form. The authors may also submit a rebuttal if there is a need especially when the authors disagree with certain comments provided by reviewers.

5. The Chief Executive Editor sends the revised manuscript out for re-review. Typically, at least 1 of the original reviewers will be asked to examine the article.

6. When the reviewers have completed their work, the Editor-in-Chief examines their comments and decides whether the manuscript is ready to be published, needs another round of revisions, or should be rejected. If the decision is to accept, the Chief Executive Editor is notified.

7. The Chief Executive Editor reserves the final right to accept or reject any material for publication, if the processing of a particular manuscript is deemed not to be in compliance with the S.O.P. of *Pertanika*. An acceptance letter is sent to all the authors.

   The editorial office ensures that the manuscript adheres to the correct style (in-text citations, the reference list, and tables are typical areas of concern, clarity, and grammar). The authors are asked to respond to any minor queries by the editorial office. Following these corrections, page proofs are mailed to the corresponding authors for their final approval. At this point, **only essential changes are accepted**. Finally, the manuscript appears in the pages of the journal and is posted on-line.

Pertanika Journal of

SCIENCE & TECHNOLOGY

Vol. 31 (3) Apr. 2023

PERTANIKA JOURNALS

A scientific journal published by Universiti Putra Malaysia Press

PJST

Pertanika Journal of Science & Technology

AN INTERNATIONAL PEER-REVIEWED JOURNAL

EDITOR-IN-CHIEF

Luqman Chuah Abdullah
Chemical Engineering

CHIEF EXECUTIVE EDITOR

Mohd Sapuan Salit

UNIVERSITY PUBLICATIONS COMMITTEE

CHAIRMAN
Nazamid Saari

EDITORIAL STAFF

Journal Officers:
Ellyianur Puteri Zainal
Kanagamalar Silvarajoo
Muhammad Shafique Ardi Abdul Rahman
Siti Zuhaila Abd Wahid
Tee Syin Ying

Editorial Assistants:
Ku Ida Mastura Ku Baharom
Siti Juridah Mat Arip
Zulinaardawati Kamarudin

English Editor:
Norhanizah Ismail

PRODUCTION STAFF

Pre-press Officers:
Nur Farrah Dila Ismail
Wong Lih Jiun

WEBMASTER

IT Officer:
Illi Najwa Mohamad Sakri

EDITORIAL OFFICE

JOURNAL DIVISION
Putra Science Park
1st Floor, IDEA Tower II
UPM-MTDC Technology Centre
Universiti Putra Malaysia
43400 Serdang, Selangor Malaysia.

General Enquiry
Tel. No: +603 9769 1622 | 1616
E-mail:
executive_editor.pertanika@upm.edu.my
URL: www.journals-jd.upm.edu.my

PUBLISHER

UPM Press
Universiti Putra Malaysia
43400 UPM, Serdang, Selangor, Malaysia.
Tel: +603 9769 8851
E-mail: penerbit@putra.upm.edu.my
URL: http://penerbit.upm.edu.my

ASSOCIATE EDITOR

2021-2023

Adem Kilicman
Mathematical Sciences
Universiti Putra Malaysia, Malaysia

Miss Laiha Mat Kiah
Security Services Sn: Digital Forensic, Steganography, Network Security, Information Security, Communication Protocols, Security Protocols
Universiti Malaya, Malaysia

Saidur Rahman
Renewable Energy, Nanofluids, Energy Efficiency, Heat Transfer, Energy Policy
Sunway University, Malaysia

EDITORIAL BOARD

2022-2024

Abdul Latif Ahmad
Chemical Engineering
Universiti Sains Malaysia, Malaysia

Ahmad Zaharin Aris
Hydrochemistry, Environmental Chemistry, Environmental Forensics, Heavy Metals
Universiti Putra Malaysia, Malaysia

Azlina Harun@Kamaruddin
Enzyme Technology, Fermentation Technology
Universiti Sains Malaysia, Malaysia

Bassim H. Hameed
Chemical Engineering: Reaction Engineering, Environmental Catalysis & Adsorption
Qatar University, Qatar

Biswajeet Pradhan
Digital image processing, Geographical Information System (GIS), Remote Sensing
University of Technology Sydney, Australia

Daud Ahmad Israf Ali
Cell Biology, Biochemical, Pharmacology
Universiti Putra Malaysia, Malaysia

Hari M. Srivastava
Mathematics and Statistics
University of Victoria, Canada

Ho Yuh-Shan
Water research, Chemical Engineering and Environmental Studies
Asia University, Taiwan

Hsiu-Po Kuo
Chemical Engineering
National Taiwan University, Taiwan

Ivan D. Rukhlenko
Nonliner Optics, Silicon Photonics, Plasmonics and Nanotechnology
The University of Sydney, Australia

Lee Keat Teong
Energy Environment, Reaction Engineering, Waste Utilization, Renewable Energy
Universiti Sains Malaysia, Malaysia

Mohamed Othman
Communication Technology and Network, Scientific Computing
Universiti Putra Malaysia, Malaysia

Mohd Shukry Abdul Majid
Polymer Composites, Composite Pipes, Natural Fibre Composites, Biodegradable Composites, Bio-Composites
Universiti Malaysia Perlis, Malaysia

Mohd Zulkifly Abdullah
Fluid Mechanics, Heat Transfer, Computational Fluid Dynamics (CFD)
Universiti Sains Malaysia, Malaysia

Mohd. Ali Hassan
Bioprocess Engineering, Environmental Biotehnology
Universiti Putra Malaysia, Malaysia

Nor Azah Yusof
Biosensors, Chemical Sensor, Functional Material
Universiti Putra Malaysia, Malaysia

Norbahiah Misran
Communication Engineering
Universiti Kebangsaan Malaysia, Malaysia

Roslan Abd-Shukor
Physics & Materials Physics, Superconducting Materials
Universiti Kebangsaan Malaysia, Malaysia

Wing Keong Ng
Aquaculture, Aquatic Animal Nutrition, Aqua Feed Technology
Universiti Sains Malaysia, Malaysia

INTERNATIONAL ADVISORY BOARD

2021-2024

CHUNG, Neal Tai-Shung
Polymer Science, Composite and Materials Science
National University of Singapore, Singapore

Hiroshi Uyama
Polymer Chemistry, Organic Compounds, Coating, Chemical Engineering
Osaka University, Japan

Mohamed Pourkashanian
Mechanical Engineering, Energy, CFD and Combustion Processes
Sheffield University, United Kingdom

Mohini Sain
Material Science, Biocomposites, Biomaterials
University of Toronto, Canada

Yulong Ding
Particle Science & Thermal Engineering
University of Birmingham, United Kingdom

ABSTRACTING AND INDEXING OF PERTANIKA JOURNALS

The journal is indexed in SCOPUS (Elsevier), Clarivate-Emerging Sources Citation Index (ESCI), BIOSIS, National Agricultural Science (NAL), Google Scholar, MyCite, ISC. In addition, Pertanika JSSH is recipient of "CREAM" Award conferred by Ministry of Higher Education (MoHE), Malaysia.

The publisher of Pertanika will not be responsible for the statements made by the authors in any articles published in the journal. Under no circumstances will the publisher of this publication be liable for any loss or damage caused by your reliance on the advice, opinion or information obtained either explicitly or implied through the contents of this publication.
All rights of reproduction are reserved in respect of all papers, articles, illustrations, etc., published in Pertanika. Pertanika provides free access to the full text of research articles for anyone, web-wide. It does not charge either its authors or author-institution for refereeing/publishing outgoing articles or user-institution for accessing incoming articles.
No material published in Pertanika may be reproduced or stored on microfilm or in electronic, optical or magnetic form without the written authorization of the Publisher.
Copyright ©2021 Universiti Putra Malaysia Press. All Rights Reserved.

Pertanika Journal of Science & Technology
Vol. 31 (3) Apr. 2023

Contents

Foreword i
Mohd Sapuan Salit

Humic Acid-Amended Formulation Improves Shelf-Life of Plant Growth-Promoting Rhizobacteria (PGPR) Under Laboratory Conditions 1137
Buraq Musa Sadeq, Ali Tan Kee Zuan, Susilawati Kasim, Wong Mui Yun, Nur Maizatul Idayu Othman, Jawadyn Talib Alkooranee, Sayma Serine Chompa, Amaily Akter and Md Ekhlasur Rahman

Effects of Density Variation on the Physical and Mechanical Properties of Empty Fruit Bunch Cement Board (EFBCB) 1157
Mohammad Nasrullah Ridzuan, Hasniza Abu Bakar, Emedya Murniwaty Samsudin, Nik Mohd Zaini Nik Soh and Lokman Hakim Ismail

Ex-Situ Development and Characterization of Composite Film Based on Bacterial Cellulose Derived from Oil Palm Frond Juice and Chitosan as Food Packaging 1173
Norshafira Syazwani Abu Hasan, Shahril Mohamad, Sharifah Fathiyah Sy Mohamad, Mohd Hafiz Arzmi and Nurul Nadia Izzati Supian

Effect of Moisture Content on Frictional Properties of Some Selected Grains in Indonesia 1189
Nursigit Bintoro, Alya Iqlima Zahra, Azizah Putri Khansa, Muftia Chairin Nissa, Aldhayu Sam Safira and Sastika Nidya Ashari

Examination of the Partial Discharge Behaviour Within a Spherical Cavity in Insulation Paper of Transformer 1209
Muhammad Hakirin Roslan, Norhafiz Azis, Mohd Zainal Abidin Ab Kadir, Jasronita Jasni and Mohd Fairouz Mohd Yousof

Sociodemographic Characteristics, Dietary Intake, and Body Image Dissatisfaction Among Saudi Adolescent Girls 1223
Abeer Ahmad Bahathig, Hazizi Abu Saad, Nor Baizura Md Yusop, Nurul Husna Mohd Sukri and Maha M. Essam El-Din

Automation of Quantifying Security Risk Level on Injection Attacks Based on Common Vulnerability Scoring System Metric 1245
Aditya Kurniawan, Mohamad Yusof Darus, Muhammad Azizi Mohd Ariffin, Yohan Muliono and Chrisando Ryan Pardomuan

The Effect of Preload, Density and Thickness on Seat Dynamic Stiffness 1267
Azmi Mohammad Hassan, Khairil Anas Md Rezali, Nawal Aswan Abdul Jalil, Azizan As'arry and Mohd Amzar Azizan

Effects of Fibre Length on the Physical Properties of Oil Palm Empty Fruit Bunch Cement Board (OPEFB-CB) 1279
Wenish Anak Maynet, Emedya Murniwaty Samsudin, Nik Mohd Zaini Nik Soh, Lokman Hakim Ismail, Hasniza Abu Bakar and Ahmed Elgadi

Review Article
A Review on Grapheme-to-Phoneme Modelling Techniques to Transcribe Pronunciation Variants for Under-Resourced Language 1291
Emmaryna Irie, Sarah Samson Juan and Suhaila Saee

Correlation Between Clinical Features of Type 2 Diabetes Mellitus with CT Findings of Fatty Liver Patients 1313
Hanady Elyas Osman, Huda Osama, Mohamed Yousef, Amal Alsalamah, Lubna Bushara and Ikhlas Abdalaziz

Highly Conductive Graphenated-Carbon Nanotubes Sheet with Graphene Foliates for Counter Electrode Application in Dye- Sensitized Solar Cells 1325
Yusnita Yusuf, Suhaidi Shafie, Ismayadi Ismail, Fauzan Ahmad, Mohd Nizar Hamidon, Pandey Shyam Sudhir and Lei Wei

Evaluation of Digital's Role in Sustainable Built Environment 1335
Theodore Wayne, Chang Saar Chai, Shirly Siew Ling Wong, Fang Lee Lim, Kai Chen Goh and Nur IzieAdiana Abidin

Server-Side Cross-Site Scripting Detection Powered by HTML Semantic Parsing Inspired by XSS Auditor 1353
Chrisando Ryan Pardomuan, Aditya Kurniawan, Mohamad Yusof Darus, Muhammad Azizi Mohd Ariffin and Yohan Muliono

Influence of Carrier Agents Concentrations and Inlet Temperature on the Physical Quality of Tomato Powder Produced by Spray Drying 1379
S. M. Anisuzzaman, Collin G. Joseph and Fatin Nadiah Ismail

Review Article
Geochemistry of Foraminifera in the Marginal Seas of the Sunda Shelf: A Review 1413
Aqilah Nur Shahruddin and Che Abd Rahim Mohamed

Railway Urbanozems: Interrelation of Physicochemical and Integral Environmental Indicators 1439
Tatyana Anatolyevna Adamovich and Anna Sergeyevna Olkova

Heat Rate Deviation Analysis of a Coal-Fired Power Plant (CFPP) with the Influence of Applicable Coal Prices (ACP) 1453
Manmit Singh Jasbeer Singh, Nawal Aswan Abdul Jalil, Sharafiz Abdul Rahim, Zamir Aimaduddin Zulkefli and Hasril Hasini

Effects of Shooting Angles and Ricochet Angles on Bullet Weight Upon Impact on Three Types of Woods (Balau, Resak, and Seraya) 1475
Mohd Najib Sam, Glenna Tan Jie Yee, Noor Hazfalinda Hamzah, Mohd Zulkarnain Embi, Ahmad Zamri Md Rejab, Gina Francesca Gabriel and Khairul Osman

The Effect of Graphene Nanoplatelets Content on the Hardness of Mg6%Zn0.2%Mn Composites 1493
Abang Mohamad Harith Abang Beniamin, Noor Hisyam Noor Mohamed and Mahsuri Yusof

Discovery of *Mycobacterium tuberculosis* CYP121 New Inhibitor via Structure-Based Drug Repurposing 1503
Tarek El Moudaka, Priya Murugan, Mohd Basyaruddin Abdul Rahman and Bimo Ario Tejo

Study and Simulation of the Electric Field-Induced Spin Switching in PZT/NiFe/CoFe Nanostructured Composites 1523
Minh Hong Thi Nguyen, Thanh Tien Pham, Nam Van La, Soo Kien Chen and Tiep Huy Nguyen

The Characteristics of Polymer Concrete Reinforced with Polypropylene Fibres Under Axial and Lateral Compression Loads 1535
Nur Aqilah Azman, Agusril Syamsir, Mohd Supian Abu Bakar, Muhammad Asyraf Muhammad Rizal, Khairul Amri Sanusi and Mohammed Jalal Abdullah

Analysis of Influence of Vertical Vibration on Natural Heat Convection Coefficients from Horizontal Concentric and Eccentric Annulus 1555
Baydaa Khalil Khudhair, Adel Mahmood Saleh and Ali Laftah Ekaid

An Alternative Count Distribution for Modeling Dispersed Observations 1587
Ademola Abiodun Adetunji and Shamsul Rijal Muhammad Sabri

Foreword

Welcome to the third issue of 2023 for the Pertanika Journal of Science and Technology (PJST)!

PJST is an open-access journal for studies in Science and Technology published by Universiti Putra Malaysia Press. It is independently owned and managed by the university for the benefit of the world-wide science community.

This issue contains 25 articles; two review articles and the rest are regular articles. The authors of these articles come from different countries namely China, Egypt, Indonesia, Iraq, Japan, Libyan, Malaysia, Nigeria, Russia Federation, Saudi Arabia, United Arab Emirates and Vietnam.

Norshafira Syazwani Abu Hasan et al. from Universiti Malaysia Pahang and International Islamic University Malaysia evaluated the *ex-situ* development and characterization of a composite film based on bacterial cellulose derived from oil palm frond juice and chitosan as potential food packaging. They successfully produced bacterial cellulose-chitosan (BCC) film composites to reduce the environmental harm caused by synthetic plastic packaging materials. BCC films were prepared via the *ex-situ* method involving immersion of bacterial cellulose (BC) derived from the static cultivation of *Acetobacter xylinum* in oil palm frond juice in various concentrations of chitosan solution. The Attenuated Total Reflection Fourier-Transform Infrared and Field Emission Scanning Electron Microscopy results confirm the successful incorporation of chitosan into the BC. Further details of the article are available on page 1173.

A regular article titled "Highly Conductive Graphenated-Carbon Nanotubes Sheet with Graphene Foliates for Counter Electrode Application in Dye-Sensitized Solar Cells" was written by Yusnita Yusuf and co-researchers from Malaysia, Japan, and China. Their research successfully synthesized graphenated-carbon nanotube sheets (g-CNT) and carbon nanotube sheets (CNT) via the floating-catalyst chemical vapor deposition method. The morphology structure of the g-CNT sheet revealed foliates growing out from the sidewalls of multi-walled CNT. The g-CNT6 showed more stability than the g-CNT8 and CNT10. High conductivity was obtained for the sample g-CNT8 (34.5 S/cm) compared to the sample g-CNT6 (11.2 S/cm) and CNT10 (4.76 S/cm). The hybrid structure of the g-CNT sheet creates efficient charge transfer in the materials resulting in higher conductivity. Thus, the g-CNT sheet, especially g-CNT8, can potentially substitute platinum as the conventional CE in the dye-sensitized solar cell. Detailed information on this study can be found on page 1325.

Another article we wish to highlight is "Discovery *of Mycobacterium tuberculosis* CYP121 New Inhibitor via Structure-based Drug Repurposing" by Tarek El Moudaka, Priya Murugan, Mohd Basyaruddin Abdul Rahman, and Bimo Ario Tejo from UCSI University and Universiti Putra Malaysia. Tuberculosis (TB) remains a serious threat to human health with the advent of multi-drug resistant tuberculosis (MDR-TB) and extensively drug-resistant tuberculosis (XDR-TB). They have found antrafenine, an anti-inflammatory drug with high promiscuity to inhibit cytochrome P450, as a potential inhibitor for *M. tuberculosis* CYP121. Antrafenine, which emerged as the top CYP121 binder after docking 8,773 compounds from the RepoDB drug repositioning database, is bound to CYP121 with a binding affinity of -12.6 kcal/mol and interacts with important residues at the CYP121 binding site. Upon binding to CYP121, antrafenine affects the dynamics of residues located distantly from the active site. Detailed information on this study is presented on page 1503.

We anticipate that you will find the evidence presented in this issue to be intriguing, thought-provoking and useful in reaching new milestones in your own research. Please recommend the journal to your colleagues and students to make this endeavour meaningful.

All the papers published in this edition underwent Pertanika's stringent peer-review process involving a minimum of two reviewers comprising internal as well as external referees. This was to ensure that the quality of the papers justified the high ranking of the journal, which is renowned as a heavily-cited journal not only by authors and researchers in Malaysia but by those in other countries around the world as well.

We would also like to express our gratitude to all the contributors, namely the authors, reviewers, Editor-in-Chief and Editorial Board Members of PJST, who have made this issue possible.

PJST is currently accepting manuscripts for upcoming issues based on original qualitative or quantitative research that opens new areas of inquiry and investigation.

Chief Executive Editor
executive_editor.pertanika@upm.edu.my

Pertanika J. Sci. & Technol. 31 (3): 1137 - 1155 (2023)

PERTANIKA JOURNALS

SCIENCE & TECHNOLOGY

Journal homepage: http://www.pertanika.upm.edu.my/

Humic Acid-Amended Formulation Improves Shelf-Life of Plant Growth-Promoting Rhizobacteria (PGPR) Under Laboratory Conditions

Buraq Musa Sadeq[1], Ali Tan Kee Zuan[1]*, Susilawati Kasim[1], Wong Mui Yun[2], Nur Maizatul Idayu Othman[3], Jawadyn Talib Alkooranee[4], Sayma Serine Chompa[1], Amaily Akter[1] and Md Ekhlasur Rahman[1,5]

[1]Department of Land Management, Faculty of Agriculture, Universiti Putra Malaysia, 43400 UPM, Serdang, Selangor, Malaysia
[2]Department of Plant Protection, Faculty of Agriculture, Universiti Putra Malaysia, 43400 UPM, Serdang, Selangor, Malaysia
[3]Faculty of Plantation and Agrotechnology, Universiti Teknologi MARA, Melaka, Kampus Jasin 77300 UiTM, Merlimau, Melaka
[4]Department of Plant Protection, Faculty of Agriculture, University of Wasit, Wasit, Iraq
[5]Divisional Laboratory, Soil Resource Development Institute, Krishi Khamar Sharak, Farmgate, Dhaka-1215, Bangladesh

ABSTRACT

Plant growth-promoting rhizobacteria (PGPR) is a soil bacterium that positively impacts soil and crops. These microbes invade plant roots, promote plant growth, and improve crop yield production. *Bacillus subtilis* is a type of PGPR with a short shelf-life due to its structural and cellular components, with a non-producing resistance structure (spores). Therefore, optimum formulations must be developed to prolong the bacterial shelf-life by adding humic acid (HA) as an amendment that could benefit the microbes by providing shelter and carbon sources for bacteria. Thus, a study was undertaken to develop a biofertilizer formulation from locally isolated PGPR, using HA as an amendment. Four doses of HA (0, 0.01, 0.05, and 0.1%) were added to tryptic soy broth (TSB) media and inoculated with *B. subtilis* (UPMB10), *Bacillus tequilensis* (UPMRB9) and the combination of both strains. The shelf-life was recorded, and

ARTICLE INFO

Article history:
Received: 01 June 2022
Accepted: 16 August 2022
Published: 31 March 2023

DOI: https://doi.org/10.47836/pjst.31.3.01

E-mail addresses:
buraqmosa1991@gmail.com (Buraq Musa Sadeq)
tkz@upm.edu.my (Ali Tan Kee Zuan)
susilawati@upm.edu.my (Susilawati Kasim)
muiyun@upm.edu.my (Wong Mui Yun)
nurmaizatul@uitm.edu.my (Nur Maizatul Idayu Othman)
jalkooranee@uowasit.edu.iq (Jawadyn Talib Alkooranee)
serinesayma@gmail.com (Sayma Serine Chompa)
amailyakter2554@gmail.com (Amaily Akter)
ekhlasurrahman02@gmail.com (Md Ekhlasur Rahman)
*Corresponding author

ISSN: 0128-7680
e-ISSN: 2231-8526

© Universiti Putra Malaysia Press

viable cells count and optical density were used to determine the bacterial population and growth trend at monthly intervals and endospores detection using the malachite green staining method. After 12 months of incubation, TSB amended with 0.1% HA recorded the highest bacterial population significantly with inoculation of UPMRB9, followed by mixed strains and UPMB10 at $1.8x10^7$ $CFUmL^{-1}$, $2.8x10^7$ $CFUmL^{-1}$and $8.9x10^6$ $CFUmL^{-1}$, respectively. Results showed that a higher concentration of HA has successfully prolonged the bacterial shelf-life with minimal cell loss. Thus, this study has shown that the optimum concentration of humic acid can extend the bacterial shelf-life and improve the quality of a biofertilizer.

Keywords: Colony forming unit, formulation, humic acid, PGPR, shelf-life

INTRODUCTION

Plant growth-promoting rhizobacteria (PGPR) has developed as an alternative method for reducing the use of agricultural chemical fertilisers to promote sustainable farming practices (Saeed et al., 2017; El-Tarabily et al., 2020; Al Raish et al., 2021; Al Hamad et al., 2021; Lahlali et al., 2022; Rizvi et al., 2022). Nowadays, much emphasis is placed on lowering the use of costly inorganic fertilizers and avoiding environmental contamination by reducing nitrogen and phosphate fertiliser doses using biofertilizers (El-Ghamry et al., 2018). Microorganisms commonly used as biofertilizer components include nitrogen fixers, phosphorous and potassium solubilizers, PGPRs, fungi, endo and ectomycorrhizal, cyanobacteria, and other useful microscopic critters (Itelima et al., 2018; Kamil et al., 2018; El-Tarabily et al., 2019; Mathew et al., 2020; El-Tarabily et al., 2021; Alblooshi et al., 2021). In addition, PGPR can directly impact the root's nutrient transportation systems. The most common issue expressed by farmers and inoculant manufacturers is the shelf life of carrier-based inoculants. If short-lived biofertilizers are not utilized or sold before expiration, they will lead to a net monetary loss to the marketing authority (Calvo et al., 2019). Furthermore, the technical restrictions include the possibility of product degradation owing to reduced shelf-life or accidental mutations throughout the fermentation or storage. Therefore, to prolong the shelf-life, an optimized formulation must be developed (Mahalakshmi et al., 2019). Moreover, the formulation should normally include the active component in an appropriate carrier and additives to stabilize and safeguard the microbial cells throughout storage, transportation, and the targeted root zone (Arriel-Elias et al., 2018).

Humic acid (HA) is still soil's most complex and physiologically active component. It is dark brown, water-soluble at higher soil pH levels, and can persist in serene soil for generations (Sootahar et al., 2020). Humic acid amendments contain beneficial effects accelerated absorption of nutrients, decreased toxins, increased water retention, improved microbial growth by providing shelter and carbon sources, and improved overall soil structure (Ekin, 2019; Meng et al., 2021). One of the humic acids' most visible and

significant effects is their contribution to soil microbial communities. Scientists are becoming increasingly aware of the importance of a healthy microbiome to soil habitats. Furthermore, because bad soils and chemicals have devastated bacteria populations, they must be recovered (Pukalchik et al., 2019; Sun et al., 2022). For the past 20 years, scientists have been studying the interactions of humic acid with microbes. Initially, HA was researched primarily as a carbon or micronutrient source or its overall impact on microorganism development (Yang et al., 2021). Moreover, humic acid (HA) is often regarded as the essential component of organic matter, influencing the behaviour of organic contaminants. Due to the huge number of reactive functional groups, there was an extensive range of reaction activities, including surface adsorption, ion exchange, and complexation (Li et al., 2022; Rashad et al., 2022).

The liquid formulations are better than solid formulations because they allow for adding nutrients and extending the bacterial shelf-life (Zvinavashe et al., 2021). It is difficult to design unique formulations, but whether the product is new or improved, it must be steady during transport and storage, easy to handle and use, boost the activities of the organisms in the fields, and be expense and practicable (Young et al., 2006; Berninger et al., 2018). Several studies have shown that mixtures of PGPR could enhance biological control activity for multiple plant diseases through the mechanisms of induced systemic resistance or antagonism (Liu et al., 2018). The isolated bacteria (*B. subtilis*) with humic acid showed good survival with minimal cell loss for up to five months of storage (Young et al., 2006).

Bacillus subtilis cells are rod-shaped, Gram-positive bacteria found in soil and vegetation; they thrive in mesophilic environments (Cho & Chung, 2020). *Bacillus subtilis* generates dormant, extremely resistant endospores in response to environmental challenges or malnutrition. As a result, *B. subtilis* has evolved mechanisms that allow it to thrive under difficult conditions (Luu et al., 2022; Mahapatra et al., 2022). These spores can survive in hostile conditions for many years without necessary nutrition, and it is a type of PGPR with a short shelf-life due to its structural, and cellular components (Luu et al., 2022). Many factors influence a *Bacillus* spore's resistance to heat, strong proteinaceous coats, peptidoglycan cortex, moderate moisture content, and large amounts of di-picolinic acid and divalent cations within the spore core are all present (Durga et al., 2021; Cho & Chung, 2020; Mukherjee et al., 2022). Moreover, *B. subtilis* secretes extracellularly during nutrient scarcity, attempting to kill proteins that affect programmed cell death in siblings, releasing nutrients and allowing a portion of the population to expand. Dormancy can be seen as a risk-aversion strategy since resting structure, and cellular components necessitate energy investment and responsiveness to signals associated with favourable situations (Pashang et al., 2022). Dorner published a method for staining endospores in 1922, and Shaeffer and Fulton refined their approach in 1933 to make the procedure of staining only bacterial endospores speedier. The primary goal of endospore staining is to

distinguish bacterial spores from other vegetative cells and spore formers from non-spore formers (Lindsay et al., 2021).

Therefore, this study was undertaken (1) to develop a biofertilizer formulation consisting of locally isolated PGPRs with an optimized rate of humic acid concentrations as an amendment and (2) to study the shelf-life of these PGPRs for up to 12 months of incubation.

MATERIALS AND METHODS

Pure Colonies Collection of PGPR Strains

Two locally isolated plant growth-promoting rhizobacteria (PGPRs), *B. subtilis* (UPMB10) and *B. tequilensis* (UPMRB9) were collected at the Microbiology laboratory Department of Land Management in the Faculty of Agriculture, Universiti Putra Malaysia. These PGPRs were collected due to their morphological, cultural, and beneficial biochemical characteristics like N_2-fixing ability, solubilizing phosphate and potassium, and producing IAA, siderophore, and pectinase. These PGPR strains were also reported to increase the concentrations of N, P, and K in shoots and storage roots (Ali-Tan et al., 2017; Shultana et al., 2020; Kapadia et al., 2021; Shultana et al., 2021). These PGPRs were grown on nutrient agar (NA) media. Tryptic soy agar (TSA) media was used for sub-culturing these strains. Twenty ml of TSA media was poured into Petri plates, and the new pure colonies of the two strains were assessed by quadrant streaking technique to obtain a single and pure colony. A loopful from the original local strains was taken and streaked into a new Petri plate with TSA media, and each sample was replicated thrice and then incubated at 30°C in the incubator (SD-310 RL, Dasol, Korea) for 24 h.

Collection and Characterization of Humic Acid

Humic acid technical purchased from Sigma-Aldrich brand purity of ≥ 98 mol.% with code: 102098564 53680-50G products of Switzerland. Humic acid, which is black in colour and low solubility in water, has a pH of 6.2; its soluble in alkali but insoluble in acid and adjusted to seven by using tryptic soy broth media (TSB), which has a pH of 7.23, an organic C component of 30–50%, hydrogen (about 5%), nitrogen (about 3%) and a CEC of 70–166 me/100g. Humic acids are not single molecular formula compounds. Figure 1 illustrates that humic acid was generally aromatic in structure, with amino acids, amino sugars, peptides, and aliphatic molecules connecting the aromatic groups. Humic acid's hypothesized structure consists of free and bound phenolic hydroxyl groups, quinines, oxygen and nitrogen bridges, and carboxy groups (Nardi et al., 2021). Model structure of humic acid according to Stevenson and Schnitzer (1982):

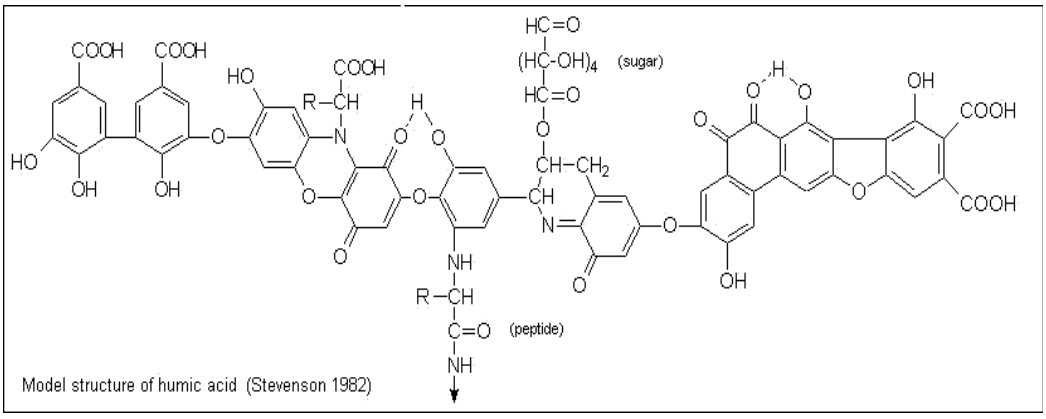

Figure 1. Model structure of humic acid (Stevenson & Schnitzer, 1982)

Shelf-Life Experimental and Treatments and Total Bacterial Population During Shelf-Life Period

A laboratory experiment was conducted with twelve treatments and three replications. The detailed treatments were as follows:

T1 = 0% Humic acid + UPMB10
T2 = 0% Humic acid + UPMRB9
T3 = 0% Humic acid + mixed strain
T4 = 0.01% Humic acid + UPMB10
T5 = 0.01% Humic acid + UPMRB9
T6 = 0.01% Humic acid + mixed strain
T7 = 0.05% Humic acid + UPMB10
T8 = 0.05% Humic acid + UPMRB9
T9 = 0.05% Humic acid + mixed strain
T10 = 0.1% Humic acid + UPMB10
T11 = 0.1% Humic acid + UPMRB9
T12 = 0.1% Humic acid + mixed strain

The microbial activity focuses on obtaining the population of bacteria in four Humic acid concentrations (0, 0.01, 0.05 and 0.1%) with two bacteria strains (*B. subtilis* (UPMB10), *B. tequilensis* (UPMRB9) and the mixture of both). Microbial development was recorded of this bacterium in laboratory circumstances for 12-months at a temperature of 30°C.

Procedure: 0, 0.01, 0.05 and 0.1 gm HA were weighted using an electric weighing machine (Precisa 1620 C) and transferred to 500 ml Erlenmeyer flasks. Tryptic Soy Broth (TSB) was prepared separately by dissolving 30 g of the media in 1 L distilled water, and about 100 ml TSB was transferred to each flask. The liquid formulations were autoclaved at 121°C for 15 minutes. After cooling at room temperature, one loopful (approximately

1 x 10^6 CFU) from UPMB10 and UPMRB9 cultures was taken and transferred into the broth media, then incubated under constant shaking at 150 rpm for 24 h at 33°C; each sample was replicated thrice. These conditions were essential so that both bacteria achieve a stationary stage of their respective growth curves at the time of their integration into the formulations. The bacterial growth population was determined by the serial dilution method 1/10 dilution series. One hundred microliters of each dilution were added to TSA Petri plates; the sample was spread evenly over the agar surface using the sterile glass spreader, and the plates were incubated in an incubator (DS-310RL, Dasol, Korea) at 33°C for 24 hours. The procedure was repeated three times for each humic acid concentration monthly for up to twelve months.

Measurements of Optical Density (OD) at Monthly Intervals for Up to 12 Months

Optical density (OD) was detected using a UV-visible spectrophotometer and checked at monthly intervals for up to 12 months. All treatments during this period were stored at room temperature at 30°C; the procedure was attempted using an 80% volume spectrophotometer cuvette. About 3.5 ml of samples were transferred from each treatment of PGPR-HA formulations (0, 0.01, 0.05, and 0.1%) and tryptic soy broth (TSB) for blank value to measure the absorbance at 600 nm wavelength. All measurements were repeated at least three times. In addition, bacterial growth trend was proposed to measure the optical density value for *B. subtilis* (UPMB10), *B. tequilensis* (UPMRB9), and mixed strains at 0, 6, 12, 18, and 24-hour periods at 30°C for 0.1% humic acid (HA) and control (without humic acid) to see the growth line trend at the 6-hour interval for 24 hours.

Endospore Stain Protocol by Using Malachite Green

According to the Schaeffer and Fulton (1933) method for staining endospores, 0.5 g of malachite green was dissolved in 100 ml of distilled water, and 2.5 g of safranin was dissolved in 100 ml of 95% ethanol. From 24 hours and 12-month-incubated cultures, endospores were detected using malachite green by the endospore staining method. The culture was spread on a slide and dried at room temperature naturally before being heat-fixed and wrapped in blotting paper. The slide was loaded with malachite green solution, which was steamed into the cells and spores using the burner's steaming light. This heating stage stained the vegetative cells and endospores; once the heating was complete, cool, rinse the dyes, and wash gently with water. Next, add safranin to the slide to colour the vegetative cells. Remove excess water, dry with a clean towel, and allow the slide to air dry. A stained smear was observed with low magnification (10X) and then switched to 100X with oil immersion. The endospores appeared green, and the vegetative cells were brownish-red or pinkish (Shen & Zhang, 2017).

Statistical Analysis

All data obtained were subjected to Analysis of Variance (ANOVA) using Statistical Analysis System (SAS) version 9.4. Means were compared by Significance Differences (LSD) at the 5% probability level. Data were subjected to ANOVA using (SAS 2004).

RESULTS AND DISCUSSION

Effect of Humic Acid Concentrations on Bacterial Population

Data presented in Figure 2 showed the bacterial population and viability in humic acid (HA) amended formulation with different strains (*B. subtilis* (UPMB10), *B. tequilensis* (UPMRB9), and mixed strain) can be enhanced by the highest concentration of HA for up to 12 months of incubation at 0.1% HA under 30°C room temperature. At 6 months of incubation, HA formulations at 0.1% and 0.05% concentrations for UPMB10, UPMRB9, and mixed strain, respectively, showed significantly highest population, then started to decline after six months of storage. While 0% HA and 0.01% HA concentration, the maximum population was recorded at 3 months of incubation by UPMB10, UPMRB9,

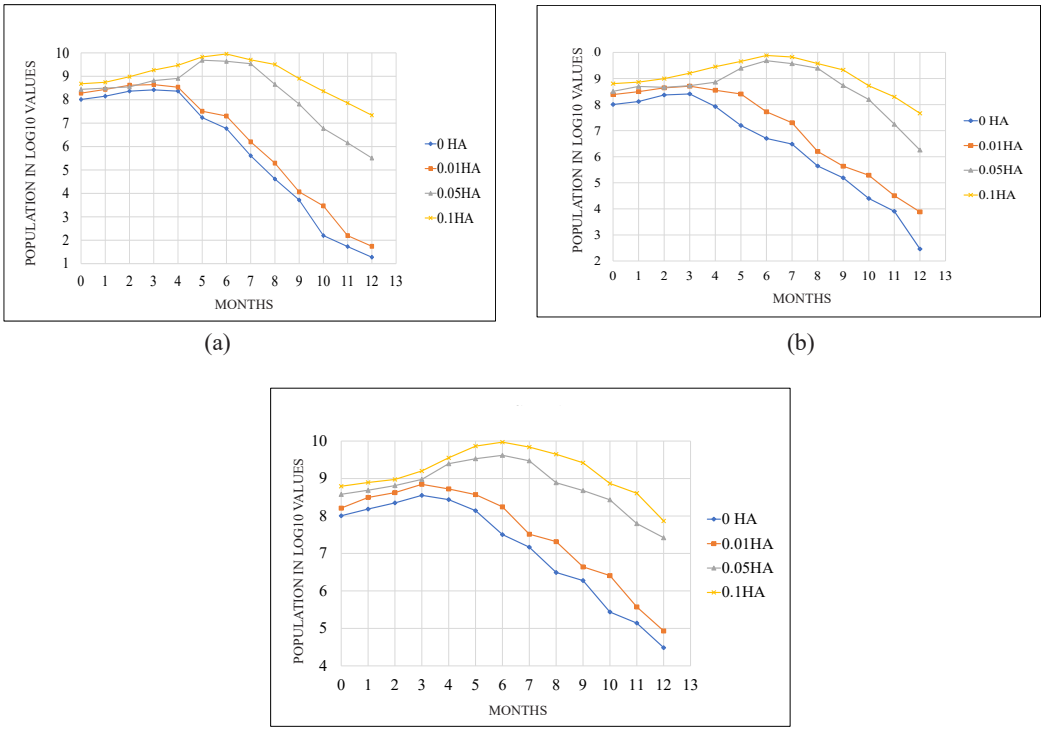

Figure 2. Effect of HA concentrations on bacterial population with three replications in (a) UPMB10, (b) UPMRB9, and (c) mixed strains for up to 12 months interval

and mixed strain, respectively, then started to decline after three months of storage. After 12 months of incubation, tryptic soy broth (TSB) amended with 0.1% of HA recorded the highest population significantly at 2.8 x10^7 CFU mL^{-1} (log 7.8) by mixed strain, followed by the UPMRB9 and UPMB10 at 1.8 x10^7 CFU mL^{-1} (log 7.6) and 8.9 x10^6 CFU mL^{-1} (log 7.3), respectively, followed by 0.05% HA compared to 0% and 0.01% HA.

Tryptic soy broth (TSB) media with humic acid as an amendment demonstrated an excellent combination as a new formulation for the bacteria shelf-life. Results showed that a higher concentration of 0.1% HA has a better shelf-life after 12 months of storage, and the bacterial strain showed excellent vitality with minimal cell loss from UPMRB9 at 1.8 x10^7, followed by UPMB10 and mixed strains at 8.9 x10^7 and 18.7 x10^5, respectively. At the same time, the lowest concentration was observed at 0% HA and 0.01%HA. A similar finding was made by Young et al. (2006), in which they reported that humic acid could enhance the viability of the encapsulated bacteria and observed minimal cell loss upon storage for five months. The steady growth of microbial activity is noticed in every treatment (bacterial formulations) due to increasing cell count and a maximum extent until its reduction.

This finding is illustrated by the time the microbial cells have adapted and grown, even if kept at temperatures other than the optimum. Since the cells are not killed by their metabolism, they can slowly take the nutrients in the formulations. Cellular activity decreases as a result of cell death if it is diminished (Mendoza-Labrador et al., 2021). We believe that one of the main reasons is that humic acids essentially offer better habitation and nutrition for beneficial bacteria, which explains why microbial communities thrive in the presence of humic acids (Li et al., 2019; Morawska et al., 2022). Many strategies have been postulated earlier to discuss the impact of humic acid on bacteria, such as changes in surface charge, chemical reactions, and steric impact caused by HA coating. Moreover, HA can also play a crucial function in altering the agglomeration of mineral particles caused by HA smears (Hong et al., 2015). Tikhonov et al. (2010) reported that the humic acid in live cells implies that it may be possible to use their energy more efficiently. ATF stores energy for cell regeneration, growth, and reproduction.

Effect of Humic Acid on Bacterial Optical Density During Shelf-Life

At monthly intervals for up to 12 months, 0.1% of humic acid (HA) significantly stimulated the optical density measurements (OD), followed by 0.05% compared to 0% and 0.01% for PGPRs shelf-life. The results show a significantly highest OD (600nm) in 0.1% HA after 12 months of incubation at (2.60) from a mixed strain followed by *B. tequilensis* (UPMRB9) and *B. subtilis* (UPMB10) at (2.46) and (2.44), respectively, followed by 0.05% HA. While 0% HA and 0.01% HA were recorded as the lowest OD readings (Figure 3).

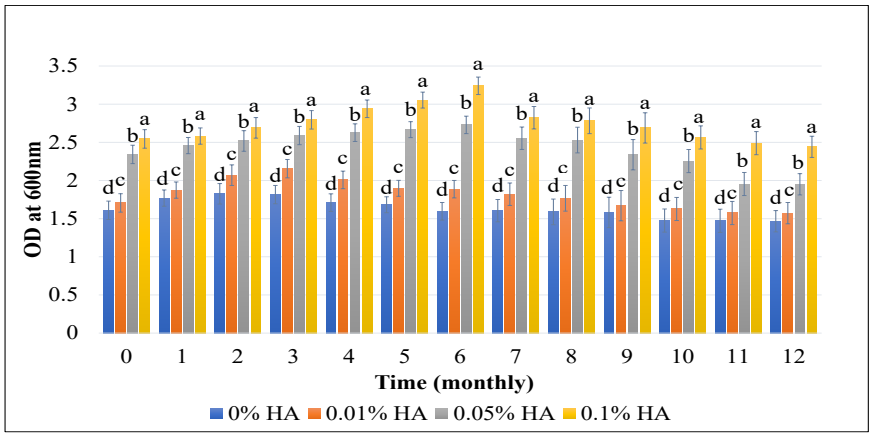

(a)

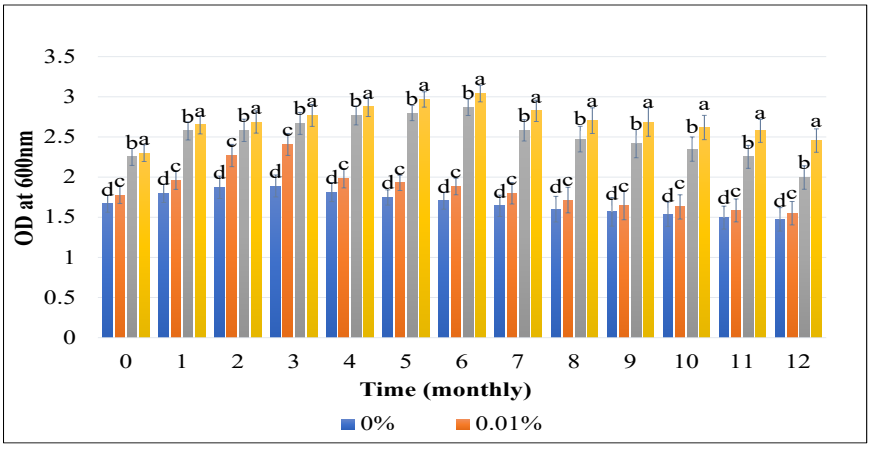

(b)

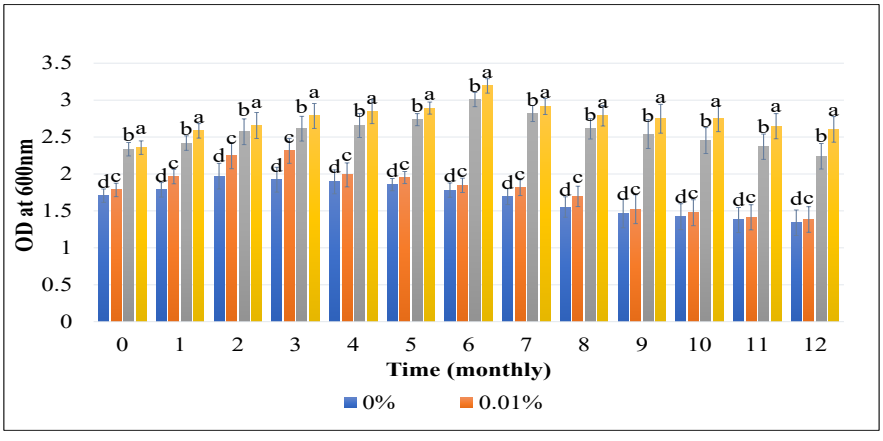

(c)

Figure 3. Optical density at 600 nm monthly intervals for 12 months of incubation in (a) UPMB10, (b) UPMRB9, and (c) mixed strain with 4 concentrations of HA and 3 replications. Means with the same letter do not significantly differ at α = 0.05 LSD.

Among all formulations, 0.1% humic acid was the best formulation for maintaining the survival of bacterial growth throughout the incubation period. After 12 months of storage and in UV-visible spectrophotometer analyses, the optical density (OD) at 600 nm has demonstrated *B. subtilis* (UPMB10), mixed strain, and *B. tequilensis* (UPMRB9) at (3.24) (3.19) and (3.04), respectively. The degradation rate depended on the time. During the first 6 months, there was an increase in bacterial growth. While from six months of storage onwards, the degradation rate of bacterial growth was slow because, in this period, the survival and development of microorganisms are affected by various variables. The inherent, intrinsic characteristics or variables are nutrient content, moisture content, pH, available oxygen, and temperature (Awulachew, 2021). Although the microbe's nutrient requirements are quite organic, the following are important: water, energy source, carbon-nitrogen supply, vitamins, and minerals. For each treatment (bacterial formulation), a progressive increase in microbial activity is noted as the number of cells increases, reaching a maximum point before decreasing (Timmis & Ramos, 2021; Bhakyaraj et al., 2022). This phenomenon is explained by the time required for microbial cells to adapt and proliferate, even when stored without agitation or at temperatures other than optimal. Since their metabolism is not disrupted, the cells continue to ingest the nutrients from the formulas, albeit at a slower rate (Arriel-Elias et al., 2018; Tapia et al., 2020). So, the degradation rate shows when the microbe's nutrient requirements start to decline.

Bacterial Growth Curves With and Without Humic Acid

Cell growth of individual bacterial strains and mixed strains was checked at 600 nm using the UV-visible spectrophotometer. An increase in optical density (OD) has been demonstrated in humic acid as an amendment. The increased bacterial growth in *Bacillus subtilis* (UPMB10), *B. tequilensis* (UPMRB9), and mixed strains with HA was gradually at the first (lag phase) at (1.83), (1.85), and (1.81) respectively, but then became drastic at12 hours on-wards at (2.74), (2.84) and (2.58), respectively. Whereas, without humic acid OD of the bacterial growth in UPMB10, UPMRB9, and the mixed strain was drastically increased from 0–6 hours of incubation and gradually became constant afterward at (1.64), (1.72) and (1.55), respectively (Figure 4). However, the final optical density (OD) was much higher than without HA. UPMB10 and UPMRB9 with and without humic acid were checked under the microscope after 24 hours of incubation, as shown in (Figures 4 & 5).

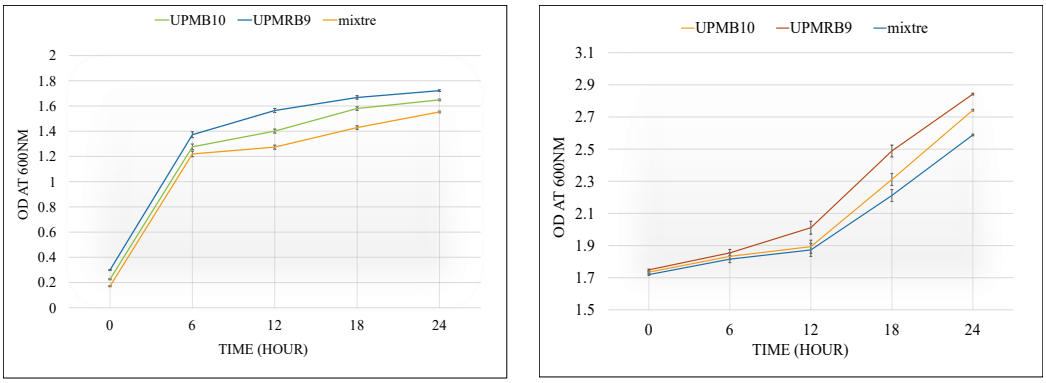

(a) (b)

Figure 4. Bacterial growth curve (a) without Humic acid, and (b) with Humic acid for 24 hours with three replicates

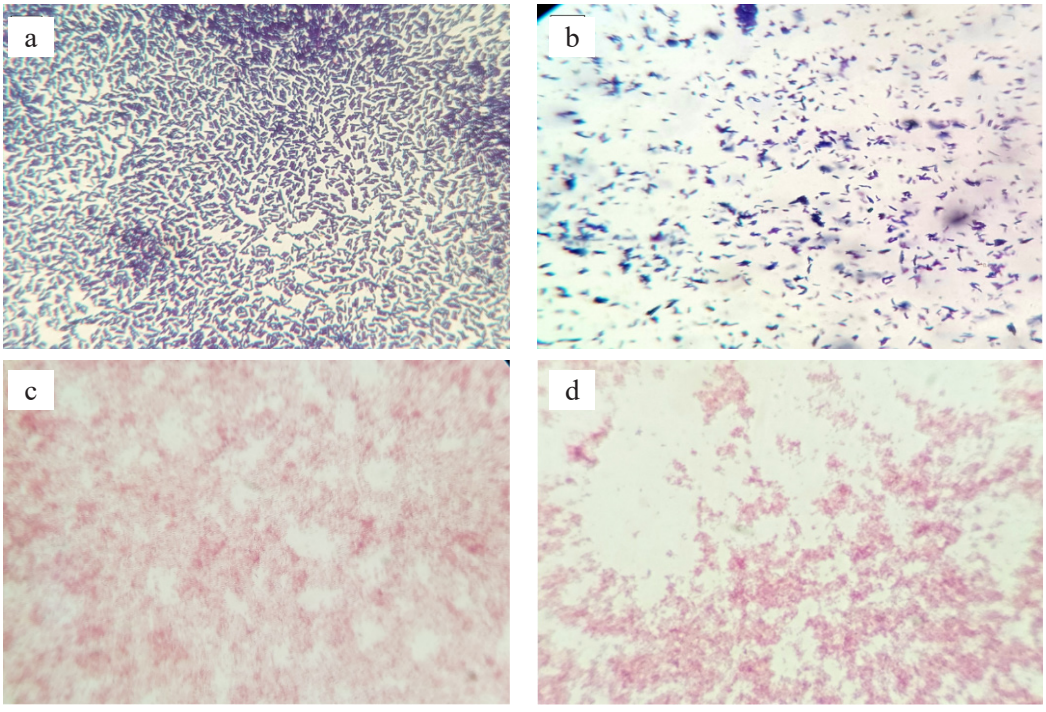

Figure 5. (a) UPMB10 with Humic acid, (b). UPMB10 without Humic acid, (c) UPMRB9 with Humic acid, and (d) UPMRB9 without Humic acid

Humic acid formulation with the concentration of 0.1% amended with tryptic soy broth (TSB) shows that the bacterial growth from *B. subtilis* (UPMB10), *B. tequilensis* (UPMRB9), and the mixed strain was significantly higher than without humic acid for 24

hours (Figure 4). The bacteria's response to HA in the medium varies, and these variances are visible even at the strain level (Tikhonov et al., 2010). The significant impact of humic acid is enhancing bacterial development, which helps to improve microbial growth by providing a carbon source. Moreover, due to its large size, humic acid serves as a food supply for microbes and a source of microflora. Vassilev et al. (2020) reported that Humic compounds had been shown to increase or decrease the populations or actions of various microbial species. In addition, *B. subtilis* encapsulated with HA ensured higher viability of the immobilized biostimulant (Nagpal et al., 2022).

Bacillus subtilis Endospores Detection After 12 Months of Shelf-Life

After 12 months of storage, *B. subtilis* species developed endospores that were detected following the Endospore staining method using malachite green. *Bacillus subtilis* (UPMB10) and mixed strains were used to detect spores. After 24 hours of incubation, results showed that UPMB10 strain, but after 12 months of incubation, there were vegetative cells with pink colour and endospores with dark green colour for both UPMB10 and mixed strain as shown in Figure 6.

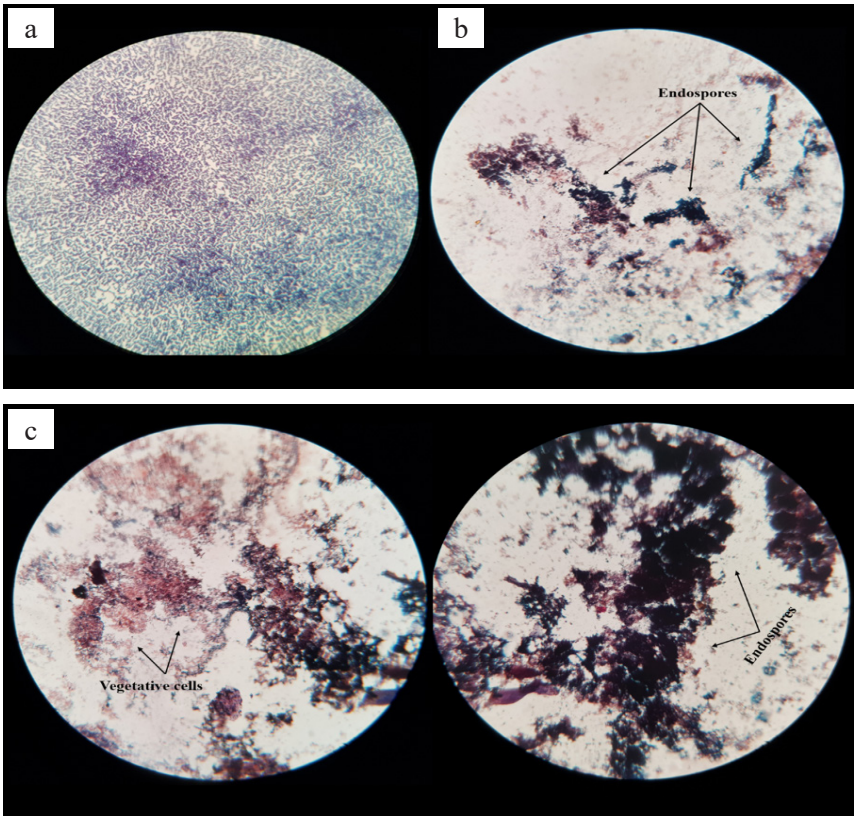

Figure 6. Spores' detection from *Bacillus subtilis* (UPMB10). (a) After 24 hours, (b) 12 months of storage, and (c) mixed strain after 12 months of storage

Endospore stain allows the bacterium to be dormant and highly resistant cells to preserve the cell genetic material during extreme stress. Endospores can survive environmental assaults that normally kill bacteria (Wrangham, 2019). When examined under a microscope, the results of endospore staining in both *B. subtilis* (UPMB10) and the mixed strains of bacteria reveal a dark green colour, indicating the presence of endospores. An endospore is a structure that can withstand harsh environmental conditions such as dryness, heat, and acidity (Rattray et al., 2021; Silaban et al., 2020). Endospores are extremely thick and refractile due to their low water content (Tehri et al., 2018). Bacteria with endospores are extremely difficult to colour, necessitating specialized staining. Spore-producing bacteria are stain-resistant. Bacteria that produce spores will significantly bind to the dye component malachite green. Moreover, it cannot be stained using safranin (Silaban et al., 2020). Połaska et al. (2021) found that the genus Alicyclobacillus contains a group of Gram-positive producing highly resistant endospores during unfavourable environmental conditions.

According to these findings, humic acid could support the combination of two different PGPR strains by demonstrating greater overall biocontrol and plant growth promotion compared to the individual PGPR strains. Microbes in a senescent stage appear to continue some metabolic activity to preserve viability and protect against stress conditions (Haruta et al., 2015; Dehsheikh et al., 2020; Pota et al., 2020). The response of the bacteria to the presence of HA in the medium is various, and these differences are manifested even at the level of the strains. Thus, the capability for the growth of humic acids is widespread among bacteria. It was shown for the first time that the mixed bacteria were compatible with the addition of HA, which provides additional evidence for symbiotic growth between the bacteria strains for a long period (Tikhonov et al., 2010; Lipczynska-Kochany, 2018).

CONCLUSION

In conclusion, as an amendment with an optimum concentration of 0.1% HA, humic acid significantly increased bacterial growth population and the optical density at monthly intervals for up to 12 months of incubation compared to 0% HA. A higher concentration of humic acid has a better shelf-life. The bacterial strain population showed excellent vitality with minimal cell loss. That may relate because humic acids can provide shelter and carbon sources for bacteria. Survival and development of microorganisms in the liquid formulation are affected by various variables: nutrient content, moisture content, pH, available oxygen, and temperature. Thus, the optimum concentration of humic acid can be used to prolong the bacteria's shelf-life and improve the quality of a biofertilizer. In this regard, the use of humic acid as an amendment for PGPR shelf-life in this study provided various advantages over the existing enrichment chemicals, demonstrating the grounds for the current investigation.

ACKNOWLEDGEMENTS

The authors sincerely acknowledge grants of the Fundamental Research Grant Scheme (FRGS) (FRGS/1/2020/STG01/UPM/02/6) by the Ministry of Higher Education, Malaysia.

REFERENCES

Al Hamad, B. M., Al Raish, S. M., Ramadan, G. A., Saeed, E. E., Alameri, S. S., Al Senaani, S. S., AbuQamar, S. F., & El-Tarabily, K. A. (2021). Effectiveness of augmentative biological control of Streptomyces griseorubens UAE2 depends on 1-aminocyclopropane-1-carboxylic acid deaminase activity against *Neoscytalidium dimidiatum*. *Journal of Fungi*, *7*(11), Article 885. https://doi.org/10.3390/jof7110885

Al Raish, S. M., Saeed, E. E., Alyafei, D. M., El-Tarabily, K. A., & AbuQamar, S. F. (2021). Evaluation of streptomycete actinobacterial isolates as biocontrol agents against royal poinciana stem canker disease caused by the fungal pathogen *Neoscytalidium dimidiatum*. *Biological Control*, *164*, Article 104783. https://doi.org/10.1016/j.biocontrol.2021.104783

Alblooshi, A. A., Purayil, G. P., Saeed, E. E., Ramadan, G. A., Tariq, S., Altaee, A. S., El-Tarabily, K. A., & AbuQamar, S. F. (2021). Biocontrol potential of endophytic actinobacteria against Fusarium solani, the causal agent of sudden decline syndrome on date palm in the UAE. *Journal of Fungi*, *8*(1), Article 8. https://doi.org/10.3390/jof8010008

Ali-Tan, K. Z., Radziah, O., Halimi, M. S., Rahim, K. B. A., Abdullah, M. Z., & Shamsuddin, Z. H. (2017). Growth and yield responses of rice cv. MR219 to rhizobial and plant growth-promoting rhizobacterial inoculations under different fertilizer-N rates. *Bangladesh Journal of Botany, 46*(1), 481-488.

Arriel-Elias, M. T., Oliveira, M. I., Silva-Lobo, V. L., Filippi, M. C. C., Babana, A. H., Conceição, E. C., & Cortes, M. D. C. (2018). Shelf-life enhancement of plant growth promoting rhizobacteria using a simple formulation screening method. *African Journal of Microbiology Research, 12*(5), 115-126. https://doi.org/10.5897/AJMR2017.8787

Awulachew, M. T. (2021). Food product shelf stability overview of sourdough-risen flatbread. *Journal of Food Technology & Nutrition Sciences, 3*(3), 1-3. https://doi.org/10.47363/JFTNS/2021(3)123

Berninger, T., González López, Ó., Bejarano, A., Preininger, C., & Sessitsch, A. (2018). Maintenance and assessment of cell viability in formulation of non-sporulating bacterial inoculants. *Microbial Biotechnology, 11*(2), 277-301. https://doi.org/10.1111/1751-7915.12880

Bhakyaraj, R., Arunkumar, D., & Anitha, A. (Eds.). (2022). *Synthetic Microbial Research-Challenge and Prospects.* Darshan Publishers.

Calvo, P., Zebelo, S., McNear, D., Kloepper, J., & Fadamiro, H. (2019). Plant growth-promoting rhizobacteria induce changes in Arabidopsis thaliana gene expression of nitrate and ammonium uptake genes. *Journal of Plant Interactions, 14*(1), 224-231. https://doi.org/10.1080/17429145.2019.1602887

Cho, W. I., & Chung, M. S. (2020). *Bacillus* spores: A review of their properties and inactivation processing technologies. *Food Science and Biotechnology, 29*(11), 1447-1461. https://doi.org/10.1007/s10068-020-00809-4

Dehsheikh, A. B., Sourestani, M. M., Zolfaghari, M., & Enayatizamir, N. (2020). Changes in soil microbial activity, essential oil quantity, and quality of Thai basil as response to biofertilizers and humic acid. *Journal of Cleaner Production*, *256*, Article 120439. https://doi.org/10.1016/j.jclepro.2020.120439

Durga, C. S. S., Ruben, N., Chand, M. S. R., Indira, M., & Venkatesh, C. (2021). Comprehensive microbiological studies on screening bacteria for self-healing concrete. *Materialia*, *15*, Article 101051. https://doi.org/10.1016/j.mtla.2021.101051

Ekin, Z. (2019). Integrated use of humic acid and plant growth promoting rhizobacteria to ensure higher potato productivity in sustainable agriculture. *Sustainability, 11*(12), Article 3417. https://doi.org/10.3390/su11123417

El-Ghamry, A., Mosa, A. A., Alshaal, T., & El-Ramady, H. (2018). Nanofertilizers vs. biofertilizers: New insights. *Environment, Biodiversity and Soil Security, 2*(2018), 51-72. https://doi.org/10.21608/jenvbs.2018.3880.1029

El-Tarabily, K. A., AlKhajeh, A. S., Ayyash, M. M., Alnuaimi, L. H., Sham, A., ElBaghdady, K. Z., Tariq, S., & AbuQamar, S. F. (2019). Growth promotion of *Salicornia bigelovii* by *Micromonospora chalcea* UAE1, an endophytic 1-aminocyclopropane-1-carboxylic acid deaminase-producing actinobacterial isolate. *Frontiers in Microbiology*, *10*, Article 1694. https://doi.org/10.3389/fmicb.2019.01694

El-Tarabily, K. A., ElBaghdady, K. Z., AlKhajeh, A. S., Ayyash, M. M., Aljneibi, R. S., El-Keblawy, A., & AbuQamar, S. F. (2020). Polyamine-producing actinobacteria enhance biomass production and seed yield in Salicornia bigelovii. *Biology and Fertility of Soils*, *56*(4), 499-519. https://doi.org/10.1007/s00374-020-01450-3

El-Tarabily, K. A., Ramadan, G. A., Elbadawi, A. A., Hassan, A. H., Tariq, S., Ghazal, E. W., Gamar, M. I. A., & AbuQamar, S. F. (2021). The marine endophytic polyamine-producing Streptomyces mutabilis UAE1 isolated from extreme niches in the Arabian Gulf promotes the performance of mangrove (*Avicennia marina*) seedlings under greenhouse conditions. *Frontiers in Marine Science*, *8*, Article 710200. https://doi.org/10.3389/fmars.2021.710200

Haruta, S., & Kanno, N. (2015). Survivability of microbes in natural environments and their ecological impacts. *Microbes and Environments*, *30*(2), 123-125. https://doi.org/10.1264/jsme2.ME3002rh

Hong, Z., Chen, W., Rong, X., Cai, P., Tan, W., & Huang, Q. (2015). Effects of humic acid on adhesion of *Bacillus subtilis* to phyllosilicates and goethite. *Chemical Geology*, *416*, 19-27. https://doi.org/10.1016/j.chemgeo.2015.10.017

Itelima, J. U., Bang, W. J., Onyimba, I. A., Sila, M. D., & Egbere, O. J. (2018). Bio-fertilizers as key player in enhancing soil fertility and crop productivity: A review. *Direct Research Journal of Agriculture and Food Science, 6*(3), 73-83.

Kamil, F. H., Saeed, E. E., El-Tarabily, K. A., & AbuQamar, S. F. (2018). Biological control of mango dieback disease caused by *Lasiodiplodia theobromae* using streptomycete and non-streptomycete actinobacteria in the United Arab Emirates. *Frontiers in Microbiology*, *9*, Article 829. https://doi.org/10.3389/fmicb.2018.00829

Kapadia, C., Sayyed, R. Z., El Enshasy, H. A., Vaidya, H., Sharma, D., Patel, N., Abd malek, R., Syed, A., Elgorban, A.M., Ahmad, K., & Zuan, A. T. K. (2021). Halotolerant microbial consortia for sustainable

mitigation of salinity stress, growth promotion, and mineral uptake in tomato plants and soil nutrient enrichment. *Sustainability, 13*(15), Article 8369. https://doi.org/10.3390/su13158369

Lahlali, R., Ezrari, S., Radouane, N., Kenfaoui, J., Esmaeel, Q., El Hamss, H., Belabess, Z., & Barka, E. A. (2022). Biological control of plant pathogens: A global perspective. *Microorganisms 2022, 10*(3), Article 596. https://doi.org/10.3390/microorganisms10030596

Li, X., Liu, H., Yang, W., Sheng, H., Wang, F., Harindintwali, J. D., Herath, H. M. S. K., & Zhang, Y. (2022). Humic acid enhanced pyrene degradation by Mycobacterium sp. NJS-1. *Chemosphere*, *288*(Part 3), Article 132613. https://doi.org/10.1016/j.chemosphere.2021.132613

Li, Y., Fang, F., Wei, J., Wu, X., Cui, R., Li, G., Zheng, F., & Tan, D. (2019). Humic acid fertilizer improved soil properties and soil microbial diversity of continuous cropping peanut: A three-year experiment. *Scientific Reports, 9*(1), Article 12014. https://doi.org/10.1038/s41598-019-48620-4

Lindsay, D., Robertson, R., Fraser, R., Engstrom, S., & Jordan, K. (2021). Heat induced inactivation of microorganisms in milk and dairy products. *International Dairy Journal*, *121*, Article 105096. https://doi.org/10.1016/j.idairyj.2021.105096

Lipczynska-Kochany, E. (2018). Humic substances, their microbial interactions and effects on biological transformations of organic pollutants in water and soil: A review. *Chemosphere*, *202*, 420-437. https://doi.org/10.1016/j.chemosphere.2018.03.104

Liu, K., McInroy, J. A., Hu, C. H., & Kloepper, J. W. (2018). Mixtures of plant-growth-promoting rhizobacteria enhance biological control of multiple plant diseases and plant-growth promotion in the presence of pathogens. *Plant Disease*, *102*(1), 67-72. https://doi.org/10.1094/PDIS-04-17-0478-RE

Luu, J., Mott, C. M., Schreiber, O. R., Giovinco, H. M., Betchen, M., & Carabetta, V. J. (2022). Nε-Lysine acetylation of the histone-like protein HBsu regulates the process of sporulation and affects the resistance properties of *Bacillus subtilis* spores. *Frontiers in Microbiology*, *12,* Article 782815. https://doi.org/10.3389/fmicb.2021.782815

Mahalakshmi, S., Vijayapriya, M., & Pandeeswari, N. (2019). Studies on developing PGPR consortium with improved shelf life. *Journal of Pharmacognosy Phytochemistry, 8*(2S), 545-548.

Mahapatra, S., Yadav, R., & Ramakrishna, W. (2022). *Bacillus subtilis* impact on plant growth, soil health and environment: Dr. Jekyll and Mr. Hyde. *Journal of Applied Microbiology*, *132*(5), 3543-3562. https://doi.org/10.1111/jam.15480

Mathew, B. T., Torky, Y., Amin, A., Mourad, A. H. I., Ayyash, M. M., El-Keblawy, A., Hilal-Alnaqbi, A., AbuQamar, S. F., & El-Tarabily, K. A. (2020). Halotolerant marine rhizosphere-competent actinobacteria promote *Salicornia bigelovii* growth and seed production using seawater irrigation. *Frontiers in Microbiology*, *11*, Article 552. https://doi.org/10.3389/fmicb.2020.00552

Mendoza-Labrador, J., Romero-Perdomo, F., Abril, J., Hernández, J. P., Uribe-Vélez, D., & Buitrago, R. B. (2021). Bacillus strains immobilized in alginate macrobeads enhance drought stress adaptation of guinea grass. *Rhizosphere*, *19*, Article 100385. https://doi.org/10.1016/j.rhisph.2021.100385

Meng, F., Huang, Q., Yuan, G., Cai, Y., & Han, F. X. (2021). The beneficial applications of humic substances in agriculture and soil environments. In *New Trends in Removal of Heavy Metals from Industrial Wastewater* (pp. 131-160). Elsevier. https://doi.org/10.1016/B978-0-12-822965-1.00007-6

Morawska, L. P., Hernandez-Valdes, J. A., & Kuipers, O. P. (2022). Diversity of bet-hedging strategies in microbial communities-Recent cases and insights. *WIREs Mechanisms of Disease, 14*(2), Article e1544. https://doi.org/10.1002/wsbm.1544

Mukherjee, S., Pandey, V., Parvez, A., Qi, X., & Hussain, T. (2022). Bacillus as a Versatile Tool for Crop Improvement and Agro-Industry. In M. T. Islam, M. Rahman & P. Pandey (Eds.), *Bacilli in Agrobiotechnology* (pp. 429-452). Springer. https://doi.org/10.1007/978-3-030-85465-2_19

Nagpal, S., Kumawat, K. C., & Sharma, P. (2022). Insights into novel cell immobilized microbial inoculants. In *New and Future Developments in Microbial Biotechnology and Bioengineering* (pp. 289-318). Elsevier. https://doi.org/10.1016/B978-0-323-85577-8.00001-9

Nardi, S., Schiavon, M., & Francioso, O. (2021). Chemical structure and biological activity of humic substances define their role as plant growth promoters. *Molecules, 26*(8), Article 2256. https://doi.org/10.3390/molecules26082256

Pashang, R., Ronan, E., Kroukamp, O., Korber, D. R., Laursen, A. E., Wenk, J., & Wolfaardt, G. M. (2022). Huddling together to survive: Population density as a survival strategy of non-spore forming bacteria under nutrient starvation and desiccation at solid-air interfaces. *Microbiological Research*, *258*, Article 126997. https://doi.org/10.1016/j.micres.2022.126997

Połaska, M., Dekowska, A., & Sokolowska, B. (2021). Isolation and identification of guaiacol producing *Alicyclobacillus fastidiosus* strains from orchards in Poland. *Acta Biochimica Polonica, 68*(2), 301-307. https://doi.org/10.18388/abp.2020_5574

Pota, G., Venezia, V., Vitiello, G., Di Donato, P., Mollo, V., Costantini, A., Avossa, J., Nuzzo, A., Piccolo, A., Silvestri, B., & Luciani, G. (2020). Tuning functional behavior of humic acids through interactions with stöber silica nanoparticles. *Polymers*, *12*(4), Article 982. https://doi.org/10.3390/polym12040982

Pukalchik, M., Kydralieva, K., Yakimenko, O., Fedoseeva, E., & Terekhova, V. (2019). Outlining the potential role of humic products in modifying biological properties of the soil-A review. *Frontiers in Environmental Science*, *7*, Article 80. https://doi.org/10.3389/fenvs.2019.00080

Rashad, M., Hafez, M., & Popov, A. I. (2022). Humic substances composition and properties as an environmentally sustainable system: A review and way forward to soil conservation. *Journal of Plant Nutrition*, *45*(7), 1072-1122. https://doi.org/10.1080/01904167.2021.2005801

Rattray, J. E., Chakraborty, A., Li, C., Elizondo, G., John, N., Wong, M., Radovic, J. R., Oldenburg, T. B. P., & Hubert, C. R. (2021). Sensitive quantification of dipicolinic acid from bacterial endospores in soils and sediments. *Environmental Microbiology*, *23*(3), 1397-1406. https://doi.org/10.1111/1462-2920.15343

Rizvi, A., Ahmed, B., Khan, M. S., El-Beltagi, H. S., Umar, S., & Lee, J. (2022). Bioprospecting plant growth promoting rhizobacteria for enhancing the biological properties and phytochemical composition of medicinally important crops. *Molecules*, *27*(4), Article 1407. https://doi.org/10.3390/molecules27041407

Saeed, E. E., Sham, A., Salmin, Z., Abdelmowla, Y., Iratni, R., El-Tarabily, K., & AbuQamar, S. (2017). *Streptomyces globosus* UAE1, a potential effective biocontrol agent for black scorch disease in date palm plantations. *Frontiers in Microbiology*, *8*, Article 1455. https://doi.org/10.3389/fmicb.2017.01455

Schaeffer, A. B., & Fulton, M. D. (1933). A simplified method of staining endospores. *Science*, *77*(1990), 194-194.

Shen, C., & Zhang, Y. (2017). Staining technology and bright-field microscope use. In *Food microbiology laboratory for the food science student* (pp. 9-14). Springer. https://doi.org/10.1007/978-3-319-58371-6_2

Shultana, R., Kee Zuan, A. T., Yusop, M. R., & Saud, H. M. (2020). Characterization of salt-tolerant plant growth-promoting rhizobacteria and the effect on growth and yield of saline-affected rice. *PLoS One*, *15*(9), Article e0238537. https://doi.org/10.1371/journal.pone.0238537

Shultana, R., Kee Zuan, A. T., Yusop, M. R., Saud, H. M., & El-Shehawi, A. M. (2021). *Bacillus tequilensis* strain 'UPMRB9'improves biochemical attributes and nutrient accumulation in different rice varieties under salinity stress. *Plos One*, *16*(12), Article e0260869. https://doi.org/10.1371/journal.pone.0260869

Silaban, S., Marika, D. B., & Simorangkir, M. (2020). Isolation and characterization of amylase-producing amylolytic bacteria from rice soil samples. *Journal of Physics: Conference Series, 1485*(1), Article 012006. https://doi.org/10.1088/1742-6596/1485/1/012006

Sootahar, M. K., Zeng, X., Wang, Y., Su, S., Soothar, P., Bai, L., Kumar, M., Zhang, Y., Mustafa, A., & Ye, N. (2020). The short-term effects of mineral-and plant-derived fulvic acids on some selected soil properties: improvement in the growth, yield, and mineral nutritional status of wheat (*Triticum aestivum L.*) under soils of contrasting textures. *Plants, 9*(2), Article 205. https://doi.org/10.3390/plants9020205

Stevenson, I. L., & Schnitzer, M. (1982). Transmission electron microscopy of extracted fulvic and humic ACIDS1. *Soil Science*, *133*(3), 179-185.

Sun, S., Abdellah, Y. A. Y., Miao, L., Wu, B., Ma, T., Wang, Y., Zang, H., Zhao, X., & Li, C. (2022). Impact of microbial inoculants combined with humic acid on the fate of estrogens during pig manure composting under low-temperature conditions. *Journal of Hazardous Materials*, *424*(Part D), Article 127713. https://doi.org/10.1016/j.jhazmat.2021.127713

Tapia, M. S., Alzamora, S. M., & Chirife, J. (2020). Effects of water activity (a_w) on microbial stability: As a hurdle in food preservation. In G. V. Barbosa-Canovas, A. J. Fontana Jr., S. J. Schmidt & T. P. Labuza (Eds.), *Water Activity in Foods: Fundamentals and Applications* (pp. 323-355). Wiley. http://dx.doi.org/10.1002/9780470376454.ch10

Tehri, N., Kumar, N., Raghu, H. V., & Vashishth, A. (2018). Biomarkers of bacterial spore germination. *Annals of Microbiology, 68*, 513-523. https://doi.org/10.1007/s13213-018-1361-z

Tikhonov, V. V., Yakushev, A. V., Zavgorodnyaya, Y. A., Byzov, B. A., & Demin, V. V. (2010). Effects of humic acids on the growth of bacteria. *Eurasian Soil Science, 43*(3), 305-313. https://doi.org/10.1134/S1064229310030087

Timmis, K., & Ramos, J. L. (2021). The soil crisis: The need to treat as a global health problem and the pivotal role of microbes in prophylaxis and therapy. *Microbial Biotechnology*, *14*(3), 769-797. https://doi.org/10.1111/1751-7915.13771

Vassilev, N., Vassileva, M., Martos, V., Garcia del Moral, L. F., Kowalska, J., Tylkowski, B., & Malusá, E. (2020). Formulation of microbial inoculants by encapsulation in natural polysaccharides: focus on beneficial properties of carrier additives and derivatives. *Frontiers in Plant Science*, *11*, Article 270. https://doi.org/10.3389/fpls.2020.00270

Wrangham, J. B. (2019, March 24). *Endospore production in response to microbiocides in the microbiologically influenced corrosion implicated genus clostridium*. Paper presented at the CORROSION 2019, Nashville, Tennessee, USA.

Yang, F., Tang, C., & Antonietti, M. (2021). Natural and artificial humic substances to manage minerals, ions, water, and soil microorganisms. *Chemical Society Reviews, 50*(10), 6221-6239. https://doi.org/10.1039/d0cs01363c

Young, C. C., Rekha, P. D., Lai, W. A., & Arun, A. B. (2006). Encapsulation of plant growth-promoting bacteria in alginate beads enriched with humic acid. *Biotechnology and Bioengineering*, *95*(1), 76-83. https://doi.org/10.1002/bit.20957

Zvinavashe, A. T., Mardad, I., Mhada, M., Kouisni, L., & Marelli, B. (2021). Engineering the plant microenvironment to facilitate plant-growth-promoting microbe association. *Journal of Agricultural and Food Chemistry*, *69*(45), 13270-13285. https://doi.org/10.1021/acs.jafc.1c00138

Pertanika J. Sci. & Technol. 31 (3): 1157 - 1172 (2023)

PERTANIKA JOURNALS

SCIENCE & TECHNOLOGY

Journal homepage: http://www.pertanika.upm.edu.my/

Effects of Density Variation on the Physical and Mechanical Properties of Empty Fruit Bunch Cement Board (EFBCB)

Mohammad Nasrullah Ridzuan, Hasniza Abu Bakar*, Emedya Murniwaty Samsudin, Nik Mohd Zaini Nik Soh and Lokman Hakim Ismail

Faculty of Civil Engineering and Built Environment, Universiti Tun Hussein Onn Malaysia, 86400 UTHM, Parit Raja, Batu Pahat, Johor Darul Takzim, Malaysia

ABSTRACT

A cement board is a composite material mostly comprised natural fibre and cement. Cement board is mainly used in roofing, raised floors, dropped ceilings, prefabricated structures, office containers, and other building components. Fibres in cement composites from discarded palm oil fruit bunches have been used to increase the quality of construction materials. Therefore, the impact density of the natural fibre cement board is essential to enhance the physical and mechanical properties. However, research on untreated fibre at various densities has not been compressively discussed in previous studies. Therefore, this research used empty fruit bunch (EFB) fibre in manufacturing empty fruit bunch cement boards (EFBCB) with a cement-to-fibre ratio of 3:1 and thickness of 12 mm. Three target density variations, 1100 kg/m^3, 1200 kg/m^3 and 1300 kg/m^3, were applied in this study to obtain their effect on physical and mechanical properties. The results revealed EFBCB sample with a target density of 1300 kg/m^3 showed the most promising results. This sample's average thickness is 12.38 mm after a 28-day curing period. Besides, at 1300 kg/m^3 target density, EFBCB achieved the lowest thickness swelling (TS) value at 1.82%, highest internal bonding (IB) at 0.164 N/mm^2, highest modulus of elasticity (MOE) and modulus of rupture (MOR) at 1398 N/mm^2 and 3.51 N/mm^2, respectively. Thus, increasing the cement board density and improving the physical and mechanical properties of EFBCB. This study demonstrates that EFB has the capacity to be one of the potential natural fibres for green building materials.

Keywords: Empty fruit bunch (EFB), empty fruit bunch cement boards (EFBCB), mechanical properties, physical properties, variation density

ARTICLE INFO

Article history:
Received: 05 June 2022
Accepted: 16 August 2022
Published: 31 March 2023

DOI: https://doi.org/10.47836/pjst.31.3.02

E-mail addresess:
muhammadnasrullah87@gmail.com (Muhammad Nasrullah Ridzuan)
hasniza@uthm.edu.my (Hasniza Abu Bakar)
emedya@uthm.edu.my (Emedya Murniwaty Samsudin)
nikzaini@uthm.edu.my (Nik Mohd Zaini Nik Soh)
lokman@uthm.edu.my (Lokman Hakim Ismail)
*Corresponding author

ISSN: 0128-7680
e-ISSN: 2231-8526

© Universiti Putra Malaysia Press

INTRODUCTION

Oil palm, by its scientific name, *Elaeis guineensis*, has become one of the most important commodities in Malaysia (Olusegun et al., 2012). Concurrently, the palm oil industry that forms the economic backbone of Malaysia also contributes to a large amount of solid waste in landfills. According to the Malaysian Palm Oil Industry (MPOB), oil palm production in Malaysia has increased over the years, from 4.1 million tonnes in 1985 to 6.1 million tonnes in 1990 to 27.8 million tonnes in 2019. However, 2020 was a challenging year for the MPOB due to the global outbreak of the COVID-19 pandemic. The industry experienced a temporary slowdown in the first half of 2020 in export demand and prices. Still, towards the second half, the scenario changed due to the re-opening of the global economic sectors with the relaxation of movement restrictions (MCO) coupled with the government's initiative under the National Economic Recovery Plan (PENJANA). Data from the Department of Statistics, MPOB (2020), the total export of palm oil in 2020 amounted to 26.7 million tonnes, lower by 4.1% than the 27.9 million tonnes exported in 2019. It is due to lower demand caused by the COVID-19 pandemic. It shows that oil palm production is still in demand yearly, even during the COVID-19 pandemic.

Along with technological development, natural fibres such as palm oil fibre have become the most valuable crop. This natural fibre composite is a cost-effective, sustainable material with low energy consumption and is environmentally friendly (Samsudin et al., 2016; Peter et al., 2020). Thus, further developments for a long-term strategy are needed for natural fibre potential as a material in structural and non-structural applications (Akasah et al., 2019). Natural fibres are typically incorporated into the cement matrix in discrete or discontinuous forms. The primary function of these fibres is to reinforce, that is, to increase tensile strength and prevent the matrix from cracking (Amel et al., 2017). Thus, transforming these wastes into cement-bonded particle boards has been found to be effective in wood waste management and producing eco-friendly development materials (Egbewole, 2017; Ogunjobi et al., 2019). Typically, due to its flexibility, such as resistance to decay and fire, good dimension stability, good insulation properties, availability, lightweight, low cost, zero-carbon footprint, toughness, biodegradability, non-toxicity to the ecosystem, thermal insulation, improved acoustic insulation and high recyclability (Momoh & Osofero, 2020; Ajayi & Badejo, 2005; Papadopoulos et al., 2006).

Cement-bonded composites have come in various forms, including cement-bonded fibreboards and particleboards. The product is easily obtained because it comes from multiple sources and is thoroughly optimised access. According to Lin (2009), empty fruit bunch (EFB) waste is mainly used as plantation fertiliser. EFB fibre may also be used as insulation, a wall divider, medium-density fibreboard, or in housing applications.

Based on Coutts's (2005) review, a study by James Hardy stated that fibre cement boards were formerly manufactured from asbestos. According to Ogonjabi et al. (2019),

asbestos fibres were previously commonly used in construction because of their low cost, relatively strong chemical, physical, and mechanical durability, and long and readily manipulated fibre. Asbestos has been utilised in sheeting/cladding, roofing, thermal and electrical insulation, moulded fittings, water cisterns, rainwater gutters, coatings, and other goods (Coutts, 2005). However, due to health and environmental concerns, efforts have been directed toward sourcing environmentally friendly and socially acceptable alternative materials. To address the issues, wood and other non-wood materials in the form of fibres or particles have been widely used with cement matrices to produce various construction materials (Asasutjarit et al., 2009; Garcez et al., 2016). The major benefit of cement boards is that they do not swell or curl when wet due to their superior drying characteristics (Akinyemi & Osasona, 2017). It is also commonly utilised in construction since it has a longer lifespan than paper-lined gypsum products and will not mould or physically degrade due to moisture or leaks. Cement boards also have the drawback of weighing in square meters and being more expensive than paper-based gypsum due to their long-term impacts (Azni et al., 2015).

Previous research concentrated more on using EFB as building materials in the form of medium-density boards and insulator boards (Khalil et al., 2010; Ibrahim, 2014) and EFB in concrete (Mayowa & Chinwuba, 2013). Furthermore, Onuorah et al. (2015) have previously researched EFB cement board, to which they have found that the mean value for MOR (3.08-16.82 MPa), MOE (2515–5291 MPa), IB (0.28–0.75 MPa) and TS (1.36–4.23%). While Peter et al. (2020) also resulted in the finding ranges in modulus of rupture (MOR) of 3.98–9.11 MPa, modulus of elasticity (MOE) of 1056–4699 MPa, internal bonding (IB) of 0.28–0.53 MPa and thickness swelling (TS) of 1.66–9.25%. Therefore, from the standpoint of mechanical and physical properties, EFB fibre also has good potential as a reinforcement of wood-based material replacement for cement board production. Based on prior research, natural fibres such as EFB fibre have been identified as an alternative material that can replace asbestos. The characteristics of EFB, which have poor thermal conductivity and superior thermal insulation, have also been devised to manufacture high-strength materials, making them appropriate for use as reinforcing materials for cement boards (Azni et al., 2015).

The more immense fibre content in cement mixtures will impact the characteristics of the cement products. This paper attempts to investigate and determine the optimal density of fibre that might contribute to the best possible performance of the finished product. Presumably, aside from studied attempts to construct empty fruit bunch cement boards (EFBCB), there are extremely few and challenging to locate published research concerning the influence of varied fibre density on the EFBCB characteristics. Hence, this study aimed to see if using a high proportion of oil palm EFB fibres might improve the cement board characteristics.

MATERIALS AND METHODS

Material Preparations

The raw material for this study was oil palm EFB obtained from Pamol Kluang Palm Oil Mill, Kluang, Malaysia. All preparation and production works of EFBCB were carried out at the Timber Fabrication Laboratory and Construction Engineering Laboratory, Faculty of Civil Engineering and Built Environment, Universiti Tun Hussein Onn Malaysia. Figure 1 shows the condition of the fibre from the source point and after being processed. It was sun-dried after transporting the raw EFB from the mill for 2 to 3 days, depending on the weather conditions to reduce the excessive moisture. The dried EFB was cut to shorter fibre using the shredder and turned into finer fibre size using the hammer mill machine. Finally, the sieving process was conducted duct using sieve equipment to remove dusk fibres. Raw EFB needed to undergo these processes due to its original conditions, which might cause difficulties in establishing good bonding between the fibre and the cement during fabrication.

Figure 1. Preparation of fibre from raw to processed fibre

Sample Preparation

The fabrication of EFBCB composites uses a mixture of portland cement, water, and EFB fibre. In this study, the density of the samples varied between 1100–1300 kg/m^3 (Asasutjarit et al., 2007). The samples were made in different densities to test the cement board's performance. Nine samples with dimensions of 350 mm x 350 mm x 12 mm with the target density of 1100 kg/m^3, 1200 kg/m^3, and 1300 kg/m^3 were manufactured using the

same cement-to-fibre ratio (3:1). EFB fibre water and cement are the materials that require for the sample fabrication need to weight before the mix. The total weight of the materials is determined by the ratio 3:1, which represents cement to fibre content. This ratio is used due to promising results of bending strength (MOR) obtained by Owoyemi et al. (2020) and Ogunjobi et al. (2019). Based on research by Akasah et al. (2019) and Onuorah et al. (2015), targeted density is achieved by maintaining the same total weight of the materials used in the mixture. The targeted density can be achieved using a calculation based on the weight of the sample divided by the volume. According to BS EN 323 (1993), the minimum density of a cement board should be equal to or greater than 1000 kg/m^3. The three densities of samples are differentiated by the total weight of the mixture according to the targeted densities of 1100 kg/m^3, 1200 kg/m^3 and 1300 kg/m^3 using the same cement-to-fibre ratio of 3:1. Based on three samples fabricated for each targeted density, the average density of 1060 kg/m^3, 1239 kg/m^3 and 1313 kg/m^3 were obtained. Table 1 shows the calculation of the design mix for EFBCB used in this research according to the targeted density. Distilled water is used to optimise the hydration rate of cement with 40% water based on cement weight (Akasah et al., 2019).

Table 1

Design mix for EFBCB

Density (kg/m^3)	1100	1200	1300
Sample size	350 x 350 x 12 mm	350 x 350 x 12 mm	350 x 350 x 12 mm
Volume sample	1.47 x 10^{-3} m^3	1.47 x 10^{-3} m^3	1.47 x 10^{-3} m^3
Dry weight	≈1617 g	≈1764 g	≈1911 g
Cement: EFB	$3x + x$ = Dry weight	$3x + x$ = Dry weight	$3x + x$ = Dry weight
3:1	1212.75 g : 404.25 g	1323 g : 441 g	1433.25 g : 477.75 g
Water	= 606.38 g	= 661.5 g	= 716.63 g

The fabrication method for Empty Fruit Bunch Cement Board (EFBCB) used in this study applied to the fabrication method used by Ashori et al. (2012), Onuorah et al. (2015), and Ghofrani et al. (2015). Recently, the same fabrication method was also used by Akasah et al., (2019) to investigate the effect of EFBCB density using different EFB fibre sizes.

This study only focused on various densities without segregating the fibre sizes. All materials (EFB fibre, water and cement) are weighted accordingly and mixed using the mechanical mixer. The raw ingredients were blended for 3 minutes in a mixer before adding the water. Then, the cement was added and mixed for about 10 minutes, which Ghorfani et al. (2015) recommended. It was then pre-formed into a wooden mould using a wire mesh and a manual lay-up procedure (Peter et al., 2020). Before being transported to a 50 tonne/m^2 cold compressor machine, the mixture was pre-pressed with another polythene sheet on top of it, with the metal plate mould put on the upper half. The cement board mixture was compressed at a 180 mm/min pressure rate for around 5 to 7 minutes until it reached

the desired thickness (Peter et al., 2020). Before the mixed materials were compacted, a 12 mm thick spacer was inserted between the steel mould. This process reduces the sample's height and helps stabilise the pressing surface. The specimen of the cement board was de-clamped after 24 hours, stacked horizontally, and cured at ambient temperature with relative humidity for 28 days allowing it to cure and increase its strength (Ghofrani et al., 2015; Onuorah et al., 2015). The EFBCB fabrication process is described in Figure 2.

(a) (b) (c)

(d) (e) (f)

(g) (h) (i)

Figure 2. EFBCB fabrication process. (a) Weighting material, (b) Mixing process, (c) Spreading process, (d) Flattening process, (e) Pre-compact process, (f) Pre-forming process, (g) Compressed using compression machine, (h) Clamped process, (i) Curing process

Thickness Monitoring (TM)

Thickness monitoring (TM) is used to investigate the density impact on the dimensional stability of EFBCB. This monitoring procedure was carried out every two days after the EFBCB had been subjected to a curing process for 28 days (BS EN 324-1:1993), and readings were collected using a digital vernier calliper throughout the process until a consistent reading was obtained. This technique was performed on three samples. The average reading of the three samples was used to calculate the thickness. The thickness of the sample was recorded on every four sides of the sample. Equation 1 was used to calculate the thickness of the cement board:

$$\text{Thickness Monitoring (TM)} = \frac{S\,1 + S\,2 + S\,3}{3} \quad (1)$$

where S is the average thickness of each sample.

Density Test

A density test was conducted after the curing process. This test aimed to analyse the dimensional stability of the EFBCB besides the physical properties themselves. The density testing procedure is based on the BS EN 32 (1993) standard. This sample's dimensions are square at 50 x 50 mm. Then, the weight and thickness of the sample were recorded. The formula for this test is in Equation 2:

$$\text{Density, } \rho = \frac{\text{m}}{V} \quad (2)$$

where m is the sample mass, and v is the sample volume.

Thickness Swelling (TS)

Due to the physical properties of EFBCB, a thickness swelling (TS) test was performed. By referring to the BS EN 317 (1993) standard, the TS test was to determine the water absorption of the samples after going through the curing process for 28 days. The sample was soaked in the water for 24 hours. The thickness of the samples before and after being immersed in water for 24 hours was recorded. The formula in Equation 3 is used to calculate the TS values:

$$\text{TS} = \frac{t2 - t1}{t1} \text{ x } 100\% \quad (3)$$

where $t1$ is the thickness before being immersed, and $t2$ is the thickness after being immersed.

Internal Bonding (IB)

This test was carried out to determine the strength of the bond between cement and EFB fibre. The test piece's dimension is a square, with each side length of 50 mm. Each test piece (top and bottom surface) was bonded to the steel-loading block using a suitable epoxy. The pulled load was then applied to the sample at a consistent action rate using a Universal Testing Machine guided by BS EN 319 (1993). The experiment was done until the sample failed. This test aimed to get the ultimate load on the sample before it breaks. Equation 4 is used to calculate the IB values:

$$\text{IB} = \frac{P}{wl} \tag{4}$$

where P is the maximum load, w is the width, and l is the length.

Modulus of Elasticity (MOE) and Modulus of Rupture (MOR)

After the curing process, the sample was cut to the prescribed size, and its mechanical characteristics of MOE and MOR were evaluated by BS EN 310 (1993). A static bending test was performed to establish the maximum load applied to the midpoint of the specimen that was simply supported. According to BS EN 310 (1993), the dimension of the specimen to be measured is 300 mm x 50 mm x 12 mm. Equations 5 and 6 are formulas to calculate the MOE and MOR values:

$$\text{MOE} = \frac{L^2 \Delta \text{W}}{4bt^3 \Delta S} \tag{5}$$

where L is the distance between the centre of support, ΔW is the increment load, ΔS is the increment of deflection at the midpoint corresponding to ΔW, b is the width of the test piece, and t is the thickness of the test piece.

$$\text{MOR} = \frac{3WL}{2bt^2} \tag{6}$$

where W is the maximum load, L is the distance between the centre of support, b is the width of the test piece, and t is the thickness of the test piece.

RESULTS AND DISCUSSION

Effects on Physical Properties of EFBCB

The dimensional stability of EFBCB was interpreted and discussed in terms of physical properties such as Thickness Monitoring (TM), Density, and Thickness Swelling (TS) performance for each density. The TM procedure was carried out every two days after the EFBCB was subjected to a curing process for 28 days. The readings were collected using a digital vernier calliper until a consistent reading was obtained. Meanwhile, the density

test was conducted after the curing process. The TS data was calculated by measuring the increase in thickness of the test piece after completing the water immersion process. The British Standard BS EN 324-1 specified all tests:1993, BS EN 323 (1993) and BS EN 317 (1993), respectively.

Thickness Monitoring (TM)

The design thickness for this study is 12 mm with an allowed thickness of ± 1 mm (BS EN 324-1, 1993), which means that the thickness must be between 11 mm and 13 mm to be suitable for use as building components in construction. Figure 3 shows the thickness monitoring results of samples in this study. Each sample recorded inconsistent readings towards the 28 days of curing. The surrounding temperature (ambient temperature) may influence the inconsistent readings of the sample thickness (Akasah et al., 2019). However, the sample with a target density of 1300 kg/m^3 showed the most horizontal graph reading, leading to a much more consistent reading to achieve the optimum thickness of EFBCB, which is 12 mm. Based on the results, the high density is one of the factors that leads the panel fabrication to achieve an optimum thickness reading due to the highest amount of cement mixed into the sample (Akasah et al., 2019). Cement is the primary binding agent for the EFB fibres in EFBCB samples (Wahab et al., 2015). Based on the results, it can be concluded that the stability of EFBCB increases when the density of EFBCB increases.

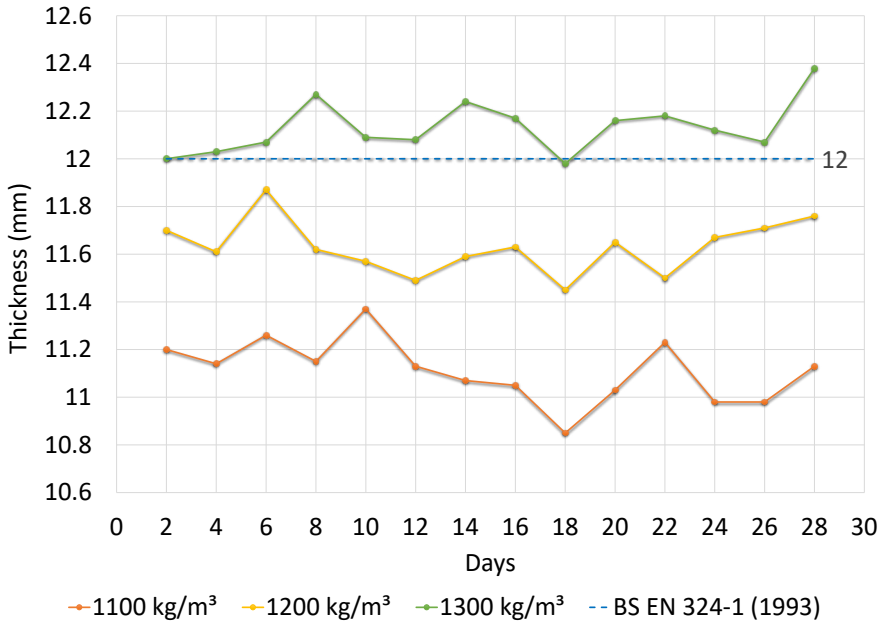

Figure 3. Thickness monitoring of EFBCB for 28 days

Density Test

The density of each sample is measured after 28 days of the curing process. The curing process allows maintenance of the sample's stability (Soydan et al., 2018). Density is measured by carefully cutting the samples into 50 mm x 50 mm. Then, samples are weighed and measured in length, width, and thickness using a vernier calliper. This density test is according to BS EN 323 (1993) standard, where the minimum requirement for a cement board density is 1000 kg/m^3. The results of the density test are shown in Figure 4.

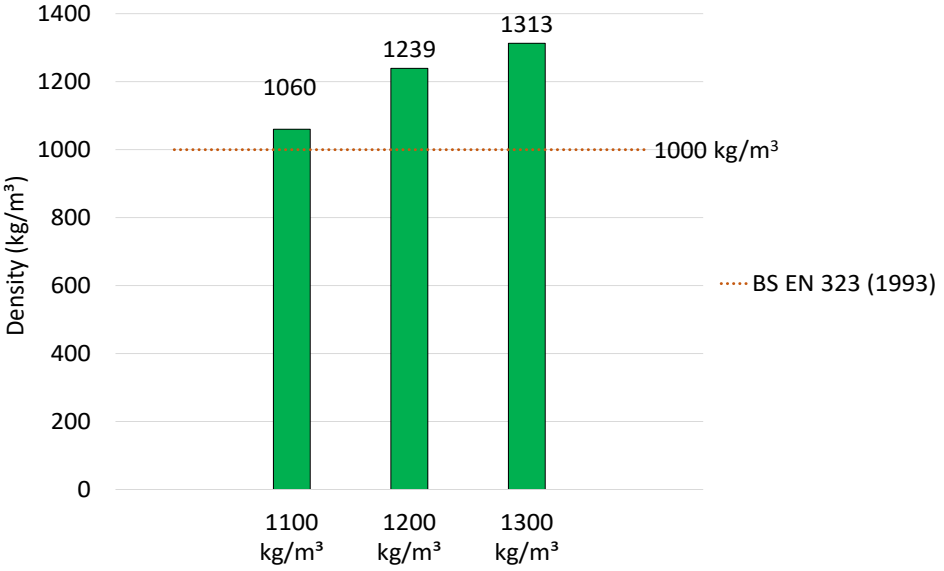

Figure 4. Average density of EFBCB

Thickness Swelling (TS)

Figure 5 shows the sample with a target density of 1100 kg/m^3 obtained 4.49% of thickness swells, which is larger than the other two samples. Voids are commonly found in low-density particleboards that generate areas to allow more water absorption (Loh et al., 2010). The low-density board's composition enhances water penetration, resulting in high water absorption, which causes the board to swell and, consequently, raises the thickness swelling (Wong et al., 2009). Hence, this research evidence that the highest density sample with a target density of 1300 kg/m^3 and 1.82% of thickness swell is the most recommended density for EFBCB with fewer TS effects that are almost complied with the recommended TS value as outlined in the BS standard requirement.

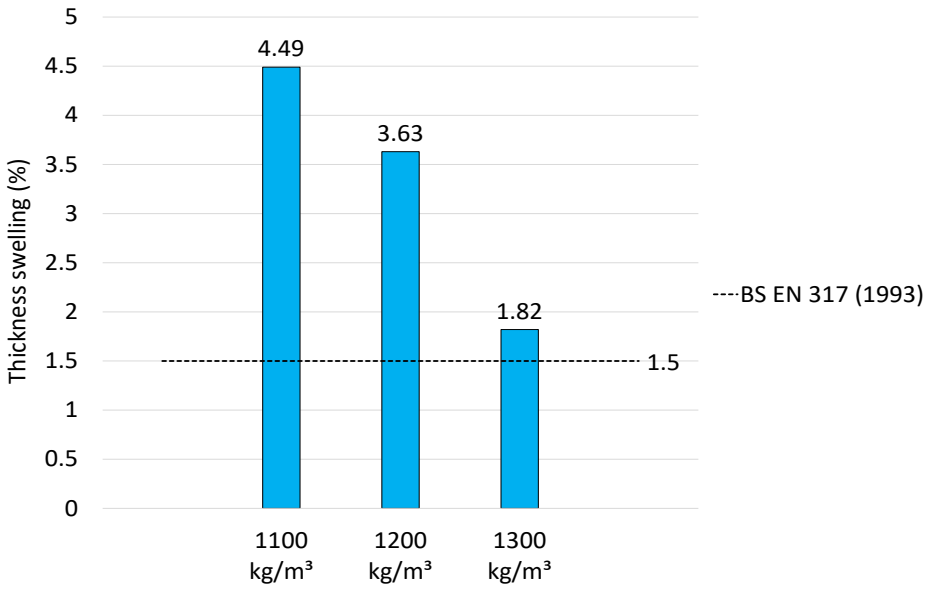

Figure 5. Thickness swelling effects of EFBCB at different target densities

Effects on Mechanical Properties of EFBCB

The mechanical characteristics of EFBCB based on densities are interpreted and discussed in terms of Internal Bonding (IB), Modulus of Rupture (MOR) and Modulus of Elasticity (MOE). The result for each targeted density is averaged from nine (9) EFBCB samples with a surface area of 50 mm x 50 mm for the IB test and using 300 mm x 50 mm for MOR and MOE testing. Testing is conducted following the British Standards BS EN 319 (1993) for IB and BS EN 310 (1993) for MOR and MOE.

Internal Bonding (IB)

Internal bonding test on the cement board samples aims to determine the internal bonding strength of the cement boards perpendicular to its surface when pressure is applied until cracks appear. The value was measured by dividing the maximum load at breaking by the sample's cross-sectional area. This testing was conducted based on the BS EN 319 (1993) procedure. Figure 6 shows that as the density of the board increase, the IB values also increase, with the EFBCB sample having a target density of 1300 kg/m^3 obtaining the highest IB at 0.164 N/mm^2 compared to the other two samples. According to Wahab et al. (2015), the bonding ability is associated with the EFBCB density. Thus, lower IB values obtained by the low-density cement boards were due to higher voids formed in the material. Those voids have caused the inter-fibre bonding to be ineffective (Ashori & Nourbaksh, 2008). Besides, inadequate compaction may also cause many of the inter-particle voids

to be left empty. Better compression and tighter particle interactions are much greater for fine and mixed particles, which may enhance the cement board's performance (Gupta et al., 2011).

This research obtained low IB results for all EFBCB samples at all three different target densities. The values are slightly below the standard requirement for a cement board, as recommended by BS EN 319 (1993), at 0.5 N/mm^2. The low IB shows incompatibility between the cement and the fibre in the mixture using 3:1 ratio.

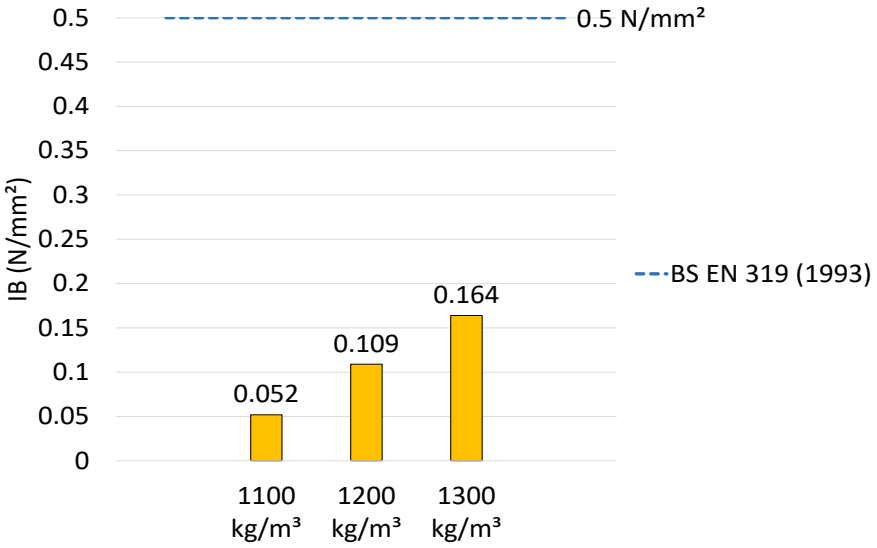

Figure 6. Internal bonding of EFBCB based on the different target density

Modulus of Elasticity (MOE) and Modulus of Rupture (MOR)

The amount of elasticity after the load applied is released and its resistance to bending define the modulus of elasticity (MOE) of an EFBCB. Meanwhile, the modulus of rupture (MOR) measures the highest load-carrying capability observed when stress is applied to a crack sample. This testing aims to determine the total strength of cement boards compared to the MOE, which only tested deflection but not the final strength of EFB cement boards. Testing was conducted according to BS EN 310:1993 guidelines.

Table 2 shows the result of the MOE and MOR for the three different densities. The sample with a target density of 1300 kg/m^3 had a greater average MOE value of 1398 N/mm^2. MOE is directly proportional to the density of the cement board, as described in a study by Wahab et al. (2015). When the MOE value is high, the board appears to be brittle; when the value is low, they tend to be ductile or flexible (Yang et al., 2003; Rasat et al., 2011). The results obtained described MOE values for all samples compared to the requirement stated in the BS EN 310:1993, Class 1: 4500 N/mm^2 and Class 2: 4000 N/mm^2.

Similarly, average MOR values for the sample with higher density shows better result compared to the lower density samples with an average MOR=3.51 N/mm^2. Based on the results, it can be concluded that the MOR value increase as the density of the sample increases. Findings from this research show that the MOR and MOE values are directly proportional to the density. Increase in the board density resulting in increasing the MOR and MOE value. The same finding was also obtained by Wahab et al. (2015); as the density of the boards increased, the MOE and MOR also increased. However, the MOR values for all samples are below the recommended value as stated in the standard, which is at 9 N/mm^2.

Table 2

Value of MOE and MOR for three different density

Target Density (kg/m^3)	Actual Density (kg/m^3)	Average Density (kg/m^3)	Mixing Ratio	MOE, N/mm^2		MOR, N/mm^2	
				Actual MOE	Average MOE	Actual MOR	Average MOR
1100	1007	1060	3:1	405.1	1006	2.39	3.1
	1051		3:1	1307		2.66	
	1121		3:1	1306		4.25	
1200	1020	1239	3:1	1122	1105.13	3.21	3.42
	1311		3:1	733.4		2.46	
	1385		3:1	1460		4.59	
1300	1214	1313	3:1	2212	1398	5.35	3.51
	1397		3:1	835		2.66	
	1327		3:1	1147		2.53	

CONCLUSION

Density had significant effects on the physical and mechanical properties of EFBCB. In this study, EFB cement boards with a target density of 1300 kg/m^3 show better performance than the other samples in terms of thickness stability, thickness swelling internal bonding, modulus of rupture and elasticity. In order to produce a higher-density panel, more cement and fibre are needed to achieve the target density. Since the same thickness is applied to all samples with regards to their target density, higher pressure needs to be applied during the fabrication process for the sample with a target density of 1300 kg/m^3, thus resulting in fewer voids left in the sample. Furthermore, voids in the EFB cement board generate areas that allow water to be absorbed, thus swelling the thickness. Since the EFB cement board with a target density of 1300 kg/m^3 contained less voids, this sample's mechanical properties are much better than the others. Density shows a directly proportional relationship with the internal bonding, modulus of rupture and modulus of elasticity of EFB cement

board at the same thickness and cement: fibre ratio. Even though the results are not very promising, this study has successfully shown that EFB fibre has a significant potential to be utilised as a green building material in the making of the building panel. However, further investigation is still needed to improve the mechanical properties of EFB cement boards to ensure their sustainability in the construction market.

ACKNOWLEDGMENT

This research is supported by Universiti Tun Hussein Onn Malaysia (UTHM) through Tier 1 (vot H900).

REFERENCES

Ajayi, B., & Badejo, S. O. O. (2005). Effects of board density on bending strength and internal board of cement bonded flake-boards. *Journal of Tropical Science*, *17*(2), 228-234

Akasah, Z. A., Dullah, H., Nik Soh, N. M. Z., & Anak Guntor, N. A. (2019). Physical and mechanical properties of empty fruit bunch fibre-cement bonded fibreboard for sustainable retrofit building. *International Journal of Material Science and Engineering*, *7*(1), 1-9. https://doi.org/10.17706/ijmse.2019.7.1.1-9

Akinyemi, O. P., & Osasona, C. O. (2017). Strength properties of bamboo-fibre cement boards used as building partitions. *Current Journal of Applied Science and Technology*, *23*(5), Article 36587.

Amel, B. A., Paridah, M. T., Rahim, S., H'ng, P. S., Zakiah, A., & Hussein, A. S. (2017). Physical-mechanical characteristics of cement-bonded kenaf bast fibres composite boards with different densities. *Journal of Engineering Science and Technology*, *12*(8), 2254-2267

Ashori, A., & Nourbakhsh, A. (2008). Effect of press cycle time and resin content on physical and mechanical properties of particleboard panels made from the underutilized low-quality raw materials. *Industrial Crops and Products*, *28*(2), 225-230. https://doi.org/10.1016/j.indcrop.2008.02.015

Ashori, A., Tabarsa, T., & Sepahvand, S. (2012). Cement-bonded composite boards made from poplar strands. *Construction and Building Materials, 26*(1), 131-134. https://doi.org/10.1016/j.conbuildmat.2011.06.001

Asasutjarit, C., Charoenvai, S., Hirunlabh, J., & Khedari, J. (2009). Materials and mechanical properties of pretreated coir-based green composites. *Composites Part B*, *40*(7), 633-637. https://doi.org/10.1016/j.compositesb.2009.04.009

Azni, M. E., Norhan, A. S., Lofflad, H., & Roslan, S. N. (2015, October 13*). Feasibility study on empty fruit bunch (EFB) cement board*. Paper presentation at Proceedings of ISER 9th International Conference. Berlin, Germany.

British Standard Institution. (1993). *Wood-based panels - Determination of modulus of elasticity in bending and of bending strength*. BS EN 310. 1993. London.

British Standard Institution. (1993). *Particleboards and fiberboards - Determination of tensile strength perpendicular to the plane of board*. BS EN 319. 1993. London.

British Standard Institution. (1993). *Wood-based panels - Determination of density*. BS EN 323. 1993. London.

British Standard Institution. (1993). *Wood-based panels - Determination of dimensions of boards.* BS EN 324-1. 1993. London.

British Standard Institution. (1993). *Particleboards and fiberboards - Determination of swelling in thickness after immersion in water*. BS EN 317.1993. London.

Coutts, R. S. (2005). A review of Australian research into natural fibre cement composites. *Cement and Concrete Composites*, *27*(5), 518-526. https://doi.org/10.1016/j.cemconcomp.2004.09.003

Egbewole, Z. T. (2017). Evaluation of strength and dimensional stability of cement bonded particle-board produced from selected wood sawdust residues. *International Journal of Applied Research and Technology*, *6*(8), 44-53.

Garcez, M. R., Garcez, E. O., Machado, A. O., & Gatto, D. A. (2016). Cement-wood composites: Effects of wood species, particle treatments and mix proportion. *International Journal of Composite Materials*, *6*(1), 1-8.

Ghofrani, M., Mokaram, K. N., Ashori, A., & Torkaman, J. (2015). Fiber-cement composite using rice stalk fiber and rice husk ash: Mechanical and physical properties. *Journal of Composite Materials*, *49*(26), 3317-3322. https://doi.org/10.1177/0021998314561813

Gupta, G., Yan, N., & Feng, M. W. (2011). Effects of pressing temperature and particle size on bark board properties made from beetle-infested lodgepole pine (*Pinus contorta*) barks. *Forest Products Journal*, *61*(6), 478-488. https://doi.org/10.13073/0015-7473-61.6.478

Ibrahim, S. H., Baharun, A., Nawi, M. N. M., & Affandi, R. (2014). Thermal performance of oil palm fibre and paper pulp as the insulation materials. *UNIMAS Journal of Civil Engineering*, *Science and Technology*, *5*(2), 22-28. https://doi.org/10.33736/jcest.135.2014

Khalil, H. P. S. A., Firdaus, M. Y. N., Jawaid, M., Anis, M., Ridzuan, R., & Mohamed, A. R. (2010). Development and material properties of new hybrid medium density fibreboard from empty fruit bunch and rubberwood. *Materials & Design*, *31*(9), 4229-4236. https://doi.org/10.1016/j.matdes.2010.04.014

Lin, C. Y. (2009). Study on effective utilization of palm oil waste (empty fruit bunch) system in Malaysia. *System Malaysia*, *3*, 1-4.

Loh, Y. W., H'ng, P. S., Lee. S. H., Lum, W. C., & Tan, C. K. (2010). Properties of particleboard produced from admixture of rubberwood and mahang species. *Asian Journal of Applied Science*, *3*(5), 310-316.

MPOB. (2020). *Overview of The Malaysian Oil Palm Industry 2020*. Malaysian Palm Oil Board. https://bepi.mpob.gov.my/

Mayowa, I. C., & Chinwuba, A. (2013). Effects of oil palm fibre on the compressive strength of mortar. *Journal of Emerging Trends in Engineering and Applied Sc*iences, *4*(5), 714-716.

Momoh, E. O., & Osofero, A. I. (2020). Recent developments in the application of oil palm fibers in cement composites. *Frontiers of Structural and Civil Engineering*, *14*(1), 94-108 https://doi.org/10.1007/s11709-019-0576-9

Ogunjobi, K. M., Ajibade, M. A., Gakenou, O. F., & Gbande, S. (2019). Physical and mechanical properties of cement-bonded particle board produced from anogeissus leiocarpus (DC.) guill and perr wood species. *African Journal of Agriculture Technology and Environment*, *8*(1), 192-199

Onuorah, E. O., Okeke, C. A., Nwabanne, J. T., Nnabuife, E. L. C., & Obiorah, S. O. M. (2015). The effects of production parameters on properties of single and 3-layer cement-bonded composites made from oil palm empty fruit bunch and tropical hardwood sawmill residue. *World Journal of Engineering*, *12*(6), 577-590. https://doi.org/10.1260/1708-5284.12.6.577

Olusegun, A., Makun, A., Ogara, H. A., Edema, I. N., Idaho, M., Olubamiwo, K. O., & Eshiett, M. E. (2012). *The Oil Palm Wastes in Malaysia*. Intech.

Owoyemi, J. M., Ogunrinde, O. S., & Oyeleye, I. O. (2020). Physical and mechanical properties of cement bonded strand board produced from *Gmelina arborea* (Roxb.) harvesting residues. *African Journal of Agricultural Research*, *16*(7), 976-982. https://doi.org/10.5897/AJAR2020.14809

Peter, P., Soh, N. M. Z. N., Akasah, Z. A., & Mannan, M. A. (2020). Durability evaluation of cement board produced from untreated and pre-treated empty fruit bunch fibre through accelerating ageing. *IOP Conf. Series: Materials Science and Engineering*, *713*, Article 012019

Papadopoulos, A. N. (2008). Mechanical properties and decay resistance of hornbeam cement bonded particleboards. *Advances in Materials Science and Engineering*, *2008*, Article 379749. http://dx.doi.org/10.1155/2008/379749

Rasat, M. S. M., Wahab, R., Sulaiman, O., Moktar, J., Mohamed, A., Tabet, T. A., & Khalid, I. (2011). Properties of composite boards from oil palm frond agricultural waste. *BioResources*, *6*(4), 4389-4403

Samsudin, E. M., Ismail, L. H., Kadir, A. A., & Mokdar, S. S. S. (2016). Comparison on acoustic performance between dust and coir form empty fruit bunches (EFB) as sound absorption material. *Jurnal Technology (Sciences & Engineering)*, *78*(5), 191-196.

Soydan, A. M., Sari, A. K., Burcu, D., Recep, A., & Bahadır, T. (2018). Air-cured fiber-cement composite mixtures with different types of cellulose fibers. *Advances in Materials Science and Engineering*, *2018*, Article 3841514. https://doi.org/10.1155/2018/3841514

Wahab, R., Dom, S. M. M., Mustafa, M. T., Samsi, H. W., Rasat, S. M., & Khalid, I. (2015). Properties of empty fruit bunch oil palm (*Elaeis guineesis*) composite boards at different densities and resin contents. *Journal of Plant Sciences*, *10*(5), 179-190. http://dx.doi.org/10.3923/jps.2015.179.190

Wong, E. D., Zhang, M., Wang, Q., & Kawai, S. (2009). Formation of the density profile and its effects on the properties of particleboard. *Wood Science Technology*, *33*(4), 327-340. https://doi.org/10.1007/s002260050119

Yang, H. S., Kim, D. J., & Kim, H. J. (2003). Rice straw-wood particle composite for sound absorbing wooden construction materials. *Bioresources Technology*, *86*(2), 117-121. https://doi.org/10.1016/S0960-8524(02)00163-3

Pertanika J. Sci. & Technol. 31 (3): 1173 - 1187 (2023)

PERTANIKA JOURNALS

SCIENCE & TECHNOLOGY

Journal homepage: http://www.pertanika.upm.edu.my/

Ex-Situ Development and Characterization of Composite Film Based on Bacterial Cellulose Derived from Oil Palm Frond Juice and Chitosan as Food Packaging

Norshafira Syazwani Abu Hasan[1], Shahril Mohamad[1], Sharifah Fathiyah Sy Mohamad[1]*, Mohd Hafiz Arzmi[2,3] and Nurul Nadia Izzati Supian[1]

[1]Faculty of Chemical of Process Engineering Technology, College of Engineering Technology, Universiti Malaysia Pahang, 26300 UMP, Kuantan, Pahang, Malaysia
[2]Department of Fundamental Dental and Medical Sciences, Kulliyyah of Dentistry, International Islamic University Malaysia, 25200 IIUM, Kuantan Campus, Pahang, Malaysia
[3]Cluster of Cancer Research Initiative IIUM (COCRII), International Islamic University Malaysia, 25200 IIUM, Kuantan, Pahang, Malaysia

ABSTRACT

The development of alternative food packaging films using bio-based residues is in great demand for replacing petroleum-based packaging materials. However, large-scale application is severely limited by costly production and poor performance. This study investigates the ex-situ modification of bacterial cellulose (BC) produced by *Acetobacter xylinum* in oil palm fronds juice to obtain BC-Chitosan (BCC) films. FTIR revealed the structure of amide I and II bands, confirming the presence of chitosan in BCC films. The FE-SEM images of BCC films showed the formation of a thick chitosan layer with increasing chitosan incorporated into the BC surface structure. The coated chitosan layer observed improved mechanical properties in BCC films due to the disappearance of empty pores between BC fibers. Increments in chitosan concentration slightly decreased the thermal behavior of BCC. The antimicrobial effects of BCC films were effective against Gram-positive bacteria (*Staphylococcus aureus*) when the concentration of chitosan incorporated was above 0.6 %w/v. This study reveals the potential of extending the application of BC derived from oil palm frond juice (OPFJ) for developing food packaging materials.

Keywords: Bacterial cellulose, chitosan, *ex-situ* method, film composite, oil palm frond juice

ARTICLE INFO

Article history:
Received: 07 June 2022
Accepted: 16 August 2022
Published: 31 March 2023

DOI: https://doi.org/10.47836/pjst.31.3.03

E-mail addresses:
nssfirawani@gmail.com (Norshafira Syazwani Abu Hasan)
shahrilm@ump.edu.my (Shahril Mohamad)
fathiyah@ump.edu.my (Sharifah Fathiyah Sy Mohamad)
hafizarzmi@iium.edu.my (Mohd Hafiz Arzmi)
diazatie@gmail.com (Nurul Nadia Izzati Supian)
*Corresponding author

ISSN: 0128-7680
e-ISSN: 2231-8526

© Universiti Putra Malaysia Press

INTRODUCTION

High consumption of non-biodegradable food packaging materials derived from petroleum-based polymers has raised environmental concerns. As a result, there is an increased interest in designing new packaging materials derived from renewable or natural sources as green alternatives for controlling the environmental impacts of the massive use of conventional plastic packaging (Oliveira et al., 2020). In this sense, bacterial cellulose (BC), produced by an inexpensive approach, can act as a base material in developing biodegradable packaging. BC is a biodegradable polymer commonly synthesized by *Acetobacter xylinum,* a widely used bacteria, due to its ability to change the sugar mixture into cellulose under specific conditions (Kongruang, 2007). In addition, BC is known to exhibit various unique properties, such as high cellulose purity, high water-holding capacity, biocompatibility, and biodegradability (Bandyopadhyay et al., 2018). Therefore, BC has found promising potential to be considered as an alternative biopolymer in medical, paper, and food applications (Azeredo et al., 2019). However, large-scale application of BC suffers from low yield as well as high cost of production due to the highly-priced Hestrin-Schramm media used in conventional BC cultivation (Lin et al., 2020). These drawbacks led to the exploration of alternative culture mediums derived from either agricultural wastes or industrial byproducts to minimize the production cost of BC.

Recently, several studies have shown the use of low-cost alternative culture media such as orange-peel wastes (Kuo et al., 2019), acerola byproducts (Leonarski et al., 2021), and wheat thin stillage (Revin et al., 2018) to produce BC. The utilization of these wastes has proven to enhance the BC yield and reduce the production cost of BC due to the abundant availability of the wastes (Hussain et al., 2019; Revin et al., 2018). The Malaysian oil palm industries produce a large quantity of oil palm biomass consisting of oil palm fronds, empty fruit bunches, oil palm trunks, palm kernel shells, mesocarp fibers, and palm oil mill effluent. The oil palm fronds, the outcome of pruning and harvesting palm oil trees, contribute to 75% of the solid wastes, at approximately 83 million tons annually (Yusof et al., 2019). The basal part of the oil palm frond (OPF) petiole can be squeezed to obtain fresh oil palm frond juice (OPFJ). The OPFJ contains a high quantity of fermentable sugars (up to 40 g/L of glucose, sucrose, and fructose), minerals, and nutrients (Zahari et al., 2012). The abundant availability of OPF all year round and the large sugars and nutrient contents of OPFJ rendered it a suitable fermentation medium. OPFJ-based culture medium was recently utilized in the fermentation of bioethanol, biobutanol, succinic acid, and poly(3-hydroxybutyrate). In addition, previous research has demonstrated the potential of producing BC using OPFJ as the only culture medium without any other nutrients or supplementation needed (Supian et al., 2021). Thus, replacing the expensive HS conventional medium with the alternative culture medium derived from OPFJ is a promising method to produce BC with minimum production cost.

BC produced from agricultural wastes could be an excellent biomaterial choice for bio-based film food packaging development. However, many issues need to be addressed before BC's unlimited potential as a choice of material can be completely realized. For example, BC films alone have low mechanical properties and poor antimicrobial resistance, hindering the broader commercialization potential of BC-based packaging material. Hence, many strategies were proposed to overcome these weaknesses, including impregnating BC with another polymer, such as chitosan. Chitosan is another natural material with antimicrobial activity, which is relatively low in cost and has abundant availability. As a food packaging material, incorporating BC film with chitosan should prevent microbial growth on the food surface by controlling the foodborne pathogenic bacteria, improving the mechanical properties, and reducing the cost (Malhotra et al., 2015).

There have been numerous studies on the development of BC-based films made from BC and chitosan. However, most studies focused on developing BC-Chitosan composites for biomedical applications and using BC produced from the commercial Hestrin-Schramm medium. However, to our knowledge, the combined effects of BC derived from the OPFJ with chitosan have never been explored. Therefore, in this study, the OPFJ was employed as the culture medium to produce BC by static cultivation of *Acetobacter xylinum*. The BC-produced synthesized BC-Chitosan (BCC) films with 0.2, 0.6, and 1.0% w/v chitosan by direct immersion into the chitosan solutions. All samples were characterized based on their chemical, morphological, mechanical, thermal, and antimicrobial properties for potential application as food packaging materials. These findings elucidate BCC films as a promising alternative for various packaging applications.

MATERIALS AND METHODS

Materials

Fresh oil palm frond was collected from LKPP Oil Palm Plantation in Pekan, Pahang, Malaysia. Chitosan of medium molecular weight, sodium hydroxide, acetic acid, microcrystalline cellulose (MCC), and α-cellulose were procured from Sigma-Aldrich. *Acetobacter xylinum* FTCC 0416 was supplied by the Malaysian Agriculture Research and Development Institute (MARDI), Serdang, Selangor, Malaysia. All other chemicals and reagents used were of the analytical grade.

Production and Purification of BC

OPFJ feedstock was extracted from OPF petioles harvested a day earlier to maintain freshness. Fresh OPFJ was obtained by pressing the OPF petiole with a hydraulic pressing machine (MATSUO Inc., Japan). Impurities contained in the extracted OPFJ were removed using a 0.5 mm stainless steel sieve followed by a muslin filter cloth. The filtered OPFJ was centrifuged (10000 rpm, 4ºC, 20 min) and kept at -20ºC before use. BC was produced

using 80% v/v OPFJ (adjusted to pH 4.5) as the culture medium. The medium was inoculated with 10% v/v *A. xylinum* and statically incubated for 14 days at 30ºC. The BC pellicles formed at the top of the culture medium were harvested at the end of 14 days and repeatedly washed using distilled water. The BC pellicles were then purified by boiling them in 0.5 M NaOH for 2 h to ensure that the BC surface was free from bacterial cell attachment. Finally, the pure BC pellicles were washed with distilled water several times until a neutral pH was attained.

Preparation of BC-Chitosan (BCC) Composite Films

The BCC composites were prepared following the method of Kim et al. (2011) with slight changes. Three different concentrations of chitosan solutions (0.2, 0.6, and 1.0% w/v) were prepared by dissolving chitosan powder in 1% v/v acetic acid at room temperature for 2 h. Preparation of BC-Chitosan (BCC) films was carried out by first positioning the neutralized BC pellicles between two filter paper sheets to absorb excessive water. The BC was then immersed in 50 ml chitosan solution for 24 h at 50ºC. Finally, the BCC films were removed from the solution, washed with deionized water, placed between two filter paper sheets to remove the excess solution, and weighed before being pressed with an iron to form dried BCC films. The samples were labeled as BC (without chitosan), BCC-0.1, BCC-0.6, and BCC-1.0 corresponding to the chitosan concentrations used (% w/v).

Characterization of BC and BCC Films

Chemical Structure by Attenuated Total Reflection Fourier-Transform Infrared (ATR-FTIR) Spectroscopy. The chemical structure of BC and BCC films was analyzed using an FTIR spectrophotometer (Nicolet iS5, Thermo Fisher Scientific, USA) with an attenuated total reflectance (ATR) mode. For each sample, 32 scans with a resolution of 4 cm^{-1} were collected over the wavenumber ranging from 400–4000 cm^{-1} in transmittance mode.

Surface Morphology by Field Emission Scanning Electron Microscopy (FE-SEM). The pure BC and BCC films' surface morphology was visualized with a DSM 940A high-resolution Field Emission Scanning Electron Microscope (FE-SEM; Zeiss, Germany) operated at 15 kV.

Mechanical Properties. The mechanical properties of the BC and BCC films were determined using a texture analyzer machine (CT3 Texture Analyzer, Brookfield, USA) equipped with TexturePro CT V1-8 Build 3.1. The samples were prepared by cutting each BC and BCC film into strips (70 mm x 10 mm) using a precise cutter. Tensile strength (TS), percentage of elongation at break (%EAB), and Young's Modulus (YM) were measured according to the standard method D-882 (ASTM, 2002). An initial grip separator of about 50 mm and a 50 mm/min of crosshead speed was used to run the tests. In every test, TS and %EAB were computed using Equations 1 and 2, respectively (Cazón et al., 2019).

$$TS(MPa) = \frac{F}{A} \quad [1]$$

$$\%EAB = \frac{L}{60} \times 100 \quad [2]$$

In Equation 1, F is the maximum load that is required in pulling apart the sample (N), and A is the cross-sectional area (m^2). Meanwhile, in Equation 2, *L* is the film elongation during the rupture (mm), and 60 is the initial length of grip (mm) of the film samples. Young's modulus was computed from the initial stress-strain curve slope, expressed in MPa.

Thermal Properties Using Thermogravimetric Analysis (TGA). TGA was carried out on all BC and BCC samples to evaluate their respective mass losses when subjected to continuous heating. TGA was performed using TGA Instrument Q500 V 6.7 (TA Instruments, USA) with a 10°C/min heating rate from 25 to 800°C under a nitrogen atmosphere.

Antimicrobial Susceptibility Testing. The antimicrobial susceptibility of pure BC and BCC films was carried out according to the Kirby-Bauer disc diffusion method. *Candida albicans* ATCC (MYA-4901), *Staphylococcus aureus* (ATCC 25923), and *Escherichia coli* (ATCC 25922) were selected as the representative of yeast, Gram-positive bacteria, and Gram-negative bacteria in the antimicrobial susceptibility tests. The stock culture was revived by inoculating the yeast and the bacteria into yeast peptone dextrose (YPD) and brain heart infusion (BHI) broth, respectively, and incubated at 37ºC overnight. Briefly, two yeast and bacteria colonies were inoculated into 5 ml of the nutrient broth. Subsequently, the inoculum was standardized to 0.5 McFarland standard, which equals OD600 nm 0.1. 100 µL of the yeast and bacteria suspension were inoculated into a nutrient agar (Oxoid, UK) plate using a sterile cotton swab. Samples of BC (control group) and BCC films priorly to sterilization were then placed onto the surface of the agar medium and incubated at 37ºC for 24 h. The inhibition zone was estimated by measuring the bacterial growth inhibition zone diameter around the samples. The diffusion assay was performed in triplicate.

RESULTS AND DISCUSSION

Characterization of BC and BCC Films

ATR-FTIR Spectroscopy Analysis. ATR-FTIR spectroscopy was performed to identify the functional groups of BC and evaluate the structural interaction between BC and chitosan due to the incorporation of different concentrations of chitosan (0.2–1.0% w/v) into the

BC film matrix by measuring the spectra in the wavenumber range of 4000-400 cm^{-1} at a spectral resolution of 4 cm^{-1}. The FTIR spectra of BC, MCC, and α-cellulose were analyzed to have a comparative view of the functional groups in cellulose. As shown in Figure 1, the BC obtained in this study showed all the typical characteristic peaks of cellulose, similar to MCC and α-cellulose, indicating that the BC had a cellulose structure. The peaks observed at 3340 cm^{-1} and 2893 cm^{-1} correspond to the stretching vibrations of the O-H groups of cellulose and the C-H stretching, respectively (Ju et al., 2020). The peak at 1630 cm^{-1} corresponds to the glucose carbonyl group (C=O) (He et al., 2020). Meanwhile, the band at 1427 cm^{-1} is from CH_2 symmetric bending, and the band at 1369 corresponds to the C-H deformation vibration. Furthermore, the peaks observed at 1161 cm^{-1} and 1107 cm^{-1} indicated the C-O-C deformation vibration and C-C bending, respectively. Finally, the peaks at 897 cm^{-1} are from the β-glycosidic linkages in the cellulose structure.

Figure 2 compares FTIR spectra between the BC and BCC films containing different chitosan amounts. The obtained spectra revealed that the prominent characteristic peaks of BC are still observed in the BCC films. The broad bands between 3300 cm^{-1} and 3278 cm^{-1} in all the samples indicated the O-H and N-H stretching vibrations. Meanwhile, the symmetric and asymmetric C-H stretching vibrations lead to peaks around 2918 cm^{-1} and 2893 cm^{-1}. Moreover, the bands at 1636 and 1541 cm^{-1} are attributed to C=O stretching (amide I) and N-H bending (amide II), respectively. Finally, the bands located between 1028-1030 cm^{-1} correspond to the stretching vibrations of C-O.

Both BC and chitosan have similar chemical compositions. Thus, the appearance of the amide groups on the IR spectra corroborated the presence of chitosan within the BCC film. IR spectra are proven useful in verifying the existence of chitosan molecules in BCC film (Lin et al., 2013). In this study, the band corresponding to the amide III could only be observed in the BCC-1.0 sample. The low peak intensity could be correlated because the chitosan signal has a lower concentration than the more vigorous BC peak intensity. The low availability of chitosan in the BCC film might also contribute to the low-intensity peak at 1371 cm^{-1} (amide III). On the other hand, higher intensity of the broad peak corresponding to the hydrogen bond absorption band was observed in pure BC than in the BCC films. It might be due to the hydrogen bonds' partial break between the BC hydroxyl groups, which is caused by the penetration of chitosan into the structure of BC (Ju et al., 2020). The decreasing and slight shift of the absorption band in the composite corresponding to Iα crystalline cellulose allomorph might indicate a disruption of BC crystallinity in the presence of chitosan interfering with BC intermolecular hydrogen bonds. Similar findings were also observed in other studies of BC/chitosan composites (Jia et al., 2017).

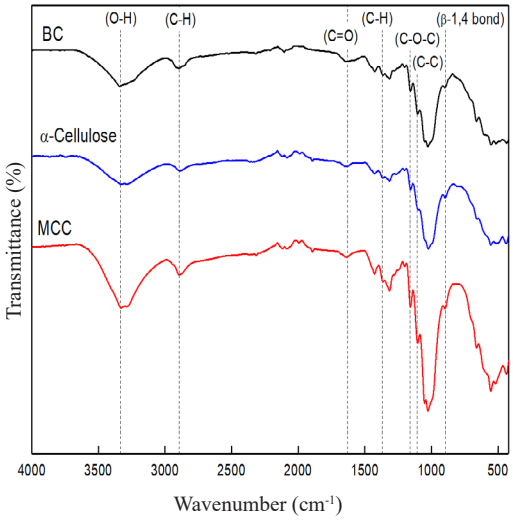

Figure 1. FTIR spectra of BC obtained from OPFJ, MCC, and α-Cellulose

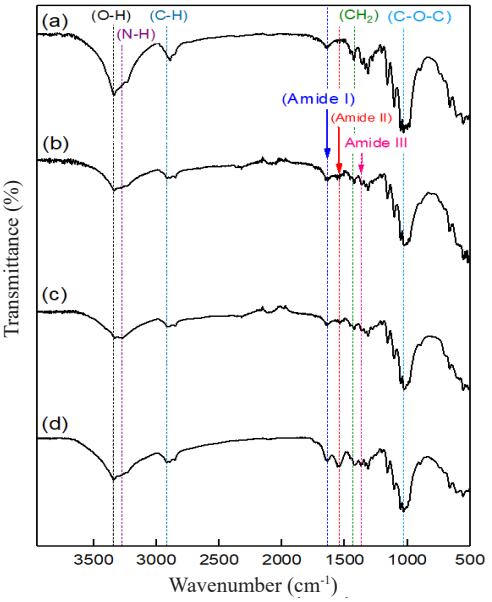

Figure 2. FTIR spectra of (a) pure BC and BCC films prepared using (b) 0.2% w/v, (c) 0.6% w/v, and (d) 1.0% w/v chitosan

Surface Morphology of BC and BCC Films. FE-SEM analysis was used to evaluate the surface morphology of the BC and BCC films and verify the degree of penetration of chitosan inside the BC. Figure 3 presents the surface morphology of each BC and BCC film examined by the FE-SEM. Figure 3a revealed that the pure BC film showed a densely packed, interwoven, connected, and randomly oriented network of fibers, with fiber diameters that range from 28 to 62 nm. The observation agrees with the morphology reported for BC produced statistically in alternative media (Dubey et al., 2017; Sharma et al., 2021). Moreover, a further increase of chitosan concentration in BCC films (Figures 3b-d) resulted in forming of a thick and coarse layer, probably due to the disappearance of the porous structure into the BC matrix that filled the gap between the adjoining BC fibers. These results implied that chitosan might penetrate within the BC microfibrils, leading to a more compact network structure with less pore size (Ul-Islam et al., 2011). Several studies also reported similar findings in the changes of the physicochemical properties with the increment of chitosan content incorporated in the BC films (Kim et al., 2011; Tanpichai et al., 2020).

Mechanical Properties. The mechanical properties of BC and BCC films were evaluated to estimate the quality of packaging materials, and the results are shown in Figure 4. In this study, the tensile strength increased with increasing chitosan concentration. Meanwhile, the elongation at break of the BC first decreased with increasing chitosan concentration and then increased when 1.0% w/v chitosan was used. In contrast, Young's modulus increased when chitosan concentration increased, reaching a maximum of BCC-0.6, then decreasing

to 1360 MPa (BCC-1.0). All these findings suggested that the BCC composites were more resilient with increasing concentrations of chitosan used.

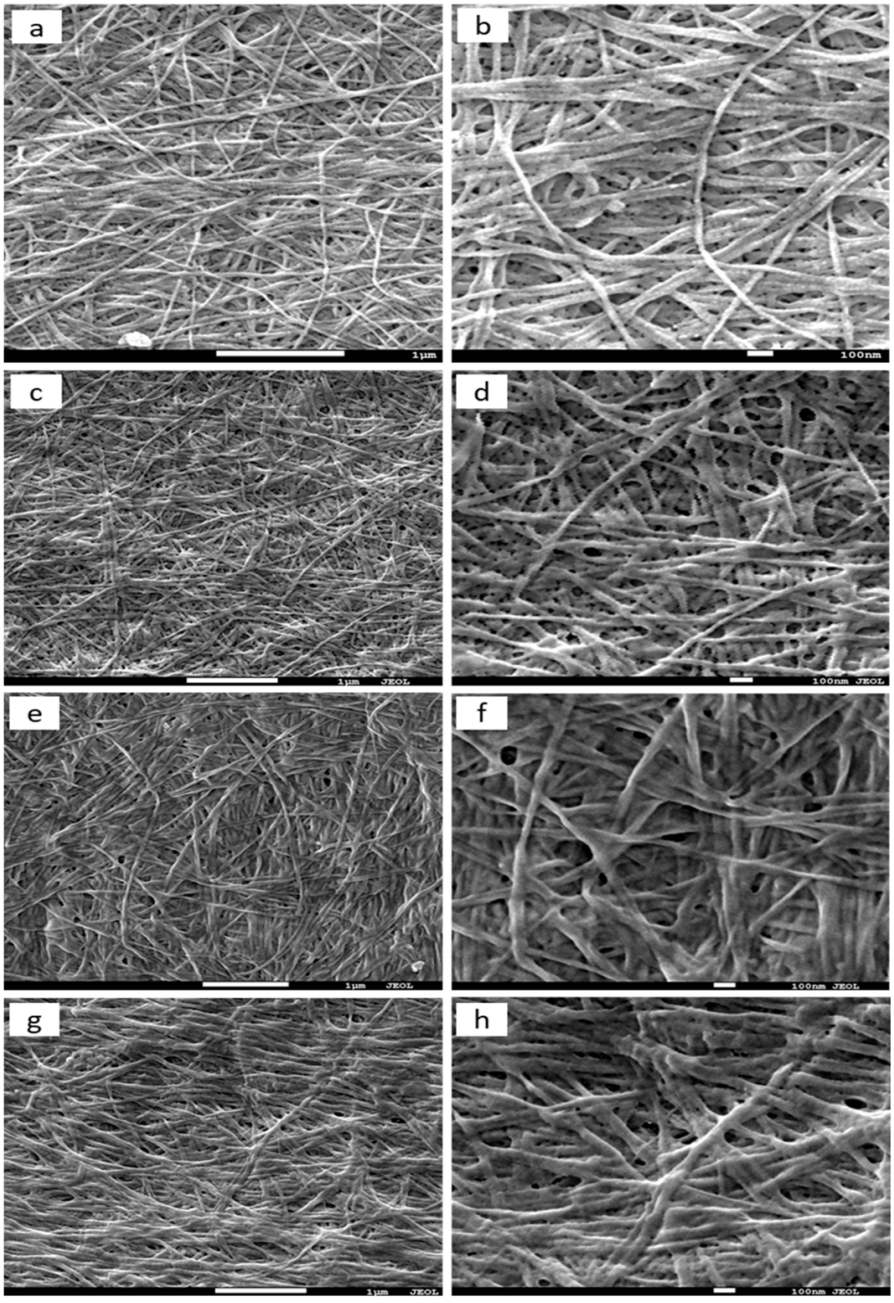

Figure 3. FE-SEM images of (a) BC ×25,000; (b) BC ×50,000; (c) BCC-0.2 ×20,000; (d) BCC-0.2 ×50,000; (e) BCC-0.6 ×25,000; (f) BCC-0.6 ×50,000; (g) BCC-1.0 ×20,000 and (h) BCC-1.0 ×50,000 magnifications

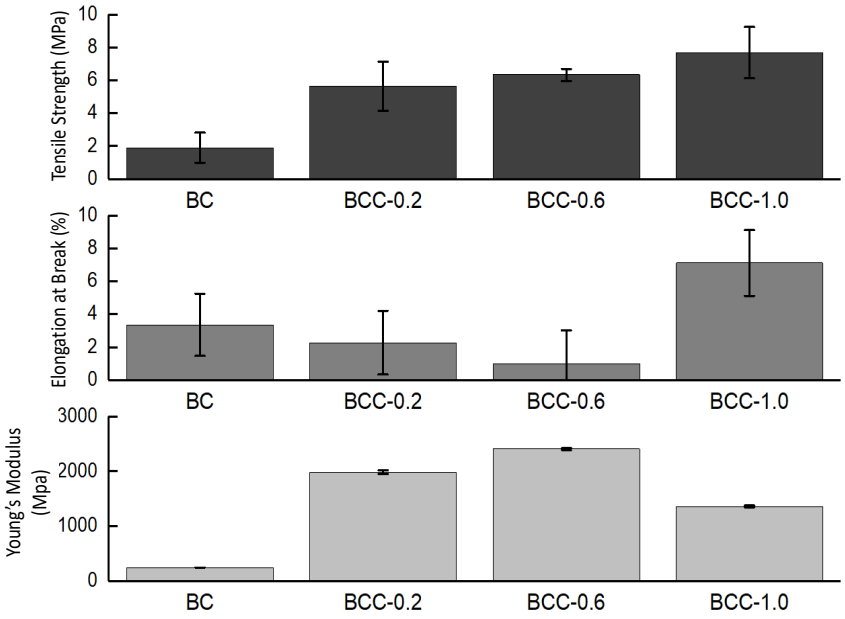

Figure 4. Tensile strength, elongation at break, and Young's modulus of BC and BCC films

The BCC films developed in this study demonstrated higher mechanical properties (tensile strength and elastic modulus) than pure BC film, indicating that the BCC could be a suitable alternative food packaging material. These results may correspond to the intermolecular hydrogen bond formation between the chemical groups in bacterial cellulose (–OH) and chitosan (–OH and –NH2), which hinders the matrix mobility while enhancing its rigidity (Liang et al., 2019). Also, we found that the BC produced from OPFJ cultivation displayed considerably high mechanical properties than the ones reported by Lin et al. (2013). The differences in mechanical properties could be due to culture time, medium supplements, or post-treatment variations for the BC (Sharma et al., 2021). Nevertheless, the elongation at the break of our BCC films was lower, contrasting with that of other BCC composites reported by Lin et al. (2013). The low elongation at break might be attributed to the brittle structure of the dried BCC films with increasing chitosan concentrations.

Thermal Properties by TGA. The thermal characteristics of BC and BCC films were tested using TGA, and the TG curves of each tested BC and BCC film as a function of temperature is presented in Figure 5. For all samples, three stages of weight loss were observed in the TGA curves. The initial stage of weight loss at 50–150°C was ascribed to the evaporation of the retained moisture in both BC and BCC samples (Du et al., 2018). The water volatilization led to a weight loss of 7.90, 9.33, 12.50, and 14.31% for samples

from BC, BCC-0.2, BCC-0.6, and BCC-1.0, respectively. The weight loss percentage until 150°C increased when chitosan concentration increased because of its hydrophilic nature. The increment of weight loss percentages observed in BCC samples might be associated with the condensation of water molecules on its surface due to the hygroscopicity character of the chitosan that retained the adsorbed moisture strongly at standard relative humidity conditions (Cazón et al., 2019).

For all BC and BCC samples, major weight losses were observed in the second stage at 200-350°C attributed to the thermal decomposition of the rapid cleavage of BC glycosidic bond and chitosan (Wahid et al., 2019). At 350°C, the total weight loss values were 85.93, 66.91, 64.11, and 66.75% for BC, BCC-0.2, BCC-0.6, and BCC-1.0 samples, respectively. The weight loss decreases as the BCC's chitosan concentration increases and becomes saturated after 0.6% w/v of chitosan concentration.

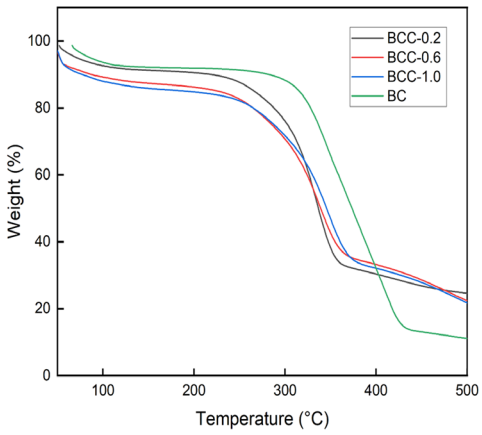

Figure 5. TGA curves of BC and BCC samples

Prior research shows BC's maximum thermal degradation temperature was 330°C (Cacicedo et al., 2020). In this study, the maximum thermal degradation temperature for BC derived from OPFJ was 342°C. The addition of chitosan to the BC matrix slightly shifted the maximum thermal degradation temperature from 342°C (BC) to 335°C (BCC-0.2), 338°C (BCC-0.6), and 328°C (BCC-1.0), indicating the presence of intermolecular interaction between BC and chitosan. However, BCC samples' thermal stability is reduced compared to BC. Similar TGA results were obtained by Jia et al. (2017). The reduced thermal stability of BCC samples could probably be due to the weaker interfacial hydrogen bonding between BC and chitosan. In addition, the thermal stability of BCC is also known to depend on these various intrinsic (degree of deacetylation, molecular weight, and purity of chitosan) and extrinsic (storage conditions and thermal processing method) factors (Szymańska & Winnicka, 2015).

The third weight loss region ranging from 360 to 500°C, was associated with the final decomposition of the vestigial carbon of BC to ash. When the heating process was almost completed, the total weight loss values were 88.86, 75.32%, 77.25, and 78.12% for BC, BCC-0.2, BCC-0.6, and BCC-1.0, respectively. The lower weight losses observed in all BCC samples implied that the BCC composites decomposed slower than BC. Nevertheless, the outcomes of thermal stability showed that the BCC composite films developed are stable at temperatures below 150°C. Therefore, this biodegradable blend material is more likely to be applied to food products post-sterilization or pasteurization.

Antimicrobial Susceptibility Testing. In the current work, since chitosan possesses antimicrobial properties, we hypothesized that the BCC films would demonstrate a similar action to the BC control film. Figure 6 presents the antimicrobial effect of BC and BCC films against Gram-positive (*S. aureus*) and Gram-negative (*E. coli*) bacteria and the antifungal activity against *C. albicans*. As expected, the BC film samples showed no antimicrobial activity against the three selected microorganisms. Interestingly, all BCC films (BCC-0.2, BCC-0.6, and BCC-1.0) also showed no inhibition of *E. coli* or *C. albicans.* The findings showed that the chitosan could be tightly incorporated in BC fibrils, preventing the diffusion of the antimicrobial component from BCC films to the surrounding agar to create the inhibition zone (Lin et al., 2013). While several authors reported significant improvement in the antimicrobial properties of BCC against Gram-positive and Gram-negative bacteria, the present results were in accordance with several studies which show the absence of antimicrobial properties of chitosan against tested microorganisms when fabricated in the solid form (Lin et al., 2013).

This study, however, demonstrated that the inhibition zone was only observed against the Gram-positive *S. aureus* for BCC-0.6 and BCC-1.0, with an inhibition zone diameter of 30.66 ± 0.28 and 32.48 ± 0.51 mm, respectively. The findings indicate that the antimicrobial activity of the BCC film was more effective against *S. aureus* than *E. coli* and *C. albicans.* The different thicknesses of the bacterial peptidoglycan layers might contribute to the high sensitivity of chitosan in BCC films against the Gram-positive *S. aureus*. By contrast, the peptidoglycan layer of Gram-positive bacteria (7–8 nm) is thinner than Gram-negative bacteria (20–80 nm). The finding also suggested that a minimum concentration of 0.6% w/v chitosan is sufficient to act as an antimicrobial agent against *S. aureus*. On the other hand, insufficient chitosan incorporated in the BCC film and the slow migration of chitosan from the BCC film matrix might be the reasons for the lack of antimicrobial activity observed for the BCC-0.2 sample (Dehnad et al., 2014).

The difference in the antimicrobial effects of chitosan was probably due to the variations in the antimicrobial mode of action and the disparities in the composition and structure of the cell walls of the three selected microorganisms (Buruaga-Ramiro et al., 2020). Although the exact antibacterial mechanism of chitosan remains unclear, several theories proposed that the antimicrobial mechanism of chitosan was probably due to the suppression of the generation of mRNA bacterial cells triggered by the electrostatic interactions between the positively charged amino groups (NH_3^+) in chitosan molecules and the anionic teichoic acids in the bacterial cell wall. As a result, the permeability of the bacteria cell membrane will also increase and causing the inhibition of cell growth (Liang et al., 2019; Wahid et al., 2019).

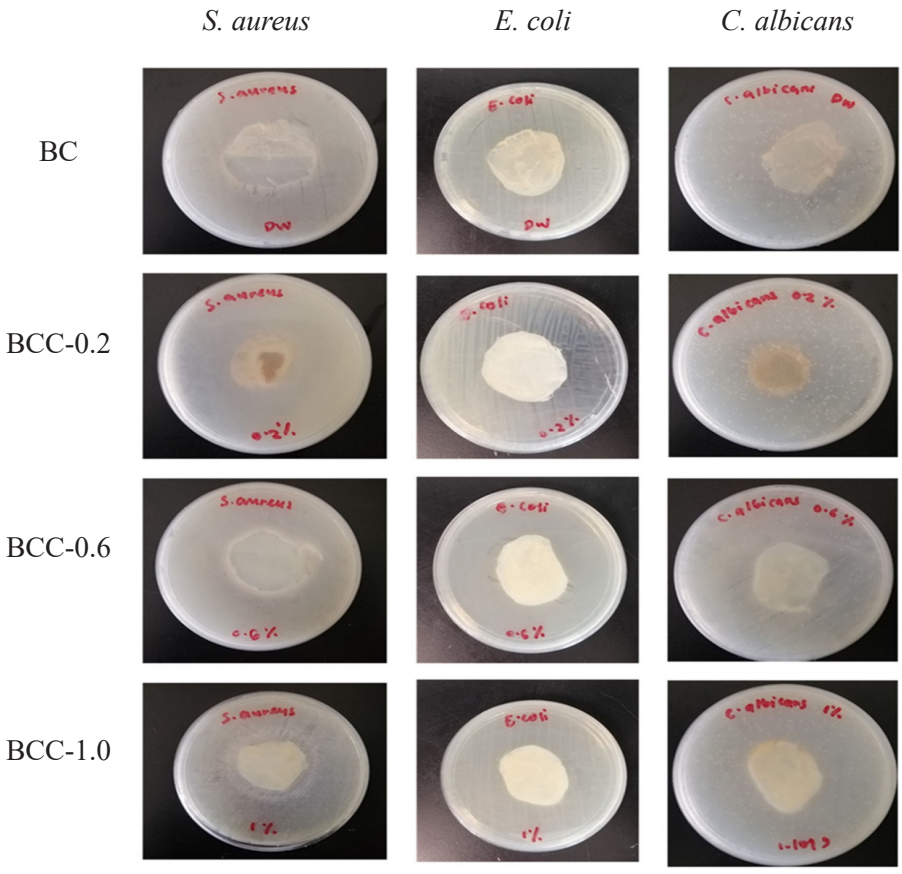

Figure 6. Disk diffusion results of BC and BCC films against three different microbes

CONCLUSION

The present study successfully produced BCC film composites to reduce the environmental harm caused by synthetic plastic packaging materials. BCC films were prepared via the *ex-situ* method involving immersion of BC derived from the static cultivation of *A. xylinum* in OPFJ in various concentrations of chitosan solution. The ATR-FTIR and FE-SEM results confirm the successful incorporation of chitosan into the BC. The BCC films also displayed enhanced mechanical properties compared to BC alone. Meanwhile, the antimicrobial properties of chitosan remained in the BCC-0.6 and BCC-1.0 against the Gram-positive *S. aureus*. The thermal behavior of the BCC films suggested the possibility of being applied in foods that are heat-treated until 150°C. Hence, BCC films from BC produced through OPFJ cultivation can offer a suitable innovative replacement for non-biodegradable food packaging materials. Further study on the effect of plasticizer type and content is recommended to obtain excellent mechanical properties, as demonstrated by commercial plastic-based materials.

ACKNOWLEDGEMENTS

The research was supported by the Fundamental Grant Research Scheme (FRGS/1/2018/TK05/UMP/03/3) received from the Malaysian Ministry of Higher Education (MOHE) and PGRS2003135 received from Universiti Malaysia Pahang.

REFERENCES

Azeredo, H. M. C., Barud, H., Farinas, C. S., Vasconcellos, V. M., & Claro, A. M. (2019). Bacterial cellulose as a raw material for food and food packaging applications. *Frontiers in Sustainable Food Systems*, *3*, 1-14. https://doi.org/10.3389/fsufs.2019.00007

Bandyopadhyay, S., Saha, N., Brodnjak, U. V., & Saha, P. (2018). Bacterial cellulose based greener packaging material: A bioadhesive polymeric film. *Materials Research Express*, *5*(11), Article 115405. https://doi.org/10.1088/2053-1591/aadb01

Buruaga-Ramiro, C., Valenzuela, S. V., Valls, C., Roncero, M. B., Pastor, F. I. J., Díaz, P., & Martinez, J. (2020). Development of an antimicrobial bioactive paper made from bacterial cellulose. *International Journal of Biological Macromolecules*, *158*, 587-594. https://doi.org/10.1016/j.ijbiomac.2020.04.234

Cacicedo, M. L., Pacheco, G., Islan, G. A., Alvarez, V. A., Barud, H. S., & Castro, G. R. (2020). Chitosan-bacterial cellulose patch of ciprofloxacin for wound dressing: Preparation and characterization studies. *International Journal of Biological Macromolecules*, *147*, 1136-1145. https://doi.org/10.1016/j.ijbiomac.2019.10.082

Cazón, P., Velázquez, G., & Vázquez, M. (2019). Characterization of bacterial cellulose films combined with chitosan and polyvinyl alcohol: Evaluation of mechanical and barrier properties. *Carbohydrate Polymers*, *216*, 72-85.

Dehnad, D., Mirzaei, H., Emam-Djomeh, Z., Jafari, S. M., & Dadashi, S. (2014). Thermal and antimicrobial properties of chitosan-nanocellulose films for extending shelf life of ground meat. *Carbohydrate Polymers*, *109*, 148-154. https://doi.org/10.1016/j.carbpol.2014.03.063

Du, R., Zhao, F., Peng, Q., Zhou, Z., & Han, Y. (2018). Production and characterization of bacterial cellulose produced by gluconacetobacter xylinus isolated from Chinese persimmon vinegar. *Carbohydrate Polymers*, *194*, 200-207. https://doi.org/10.1016/j.carbpol.2018.04.041

Dubey, S., Sharma, R. K., Agarwal, P., Singh, J., Sinha, N., & Singh, R. P. (2017). From rotten grapes to industrial exploitation: Komagataeibacter europaeus SGP37, a micro-factory for macroscale production of bacterial nanocellulose. *International Journal of Biological Macromolecules*, *96*, 52-60. https://doi.org/10.1016/j.ijbiomac.2016.12.016

He, F., Yang, H., Zeng, L., Hu, H., & Hu, C. (2020). Production and characterization of bacterial cellulose obtained by Gluconacetobacter xylinus utilizing the by-products from Baijiu production. *Bioprocess and Biosystems Engineering*, *43*, 927-936. https://doi.org/10.1007/s00449-020-02289-6

Hussain, Z., Sajjad, W., Khan, T., & Wahid, F. (2019). Production of bacterial cellulose from industrial wastes: A review. *Cellulose*, *26*, 2895-2911. https://doi.org/10.1007/s10570-019-02307-1

Jia, Y., Wang, X., Huo, M., Zhai, X., Li, F., & Zhong, C. (2017). Preparation and characterization of a novel bacterial cellulose/chitosan bio-hydrogel. *Nanomaterials and Nanotechnology*, *7*, 1-8. https://doi.org/10.1177/1847980417707172

Ju, S., Zhang, F., Duan, J., & Jiang, J. (2020). Characterization of bacterial cellulose composite films incorporated with bulk chitosan and chitosan nanoparticles: A comparative study. *Carbohydrate Polymers*, *237*, Article 116167. https://doi.org/10.1016/j.carbpol.2020.116167

Kim, J., Cai, Z., Lee, H. S., Choi, G. S., Lee, D. H., & Jo, C. (2011). Preparation and characterization of a bacterial cellulose/chitosan composite for potential biomedical application. *Journal of Polymer Research*, *18*, 739-744. https://doi.org/10.1007/s10965-010-9470-9

Kongruang, S. (2007). Bacterial cellulose production by acetobacter xylinum strains from agricultural waste products. In W. S. Adney, J. D. McMillan, J. Mielenz, K. T. Klasson (Eds.), *Biotechnology for Fuels and Chemicals* (pp. 763-774). Springer. https://doi.org/10.1007/978-1-60327-526-2_70

Kuo, C. H., Huang, C. Y., Shieh, C. J., Wang, H. M. D., & Tseng, C. Y. (2019). Hydrolysis of orange peel with cellulase and pectinase to produce bacterial cellulose using gluconacetobacter xylinus. *Waste and Biomass Valorization*, *10*, 85-93. https://doi.org/10.1007/s12649-017-0034-7

Leonarski, E., Cesca, K., Zanella, E., Stambuk, B. U., de Oliveira, D., & Poletto, P. (2021). Production of kombucha-like beverage and bacterial cellulose by acerola byproduct as raw material. *LWT*, *135*, Article 110075. https://doi.org/10.1016/j.lwt.2020.110075

Liang, J., Wang, R., & Chen, R. (2019). The impact of cross-linking mode on the physical and antimicrobial properties of a chitosan/bacterial cellulose composite. *Polymers*, *11*(3), Article 491. https://doi.org/10.3390/polym11030491

Lin, D., Liu, Z., Shen, R., Chen, S., & Yang, X. (2020). Bacterial cellulose in food industry: Current research and future prospects. *International Journal of Biological Macromolecules*, *158*, 1007-1019. https://doi.org/10.1016/j.ijbiomac.2020.04.230

Lin, W. C., Lien, C. C., Yeh, H. J., Yu, C. M., & Hsu, S. H. (2013). Bacterial cellulose and bacterial cellulose-chitosan membranes for wound dressing applications. *Carbohydrate Polymers*, *94*(1), 603-611. https://doi.org/10.1016/j.carbpol.2013.01.076

Malhotra, B., Keshwani, A., & Kharkwal, H. (2015). Antimicrobial food packaging: Potential and pitfalls. *Frontiers in Microbiology*, *6*, Article 611. https://doi.org/10.3389/fmicb.2015.00611

Oliveira, M. A., Gonzaga, M. L. C., Bastos, M. S. R., Magalhães, H. C. R., Benevides, S. D., Furtado, R. F., Zambelli, R. A., & Garruti, D. S. (2020). Packaging with cashew gum/gelatin/essential oil for bread: Release potential of the citral. *Food Packaging and Shelf Life*, *23*, Article 100431. https://doi.org/10.1016/j.fpsl.2019.100431

Revin, V., Liyaskina, E., Nazarkina, M., Bogatyreva, A., & Shchankin, M. (2018). Cost-effective production of bacterial cellulose using acidic food industry by-products. *Brazilian Journal of Microbiology*, *49*, 151-159. https://doi.org/10.1016/j.bjm.2017.12.012

Sharma, C., Bhardwaj, N. K., & Pathak, P. (2021). Static intermittent fed-batch production of bacterial nanocellulose from black tea and its modification using chitosan to develop antibacterial green packaging material. *Journal of Cleaner Production*, *279*, Article 123608. https://doi.org/10.1016/j.jclepro.2020.123608

Supian, N. N. I., Zakaria, J., Amin, K. N. M., Mohamad, S., & Sy Mohamad, S. F. (2021). Effect of fermentation period on bacterial cellulose production from oil palm frond (OPF) juice. *IOP Conference Series: Materials Science and Engineering*, *1092*, Article 012048. https://doi.org/10.1088/1757-899X/1092/1/012048

Szymańska, E., & Winnicka, K. (2015). Stability of chitosan-A challenge for pharmaceutical and biomedical applications. *Marine Drugs*, *13*(4), 1819-1846. https://doi.org/10.3390/md13041819

Tanpichai, S., Witayakran, S., Wootthikanokkhan, J., Srimarut, Y., Woraprayote, W., & Malila, Y. (2020). Mechanical and antibacterial properties of the chitosan coated cellulose paper for packaging applications: Effects of molecular weight types and concentrations of chitosan. *International Journal of Biological Macromolecules*, *155*, 1510-1519. https://doi.org/10.1016/j.ijbiomac.2019.11.128

Ul-Islam, M., Shah, N., Ha, J. H., & Park, J. K. (2011). Effect of chitosan penetration on physico-chemical and mechanical properties of bacterial cellulose. *Korean Journal of Chemical Engineering*, *28*, 1736-1743. https://doi.org/10.1007/s11814-011-0042-4

Wahid, F., Hu, X. H., Chu, L. Q., Jia, S. R., Xie, Y. Y., & Zhong, C. (2019). Development of bacterial cellulose/chitosan based semi-interpenetrating hydrogels with improved mechanical and antibacterial properties. *International Journal of Biological Macromolecules*, *122*, 380-387. https://doi.org/10.1016/j.ijbiomac.2018.10.105

Yusof, S. J. H. M., Roslan, A. M., Ibrahim, K. N., Abdullah, S. S. S., Zakaria, M. R., Hassan, M. A., & Shirai, Y. (2019). Life cycle assessment for bioethanol production from oil palm frond juice in an oil palm based biorefinery. *Sustainability*, *11*(24), Article 6928. https://doi.org/10.3390/SU11246928

Zahari, M. A. K. M., Ariffin, H., Mokhtar, M. N., Salihon, J., Shirai, Y., & Hassan, M. A. (2012). Factors affecting poly(3-hydroxybutyrate) production from oil palm frond juice by cupriavidus necator (CCUG52238 T). *Journal of Biomedicine and Biotechnology*, *2012*, Article 125856. https://doi.org/10.1155/2012/125865

Pertanika J. Sci. & Technol. 31 (3): 1189 - 1207 (2023)

PERTANIKA JOURNALS

SCIENCE & TECHNOLOGY

Journal homepage: http://www.pertanika.upm.edu.my/

Effect of Moisture Content on Frictional Properties of Some Selected Grains in Indonesia

Nursigit Bintoro*, Alya Iqlima Zahra, Azizah Putri Khansa, Muftia Chairin Nissa, Aldhayu Sam Safira and Sastika Nidya Ashari

Department of Agricultural Engineering and Biosystem, University of Gadjah Mada, Yogyakarta 55281, Indonesia

ABSTRACT

The frictional property of grains is one of the most important engineering parameters in developing solid bulk handling of grains. It is necessary for designing agricultural facilities and production process activities. These properties are expressed as internal friction angle (φ) and wall friction angle (θ), which are known to be affected by the moisture content of the grains. This research investigates the effect of moisture content on the values of φ and θ of some selected grains. In the research, some indigenous Indonesian grain types, including rough rice, white rice, corn, soybean, and coffee, each in three varieties and three level of moisture contents, were used as the research samples. Those angles were measured using a self-constructed direct shear cell apparatus. Three different normal loads for each grain type were used with three replications. It is concluded that φ and θ of the tested grains increase with moisture contents with different trends of increments. The relationship of those angles with moisture contents can be expressed as linear regression equations. The slope of the regression lines for both φ and θ is significantly affected by grain type (p<0.05). For φ, coffee (*Excelsa*) is the most susceptible to the change in moisture content, while dent corn (*Hibrida*) is the least affected one. For θ, soybean (*Galunggung*) is the most susceptible to the change in moisture content, while rough rice (*Mapan 5*) is the least affected one.

Keywords: Direct shear cell, grain, moisture content, φ, θ

ARTICLE INFO

Article history:
Received: 09 June 2022
Accepted: 16 August 2022
Published: 31 March 2023

DOI: https://doi.org/10.47836/pjst.31.3.04

E-mail addresses:
nursigit@ugm.ac.id (Nursigit Bintoro)
alyaiqlimazahra88@gmail.com (Alya Iqlima Zahra)
azizahputrik@gmail.com (Azizah Putri Khansa)
muftiachairin@gmail.com (Muftia Chairin Nissa)
aldhyusfra@gmail.com (Aldhayu Sam Safira)
swastika.nidyaa@gmail.com (Sastika Nidya Ashari)
*Corresponding author

ISSN: 0128-7680
e-ISSN: 2231-8526

© Universiti Putra Malaysia Press

INTRODUCTION

Indonesia is an agricultural country located in the tropics. Therefore, the climate conditions in Indonesia support the cultivation of perennial plants and annual crops all year round. It causes abundant agricultural products yearly in Indonesia, especially for grains such as rough rice, white rice, corn, soybean, and coffee. Various data sources have shown that the production of rough rice in Indonesia reaches 55,269,619.39 tons, white rice reaches 31,627,132 tons (BPS-Statistics Indonesia, 2021), corn 11,800,000 metric tons, soybean 480,000 metric tons (USDA, 2022), and coffee 726,000 tons (ICO, 2021). Indonesia is the third country with the largest paddy rice production (USDA, 2022) and the fourth country with the world's largest coffee export (ICO, 2021). This illustration may give an idea of how high grain production in Indonesia is yearly. However, high-grain productions are still handled manually in post-harvest activities. Harvesting is mostly done manually, transportation and storage are done using a sack while drying, cleaning, and other activities are still handled manually. This handling method has many drawbacks, such as high grain losses, high labor demand, high cost of production, slow handling activity, and finally results in inefficient post-harvest handling practices.

Presently, most post-harvest handling of cereal grains, especially maize, and sorghum, are done manually in Nigeria and other developing countries (Okolo et al., 2020). It is reported that in developing countries, crop harvesting activity is mainly conducted manually. Meanwhile, in developed countries, almost all crops are harvested using a combined harvester. It is reported that around one-third of the produced food is lost. This loss may occur during harvest and post-harvest periods due to problems in processing, handling, packing, transportation, and retail. One of the underlying causes of food losses is inadequate infrastructure (Vagsholm et al., 2020). It is common for many developing countries to have overall post-harvest losses of cereals and legumes reaching 10 to 15% (FAO, 2021). If it is related to the large grain production in Indonesia, the loss of grains will reach millions of tons yearly. The new postharvest handling methods should be investigated to save grain production in Indonesia.

Developed countries started handling grains mechanically in bulk long ago, and this method has been revealed to give very efficient postharvest handling in the grain production system. Material handling is moving and storing materials at the lowest possible cost using proper methods and equipment. Material handling is a very important step since this will handle the material properly, keep it from damage, and deliver it safely to the destination with the desired quality and conditions. Adequate material handling will give efficient handling and avoid accidents during the process (Alghalayini, 2020). In bulk grain handling, the grain is handled mechanically using various machines, from harvesting to storage. This method of handling is capable of handling very large grain volumes in every activity with minimum losses. Losses during the post-harvest period in developed countries are lower

than in developing countries due to more efficient farming systems, better transportation services, and other supported facilities (Pawlak & Kołodziejczak, 2020; Nicastro & Carillo, 2021). This high agricultural production needs to be handled quickly and efficiently to avoid high losses during postharvest.

In order to improve post-harvest grain handling in Indonesia, there is a need to change the method of grain handling from traditional and manual handling to modern mechanical bulk handling practices. Improvements in material handling have positively affected workers more than any other area of work design and ergonomics. Further, it is stated that the equipment for material handling has reduced the boredom of work. It reduces production costs and improves work-life quality for almost everyone in the modern industry (Stephens & Meyers, 2013). Developing and improving the machine in the agricultural area, commonly known as mechanization, can also overcome aging rural labor (Liu et al., 2021). It is also mentioned that mechanizing the post-harvest handling process using various equipment will add value to the process and product and minimize handling time (Okolo et al., 2020). However, problems arise in changing the handling method, such as the unavailability of research facilities and lack of data sources. Activities correlating to developing and promoting bulk grain handling are still very limited. Many challenges need to be solved, and it should start by increasing research activities related to bulk grain handling. In modern bulk grain handling, it is necessary to design the process, equipment, and machines to handle the grains scientifically.

This design process needs some information when dealing with grain properties. In general, the engineering properties of grains are very important for designing the basic parameters required for drying, storage, and equipment, particularly for their handling, processing, and storage (Bako & Bardey, 2020). This similar statement is also reported in various research works (Rodrigues et al., 2019; Wang & Wang, 2019; Fayed et al., 2020; Kaliniewicz et al., 2020; Etim et al., 2021; Kruszelnicka, 2021; Fadeyibi et al., 2021; Gierz et al., 2022).

One of the parameters needed to develop modern bulk grain handling is the friction properties of the grain, which are the internal friction angle (φ) and the wall friction angle (θ). φ is a quantification expressed in the angle value of the friction between the grain on itself, while θ is the angle formed when the grain slides on the surface of the wall material. These two parameters can be determined using direct shear cell apparatus. These values are needed in designing silos, hoppers, some conveyor types, and others. Parameters of φ and θ are among the basic parameters of bulk materials (Vagová et al., 2019). Knowledge of the frictional properties of plant materials is essential in designing mechanical units of machines and selecting parameters for many post-harvesting processes (Wójcik et al., 2020; Tang et al., 2021; Shi et al., 2022). A similar expression of the importance of frictional properties of the grain for machinery or facilities design is also pointed out by many other researchers (Wang & Wang, 2019; Li et al., 2020; Kopeć-Jarosz & Wójcik, 2021).

Frictional properties of agricultural grains are often measured using a direct shear cell. The direct shear test is widely used to determine frictional properties of agricultural materials for various purposes, such as designing storage structures, processing equipment, and machinery (Zeng & Wang, 2019; Mohite et al., 2019). In this apparatus, the grains are accommodated in the hole of the shear cell, then loaded with a certain normal weight, after which it is sheared by pushing one of the cells to move. This shearing process can calculate the magnitude of normal stress and shear stress. By varying the magnitude of the normal load, the related values of shear forces for each normal load applied will be obtained. Using Coulomb's theory, the angle of friction can be determined. It is done by graphically drawing the normal stress as the abscissa, and the shear stress as the ordinate, the angle of friction can then be determined from the slope of the line. Researchers in various works have also used this shear cell apparatus in their studies (Zou et al., 2020; Rasti et al., 2021; Tabari & Shooshpasha, 2021; de Oliveira et al., 2022; Zhu et al., 2022).

One of the most important factors which affect these angles is the moisture content of the grain. As the moisture content of the grain changes, the properties of the grain will also change, including the frictional properties of that grain. The effect of moisture content on the physical and mechanical properties of the grain is an important factor to be evaluated in determining machine design and storage facility (Jan et al., 2019). A similar statement is also conveyed by many other researchers (Dawange & Jha, 2019; Inekwe, 2019; Sadiku & Omogunsoye, 2021; Hasmadi, 2021; Wang et al., 2022). Therefore, it is necessary to find the relationship between φ and θ of the grains with their moisture contents. This research investigates the effect of moisture content on the φ and θ values of selected grains in Indonesia. The measurement methods, construction of the used apparatus, and the obtained values of these two parameters (φ and θ) will be very useful in developing modern bulk grain handling in Indonesia.

MATERIALS AND METHODS

Materials

In this research, indigenous Indonesian grains, including rough rice, white rice, corn, soybean, and coffee, each in three varieties or grain types, and three levels of moisture contents were used as the research samples. Two types of grains, i.e., *Koshihikar*i (japonica) and *Basmati* (indica) white rice, were not indigenous Indonesian grains, but they were included here to compare for indigenous white rice of *IR 64* (local). Those grain samples were chosen as they were the most commonly encountered grains in Indonesia; some were used as a staple food, such as white rice and corn, while others were mostly used as raw materials in several industries. The grain samples were bought from a local grain trader in Yogyakarta, Indonesia, while *Khosihikari* and *Basmati* white rice were bought through an online shop. Those grains were then transported to the laboratory, and some preparations

began. The grains were cleaned manually to discard the impurities, broken grain, and discolored grain, and only healthy whole grain was used in the experiment. The grains went through heating and wetting to create the desired moisture content for the experiment. After the grains achieved the desired moisture contents, they were packaged in a plastic bag and stored in cold storage to be further used as the sample in the experiment. Each of the grains was measured for their frictional properties at three different moisture contents. Average values of major, intermediate, and minor diameters of the grains used in the research are presented in Table 1, while grain types, range of tested moisture contents, and the applied vertical loads used in the research are presented in Table 2.

Table 1

Average values of major, intermediate, and minor diameters of the grains used in the research

Grain Types	a			b			c		
	Moisture content (% wb)								
White rice	**9**	**14**	**19**	**9**	**14**	**19**	**9**	**14**	**19**
Local (*IR 64*)	0.698	0.710	0.725	0.234	0.238	0.245	0.174	0.178	0.185
Japonica (*Koshihikari*)	0.513	0.521	0.534	0.303	0.319	0.322	0.209	0.224	0.227
Indica (*Basmati*)	0.882	0.898	0.921	0.194	0.204	0.208	0.159	0.172	0.175
Rough rice	**14**	**20**	**25**	**14**	**20**	**25**	**14**	**20**	**25**
Local (*Inpari 19*)	0.983	0.999	1.023	0.281	0.276	0.282	0.211	0.222	0.231
Local (*Mentik wangi*)	0.870	0.891	0.922	0.326	0.338	0.338	0.220	0.235	0.243
Local (*Mapan 5*)	0.998	1.070	1.107	0.269	0.284	0.287	0.210	0.229	0.243
Corn	**14**	**20**	**25**	**14**	**20**	**25**	**14**	**20**	**25**
Dent corn (*Local-Hibrida*)	1.126	1.166	1.273	0.799	0.813	0.944	0.422	0.433	0.498
Flint corn (*Local-Mutiara*)	1.026	1.068	1.125	0.816	0.872	0.909	0.429	0.478	0.493
Popcorn (*Imported*)	0.823	0.899	0.951	0.620	0.687	0.729	0.412	0.411	0.478
Soybean	**10**	**13**	**16**	**10**	**13**	**16**	**10**	**13**	**16**
Local (*Galunggung*)	0.680	0.787	0.855	0.567	0.662	0.717	0.452	0.549	0.572

Table 1 *(Continue)*

Grain Types	a			b			c		
	Moisture content (% wb)								
Local-Black (*Malika*)	0.757	0.791	0.845	0.570	0.621	0.632	0.413	0.460	0.490
Imported (*America*)	0.735	0.833	0.909	0.676	0.722	0.768	0.587	0.634	0.675
Coffee	**9**	**14**	**19**	**9**	**14**	**19**	**9**	**14**	**19**
Local (*Robusta*)	1.034	1.213	1.247	0.831	0.919	0.935	0.535	0.573	0.625
Local (*Arabica*)	0.919	0.977	1.101	0.711	0.711	0.769	0.471	0.505	0.525
Local (*Excelsa*)	0.952	0.972	1.119	0.671	0.714	0.796	0.483	0.486	0.538

**a, b*, and *c* were the grain's major, intermediate, and minor diameters (cm), respectively.

Table 2

Grain types, range of tested moisture contents, and the applied vertical loads used in the research

Grains Type	Moisture content (% wb)	Normal stress (kPa)	
		φ	θ
White rice			
Local (*IR 64*) Japonica (*Koshihikari*) Indica (*Basmati*)	9, 14, 19	27.6, 34.6, 41.5	6.9, 10.4, 13.8
Rough rice			
Local (*Inpari 19*) Local (*Mentik wangi*) Local (*Mapan 5*)	14, 20, 25	20.8, 27.7, 34.6	6.9, 13.8, 20.8
Corn			
Dent corn (*Local-Hibrida*) Flint corn (*Local-Mutiara*) Popcorn (*Imported*)	14, 20, 25	20.8, 27.7, 34.6	6.9, 13.8, 20.8
Soybean			
Local (*Galunggung*) Local-Black (*Malika*) Imported (*America*)	10, 13, 16	27.6, 34.6, 41.5	6.9, 13.8, 20.8
Coffee			
Local (*Robusta*) Local (*Arabica*) Local (*Excelsa*)	9, 14, 19	27.6, 34.6, 41.5	6.9, 10.4, 13.8

The applied vertical stresses ranged from 20.75 to 41.53 kPa and 6.92 to 20.75 kPa for the measurement of φ and θ, respectively. Various normal stresses were used in the research, with normal stresses of 1.209 to 6.045 kPa for barley malt and malt crush (Vagová et al., 2019). Normal stresses ranged from 100 to 250 kPa for root-soil composite (Sui et al., 2021). It was also reported that in measuring the frictional properties of rape seed, the used normal stresses ranged from 25 to 100 kPa for φ and θ (Xu et al., 2019). The emphasis of this research was to find the relationship between moisture content and the frictional properties of the grains; for that reason, the moisture content level used was not the same for all the tested grains. However, it was considered that the range of moisture contents used in this research falls within the range of moisture contents commonly encountered in real postharvest handling practices in Indonesia.

Direct Shear Cell

The measurement of φ and θ were carried out using a direct shear cell constructed for this research (Figure 1). The main parts of this apparatus consist of upper and lower shear cells, loadcell (Keli, AMI Sensing Technology, 50 kg), threaded shaft, direct current (DC) electric motor (RWB, 12V), DC speed regulator (10A), AC to DC adapter (SPC 20A/12V), Analog Digital Converter (Single Channel 24 Bit Digital Interface with USB, Loadstar DI-1000U), and a computer. The shear cells' upper and lower cells were made from square-shaped steel with a circular hole at the center. The dimension of the upper cell was 24.5 × 15.5 × 1 cm, with a center hole diameter of 9.5 cm, whereas the lower cell was 18.5 × 12.5 × 1 cm, with a center hole diameter of 9.5 cm. The upper cell was supported by four roller wheels 3 cm in diameter and rested on an adjustable constructed rail, while the lower cell was fixed on the table surface. For the measurement of θ, the lower cell was replaced by the wall sample, where in this experiment, it was stainless steel plate 32 × 12 × 0.5 cm. This wall sample was also fixed on the surface of the table.

The vertical position of the upper cell could be adjusted by adjusting the height of the rail. This adjustment was needed to ensure no contact between the upper and lower cells in the measurement of φ or between the upper cell and the wall sample plate in measuring θ; this clearance was around 1mm. A load cell was used to measure the values of shearing force during measurement. This load cell was installed using 4 bolts on a specially constructed frame at the edge of the pushing rod. This shearing force was inputted to the Analog Digital Converter (interface) and finally recorded in the computer. The normal load was applied manually by putting a certain known weight on the surface of the grain in the upper cell. Normal loads were chosen as needed in the measurement, especially depending on the grain's types. In this study, a pre-experiment was carried out to determine the range of reasonable normal load to find a good measurement result. It was found that the normal load range for white rice, soybean, and coffee was the same, while rough rice had the

same as corn. The normal load range was also different in the measurement of φ and θ. The shearing speed used in the measurement was around 3.0 mm/minute, which could be regulated by adjusting the DC speed regulator equipped in the apparatus.

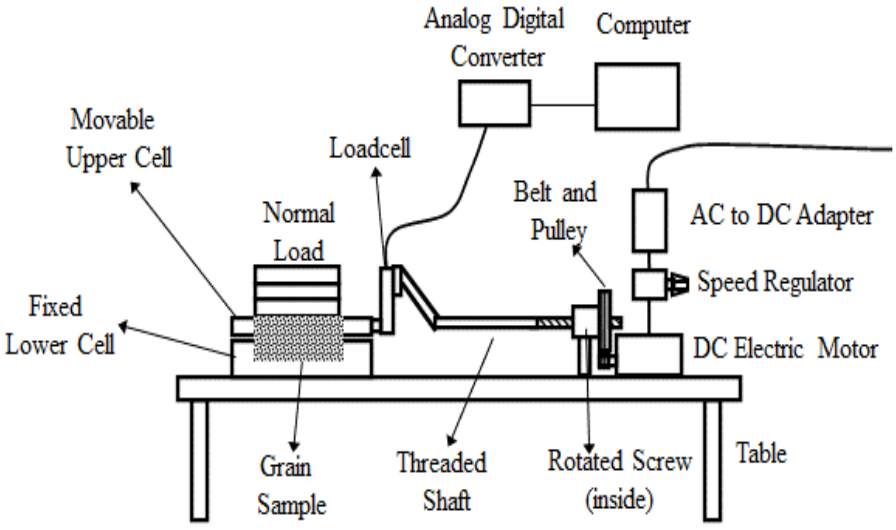

Figure 1. Constructed direct shear cell apparatus used in the experiment

Measurement of φ (Internal Friction Angle)

In this measurement, the first step was positioning the apparatus in the ready-for-measurement condition, with the upper and lower cell in parallel positions in the vertical direction, the grains were then poured into the hole of the cell, and the excess of the grain was gently cleaned using a steel plate so that it was aligned with the top cell surface. The desired normal/vertical load was gently put on the grain surface, then the apparatus was ready to be used for measurement. By turning on the electric motor, the threaded shaft would lengthen and push the upper cell, and the grain would be sheared. The shearing force was measured by loadcell and directly recorded in the computer through an ADC device. The shearing operation finished when the maximum shearing force had been achieved, as indicated by the computer monitor's constant value of the shearing curve. After the first measurement, the grain sample was removed, and the apparatus was again positioned in the ready-for-measurement condition. The next measurements were done the same way by using the new sample and replacing different normal loads as desired on the surface of the grains. Each grain sample was measured in three replications for each normal load used. Normal stress (σ) and shear stress (τ) were found by dividing normal load (P) and shear force (F) with the area of the cell hole (A), respectively. Assigning the shear stress as the ordinate and normal stress as the abscissa from the three measurements of different normal loads, a straight line could be drawn through the coordinate center, and the slope

of that line was known as tan φ. The value of φ in degree*s* was determined as the arctan φ, as shown in Equations 1 to 3.

$$\sigma = \frac{P}{A} \quad (1)$$

$$\tau = \frac{F}{A} \quad (2)$$

$$\varphi = \arctan\left(\frac{\tau}{\sigma}\right) \quad (3)$$

This analysis meant that the grains were treated as non-cohesive material or had no cohesion stress in the following research. For dry granular materials with particles larger than 100 µm, the interparticle forces were often neglected when determining their mechanical properties, and the granular material was considered non-cohesive (Larsson, 2019). Furthermore, agricultural grains were free-flowing bulk materials, and in structural design, the cohesion between grains was usually not taken into account (Bucklin et al., 2013). Typically, grains did not have a significant, cohesive force to create surface tension between two types of granular materials (McLaren et al., 2019). It was also reported that for loose sand, which was comparable to dry agricultural grains, the cohesion force should be neglected (Elyashiv et al., 2020).

Measurement of θ (Wall Friction Angle)

The measurement of θ was also carried out using the same apparatus used in the measurement of φ. The important difference was the replacement of the lower cell with a piece of wall sample and fixing it beneath the lower surface of the upper cell. Height adjustment should be made to ensure that the wall sample did not touch the cell; this was done by adjusting the height of the sample wall or the upper cell. The procedures of measurement and determination of the value of θ were the same as measuring the φ above; the difference was only in the normal loads used. In this research, the sample of wall material was only a stainless-steel plate (32 × 12 × 0.5 cm) with an average surface roughness of 0.4294 µm. It was done with the consideration that there were quite a lot of grains tested, and the purpose was to find the trend of the effect of moisture content on θ and was not intended to collect the value of θ of those grains on various wall materials. As was in the measurement of φ, the measurement of θ was also to find the values of normal stress (σ) and shear stress (τ) for each sample. The value of θ was determined from Equation 4.

$$\varphi = \arctan\left(\frac{\tau}{\sigma}\right) \quad (4)$$

Data Analysis

In this research, the values of φ and θ of 15 types of grain were evaluated in relation to their three levels of moisture contents. The collected data were analyzed using linear regression analysis to find the relationship between the friction angles of the grains with the moisture content to find the regression equations and the coefficients of determination. Further, as the ranges of moisture content of the tested grains were not the same in this research, the value of φ and θ was not directly subjected to statistical analysis. However, the slopes of regression equations of those friction angles were used in the statistical analysis using a one-way analysis of CRD (Completely Randomized Design), and the means were compared with DMRT (Duncan's Multiple Range Test) with a significant level of 0.05.

RESULTS AND DISCUSSION

Internal Friction Angle (φ)

Figure 2 presented the results of φ values from the 15 tested grains in three different moisture contents. It could be observed that the value of φ of the tested grains differed considerably, ranging from 20.95^{o} for white rice (*Koshihikari*) at 9% moisture content to 31.89^{o} for local soybean (*Galunggung*) at 16% moisture content. All grains indicated a significant increase of φ values with the increase in moisture contents. Similar phenomena were also reported in several research works (Xu et al., 2019; Brar et al., 2016). It was suspected that increasing grain moisture content caused the grain surface to become wetter so that it would increase the cohesive forces between grains and finally produce a larger φ value. In the range of the tested moisture contents, the increments of the φ values ranged from 7.82% for dent corn (*Hibrida*) to 23.13% for coffee (*Excelsa*).

It was reported that when moisture content increased from 6,56 to 11.16% (wb), the value of φ for rape seed increased by 27.47, 17.68, 14.27, and 11.08% for normal stress used of 25, 50, 75, and 100 kPa, respectively (Xu et al., 2019). These increments were comparable with the results from this study. The trends of the increment of φ differed among the tested grains, as shown by the steepness of the slope of those lines. These slopes ranged from 0.159 to 0.598, with an average of 0.363, in which the smallest slope was for dent corn (*Hibrida*), and the largest was for coffee (*Excelsa*). The higher the slope, the more susceptible the value of φ to the change in moisture content, and vice-versa. It meant that the value of φ for coffee (*Excelsa*) was the most susceptible to the change in moisture content, while dent corn (*Hibrida*) was the least affected one. It was possible that coffee (*Excelsa*) easily absorbed the moisture which accumulated on the kernel's surface, causing an increase in its cohesion force and finally producing a high φ value, while the opposite condition occurred for dent corn (*Hibrida*).

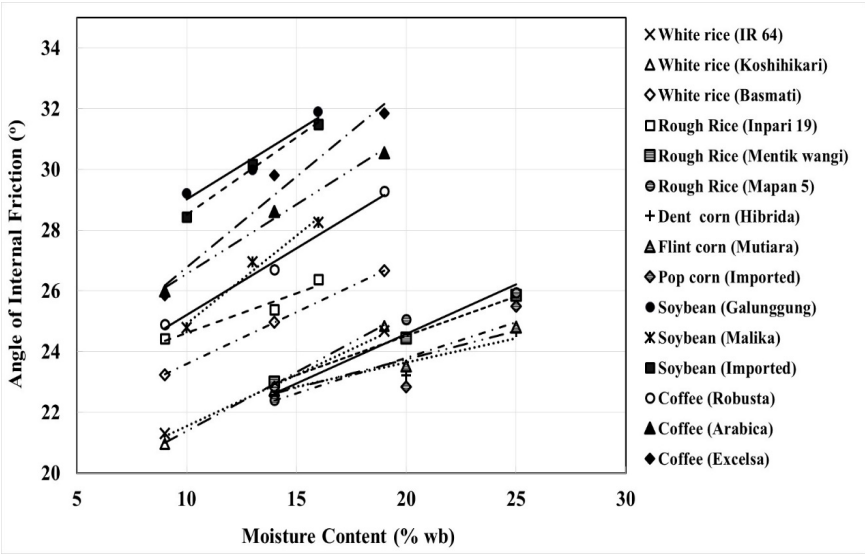

Figure 2. The values of φ as a function of moisture contents of the tested grains

The relationship between φ values and moisture contents of the grains could be expressed satisfactorily using linear regression, as indicated with high coefficients of determinations (Table 3). It was also reported that the relationship between φ and moisture content was linear for rape seed (Xu et al., 2019) and *Canarium schweifurthii* (Ehiem et al., 2015). Another study reported that the relationships between the coefficient of internal friction and moisture content were also linear for oat grain (Brar et al., 2016).

Statistical analysis indicated that the slopes of those regression lines were significantly influenced by grain type ($p<0.05$). This finding indicated that the frictional properties of each grain behaved differently in relation to the change in moisture content. This phenomenon was thought to be the effect of differences like the grain in relation to the change in its moisture content.

Table 3

Equations of the relationship between φ (y) and moisture content (x) of all tested grains

Grain Types	Equation	Coeff. of determination
White rice (*IR 64*)	y = 0.337x + 18.164	$R^2 = 0.99$
White rice (*Koshihikari*)	y = 0.389x + 17.481	$R^2 = 0.99$
White rice (*Basmati*)	y = 0.343x + 20.16	$R^2 = 1.00$
Rough rice (*Inpari 19*)	y = 0.177x + 21.92	$R^2 = 0.99$
Rough rice (*Mentik wangi*)	y = 0.259x + 19.344	$R^2 = 0.99$
Rough rice (*Mapan 5*)	y = 0.326x + 18.067	$R^2 = 0.95$

Table 3 *(Continue)*

Grain Types	Equation	Coeff. of determination
Corn (Dent corn, *Hibrida*)	y = 0.159x + 20.457	$R^2 = 0.85$
Corn (Flint corn, *Mutiara*)	y = 0.187x + 20.005	$R^2 = 0.96$
Corn (Popcorn, *Imported*)	y = 0.235x + 19.096	$R^2 = 0.71$
Soybean (*Galunggung*)	y = 0.448x + 24.528	$R^2 = 0.94$
Soybean (*Malika*)	y = 0.578x + 19.145	$R^2 = 0.98$
Soybean (*Imported*)	y = 0.508x + 23.425	$R^2 = 0.99$
Coffee (*Robusta*)	y = 0.439x + 20.811	$R^2 = 0.99$
Coffee (*Arabica*)	y = 0.456x + 22.003	$R^2 = 0.99$
Coffee (*Excelsa*)	y = 0.598x + 20.798	$R^2 = 0.97$

Table 4 compares the means using DMRT of the slopes for all tested grains. It was found that dent corn (*Hibrida*), rough rice (*Inpari 19*), flint corn (*Mutiara*), popcorn (*Imported*), and rough rice (*Metik wangi*) were not significantly different and belonged to the lowest values of line slope while soybean (*Malika*) and coffee (*Excelsa*) were not significantly different and had the largest slope values.

Table 4

Means comparison (DMRT) of the line slopes of the φ of the tested grains

Grain types	N	Slope means
White rice (*IR 64*)	3	0.3373^{cd}
White rice (*Koshihikari*)	3	0.3897^{def}
White rice (*Basmati*)	3	0.3429^{cde}
Rough rice (*Inpari 19*)	3	0.1766^{a}
Rough rice (*Mentik wangi*)	3	0.2586^{abc}
Rough rice (*Mapan 5*)	3	0.3256^{bcd}
Corn (Dent corn, *Hibrida*)	3	0.1591^{a}
Corn (Flint corn, *Mutiara*)	3	0.1873^{a}
Corn (Popcorn, *Imported*)	3	0.2350^{ab}
Soybean (*Galunggung*)	3	0.4482^{fg}
Soybean (*Malika*)	3	0.5861^{h}
Soybean (*Imported*)	3	0.5088^{gh}
Coffee (*Robusta*)	3	0.4385^{efg}
Coffee (*Arabica*)	3	0.4568^{fg}
Coffee (*Excelsa*)	3	0.5982^{h}

*The values followed with the same letter were not significantly different

For the same grain types, some of them were significantly different, while some of the others were the same. For example, white rice of *IR 64*, *Basmati*, and *Koshihikari* were not significantly different, and the same was true for corn grains. However, the coffee of *Excelsa* was significantly different from *Robusta* and *Arabica*; the same was true for rough rice and soybean grains.

Wall Friction Angle (θ)

Figure 3 presents the relationship between μ values and moisture contents for all tested grains. The same phenomenon could also be observed where the values of θ increased with moisture contents. The same phenomenon was also reported by other researchers (Dauda et al., 2019; Inekwe, 2019; Jan et al., 2019; Larsson, 2019; Mohite et al., 2019; Etim et al., 2021; Kopeć-Jarosz & Wójcik, 2021; Wang et al., 2022; Zhang et al., 2022). As can be observed, all the linear regression lines of the grains showed positive increments but differed in steepness, indicating that θ of the tested grains increased with moisture content. This increment was possibly caused by the fact that increasing moisture content would increase water content on the surface of the grain, causing the grain surface to become wetter, and this condition caused more intensive friction between the grain and the wall surface as the result of increasing adhesion force between the grain and wall sample. The same condition applied for φ values; the values of θ of the tested grains differed considerably, ranging from 10.83^{o} for rough rice (*Mapan 5*) at a moisture content of 14% to 24.76^{o} for white rice (*IR 64*) at 19% moisture content. However, as compared with the value of φ, the type of the grains and the values were different, where for φ, the lowest was 20.95^{o} for white rice (*Koshihikari*) at 9% moisture content, and the largest was 31.89^{o} for local soybean (*Galunggung*) at 16% moisture content. In general, the values of θ were considerably smaller as compared to the values of φ for all the grains tested.

The smoother sliding surface of the stainless-steel plate created less friction force to the grain than the friction force between the grain on itself and resulted in smaller values of θ. In the range of moisture contents tested, the increments of the μ values ranged from 1.521% for rough rice (*Inpari 19*) to 90.309% for white rice (*IR 64*), while in the same condition for φ, the values were 7.82% for dent corn (*Hibrida*) and 23.13% for coffee (*Excelsa*). White rice showed the largest increment, followed by soybean, coffee, and corn, whereas the smallest increments were found for rough rice. It was known that rice had an open surface so that when it was wet, the water would immediately react with the ingredients, making it stickier and causing an increase in its adhesion force and finally producing a high θ value as compared with the other tested grains. The opposite condition occurred in rough rice, as there was a husk layer on the grain.

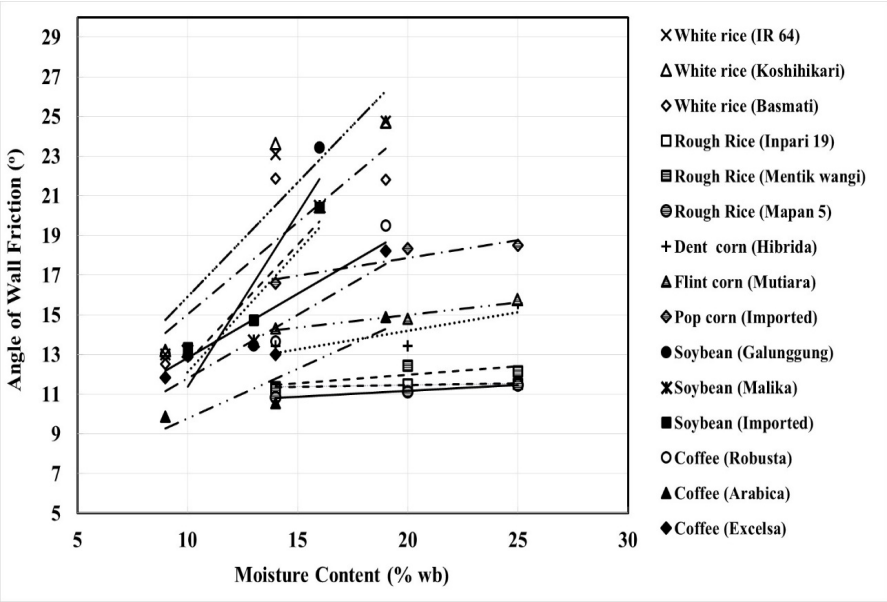

Figure 3. The values of θ as a function of moisture contents of the tested grains

The sliding friction coefficient of tiger nut on steel, aluminum, plexiglass, and polyurethane was reported to have a linear increase in moisture content (Zhang et al., 2022). The same phenomenon was reported for mucuna beans on plywood, aluminum, glass, galvanized steel, and rough wood (Etim et al., 2021). The trends of the increment of the θ values with the moisture contents also differed among the tested grains, as shown by the slopes of those lines. These slopes ranged from 0.016 to 1.745, with an average of 0.661, in which the smallest slope was for rough rice (*Mapan 5*) and the largest was for soybean (*Galunggung*). This phenomenon was also different from the condition for φ, where for φ values, these slopes ranged from 0.159 to 0.598, with an average of 0.363, in which the smallest slope was for dent corn (*Hibrida*), and the largest was for coffee (*Excelsa*). Table 5 summarizes the equations that explain the relationship between θ and the moisture content of the grains, along with their determination coefficients. These equations might approximate the values of θ of those grains on stainless steel for machinery or facility design. Statistical analysis indicated that the values of the slopes of those lines were significantly affected by the grain type (p<0.05). It strengthened the above finding that moisture content affected the frictional properties of the grains for the φ and θ in the same manner.

Table 5

Equations of the relationship between θ (y) and moisture content (x) of all tested grains

Grain Types	Equation	Coeff. of determination
White rice (*IR 64*)	y = 1.175x + 3.8411	R^2 = 0.85
White rice (*Koshihikari*)	y = 1.153x + 4.3818	R^2 = 0.82
White rice (*Basmati*)	y = 0.929x + 5.7212	R^2 = 0.75
Rough Rice (*Inpari 19*)	y = 0.016x + 11.14	R^2 = 0.81
Rough Rice (*Mentik wangi*)	y = 0.086x + 10.279	R^2 = 0.59
Rough Rice (*Mapan 5*)	y = 0.059x + 9.9933	R^2 = 0.99
Dent corn (*Hibrida*)	y = 0.188x + 10.446	R^2 = 0.71
Flint corn (*Mutiara*)	y = 0.128x + 12.434	R^2 = 0.94
Popcorn (*Imported*)	y = 0.179x + 14.31	R^2 = 0.85
Soybean (*Galunggung*)	y = 1.745x – 6.0685	R^2 = 0.79
Soybean (*Malika*)	y = 1.215x – 0.0244	R^2 = 0.80
Soybean (*Imported*)	y = 1.180x + 0.8301	R^2 = 0.89
Coffee (*Robusta*)	y = 0.648x + 6.3424	R^2 = 0.82
Coffee (*Arabica*)	y = 0.501x + 4.7656	R^2 = 0.85
Coffee (*Excelsa*)	y = 0.639x + 5.4058	R^2 = 0.88

From Table 6, it was also observed that for the same grain types, some of them were significantly different while some of the others were the same. Rough rice was not significantly different among all types tested, and the same was true for corn grains. However, *Arabica* coffee differed from *Excelsa* and *Robusta*; the same was true for white rice and soybean grains.

Table 6

Means comparison (DMRT) of the line slopes of θ of the tested grains

Grain types	N	Slope means	Grain types	N	Slope means
White rice (*IR 64*)	3	1.1750^{g}	Corn (Dent corn, *Hibrida*)	3	0.1877^{c}
White rice (*Koshihikari*)	3	1.1526^{g}	Corn (Flint corn, *Mutiara*)	3	0.1282^{bc}
White rice (*Basmati*)	3	0.9298^{f}	Corn (Popcorn, *Imported*)	3	0.1785^{c}
Rough rice (*Inpari 19*)	3	0.0913^{ab}	Soybean (*Galunggung*)	3	1.7451^{h}
Rough rice (*Mentik wangi*)	3	0.0848^{ab}	Soybean (*Malika*)	3	1.2180^{g}
Rough rice (*Mapan 5*)	3	0.0587^{a}	Soybean (*Imported*)	3	1.1803^{g}
Corn (Dent corn, *Hibrida*)	3	0.1877^{c}	Coffee (*Robusta*)	3	0.6476^{e}
			Coffee (*Arabica*)	3	0.5007^{d}
			Coffee (*Excelsa*)	3	0.6393^{e}

* The values followed with the same letter were not significantly different

CONCLUSION

It is concluded that both the values of φ and θ of the tested grains increased with moisture contents with different trends of increments. The relationship of those angles with moisture contents can be expressed as linear regression equations with high prediction coefficients. The slope of the regression lines for both φ and θ is found to be affected by grain type ($p<0.05$). For φ values, coffee (*Excelsa*) is the most susceptible to the change in moisture content, while dent corn (*Hibrida*) is the least affected one. For θ values, soybean (*Galunggung*) was the most susceptible to the change in moisture content, while rough rice (*Mapan 5*) was the least affected one.

ACKNOWLEDGMENTS

The authors wish to thank The Department of Agricultural Engineering and Biosystems, University of Gadjah Mada, Indonesia for providing laboratory facilities during the experiment.

REFERENCES

Alghalayini, R. (2020). *Improving an internal material handling system. A case study of a Swedish company in food industry*. Jönköping University, Sweden. https://www.diva-portal.org/smash/get/diva2:1458374/FULLTEXT01.pdf

Bako, T., & Bardey, I. A. (2020). Engineering properties of acha (*digitaria exilis*) grains in relation to the design of grain processing machines. *Agricultural Engineering International: CIGR Journal*, *22*(3), 159-170.

BPS-Statistics Indonesia. (2021). *Statistical Yearbook of Indonesia 2021*. Badan Pusat Statistik. https://www.bps.go.id/publication/2021/02/26/938316574c78772f27e9b477/statistik-indonesia-2021.html

Brar, H. S., Sidhu, G. K., & Singh, A. (2016). Effect of moisture content on engineering properties of oats (*Avena sativa* L.). *Agricultural Engineering International: CIGR Journal*, *18*(3), 186-193.

Bucklin, R., Thompson, S., Montross, M., & Abdel-Hadi, A. (2013). Grain storage systems design. In M. Kutz (Ed.), *Handbook of Farm, Dairy and Food Machinery Engineering*, (pp. 123-175). Elsevier. https://doi.org/10.1016/B978-0-12-385881-8.00007-0

Dauda, S. M., Ismail, F., Balami, A. A., Aliyu, M., Mohammed, I. S., & Ahmad, D. (2019). Physical and mechanical properties of raphia palm kernel at different moisture contents. *Food Research*, *3*(4), 305-312.

Dawange, S. P., & Jha, S. K. (2019). Moisture dependent physical properties of quality protein maize. *Journal of Agricultural Engineering*, *56*(3), 48-65.

de Oliveira, G. H. H., Corrêa, P. C., de Oliveira, A. P. L. R., Vargas-Elías, G. A., & Júnior, C. C. (2022). Arabica coffee flow properties assessed using different roasts and particle sizes during storage. *Brazilian Journal of Food Technology*, *25*, 1-12, https://doi: 10.1590/1981-6723.02621

Ehiem, J. C., Ndirika, V. I. O., & Raghavan, G. S. V. (2015). Frictional properties of canarium schweifurthii engl. fruits and their interaction with moisture content and shape. *International Journal of Engineering and Applied Sciences (IJEAS)*, *2*(8), 30-34.

Elyashiv, H., Bookman, R., Siemann, L., Brink, U., & Huhn, K. (2020). Numerical characterization of cohesive and non-cohesive 'sediments' under different consolidation states using 3D DEM triaxial experiments. *Processes*, *8*(10), Article 1252. https://doi.org/10.3390/pr8101252

Etim, P. J., Alonge, A. F., & Akpan, G. E. (2021). Effect of moisture content on some mechanical and frictional properties of mucuna bean (*Mucuna crens*) relevant to its cracking. *Agricultural Engineering International: CIGR Journal*, *23*(4), 265-273.

Fadeyibi, A., Lamidi, W. A., & Ademola, S. M. (2021). Engineering and proximate properties of miracle berry fruit (*Synsepalum dulcificum* L.). *Agricultural Engineering International: CIGR Journal*, *23*(4)*,* 227-235.

Fayed, M. I. A., El-Shal, M. S., & Omar, O. A. (2020). Determination of some apricot seed and kernel physical and mechanical properties. *Agricultural Engineering International: CIGR Journal*, *22*(4), 229-237.

FAO. (2021). *Post-harvest Losses*. Food and Agricultural Organization. https://www.fao.org/3/t0522e/T0522E04.htm#Post-harvest%20losses

Gierz, L., Kolankowska, E., Markowski, P., & Koszela, K. (2022). Measurements and analysis of the physical properties of cereal seeds depending on their moisture content to improve the accuracy of DEM simulation. *Applied Science*, *12*(2)*,* Article 549. https://doi: 10.3390/app12020549

Hasmadi, M. (2021). Effect of water on the caking properties of different types of wheat flour. *Food Research*, *5*(1), 266-270. https://doi: 10.26656/fr.2017.5(1).412

Inekwe, G., Kiniyi, B. U., Umunna, M., & Udensi, N. K. (2019). Effect of moisture content on physical properties of mung bean (*Vignaradiata* L.). *International Journal of Engineering Research*, *8*(07), 54-59.

International Coffee Organization. (2021). *Coffee Year Production by Country*. https://www.ico.org/prices/po-production.pdf

Jan, K. N., Panesar, P. S., & Singh, S. (2019). Effect of moisture content on the physical and mechanical properties of quinoa seeds. *International Agrophysics*, *33*(1), 41-48. https://doi.org10.31545/intagr/104374

Kaliniewicz, Z., Jadwisieńczak, K., Żuk, Z., Konopka, S., Frączyk, A., & Krzysiak, Z. (2020). Effects of friction plate hardness and surface orientation on the frictional properties of cereal grain. *International Journal of Food Science*, *2020*, Article 6639233. https://doi.org/10.1155/2020/6639233

Kopeć-Jarosz, A., & Wójcik, A. (2021). The impact of moisture and number of contact points on the process of friction in plant granular materials. *Processes, 9*(2), Article 215. https://doi.org/10.3390/pr9020215

Kruszelnicka, W. (2021). Study of selected physical-mechanical properties of corn grains important from the point of view of mechanical processing systems designing. *Materials*, *14*(6)*,* Article 1467. https://doi:10.3390/ma14061467

Larsson, S. (2019). *Particle Methods for Modelling Granular Material Flow*. [Doctoral dissertation]. Lulea University of Technology, Sweden. https://www.diva-portal.org/smash/get/diva2:1296317/FULLTEXT01.pdf

Li, X., Du, Y., Guo, J., & Mao, E. (2020). Design, simulation, and test of a new threshing cylinder for high moisture content corn. *Applied Science*, *10*(14), Article 4925. https://doi.org/10.3390/app10144925

Liu, J., S. Du, S., & Fu, Z. (2021). The impact of rural population aging on farmers' cleaner production behavior: Evidence from five provinces of the north China plain. *Sustain*, *13*(21), Article 12199. https://doi: 10.3390/su132112199

McLaren, C. P., Kovar, T. M., Penn, A., Müller, C. R., & Boyce, C. M. (2019). Gravitational instabilities in binary granular materials. *Proceeding of The National Academy of Science*, *USA*, *116*(19), 9263-9268. https://doi.org/10.1073/pnas.1820820116

Mohite, A. M., Sharma, N., & Mishra, A. (2019). Influence of different moisture content on engineering properties of tamarind seeds. *International Agricultural Engineering Journal*, *21*(1), 220-224.

Nicastro, R., & Carillo, P. (2021). Food loss and waste prevention strategies from farm to fork. *Sustainability, 13*(10), Article 5443. https://doi.org/10.3390/su13105443

Okolo C. A., Haruna S. A., Chukwu O., & Madu U. O. (2020). Comparative studies of material handling time for maize (*Zea mays*. Linn.) and sorghum (*Sorghum bicolor* L. Moench) in a typical 50 metric tonnes (MT)/hr Silo. *International Journal of Engineering Research and Technology*, *9*(1), 457-461.

Pawlak, K., & Kołodziejczak, M. (2020). The role of agriculture in ensuring food security in developing countries: Considerations in the context of the problem of sustainable food production. *Sustainability*, *12*(13), Article 5488. https://doi.org/10.3390/su12135488

Rasti, A., Adarmanabadi, H. R., Pineda, M., & Reinikainen, J. (2021). Evaluating the effect of soil particle characterization on internal friction angle. *American Journal of Engineering and Applied Sciences*, *14*(1), 129-138. https://doi: 10.3844/ajeassp.2021.129.138

Rodrigues, G. B., Resende, O., de Oliveira, D. E. C., Silva, L. C. M., & Junior, W. N. F. (2019). Mechanical properties of grains sorghum subjected to compression at different moisture contents. *Journal of Agricultural Science*, *11*(4), Article 279. https://doi: 10.5539/jas.v11n4p279

Sadiku, O. A., & Omogunsoye, D. (2021). Moisture - Influenced friction properties of ackee apple (*Blighia sapida*) seeds. *Research in Agricultural Engineering*, *67*(1), 26-33. https://doi: 10.17221/75/2020-RAE

Shi, G., Li, J., Ding, L., Zhang, Z., Ding, H., Li, N., & Kan, Z. (2022). Calibration and tests for the discrete element simulation parameters of fallen jujube fruit. *Agriculture*, *12*(1), Article 38. https://doi.org/10.3390/agriculture12010038

Stephens, M. P., & Meyers, F. E. (2013). *Manufacturing facilities design and material handling*. Purdue University Press.

Sui, Z. F., Yi, W., Lu, Y. G., & Deng, L. (2021). Experimental and numerical simulation study on the shear strength characteristics of magnolia multiflora root-soil composites. *Advances in Civil Engineering*, *2021*, Article 6642594. https://doi: 10.1155/2021/6642594

Tabari, S. A. M., & Shooshpasha, I. (2021). Evaluation of coarse-grained mechanical properties using small direct shear test. *International Journal of Geotechnical Engineering*, *15*(6), 667-679. https://doi.org/10.1080/19386362.2018.1505310

Tang, H., Xu, C., Jiang, Y., Wang, J., Wang, Z., & Tian, L. (2021). Evaluation of physical characteristics of typical maize seeds in a cold area of north China based on principal component analysis. *Processes*, *9*(7). Article 1167. https://doi.org/10.3390/pr9071167

United States Department of Agriculture. (2022). *World Agricultural Production*. United States Department of Agriculture, Foreign Agricultural Service. https://usdabrazil.org.br/

Vagová, A., Hromasová, M., Linda, M., & Vaculík, P. (2019). Determining external friction angle of barley malt and malt crush. *Agronomy Research*, *17*(5), 2106-2114. https://doi.org/10.15159/ar.19.149

Vagsholm, I., Arzoomand, N. S., & Boqvist, S. (2020). Food security, safety, and sustainability-getting the trade-offs right. *Frontier in Sustainable Food Systems*, *4*(16), 1-4. https://doi.org/10.3389/fsufs.2020.00016

Wang, B., & Wang, J. (2019). Mechanical properties of maize kernel horny endosperm, floury endosperm and germ. *International Journal of Food Properties*, *22*(1), 863-877. https://doi.org/10.1080/10942912.2019.1614050

Wang, J., Xu, C., Qi, X., Zhou, W., & Tang, H. (2022). Discrete element simulation study of the accumulation characteristics for rice seeds with different moisture content. *Foods*, *11*(3)*,* Article 295. https://doi: 10.3390/foods11030295

Wojcik, A., Fraczek, J., & Niemczewska-Wojcik, M. (2020). The relationship between static and kinetic friction for plant granular materials. *Powder Technology*, *361*, 739-747. https://doi.org/10.1016/j.powtec.2019.11.048

Xu, Q., Cheng, X., & Chen, X. (2019). Models for predicting frictional properties of rapeseed. *International Agrophysics*, *33*(1), 61-66. https://doi.org/10.31545/intagr/104377

Zeng, C., & Wang, Y. (2019). The shear strength and dilatancy behavior of wheat stored in silos. *Complexity, 2019*, Article 1547616. https://doi.org/10.1155/2019/1547616

Zhang, S., Fu, J., Zhang, R., Zhang, Y., & Yuan, H. (2022). Experimental study on the mechanical properties of friction, collision and compression of tiger nut tubers. *Agriculture*, *12*(1), Article 65. https://doi.org/10.3390/agriculture12010065

Zhu, Y., Miao, S., Li, H., Han, Y., & Lan, H. (2022). An empirical shear model of interface between the loess and hipparion red clay in a loess landslide. *Frontiers in Earth Science*, *9*, 1-18. https://doi.org/10.3389/feart.2021.806832

Zou, Z., Zhang, Q., Xiong, C., Tang, H., Fan, L., Xie, F., Yan, J., & Luo, Y. (2020). *In situ* shear test for revealing the mechanical properties of the gravelly slip zone soil. *Sensors*, *20*(22)*,* Article 6531. https://doi.org/10.3390/s20226531

Pertanika J. Sci. & Technol. 31 (3): 1209 - 1221 (2023)

PERTANIKA JOURNALS

SCIENCE & TECHNOLOGY

Journal homepage: http://www.pertanika.upm.edu.my/

Examination of the Partial Discharge Behaviour Within a Spherical Cavity in Insulation Paper of Transformer

Muhammad Hakirin Roslan[1,2], Norhafiz Azis[2,3]*, Mohd Zainal Abidin Ab Kadir[2], Jasronita Jasni[2] and Mohd Fairouz Mohd Yousof[4]

[1]Faculty of Engineering, Universiti Pertahanan Nasional Malaysia, 57000 Kem Sg Besi, Malaysia
[2]Advanced Lightning, Power and Energy Research Centre (ALPER), Universiti Putra Malaysia, 43400 UPM, Serdang, Selangor, Malaysia
[3]Institute of Nanoscience and Nanotechnology (ION2), Universiti Putra Malaysia, 43400 UPM, Serdang, Selangor, Malaysia
[4]Faculty of Electrical and Electronics Engineering, Universiti Tun Hussein Onn Malaysia, 86400 UTHM, Parit Raja, Johor, Malaysia

ABSTRACT

This paper investigates the behaviour of partial discharge (PD) in transformer insulation paper based on the Finite Element Method (FEM). The three-dimensional (3D) FEM model consists of conductor and insulation paper, representing part of a transformer's high voltage winding. The conductor's width, height, and length used in this study were 2.4 mm, 11.5 mm, and 16 mm. An insulation paper thickness of 1 mm was modelled around the conductor. An internal cavity with a diameter of 0.5 mm cavity was introduced within the insulation paper. This study introduced two locations of the spherical cavities at the centre and left corner of the insulation paper: Location 1 (L1) and Location 2 (L2). An AC voltage of 33 kV, 50 Hz, was applied to the conductor while the bottom of the insulation paper was grounded. The model was used to study the electric field distribution within the insulation paper and its effect on PD current and charge magnitude. The influence of cavity location on the charge magnitude was also examined. It is found that the electric field distribution is influenced by the conductor configuration as well as the location of the cavity. The electric field in the cavity is the highest at L1 compared to L2. The first PD occurs faster for the cavity with a high electric field. Due to the PD occurrence at the same inception field, the real PD current

ARTICLE INFO

Article history:
Received: 16 June 2022
Accepted: 13 September 2022
Published: 31 March 2023

DOI: https://doi.org/10.47836/pjst.31.3.05

E-mail addresses:
hakirin@upnm.edu.my (Muhammad Hakirin Roslan)
norhafiz@upm.edu.my (Norhafiz Azis)
mzk@upm.edu.my (Mohd Zainal Abidin Ab Kadir)
jas@upm.edu.my (Jasronita Jasni)
fairouz@uthm.edu.my (Mohd Fairouz Mohd Yousof)
* Corresponding author

ISSN: 0128-7680
e-ISSN: 2231-8526

© Universiti Putra Malaysia Press

and charge magnitude is similar at different locations. The apparent PD current and charge magnitude induced at the ground electrode is slightly higher at L1 than at L2.

Keywords: Insulation paper, partial discharge modelling, spherical cavity, transformer

INTRODUCTION

Among the critical equipment in the electrical power system network is transformers. Transformers can be subjected to different types of electrical issues, which can reduce their reliabilities. One common issue in the insulation of transformers is Partial Discharge (PD) (Hussain et al., 2021). PD is an electrical discharge that originates from a defective area within the insulation system (Naidu & Kamaraju, 2013). During the PD occurrence, solid insulation can degrade over time and extend to full electrical discharge. The most known defective areas are the void, cavity, and crack in the solid insulation (E-CIGRE, 2017). In recent years, PD assessment has become an important tool for evaluating the integrity of transformer insulation. Generally, the PD phenomenon is quite complex and requires further analyses through modelling the physical process. The electric field distributions before and after PD can be further evaluated based on the analyses.

The PD models with regard to a spherical cavity within solid dielectric material can be categorized into three capacitance, induced charge concept (ICC) and Finite Element Method (FEM) models (Illias et al., 2017). The three-capacitance or ABC model represents the model of PD as a capacitance circuit (Whitehead, 1952). This model is simple; however, the surface charge decay and charge accumulation along the cavity surface are not considered in the analysis. The PD occurrence of this model does not relate to the changes in capacitance as in the ICC model. The ICC model is derived based on the phenomenon of charge distribution on the cavity surface due to PD (Pedersen et al., 1995; Pedersen et al., 1991). The ICC model is also known as the analytical equation PD model, which is based on streamer-type PD whereby consideration on the surface charge accumulation on the cavity surface due to a PD occurrence is considered. The simulation time for the ICC model is short, but it is only suitable if the cavity size is small and has a uniform field distribution.

In recent years, the FEM model has been widely used for the PD model of a spherical cavity (Borghei et al., 2021; Illias et al., 2009, 2010, 2011a, 2011b, 2011c; Illias et al., 2012a; Illias et al., 2012b; Illias et al., 2015a, 2015b). This approach is promising for developing the PD model since it can be simulated dynamically. The FEM model solves the electric field distribution in a cavity numerically and can be applied to solve non-uniform electric field distribution. The electric field distribution during the PD process can also be obtained through the FEM model. The apparent and real charges based on the FEM model are also comparable with the experimental data (Borghei et al., 2021; Forssén & Edin, 2008; Illias, 2011; Illias et al., 2012a). The FEM model can be considered a reliable tool to simulate PD due to its credibility in simulating PD in complex geometry. The FEM

model has also been applied to examine the PD activities in cables (Anagha et al., 2018; Joseph et al., 2019).

This paper presents the investigation of PD behaviour within a spherical cavity in the insulation paper of a transformer through FEM modelling. The 3D model consists of a conductor, insulation paper and a spherical cavity, whereby it is developed and solved through a transient electric solver. The electric field distribution in the insulation paper with consideration of the spherical cavity is evaluated, and its effect on the PD current and charge magnitude is examined.

PARTIAL DISCHARGE MODELLING

Two important criteria need to be considered for PD modelling:

1. The electric field in the cavity should exceed the cavity PD inception field, E_{inc}.
2. The presence of the free electron initiates the ionization process.

The discharge process of PD can be delayed if there is no presence of the free electron, even though the electric field already exceeds the E_{inc}. Thus, the free electron in the cavity is a crucial parameter to initiate PD. The Electron Generation Rate (EGR) controls the number of free electrons in the cavity. Two main contributions of EGR are surface emission and volume ionization. Once all the requirements were satisfied, the discharge process simulation was initiated to model the PD occurrence. The simulation continued until the cavity's electric field was lower than the PD extinction field, E_{ext}.

PD Physical Parameter

Four parameters need to be acquired to model the PD. These parameters are known as the physical process parameter, which consists of the E_{inc}, E_{ext}, EGR and surface charge decay.

PD Inception Field. E_{inc} was determined based on Equation 1, where the PD was considered a streamer type (Borghei et al., 2021; Niemeyer, 1995; Pan et al., 2019).

$$E_{inc} = \left(\frac{E_1}{P}\right)_{cr} P\left(1 + \frac{B}{\sqrt{Pd}}\right) \qquad [1]$$

In the case of air, the ionization parameters for $(E_1/p)_{cr}$ and B are defined as 24.2 $VPa^{-1}m^{-1}$ and 8.6, respectively (Illias, 2011). P and d are the pressure and diameter of the cavity, respectively. Equation 1 can be simplified into Equation 2 if the cavity contains air.

$$E_{inc} = 24.2P\left(1 + \frac{8.6}{\sqrt{Pd}}\right) \qquad unit\ in \frac{V}{m} \qquad [2]$$

The pressure and diameter of the cavity were set to 100 kPa and 0.5 mm. Based on Equation 2, the computed E_{inc} was 5.4 kV/mm.

PD Extinction Field. E_{ext} is the minimum electric field required to stop the discharge process during the PD occurrence. E_{ext} was determined based on Equation 3, where the value was set to 10% of E_{inc} obtained from Equation 2 (Joseph et al., 2019).

$$E_{ext} = 0.1E_{inc} \qquad unit\ in \frac{V}{m} \qquad [3]$$

Electron Generation Rate (EGR). EGR in the cavity is one of the crucial parameters that control the condition of PD occurrence. The free electron must exist in the cavity to start the ionization process. The lack of the free electron will delay the PD occurrence even if the first condition of the cavity E_{inc} is already satisfied. The delay time from the time occurrence of E_{inc} to the time of PD occurrence was defined as statistical time lag, τ_{stat}. The EGR affects the τ_{stat}, which is contributed by the cavity surface emission and volume ionization (Illias et al., 2015a). The EGR contributed by the volume ionization was considered since only the first discharge was simulated in this study, whereby the free electron was always considered available. There was no free electron contributed by the surface emission and the surface charge decay effect since the subsequent discharge was not simulated in this study.

Discharge Process

Two methods to develop the discharge process during PD occurrence based on the FEM model are electrostatic and electric transient (Illias et al., 2017). This study used the electric transient method to model the discharge process based on the conductance model. The discharge channel was included in the model due to the high charge development in the cavity. As a result, the discharge process influenced the entire cavity, which increased the cavity conductivity from the initial value to a high value during the PD occurrence. It will lead to the decrement of the electric field in the cavity. Once the electric field in the cavity was less than the E_{ext}, the conductivity of the whole cavity was set to non-conducting. Figure 1 shows the flowchart of the discharge model for the first PD.

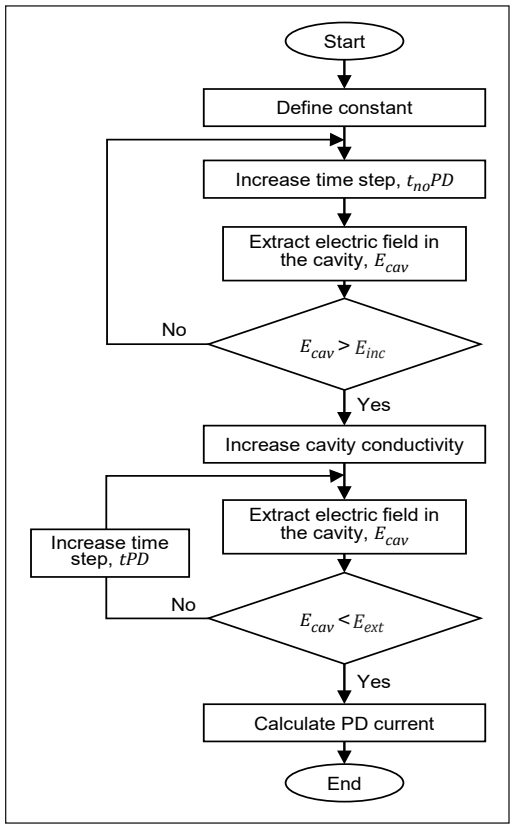

Figure 1. Flowchart of the discharge model

Model Geometry

Figure 2 shows the three-dimensional (3D) FEM model geometry of the insulation paper and conductor in Ansys Maxwell. The transient electric solver was used to solve the electric potential distribution in insulation paper. The model was modelled based on the part of the disc layered high voltage winding in a 33/11 kV, 30 MVA transformer.

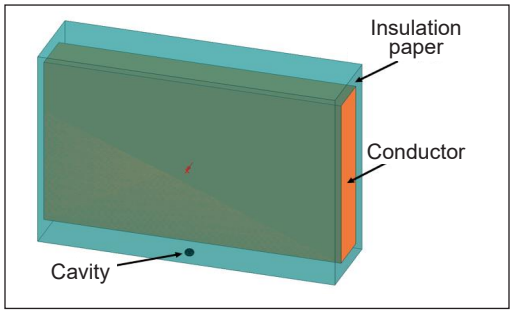

Figure 2. 3D FEM model of insulation paper and conductor of high voltage winding

The model consisted of conductor and insulation paper. To represent the defect area, a diameter of 0.5 mm cavity was located within the insulation paper. The detail of the geometrical design can be seen in Table 1 (Murthy et al., 2020).

In this study, there were two locations of the cavities, namely Location 1 (L1) and Location 2 (L2), as shown in Figure 3. L1 is the location of the cavity at the centre of the insulation paper, and L2 is the location of the cavity at the left corner of the insulation paper.

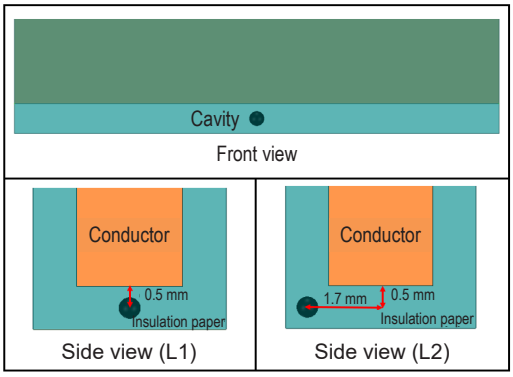

Figure 3. Two different cavity locations within the insulation paper

Simulation of Model

The electric potential calculation in the model was performed through the transient electric solver. The details of the other parameters for the simulation are shown in Table 2. A 33 kV, 50 Hz AC was supplied at the conductor while the bottom of the insulation paper was grounded. The simulation time was set to 100 µs during no PD to reduce the simulation time while maintaining the accuracy of the electric field in one time step. The time step during the occurrence of PD was set to 1 ns to maximize the accuracy in one time step due to the sudden reduction of the electric field in the cavity once the PD was initiated. The fast change in the electric field within the cavity was controlled by the conductivity during the

Table 1
Parameters for 3D Finite Element Method model

Parameters	Values
Power rating	30 MVA
High voltage winding rating	33 kV
Low voltage winding rating	11 kV
Height (conductor)	11.5 mm
Width (conductor)	2.4 mm
Length (conductor)	16 mm
The thickness of the insulation paper	1 mm
Cavity diameter	0.5 mm

discharge process. In this study, the conductivity during PD was set to 0.005 s/m to reduce the simulation time and avoid the fast reduction of the electric field. The apparent and real charges were determined based on the current integration flowing through the electrode and cavity centre surface area, as shown in Equations 4 - 7 (Borghei et al., 2021).

$$I_{real}(t) = \int_{S_{cav}} \overrightarrow{J(t)} . \vec{n}\ dS \quad [4]$$

$$I_{app}(t) = \int_{S_{ground}} \overrightarrow{J(t)} . \vec{n}\ dS \quad [5]$$

$$Q_{real} = \int_{t_{inc}}^{t_{ext}} I_{real}(t)\ dt \quad [6]$$

$$Q_{app} = \int_{t_{inc}}^{t_{ext}} I_{app}(t)\ dt \quad [7]$$

Where $\overrightarrow{J(t)}$ is the current density, S_{cav} is the cavity centre surface area, and S_{ground} is the ground electrode surface area. The t_{inc} and t_{ext} are the time occurrence of the inception and extinction fields.

Table 2
Parameter for partial discharge modelling of the insulation paper and cavity

Parameters	Values	Units
Insulation paper (relative permittivity), ε_{mat}	2.3	
Cavity (relative permittivity), ε_{cav}	1	
Insulation paper (conductivity), σ_{mat}	1×10^{-10}	s/m
Conductivity of cavity during no PD, $\sigma_{cav,0}$	0	s/m
Conductivity of cavity during PD, $\sigma_{cav,PD}$	5×10^{-3}	s/m
Simulation time step (no PD), t_{noPD}	100	µs
Simulation time step during PD, t_{PD}	1	ns

RESULTS AND DISCUSSION

Electric Field Distribution in the Paper Insulation for Different Locations of the Cavity

The electric field distribution in the insulation paper before the occurrence of the PD for the cavity at L1 can be seen in Figure 4. The electric field distribution at the centre of the cavity is higher than the insulation paper. It is expected since the cavity's relative permittivity is lower than the insulation paper. Since the cavity surface at the top and bottom is near the

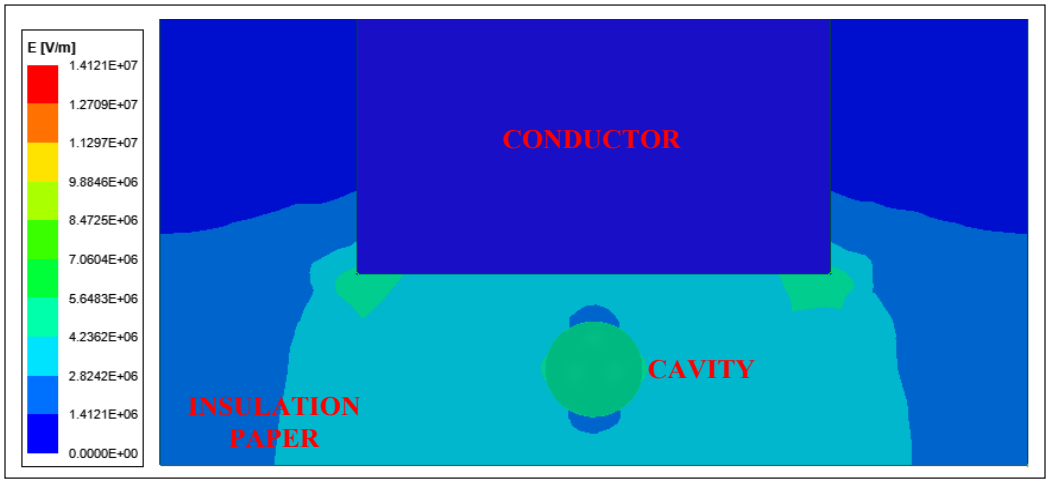

Figure 4. Electric field distribution before PD occurrence for cavity location at L1

electrode, the electric field distribution in the insulating paper is low at the top and bottom of the cavity surface. The electric field around the edges of the conductor is higher than the left and right of the insulation paper.

After the occurrence of the PD, the electric field inside the cavity rapidly decreases, as shown in Figure 5. It is due to the cavity conductivity being higher than the initial value during the discharge process. The highest electric fields are located at the top and bottom surfaces of the cavity. The conductor edge affects the electric field distribution in the insulation paper, which is higher at the centre than at the left and right of the insulation paper.

The electric field distribution in the insulation paper before the PD occurrence for the cavity at L2 is shown in Figure 6. The electric field distribution is higher at the centre of the insulation paper. It is due to the influence of the sharp edge of the conductor. The electric field in the cavity is slightly lower than the centre of the insulation paper since the cavity is slightly far from the centre of the insulation paper.

A similar pattern of the electric field distribution in the cavity compared to Figure 5 is found after the PD occurrence, as shown in Figure 7. During the PD occurrence, the cavity conductivity increases, allowing the PD pulse current to appear, which results in the electric field reduction in the cavity. The electric field distribution at the top surface of the cavity has a similar pattern in Figure 5, whereby the highest electric field is at the right of the conductor's edge.

The sharp edge of the conductor and the location of the cavity within the insulation paper can affect the electric field distribution in the system. Figure 8 shows the electric field in the cavity without the PD activity for one cycle. At the same electric potential injected at the conductor, the electric field at L1 is slightly higher than at L2. The time to reach the

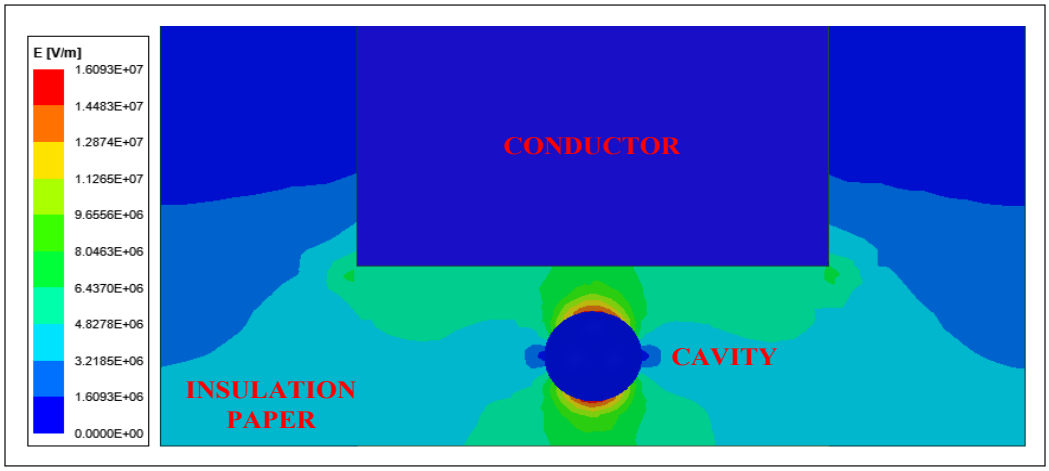

Figure 5. Electric field distribution after PD occurrence for cavity location at L1

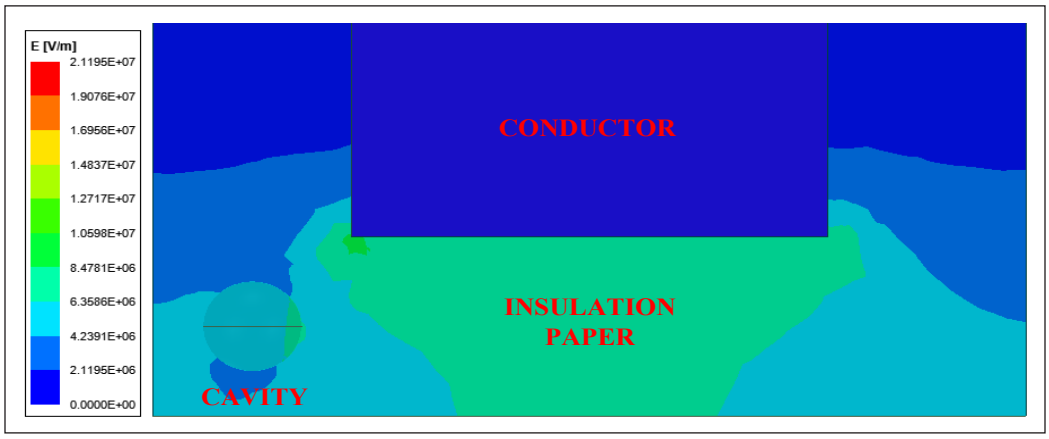

Figure 6. Electric field distribution before PD occurrence for cavity location at L2

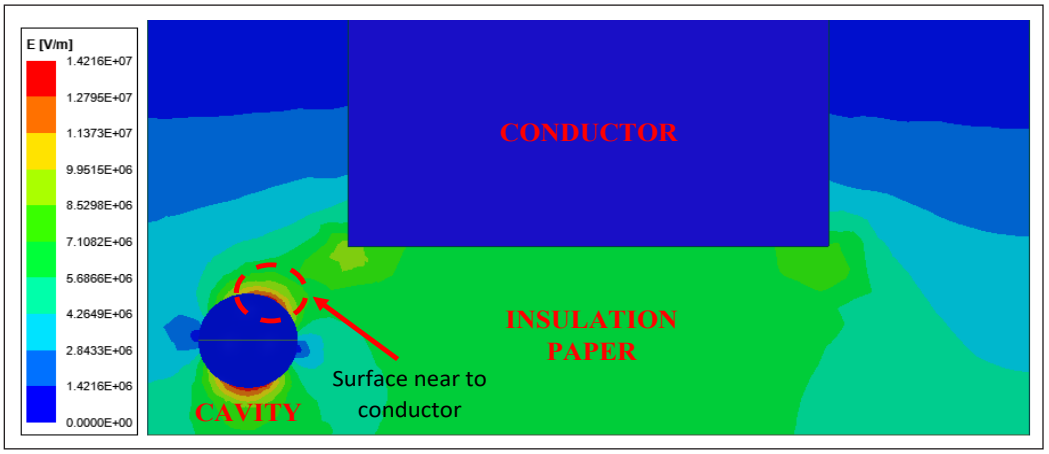

Figure 7. Electric field distribution after PD occurrence for cavity location at L2

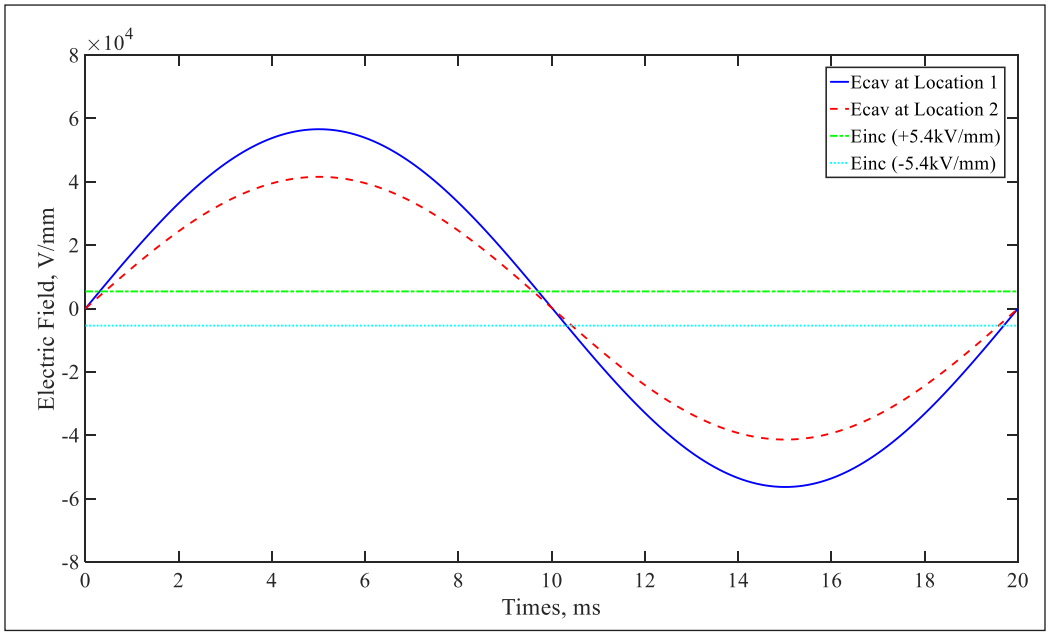

Figure 8. Electric field in the cavity versus time for one cycle in the absence of PD activity

E_{inc} is faster at L1 than at L2. It is due to the sharp edge of the conductor as well as the location of the cavity in the insulation paper.

PD Current and First Discharge Magnitude as A Function of Cavity Location

The simulated real and apparent PD currents for different cavity locations can be seen in Figure 9. The real PD current recorded at L1 is close to L2 since the first PD occur at the same E_{inc} due to the same cavity size. However, the PD occurrence time is different because the electric field in the cavity at L1 is slightly higher than at L2, which can be seen in Figure 8. The simulated apparent PD current at L1 is slightly higher than at L2. The difference is affected by the cavity's location and the electric field distribution in the insulation paper.

The simulated real and apparent charge magnitudes for different cavity locations are shown in Figure 10. The charge magnitude was obtained from the integrated PD current. The real and apparent charges range for both locations from 0.015 to 0.05 nC. The electric field distribution in the insulation paper affects the apparent charge magnitude induced at the ground electrode, where its value at L2 is slightly lower than L1. The real charge magnitude is close at both locations.

The electric field distribution in the insulation paper is influenced by the shape of the conductor as well as the electric field in the cavity, which depends on the cavity's location. The highest electric field distribution is found at the centre of the insulation

paper, which is close to the sharp edges of the conductor. The electric field in the cavity at L1 is the highest. The shape of the conductor is expected to affect the subsequent PD and its intensity due to its influence on the electric field distribution in insulation paper. The location of the cavity can also affect the PD current and charge magnitude due to the differences in the electric field distribution.

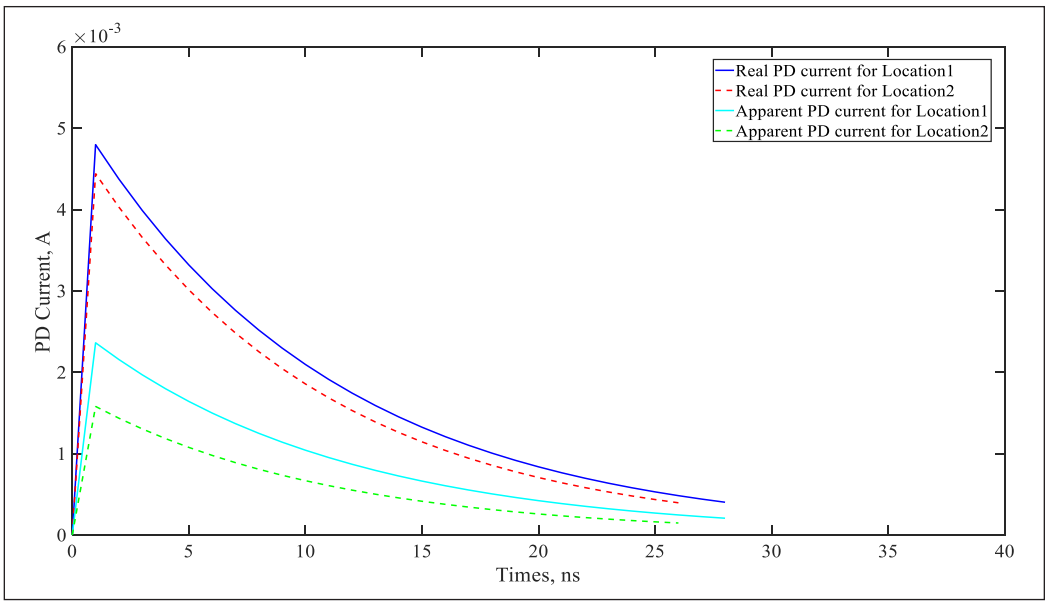

Figure 9. Real and apparent PD current for different cavity locations

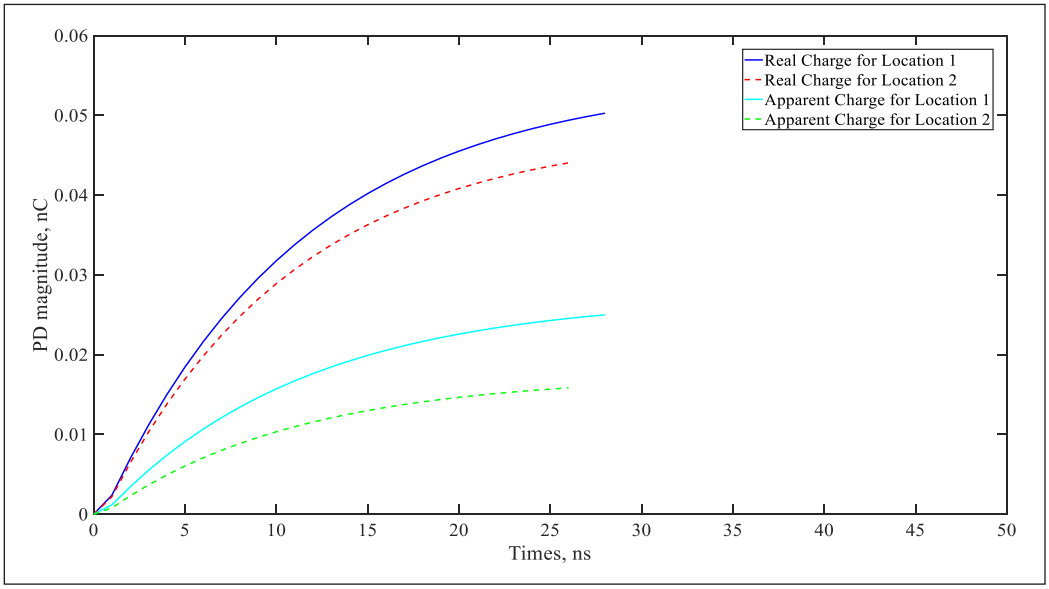

Figure 10. Real and apparent charge magnitudes for different cavity locations

CONCLUSION

In conclusion, PD modelling based on FEM can be used to examine the behaviour of PD in terms of electric field distribution as well as PD current and charge magnitude within a spherical cavity in the insulation paper of the transformer. The electric field distribution in the insulation paper is affected by the sharp edge of the electrode. This condition causes the electric field in the cavity to change dependent on the location of the cavity. The cavity location affects the first apparent PD current and charge magnitude induced at the ground electrode. The real PD current and charge magnitude of the first PD is similar at both cavity locations due to the PD occurrence at the same E_{inc}. The cavity location can affect the time of PD occurrence, whereby L1 is faster than L2.

ACKNOWLEDGMENT

The authors would like to express their sincere gratitude for the funding by the Matching Grant Universiti Putra Malaysia-Kyushu Institute of Technology (UPM.RMC/800/2/2/4/ Matching UPM-KYUTECH/2021/ 9300481). Special thanks to Advanced Lightning, Power and Energy Research (ALPER), UPM, for technical support to this research.

REFERENCES

Anagha, E. R., Joseph, J., & Sindhu, T. K. (2018). *A finite element method based approach for modeling of partial discharges in HVDC cables.* In *2018 Electrical Insulation Conference (EIC)* (pp. 533-537). IEEE Publishing. https://doi.org/10.1109/EIC.2018.8481089

Borghei, M., Ghassemi, M., Rodriguez-Serna, J. M., & Albarracin-Sanchez, R. (2021). A finite element analysis and an improved induced charge concept for partial discharge modeling. *IEEE Transactions on Power Delivery*, *36*(4), 2570-2581. https://doi.org/10.1109/tpwrd.2020.2991589

E-CIGRE. (2017). *Partial Discharges in Transformers*. e-cigre.org. https://e-cigre.org/publication/676-partial-discharges-in-transformers

Forssén, C., & Edin, H. (2008). Partial discharges in a cavity at variable applied frequency part 2: Measurements and modeling. *IEEE Transactions on Dielectrics and Electrical Insulation*, *15*(6), 1610-1616. https://doi.org/10.1109/TDEI.2008.4712664

Hussain, M. R., Refaat, S. S., & Abu-Rub, H. (2021). Overview and partial discharge analysis of power transformers: A literature review. *IEEE Access*, *9*, 64587-64605. https://doi.org/10.1109/access.2021.3075288

Illias, H. A., Chen, G., & Lewin, P. L. (2017). Comparison between three-capacitance, analytical-based and finite element analysis partial discharge models in condition monitoring. *IEEE Transactions on Dielectrics and Electrical Insulation*, *24*(1), 99-109. https://doi.org/10.1109/tdei.2016.005971

Illias, H. A., Tunio, M. A., Mokhlis, H., Chen, G., & Bakar, A. H. A. (2015a). Determination of partial discharge time lag in void using physical model approach. *IEEE Transactions on Dielectrics and Electrical Insulation*, *22*(1), 463-471. https://doi.org/10.1109/tdei.2014.004618

Illias, H. A., Tunio, M. A., Mokhlis, H., Chen, G., & Bakar, A. H. A. (2015b). Experiment and modeling of void discharges within dielectric insulation material under impulse voltage. *IEEE Transactions on Dielectrics and Electrical Insulation*, *22*(4), 2252-2260. https://doi.org/10.1109/tdei.2015.004817

Illias, H. A., Chen, G., & Lewin, P. L. (2012a). Partial discharge within a spherical cavity in a dielectric material as a function of cavity size and material temperature. *IET Science, Measurement & Technology*, *6*(2), 52-62. https://doi.org/10.1049/iet-smt.2011.0091

Illias, H. A., Jian, L. T., Bakar, A. H. A., & Mokhlis, H. (2012b). Partial discharge simulation under various applied voltage waveforms. In *2012 IEEE International Conference on Power and Energy (PECon)*, (pp. 967-972). IEEE Publishing. https://doi.org/10.1109/PECon.2012.6450358

Illias, H. A. (2011). *Measurement and simulation of partial discharges within a spherical cavity in a solid dielectric material* [Doctoral dissertation]. University of Southampton, UK. https://eprints.soton.ac.uk/194921/

Illias, H. A., Chen, G., & Lewin, P. L. (2011a). The influence of spherical cavity surface charge distribution on the sequence of partial discharge events. *Journal of Physics D: Applied Physics*, *44*(24), 245202. https://doi.org/10.1088/0022-3727/44/24/245202

Illias, H. A., Chen, G., & Lewin, P. L. (2011b). Partial discharge behavior within a spherical cavity in a solid dielectric material as a function of frequency and amplitude of the applied voltage. *IEEE Transactions on Dielectrics and Electrical Insulation*, *18*(2), 432-443. https://doi.org/10.1109/TDEI.2011.5739447

Illias, H. A., Chen, G., & Lewin, P. L. (2011c). Partial discharge behaviour within two spherical cavities in a dielectric material. In *2011 Annual Report Conference on Electrical Insulation and Dielectric Phenomena* (pp. 456-459). IEEE Publishing. https://doi.org/10.1109/CEIDP.2011.6232693

Illias, H. A., Chen, G., & Lewin, P. L. (2010). Comparison of partial discharge measurement and simulation results for spherical cavities within solid dielectric materials as a function of frequency using finite element analysis method. In *2010 IEEE International Symposium on Electrical Insulation* (pp. 1-5). IEEE Publishing. https://doi.org/10.1109/ELINSL.2010.5549733

Illias, H. A., Chen, G., & Lewin, P. L. (2009). *Partial* discharge measurements for spherical cavities within solid dielectric materials under different stress and cavity conditions In *2009 Annual Report Conference on Electrical Insulation and Dielectric Phenomena* (pp. 388-391). IEEE Publishing. https://doi.org/10.1109/CEIDP.2009.5377831

Joseph, J., Mohan, S., & Krishnan, S. T. (2019). Numerical modelling, simulation and experimental validation of partial discharge in cross-linked polyethylene cables. *IET Science, Measurement & Technology*, *13*(2), 309-317. https://doi.org/10.1049/iet-smt.2018.5248

Murthy, A. S., Azis, N., Jasni, J., Othman, M. L., Yousof, M. F. M., & Talib, M. A. (2020). Extraction of winding parameters for 33/11 kV, 30 MVA transformer based on finite element method for frequency response modelling. *PLoS One*, *15*(8), Article e0236409. https://doi.org/10.1371/journal.pone.0236409

Naidu, M. S., & Kamaraju, V. (2013). *High Voltage Engineering*. McGraw Hill.

Niemeyer, L. (1995). A generalized approach to partial discharge modeling. *IEEE Transactions on Dielectrics and Electrical Insulation*, *2*(4), 510-528. https://doi.org/10.1109/94.407017

Pan, C., Chen, G., Tang, J., & Wu, K. (2019). Numerical modeling of partial discharges in a solid dielectric-bounded cavity: A review. *IEEE Transactions on Dielectrics and Electrical Insulation*, *26*(3), 981-1000. https://doi.org/10.1109/tdei.2019.007945

Pedersen, A., Crichton, G. C., & McAIIister, I. W. (1995). The functional relation between partial discharges and induced charge. *IEEE Transactions on Dielectrics and Electrical Insulation*, *2*(4), 535-543. https://doi.org/10.1109/94.407019

Pedersen, A., Crichton, G. C., & McAlIister, I. W. (1991). The theory and measurement of partial discharge transients. *IEEE Transactions on Electrical Insulation*, *26*(3), 487-497. https://doi.org/10.1109/14.85121

Whitehead, S. (1952). Electrical breakdown of solids. *Nature, 170,* Article 219. https://doi.org/10.1038/170219a0

Pertanika J. Sci. & Technol. 31 (3): 1223 - 1244 (2023)

PERTANIKA JOURNALS

SCIENCE & TECHNOLOGY

Journal homepage: http://www.pertanika.upm.edu.my/

Sociodemographic Characteristics, Dietary Intake, and Body Image Dissatisfaction Among Saudi Adolescent Girls

Abeer Ahmad Bahathig[1,2], Hazizi Abu Saad[1]*, Nor Baizura Md Yusop[3], Nurul Husna Mohd Sukri[1] and Maha M. Essam El-Din[2,4]

[1]Department of Nutrition, Faculty of Medicine and Health Sciences, Universiti Putra Malaysia, UPM Serdang, Selangor 43400, Malaysia

[2]Department of Nutrition and Food Science, College of Home Economics, Northern Border University, Arar 91431, Saudi Arabia

[3]Department of Dietetics, Faculty of Medicine and Health Sciences, Universiti Putra Malaysia, UPM Serdang, Selangor 43400, Malaysia

[4]Department of Nutrition and Food Science, Faculty of Home Economics, Helwan University, Cairo 11795, Egypt

ABSTRACT

This study assesses sociodemographic characteristics, dietary intake and body image dissatisfaction (BID) among Saudi adolescent girls. A total of 399 girls ages 13-14 were randomly selected from intermediate schools in Arar, Saudi Arabia. Data on anthropometric measurements, sociodemographic characteristics, dietary intake and body image (BI) were collected. Multiple linear regression was used to predict the association between variables. Most adolescents had a normal weight based on their body mass index (BMI), normal waist circumference (WC), and normal waist-to-height ratio (WHtR). Fried chicken and Kabsa rice were the most frequently consumed foods; most girls consumed excessive fat. Most girls had BID (81.5%), and 51.4% desired to lose weight. BMI was positively correlated with age and current BI ($p<0.001$) and negatively associated with dairy product intake ($p=0.004$) and desired BI ($p<0.001$). WC had a positive association with age ($p=0.001$) and current BI ($p<0.001$) and a negative association with dairy product intake, cereal and grain intake ($p=0.001$) and ideal BI ($p<0.001$). WHtR was positively associated with current BI ($p<0.001$) and negatively associated with cereal and grain intake ($p=0.005$), dairy product intake and desired BI ($p<0.001$). Although most participants had a normal weight, they

ARTICLE INFO

Article history:
Received: 03 October 2021
Accepted: 18 April 2022
Published: 31 March 2023

DOI: https://doi.org/10.47836/pjst.31.3.06

E-mail addresses:
abeer-ahmad-b@hotmail.com (Abeer Ahmad Bahathig)
hazizi@upm.edu.my (Hazizi Abu Saad)
norbaizura@upm.edu.my (Nor Baizura Md Yusop)
n_husna@upm.edu.m (Nurul Husna Mohd Sukri)
mahaaessam82@gmail.com (Maha M. Essam El-Din)
* Corresponding author

ISSN: 0128-7680
e-ISSN: 2231-8526

© Universiti Putra Malaysia Press

consumed excessive fat and were dissatisfied with their BI, which are significant predictors of obesity. Saudi adolescent girls require nutritional interventions to help them transition to a healthy diet, positive BI and healthy lifestyle.

Keywords: Body image dissatisfaction, dietary intake, obesity, Saudi female, unhealthy food, waist-to-height ratio

INTRODUCTION

Obesity and overweight exacerbate health problems and the risk of noncommunicable diseases (NCDs), such as musculoskeletal disorders, some cancers, cardiovascular diseases, breathing difficulties and diabetes (WHO, 2021a). They pose a significant public health challenge among children and adolescents in countries with high, middle and low incomes (WHO, 2021a) (El Kabbaoui et al., 2018). In the United States, 14.4 million children and adolescents are obese (CDC, 2021). In Europe, one in three children is overweight or obese (Bell et al., 2019). A recent study on Saudi adolescent nutritional profiles reported that 15.8% and 14.2% of participants were obese and overweight, respectively (Musharrafieh et al., 2020).

The rapid economic growth of Saudi Arabia has coincided with negative changes in lifestyle, such as a shift toward high-caloric-density food consumption, which has been accompanied by an increase in NCDs (Al-Hazzaa, 2018). One study found that 19.4% of Saudi females consumed a large amount of unhealthy food, while 21.1% and 60.4% consumed less healthy foods, such as French fries and chocolate, respectively, for ≥ 3 days (Alzamil et al., 2019). Saudi adolescents consume large quantities of fat, carbohydrates and proteins, especially among obese subjects (Al-Kutbe et al., 2017). A systematic review revealed that Middle Eastern children, including Saudis, engaged in several unhealthy dietary behaviours. These included consuming excessive amounts of refined carbohydrates and fat and having a low intake of vegetables, fruits and dairy products, increasing their risk of obesity (Albataineh et al., 2019). An unhealthy diet is an NCD risk factor (WHO, 2021b). It must be addressed in the adolescent period to prevent NCDs from becoming more prevalent in adults (Draper et al., 2015). Consequently, nutritionists recommend that adolescents consume healthy foods, including whole grains, vegetables and fruits, and limit their junk food consumption to promote a healthy lifestyle and avoid risky behaviours (Tabbakh & Freeland-Graves, 2016; WHO, 2021a). It would support their growth and development (Hijji et al., 2021).

Adolescence involves physical, intellectual, psychological, cognitive and social changes between childhood and adulthood (WHO, 2021c); it affects adolescent bodies' weight, shape and appearance (Voelker et al., 2015). Family members, friends, gender and age, play a role in shaping one's body image (BI) (Cafri et al., 2005). However, adolescents with negative BI are more likely to adhere to an unhealthy lifestyle involving behaviours

such as disordered eating (Cruz-Sáez et al., 2020). Obesity and body image dissatisfaction (BID) are linked to depression and low self-esteem. However, those who are obese are not all equally prone to BID, and this association may also exist among those with normal body weight (Weinberger et al., 2016). A previous study indicated that body mass index (BMI) was significantly associated with the proportion of BID (p<0.001) among Saudi females (Albawardi et al., 2021). Therefore, a key to weight management and health is body satisfaction and a healthy self-perception (Lynch et al., 2009; Radwan et al., 2019). The results indicated that the percentage of underweight Saudi adolescent girls who wanted to lose weight between the ages of 10 and 14 years was 16%, and it was 5% for boys (Hijji et al., 2021). Khalaf et al. (2015) found that only 23.3% of Saudi female adolescents were satisfied with their ideal, visible and current BI, while most desired a thinner body shape. Children and adolescents with BID are generally at risk of being inactive, eating uncontrollably, smoking or exhibiting depression (Baceviciene et al., 2020; Bray et al., 2018).

To our knowledge, many Saudi adolescent studies focus on the connections between dietary intake, BI and anthropometric measurements. The current study aims to assess sociodemographic characteristics, dietary intake and BID and to predict their association with anthropometric measurements among Saudi adolescent girls between 13 and 14 in Arar.

METHODOLOGY

Design and Location of the Study

This cross-sectional study was carried out in September-October 2019 in Arar City, located in the northern border region of Saudi Arabia. Saudi female adolescent students were recruited from government schools randomly. Among Arar's 22 all-girl public intermediate schools, one school from each identified region was randomly selected (Figure 1).

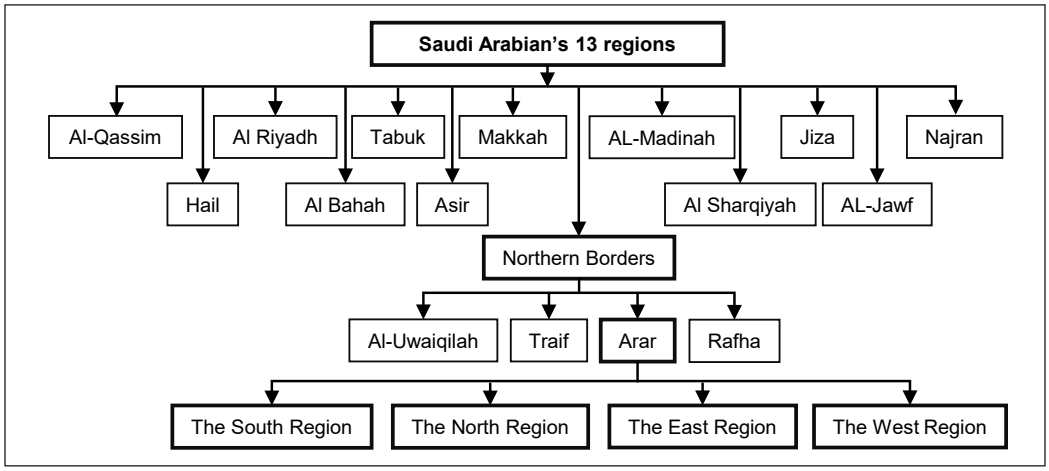

Figure 1. Recruitment of participants in Arar, Saudi Arabia

Ethical Considerations

Ethical approval was obtained from the Ministry of Education, the Local Committee of Bio-Ethics HAP-09-A-043 at Northern Border University, Arar, Saudi Arabia (reference no. 13/40/H) and the research ethics committee of Universiti Putra Malaysia involving human subjects (reference no. UPM/TNCPI/RMC/JKEUPM/1.4.18.2 (JKEUPM)) to conduct this study. Participation was voluntary. The participants and their parents signed an informed consent form to participate. The purpose of the study was explained to them before the study commenced. The identities of the participants were kept confidential.

Participants and Sample Size

The researchers recruited only Saudi girls (13–14 years old) who enrolled in an intermediate public school in Arar during the 2019–2020 academic year. The sample size was calculated using the commonly used formula of Lemeshow et al. (1990). A total of 399 participants were obtained, indicating a 93.2% response rate. The inclusion and exclusion criteria details and sample size determination were previously published elsewhere (Bahathig et al., 2021).

Data Collection

The researcher provided face-to-face guidance to the students who were asked to complete the questionnaire, which consisted of sociodemographic characteristics, food habits and BID. Anthropometric indicator data were measured for all students.

Sociodemographic Characteristics. In addition to specifying their age and date of birth, the participants indicated their number of siblings and household members, the education levels of their mothers and fathers and monthly income in the sociodemographic data.

Participants' Anthropometries. All measurements were repeated twice for accuracy, and further analysis was conducted using the mean value. The participants were initially asked to remove their shoes, wear light clothes, stand up straight, hold their heads upright and relax their shoulders and arms at their sides. The girls' body weight and height were measured using a special digital body weight scale (Detecto solo Digital Clinical Scale; Webb City, MO, USA) to the nearest 0.1 kg and 0.1 cm, respectively. According to a growth reference for girls aged 5–19, body mass index-for-age (BMI z-score) was measured. BMI was categorised as follows: (thinness: < -2 standard deviation SD; normal weight: ≤ 2 SD and ≥ 1 SD; overweight: $> +1$ SD; and obesity: $> +2$ SD) (WHO, 2021d). A non-stretchable tape marked in centimetres was used to measure the waist circumference (WC) in the area between the iliac crest and the last rib of the ribcage to the nearest 0.1 cm. The cut-off points were 77 cm (obesity) and 72.3 cm (overweight) (Motlagh et al., 2018). Waist-to-height

ratio (WHtR) was calculated in centimetres by dividing WC by height. WHtR ≥ 0.5 was considered abdominal obesity (Maffeis et al., 2008).

Assessment of Food Habits. The Arabic version (original) of a semi-quantitative food frequency questionnaire (SFFQ) developed by Almajwal et al. (2018) was used to assess the dietary intake of the participants. The SFFQ involves 74 food items categorised into once, 2–3, 4–5 and 6–7 times/day; 1–2, 3–4 and 5–6 times/week; once and 2–3 times/monthly; and never. The nutrient and food groups had an average percentage agreement of 70.1% and 70.9%, respectively (Almajwal et al., 2018). The participants were asked to determine the food they consumed and its size. The mean score of calories for each type of food, the 10 most and least frequently consumed food and the frequency of consumption of food groups were determined using Nutritionist Pro™ Diet version 6 (Axxya Systems, USA; Axxya Systems, 2014). According to the guidelines provided by Hackshaw (2014), food items with a frequency of ≥ 0.5 were referred to as the most frequently consumed food.

Assessment of Body Image Dissatisfaction (BID). Figure drawings or questionnaires are usually used to assess BI (Moehlecke et al., 2020). BID in this study was determined by adopting the Stunkard Figure Rating Scale (Stunkard, 1983). The test–retest of this scale was 0.8 (Cardinal et al., 2006). The scale is reliable in a wide range of populations, including the Middle East; it consisted of nine figures coded from (one) thinnest to (nine) heaviest (McElhone et al., 1999; Shaban et al., 2016). Each participant was required to choose a figure representing her present image, the desired BI and the perfect BI figure based on her perception. BID was calculated as follows: desired BI minus current BI. A score is other than zero means that the participants were unsatisfied with their BI (Sánchez et al., 2018). The pre-test was conducted among 30 students to ensure the scale was appropriate and understandable.

Statistical Analysis

SPSS Statistics for Windows (version 25; Chicago, USA) was used for data analysis, with a 95% confidence interval (CI). The mean, standard deviation, percentage and frequency were used to present the data. The chi-square test was used to determine the correlation between the actual BMI and the perceived BMI. A multiple linear regression model was used to determine the association between the anthropometric measurements and the variables. A p-value < 0.05 was considered statistically significant.

RESULTS

Study Sample and Anthropometric Measurements

Table 1 shows the sociodemographic characteristics of the 399 girls aged 13–14 years who were satisfied (N = 74; 18.5%) and dissatisfied with their BI (N = 325; 81.5%).

Approximately 52.9% of the girls with BID reported having 5–10 siblings, and 76.9% had 5–10 family members. Among the participants, 48.3% and 54.8% of the girls' mothers and fathers had at least some college education, respectively. Among the girls who were satisfied with their BI, 54% and 78.3% had 5–10 siblings and lived with 5–10 household members, respectively. Among them, 47.3% and 54.1% of the girl's mothers and fathers obtained a university education or higher, indicating that most participants had educated parents.

Table 1
Participants' sociodemographic data and anthropometric indicators

Items	Body image satisfaction (BIS), (N=74)		Body image dissatisfaction (BID), (N=325)		
	Mean (SD)	**N (%)**	**Mean (SD)**	**N (%)**	***p*-value**
Age group (years)	13.39±.49		13.32±0.47		0.258
School(s)					0.795
The Northern Region		22(29.7)		88(27.1)	
The South Region		20(27.0)		91(28.0)	
The East Region		11(14.9)		63(19.4)	
The West Region		21(28.4)		83(25.5)	
Number of Siblings					0.500
< 5		29(39.2)		140(43.1)	
5 - 10		40(54.0)		172(52.9)	
> 10		5(6.8)		13(4.0)	
Number of households					0.750
< 5		3(4.1)		14(4.3)	
5 - 10		58(78.3)		250(76.9)	
> 10		13(17.6)		61(18.8)	
Mother's education					0.923
Intermediate school or lower		15(20.3)		70(21.5)	
High school		24(32.4)		98(30.2)	
Undergraduate or higher		35(47.3)		157(48.3)	
Father's education					0.347
Intermediate school or lower		6(8.1)		44(13.5)	
High school		28(37.8)		103(31.7)	
Undergraduate or higher		40(54.1)		178(54.8)	
Family monthly income (SAR) *					0.462
< 5000		8(10.8)		49(15.1)	
5000 - 14999		38(51.4)		160(49.2)	
≥ 15 000		28(37.8)		116(35.7)	

Table 1 *(continue)*

Items	Body image satisfaction (BIS), (N=74)		Body image dissatisfaction (BID), (N=325)		
	Mean (SD)	**N (%)**	**Mean (SD)**	**N (%)**	***p*-value**
Person in charge of preparing cook food					0.340
Mother		64(86.5)		295(90.8)	
Father		1(1.4)		1(0.3)	
Housekeeper		5(6.8)		21(6.5)	
Others		4(5.4)		8(2.5)	
Person spent most time on weekdays					0898
Mother		54(73.0)		235(72.3)	
Father		5(6.8)		16(4.9)	
Friends		7(9.5)		32(9.8)	
Others		8(10.8)		42(12.9)	
Person spent most time on weekends					0.102
Mother		51(68.9)		198(60.9)	
Father		6(8.1)		25(7.7)	
Friends		12(16.2)		42(12.9)	
Others		5(6.8)		60(18.5)	
Anthropometric measurements					
Height (cm)	151±0.06		152±0.07		0.190
Weight (kg)	46.63±8.42		52.07±14.36		<0.001
BMI (kg/m^2)	20.45±3.32		22.36±5.35		<0.001
BMI z-score	0.29±1.07		0.63±1.46		<0.022
WC (cm)	67.89±7.25		71.35±10.59		0.001
WHtR (cm)	1.51±0.06		1.52±0.07		0.003
BMI status					0.013
Thinness <−2 SD		1(1.4)		19(5.8)	
Normal ≤ −2 SD and ≥1		69(93.2)		248(76.3)	
Overweight > +1 SD		4(5.4)		48(14.8)	
Obese > +2 SD		0(0)		10(3.1)	
WC					0.001
Normal		56(75.7)		193(59.4)	
Overweight 72.3 cm		12(16.2)		40(12.3)	
Abdominal Obesity 77 cm		6(8.1)		92(28.3)	
WHtR					0.001
WHtR < 0.5		67(90.5)		231(71.1)	
WHtR ≥ 0.5		7(9.5)		94(28.9)	

* 1 USD = 3.75 SAR (Saudi Arabia Riyal). Abbreviations: BMI—body mass index; WHtR—waist to height ratio; WC—Waist circumference.

Among the participants, 49.2% and 54.1% with BID and BIS came from middle-income families earning 5,000–14,999 Saudi riyals, respectively. Most students reported that their mothers usually prepared their food. Among the girls with BID, 72.3% and 60.9% spent most of their time with their mothers on weekdays and weekends, respectively; among girls with BIS, 73% and 68.9% spent most of their time with their mothers on weekdays and weekends, respectively. The results indicated no significant differences between the two groups for sociodemographic variables ($p > 0.05$).

The anthropometric indicators of the participants are presented in Table 1. The mean value was 152.00 ± 0.07 cm for height, 52.07 ± 14.36 kg for weight, 0.63 ± 1.46 for the BMI z-scores, 71.35 ± 10.59 cm for WC and 1.52 ± 0.07 cm for WHtR for the girls with BID. The mean value was 151 ± 0.06 cm for height, 46.63 ± 8.42 kg for weight, 0.29 ± 1.07 for the BMI z-scores, 67.89 ± 7.25 cm for WC and 1.51 ± 0.06 kg for WHtR for the girls with BIS. Thus, most respondents in both groups had normal average BMI, WC and WHtR. In the BID group, 14.8% were overweight, and 3.1% were obese based on BMI; 12.3% were overweight, 28.3% were obese based on WC, and 28.9% did not have normal weight based on WHtR. In the BIS group, only 5.4% were overweight, and none were obese based on BMI; 16.2% were overweight, 8.1% were obese based on WC, and 9.5% did not have normal weight based on WHtR. The results showed significant differences between the two groups for all anthropometric variables except height ($p = 0.190$). Thus, girls with BID were more likely to gain weight, whereas those with BIS were more likely to have normal weight.

Distribution of Respondents Based on Dietary Intake

Table 2 shows the percentage contribution of each nutrient intake to the girls' energy assessed by the SFFQ at least once a week. In this study, the top ten most frequently consumed and least frequently consumed food items were selected. Most of the girls who had BIS consumed fried chicken and Kabsa rice (100.0%), both of which are high in energy and fat content, followed by potato chips (97.3%), ice cream milk and sugar (94.6%), with mean scores of 69.14 ± 51.49, 764 ± 342.73, 222.27 ± 100.33 and 209.89 ± 103.99 calories, respectively. The least frequently consumed food items were canned unsweetened (1.4%), liver sandwich (2.7%) and low-fat cow's milk, with mean scores of 1.42 ± 10.67, 2.9 ± 6.96 and 28.6 ± 105.71 calories, respectively. Most of the participants with BID consumed fried chicken and rice Kabsa (100%), sugar (95.1) and aerated cola drinks (93.8), with mean scores of 65.21 ± 47.4, 758.39 ± 305.88, 200.19 ± 101.98 and 118 ± 59.14 calories, respectively. The least consumed foods were fresh tomatoes (11.4%), cream desserts (11.5%), low-fat cow's milk (9.2%), coconut (8.9%) and liver sandwiches (0.9%), with mean scores of 32.49 ± 47.94, 27.63 ± 42.29, 243.39 ± 595.14, 81.63 ± 65.13 and 7.75 ± 13.69 calories, respectively.

Table 2
Top 10 contributors and less according to per cent contribution to total energy intake (at least once a week), frequency of consumption for the seven food groups, and the adequate, inadequate and excess intake of macronutrients per day among girls BIS and those who had BID

Body image satisfaction (BIS), (N=74)			Body image dissatisfaction (BID), (N=325)			*p*-value
	Mean (SD) of calorie	N (%)		Mean (SD) of calorie	N (%)	
Top 10 most frequently consumed food (at least once a week)			**Top 10 most frequently consumed food (at least once a week)**			
Fried chicken	69.14±51.49	74(100)	Fried chicken	65.21±47.4	325(100)	
Rice kabsa	764±342.73	74(100)	Rice kabsa	758.39±305.88	325(100)	
Potato chips	222.27±100.33	72(97.3)	Sugar	200.19±101.98	309(95.1)	
Ice cream milk	469.57±184.33	70(94.6)	Aerated cola drink	118±59.14	305(93.8)	
Sugar	209.89±103.99	70(94.6)	Ice cream milk	448.01±200.43	300(92.3)	
Bread	105.05±54.99	69(93.2)	Potato chips	241.25±233.99	300(92.3)	
Aerated cola drink	115.08±63.55	68(91.9)	Bread	129.72±142.06	298(91.7)	
Poached chicken	66.87±86.11	64(86.5)	Biscuits	20.47±25.73	279(85.8)	
Biscuits	224.76±323.12	63(85.1)	Poached chicken	54.52±58	270(83.1)	
Cappuccino	1.29±0.86	63(85.1)	Cake	5.94±7.74	264(81.2)	
Top 10 less frequently consumed food (at least once a week)			**Top 10 less frequently consumed food (at least once a week)**			
Kofta kebab meat	6.67±15.88	9(12.2)	Fresh tomatoes	32.49±47.94	37(11.4)	
Cream desserts	10.59±9.42	9(12.2)	Cream desserts	27.63±42.29	34(10.5)	
Coconut	9.01±25.18	8(10.8)	Low-fat cow's milk	243.39±595.14	30(9.2)	
Sandwich mixed	6.21±18.37	6(8.1)	Sandwiches meat	0.3±0.38	29(8.9)	
Konafa cream	77.37±345.3	6(8.1)	Coconut	81.63±65.13	29(8.9)	
Sandwiches meat	2.98±8.81	4(5.4)	Samosas meat	241.25±233.99	23(7.1)	
Samosas meat	11.28±36.77	3(4.1)	Sandwich mixed	4.15±4.03	16(4.9)	
Low-fat cow's milk	28.6±105.71	3(4.1)	Konafa cream	190.11±262.43	16(4.9)	
Liver sandwiches	2.9±6.96	2(2.7)	Canned unsweetened	65.21±47.4	6(1.8)	

Table 2 *(continue)*

Body image satisfaction (BIS), (N=74)			Body image dissatisfaction (BID), (N=325)			*p*-value
	Mean (SD) of calorie	N (%)		Mean (SD) of calorie	N (%)	
Canned unsweetened	1.42±10.67	1(1.4)	Liver sandwiches	7.75±13.69	3(0.9)	
Frequently consumed food groups						
Cereal and grain	0.63±0.23			0.64±0.23		0.507
Dairy products	0.54±0.18			0.54±0.17		0.275
Fish, poultry, and meat products	0.4±0.15			0.4±0.15		0.949
Sweeten beverage	0.54±0.14			0.56±0.15		0.696
Fruit and vegetables	0.5±0.15			0.5±0.13		0.873
Sweet baked goods	0.45±0.14			0.44±0.14		0.504
Mixed dishes	0.40±0.14			0.40±0.15		0.892
Intake of macronutrients per day						
Carbohydrate						0.851
Inadequate < 45 %		17(23)			78(24)	
Adequate (45-65) %		57(77)			247(76)	
Excess > 65 %		0(0)			0(0)	
Fat						0.798
Inadequate < 25 %		0(0)			0(0)	
Adequate (25-35) %		7(9.5)			34(10.5)	
Excess > 35 %		67(90.5)			291(89.5)	
Protein						0.086
Inadequate < 10 %		0(0)			0(0)	
Adequate (10-30) %		71(95.9)			291(89.5)	
Excess > 30 %		3(4.1)			34(10.5)	

As shown in Table 2, cereals and grains, dairy products and sweet beverages were the most frequently consumed food groups by all BIS and BID respondents. By contrast, fish, poultry, meat products, and sweet baked goods were less frequently consumed in both groups.

The average daily dietary intakes of the respondents of both groups were 777.3 ± 238.4 g of carbohydrates, 292.6 ± 132.8 g of fat and 275.7 ± 172.8 g of protein. Among the girls with BIS and BID, the majority had an adequate intake of carbohydrates (77% and 76%) and protein (95.9% and 89.5%), respectively. As shown in Table 2, 23% and 24% of the girls with BIS and BID consumed insufficient amounts of carbohydrates, and 90.5% and 89.5% consumed excessive amounts of fat due to a high intake of unhealthy food, respectively. The intake of carbohydrates, fat and protein of the two groups did not show a significant difference ($p > 0.05$).

Body Image Dissatisfaction (BID) Among the Respondents

According to the Stunkard Figure Rating Scale (FRS), Table 3 shows that more than 81.5% of the participants were dissatisfied with their BI, whereas only 18.5% expressed satisfaction with their BI. Among the participants, 51.4% desired a smaller body size, and 30.1% preferred a larger body type.

Table 3
BI discrepancy score (BIDS) and girl distribution based on image discrepancy score categories among participants

Variable	Body image satisfaction (BIS), (N=74)		Body image dissatisfaction (BID), (N=325)	
	N	%	N	%
Total numbers and percentage	74	18.5	325	81.5
Perceptions of participants				
Underweight	1	1.4	19	5.8
Normal	69	93.2	248	76.3
Overweight	4	5.4	48	14.8
Obese	0	0	10	3.1
BIDS status				
Desired to reduce			205	51.4
Desire to increase			120	30.1

Table 4 presents the significant relationship between the perceived BMI and the actual BMI ($X^2 = 215.636$, $p < 0.001$). The participants who identified their BMI as normal had a normal BMI (39.3%), but those who perceived their BMI as underweight (38.3%) had a normal BMI. Moreover, 7% of overweight girls considered themselves normal, and 5% considered themselves overweight. Only two obese girls correctly identified themselves as obese.

Table 4
Actual BMI and perceived BMI among participants

Actual BMI	Perception BMI				$\chi 2$	*P*-value
	Thinness N (%)	Normal N (%)	Overweight N (%)	Obese N (%)		
Thinness	19(4.8)	1(0.3)	0(0)	0(0)	215.636	<0.001
Normal	153(38.3)	157(39.3)	7(1.8)	0(0)		
Overweight	1(0.3)	28(7)	22(5.5)	1(0.3)		
Obese	0(0)	2(0.5)	6(1.5)	2(0.5)		

Association Between Body Weight Indicator, Sociodemographic, Dietary Intake and Body Image Perception

Table 5 presents the strong association among BMI, WC, WHtR, sociodemographic data, dietary intake, and BI explored using simple and multiple regression analyses. A simple regression was conducted, and all significant ($p < 0.05$) factors were selected and used in the multiple regression analysis. The results of the multiple regression analysis using a backward stepwise approach showed a significant and positive association between BMI and the participants' age ($\beta = 1.252$, $p < 0.001$) and current body size ($\beta = 2.826$, $p < 0.001$) and a negative association between dairy products ($\beta = -0.080$, $p = 0.004$) and desired body size ($\beta = -0.734$, $p < 0.001$). The results indicated that the respondents with a perception of their (current and desired) body size as different from their actual body size tended to have a higher BMI. In terms of BMI, these four variables were observed to affect the final model ($p < 0.05$) and significantly predicted the body weight indicator of the study subjects [$F(4,394) = 151.737$, $p = 0.00$]. A moderate relationship was observed between the four predictor variables ($R^2 = 0.602$). In the final model, 62% of the body weight indicators (BMI) could be explained by this model. The body weight indicator is the equation of the backward stepwise multiple regression model: BMI = 1.716 + [1.252 age] + [− 0.080 dairy products] + [2.826 current body size] **-** [0.734 desired body size].

The WC results of the stepwise regression model showed a significant and positive association with age ($B = 2.324$, $p = 0.001$) and current body size ($B = 5.369$, $p = 0.001$), as well as a significant and negative relationship with dairy products ($B = -0.189$, $p = 0.001$), cereal and grain ($B = -0.171$, $p = 0.001$) and ideal body size ($B = -1.537$, $p < 0.001$). The current and ideal body sizes perceived differently from the actual BI were associated with a higher BMI among the girls. In terms of WC, these five variables predicted the body weight indicators [$F(5,393) = 96.741$, $p < 0.001$]. A moderate relationship was found among these predictor variables ($R^2 = 0.546$). A 54.6 % change in body weight indicators for WC could be explained as 29.120 + [2.342 age] + [-0.171 cereal and grain] + [-0.189 dairy products] + [5.369 current body size] + [-1.537 ideal body size].

Table 5
Relationship between sociodemographic characteristics, dietary intake, and BI with BMI, WC, and WHtR explored using multiple regression analyses

Variable(s)	BMI			WC			WHtR		
	Adjusted (Multiple regression)			Adjusted (Multiple regression)			Adjusted (Multiple regression)		
	B (β) (95% CI)	*p*-Value	VIF	B (β) (95% CI)	*p*-Value	VIF	B(β) (95% CI)	*p*-Value	VIF
Sociodemographic characteristics									
Age (years)	1.252(0.583 -1.921)	<0.001	1.059	2.342(0.889 - 3.749)	0.001	1.059			
Number of siblings									
Number of household members									
Mother's education									
Father's education									
Family's monthly income									
Dietary intake									
Cereal and grain				-0.171(-0.307-- 0.036)	0.001	1.039	-0.125(-0.212-- 0.038)	0.005	1.014
Dairy products	-0.08(-0.135 -- 0.026)	0.004	1.028	-0.189(-0.305 -- 0.073)	0.001	1.039	-0.134(-0.208 -- 0.06)	<0.001	1.025
Fish, poultry, and meat products									
Sweeten beverage									
Fruit and vegetables									
Sweet baked goods									
Mixed dishes									
Body image discrepancy									
Current body size (BI)	2.826(2.584 -3.068)	<0.001	1.121	5.369(4.853 - 5.886)	<0.001	1.123	3.21(2.885 - 3.534)	<0.001	1.071
Desired body size (BI)	-0.734(-1.045 -- 0.423)	<0.001	1.064				-0.931(-1.359 -- 0.504)	<0.001	1.065
Ideal body size (BI)				-1.537(-2.200 -- 0.874)	<0.001	1.064			
F value	151.737			96.741			95.944		
p-value	0			0			0		
Adj R^2	0.602			0.546			0.488		

Abbreviations: BI —body image; BMI—body mass index; WC — waist circumference; WHtR—waist to height ratio; β —regression coefficient; CI—confidence interval; VIF—variance inflation factor

The WHtR results showed a significant and negative association with cereal and grain ($\beta = -0.125$, $p = 0.005$), dairy products ($\beta = -0.134$, $p < 0.001$) and desired body size ($\beta = -0.931$, $p < 0.001$), and a positive and significant association with current body size ($\beta = 3.21$, $p < 0.001$). The multiple regression analysis used all significant factors ($p < 0.05$) selected in the simple regression. These factors were WHtR-based variables ($F(4,394) = 95.944$, $p \leq 0.001$), and a moderately significant relationship was observed ($R^2 = 0.488$). A 48.8% change in body weight indicators for WHtR could be explained as 40.880 + [−0.125 cereal and grain] + [−0.134 dairy products] + [3.21 current body size] + [−0.931 desired body size].

In summary, the body weight indicator was positively associated with age and current body size and negatively associated with cereal, grain, dairy products, desired body size, and ideal body size. The results of the multiple linear regression models revealed that fish, poultry and meat products, sweetened beverages, fruit and vegetables, sweet baked goods and mixed dishes did not significantly predict body weight indicators ($p > 0.05$).

DISCUSSION

According to a previous study, sociodemographic characteristics such as age, sex and socioeconomic status are associated with overweight or obesity (Bel-Serrat et al., 2018). Conversely, the present study showed a significant association between anthropometric measurements (BMI and WC) and age only, and it did not find a significant relationship with the other sociodemographic characteristics analysed ($p > 0.05$). It is possible that the homogeneity of the sample influenced our results. Moreover, all the participants were Saudi girls aged 13 and 14, and all other nationalities were excluded. We found a significant positive association between body weight indicators with age and current body size and a negative association with cereal and grain, dairy products, and desired and ideal body size at ($p < 0.05$). The participants' BMI was [$F(4,394) = 151.737$, $p = 0.00$], the WC was [$F(5,393) = 96.741$, $p < 0.001$], and the WHtR was ($F(4,394) = 95.944$, $p \leq 0.001$). A significant moderate relationship was found among the following predictor variables: ($R^2 = 0.602$ (BMI), 0.546 (WC), and 0.488 (WHtR)).

Adolescence marks a period of rapid growth; thus, the results were unsurprising. Al-Kutbe et al. (2017) reported that excessive energy intake predicted body weight as positive ($p = 0.001$) among Saudi children based on BMI and WC, consistent with our results. A significant difference was found in the mean daily energy intake, with higher consumption among obese participants than those with normal body weight (2677 ± 804 vs 1806 ± 403 kcal/d at $p < 0.001$). Conversely, 30% were found to be overweight or obese, with a mean WC of 72.1 ± 5.3 and 79.8 ± 7.9 and BMI of 90 ± 3.6 and 97.9 ± 0.9, respectively. Thus, higher consumption of unhealthy foods was significantly inversely correlated with a lower risk of abdominal obesity. Our findings are consistent with those of Gosadi et al. (2017),

who found a statistically significant association between BMI and consumption of meat and dairy products ($p = 0.03$) among Saudi adolescents. Moreover, a study among Qatari female adolescents indicated that the frequency/week of an unhealthy diet, i.e., fast food, fries, sweets and cake intake, were significantly associated with high WHtR/ WC ($p < 0.05$) (Kerkadi et al., 2019).

The association between body weight indicators and (current, desired and ideal) BI was significant. The (current, desired and ideal) body size of the participants contributed to and predicted the body weight indicators of BMI, WC and WHtR, whether positively or negatively. According to previous studies, 60.1% of students had BID. BID was significantly associated with BMI ($p < 0.001$), and it was 4.06 times greater among overweight/obese participants ($p < 0.001$) than among those with normal BMI (Latiff et al., 2018). However, in accordance with our findings, Albawardi et al. (2021) reported that 87% of Saudi university students were unhappy with their physical shape and that 68% had normal body weight. Gaddad et al. (2018) revealed that most subjects (90.05%) had no concerns about BI, 75% had a normal BMI, only one was overweight, and none were obese. Our results are not consistent with a study that showed the prevalence of overweight (28.2%), obesity (19.5%) and BID (13.2%) among children from Chile. A significant association was found between BID and the anthropometric parameters of obesity/overweight ($p < 0.001$) and WHtR ($p < 0.001$) (Delgado-Floody et al., 2018). The different work environments could have contributed to the different results.

Our results revealed that most of the adolescents had poor nutritional habits. Fried chicken and rice Kabsa (100.0%) were consumed the most. Many adolescents with BIS and BID also consumed potato chips (97.3% and 92.3%), sugar (94.6% and 95.1%) and cola drinks (91.9% and 93.8%), respectively, which are known to be high in fat and energy content. Around 90.5% of girls with BIS and 89.5% of those with BID consumed excessive fat daily. Our results support the Moradi-Lakeh et al. (2017) study of Saudi adolescents and adults, which showed that only a small proportion met the dietary recommendations. Only 5.2%, 7.5% and 44.7% of the participants consumed fruits, vegetables and fish, respectively, and most young adults consumed large amounts of sweetened beverages (115.5 ± 2.6 ml/ day). Although the survey included only 42 items in the diet history questionnaires, this shows a larger picture of adolescents' dietary habits. In line with other studies, Saudi females consumed chicken Kabsa (77.5%) the most, followed by rice and chicken burgers (60%). At the same time, fruit syrup (12%) and cabbage (11.5%) were consumed less frequently (Gosadi et al., 2017). Consistent with our results, Song and Shim (2019), who analysed data from 2007 to 2017, found that 11-year-old Korean children increased their fat intake from 21.7% kcal (54.3 g) to 25.2% kcal (61.8 g). The percentage of children with fat intake above the recommended values increased from 3.7% to 27.5%. In accordance with our results, Al Bahhawi et al. (2018) found that 90%, 81%, 71% and 75% of Saudi girls

consumed sugary desserts, fast food, canned food and caffeine, respectively, and that 97%, 86% and 90% consumed meat, fish and fruits, respectively. Thus, previous studies revealed that people still have unhealthy eating habits and that Saudi girls are no exception. For instance, our participants with BIS and BID consumed more sweetened beverages than fruits and vegetables, possibly due to a lack of nutrition knowledge.

The current findings reported that 81.5% of the participants were dissatisfied with their BI and that 51.4% desired to reduce their body size. Among the participants with an actual normal BMI, only 39.3% believed they had a normal BMI, while the rest were mistaken. Most overweight or obese students consider themselves to have a lower BMI than their actual BMI. These results are close to those of Farias et al. (2018), who found that most Brazilian participants were unsatisfied with their BI and that 71% were female. As the participants were adults, their BID continued into adulthood. Similarly, Hijji et al. (2021) reported that underweight Saudi girls (44.8% and 39.4%) and boys (49.4% and 45.2%) 10–14 and 15–19 years of age were satisfied with their BI, respectively. This work is consistent with a study conducted among Turkish adolescents with a normal BMI, which reported that only 22.8% were satisfied with their BI (Düzçeker et al., 2021).

The present study shows a significant association between the perceived BMI and actual BMI ($p < 0.001$). Around half of our adolescents did not misinterpret their BMI status. Radwan et al. (2019) showed that 80.9% of Emirati university students had BID and that 57.5% wanted to lose weight. The perceived BMI significantly influenced the actual BMI ($X^2 = 546$, $p < 0.001$). Most participants considered their BMI normal indeed had a normal BMI, and 19.8% of the overweight participants reported a normal BMI. Cid et al. (2018) reported that among Spanish participants with a mean age of 12.46 ± 2.14, 47 had a mean BMI of 20.18 ± 3.58, and 41.14% were overweight or obese. Among the overweight participants, the majority (69.23%) misperceived their weight, mainly believing they had normal weight (62.82%). Among the obese, the majority (88.63%) misperceived their weight, and (84.09%) considered themselves slightly overweight or normal. A significant correlation was found between BMI and BID/restricted eating ($p < 0.0001$).

The present study aimed to assess the sociodemographic characteristics, dietary intake and BID and predict their association with anthropometric measurements among Saudi adolescent girls aged 13–14. The findings showed that most study population consumed fat in excessive amounts and that the prevalence of BID was high among them. Moreover, age, dairy products, cereal and grain, and (current, desired and ideal) body size predicted the body weight of the girls based on regression analyses. A previous study found that BID with a desire to reduce weight among adolescents was associated with being female ($p = 0.007$) and that a desire to gain weight was associated with eating between meals ($p = 0.01$) and frequent fast food consumption ($p = 0.038$) (Ayed et al., 2019). Ribeiro-Silva et al. (2018) reported that among overweight and obese Brazilian adolescents, a pattern

of a Western diet of fast food, sweets and sugars, soft drinks, milk and dairy products was negatively associated with a slight BID (OR: 0.240, 95% CI: 0.100–0.576). However, no association between normal weight or underweight between the BID and any dietary pattern was found. Note that most of the participants were of normal weight (77.3%) and were satisfied with their BI (80.5%) (Ribeiro-Silva et al., 2018). Cereal and grain, and dairy products were the most frequently consumed food groups by our participants with BIS and BID. Conversely, they consumed insufficient fish, poultry and meat products. However, no significant differences were found between the two participant groups in terms of food groups. This study's multiple linear regression models showed that the self-assessment of fish, poultry and meat products, sweetened beverages, fruit and vegetables, sweet baked goods and mixed dishes did not significantly predict anthropometric measurements (BMI, WC and WC WHtR; $p > 0.05$). Previous studies used different methods to assess dietary intake and reported a correlation with BMI. For example, Al-Kutbe et al. (2017) and Gosadi et al. (2017) found that dietary intake predicted obesity using a 24-h record for four days and the SFFQ including 120 food items, respectively. The Drawing Scale (Latif et al., 2018) and the Stunkard Scale (Kops et al., 2019) were also used, and a significant association between BMI and BID was found to determine BID.

To our knowledge, this study is the first to focus on measuring the relationships among the sociodemographic characteristics, dietary intake, BID, and anthropometric measurements (BMI, WC and WHtR) of young Saudi adolescent girls in Arar. The results are important for those interested in future nutrition education and obesity prevention programmes, as the results can provide them with methodological support. This study is a source of information on anthropometric status, nutrition and BID status among children and adolescents. The use of validated questionnaires is another advantage of this study.

This study has several limitations. First, it was conducted in only one Saudi Arabian city (Arar). Time constraints restricted the expansion to other cities. Second, boys were not included in this study because of the nature of Saudi society, which separates the genders in schools. We recommend that males be included in future research of similar populations to study nutritional intake and male image dissatisfaction with female outcomes. Third, biological maturation variables were not evaluated. Future research should include this variable in similar population groups. Finally, the FFQ was used to determine the nutritional intake of female students. The FFQ may not give many details because it depends on the girls' memories, which could lead to errors. Including a 24-h dietary recall to assess the participants' dietary intake and food habits would be more accurate.

CONCLUSION

The percentage of Saudi girls aged 13–14 with normal weight was higher in BIS than in BID in terms of BMI, WC and WHtR. Fried chicken, Kabsa rice and sugar were the most

frequently consumed foods of most respondents, and fish, poultry and meat products were the least frequently consumed. Adolescent girls consume an excess intake of fat per day. The prevalence of BID was high, and half of the girls desired to reduce their body weight. The percentage of BID adolescents found to be overweight/obese based on WHtR was higher than that of BIS girls; this is not considered healthy. Only age, cereal and grain, dairy products and (current, desired and ideal) body size were significantly associated with body weight indicators. Therefore, school-based intervention programmes for Saudi girls are required to address unhealthy behaviours, such as eating unhealthy food and having a negative BI. Increasing knowledge, attitudes and practices through nutritional education and creating awareness about nutrition and positive BI can positively change eating behaviour and encourage BI satisfaction.

ACKNOWLEDGMENTS

Thanks to the Saudi Arabian Culture Mission, Northern Border University, Ministry of Education, and Northern Border Region of Saudi Arabia for supporting this study. We are very grateful to Lmyaa Abdullah Abdul Hussin for editing the Arabic questionnaire.

REFERENCES

Al Bahhawi, T., Doweri, A. A., Sawadi, R. M., Awaji, M. Y., Jarad, M. M., Sulays, Z. Y., & Madkor, K. A. (2018). Consumption habits of pregnant women in the Jazan region, Saudi Arabia: A descriptive study. *BMC Research Notes*, *11*(1), Article 817. https://doi.org/10.1186/s13104-018-3921-5

Albataineh, S. R., Badran, E. F., & Tayyem, R. F. (2019). Dietary factors and their association with childhood obesity in the Middle East: A systematic review. *Nutrition and Health*, *25*(1), 53-60. https://doi.org/10.1177/0260106018803243

Albawardi, N. M., AlTamimi, A. A., AlMarzooqi, M. A., Alrasheed, L., & Al-Hazzaa, H. M. (2021). Associations of body dissatisfaction with lifestyle behaviors and socio-demographic factors among Saudi females attending fitness centers. *Frontiers in Psychology*, *12*, Article 199. https://doi.org/10.3389/fpsyg.2021.611472Al-Hazzaa, H. M. (2018). Physical inactivity in Saudi Arabia revisited: A systematic review of inactivity prevalence and perceived barriers to active living. *International Journal of Health Sciences*, *12*(6), 50-64.

Al-Kutbe, R., Payne, A., de Looy, A., & Rees, G. A. (2017). A comparison of nutritional intake and daily physical activity of girls aged 8-11 years old in Makkah, Saudi Arabia according to weight status. *BMC Public Health*, *17*(1), 1-9. https://doi.org/10.1186/s12889-017-4506-2

Almajwal, A., AL-zahrani, S., Abulmeaty, M., Alam, I., Razzak, S., & Alqahtani, A. (2018). Development of food frequency questionnaire (FFQ) for the assessment of dietary intake among overweight and obese Saudi young children. *Nutrire*, *43*(1), Article 29. https://doi.org/10.1186/s41110-018-0088-8

Alzamil, H. A., Alhakbany, M. A., Alfadda, N. A., Almusallam, S. M., & Al-Hazzaa, H. M. (2019). A profile of physical activity, sedentary behaviors, sleep, and dietary habits of Saudi college female students. *Journal of Family & Community Medicine*, *26*(1), 1-8. https://doi.org/10.4103/jfcm.JFCM_58_18

Axxya Systems. (2019). *Nutritionist ProDiet Analysis. 2014*. https://nexgen1.nutritionistpro.com/shop/product-detail/nutritionist-pro-diet-analysis-software-13.

Ayed, H. B., Yaich, S., Jemaa, M. B., Hmida, M. B., Trigui, M., Jedidi, J., Sboui, I., Karray, R., Feki, H., Mejdoub, Y., Kassis, M., & Damak, J. (2019). What are the correlates of body image distortion and dissatisfaction among school-adolescents? *International Journal of Adolescent Medicine and Health, 33*(5), 1-12. https://doi.org/10.1515/ijamh-2018-0279

Baceviciene, M., Jankauskiene, R., & Balciuniene, V. (2020). The role of body image, disordered eating and lifestyle on the quality of life in Lithuanian university students. *International Journal of Environmental Research and Public Health*, *17*(5), Article 1593. https://doi.org/10.3390/ijerph17051593

Bahathig, A. A., Saad, H. A., Yusop, N. B. M., Shukri, N. H. M., & El-Din, M. M. E. (2021). Relationship between physical activity, sedentary behavior, and anthropometric measurements among Saudi female adolescents: A cross-sectional study. *International Journal of Environmental Research and Public Health*, *18*(16), Article 8461. https://doi.org/10.3390/ijerph18168461

Bell, M. J., Zeiler, M., Herrero, R., Kuso, S., Nitsch, M., Etchemendy, E., Fonseca-Baeza, S., Oliver, E., Adamcik, T., Karwautz, A., Wagner, G., Banos, R., Botella, C., Gorlich, D., Jacobi, C., & Waldherr, K. (2019). Healthy Teens@ School: Evaluating and disseminating transdiagnostic preventive interventions for eating disorders and obesity for adolescents in school settings. *Internet Interventions*, *16*, 65-75. https://doi.org/10.1016/j.invent.2018.02.007

Bel-Serrat, S., Heinen, M. M., Mehegan, J., O'Brien, S., Eldin, N., Murrin, C. M., & Kelleher, C. C. (2018). School sociodemographic characteristics and obesity in schoolchildren: Does the obesity definition matter? *BMC Public Health*, *18*(1), 1-12.https://doi.org/10.1186/s12889-018-5246-7

Bray, I., Slater, A., Lewis-Smith, H., Bird, E., & Sabey, A. (2018). Promoting positive body image and tackling overweight/obesity in children and adolescents: A combined health psychology and public health approach. *Preventive Medicine*, *116*, 219-221. https://doi.org/10.1016/j.ypmed.2018.08.011

Cafri, G., Yamamiya, Y., Brannick, M., & Thompson, J. K. (2005). The influence of sociocultural factors on body image: A meta-analysis. *Clinical Psychology: Science and Practice*, *12*(4), 421-433. https://doi.org/10.1093/clipsy.bpi053

Cardinal, T. M., Kaciroti, N., & Lumeng, J. C. (2006). The figure rating scale as an index of weight status of women on videotape. *Obesity*, *14*(12), 2132-2135. https://doi.org/10.1038/oby.2006.249

CDC. (2021). *Childhood Obesity Facts, Prevalence of Childhood Obesity in the United States*. Center for Disease Control and Prevention. https://www.cdc.gov/obesity/data/childhood.html

Cid, J. A., Ramírez, C. A., Rodríguez, J. S., Conde, A. I., Jáuregui-Lobera, I., Martín, G. H., & Ríos, P. B. (2018). Self-perception of weight and physical fitness, body image perception, control weight behaviors and eating behaviors in adolescents. *Nutrición Hospitalaria: Organo Oficial De La Sociedad Española De Nutrición Parenteral Y Enteral*, *35*(5), 1115-1123.

Cruz-Sáez, S., Pascual, A., Wlodarczyk, A., & Echeburúa, E. (2020). The effect of body dissatisfaction on disordered eating: The mediating role of self-esteem and negative affect in male and female adolescents. *Journal of Health Psychology*, *25*(8), 1098-1108. https://doi.org/10.1177/1359105317748734

Delgado-Floody, P., Caamaño-Navarrete, F., Jerez-Mayorga, D., Guzmán-Guzmán, I. P., Cofré-Lizama, A., & Martínez-Salazar, C. (2018). Body image dissatisfaction and its association with antropometrics parameters, weight status and self-esteem in Chilean schoolchildren. *Archivos Latinoamericanos De Nutricion*, *68*(4). https://www.doi.org/10.37527/2018.68.4.006

Draper, C. E., Grobler, L., Micklesfield, L. K., & Norris, S. A. (2015). Impact of social norms and social support on diet, physical activity and sedentary behaviour of adolescents: A scoping review. *Child: Care, Health and Development*, *41*(5), 654-667. https://doi.org/10.1111/cch.12241

Düzçeker, Y., Akgül, S., Durmaz, Y., Yaman, M., Örs, S., Tüzün, Z., Büyüktuncer, Z., & Kanbur, N. (2021). Is Ramadan fasting correlated with disordered eating behaviours in adolescents? *Eating Disorders*, *29*(1), 74-87. https://doi.org/10.1080/10640266.2019.1642032

El Kabbaoui, M., Chda, A., Bousfiha, A., Aarab, L., Bencheikh, R., & Tazi, A. (2018). Prevalence of and risk factors for overweight and obesity among adolescents in Morocco. *Eastern Mediterranean Health Journal*, *24*(6), 512-521. https://doi.org/10.26719/2018.24.6.512

Farias, R. R., Martins, R. B., Ulrich, V., Kanan, J. H. C., Silva, I. G. D., & Resende, T. D. L. (2018). Body image satisfaction, sociodemographic, functional and clinical aspects of community-dwelling older adults. *Dementia & Neuropsychologia*, *12*, 306-313. https://doi.org/10.1590/1980-57642018dn12-030012

Gaddad, P., Pemde, H. K., Basu, S., Dhankar, M., & Rajendran, S. (2018). Relationship of physical activity with body image, self esteem sedentary lifestyle, body mass index and eating attitude in adolescents: A cross-sectional observational study. *Journal of Family Medicine and Primary Care*, *7*(4), 775-779. https://doi.org/10.4103/jfmpc.jfmpc_114_18

Gosadi, I. M., Alatar, A. A., Otayf, M. M., AlJahani, D. M., Ghabbani, H. M., AlRajban, W. A., Alrsheed, A. M., & Al-Nasser, K. A. (2017). Development of a Saudi food frequency questionnaire and testing its reliability and validity. *Saudi Medical Journal*, *38*(6), 636-641. https://doi.org/10.15537/smj.2017.6.20055

Hackshaw, A. (2014). *A Concise Guide to Observational Studies in Healthcare*. John Wiley & Sons. https://doi.org/10.1002/9781118527122

Hijji, T. M., Saleheen, H., & AlBuhairan, F. S. (2021). Underweight, body image, and weight loss measures among adolescents in Saudi Arabia: Is it a fad or is there more going on? *International Journal of Pediatrics and Adolescent Medicine*, *8*(1), 18-24. https://doi.org/10.1016/j.ijpam.2020.01.002

Kerkadi, A., Sadig, A. H., Bawadi, H., Al Thani, A. A. M., Al Chetachi, W., Akram, H., Al-Hazzaa, H. M., & Musaiger, A. O. (2019). The relationship between lifestyle factors and obesity indices among adolescents in Qatar. *International Journal of Environmental Research and Public Health*, *16*(22), Article 4428. https://doi.org/10.3390/ijerph16224428

Khalaf, A., Westergren, A., Berggren, V., Ekblom, Ö., & Al-Hazzaa, H. M. (2015). Perceived and ideal body image in young women in South Western Saudi Arabia. *Journal of Obesity*, *2015*, Article 697163. https://doi.org/10.1155/2015/697163

Kops, N. L., Bessel, M., Knauth, D. R., Caleffi, M., & Wendland, E. M. (2019). Body image (dis) satisfaction among low-income adult women. *Clinical Nutrition*, *38*(3), 1317-1323. https://doi.org/10.1016/j.clnu.2018.05.022

Latiff, A. A., Muhamad, J., & Rahman, R. A. (2018). Body image dissatisfaction and its determinants among young primary-school adolescents. *Journal of Taibah University Medical Sciences*, *13*(1), 34-41. https://doi.org/10.1016/j.jtumed.2017.07.003

Lemeshow, S., Hosmer, D. W., Klar, J., Lwanga, S. K., & World Health Organization. (1990). *Adequacy of Sample Size in Health Studies*. Chichester: Wiley.

Lynch, E., Liu, K., Wei, G. S., Spring, B., Kiefe, C., & Greenland, P. (2009). The relation between body size perception and change in body mass index over 13 years: The coronary artery risk development in young adults (CARDIA) study. *American Journal of Epidemiology*, *169*(7), 857-866. https://doi.org/10.1093/aje/kwn412

Maffeis, C., Banzato, C., Talamini, G., & Italian, O. S. G. (2008). Waist-to-height ratio, a useful index to identify high metabolic risk in overweight children. *The Journal of Pediatrics*, *152*(2), 207-213. https://doi.org/10.1016/j.jpeds.2007.09.021

McElhone, S., Kearney, J. M., Giachetti, I., Zunft, H. J. F., & Martínez, J. A. (1999). Body image perception in relation to recent weight changes and strategies for weight loss in a nationally representative sample in the European Union. *Public Health Nutrition*, *2*(1a), 143-151. https://doi.org/10.1017/S1368980099000191

Moehlecke, M., Blume, C. A., Cureau, F. V., Kieling, C., & Schaan, B. D. (2020). Self-perceived body image, dissatisfaction with body weight and nutritional status of Brazilian adolescents: A nationwide study. *Jornal de Pediatria*, *96*, 76-83. https://doi.org/10.1016/j.jped.2018.07.006

Moradi-Lakeh, M., El Bcheraoui, C., Afshin, A., Daoud, F., AlMazroa, M. A., Al Saeedi, M., Basulaiman, M., Memish, Z. A., Al Rabeeah, A. A., & Mokdad, A. H. (2017). Diet in Saudi Arabia: Findings from a nationally representative survey. *Public Health Nutrition*, *20*(6), 1075-1081. https://doi.org/10.1017/S1368980016003141

Motlagh, M., Shirvani, S., Hassanzadeh-Rostami, Z., Taheri, M., & Ghadimi, R. (2018). Assessment of overweight and obesity in Iranian adolescents: Optimal cut-off values of anthropometric indices. *Eastern Mediterranean Health Journal*, *24*(10), 975-987. https://doi.org/10.26719/2018.24.10.975

Musharrafieh, U., Tamim, H., Houry, R., & AlBuhairan, F. (2020). A nationwide study of asthma correlates among adolescents in Saudi Arabia. *Asthma Research and Practice*, *6*, 1-8. https://doi.org/10.1186/s40733-020-00056-8

Radwan, H., Hasan, H. A., Ismat, H., Hakim, H., Khalid, H., Al-Fityani, L., Mohammed, R., & Ayman, A. (2019). Body mass index perception, body image dissatisfaction and their relations with weight-related behaviors among university students. *International Journal of Environmental Research and Public Health*, *16*(9), Article 1541. https://doi.org/10.3390/ijerph16091541

Ribeiro-Silva, R. D. C., Fiaccone, R. L., Conceição-Machado, M. E. P. D., Ruiz, A. S., Barreto, M. L., & Santana, M. L. P. (2018). Body image dissatisfaction and dietary patterns according to nutritional status in adolescents. *Jornal de Pediatria*, *94*(2), 155-161. https://doi.org/10.1016/j.jped.2017.05.005

Sánchez, G. F. L., Suárez, A. D., & Smith, L. (2018). Analysis of body image and obesity by Stunkard's silhouettes in 3-to 18-year-old Spanish children and adolescents. *Anales de Psicología*, *34*(1), 167-172. http://dx.doi.org/10.6018/analesps.34.1.294781

Shaban, L. H., Vaccaro, J. A., Sukhram, S. D., & Huffman, F. G. (2016). Perceived body image, eating behavior, and sedentary activities and body mass index categories in Kuwaiti female adolescents. *International Journal of Pediatrics*, *2016*, Article 1092819. https://doi.org/10.1155/2016/1092819

Song, S., & Shim, J. E. (2019). Trends in dietary intake of total fat and fatty acids among Korean adolescents from 2007 to 2017. *Nutrients*, *11*(12), Article 3073. https://doi.org/10.3390/nu11123073

Stunkard, A. J. (1983). Use of the Danish adoption register for the study of obesity and thinness. *Research publications - Association for Research in Nervous and Mental Disease, 60*, 115-120.

Tabbakh, T., & Freeland-Graves, J. H. (2016). The home environment: A mediator of nutrition knowledge and diet quality in adolescents. *Appetite*, *105*, 46-52. https://doi.org/10.1016/j.appet.2016.05.002

Voelker, D. K., Reel, J. J., & Greenleaf, C. (2015). Weight status and body image perceptions in adolescents: current perspectives. *Adolescent Health, Medicine and Therapeutics*, *6*, 149-158. https://doi.org/10.2147/AHMT.S68344

Weinberger, N. A., Kersting, A., Riedel-Heller, S. G., & Luck-Sikorski, C. (2016). Body dissatisfaction in individuals with obesity compared to normal-weight individuals: A systematic review and meta-analysis. *Obesity Facts*, *9*(6), 424-441. https://doi.org/10.1159/000454837

WHO. (2021a). *Adolescent Health and Development*. World Health Organisation. https://www.who.int/westernpacific/news/q-a-detail/adolescent-health-and-development

WHO. (2021b). *Growth Reference Data for 5-19 Years*. World Health Organisation. https://www.who.int/tools/growth-reference-data-for-5to19-years/indicators/bmi-for-age

WHO. (2021c). *Noncommunicable Diseases; Unhealthy Food*. World Health Organisation. http://www.emro.who.int/noncommunicable-diseases/causes/unhealthy-diets.html

WHO. (2021d). *Obesity and overweight*. World Health Organisation. http://www.who.int/news-room/fact-sheets/detail/obesity-and-overweight

Pertanika J. Sci. & Technol. 31 (3): 1245 - 1265 (2023)

PERTANIKA JOURNALS

SCIENCE & TECHNOLOGY

Journal homepage: http://www.pertanika.upm.edu.my/

Automation of Quantifying Security Risk Level on Injection Attacks Based on Common Vulnerability Scoring System Metric

Aditya Kurniawan[1]*, Mohamad Yusof Darus[2], Muhammad Azizi Mohd Ariffin[2], Yohan Muliono[1] and Chrisando Ryan Pardomuan[1]

[1]*School of Computer Science, Bina Nusantara University, Kota Jakarta Barat, Daerah Khusus Ibukota 11530, Jakarta, Indonesia*
[2]*Faculty of Computer and Mathematical Sciences, UiTM, Shah Alam, 40450, Malaysia*

ABSTRACT

An injection attack is a cyber-attack that is one of The Open Web Application Security Project Top 10 Vulnerabilities. These attacks take advantage of insufficient user input validation into the system through the input surface of a Web application as that user in the browser. The company's cyber security team must filter thousands of attacks to prioritize which attacks are considered the most dangerous to be mitigated first. This activity of filtering thousands of attacks takes much time because you have to check these attacks one by one. Therefore, a method is needed to assess how dangerous a cyber-attack is that enters an organization's or company's server. Injection attack detection can be done by analyzing the request data in the web server log. Our research attempts to perform quantification modeling of the variations of two types of injection attacks, SQL Injection (SQLi) and Cross-Site Scripting (XSS), using Common Vulnerability Scoring System Metrics (CVSS). CVSS metrics are generally used to calculate the level of dangerous weakness in the system. This metric is never used to calculate the level of how dangerous an attack is. The modeling that we have made shows that SQLi and XSS attacks have many variations in levels ranging from low to high levels. We discovered that when classified with Common Weakness Enumeration Database, SQLi and XSS attacks CVE values would have high-level congruence with almost 94% value between one another vector on CVSS.

Keywords: Common vulnerability scoring system, injection attack, metrics security risk level

ARTICLE INFO

Article history:
Received: 07 February 2022
Accepted: 24 May 2022
Published: 31 March 2023

DOI: https://doi.org/10.47836/pjst.31.3.07

E-mail addresses:
adkurniawan@binus.edu (Aditya Kurniawan)
yusof@tmsk.uitm.edu.my (Mohamad Yusof Darus)
mazizi@fskm.uitm.edu.my (Muhammad Azizi Mohd Ariffin)
ymuliono@binus.edu (Yohan Muliono)
chrisando.pardomuan@binus.edu (Chrisando Ryan Pardomuan)
* Corresponding author

ISSN: 0128-7680
e-ISSN: 2231-8526

© Universiti Putra Malaysia Press

INTRODUCTION

An injection attack on a website is one of the malicious hackers' most executed attack vectors. When an injection attack is executed, the hacker will enter malicious input into an application or program. The interpreter or compiler will process this input to get the expected output from the injection attack, such as data theft, denial of service, loss of data integrity, or bypassing system authentication. Malicious hackers exploit flaws and errors in validating user input on input surfaces such as forms or URLs (Kindy & Pathan, 2011).

Retrieving hidden data is a type SQLi that can modify SQL Query to return expected additional data results. Subverting application logic is a type SQLi that changes the query to interfere with the application's algorithm (Pramod et al., 2015). Aliero & Qureshi et al. (2020) conducted literature review research on SQL injection attacks published between 2006 and 2019. Their research found that of 82 papers filtered from 1261 papers, 85.4% or 70 papers proposed SQLIA mitigation & prevention methods and tools, 8.5% or seven papers proposed experimental evaluation methods, and 6.1% or five papers proposed analytical methods. The results of the study literature review by them have not found any research on assessing the dangerous level of an SQL injection attack. UNION attacks are a type SQLi that can retrieve data from different database tables. Examining the database is a type SQLi that can extract the structure of database information. Blind SQL injection is a type SQLi that use to test whether a website is SQLi vulnerable or not through query response that shows in the application's response (Aliero & Ghani, et al., 2020; Sadeghian et al., 2013). The malicious hacker usually executed SQLi attacks via automation tools such as NMAP (Alazmi & de Leon, 2022; Kieyzun et al., 2009).

Javascript code injection vulnerabilities have three variations: Reflected, Store, and Dom-based (Fogie et al., 2007). The Reflected type is an XSS vulnerability that originates from an HTTP request as a URL (Sarmah et al., 2018). Type Store is the type of XSS vulnerability coming from the JavaScript code that is deliberately inputted into the database by a malicious hacker with the purpose when the JavaScript code is read by the process of querying the database for display in the user interface web, executed during the process of web page loading and processing processes that malicious. The DOM-based type is an XSS attack that exploits JavaScript code that processes data from untrusted sources with insecure processing methods (Bisht & Venkatakrishnan, 2008). Several studies on detecting cross-site scripting vulnerabilities have been carried out on several types of cross-site scripting vulnerabilities (Sarmah et al., 2018). According to Sarmah et al., research on cross-site scripting is divided into two approaches, namely client-side and server-side approaches. Several studies using a client-side approach have been carried out using the static analysis method, as many as 10 studies, and the hybrid analysis method, as many as four studies. While the number of studies using the server-side approach with the static analysis method is as many as 12 studies, the dynamic analysis method has as many

as nine studies, and the hybrid analysis method has as many as two studies. This study shows that research in the server-side approach area with the static analysis method is the most studied. Reflected XSS detection has been widely studied using regular expression and string-matching methods (Bates et al., 2010; Gupta & Gupta, 2016; Pelizzi & Sekar, 2012; Rao et al., 2016; Wang & Zhou, 2016) (cite xx auditor, xss filt, no script, ie 2008, xss immune, xbuster, rule based). Meanwhile, for the detection of weaknesses in cross-site scripting types of DOM and Stored XSS, little research is done with string matching and string comparison.

Most injection attacks research only focuses on how to detect these injection attacks, filtering input as a defense mechanism, or also preventing the entry of injection attacks code by utilizing third-party software such as intrusion detection system (Bisht & Venkatakrishnan, 2008; Bozic & Wotawa, 2013; Gupta & Gupta, 2017; Kumar Singh & Roy, 2012). However, no research discusses how to assess the ability of malicious hackers to exploit injection vulnerabilities of the complexity of the injection attacks. Knowing the complexity of the attacks launched by these malicious hackers, the incident response team's resources can be focused on attacks that can be considered dangerous to the system (Athanasopoulos et al., 2010).

Measuring cyber security in a company's digital assets can help them define an organization's security posture. Appropriate cyber security measures can help companies (1) verify whether their control security has complied with a policy, process, or procedure, (2) help identify strengths and weaknesses and findings of exploitation of the company's digital assets, and (3) help identify trends in security, both in the internal and external environment of the organization (Voeller, 2008). Companies can monitor their cyber security and defense performance by keeping abreast of the latest cyber security trends. CVSS metrics help companies measure how big a weakness is in the system. In this study, we use CVSS metrics to measure how dangerous a cyber-attack is combined with NVD data.

The accuracy of the CVSS calculation score is influenced by the knowledge of the security researcher and its analysis. It contains an element of their subjectivity in determining each score of the CVSS variables. Security researchers worldwide will upload their calculations for every type of vulnerability they find in technology or system to organizations such as NVDs. NVD organizations use the Common Vulnerabilities and Exposures (CVE) standard for recording the uploaded weakness catalog (Aksu et al., 2018). NVD organizations modify CVE by providing a classification for each weakness known as Common Weakness Enumeration (CWE). This study uses CWE to classify weaknesses and insert some CWE values into the CVSS variables.

Several studies propose several uses of CVSS in certain cybersecurity fields. CVSS is used to analyze the risk of vulnerabilities in system assets as measured by the frequency and process of risk management and cybersecurity strategies in corporate and industrial

environments (Figueroa-Lorenzo et al., 2021; Houmb et al., 2010a). CVSS is also trying to be implemented to illustrate the graph of cyber-attacks (Gallon & Bascou, 2011a). The application of CVSS has also tried to be automated and use machine learning from the findings of weaknesses in the system (Beck & Rass, 2016; Elbaz et al., 2020; Minh Le et al., 2021; Radack & Kuhn, 2011). From a literature review study conducted regarding the application of CVSS, it was found that there was no CVSS automation application to measure the dangerous level of a cyber-attack, especially in SQL injection attacks and cross-site scripting attacks.

The paper is organized into the following section. Section 2 discussed the material and methodology of the CVSS method and its implementation on level attack scoring. Section 3 discussed the result and evaluation of level attack scoring CVSS on SQL injection and cross-site scripting attacks. Finally, we wind up in Section 4 with the conclusion of our research.

MATERIAL

Related Works

Common Vulnerability Scoring System. Common Vulnerability Scoring System is a system for conducting a quantitative assessment of a vulnerability by Common Weakness Enumeration, giving metrics to the properties of a vulnerability built and maintained by the Forum of Incident Response (Scarfone & Mell, 2009). Quantitative assessments are calculated based on formulas that depend on several metrics representing the ease of exploitation, the impact of mitigation, and the way the vulnerability is spread (Houmb et al., 2010b, 2010a). Quantitative assessment can be represented qualitatively (Low, Medium, High, and Critical) to help the organization assess and prioritize changes to their system.

CVSS has also become a standard system used by many agencies and companies. This research uses CVSS 3.0 version (Gallon & Bascou, 2011b; Houmb & Franqueira, 2009). CVSSv3 has three main metrics as follows:

(1) Base Metrics

This metric describes the vulnerability's characteristics and traits. This metric consists of the following:

(a) Exploitability Metrics

Metrics that represent the characteristics of a security hole, where vulnerable components will be given a score based on indications of a security hole that leads to the success of an attack. Exploitability metrics consist of Attack Vector (AV), Attack Complexity (AC), Privilege Required (PR), and User Interaction (UI).

(b) Scope

Scope metric (S) represents the scope of the impact of the security gap. Does

the security gap provide an opportunity for attackers to get coverage of access rights regulated by other access rights coverage. For example, the attacker can access and perform activities on the host OS by attacking VMware.

(c) Impact Metrics
Metrics that represent the impact of Vulnerability on the CIA triad (Confidentiality, Integrity, and Availability) of an infrastructure.

(2) Temporal Metrics
This metric reviews the current conditions based on exploitation techniques, the certainty of information about exploitation codes, or whether a solution is offered to correct the security hole itself.

(3) Environmental Metrics
This metric allows users or analysts to adjust Base Metrics to the organizational needs of the user itself, which will later be applied to the organization's infrastructure in terms of place security controls or CIA triads (Confidentiality, Integrity, and Availability).

This research uses Exploitability metrics, Scope metrics, and Impact metrics.

METHODOLOGY

The steps of this research methodology have been prepared and executed by processing the data in the National Vulnerability Database (NVD) and SQL Injection attack data and cross-site scripting. The following are the detailed steps of this research methodology:

(1) Data Pre-processing
  (a) Standard Deviation of CVSS for Constant Variable
  (b) CVSS Calculation Simulation on Injection Attacks
(2) Analysis & Design CVSS Formulation
  (a) Dynamic CVSS Vector Calculation
  (b) CVSS Base Score Calculation
(3) Algorithm Implementation
(4) Evaluation

Data Pre-Processing

Standard Deviation of CVSS for Constant Variable. NVD data is downloaded and updated periodically to perform a static calculation of scores of multiple CVSS vectors. The data is then used to determine the majority score of each vector generally assigned to a type of attack. Based on the calculation of standard error and standard deviation of the two types of attacks on NVD data, the following results were obtained in Tables 1 and 2. SQL Injection and Cross-site Scripting attacks have very low standard deviation and standard errors; These observations indicate that NVD data has a low variation. Therefore, by using

the majority value of each vector in the NVD data (the score of each vector is determined based on the highest score on the NVD data for each vector), the score for each vector in the newly detected attack can be determined only based on the type of attack detected.

Table 1
Results of SQL injection statistical calculations on NVD dataset (as of 23 March 2020)

Vector	stderr	mean	std
AV	0.000795	0.847520	0.029299
AC	0.001051	0.765386	0.038760
PR	0.004775	0.748227	0.176041
UI	0.000608	0.847800	0.022396
S	0.001040	1.001472	0.038348
C	0.555629	0.555629	0.067088
I	0.003348	0.587947	0.123428
A	0.003630	0.598764	0.133822

Table 2
Results of XSS injection statistical calculations on NVD dataset (as of 23 March 2020)

Vector	Stderr	Mean	std
AV	0.000145	0.849619	0.010214
AC	0.000281	0.768804	0.019834
PR	0.001666	0.764082	0.117414
UI	0.000273	0.621621	0.019243
S	0.001485	1.988925	0.104665
C	0.000754	0.225554	0.053156
I	0.000638	0.224591	0.044990
A	0.000668	0.995276	0.047085

CVSS Calculation Simulation on Injection Attacks. This research uses eight field parameter that showed in Table 3 as follow:

- URL: URL string read from the Apache engine.
- body: Name and parameter value that will be checked whether there is a string injection pattern or not
- source_address: The attacker's IP address
- has_sql: Did the request trigger a connection to the database
- source_port: The attacker's (inbound) port number
- arrived_at: Time the request was received
- audit_xss: XSS detection result data by SIEM
- inspect_sqli: Data from SIEM's SQL Injection detection results

Table 3
Data logs generated for SQL injection attacks

Attribute	Value
url	http://server.com/products.php?id=1' OR 1=1-- -
body	id=1' OR 1=1-- -
source_address	115.166.114.89
source_port	33527
has_sql	true
arrived_at	2021-04-21T13:24:22+00:00
audit_xss	Not Detected
inspect_sqli	Detected

Table 4
SQL injection NVD scores

SQL								
Score	**AV**	**AC**	**PR**	**UI**	**S**	**C**	**I**	**A**
0						12	101	129
00.02	1							
00.22						33	19	12
00.27			120					
00.44		19						
00.05			0					
00.55	6							
00.56						1314	1239	1218
0,043	4		298	13				
0,047			1					
0,053		1340						
0,059	1348		940	1346				
C					2			
U					1357			

The measurement variables contained in CVSS will be calculated statically and dynamically. Static calculations will be carried out to obtain PR (Privileges Required) vectors, AC (Attack Complexity), UI (User Interaction), S (Scope), C (Confidentiality), I (Integrity), and A (Availability) based on CVSSv3 data NVD published regularly. Meanwhile, a dynamic calculation will be carried out to get a vector score of AV (Attack Vector).

NVD data will be retrieved periodically to ensure the data used in the static calculation is the most up to date. The next step is that the system will filter the data for attacks that are out of context, leaving only NVD data for SQL Injection and Cross-site Scripting. Furthermore, from the log data provided by SIEM, it is known that the attack that occurred on the HTTP Request was a SQL Injection attack or Cross-site Scripting. Therefore, the NVD data used is SQL Injection attack data, as shown in Table 4. The NVD data used in this simulation is from 2017 to 2019, taken on 23 March 2020.

The value of each metric is taken based on the majority score for the attacks identified by SIEM. Based on the table, for example, it can be determined that the value for the AC metric in this HTTP Request is 0.77 because it is the majority value (1340 data on NVD shows SQL Injection attacks have an AC score of 0.77). The calculation results show the scores assigned to each CVSS vector on this HTTP as follows:

- AC: 0.77 (Low)
- PR: 0.85 (None)
- UI: 085 (None)

- S: Unchanged (U)
- C: 0.56 (High)
- I: 0.56 (High)
- A: 0.56 (High)

Analysis and Design CVSS Applied Formulation

Dynamic CVSS Vector Calculation. From the log data provided by SIEM, the attacker's IP is 115.166.114.89. Then, to perform AV calculations, the system needs to get the IP of the server it wants to protect (Host IP). Host IP can be retrieved automatically via the ipconfig command, which is run automatically or set manually by the administrator. As a simulation, it is assumed that the Host IP is 10.20.20.122 with a subnet of 255.255.0.0. Next, the system performs a subnet calculation against the Host IP to determine whether the attacker's IP is on the same subnet as the Host, with the following calculation in Table 5. From the results of these calculations, the attacker's IP (115.166.114.89) is on a different subnet from the Host's IP (10.20.20.122), where only IPs are in the range 10.20.0.1 to 10.20.255.254 are on that subnet. Because the two IPs are on different subnets, it can be concluded that the AV from the attack was Network with a score of 0.85.

Table 5
Subnet calculation results based on host IP

IP Address:	**10.20.20.122**
Network Address:	10.20.0.0
Usable Host IP Range:	10.20.0.1 - 10.20.255.254
Broadcast Address:	10.20.255.255
Total Number of Hosts:	65,536
Number of Usable Hosts	65,534
Subnet Mask:	255.255.0.0
Wildcard Mask:	0.0.255.255

Base Score CVSS Calculation. From the results of these calculations, the CVSS Vector String is obtained as follows:

CVSS:3.0/AV:N/AC:L/PR:N/UI:N/S:U/C:H/I:H/A:H

To determine the CVSS Base Score from this HTTP Request, the Exploitability Score and Impact Score were calculated; because the scope of this attack is Unchanged, the CVSS calculation formula used is Equation 1:

$$Impact = 6.42 \times ISS$$

$$ISS = 1 - ((1 - C) \times (1 - I) \times (1 - A))$$

$$Exploitability = 8.22 \times AV \times AC \times PR \times UI$$

$$BaseScore = Roundup(Min((Impact + Exploitability), 10)) \quad (1)$$

Based on this formula, the Exploitability Score is calculated as Equation 2:

$$Exploitability = 8.22 \times 0.85 \times 0.77 \times 0.85 \times 0.85 = 3.887 \quad (2)$$

Next, the Impact Score is calculated by calculating the Impact Sub Score (ISS) first, as Equation 3:

$$ISS = 1 - \big((1 - 0.56) \times (1 - 0.56) \times (1 - 0.56)\big) = 0.914 \quad (3)$$

Because the scope of this attack is Unchanged, the Impact Score (Equation 4):

$$Impact = 6.45 \times 0.914 = 5.895 \quad (4)$$

From these calculations, because the scope of this attack is Unchanged, the Base Score is obtained (Equation 5):

$$BaseScore = Roundup\Big(Min\big((3.887 + 5.895), 10\big)\Big) = 9.8 \quad (5)$$

From the calculation of the score is 9.8, it can be concluded that the severity level of the attack is Critical.

Algorithm Implementation

The implementation of this algorithm uses several server technologies, including Apache Server, Nginx, Redis, Elastic Kibana, and Logstash. The system diagram in Figure 1 illustrates the workflow of the system built in this study. Overall, there are five types of flow or data flow between modules, namely: initial flow, return flow, process flow, periodic flow, and concurrent flow, that described in Table 6.

The HTTP Sniffer module catches every HTTP packet that the system receives from the client, i.e., an HTTP request packet, when it is forwarded to the web server service (e.g., Apache, Nginx, among others). The HTTP Sniffer module normalizes the captured packets and sends them to the SQLi Feature Selector module for further processing. In addition, normalized HTTP packets are also sent to be stored on the Redis server, which is an in-memory data storage available in the system. This storage is done so that HTTP packets are still available and can be used in subsequent processes and so that they can be retrieved quickly. In the SQLi Feature Selector module, the input data received from

the user, whether it contains SQL syntax or not, is generalized into a token. The goal is to reduce the data's very high dimensionality or diversity to a simpler form. The results of the processing are then sent to the Audit Control module. From there, all received data will be used to detect SQLI and XSS attacks.

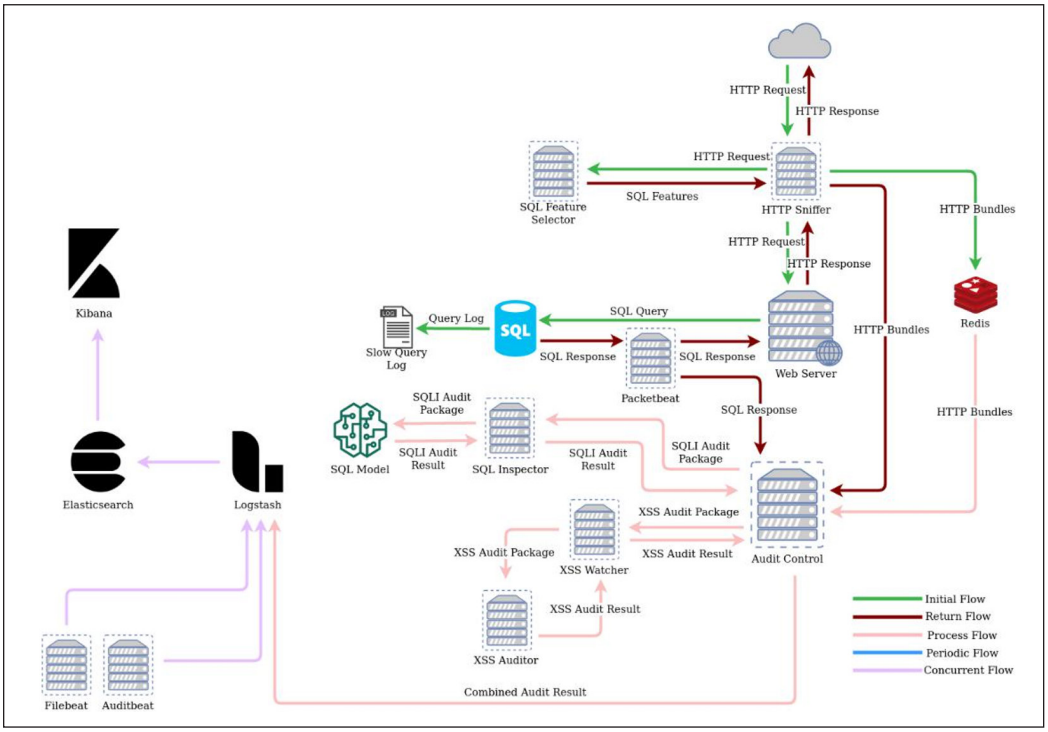

Figure 1. Inflow and outflow data traffic on system

Table 6
Data flow type description

Flow Type	Description	Example
Initial Flow	Occurs when a request comes from a client until before the response is returned	HTTP Request Packet Data
Return Flow	Occurs when a response has been received from client, processed, and returned to the client	HTTP Response Packet Data
Process Flow	Executed specifically by a module when all information needs have been met and are ready to be processed. It is on the fly and not tied to the initial flow or return flow	Data from the Redis server to the Audit Control module
Periodic Flow	Data flow is carried out periodically within a certain time	Data from Elastic Search to Kibana module
Concurrent Flow	The data flow always runs at any time, does not depend on a particular condition, and is not bound to other flows	Data from Filebeat and Auditbeat to Logstash

After the request from the client is processed by the web server and the response is sent back to the client in the form of an HTTP response packet, the packet is again captured by the HTTP Sniffer module and then forwarded to the Audit Control module along with the query result data from MySQL for XSS Auditing. The process results are returned to Audit Control and then sent to the Logstash server, which is also available in the system. Logstash servers receive, parse, and process information from various sources and then send it to the Elasticsearch servers as long-term storage.

Evaluation

Evaluation of the algorithm implementation uses a series of test procedures conducted against a server that runs a vulnerable web application.

RESULT

Result of Experiment

This research uses data feeds from the National Vulnerability Database (NVD) in 2017, 2018, and 2019. The table structure in the NVD will take the following data:

(1) CVE: CVE data has a \textbf{problemtype} column that has a CWE classification value
(2) Configuration: This section has the effect of weakness on the system
(3) Impact: This section has valuable information from CVSS
(4) Published Date: Publish date for a CVE record
(5) Last Modified: The last modified date for a CVE record

CWEs and CVEs data are important in assessing a software's vulnerability, and it provides an easy reference to understand existing vulnerabilities, which can ease software quality testing. Therefore, this research uses CWE as part of the classification of injection attacks. The CWE identifier is CWE-89 for SQL injection attacks and CWE-1033 for cross-site scripting injection attacks.

JSON data feeds from NVD and CVE have inconsistent scores, which can be seen in Figures 2, 3, and 4. Therefore, this research tries to find the congruence of each CVSS by using Equation 6:

$$c = \sum_{n=1}^{\infty} \frac{mode(t)}{y} \tag{6}$$

Where:
t = Each Vector's Possible values (Such as N, L, A, P for Attack Vector)
y = The total data gathered for such a vector.
c = Congruence

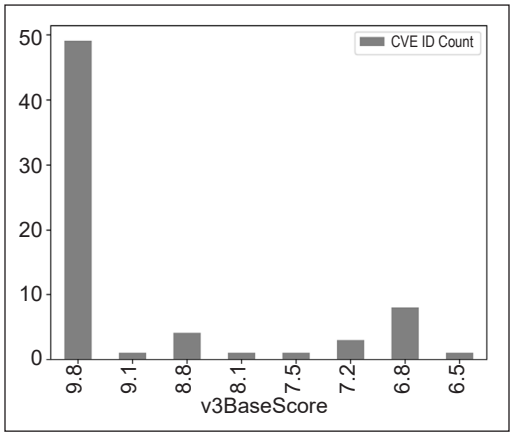

Figure 2. SQL injection CVSS3 scores in 2019

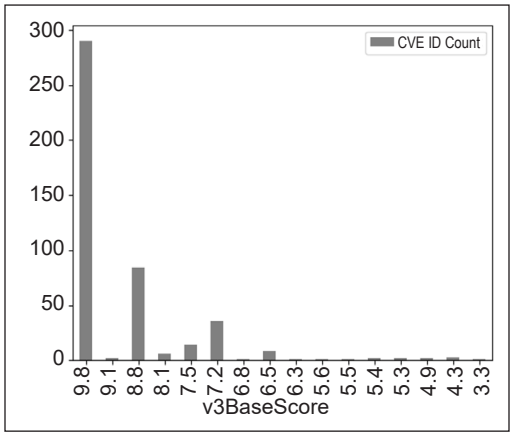

Figure 3. SQL injection CVSS3 scores in 2018

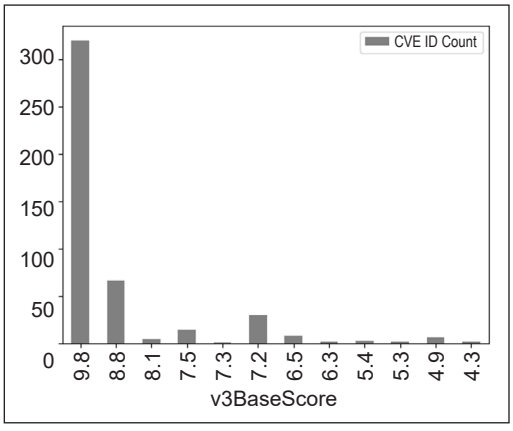

Figure 4. SQL injection CVSS3 scores in 2017

Table 7
Congruence values of CVE

Parameter	SQL	XSS
AV	99.3\%(N)	99.8\%(N)
AC	98.7\%(L)	99.6\%(L)
PR	73.0\%(N)	60.56\%(N)
UI	98.8\%(N)	99.2\%(R)
S	100\%(U)	98.8\%(C)
C	97.8\%(H)	98.7\%(L)
I	92.6\%(H)	98.8\%(L)
A	91.9\%(H)	98.9\%(N)
Total	985 CVEs	4681 CVEs

The calculation results of the above formula can be seen in Table 7. This research does not use the Attack Vector (AV) parameter in the calculation results because this parameter becomes invalid. After all, the attack surface can be accessed by hackers in a network interface protocol. Therefore, to check an attacker's IP address, whether it is still in one subnet or not, with the following algorithm:

Algorithm 1: AV String Vector Generation Algorithm

```
Result: Attack Vector (Network / Adjacent)
let compare = getInputIP() ;
let localip.prefix = getNetworkInterfaceInfo();
let subnets = GenerateSubnet(localip.prefix);
procedure findMatchingSubnet(ip)
for (subnet in subnets) do
```

```
    if IP is in the subnet, then
        return subnet
    else
        return -1
    end
end
if findMatchingSubnet(localip) is equal to findMatchingSubnet(compare) then
    return "A";
else
    return "N";
end
```

The Privileged Require (PR) vector is the lowest vector of all existing CVSS vectors. This vector can be assessed manually using the Principle of Least Privilege method, which uses restrictions on access to user roles or privileges.

Detection of user privileges, in general, can use the Cookies variable. This method is effective when the attacker is using a browser. Cookies have an interesting section containing a URL Path that can indicate the user's access rights. The Path variable contains information about where Cookie headers can be sent for authentication from the server.

This research uses the Path URL Cookies Header to identify whether an attacker has fully gained access to a specific Path. Since the Cookies header was sent to a specified path, we can conclude that if the attacker managed to access the specified path without generating an HTTP error, the attacker has essentially gained the privilege to access that Path and retrieved the server's corresponding resources. It can be done without forcefully checking the Cookie header from the incoming Request.

The privileges declared can vary; however, the Super User is one absolute privilege. Like the Linux counterpart, a superuser is allowed to execute any command in the server, giving them the highest level of privilege. If that is the case, the PR would be scored as "H" or High since the attacker has gained the highest privilege within the web server. Other privileges specified within the URL are relative to the use.

DISCUSSION

In this study, we used many log entries considered malicious and detected by the IDS or SIEM system. This study develops a log parser tool to convert logs from the detection system into a file with a .csv extension. The output taken from the log is IP Address; URL; Score; Vector String.

We would also use VSS, a Python library, to calculate the CVSS3.0 score. The script that implements the library takes an input of a CVSS:3.0 vector string and prints out the generated CVSS3.0 score.

Table 7 shows the results of the testing procedure. It all comprised SQL Injection attempts toward a victim web server located at 172.17.0.2 with a prefix of 16.

We can see from the table below that the score changes corresponding to the *URL* and *IP* parameter given.

There are a few things to take note of:

(a) We omit the queries of the URL string to shorten the sentence length in this paper.

(b) We omit the request method.

The following are the explanations of each row of the result table.

(1) In this case, the SIEM System recorded an attack in the first row with the following data.
   (a) IP: 171.25.193.77
   (b) URL: /
   (c) Timestamp: 1564284545
   (d) Is a threat: yes
   (e) SQLi type: tautology

Since the attacker is located outside the system's subnet, it is classified as a remote attack. The URL appears to be a non-privileged URL based on the configuration.

So, from there, the dynamically designed vector, which consists of *AV* and *PR*, would be scored *N* and *N*, respectively.

Since the vulnerability is classified as SQL Injection, the predetermined values would be **C:H/I:H/A:H/UI:N/S:U/AC:L**. Thus, the final CVSS vector string would be **C:H/I:H/A:H/AV:N/UI:N/S:U/PR:N/AC:L**, which is scored as *9.8* according to CVSS:3.0.

(2) In the second row, the SIEM System recorded an attack with the following data in this case.
   (a) IP: 171.25.193.235
   (b) URL: /index
   (c) Timestamp: 1564284545
   (d) Is a threat: yes
   (e) SQLi type: tautology

This row is very similar to the first row. The attacker is outside of the subnet the machine is in and has a URL with no privilege.

(3) In the third row, the SIEM System recorded an attack with the following data in this case.
   (a) IP: 172.17.0.9
   (b) URL: /2006
   (c) Timestamp: 1564284548
   (d) Is a threat: yes
   (e) SQLi type: tautology

This row features an adjacent attacker with an IP of *172.17.0.9*, which would modify the Attack Vector into *A* or Adjacent. Other than that, it is still the same as the previous row with a vector string of **C:H/I:H/A:H/ AV:A/UI:N/S:U/PR:N/AC:L** and a score of **8.8**.

(4) In this case, the SIEM System recorded an attack in the fourth row with the following data.
   (a) IP: 172.25.193.20
   (b) URL: /crack
   (c) Timestamp: 1564284548
   (d) Is a threat: yes
   (e) SQLi type: tautology

This row features an attack with a URL specified as having high privilege, which would modify the Privilege Required vector into *H* or Adjacent. Other than that, it is still the same as the previous row with a vector string of **C:H/I:H/A:H/ AV:A/UI:N/S:U/PR:H/ AC:L** and a score of **7.2**.

Table 8
Automatic summarizing (Victim IP is 172.17.0.2)

IP **URL** **timestamp** **category** **class**	**Vector**	**Score**
171.25.193.77 **/** **1564284545** **threat** **tautology**	C:H/I:H/A:H/AV:N/UI:N/S:U/PR:N/AC:L/	9.8
171.25.193.235 **/index** **1564284545** **threat** **tautology**	C:H/I:H/A:H/AV:N/UI:N/S:U/PR:N/AC:L/	9.8
172.17.0.9 **/2006** **1564284548** **threat** **tautology**	C:H/I:H/A:H/AV:A/UI:N/S:U/PR:N/AC:L/	8.8
171.25.193.20 **/crack** **1564284549** **threat** **tautology**	C:H/I:H/A:H/AV:N/UI:N/S:U/PR:H/AC:L/	7.2

EVALUATION

A series of test procedures were conducted against a server that runs a vulnerable web application to evaluate the overall performance of the methods. The server was assigned 10.20.153.52/20 as the IP address. Note that the /20 CIDR notation indicates that the IP is a Class C. The first test procedure involves a potential Cross-site scripting attack that has been detected, and the detection data is fed to the system. The data is shown in Figure 6.

After the summarizing process, data that indicates the severity measurement result (Figure 6, is emitted by the system. From the data, it can be concluded that the attack has a severity score of 6.1, denoted **medium** severity, with a likelihood percentage of 94%. The data also shows the vector string of the attack, which is very helpful for a vulnerability assessment and incident report.

The attack is analyzed based on the CWE tag. The IP and server prefix (CIDR) are obtained, then the system detects that the attack can be categorized as a Network Attack. P_ERRORS attribute in the output data indicates that the endpoint URL does not exist in the database. Hence, the system directly inserts the URL into the database so that future detections involving the same attack and endpoint will use the measured severity as precedence.

Same for the SQL Injection attack testing, the detection data (Figure 7, is fed to the system to be analyzed.

After the summarizing process, data in Figure 8, is emitted. From the data, it can be concluded that the attack also has a severity score of 6.1, denoted **medium** severity, with a likelihood percentage of 94%.

The system measures an attack with SQL Injection payload (CWE-89 based on

```
 {
"_id": "124",
"timestamp":str(datetime.datetime.now()),
"vul":"XSS",
"ip":"10.20.30.40",
"url":"/xss/stored"
}
```

Figure 5. Data input for cross-site scripting testing


```
{
   "_index" : "nethive-cvss",
   "_type" : "_doc",
   "_id" : "YhVwOG8BWtOlYx1xVPQM",
   "_\textit{score}" : 1.0,
   "_source" : {
     "corr_id" : "124",
     "timestamp" : "2020-01-23T03:26:56.147001",
     "SUMMARIZE_RESULT" : {
       "vector" : "AV:N/AC:L/PR:N/UI:R/S:C/C:L/I:L/A:N/",
       "\textit{score}" : 6.1,
       "severity" : "MEDIUM",
       "errors" : {
         "PR_ERRORS" : "2020/01/23 03:26:58 sql: no rows in
                        result set\n"
       },
       "likelyhood" : 94
     }
   }
}
```


Figure 6. Data output for cross-site scripting testing

tag classification). The IP source of the attack indicates that the attack was carried out from a machine under the same network. Hence, the attack is categorized as an Adjacent attack.

Overall, 1359 SQL Injection and 4966 Cross-site Scripting attack simulations are conducted against the system. The accuracy of the automatic measurement is calculated, with human-assessed severity as the ground truth. The result is shown in Table 9.

Apart from the accuracy measurement, the *common error cause* is also measured for every vulnerability metric on SQL Injection and Cross-site Scripting attack data. The result is shown in Table 10. The *common error cause* illustrates the amount of attack data for each metric that are incongruent with the rest of the data.

```
{
    "_id": "124",
    "timestamp":str(datetime.datetime.now()),
    "vul":"SQLi",
    "ip":"10.20.153.54",
    "url":"/vulnerabilities/sqli"
}
```

Figure 7. Data input for SQL injection testing

```
{
   "_index" : "nethive-cvss",
   "_type" : "_doc",
   "_id" : "YxV20G8BWtOlYx1x5PQh",
   "_\textit{score}" : 1.0,
   "_source" : {
     "corr_id" : "124",
     "timestamp" : "2020-01-23T03:34:07.456804",
     "SUMMARIZE_RESULT" : {
       "vector" : "AV:N/AC:L/PR:N/UI:R/S:C/C:L/I:L/A:N/",
       "\textit{score}" : 6.1,
       "severity" : "MEDIUM",
       "errors" : { },
       "likelyhood" : 94
     }
   }
 }
```

Figure 8. Data output for SQL injection testing

Table 9
Accuracy percentage of SQL injection and cross-site scripting

Attack Type	String Accuracy %	Score Accuracy %
SQL Injection	62,61957321559971	62,61957321559971
Cross-site Scripting	59,30326218284333	59,28312525171164

Table 10
Common error cause breakdown for SQL injection and cross-site scripting

Attack Type	Common Error Cause							
	AV	**AC**	**PR**	**UI**	**S**	**C**	**I**	**A**
SQL Injection	7	19	419	13	2	45	120	7
Cross-site Scripting	4	18	1964	35	55	63	58	4

CONCLUSION

In this paper, the author designed a novel system to automate the calculation of CVSSv3.0 scores on SQL Injection and XSS vulnerabilities based on data from NVD and network logs. Dynamic analysis can be performed on AV Vector (Attack Vector) metric, while the PR (Privilege Required) metric is shown to be able to be calculated pseudo-dynamically, with a note that the accuracy rate is 59.28% for Cross-site Scripting attacks, and 62.62% for SQL Injection attack. For other vectors, the data from NVD has a high enough congruence that can be used as an element of static calculations.

Although, the authors have to admit that the methods we suggested are hardly flawless since it relies on the congruence of currently existing vector strings in NVD. If, in any case, the NVD data feeds become highly incongruent, then this paper becomes deprecated. Another point we should mention is that perhaps further research is required in detecting privilege. Since what we propose perhaps is effective, it is slightly hard coded. Though now it is statistically proven that a vulnerability's base vectors, most of the time, do have similar values, disregarding the software it is exploited in. Finally, the author suggests further researchers examine data from other sources, such as the Open Source Vulnerability Database (OSVDB) (Kouns, 2008), and extensively test the theory used in this paper.

ACKNOWLEDGEMENT

This work was supported by the Collaboration International Grant 2021 between Bina Nusantara University, Indonesia and Universiti Teknologi MARA (UiTM) Shah Alam, Malaysia.

REFERENCES

Aksu, M. U., Bicakci, K., Dilek, M. H., Ozbayoglu, A. M., & Tatli, E. I. (2018). Automated generation of attack graphs using NVD. In *Proceedings of the Eighth ACM Conference on Data and Application Security and Privacy* (pp. 135-142). ACM Publishing. https://doi.org/10.1145/3176258.3176339

Alazmi, S., & de Leon, D. C. (2022). A systematic literature review on the characteristics and effectiveness of web application vulnerability scanners. *IEEE Access*, *10*, 33200-33219. https://doi.org/10.1109/ACCESS.2022.3161522

Aliero, M. S., Ghani, I., Qureshi, K. N., & Rohani, M. F. (2020). An algorithm for detecting SQL injection vulnerability using black-box testing. *Journal of Ambient Intelligence and Humanized Computing*, *11*, 249-266. https://doi.org/10.1007/s12652-019-01235-z

Aliero, M. S., Qureshi, K. N., Pasha, M. F., Ghani, I., & Yauri, R. A. (2020). Systematic review analysis on SQLIA detection and prevention approaches. *Wireless Personal Communications*, *112*, 2297-2333. https://doi.org/10.1007/s11277-020-07151-2

Athanasopoulos, E., Pappas, V., Krithinakis, A., Ligouras, S., Markatos, E. P., & Karagiannis, T. (2010, June 23-24). *xJS: Practical XSS prevention for web application development* [Paper presentation]. USENIX Conference on Web Application Development, Boston, MA, USA.

Bates, D., Barth, A., & Jackson, C. (2010). Regular expressions considered harmful in client-side XSS filters. In *Proceedings of the 19th International Conference on World Wide Web - WWW '10* (pp. 91-100). ACM Publishing. https://doi.org/10.1145/1772690.1772701

Beck, A., & Rass, S. (2016). Using neural networks to aid CVSS risk aggregation - An empirically validated approach. *Journal of Innovation in Digital Ecosystems*, *3*(2), 148-154. https://doi.org/10.1016/j.jides.2016.10.002

Bisht, P., & Venkatakrishnan, V. N. (2008). XSS-GUARD: Precise dynamic prevention of cross-site scripting attacks. In D. Zamboni (Ed.), *Detection of Intrusions and Malware, and Vulnerability Assessment* (Vol. 5137, 23-43). Springer. https://doi.org/10.1007/978-3-540-70542-0_2

Bozic, J., & Wotawa, F. (2013). XSS pattern for attack modeling in testing. In *2013 8th International Workshop on Automation of Software Test (AST)* (pp. 71-74). IEEE Publishing. https://doi.org/10.1109/IWAST.2013.6595794

Elbaz, C., Rilling, L., & Morin, C. (2020). Fighting N-day vulnerabilities with automated CVSS vector prediction at disclosure. In *Proceedings of the 15th International Conference on Availability, Reliability and Security* (pp. 1-10). ACM Publishing. https://doi.org/10.1145/3407023.3407038

Figueroa-Lorenzo, S., Añorga, J., & Arrizabalaga, S. (2021). A survey of IIoT protocols: A measure of vulnerability risk analysis based on CVSS. *ACM Computing Surveys*, *53*(2), 1-53. https://doi.org/10.1145/3381038

Fogie, S., Grossman, J., Hansen, R., & Petkov, P. D. (2007). *XSS Attacks: Cross Site Scripting Exploits and Defense* (1st ed.). Syngres Media.

Gallon, L., & Bascou, J. J. (2011a). Using CVSS in attack graphs. In *2011 Sixth International Conference on Availability, Reliability and Security* (pp. 59-66). IEEE Publishing. https://doi.org/10.1109/ARES.2011.18

Gallon, L., & Bascou, J. J. (2011b). Using CVSS in attack graphs. In *2011 Sixth International Conference on Availability, Reliability and Security* (pp. 59-66). IEEE Publishing. https://doi.org/10.1109/ARES.2011.18

Gupta, S., & Gupta, B. B. (2016). XSS-immune: A google chrome extension-based XSS defensive framework for contemporary platforms of web applications. *Security and Communication Networks*, *9*(17), 3966-3986. https://doi.org/10.1002/sec.1579

Gupta, S., & Gupta, B. B. (2017). Cross-site scripting (XSS) attacks and defense mechanisms: Classification and state-of-the-art. *International Journal of System Assurance Engineering and Management*, *8*(Suppl 1), 512-530. https://doi.org/10.1007/s13198-015-0376-0

Houmb, S. H., & Franqueira, V. N. L. (2009). Estimating ToE risk level using CVSS. In *2009 International Conference on Availability, Reliability and Security* (pp. 718-725). IEEE Publishing. https://doi.org/10.1109/ARES.2009.151

Houmb, S. H., Franqueira, V. N. L., & Engum, E. A. (2010a). Quantifying security risk level from CVSS estimates of frequency and impact. *Journal of Systems and Software*, *83*(9), 1622-1634. https://doi.org/10.1016/j.jss.2009.08.023

Houmb, S. H., Franqueira, V. N. L., & Engum, E. A. (2010b). Quantifying security risk level from CVSS estimates of frequency and impact. *Journal of Systems and Software*, *83*(9), 1622-1634. https://doi.org/10.1016/j.jss.2009.08.023

Kieyzun, A., Guo, P. J., Jayaraman, K., & Ernst, M. D. (2009). Automatic creation of SQL Injection and cross-site scripting attacks. In *2009 IEEE 31st International Conference on Software Engineering* (pp. 199-209). IEEE Publishing. https://doi.org/10.1109/ICSE.2009.5070521

Kindy, D. A., & Pathan, A.-S. K. (2011). A survey on SQL injection: Vulnerabilities, attacks, and prevention techniques. In *2011 IEEE 15th International Symposium on Consumer Electronics (ISCE)* (pp. 468-471). IEEE Publishing. https://doi.org/10.1109/ISCE.2011.5973873

Kouns, J. (2008). *Open source vulnerability database project*. TIM Review. https://timreview.ca/article/155

Le, T. H. M., Hin, D., Croft, R., & Babar, M. A. (2021). DeepCVA: Automated commit-level vulnerability assessment with deep multi-task learning. In *2021 36th IEEE/ACM International Conference on Automated Software Engineering (ASE)* (pp. 717-729). IEEE Publishing. https://doi.org/10.1109/ASE51524.2021.9678622

Pelizzi, R., & Sekar, R. (2012). Protection, usability and improvements in reflected XSS filters. In *Proceedings of the 7th ACM Symposium on Information, Computer and Communications Security - ASIACCS '12* (pp. 1-5). ACM Publishing. https://doi.org/10.1145/2414456.2414458

Pramod, A., Ghosh, A., Mohan, A., Shrivastava, M., & Shettar, R. (2015). SQLI detection system for a safer web application. In *2015 IEEE International Advance Computing Conference (IACC)* (pp. 237-240). IEEE Publishing. https://doi.org/10.1109/IADCC.2015.7154705

Radack, S., & Kuhn, R. (2011). Managing security: The security content automation protocol. *IT Professional*, *13*(1), 9-11. https://doi.org/10.1109/MITP.2011.11

Rao, K. S., Jain, N., Limaje, N., Gupta, A., Jain, M., & Menezes, B. (2016). Two for the price of one: A combined browser defense against XSS and clickjacking. In *2016 International Conference on Computing, Networking and Communications (ICNC)* (pp. 1-6). IEEE Publishing. https://doi.org/10.1109/ICCNC.2016.7440629

Sadeghian, A., Zamani, M., & Manaf, A. A. (2013). A taxonomy of SQL injection detection and prevention techniques. In *2013 International Conference on Informatics and Creative Multimedia* (pp. 53-56). IEEE Publishing. https://doi.org/10.1109/ICICM.2013.18

Sarmah, U., Bhattacharyya, D. K., & Kalita, J. K. (2018). A survey of detection methods for XSS attacks. *Journal of Network and Computer Applications*, *118*, 113-143. https://doi.org/10.1016/j.jnca.2018.06.004

Scarfone, K., & Mell, P. (2009). An analysis of CVSS version 2 vulnerability scoring. In *2009 3rd International Symposium on Empirical Software Engineering and Measurement* (pp. 516-525). IEEE Publishing. https://doi.org/10.1109/ESEM.2009.5314220

Singh, A. K., & Roy, S. (2012). A network based vulnerability scanner for detecting SQLI attacks in web applications. In *2012 1st International Conference on Recent Advances in Information Technology (RAIT)* (pp. 585-590). IEEE Publishing. https://doi.org/10.1109/RAIT.2012.6194594

Voeller, J. G. (2008). *Wiley Handbook of Science and Technology for Homeland Security*. John Wiley & Sons, Inc. https://doi.org/10.1002/9780470087923

Wang, C. H., & Zhou, Y. S. (2016). A new cross-site scripting detection mechanism integrated with HTML5 and CORS properties by using browser extensions. In *2016 International Computer Symposium (ICS)* (pp. 264-269). IEEE Publishing. https://doi.org/10.1109/ICS.2016.0060

Pertanika J. Sci. & Technol. 31 (3): 1267 - 1278 (2023)

PERTANIKA JOURNALS

SCIENCE & TECHNOLOGY

Journal homepage: http://www.pertanika.upm.edu.my/

The Effect of Preload, Density and Thickness on Seat Dynamic Stiffness

Azmi Mohammad Hassan[1], Khairil Anas Md Rezali[1]*, Nawal Aswan Abdul Jalil[1], Azizan As'arry[1] and Mohd Amzar Azizan[2,3]

[1]Sound and Vibration Research Group (SVRG), Department of Mechanical and Manufacturing Engineering, Faculty of Engineering, Universiti Putra Malaysia (UPM), 43400 UPM Serdang, Selangor, Malaysia
[2]Higher Colleges of Technology (HCT), Abu Dhabi 25026, United Arab Emirates
[3]Khalifa bin Zayed Air College (KBZAC), Abu Dhabi, United Arab Emirates

ABSTRACT

The vibration transferred to the car floor transmits to the human body through the seat structure, and the typical design of the seat structure consists of several components such as seat frame and seat cushion. The material widely used as seat cushion is open-cell polyurethane (PUR) foam; when under vibration, it will behave dynamically. Factors such as mechanical properties and material thickness of PUR can affect its behaviour and performance and the amount of vibration transmits to the human body. This work measures the PUR dynamic stiffness for different material densities and thicknesses. The test was conducted using an indenter head with a flat surface since it was a less expensive method, and quicker measurement could be done. The force sensor was placed within the indenter structure to measure the load transmitted to the seat and acceleration data acquired by the accelerometer, which was mounted on a shaker test plate. Foam materials with 30 kg/m^3 and 44 kg/m^3 with 30 mm and 50mm thickness are used in the experiment with the amount of preload applied of 20 N,30 N and 40 N. Seat stiffness increased when the preload increased from 20 N to 40 N, and a similar trend occurred when foam thickness decreased. The lower density of PUR resulted in a greater increase of seat stiffness and damping across the frequency 0-30 Hz compared to a higher density of PUR. This study concluded that thickness, preload, and density significantly affect seat dynamic stiffness.

Keywords: Dynamic stiffness, seat cushion, seat dynamic, seat vibration

ARTICLE INFO

Article history:
Received: 25 February 2022
Accepted: 16 August 2022
Published: 31 March 2023

DOI: https://doi.org/10.47836/pjst.31.3.08

E-mail addresses:
azmi@outlook.my (Azmi Mohammad Hassan)
khairilanas@upm.edu.my (Khairil Anas Md Rezali)
nawalaswan@upm.edu.my (Nawal Aswan Abdul Jalil)
zizan@upm.edu.my (Azizan As'arry)
mazizan@hct.ac.ae (Mohd Amzar Azizan)
* Corresponding author

ISSN: 0128-7680
e-ISSN: 2231-8526

© Universiti Putra Malaysia Press

INTRODUCTION

The seat is a critical structure of a vehicle because vibration transmitted through the seat can affect both human health and driving comfort (Griffin, 1990). Many methods have been developed numerically and experimentally to assess seat performance in attenuating or influencing vibration; however, the findings have not always been consistent due to the nonlinearity of the material used for the seat and the human responses (Karen et al., 2012). The seat vibrations due to the movement of a car are transmitted to the car floor, which is later transmitted to the human body through seat structure and can be complex, involving many factors. The seat can be considered a structure that can influence comfort significantly compared to other factors such as air conditioning and noise level (Kamp, 2012). It is because the human body has the most direct contact with the vehicle seat (Bang et al., 2017).

Typical seat components include several components, such as a seat frame and seat cushion. Open-cell polyurethane (PUR) foam has been widely used in the automotive industry as a cushion for seat structure (Patten et al., 1998). Open cell PUR provides advantages such as excellent compression properties, ease of hardness adjustment, superior resilience, and ability to mould shapes, and it is cheap, too (Murata et al., 2014; Patten et al., 1998). The material structure comprises a cellular matrix filled with air free from loads. When subjected to impact, the air trapped in the cell will squeeze through the cell structure. Hence the cell size of the cellular matrix will affect its mechanical properties and behaviour under compression.

The static and dynamic properties of PUR used as a seat cushion can affect the comfort level experienced by the human body (Choi & Kim, 2020). Hence modification of material structure, such as increasing crosslinking density of the polymer matrix, can improve the comfort level (Wada et al., 2008). Instead of modifying the structure of the material, the use of an optimal thickness relative to its mechanical property can also improve the level of comfort (Deng et al., 2003; Patten et al., 1998; Zhang & Dupuis, 2011). Dynamic stiffness of the foam becomes one of the important parameters in determining the seat performance (Kreter, 1985) and by measuring dynamic stiffness, the behaviour of the foam under load can be investigated.

Dynamic stiffness property can be evaluated using the indentation test method by applying preloads using an indenter pad with an SIT-BAR shape (Wei & Griffin, 1998; Tufano & Griffin, 2013; Whitham & Griffin, 2010; Zhang et al., 2015). The load imposed on the PUR material significantly affects material stiffness; when the load increases, the stiffness and damping increase (Wei & Griffin, 1998). Other findings showed that foam thickness less affected damping, but it depends more on the frequency (Zhang et al., 2015).

The seat dynamic stiffness is an important characteristic of predicting seat transmissibility. As mentioned previously, the dynamic stiffness of seat material can be affected by various factors. Three main factors are usually assessed when selecting seat

material with respect to its dynamic stiffness: the effects of seat thickness, the preload force and seat densities apart from the seat design. However, it is still unclear how significantly seat dynamic stiffness is affected by the mentioned factors. In addition, all previous studies did not investigate the effects of contact area, contact force, and material density in a single study. The seat foam usually behaves non-linearly, so a study of this will help us further understand how all variables influence the material dynamic stiffness. This work aimed to investigate the dynamic stiffness characteristics of automotive seats, emphasising the effects of thickness, preload, and material densities. The increase in thickness was expected to reduce seat dynamic stiffness. Seat foam density can be between 30 kg/m^3 to 50 kg/m^3 in accordance with Euromoulder Association (http://euromoulders.org). It was also expected that the dynamic stiffness of the seat would increase as the density of the material decreased. The findings in this work can provide the researchers and seat designers with an insight into how density and thickness will affect vibration transmission. Even though few previous publications are studying the effect of the thickness of seat foam on dynamic stiffness, it was not discussed thoroughly, and so far, the effect of foam density was not properly studied.

METHODS

Test Apparatus and Setup

The study employed a test rig for the measurement of dynamic stiffness testing, including the structural test frame, force sensor, vibration shaker, and accelerometer (Figure 1). The force sensor used in the experiment was Futek LTH-350, a doughnut-type sensor which

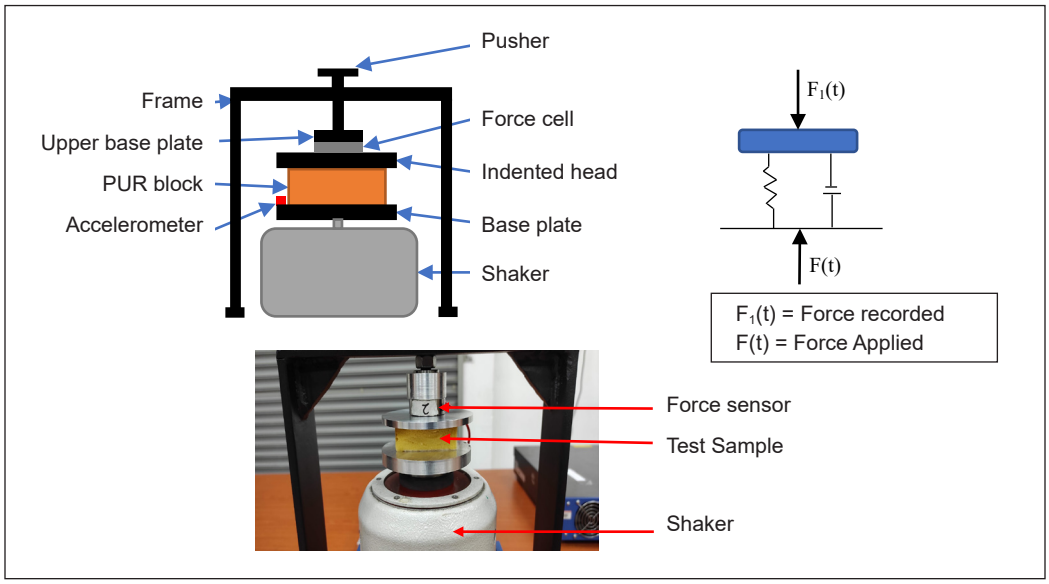

Figure 1. Schematic and actual view of the test setup

has a maximum loading capacity of 500lb (~227kg). The acceleration in the vertical direction was measured using a triaxial IEPE Dytran 3023A accelerometer with a sensitivity of 10.78 mV/g in the respective axis. The vibration was generated using Tira Vibration Test System, and vibration input was configured using the LMS SCADA Mobile system. LABVIEW software provided real-time load control monitored the power spectral density and acquired fresh measurement data for both the force sensor and accelerometer. The coherence of system input and output was monitored during experimental works, and the coherence within the frequency of interest is shown in Figure 2. Coherence close to 1 indicated that the output signal was linearly correlated with the input signal (Zhang et al., 2015).

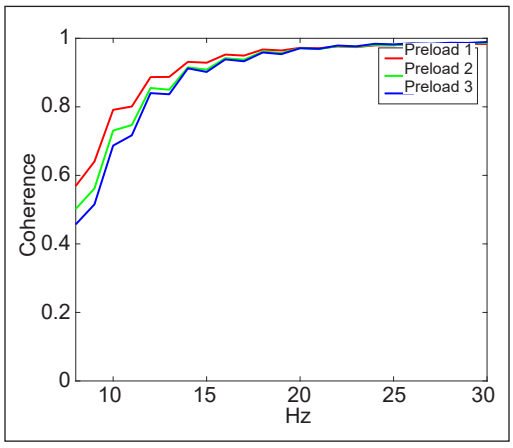

Figure 2. System input-output coherence

Test Sample and Procedures

The test sample was an open cell polyurethane foam (PUR) with a density of 44 kg/m^3 and 30 kg/m^3 with a sample's dimension of 60 mm × 60 mm and thickness of 30 mm, 40 mm and 50 mm as shown in Table 1. All samples in this study agreed with Euromoulders Association's suggestion for actual seat applications (http://euromoulder.org). Samples 1 and 2 were used to investigate the effects of foam density and preload, whilst Samples 2, 3 and 4 were employed to study the effects of material thickness on seat dynamic stiffness. Three different preloads were applied in this study which was 30 N, 40 N and 50 N. The test frequency the shaker (TIRAvib with a maximum force of 200 N) generated was between 1 and 100Hz and 8 ms^{-2} r.m.s. acceleration (unweighted) or 1.5 r.m.s acceleration (weighted W_k according to ISO-2361-1) with a spectral density, as shown in Figure 3. The input spectra were high, between 10 to 30Hz and similar across different settings. The study measured the vibration and force signals of the material at the lower and upper surfaces of the foam (Figure 1). The data recorded were sampled at 2048 samples per second and

Table 1
Test sample characteristics

Parameter	***Sample 1***	***Sample 2***	***Sample 3***	***Sample 4***
Size	60 mm × 60 mm	60 mm × 60 mm	60 mm × 60 mm	60 mm × 60 mm
Thickness	50 mm	50mm	40 mm	30mm
Density	30 kg/m^3	44 kg/m^3	44 kg/m^3	44 kg/m^3
Origin	Foam Block	Car Seat	Car Seat	Car Seat

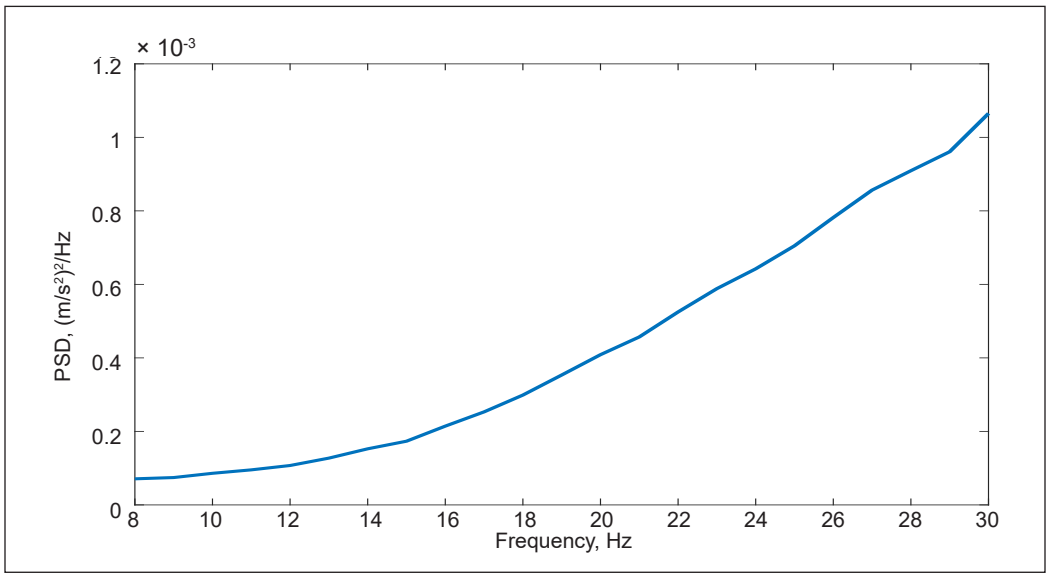

Figure 3. Median power spectral density for input acceleration weighted W_k according to ISO2631-1 in logarithmic scale

filtered by Butterworth low pass filter with 2 poles and a cut-off frequency of 50 Hz the analysis of the data was done using MATLAB.

Sample Scale

This experiment was conducted using a small-scale shaker and sample size. The maximum load applied to the small shaker was about 200 N. Because the samples used in this study were much smaller than the actual seat size studied previously (Wei & Griffin, 1998), the loads applied to the materials differed. The loads applied in this study were chosen based on similar force per unit area to make it comparable to the actual size and load on the actual seat, as conducted in previous studies. The PUR sample sizing was estimated based on the approximated actual seat size and load applied by (Wei & Griffin, 1998).

As shown in Table 2, the force per unit area for small-scale foam samples used in this work was identical to the force per unit area for the actual seat foam size used (Wei & Griffin, 1998). It can be concluded that the amount of preload for small-scale samples of 30 N, 40 N, and 50 N was identical to full-scale samples of 400 N, 500 N and 600 N, accordingly. Force per unit area, *P*, is calculated using Equation 1.

$$P = \frac{F}{A} \qquad (1)$$

Where *F* is the applied force and *A* is the area impacted by the applied force.

Table 2
Force per unit area

Area, mm²	Force, N	Force per unit area, MPa	Source
3600	30	0.0083	
3600	40	0.011	This work
3600	50	0.014	
47047	400	0.0085	
47047	500	0.011	(Wei & Griffin, 1998)
47047	600	0.013	

Theory of Dynamic Stiffness

Dynamic stiffness of the seat, *S(f),* was given by Griffin (1990) in Equation 2:

$$S(f) = \frac{F_{io}(f)}{(-(2\pi f)^{-2})\ A_{ii}(f)} \qquad (2)$$

Where $F_{io}(f)$ is the cross-spectral density of the input acceleration and the output force transmitted by the material, $A_{ii}(f)$ is the power spectral density of the input acceleration, and f is the frequency in Hz.

The dynamic stiffness was assumed to be represented by the Kelvin Voigt model (Equation 3).

$$S(f) = K(f) + 2\pi f C(f) * i \qquad (3)$$

Where K is the stiffness of the material and C is the material viscous damping coefficient.

The complex number, $S(f)$, is called dynamic stiffness and was used in preference to the mechanical impedance (the ratio of force over velocity) because dynamic stiffness provided an easier approach to identifying the equivalent stiffness, K and the equivalent damping, C. Both seats/foam parameters of K and C can be obtained using the curve fitting method from real and imaginary components of dynamic stiffness, $S(f)$ (Wei & Griffin, 1998; Tufano & Griffin, 2013; Zhang et al., 2015) but are not conducted in this study.

RESULTS

Effect of Preload on the PUR Dynamic Stiffness

Figure 4 displays the dynamic stiffness for density 44kg/m^3 at the variation of preloads at 20N, 30N and 40N. From the plot, stiffness increases with increasing preload force from 20 N to 40 N. A similar trend was also observed for PUR foam with lower density (30 kg/m^3). Increasing the preload will increase the dynamic stiffness of the foam.

At all preloads, foam stiffness increased as the vibration frequency increased for frequencies between 8 to 15 Hz. The damping of PUR foam was also found to increase with the increased preload amount, although they were not significant for each preload.

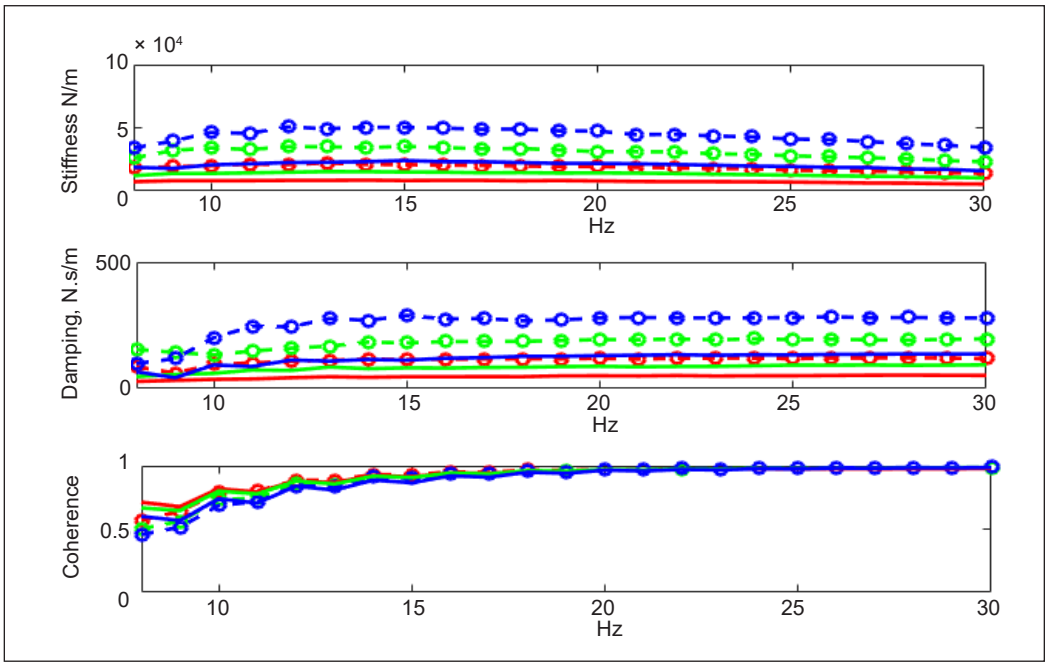

Figure 4. Dynamic stiffness for PUR with 30 kg/m^3(-o-) and 44 kg/m^3 (-) at preload of 20 N (----), 30 N (----) and 40 N (----)

Effect of Material Density on PUR Dynamic Stiffness

Figure 5 presents the effects of foam density on the modulus of dynamic stiffness. PUR foam with a density of 30 kg/m^3 produced greater stiffness than PUR foam with 44 kg/m^3. Also, the damping of lower-density PUR foam was greater than PUR foam with higher density.

Open-celled PU foam material structure consists of PU material and air-filled cells. The entrapped air movement is unrestricted. Under applied preload, the PU foam with lower density loses more air (due to greater compression) than the PU foam with higher density. Greater reduction of air in the cells makes the PU foam stiffer and less flexible. The result is consistent with findings by (Tufano & Griffin, 2013).

Figure 6 exhibits the minimum and maximum stiffness for PUR foam with a density of 30 kg/m^3 and 44 kg/m^3. The differences in maximum stiffness at 20 N, 30 N and 40 N vary by 61%, 56% and 52%, respectively, for both densities.

Effect of Material Thickness on PUR Dynamic Stiffness

Figure 7 shows that foam stiffness increased when the thickness decreased. The result was in line with Zhang et al. (2015). For both thicknesses, at all preloads, the stiffness had slightly increased up to 15 Hz, and beyond 15 Hz, it produced a slight decrease to 30 Hz. The damping had a slightly increased trend up to 30 Hz at all preloads for both thicknesses, and the damping increased when the thickness increased.

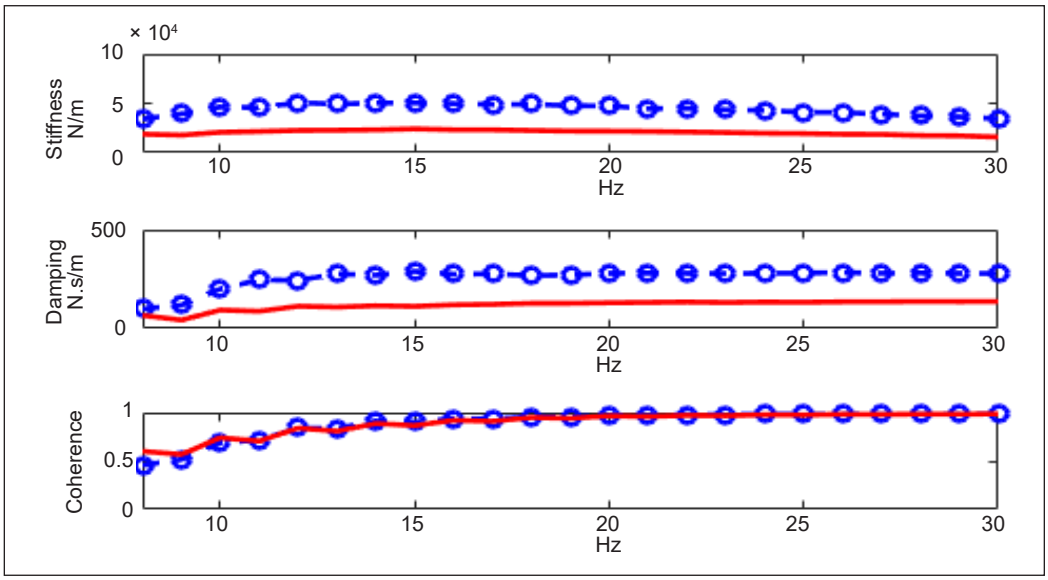

Figure 5. Dynamic stiffness for PUR with 30 kg/m³ (-o-) and 44 kg/m³ (-) at 40 N

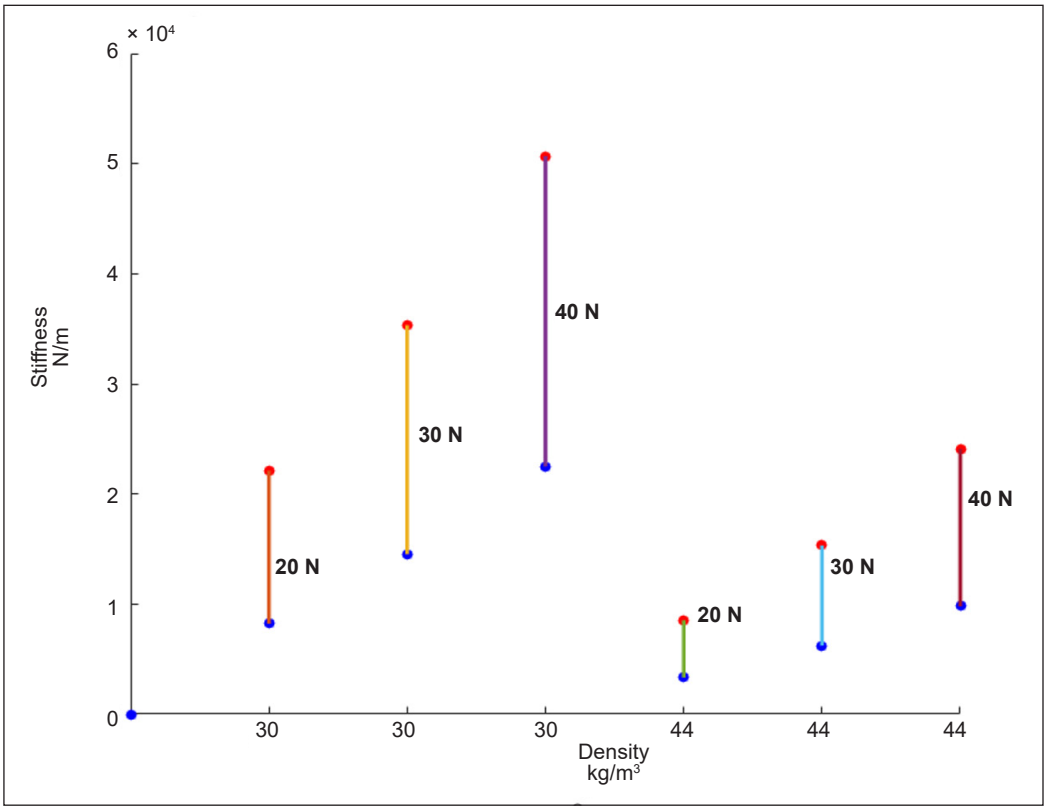

Figure 6. Maximum and minimum stiffness for PUR foam samples at preload of 20 N, 30 N and 40 N in the frequency range of 0-30 Hz

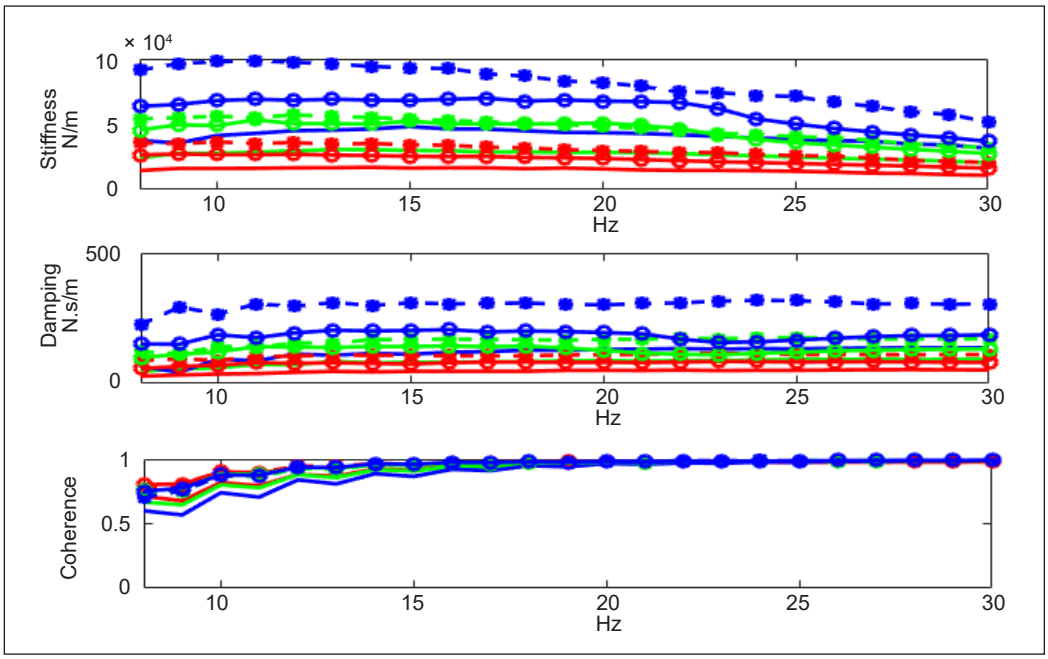

Figure 7. Dynamic stiffness of PUR foam with density 44 kg/m^3 a thickness of 50 mm (-), 40 mm (-o-) and 30 mm (-*-) at preload of 20 N (----), 30 N (----) and 40 N (----)

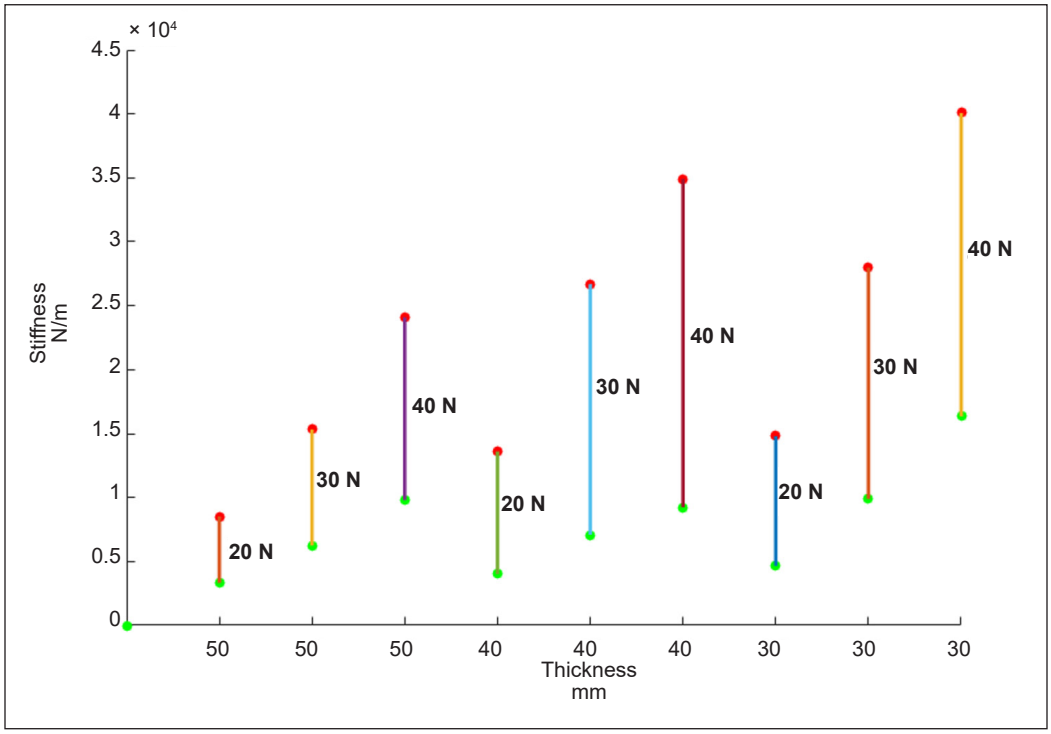

Figure 8. Maximum and minimum foam stiffness for PUR with density 44 kg/m^3 at 50 mm and 30 mm

As shown in Figure 8, a higher maximum stiffness was observed for the lower thickness of PUR foam, while at each thickness, the maximum stiffness increased when the preload increased. At 40 N, the PUR sample with a thickness of 50 mm produced the lowest maximum stiffness of 2.4×10^4 N/m and the higher maximum stiffness increased by 40% and 46% when using a PUR sample with a thickness of 40 mm and 30 mm. Similarly, the maximum stiffness at 50mm thickness is 1.53×10^4 N/m and 0.8×10^4 N/m which increased by 37% and 42% at preload of 30 N and 43% and 45% at 20 N, accordingly.

DISCUSSION

Effect of Preloads on the Material Stiffness and Damping

The stiffnesses of PUR foams were found to be affected when the applied force on the PUR foam varied. The results align with previous studies' findings (Wei & Griffin, 1998; Tufano & Griffin, 2013; Zhang et al., 2015). A similar finding was also obtained by Zhang et al. (2015) when evaluating static stiffness, where a higher thickness of seat foam will decrease its stiffness. As reported by Ebe & Griffin (2001), higher stiffness of seat foam will reduce seat comfort; however, this still depends on the damping coefficient because the damping coefficient can affect the system's settling time.

Effect of Material Thickness on the Material Stiffness and Damping

PUR foam behaviour under vibration might be influenced by the damping and entrapped air in the cells. As shown in the results, at 40 N, the preload applied on PUR foam density of 30 kg/m^3 will require more displacement than PUR foam with a density of 44 kg/m^3. Under greater displacement, the cell's structure becomes denser, and more resistance from the entrapped air will require a higher load. This behaviour indicated that the foam material might be in the densification stage when subjected to preload of 40N (Qiu et al., 2019). Similar behaviour was also observed when changing the thickness from 50 mm to 30 mm, as the thinner foam will generate more entrapped air resistance under a similar preload compared to thicker foam. As shown in Figure 5, even though the damping decreased when the thickness increased, there is only a slightly different between both thicknesses. Therefore, the thickness of foam has a less significant impact on the damping of PUR foam, while Zhang et al. (2015) reported that damping has more impact due to frequency variation.

Limitations of the Study

Although the results are in line with all previous work, the study was conducted on samples significantly smaller than the one installed in a vehicle seat. The smaller size of foam is expected to produce lower air-trapped responses compared to a larger sample. In addition,

a greater density of the foam should also be employed. Vehicle manufacturers may use greater density than the one studied here in the range of 40 kg/m^3 to 60 kg/m^3.

Also, both materials were selected based on their type (open-celled polyurethane foam) and density. Other factors such as composition, number of cells and chemical properties were unknown, which can be a factor in the difference they had in this study.

CONCLUSION

This study found that over the frequency of 10–30 Hz, the lower density of PUR foam will produce greater stiffness. Similar behaviour was observed when using thinner foam and when subjected to greater preload. From the findings, it can be concluded that using different densities of foam and thickness will affect the comfort of sitting on the seat. It is important for engineers to properly select seat foam and verify its performance because the dynamic stiffness, based on this study, is significantly influenced by its thickness, density, and preload.

ACKNOWLEDGEMENT

The authors would like to appreciate and acknowledge the financial support provided by the Universiti Putra Malaysia (UPM) via Geran Putra (GP-IPS) (Vot. number: 9689600).

REFERENCES

Bang, J. H., Lee, C. A., Kim, H. Y., Kim, H. J., & Choi, K. Y. (2017). Optimization of the static properties of seat foam to improve the seating comfort. *Proceedings of the Institution of Mechanical Engineers, Part D: Journal of Automobile Engineering*, *231*(14), 1945-1960. https://doi.org/10.1177/0954407016688782

Choi, H. J., & Kim, J. H. (2020). Static and dynamic comfort properties of polyurethane foams including a flexible amine crosslinker. *Journal of Industrial and Engineering Chemistry*, *90*, 260-265. https://doi.org/10.1016/j.jiec.2020.07.021

Deng, R., Davies, P., & Bajaj, A. K. (2003). Flexible polyurethane foam modelling and identification of viscoelastic parameters for automotive seating applications. *Journal of Sound and Vibration*, *262*(3), 391-417. https://doi.org/10.1016/S0022-460X(03)00104-4

Ebe, K., & Griffin, M. J. (2001). Factors affecting static seat cushion comfort. *Ergonomics*, *44*(10), 901-921. https://doi.org/10.1080/00140130110064685

Griffin, M. J. (1990). *Handbook of Human Vibration*. Academic Press.

Kamp, I. (2012). The influence of car-seat design on its character experience. *Applied Ergonomics*, *43*(2), 329-335. https://doi.org/10.1016/j.apergo.2011.06.008

Karen, I., Kaya, N., Öztürk, F., Korkmaz, I., Yildizhan, M., & Yurttaç, A. (2012). A design tool to evaluate the vehicle ride comfort characteristics: Modeling, physical testing, and analysis. *International Journal of Advanced Manufacturing Technology*, *60*, 755-763. https://doi.org/10.1007/s00170-011-3592-z

Kreter, P. E. (1985). Polyurethane foam physical properties as a function of foam density. *Journal of Cellular Plastics, 21*(5), 306-310. https://doi.org/10.1177/0021955X8502100502

Murata, S., Ito, H., & Sopher, S. (2014). Polyurethane-free lightweight automotive seat. *SAE International Journal of Materials and Manufacturing*, *7*(3), 655-661. https://doi.org/10.4271/2014-01-1033

Patten, W. N., Sha, S., & Mo, C. (1998). A vibrational model of open celled polyurethane foam automotive seat cushions. *Journal of Sound and Vibration*, *217*(1), 145-161. https://doi.org/10.1006/jsvi.1998.1760

Qiu, D., He, Y., & Yu, Z. (2019). Investigation on compression mechanical properties of rigid polyurethane foam treated under random vibration condition: An experimental and numerical simulation study. *Materials*, *12*(20), Article 3385. https://doi.org/10.3390/ma12203385

Tufano, S., & Griffin, M. J. (2013). Nonlinearity in the vertical transmissibility of seating: The role of the human body apparent mass and seat dynamic stiffness. *Vehicle System Dynamics*, *51*(1), 122-138. https://doi.org/10.1080/00423114.2012.715652

Wada, H., Toyota, Y., Horie, A., Sasaki, T., Suzuki, C., & Fukuda, H. (2008). Automotive seating foams with excellent riding comfort prepared by a novel polypropylene glycol. *Polymer Journal*, *40*(9), 842-845. https://doi.org/10.1295/polymj.pj2008098

Wei, L., & Griffin, J. (1998). The prediction of seat transmissibility from measures of seat impedance. *Journal of Sound and Vibration*, *214*(1), 121-137. https://doi.org/10.1006/jsvi.1998.1540

Whitham, E. M., & Griffin, M. J. (2010). Measuring vibration on soft seats. In *1977 International Automotive Engineering Congress and Exposition* (pp. 1-12). SAE International in United States. https://doi.org/10.4271/770253

Zhang, L., & Dupuis, R. (2011). Measurement and identification of dynamic properties of flexible polyurethane foam. *Journal of Vibration and Control*, *17*(4), 517-526. https://doi.org/10.1177/1077546310363777

Zhang, X., Qiu, Y., & Griffin, M. J. (2015). Transmission of vertical vibration through a seat: Effect of thickness of foam cushions at the seat pan and the backrest. *International Journal of Industrial Ergonomics*, *48*, 36-45. https://doi.org/10.1016/j.ergon.2015.03.006

Pertanika J. Sci. & Technol. 31 (3): 1279 - 1290 (2023)

PERTANIKA JOURNALS

SCIENCE & TECHNOLOGY

Journal homepage: http://www.pertanika.upm.edu.my/

Effects of Fibre Length on the Physical Properties of Oil Palm Empty Fruit Bunch Cement Board (OPEFB-CB)

Wenish Anak Maynet[1], Emedya Murniwaty Samsudin[1]*, Nik Mohd Zaini Nik Soh[1], Lokman Hakim Ismail[1], Hasniza Abu Bakar[1] and Ahmed Elgadi[2]

[1]Faculty of Civil Engineering and Built Environment, Universiti Tun Hussein Onn Malaysia, 86400 UTHM, Parit Raja, Batu Pahat, Johor, Malaysia

[2]Department of Civil Engineering, Faculty of Engineering, University of Azzaytuna, Tarhuna, Libyan

ABSTRACT

In a cement board (CB) composite, fibres reinforce the board. It is because the length of the fibres significantly impacts the strength of the CB composite. Nonetheless, the physical properties of the CB are also an important aspect when dealing with the quality control of the final product. This study investigates the effects of various fibre lengths in CB fabrication on its physical properties, including the cement-hydration rate, tensile strength, density stability and thickness swelling (TS). Oil palm empty fruit bunch (OPEFB) fibres at different lengths are used based on the mesh retained size of R7M, R14M, and R30M. The OPEFB-CB mixture used in this research is 3:1 (cement: fibre ratio), with a target density of 1,300 kg/m^3. The sample is compressed using a 1000 psi cold-compression load to achieve the desired composite thickness of 12 mm. This research revealed that the longest fibres retained on the R7M mesh with an average length of 5 mm resulted in lower density and the highest TS value. Meanwhile, lower dimensional stability was achieved by OPEFB-CB composites using fibre that retained on the R14M and R30M, having an average length of 3 mm and 1 mm, respectively. Based on the results, the optimum fibre length recommended in the fabrication of OPEFB-CB composites is processed fibres retained on the R14M sieve with an average length of 3 mm. This recommendation is made based on the most stable density and lowest TS results achieved by the R14M retained fibres which is in the range of 1,231–1,309.4 kg/m^3 and TS of 0.65 %.

Keywords: Density, fibre length, hydration rate, OPEFB-CB, ratio, tensile strength, thickness swelling

ARTICLE INFO

Article history:
Received: 23 March 2022
Accepted: 07 September 2022
Published: 31 March 2023

DOI: https://doi.org/10.47836/pjst.31.3.09

E-mail addresses:
wenish.mae@gmail.com (Wenish Anak Maynet)
emedya@uthm.edu.my (Emedya Murniwaty Samsudin)
nikzaini@uthm.edu.my (Nik Mohd Zaini Nik Soh)
lokman@uthm.edu.my (Lokman Hakim Ismail)
hasniza@uthm.edu.my (Hasniza Abu Bakar)
elgadi.uthm@gmail.com (Ahmed Elgadi)
* Corresponding author

ISSN: 0128-7680
e-ISSN: 2231-8526

© Universiti Putra Malaysia Press

INTRODUCTION

Recently, research and development of eco-friendly or green construction materials have been gaining interest among researchers. Recycling waste materials, especially from agricultural activities, into building components is one of the most popular eco-friendly approaches among researchers. The use of wood as natural reinforcement in cement boards (CB) has increased rapidly due to the high demand of construction industries (Kochova et al., 2015). Cement boards are building and construction materials mostly applied in roofing and/or facades due to their strength and durability. They are made up of primarily cement-bonded particle boards and cement-fibre boards, usually applied as roofs and other high-security building elements. Several factors affect the performance of the physical properties of CB, for example, various lengths of the fibre (Akasah et al., 2019). Research conducted by Sugiman et al. (2019) found that the fibre length influenced the workability and increasing impact strength of cement board. Heterogeneous fibre length can improve various mechanical properties of CB as compared to only one larger fibre size. Most outcomes have agreed that reinforced natural fibre has a better-performing load transfer mechanism and results in higher mechanical properties (Jeyapragash et al., 2020). The empty fruit bunch fibre was selected as an economical and sustainable natural fibre compared to others and has shown comparable quality to high-strength kenaf bast fibres (Ayu et al., 2020).

Numerous studies on the subject have been done and are being examined. Flexible board panels or loose-fill insulation in structures can be insulated with insulation fibre manufactured from EFB. With other materials like kenaf, coconut fibre, or hemp, the lambda value is thus fairly comparable. The material is not as widely accessible as EFB fibre and is quite pricey. The insulation also benefits from applying to roof insulation systems (Kaliwon et al., 2012).

However, research using various lengths of oil palm empty fruit bunch (OPEFB) fibres in producing empty fruit bunch-cement board (OPEFB-CB) is still lacking. Therefore, this research analysed and determined the appropriate fibre length used in the fabrication of OPEFB-CB composite with a constant mix design of 3:1 and density of 13000 kg/m^3 that is able to give significant impact to EFBCB contributes to a good performance of OPEFB-CB.

MATERIALS AND METHODS

This research used EFB fibres obtained from a local palm oil processing mill. The EFB was processed in the laboratory and used to fabricate the CB panel size of 350 mm × 350 mm × 12 mm (thickness). This study comprised three stages of laboratory work. The first stage is OPEFB fibre preparation, which involves the pre-treatment of fibre using sodium hydroxide (NaOH). The next stage was stage 2, the fabrication process. The mixture of cement, water, and fibre was prepared according to a ratio of 3:1, followed by the moulding and cutting of the OPEFB-CB samples for testing. Stage 3, the OPEFB-CB underwent

physical and mechanical properties tests (hydration rate, tensile strength, density, and thickness swelling).

Fibre Preparation

The OPEFB fibres were collected from Ban Dung Palm Oil Industries Sdn. Bhd. in Parit Sulong, Batu Pahat, Johor. Loose OPEFB fibres were sun-dried for two days to remove the excessive moisture. The sun-dried fibres were hammer-milled and filtered using sieves according to different fibre lengths. The fibre length consisted of three passing mesh sizes (R7M, R14M, and R30M), as classified in Table 1. During this process, all sieves were placed on the top of the vibrating table and vibrated for 1–2 minutes. This process separates most of the fibres' dust while retaining some shorter fibres in the sieves.

Table 1
OPEFB fibre lengths based on the mesh sizes

OPEFB Fibre Length (mm)		
Passing 4 mesh, Retained 7 mesh (R7M)	**Passing 7 mesh, Retained 14 mesh (R14M)**	Passing 14 mesh, Retained 30 mesh (R30M)
5 mm	3 mm	1 mm

According to Ibrahim et al. (2015), pre-treatment is needed to remove contaminants from the fibre surface and lignin, wax, and oil, which might affect cement hydration. Many studies recommended using sodium hydroxide (NaOH) in the pre-treatment of EFB (Izani et al., 2013; Akasah et al., 2019). As Izani et al. (2013) mentioned, the most effective amount of NaOH for EFB treatment is soaking in a 2% NaOH solution for 30 min. Meanwhile, Elkordi (2014) preferred a 4% NaOH concentration for 24 h to pre-treatment fan palm fibres. Fewer studies have attempted using a very low NaOH concentration in the fibre pre-treatment, except for Ibrahim et al. (2015), which applied various concentrations below 1%. Their research used 0.2%, 0.4%, 0.6%, and 0.8% of NaOH in the pre-treatment but with the addition of acetic acid into the solutions. OPEFB fibre was soaked in this research with 0.4 % NaOH concentration for 24 hours. After being soaked for 24 hours, fibres were rinsed thoroughly to remove the remaining alkali content due to the pre-treatment process. Next, the washed fibres were sun-dried to remove excess moisture and dried using a controlled oven-dry at 100°C for 24 hours. The oven-dry method allowed the moisture content of the fibre to be controlled at approximately ±5 %.

OPEFB Cement Board Fabrication

The size of the OPEFB-CB sample fabricated in this research is 350 mm × 350 mm × 12 mm with a targeted density of 1,300 kg/m^3. The fabrication of OPEFB-CB composites used

a mixture of Portland cement, water, and EFB fibre, as shown in Figure 1. Fibre, water, and cement were mixed in a mixer for 8–10 min at 60–80 rpm, whereas the hand-forming method was used to fill the mixture into the mould. After that, the mixture was hand-pressed using a plywood plate. A polythene sheet was placed on top of the mixture, followed by a steel plate prior to the machine-pressing procedure. Next, the OPEFB-CB mixture was set for final pressing within 5–7 minutes at an applied pressure of 1000 psi at an 18 mm/min rate using a hydraulic cold-press machine until the thickness reached 12 mm. The pressed sample is tightly clamped before the load is released, and the sample is removed from the machine. The sample was de-clamped after 24 hours and stacked vertically for 28 days for the air-curing process at room temperature (Onuorah et al., 2016). The fabrication process of the OPEFB-CB composite is illustrated in Figure 2.

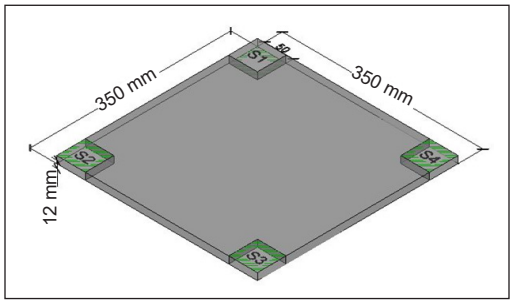

Figure 1. OPEFB-CB test sample based on different locations

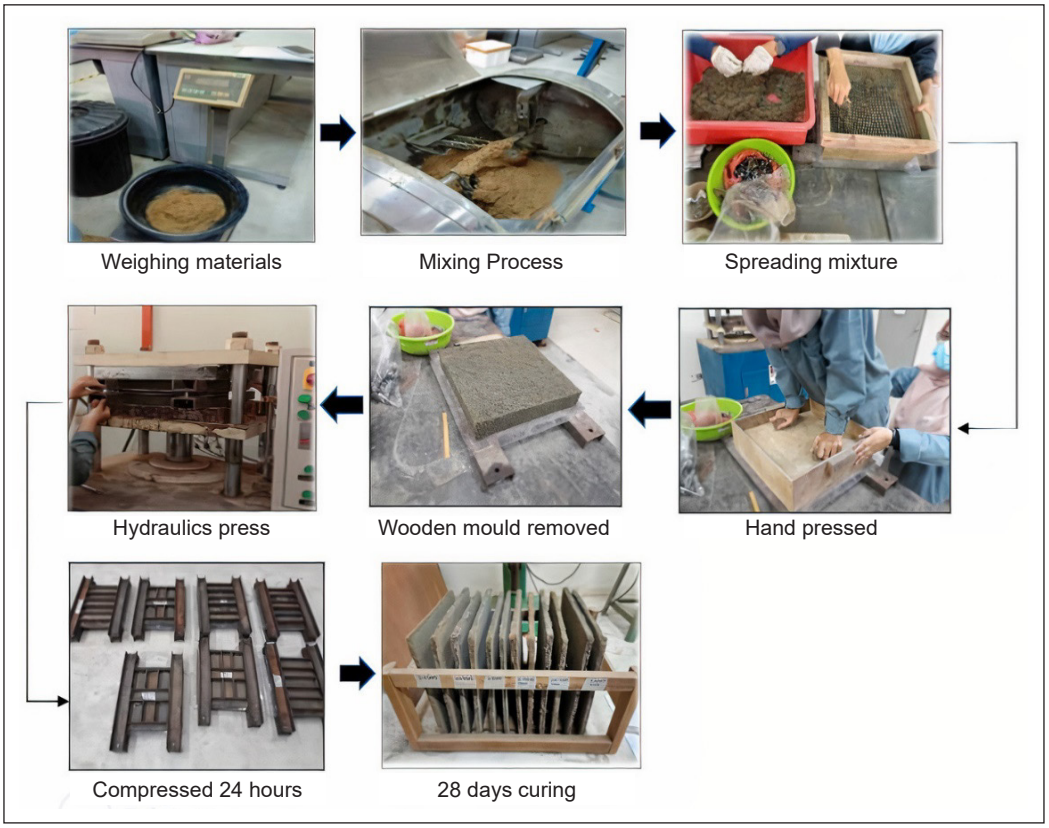

Figure 2. Fabrication process of OPEFB-CB composites

Physical Properties Testing

In this research, the physical properties determined were the selection criteria of OPEFB fibre pre-treatment using sodium hydroxide, hydration rate, tensile strength, density and thickness swelling. The physical properties of OPEFB-CB composites were analysed and discussed based on different fibre lengths of 5 mm for R7M, 3 mm for R14M, and 1 mm for R30M.

The selection criteria of sodium hydroxide (NaOH) for pre-treatment are based on the untreated fibre of 0% and treated fibre of 0.4%. Pre-treatment on OPEFB fibre significantly removes a certain amount of silica bodies that can potentially increase the fibre's workability. At the same time, untreated (UT) fibre has excess impurities and oil content and can reduce the compatibility between fibre and cement, thereby reducing the strength of the fibre. Natural fibre-to-cement compatibility is a main problem in OPEFB-CB production. Adding a certain amount of natural fibre into cement composites significantly reduces the hydration temperature of the mixture. This research also observed the hydration rates of neat cement and cement with OPEFB fibre within 24 hours for both UT and treated fibres. Data were recorded to observe the temperature changes and compared between the neat cement with the mixed material based on the treatment.

The chemical composition of EFB fibres includes lignin, hemicellulose, and cellulose. Cellulose is a significant strength and stability component (Supranto et al., 2014). Higher cellulose content can be obtained by increasing the solutions in NaOH concentrations during pre-treatment. However, increasing the NaOH concentration caused the hemicellulose and lignin in EFB fibre to decrease much more than cellulose, as Aanifah et al. (2014) observed. Cellulose is the main structural component of the strand cell walls. As a result, the lower cellulose content of untreated EFB fibre explicates its low tensile strength. Furthermore, when NaOH pre-treatment was used, the cellulose content showed a better effect on the strength of EFB fibre.

The density of OPEFB-CB composites was determined using a weighing balance by determining the weight of the sample after the curing period. The parameter measurement result was examined based on an average of four locations on the CB, labelled S1, S2, 23, and S4, as shown in Figure 4. The TS experimental test measured the water absorption of OPEFB-CB composites after 28 days of curing. The test procedure follows the British Standard requirement below 1.5%. The dimension of the test piece was 50 mm × 50 mm × 12 mm. The samples were immersed in water for 24 h at room temperature. The thickness of the sample (t_1) was recorded on every four sides of the sample, as shown in Figure 4. The thickness after immersion (t_2) was also recorded, and the average of each side of the sample was calculated. The thickness increases as the sample absorb water. The TS was calculated using Equation 1 based on the difference in thickness:

$$\text{TS}\ (\%) = \frac{t2 - t1}{t1} \times\ 100\% \qquad [1]$$

This study used the hand-forming method for OPEFB-CB fabrication based on different lengths and a fixed mixing ratio of 3:1. Figure 1 shows the selection of sample area for the density test of the OPEFB-CB composites based on different locations.

This method is based on four locations for the OPEFB-CB samples presented in Figure 3. Its purpose is to identify the consistency of the density distribution of the cement-fibre mixture for the OPEFB-CB samples. The density values at each location were recorded and analysed through the plotted graph. The results determine if the OPEFB-CB samples have an evenly distributed density during the hand-forming method in this fabrication stage.

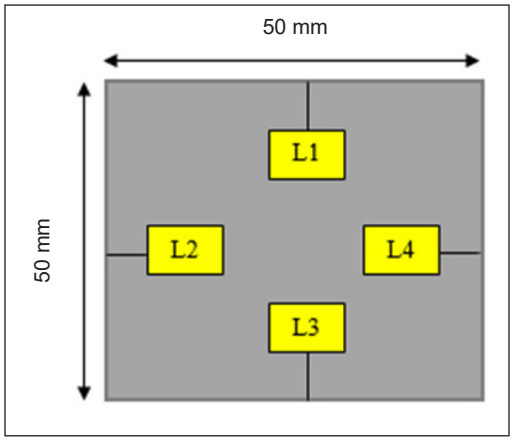

Figure 3. OPEFB-CB test sample (50 mm × 50 mm) based on four sides

RESULTS AND DISCUSSION

Table 2 shows the selection criteria for pre-treatment with sodium hydroxide through scanning electron miscroscopy (SEM). The SEM images of fibre treated with 0.4% NaOH show that the silica bodies were slightly removed with much remaining on the surface of the EFB fibre. Low NaOH concentrations in the pre-treatment cannot fully remove the silica bodies from the strand.

Table 2
Selection criteria for pre-treatment sodium hydroxide, NaOH

NaOH Treatment (%)	Untreated (UT)	Treated (0.4)
Scanning electron Microscopy (SEM)	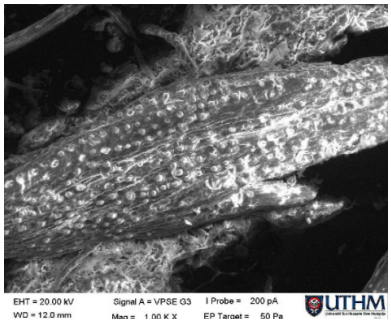	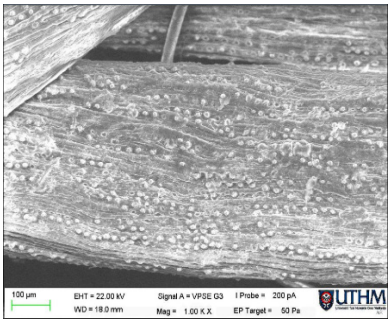

Observation and analysis of the hydration behaviour in terms of hydration properties, specifically, maximum hydration temperature and its necessary time to attain maximum

temperature, the compatibility between cement and fibre and its enhancement with different types of accelerators can be explored (Amel et al., 2014). Recent research by Soh et al. (2018) revealed that the presence of hemicellulose, lignin, and extractives (oil, sugar, and starch) impacts the incompatibility of EFB fibre and cement. The heat of hydration of cement constituents influences cement formulation in various applications, along with its effectiveness in preventing water in cement paste from freezing in the winter and trying to improve the setting and hardening processes. Serious stress cracking can occur if heat is not easily depleted, especially for large structures. Thus, the adhesion of cement with natural fibre remains a major issue in the production of EFB fibre-cement board since adding a specific amount of natural fibre to a cement composition may cause a direct decrease in a compound's hydration temperature.

The hydration test was conducted in a sealable polyethene bag using 20g of EFB particles thoroughly mixed with 250g of Ordinary Portland cement (OPC). The mixture was then mixed with 114 mL of water for 2 minutes. The amount of water was calculated using 0.7 mL/g of EFB fibre (oven-dried basis) and 0.4 mL/g of cement. The samples were prepared in accordance with the fibre length. A thermocouple temperature (type K) is taped outside the sample bag immediately after thoroughly blending the mixture. The polyethene bag was neatly folded around the thermocouple to ensure that the temperature released by the mixture was correctly detected. The bag was then sealed inside a thermos flask and placed inside a polystyrene cup. Thermocouples were connected to the data logger (Graphtec GL240 Midi Logger) to record the temperature for each sample for 24 hours (Soh et al., 2018).

The hydration level of neat cement and cement-EFB fibre were monitored for 65 hours to track changes in the mixed material's temperature. Figures 4 and 5 show the hydration rate of the untreated and treated fibre using 0.4 % sodium hydroxide (NaOH).

The hydration rate for cement mixed with EFB fibre for passing R14M increased steadily for the first 11 hours at 44.9^{o}C for the treated fibre and 43.8^{o}C for the untreated fibre. The hydration temperature increases steadily for the treated fibre. Results show that the shortest fibre length R30M treated with 0.4% NaOH reached the maximum temperature of 47^{o}C after 11.2 hours. Meanwhile, the untreated fibre of the same retained mesh only reached 45.9^{o}C after 10.5 hours. Findings from this research are similar to Schackow et al. (2016) for the treated fibre, where the shorter the fibre length, the higher the hydration temperature was recorded.

According to Izani et al. (2013), the single fibre tensile test method determines natural fibres' modulus and tensile strength. Figure 6 shows the results of tensile strength using a single fibre strand done in this research based on the respective pre-treatment. The treated fibre shows higher tensile strength compared to the untreated fibres. In the recent research by Ramlee et al. (2019), the OPEFB was compared to sugarcane bagasse fibre.

This research has discovered that the presence of lignin affects the tensile strength of SCB fibre. Furthermore, SCB fibre contained more lignin than OPEFB fibres, and the tensile property of composites is influenced by the compatibility of the hydroxyl groups of lignin. Increased lignin content in the composite resulted in greater water absorption and swelling values. The lignin dispersion may have created voids that allowed water to be absorbed.

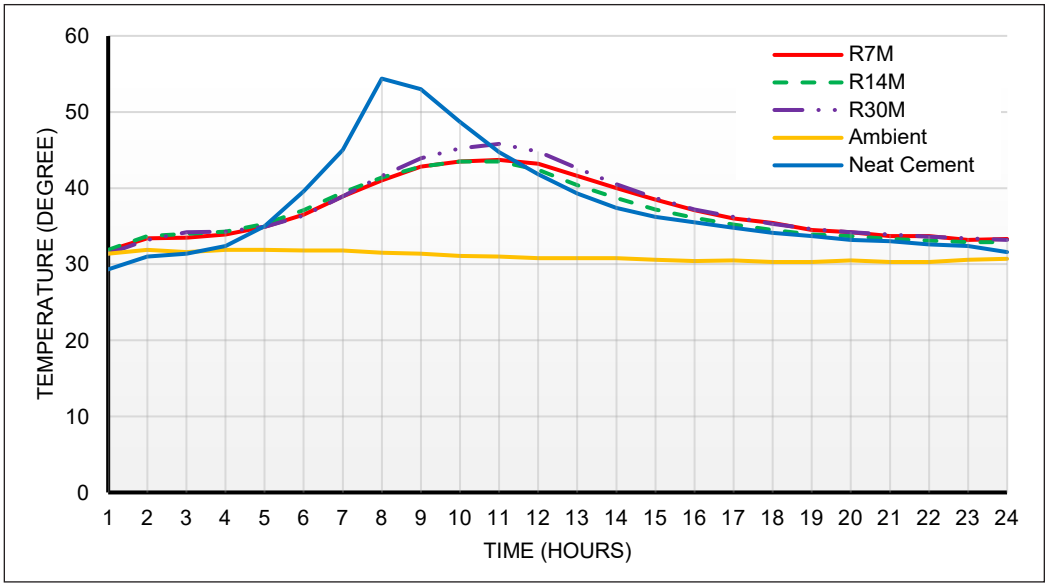

Figure 4. Hydration rate of 0% using different fibre length

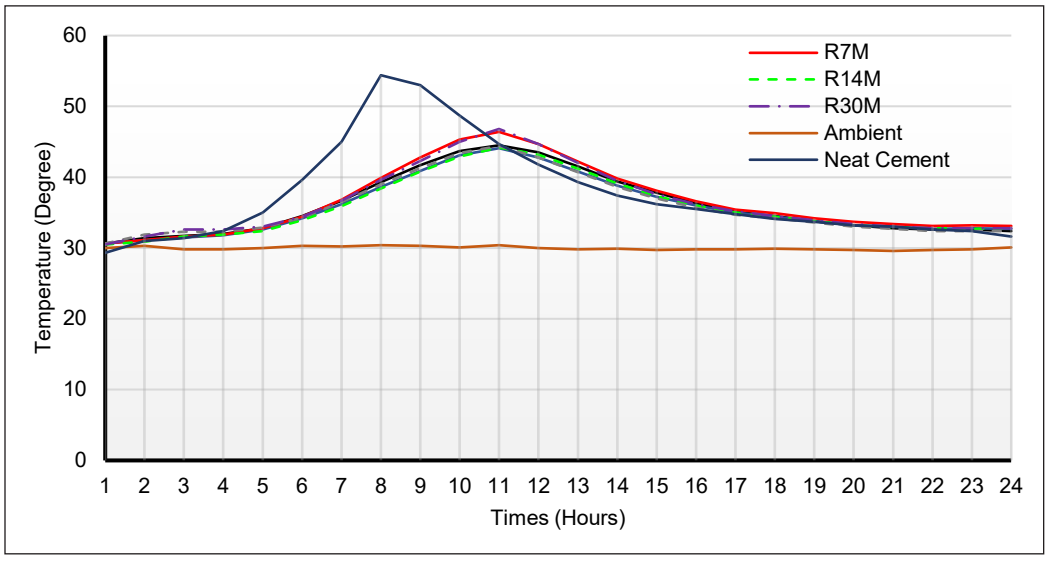

Figure 5. Hydration rate of 0.4% using different fibre length

Based on Figure 7, a moderate decrease in density was recorded by the OPEFB-CB composites using the treated fibres retained on R7M. From this result, the density of the sample decreased from 1,245.6 kg/m^3 to 1,155.6 kg/m^3. It is due to the presence of long fibres in the composite mixture that reduced the compaction between cement and fibre, hence affecting fibre distribution and resulting in large void spaces in the composite. The higher void content leads to lower composite density. According to Ramlee et al. (2019), EFB fibre board has a higher void content than sugarcane bagasse (SCB) and other hybrid EFB/SCB mixtures at the same fibre sieve size of ±13mm**.** The matrix's incompatibility causes high void formation with the fibre. Hence, this will result in a low internal bonding (IB) of the OPEFBCB. Since higher void content is most common in low-density materials, more areas were created, which allowed higher water absorption, thus an increase in the thickness swelling (TS) (Loh et al., 2010). According to Zuraida et al. (2011), long fibres will produce larger void spaces and consequently affect the density of the samples. Furthermore, based on the chemical constitution, EFB, which contained higher cellulose than the SCB,

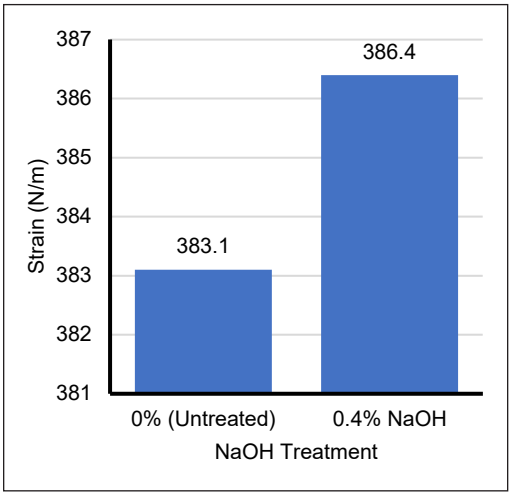

Figure 6. Tensile strength for single fibre with different percentages of NaOH Treatment

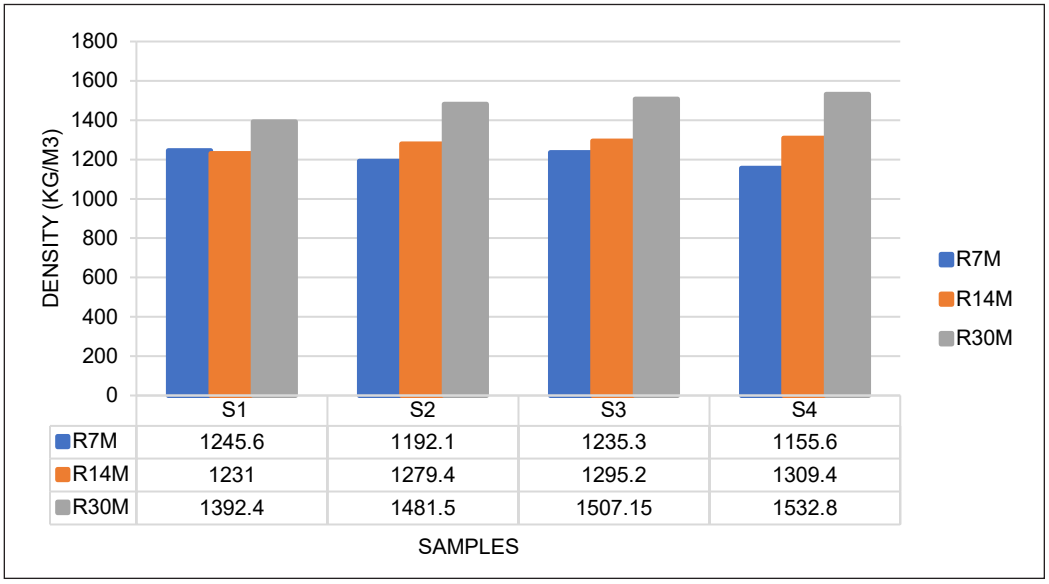

Figure 7. Density distribution of OPEFB-CB composites

achieved higher specific strength, stiffness in the matrix and stability Ramlee et al. (2019). Meanwhile, the OPEFB-CB composites fabricated using the fibres retained on R14M (fibre size 3 mm) demonstrated better consistency in density distribution, ranging from 1,231 kg/m^3 to 1,309.4 kg/m^3 compared to the others.

The results of the thickness swelling for OPEFB-CB composites based on treated fibre are shown in Figure 8. In general, TS also represents the dimensional stability of OPEFB-CB composites. Longer fibres tend to ball up, reducing workability and strength (Zuraida et al., 2011). The shorter fibre used in the fabrication of OPEFB-CB significantly reduced the void spaces in the composite, thus resulting in less water being absorbed. High water absorption influences the composite's thickness, thus affecting its dimensions' stability. The effective moisture balance should be achieved continually after the thickness swelling test is conducted until a consistent weight is acquired (Fang et al., 2017). This research evidence that shorter fibre length demonstrated less TS effects on EFBCB.

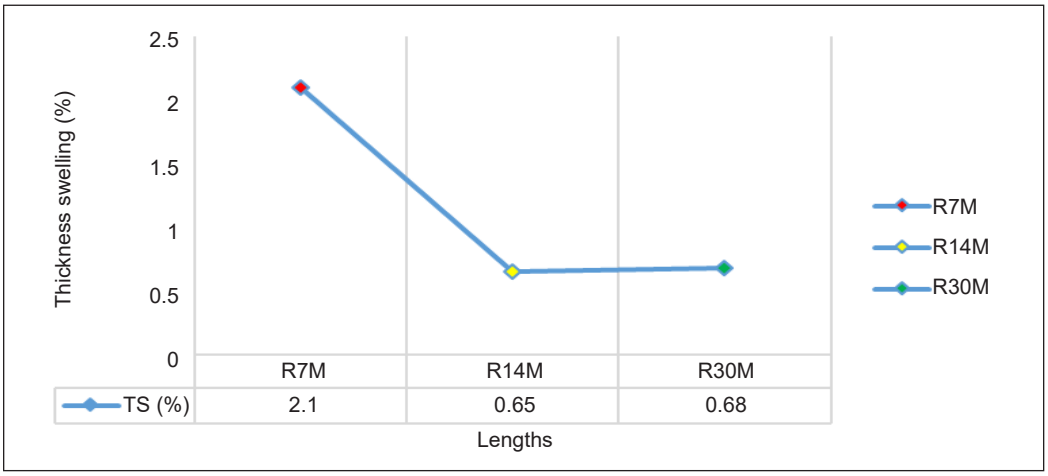

Figure 8. Average thickness swelling of OPEFB-CB composites

CONCLUSION

This research has revealed that the fibre length influenced the OPEFB-CB properties. The shorter fibre, which retains at R14M and R30M, results in a better density value near the target density of 1300 kg/m^3. Longer fibre lengths, particularly for fibre retained at R7M, result in a lower-density composite, thus creating more voids. Furthermore, shorter-treated EFB also results in higher hydration temperatures in the hydration test. Treated fibre removes the lignin layer and causes the cellulose content of OPEFBCB to increase and resulting in better tensile strength of a single fibre. It will allow better incompatibility between cement and fibre. The less void area in OPEFB-CB fabricated using shorter fibre also contributes to lower thickness swelling and gives better dimensional stability to the cement board.

ACKNOWLEDGEMENT

This research was supported by the Ministry of Higher Education (MOHE) through the Fundamental Research Grant Scheme (FRGS/1/2020/TK01/UTHM/03/3 and Research Management Centre, Universiti Tun Hussein Onn Malaysia (UTHM) through Research Fund E15501 and Vot no. H652.

REFERENCES

Aanifah, F. J. M., Yee, P. L., Wasoh, H., & Abd-Aziz, S. (2014). Effect of different alkaline treatment on the release of ferulic acid from oil palm empty fruit bunch fibres. *Journal of Oil Palm Research*, *26*(4), 321-331.

Akasah, Z. A., Mohd, N., Nik, Z., & Dullah, H. (2019). The influence of oil palm empty fruit bunch fibre geometry on mechanical performance of cement bonded fibre boards. *International Journal of Mechanical Engineering and Robotics Research, 8*(4), 547-552. https://doi.org/10.18178/ijmerr.8.4.547-552

Amel, B. A., Paridah, M. T., Rahim, S., Osman, Z., Zakiah, A., & Ahmed, S. H. (2014). Effects of kenaf bast fibres on hydration behaviour of cement. *Journal of Tropical Forest Science*, *26*(3), 340-346.

Ayu, R. S., Khalina, A., Harmaen, A. S., Zaman, K., Isma, T., Liu, Q., Ilyas, R. A., & Lee, C. H. (2020). Characterization study of empty fruit bunch (EFB) fibers reinforcement in poly(butylene) succinate (PBS)/ starch/glycerol composite sheet. *Polymers*, *12*(7), Article 1571. https://doi.org/10.3390/polym12071571

Elkordi, A. (2014). Alkali treatment of fan palm natural fibers for use in fiber reinforced concrete. *European Scientific Journal, 10*(12), 186-195.

Fang, T. W., Asyikin, N. S. S. N., Shawkataly, A. K. H. P., Kassim, M. H. M., & Syakir, M. I. (2017). Water absorption and thickness swelling of oil palm empty fruit bunch (OPEFB) and seaweed composite for soil erosion mitigation. *Journal of Physical Science*, *28*(2), 1-17.

Ibrahim, Z., Aziz, A. A., & Ramli, R. (2015). Effect of treatment on the oil content and surface morphology of oil palm (*Elaeis Guineensis*) empty fruit bunches (EFB) fibres. *Wood Research, 60*(1), 157-166.

Izani, M. N., Paridah, M. T., Anwar, U. M. K., Nor, M. M., & H'ng, P. S. (2013). Effects of fiber treatment on morphology, tensile and thermogravimetric analysis of oil palm empty fruit bunches fibers. *Composites Part B: Engineering, 45*(1), 1251-1257. https://doi.org/10.1016/j.compositesb.2012.07.027

Jeyapragash, R., Srinivasan, V., & Sathiyamurthy, S. J. M. T. P. (2020). Mechanical properties of natural fiber/ particulate reinforced epoxy composites - A review of the literature. *Materials Today: Proceedings, 22*, 1223-1227. https://doi.org/10.1016/j.matpr.2019.12.146

Kaliwon, J., Ahmad, S. S., & Aziz, A. A. (2009). *Oil Palm Empty Fruit Bunch (EFB) as Energy*. Malaysian Palm Oil Board.

Kochova, K., Schollbach, K., & Brouwers, H. J. H. (2015, September 16-18). Use of alternative fibres in Wood Wool cement boards and their influence on cement hydration. In *Proceedings of the 19th International Conference on Building Materials, Ibausil* (pp. 1375-1382). Bauhaus University, Weimar, Germany.

Loh, Y. W., H'ng, P. S., Lee, S. H., Lum, W. C., & Tan, C. K. (2010). Properties of particleboard produced from admixture of rubberwood and Mahang species. *Asian Journal of Applied Sciences, 3*(5), 310-316.

Onuorah, E. O., Okeke, C. A., Nwabanne, J. T., Nnabuife, E. L. C., & Obiorah, S. O. M. (2016). The effects of production parameters on properties of single and 3-layer cement-bonded composites made from oil palm empty fruit bunch and tropical hardwood sawmill residue. *World Journal of Engineering*, *12*(6), 577-590. https://doi.org/10.1260/1708-5284.12.6.577

Ramlee, N. A., Jawaid, M., Zainudin, E. S., & Yamani, S. A. K. (2019). Tensile, physical and morphological properties of oil palm empty fruit bunch/sugarcane bagasse fibre reinforced phenolic hybrid composites. *Journal of Materials Research and Technology*, *8*(4), 3466-3474. https://doi.org/10.1016/j.jmrt.2019.06.016

Schackow, A., Effting, C., Gomes, I. R., Patruni, I. Z., Vicenzi, F., & Kramel, C. (2016). Temperature variation in concrete samples due to cement hydration. *Applied Thermal Engineering, 103*, 1362-1369. https://doi.org/10.1016/j.applthermaleng.2016.05.048

Soh, N. M. Z. N., Akasah, Z. A., Dullah, H., Aziz, A. A., & Aminudin, E. (2018). Alkaline treatments on EFB fibre: The effect on mechanical-physical properties and fibre-cement hydration rate. *Malaysian Construction Research Journal*, *4*(2 Special Issue), 117-128.

Sugiman, S., Setyawan, P. D., & Anshari, B. (2019). Effect of fiber length on the mechanical properties and water absorption of bamboo fiber/polystyrene-modified unsaturated polyester composites. In *IOP Conference Series: Materials Science and Engineering* (Vol. 532, No. 1, p. 012008). IOP Publishing.

Supranto, S., Tawfiequrrahman, A., Yunanto, D. E., & Kurniawan, I. (2014, December 2-3). Oil palm empty fruit bunch fiber conversion to high refined cellulose using nitric acid and sodium hydroxide as the delignificating agents. *AUN/SEEED-Net Regional Conference on Chemical Engineering* (pp. 1-15). Yogyakarta, Indonesia.

Zuraida, N., Sopyan, I., & Zahurin, H. (2011). Effect of fiber length variations on mechanical and physical properties of coir fiber reinforced cement-albumen composite (CFRCC). *IIUM Engineering Journal, 12*(1), 65-77.

Pertanika J. Sci. & Technol. 31 (3): 1291 - 1311 (2023)

PERTANIKA JOURNALS

SCIENCE & TECHNOLOGY

Journal homepage: http://www.pertanika.upm.edu.my/

Review Article

A Review on Grapheme-to-Phoneme Modelling Techniques to Transcribe Pronunciation Variants for Under-Resourced Language

Emmaryna Irie, Sarah Samson Juan* and Suhaila Saee

Faculty of Computer Science and Information Technology, Universiti Malaysia Sarawak, 94300 UNIMAS, Kota Samarahan, Sarawak, Malaysia

ABSTRACT

A pronunciation dictionary (PD) is one of the components in an Automatic Speech Recognition (ASR) system, a system that is used to convert speech to text. The dictionary consists of word-phoneme pairs that map sound units to phonetic units for modelling and predictions. Research has shown that words can be transcribed to phoneme sequences using grapheme-to-phoneme (G2P) models, which could expedite building PDs. The G2P models can be developed by training seed PD data using statistical approaches requiring large amounts of data. Consequently, building PD for under-resourced languages is a great challenge due to poor grapheme and phoneme systems in these languages. Moreover, some PDs must include pronunciation variants, including regional accents that native speakers practice. For example, recent work on a pronunciation dictionary for an ASR in Iban, an under-resourced language from Malaysia, was built through a bootstrapping G2P method. However, the current Iban pronunciation dictionary has yet to include pronunciation variants that the Ibans practice. Researchers have done recent studies on Iban pronunciation variants, but no computational methods for generating the variants are available yet. Thus, this paper reviews G2P algorithms and processes we would use to develop pronunciation variants automatically. Specifically, we discuss data-driven techniques such as CRF, JSM, and JMM. These methods were used to build PDs for Thai, Arabic, Tunisian, and Swiss-German languages. Moreover, this paper also highlights the importance of pronunciation variants and how they can affect ASR performance.

Keywords: Automatic speech recognition, G2P technique, grapheme-to-phoneme, pronunciation variants, under-resourced language

ARTICLE INFO

Article history:
Received: 31 May 2022
Accepted: 04 November 2022
Published: 31 March 2023

DOI: https://doi.org/10.47836/pjst.31.3.10

E-mail addresses:
emmaryna.ji@gmail.com (Emmaryna Irie)
sjsflora@unimas.my (Sarah Samson Juan)
ssuhaila@unimas.my (Suhaila Saee)
*Corresponding author

ISSN: 0128-7680
e-ISSN: 2231-8526

© Universiti Putra Malaysia Press

INTRODUCTION

Iban language is an isolect or neutral language of the Austronesian language family (Sutlive, 1994). The iban language is associated with the Malayic subgroup, the Malay language, but they are not the same. The difference gap is big in terms of spelling, pronunciation, and meaning. The addition rule of prefixes and suffixes still applies to the Iban language.

According to Sutlive (1994), there were initially 22 phonemes in the Iban language. Currently, 34 phonemes of the Iban language are found in the studies made by Juan et al. (2015). The recent study focused on the Iban language in general, noting the words and phonemes of the standard Iban language. These phonemes have potential pronunciation variants, especially in the Iban language. The Iban language has no slang or dialect (Sutlive, 1994). Nevertheless, variations of pronunciation in the language exist, distinct from each other throughout the Sarawak region, as stated by Shin (2021). The region or area is the river from which it came, for example, the Engkari river, Undop river, Sebuyau river, and Baloh River.

The Iban language is considered an under-resourced language in terms of language technology and application. Under-resource languages are mostly less studied, and lack digitalised documents because there are few language resources, and languages are passed down verbally through generations (Singh, 2008). Other examples of under-resourced languages from different parts of the globe are Tunisia (Masmoudi et al., 2016), Bangla, or Bengali (Chowdhury et al., 2018), and Thai language (Rugchatjaroen et al., 2019; Saychum et al., 2016). For Iban, a language corpus exists with thirty-one thousand (31k) Iban words collected and used for building an Iban ASR (Juan et al., 2015). Language corpora here refers to the collection of written or spoken texts that can be used to analyse speech patterns. The written texts will be laid out or listed as a pronunciation dictionary.

There are no systematic methods for generating pronunciation variants for the Iban language. Therefore, a suitable modelling technique or method is needed. This paper aims to review ASR G2P modelling techniques available for generating pronunciation variants.

BACKGROUND OF STUDY

Pronunciation Dictionary for an ASR for Iban, an Under-Resourced Language

A pronunciation dictionary is a term for a list of words that consists of word and phoneme pairing. The phonemes are phonetic symbols that comply with the International Pronunciation association (IPA) standards. They can be generated via grapheme-to-phoneme (G2P) conversion using G2P techniques, which will be discussed further in the literature review.

The current Iban ASR holds 34 phonemes of the Iban language, as mentioned and studied by Juan et al. (2015). Furthermore, the study has compiled a total of 31k Iban words, resulting from the bootstrapping method, a closely related language to the Iban language,

which is the Malay language. The experiment conducted in the study uses the Deep Neural Network (DNN) system, which resulted in a 15.8%-word error rate. The compilation was then used as the pronunciation dictionary for the Iban ASR.

Figure 1 shows a sample pronunciation dictionary Juan and Flora (2015) developed for the Iban ASR.

```
penerang        p @ n @ r a NG
tadi    t a d i KK
pesisir p @ s i s i @ r
taja    t a dZ @ KK
berita  b @ r i t a
kepala  k @ p a l a KK
sepuluh s @ p u l u @ h
aum     a w u e m
lebih   l @ b i @ h
parlimen        p a r l i m @ n
ketuai  k @ t u w aj
iban    i b a n
sibu    s i b u
mujur   m u dZ u r
asal    a s a l
kuching k u tS i @ NG
```

Figure 1. Parts of words and phoneme pairing from the Iban pronunciation dictionary

From Figure 1, the left side of the column is the Iban word or graphemes. The right side of Figure 1 shows the phonemes of the Iban word in SAMPA format. SAMPA (Speech Assessment Methods Phonetic Alphabet) is a format for phonetic script in a machine. It uses 7-bit printable ASCII characters based on IPA (International Pronunciation Alphabet). For example, Table 1 shows the Iban IPA according to Omar (1981).

Table 1 shows 19 consonant phonemes and 11 vowel cluster phonemes. Examples shown in Table 1 are given to show how it is applied in Iban's common words.

Table 1

Iban vowel and consonant phonemes with examples by Omar (1981)

	Classification	Phoneme	Place of articulation	Example
Consonant	Plosive/ stop	/p/	Bilabial	/pandak/ (short), /pintu/ (door)
		/b/	Bilabial	/badas/ (good), /baruh/ (down)
		/t/	Alveolar	/tanʧaŋ/ (tie up), /tiluək/ (scoop)
		/d/	Alveolar	/dampiəh/ (nearby), /duɲa/ (world)
		/k/	Velar	/pekakas/ (tool), /kibaʔ/ (left)
		/g/	Velar	/gagit/ (excited), /gerau/ (spook)
		/ʔ/	Glottal	/mukaʔ/ (open), /ɲemaʔ/ (if)
	Nasal	/m/	Bilabial	/majaw/ (cat), /merindaŋ/ (entertain)
		/n/	Alveolar	/menoa/ (world), /mansaŋ/ (forward)
		/ɲ/	Palatal	/meɲa/ (long time ago), /ɲirap (slice)
		/ŋ/	Velar	/eŋkabaŋ/ (light red meranti), /ŋabaŋ/ (to visit)
	Affricate	/ʧ/	Palatal	/ʧelap/ (cold), /tinʧin/ (ring)
		/ʤ/	Palatal	/ʤampat/ (hurry), /ʤera/ (guilty)

Table 1 *(Continue)*

	Classification	Phoneme	Place of articulation	Example
	Fricative	/s/	Alveolar	/sampi/ (prayer), /siŋkaŋ/ (footsteps)
		/h/	Glottal	/luhus/ (straight), /ŋehembai/ (spread out)
	Trill/ rolled	/r/	Alveolar	/riŋat/ (angry), /ŋerembaŋ/ (get across)
	Lateral	/l/	Alveolar	/telai/ (whisper), /tilok/ (scoop)
	Semi-vowel	/j/	Palatal	/gaja/ (looks like), /ukuj/ (dog)
		/w/	Bilabial	/gawa/ (work), /wai/ (calling someone older than us)
Vowel	Vowel cluster	/ai/	Fronting	/makai/ (eat)
		/ui/		/ukui/
		/ia/	Backing	/maia/ (at the time)
		/ea/		/mageaŋ/ (all)
		/ua/		/muai/ (throw away)
		/oa/		/menoa/
		/iu/		/tiup/ (blow away)
		/au/		/tauka/ (or)
		/iə/	Centering	/niliək/ (glance)
		/uə/		/puən/ (the beginning)
		/oə/		/tusoək/ (to insert a thread, to suck)

Pronunciation Variants and Why It Matters

A pronunciation variant is a term for a language that has an alternate way of speaking or different intonations of the base word and has a slight difference in terms of spelling. Examples of pronunciation variations are typically known as dialect or slang of the language. Pronunciation variants happen when two or more cultures are mixed from migration to an area (Shin, 2021).

Having a basic pronunciation dictionary is beneficial for an under-resource language, but including the pronunciation, variants can be much more beneficial. For example, some other languages have their dialects and slang added to their ASR pronunciation dictionary, as mentioned in the study by Stadtschnitzer and Schmidt (2018); Masmoudi et al. (2016).

In Stadtschnitzer and Schmidt (2018), the language in focus is Swiss German, a dialectal form of the Swiss language. The people of Switzerland use this dialect in their conversations and switch to the German language when it comes to conversing with visitors so that they can understand (Stadtschnitzer & Schmidt, 2018). The dialect is highly used in Swiss broadcasts. However, there is no standardised writing on the dialect itself. When it is tested in the ASR, the system cannot detect the language- the desired outcome is that when the dialect is inserted into the system, the output comes out as standard German writing.

The study has successfully implemented the dialect into the system by training the Swiss-German model using the standard German model, thus creating its pronunciation dictionary.

Another example of dialect added to the ASR system is the Tunisian dialect, as Masmoudi et al. (2016) studied. Including the dialect enhances the Tunisian ASR system and the pronunciation dictionary of the Tunisian language, which is called TunDPDic (The Tunisian Dialect Phonetic Dictionary). The pronunciation dictionary contains the rules and exceptions of Tunisian words, base words, and dialects. This dictionary is useful for future studies of the Tunisian language as it guides the user on the rules of base and dialect words when developing an ASR system of the language.

Common languages such as English and French also have variations in their dictionary. Take English as the prime example, where two common English instances are separated by variations or accents- British English and American English. The accents have different dictionaries for each other. For instance, Accents of British Isles corpus (Tjalve & Huckvale, 2005) and BEEP dictionary (http://svr-www.eng.cam.ac.uk/comp.speech/Section1/Lexical/beep.html) are for British English, while CMUDict corpus (Yolchuyeva et al., 2019) is for American English. The Cambridge Dictionary and Oxford Dictionary have compiled variations of the English language, including pronouncing and spelling the words. The most straightforward comparison of spelling and pronunciation of the words are such:

- The word "water" is pronounced as /ˈwɔtəɹ/ (w-a-t-e-r) in American English, /ˈwɔːtə/ (w-o-t-a-h) in British English.
- The spelling of the word "colour" is/ˈkʌlər/ (American English), and "colour" is /ˈkʌlə/ (British English).

There are reasons to include these pronunciation variants, both cultural and technical. Preserving the language's culture and uniqueness helps expose the differences and the importance of the language's history. When a language such as English is known to others, it can identify the speaker's ethnicity and cultural identity, thus making people recognise the existence of the language (Guazzi et al., 1983).

Furthermore, including the variants in an ASR system helps improve- but does not necessarily do- the system's quality (Karanasou, 2013). It also helps increase the probability for the ASR system to analyse word variations and the base word of the targeted language, thus enriching the system's dictionary with various possibilities. Finally, including pronunciation variants into the system can also be used as a bootstrap for another language with almost the same base as the selected language, as used in Juan and Besacier (2013), where Malay language data was used as the seed data for the bootstrapping method.

However, the current pronunciation dictionary for Iban ASR does not consist of pronunciation variants. The current pronunciation dictionary contains the standard form of Iban words. Word variants are yet to be included as the method mentioned earlier only

focuses on developing a base Iban pronunciation dictionary. The pronunciation variant of the Iban language exists according to different areas across Sarawak. Based on Shin's (2021) findings, the pronunciation variants exist because Ibanic speakers' migration from West Kalimantan happened in the 19th century. Some highlighted Iban word variants; examples are shown in Table 2.

Table 2
The comparison between base Iban word and its variants

Base word	Variant 1 (Kapit)	Variant 2 (Sibu)
Rumah (House)	*Humeah*	*Rumeah*
Urang (People or Humans)	*Uheang*	*Ureang*
Barang (Stuff, like an object)	*Baheang*	*Bareang*

From Table 2, the variants shown are the additional or replacement of letters from the base word. The additional *'ea'* instead of /a/ and the replacement of /r/ with /h/ are obvious differences in variants found in Iban speakers from different areas in Sarawak.

Thus, this paper aims to investigate grapheme-to-phoneme methods that can generate Iban pronunciation variants to improve the current pronunciation dictionary. Moreover, a general G2P framework is described in this paper to illustrate the flow of grapheme-to-phoneme conversion and selecting candidates for pronunciation variants.

LITERATURE REVIEW

Modelling pronunciation data by leveraging statistical approaches can help generate more word-phoneme pairs for a pronunciation dictionary. It can replace the manual labour efforts by linguists to transcribe all words to phonemes and reduce human mistakes during the transcribing process. We reviewed selected Grapheme-to-phoneme (G2P) modelling for the motivation in improving our current pronunciation dictionary with pronunciation variants. Furthermore, we briefly describe under-resourced language and its G2P challenges.

Grapheme-to-Phoneme Conversion

Grapheme-to-phoneme conversion (G2P) is the task of finding the pronunciation of a word in its written form (Bisani & Ney, 2008). It was also essential in ASR and TTS (text-to-speech) systems (Yu et al., 2020). The term phoneme refers to the smallest unit of sound that makes up a complete word, while grapheme refers to a letter or a group of letters to represent the sound of the phoneme. Figure 2 shows the basic flowchart of G2P conversion.

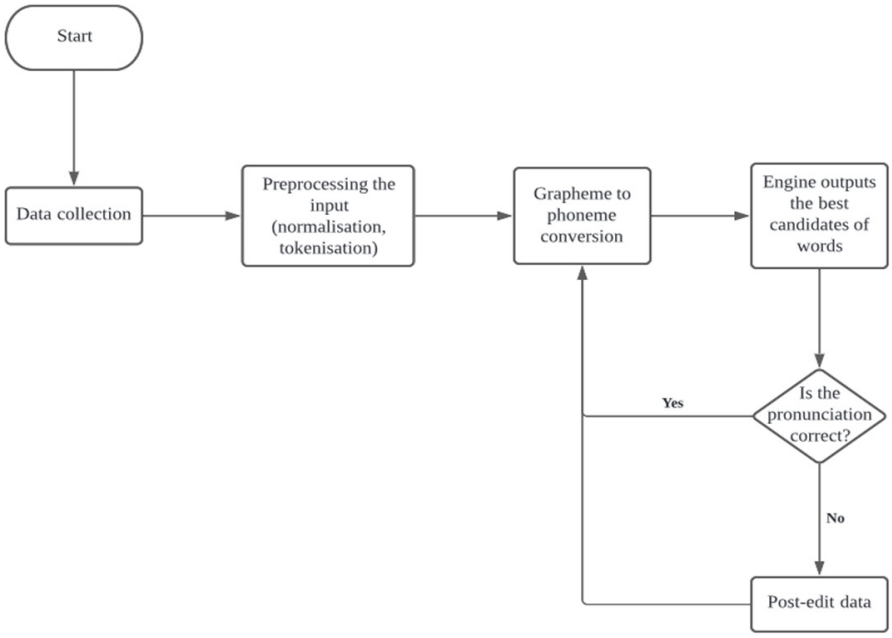

Figure 2. Basic flowchart of G2P conversion in a G2P technique

Figure 2 simplifies the data-driven flowchart from Juan and Flora (2015), which have implemented the G2P technique in their work. The following will explain the steps in detail.

Data Collection

In this process, raw text data are collected and compiled into a database or in an excel sheet. The data collection format can be formal texts, scripts, newspapers, websites, and other text-based platforms. The amount of data collected may vary from one to another, depending on the availability of the targeted language. For example, from an online news portal, Juan and Flora (2015) collected 7,000 articles in the Iban language from 2009-2012 related to sports, entertainment and general matters. From these articles, there were 2.08 million words found.

Pre-Processing the Input

The data that has been collected will be pre-processed to remove noise and unwanted symbols. This process is based on Ramli et al. (2015), where pre-processing involved tokenising the words, normalising the data into a machine-readable format, and sampling and grouping the data according to the amount of data of the chosen parameters. Lastly, the data are transformed into text in their orthographic form. An example of normalisation is as follows: the number '4' will be changed into 'four', and symbols such as *'$'* will be changed to 'dollar'. The tokenisation process includes spaces between the normalised words or letters, depending on the G2P modelling techniques. Iban data were pre-processed using

the above techniques, and the sentences were segmented to obtain 36 thousand unique words, which will then be used in the G2P conversion (Juan & Flora, 2015).

Grapheme-to-Phoneme Conversion

Converting the sequence of letters into sequences of phones is called G2P conversion. Its job is to convert a letter string into a phoneme string form (Jurafsky & Martin, 2000). The conversion process needs rules or learning from the seed data given during the process. The data-driven approach derives the pronunciation data from the seed data (Laurent et al., 2014). This study focuses on data-driven modelling techniques, which will be explained further in *Data-Driven G2P techniques*.

The G2P Engine Output the Best Candidates for Words

After the previous process, the outputs are compiled together and checked for errors. Language experts or native speakers can verify the outputs by conducting post-editing tasks, as shown in a previous study, to obtain a gold standard letter-phoneme pair (Juan & Flora, 2015). Then, the performance of the G2P model can be evaluated using metrics such as phoneme error rate, word error rate, and perplexity by comparing the gold standard with the G2P outputs (Chen et al., 1998).

Post-Edited Data

The post-edited letter-phoneme pairs can then be added to the training data to improve samples for the G2P model, and the next sequence of words is predicted using the improved model. This bootstrapping strategy reduces the time to transcribe graphemes to phonemes manually and systematically improves the quality of a G2P model as this approach can be repeated many times according to the language vocabulary size.

Previous work applied the bootstrapping strategy based on the semi-supervised method using a local dominant language, Malay, to create a base Iban phoneme sequence (Juan & Besacier, 2013). In this work, a Malay G2P was developed using an existing Malay pronunciation dictionary (Tan et al., 2009) as the source for the model. From the 36 thousand entries of the Iban word lexicon, about 1,000 words were phonetised using Malay G2P to obtain phonetic transcripts, and the outputs were post-edited to match with Iban pronunciations. Subsequently, another 1,000 words were phonetised by the same G2P, and the outputs were post-edited to get Iban phonemes. Hence, bootstrapping outputs from Malay G2P became the base for Iban G2P to convert the remaining entries in the Iban word lexicon.

Data-Driven G2P Techniques

The selected G2P modelling techniques have been used in research and experiments in the past years.

Conditional Random Fields. Conditional random fields, or CRF in short, are one of the techniques used for grapheme-to-phoneme conversion. This technique utilises a network of non-directional nodes and vertices. The nodes contain every possibility or probability of the next sequence word or letter being trained and tested. This technique shares a similar inner working with Hidden Markov Model (HMM); the only difference is that CRF did not make any assumptions about the data interdependence or independence chosen as the model (Morris, 2010). It is a framework for building probabilistic models to segment and label sequence data (Lafferty et al., 2001).

In G2P conversion, CRF defines a conditional probability distribution over label sequences by a given observation sequence rather than a joint distribution of label and observation sequences (Illina et al., 2011). Given the training grapheme or letter-to-phoneme associations and some predefined feature sets, CRF learns a set of weights *w*. The learning process of set *w* parameters is usually done by maximum likelihood learning for $p(\bar{y} \mid \bar{x};\ w)$ as in Equations 1 and 2:

$$p(\bar{y} \mid \bar{x};\ w) = \frac{1}{Z(\bar{x},\ w)} \exp \sum_j w_j F_j(\bar{x},\ \bar{y}) \tag{1}$$

$$F_j(\bar{x}, \bar{y}) = \sum_{i=1}^{n} f_j(\bar{y}_{i-1}, \bar{y}_i, \bar{x}, i) \tag{2}$$

Where,
$\bar{x}$: sequence of letters
$\bar{y}$: sequence of phonemes
w: weights
fj: feature function

The feature function can depend on the sequence of word letters, the current and previous phonemes, and the current position in the given the word. For example, in Equation 2, unigram features are shown as $f_j(\bar{y}_i, \bar{x}, i)$, while bigram features are represented as $f_j(\bar{y}_{i-1}, \bar{y}_i, \bar{x}, i)$. The unigram features will only be utilised when the bigram features use the current and previous phoneme sequence.

There has been a discussion regarding methods such as HMM, MEMM (maximum entropy Markov Model), and CRF, and ultimately, CRF can solve HMM and MEMM issues of bias labelling in experimental stages, as stated in Morris (2010) and Lafferty et al. (2001).

Joint Multigram Modelling. The joint multigram model (JMM) was pioneered by Deligne et al. (1995). It is a statistical model for matching streams of symbols under the hypothesis that all came from a common underlying stochastic process. JMM utilises the segmentation

process, in which it segments the letter of the word and phoneme and pairs them in every possible way. Figure 3 illustrates the segmentation of JMM.

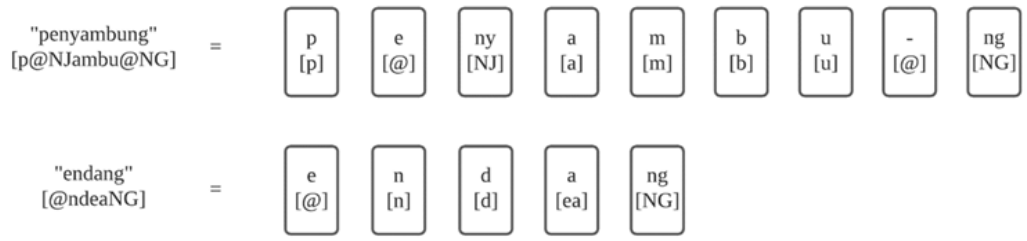

Figure 3. Examples of the segmentation process by JMM

To explain the JMM process illustrated in Figure 3, two streams of symbols in Equation 3 present a pair of sequences of $\begin{bmatrix} S_t \\ \omega_t \end{bmatrix}$.

$$\begin{pmatrix} O = o_{(1)} \dots o_\tau \\ \Upsilon = \varepsilon_{(1)} \dots \varepsilon_{(\Theta)} \end{pmatrix} \tag{3}$$

A (n, υ) JMM is a model in which the longest size of sequences in *O* and ϒ are, respectively, *n* and *υ*. Furthermore, the model allows the pair sequences s_t and ω_t to be of unequal length, which further assumes a many-to-many alignment between two strings. Taking L_o and L_Υ as a cosegmentation of *O* and *ϒ*, where *L* is the corresponding joint segmentation of *O* and ϒ, which *L* can be denoted as Equation 4:

$$L = (L_O, L_\Upsilon) \tag{4}$$

where *L* consists of all possible cosegmentation. Meanwhile, the overall likelihood of (*0*, ϒ) is computed as the sum of all cosegmentation (Equation 5).

$$L(O, \Upsilon) = \sum_{L \in \{L\}} L(O, , \Upsilon\, L) \tag{5}$$

Assuming the concatenated consequences independent, the likelihood will be denoted as Equation 6.

$$L(O, \Upsilon, L) = \prod_t p \begin{bmatrix} S_t \\ \omega_t \end{bmatrix} \tag{6}$$

A decision-oriented version of the model approximates the likelihood of the corpus as Equation 7:

$$L^*(O, \Upsilon) = max_{L \,\epsilon\, \{L\}}\, L(O, \Upsilon, L) \tag{7}$$

and defines the most likely cosegmentation of *L** as Equation 8.

$$L^* = argmax_{L \,\epsilon\, \{L\}}\, L(O, \Upsilon, L) \tag{8}$$

Taking another example from an Iban word "urang" and "ureaNG", where O = *"urang"* and Υ = *"ureaNG"*; the best segmentation obtained using Equation 8 will be pictured as the following Equation 9:

$$p\begin{bmatrix}u\\u\end{bmatrix}\cdot p\begin{bmatrix}rang\\reaNG\end{bmatrix},\ p\begin{bmatrix}ur\\ur\end{bmatrix}\cdot p\begin{bmatrix}ang\\eaNG\end{bmatrix},\dots$$

$$p\begin{bmatrix}u\\u\end{bmatrix}\cdot p\begin{bmatrix}r\\r\end{bmatrix}\cdot p\begin{bmatrix}ang\\eaNG\end{bmatrix},p\begin{bmatrix}ura\\urea\end{bmatrix}\cdot p\begin{bmatrix}ng\\NG\end{bmatrix},\dots \quad (9)$$

$$p\begin{bmatrix}u\\u\end{bmatrix}\cdot p\begin{bmatrix}r\\r\end{bmatrix}\cdot p\begin{bmatrix}a\\ea\end{bmatrix}\cdot p\begin{bmatrix}ng\\NG\end{bmatrix},\dots$$

All consequence probabilities are estimated on a training corpus. Besides that, the JMM model can automatically decode a test input string O into an output string Υ through a sequence-by-sequence transcription process (Deligne et al., 1995). It can be a standard maximum of a posteriori decoding problem, which consists of finding the most likely string $\hat{\Upsilon}$ given the stream of O (Equation 10).

$$\hat{\Upsilon} = argmax_{\Upsilon}\, L(\Upsilon|O) = argmax_{\Upsilon}\, L(O,\Upsilon) \quad (10)$$

Assuming $L^* = (L_O^*, L_\Upsilon^*)$ - most likely joint segmentation of O and Υ representing most of the likelihood, Equation 7 will be maximised as Equation 11:

$$\widehat{\Upsilon^*} = argmax_{\Upsilon}\, L(O, \Upsilon, L_O^*,\ L_\Upsilon^*) \quad (11)$$

By using the Bayes rule, Equation 11 can be rewritten as Equation 12:

$$\widehat{\Upsilon^*} = argmax_{\Upsilon}\, L(O, L_O^*|\Upsilon, L_\Upsilon^*)\, L(\Upsilon, L_\Upsilon^*) \quad (12)$$

where $L(O, L_O^*|\Upsilon, L_\Upsilon^*)$ measures the likelihood of the matching between O and Υ along with their best cosegmentation.

Several studies, such as Cherifi and Guerti (2021), Masmoudi et al. (2016), and Wang and Sim (2013), have been using this G2P method in their experimentations.

Joint Sequence Modelling. Joint sequence modelling, or JSM in short, was founded by Bisani and Ney (2008). The overview of JSM is that the relation of input and output sequences was generated from the common sequence of the joint unit that carried input and output symbols. The term *consequence* and *joint multigram* refers to the unit that carries multiple input-output symbols (Deligne et al., 1995; Bisani & Ney, 2008). In JSM, the joint units, the grapheme-phoneme joint multigram, were stated as graphones. Figure 4 shows an example of JSM segmentation.

An orthographic form is given a sequence of letters or characters. It is sometimes referred to as graphemes. Pronunciation, on the other hand, is represented in phonemic transcription, a sequence of phoneme symbols. By denoting a set of graphemes as ***G*** and

a set of phonemes as ϕ, the task of G2P conversion is following Bayes' decision rule to obtain the optimal phone sequence (Equation 13)

$$\varphi(g) = arg \max_{\boldsymbol{\varphi' \epsilon \phi^*}} P(\boldsymbol{g}, \boldsymbol{\varphi'}) \tag{13}$$

where in each orthographic form $g \epsilon G^*$, we seek the most likely pronunciation $\varphi \epsilon \phi^*$.

A graphone is a pair of letter and phoneme sequences of possibly different lengths. It is denoted as Equation 14:

$$q = (g, \varphi) \epsilon Q \subseteq G^* \times \phi^* \tag{14}$$

The expressions of $\boldsymbol{g_q}$ and $\boldsymbol{\varphi_q}$ referred to the first and the second component of $\boldsymbol{q}$, respectively. A graphone is mentioned as *singular* if it has one letter and one phoneme at most. In JMM, a common sequence of graphones assumes the orthographic sequence of the word and the phoneme. The letter and phoneme sequences are grouped according to an equal amount of segmentation called *cosegmentation* (Deligne et al., 1995). This segmentation uses many-to-many alignment, which has the advantage of grouping input letters because of its ambiguity. As for JSM, sequence segmentation utilises one-to-one alignment. An example of the segmentation is shown in Figure 4.

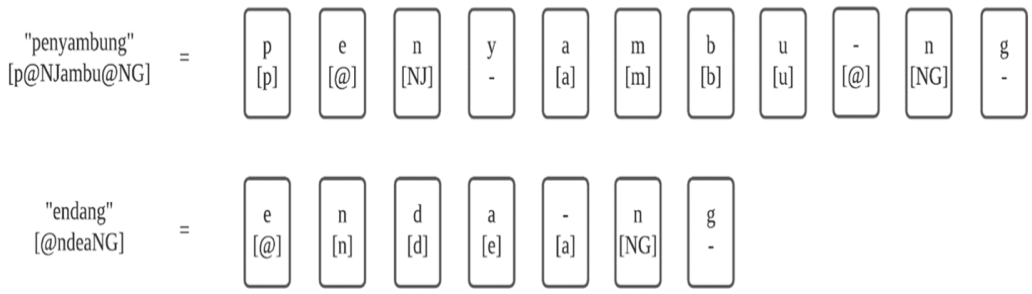

Figure 4. Segmentation sequence according to JSM

Hence, the joint probability of obtaining the sequence is determined by the total of all matching graphone sequences (Equation 15):

$$p(g, \varphi) = \sum_{q \epsilon S(g, \varphi)} p(\boldsymbol{q}) \tag{15}$$

where $q \epsilon Q^*$ is a sequence of graphones and $S(g, \varphi)$ contains all cosegmentations of $\boldsymbol{g}$ and $\boldsymbol{\varphi}$ (Equation 16).

$$S(g, \varphi) \coloneqq \left\{ q \epsilon Q^* \middle| \begin{matrix} g_{q_1} \frown \cdots \frown g_{q_K} = g \\ \varphi_{q_1} \frown \cdots \frown \varphi_{q_K} = \varphi \end{matrix} \right\} \tag{16}$$

Equation 16 ⌣ denotes the sequence concatenation, and K = |*q*| is the sequence length by ***q***. The joint probability can be modelled using a standard M-gram approximation as Equation 17:

$$p(q_1^K) \cong \prod_{j=1}^{K+1} p\left(q_j \middle| q_{j-1}, \ldots, q_{j-M+1}\right) \quad (17)$$

where the positions $j < 1$ and $j > K$ have a boundary that allows modelling characteristic phenomena at the start and end of the word.

A few numbers of studies have been using these methods for grapheme-to-phoneme conversions, such as the study of Saychum et al. (2016), Wang and Sim (2013), and Masmoudi et al. (2016).

Table 3 shows the summary of all reviewed G2P techniques. The summary includes the name of the techniques, the overall working process and the studies that have adopted the techniques in their experiments or journals.

Table 3

Summary of G2P techniques

G2P technique	How does it work	Studies that used the technique
CRF	Using a network of non-directional nodes and vertices	Illina et al. (2011), Zweig and Nguyen (2009), Yamazaki et al. (2014), Al-Shareef and Hain (2012), Masmoudi et al. (2016)
JMM	Segments of the word letter sequence in the many-to-one alignment	Cherifi and Guerti (2021), Masmoudi et al. (2016), Wang and Sim (2013)
JSM	Segments the word letter sequences using one-to-one alignment	Saychum et al. (2016), Wang and Sim (2013), Masmoudi et al. (2016)

G2P for Building Pronunciation Variants

As discussed in the earlier part of this paper, pronunciation variants are important, as shown by the English language, commonly known as British and American English. Including pronunciation variants in the system helps to show that another form of intonation and spelling exists for the words. Most rich-resource languages have included pronunciation variants (dialect, slang) in the system; including the variants is less challenging for this category, as their resources are ample.

However, such is not the case for under-resourced language. In the last few years, some studies focused on under-resourced language, which deserved the recognition of

researchers and developers. However, the efforts of building a G2P system for under-resourced languages vary, such as bootstrapping (Juan & Flora, 2015), web-mining, and segmentation (Saychum et al., 2016; Tsuboi et al., 2008).

Only one study investigated G2P for building pronunciation variants where the target language comes from an under-resourced language. Such analysis has been described by (Lukeš et al., 2019), where the study used the Czech language from two sources to generate pronunciation variants. The number of studies that are alike is very scarce. There is still little work on G2P modelling to produce pronunciation variants. Thus, there is a need to study the computational approach for this research gap. By following the example of the study mentioned, it is possible to use an under-resourced language, such as the Iban language, as the target language to generate pronunciation variants. Thus, it needs to include the variants in the pronunciation dictionary systematically.

Under-Resource Language and G2P Challenges

Joshi et al. (2020) mention that languages worldwide are grouped according to classes. There are six (6) class 'races', as shown in Table 4.

From Table 4, under-resourced languages fall in positions 0, 1, and 2, and a few managed to get into position 3. The number of speakers from these positions ranges from 1.8 billion and below (Joshi et al., 2020); meanwhile, the number of speakers for position 4 and 5 are 2.0 billion and above. Languages in these positions are known as 'rich-resourced languages', such as Russian, Korean, English, Spanish, German, Japanese, and French.

Under-resourced languages are almost endangered because they are fewer studied and digitalised records regarding the language (Singh, 2008). They are also losing to extinction as the native under-resourced speakers resorted to using high-resource languages such as English and French. Furthermore, fewer and fewer people can talk using under-resourced language, other than a very little guide to that language in the community themselves (Brenzinger et al., 2003).

Table 4
Positions and class 'race' of languages

Position	Class 'race'
0	The Left-Behinds
1	The Scraping-Bys
2	The Hopefuls
3	The Rising Stars
4	The Underdogs
5	The Winners

Some prime examples of under-resourced languages have been stated in the introduction of this paper. In addition, studies focus on these under-resourced languages and how to preserve them. Still, there are limitations in pursuing the conservation of the languages-insufficient amount of data, fewer language experts on the language, and limitations of the software used to emulate the experiments.

These limitations are also applied in G2P conversion and modelling techniques. An immense amount of data is needed for the experiments (training and testing). Since under-resourced languages have limited data, some researchers such as Juan and Flora (2015), Juan & Besacier (2013) and Juan et al. (2015) use an approach where the language is closely related to the under-resourced language that is being used for training. The process, known as bootstrapping, has generated the baseline dictionary for the under-resourced language. However, the process consumed much time as it started the baseline from scratch and depended on the equipment used.

As Besacier et al. (2014) stated, the challenge of bridging the gap between language and technology experts still holds until recent years. Language experts regarding under-resourced languages are rare and mainly originated outside the said language's country. Only a few pursue such language and give effort to researching and including them in language technology. Efforts are made because they realise the danger of language extinction and how it affects the world languages, which many people, especially native speakers, do not. It is also quite rare to find a language expert with the knowledge of developing ASR that is native to the under-resourced language itself.

DISCUSSION

As discussed earlier regarding G2P conversion techniques, three G2P modelling techniques are available: CRF, JMM and JSM. All three modelling techniques have been used in G2P conversion for rich and under-resourced languages.

CRF modelling technique has non-directional nodes and vertices, making the training process in the conversion have more match-up probability and a wide selection of letter-phone pairing. Since CRF is an upgrade from HMM and MEMM, the modelling technique has solved labelling and observation biases (McCallum, 2012). CRF is said to be independent and flexible in creating segmentations if the selected feature is correct. However, this can also invite unwanted errors in the generated output. It is mentioned to have high computational complexity during the algorithm's training stage, making it harder for model re-training when new data is included. It is also difficult for CRF training to detect and learn unknown words not included in the training data.

JSM and JMM look almost the same, but there is a slight difference during the segmentation process. JSM segmentation alignment focuses on one-to-one alignment. Meanwhile, JMM utilises many-to-any alignments. However, the main concern for both modelling techniques is the sparseness problem (Bisani & Ney, 2002). Each word's various sizes or lengths can yield different results; features such as evidence trimming and maximum approximation (Viterbi training) are important in segmentation. The features must be balanced and used when appropriate to yield a better result.

Another term that has been mentioned before is the term bootstrapping, or bootstrap. It is "to change the state using existing resources" (Zoubir & Iskander, 2007). As a data-driven approach, this method can substitute tedious and often impossible analytical deviations with computational analysis and calculations. For bootstrapping to succeed, the most suitable resampling schemes must be identified. Initial decisions must be based on examining the data and the problem. Next, determine whether the data in hand is independently and identically distributed (IID in short) or non-IID. IID data is the collection of data that are unlikely to happen in an actual situation, but for study simulations, it is sufficient. If the data is identified as IID, standard bootstrap resampling techniques like independent data bootstrap can be used. If it is non-IID, consider using a parametric approach where a specific structure is assumed, which helps reduce the problem difficulty of dependent data bootstrap to standard resampling of the assumed IID model error estimates. The flow of the strategy process can be seen in Figure 5.

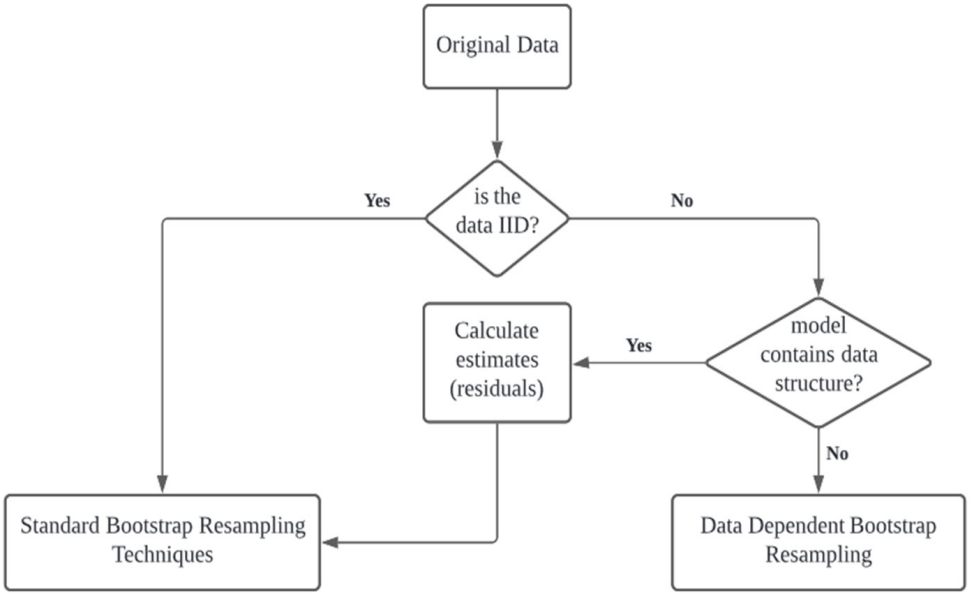

Figure 5. Practical strategy for bootstrapping data (Zoubir & Iskander, 2007)

The bootstrapping method can be applied to estimate statistical characteristics such as bias, variance, distribution functions and, thus, confidence intervals. The method itself is a computational tool for statistical inference. Furthermore, the bootstrap method can estimate hypothesis tests and model selection (Zoubir & Iskander, 2007). Zoubir and Iskander (2007) state that the bootstrap method can be used in experiments with very little data on hand to avoid using asymptotic results. In terms of G2P, the bootstrap method is being used in a data-driven approach, where the estimation and substitution to the unknown while

referring to the available data. One example has been portrayed in the study of Juan and Besacier (2013), where it has been done by filling and substituting unknown data into the Iban pronunciation dictionary using a closely-related language, Malay.

Out-of-Vocabulary, or OOV in short, is a term for words of the selected language in the dictionary that is not a part of the dictionary list of words. It is one of the causes of error in recognising spontaneously spoken utterances (Young, 1994).

The modelling techniques mentioned are based on a data-driven approach, which means the learning or training process uses the input seed data as a reference. The data-driven approach can be semi-supervised or unsupervised most of the time since no default rules are needed in the learning process. Other than that, a data-driven approach may be the best option for generating pronunciation variations. Especially in under-resourced language, when there is scarce information regarding linguistic information (Amdal et al., 2000). In the case of the Iban language, the documentation of rules and exceptions of the language structure is incomplete. Hence, the best approach is to use closely related language data as the seed data for training and testing. Based on the study made by Amdal et al. (2000), the pattern of the data-driven approach in any modelling technique usually follows these steps in G2P conversion:

- Automatically generate alternative transcription.
- Align reference and alternative transcription
- Derive the initial rule from the alignment

However, a data-driven approach can also be rule-based, like a knowledge-based approach that uses data to learn and modify pre-determined pronunciation rules.

CONCLUSION

Pronunciation dictionary plays an important role in ASR systems, especially for an under-resourced language such as the Iban language. It helps to show the variation of word spellings and language pronunciation. Culturally, the Iban language has its pronunciation variants, varying across Sarawak's region. However, the variants are not explicitly depicted in the Iban pronunciation dictionary developed for ASR tasks.

Currently, there is no efficient way of generating Iban pronunciation variants; thus, this paper reviewed selected G2P methods for generating pronunciation variants. Furthermore, this paper reviewed methods used for G2P conversions, such as CRF, JMM and JSM. These methods produced pronunciation variants by converting grapheme sequences to phoneme sequences from any target language.

We described the importance of pronunciation variants, particularly for ASR systems. The variants in the pronunciation dictionary can increase the ASR system's probability of analysing word variations and the base word of the targeted language, thus enriching the system's lexicon with various possibilities. Thus, there is a need to develop systematic

approaches to include significant variants in the dictionary to cater to speakers' speech variabilities when using ASR applications. Articles highlighted in this paper can bring insights to researchers on recent works. These works are related to developing pronunciation variants for under-resourced languages and state-of-the-art techniques for producing G2P models that are reliable in predicting pronunciations for Out-Of-Vocabulary (OOV) words.

We have also briefly discussed the bootstrap method and its correlation with the data-driven approach. The discussion has included the bootstrap application, how it works in a data-driven environment, and the practical bootstrapping strategy in G2P techniques, as shown in Figure 5. Moreover, this paper can be used as a guide or a baseline study on G2P modelling pronunciation variants for under-resourced languages.

ACKNOWLEDGEMENTS

This work was supported by the Malaysia Comprehensive University Network (Grant number: GL/F08/MCUN/ 11/2020). We are grateful for the support enabling us to conduct this research.

REFERENCES

Al-Shareef, S., & Hain, T. (2012). Crf-based diacritisation of colloquial Arabic for automatic speech recognition. In *Thirteenth Annual Conference of the International Speech Communication Association* (pp. 1824-1827). ISCA Publishing.

Amdal, I., Korkmazskiy, F., & Surendran, A. C. (2000, October 16-20). Joint pronunciation modelling of non-native speakers using data-driven methods. In *INTERSPEECH* (pp. 622-625). Beijing, China.

Besacier, L., Barnard, E., Karpov, A., & Schultz, T. (2014). Automatic speech recognition for under-resourced languages: A survey. *Speech Communication*, *56*(1), 85-100. https://doi.org/10.1016/j.specom.2013.07.008

Bisani, M., & Ney, H. (2002, September 16-20). Investigations on joint-multigram models for grapheme-to-phoneme conversion. In *INTERSPEECH* (pp. 1-4). Colorado, USA

Bisani, M., & Ney, H. (2008). Joint-sequence models for grapheme-to-phoneme conversion. *Speech Communication*, *50*(5), 434-451. https://doi.org/10.1016/j.specom.2008.01.002

Brenzinger, M., Yamamoto, A., Aikawa, N., Koundiouba, D., Minasyan, A., Dwyer, A., Grinevald, C., Krauss, M., Miyaoka, O., Sakiyama, O., Smeets, R., & Zepeda, O. (2003, March 10-12). Language vitality and endangerment. In *International Expert Meeting on the UNESCO Programme Safeguarding of Endangered Languages*. Fontenoy, Paris.

Chen, S., Beeferman, D., & Rosenfeld, R. (1998, February 8-11). Evaluation metrics for language models. In *Proceedings of the DARPA Broadcast News Transcription and Understanding Workshop* (pp. 275-280). Lansdowne, Virginia. http://repository.cmu.edu/cgi/viewcontent.cgi?article=2330&context=compsci

Cherifi, E. H., & Guerti, M. (2021). Arabic grapheme-to-phoneme conversion based on joint multi-gram model. *International Journal of Speech Technology*, *24*(1), 173-182. https://doi.org/10.1007/s10772-020-09779-8

Chowdhury, S. A., Alam, F., Khan, N., & Noori, S. R. H. (2018). Bangla grapheme to phoneme conversion using conditional random fields. In *2017 20th International Conference of Computer and Information Technology (ICCIT)* (pp. 1-6). IEEE Publishing. https://doi.org/10.1109/ICCITECHN.2017.8281780

Deligne, S., Yvon, F., & Bimbot, F. (1995, September 18-21). Variable-length sequence matching for phonetic transcription using joint multigrams. In *Fourth European Conference on Speech Communication and Technology* (pp. 2243-2246). Madrid, Spain.

Guazzi, M. D., Cipolla, C., Sganzerla, P., Agostoni, P. G., Fabbiocchi, F., & Pepi, M. (1983). Language vitality and endangerment. *European Heart Journal*, *4*(Suppl. A), 181-187. https://doi.org/10.1093/eurheartj/4.suppl_a.181

Illina, I., Fohr, D., & Jouvet, D. (2011, August 28-31). Grapheme-to-phoneme conversion using Conditional Random Fields. In *Twelfth Annual Conference of the International Speech Communication Association* (pp. 2313-2316). Florence, Italy.

Joshi, P., Santy, S., Budhiraja, A., Bali, K., & Choudhury, M. (2020). *The state and fate of linguistic diversity and inclusion in the NLP world*. arXiv Preprint. https://doi.org/10.18653/v1/2020.acl-main.560

Juan, S., & Flora, S. (2015). *Exploiting resources from closely-related languages for automatic speech recognition in low-resource languages from Malaysia* (Doctoral dissertation). Université Grenoble Alpes, France. https://www.theses.fr/2015GREAM061

Juan, S. S., & Besacier, L. (2013, October 14-18). Fast bootstrapping of grapheme to phoneme system for under-resourced languages-application to the iban language. In *Proceedings of the 4th Workshop on South and Southeast Asian Natural Language Processing* (pp. 1-8). Nagoya, Japan.

Juan, S. S., Besacier, L., Lecouteux, B., & Dyab, M. (2015, September 6-10). Using resources from a closely-related language to develop ASR for a very under-resourced language: A case study for iban. In *Proceedings of the Annual Conference of the International Speech Communication Association* (pp. 1270-1274). Dresden, Germany.

Jurafsky, D., & Martin, J. (2000). *Speech & Language Processing*. Pearson Education India.

Karanasou, P. (2013). *Phonemic variability and confusability in pronunciation modeling for automatic speech recognition* (Doctoral dissertation). Université Paris Sud-Paris, France. http://hal.archives-ouvertes.fr/tel-00843589/

Lafferty, J., McCallum, A., & C.N. Pereira, F. (2001). Conditional rndom fileds: Probabbilistic models for segmenting and labeling sequence data. In *Proceedings of the 18th International Conference on Machine Learning 2001 (ICML 2001)* (pp. 282-289). ACM Publishing. https://doi.org/10.29122/mipi.v11i1.2792

Laurent, A., Meignier, S., & Deléglise, P. (2014). Improving recognition of proper nouns in ASR through generating and filtering phonetic transcriptions. *Computer Speech & Language, 28*(4), 979-996. https://doi.org/10.1016/j.csl.2014.02.006

Lukeš, D., Kopřivová, M., Komrsková, Z., & Poukarová, P. (2018, May 7-12). Pronunciation variants and ASR of colloquial speech: A case study on Czech. In *Proceedings of the Eleventh International Conference on Language Resources and Evaluation (LREC 2018)* (pp. 2704-2709). Miyazaki, Japan.

Masmoudi, A., Ellouze, M., Bougares, F., Esètve, Y., & Belguith, L. (2016). Conditional random fields for the tunisian dialect grapheme-to-phoneme conversion. In *Proceedings of the Annual Conference of the International Speech Communication Association* (pp. 1457-1461). ISCA Publishing. https://doi.org/10.21437/Interspeech.2016-1320

McCallum, A. (2012). *Efficiently Inducing Features of Conditional Random Fields*. arXiv Preprint. http://arxiv.org/abs/1212.2504

Morris, J. J. (2010). *A study on the use of conditional random fields for automatic speech recognition* (Doctoral dissertation). The Ohio State University, USA. https://etd.ohiolink.edu/apexprod/rws_olink/r/1501/10?clear=10&p10_accession_num=osu1274212139

Omar, A. (1981). *The Iban language of Sarawak; A grammatical description*. Kuala Lumpur: Dewan Bahasa dan Pustaka.

Ramli, I., Jamil, N., Seman, N., & Ardi, N. (2015). An improved syllabification for a better Malay language text-to-speech synthesis (TTS). *Procedia Computer Science*, *76*, 417-424. https://doi.org/10.1016/j.procs.2015.12.280

Rugchatjaroen, A., Saychum, S., Kongyoung, S., Chootrakool, P., Kasuriya, S., & Wutiwiwatchai, C. (2019). Efficient two-stage processing for joint sequence model-based Thai grapheme-to-phoneme conversion. *Speech Communication*, *106*, 105-111. https://doi.org/10.1016/j.specom.2018.12.003

Saychum, S., Kongyoung, S., Rugchatjaroen, A., Chootrakool, P., Kasuriya, S., & Wutiwiwatchai, C. (2016, September 8-12). Efficient Thai grapheme-to-phoneme conversion using CRF-based joint sequence modeling. In *Proceedings of the Annual Conference of the International Speech Communication Association* (pp. 1462-1466). ISCA Publishing. https://doi.org/10.21437/Interspeech.2016-621

Shin, C. (2021). Iban as a koine language in Sarawak. *Wacana*, *22*(1), 102-124. https://doi.org/10.17510/wacana.v22i1.985

Singh, A. K. (2008). Natural language processing for less privileged languages: Where do we come from? Where are we going? In *Proceedings of the IJCNLP-08 Workshop on NLP for Less Privileged Languages* (pp. 7-12). Asian Federation of Natural Language Processing. http://www.aclweb.org/anthology/I08-3004

Stadtschnitzer, M., & Schmidt, C. (2018, May 7-12). Data-driven pronunciation modeling of swiss german dialectal speech for automatic speech recognition. In *Proceedings of the Eleventh International Conference on Language Resources and Evaluation (LREC 2018)* (pp. 3152-3156). Miyazaki, Japan.

Sutlive, V. H. (1994). *A handy Reference Dictionary of Iban and English*. Tun Jugah Foundation.

Tjalve, M., & Huckvale, M. (2005, September 4-8). Pronunciation variation modelling using accent features. In *9th European Conference on Speech Communication and Technology* (pp. 1341-1344). Lisbon, Portugal.

Tsuboi, Y., Kashima, H., Mori, S., Oda, H., & Matsumoto, Y. (2008, August 18-22). Training conditional random fields using incomplete annotations. In *Coling 2008 - 22nd International Conference on Computational Linguistics, Proceedings of the Conference* (pp. 897-904). Manchester, UK. https://doi.org/10.3115/1599081.1599194

Tan, T. P., Xiao, X., Tang, E. K., Chng, E. S., & Li, H. (2009). MASS: A Malay language LVCSR corpus resource. In *2009 Oriental COCOSDA International Conference on Speech Database and Assessments* (pp. 25-30). IEEE Publishing. https://doi.org/10.1109/ICSDA.2009.5278382.

Wang, X., & Sim, K. C. (2013). Integrating conditional random fields and joint multi-gram model with syllabic features for grapheme-to-phone conversion. In *INTERSPEECH* (pp. 2321-2325). ISCA Publishing.

Yamazaki, M., Morita, H., Komiya, K., & Kotani, Y. (2014). Extracting the translation of anime titles from web corpora using CRF. In *Knowledge-Based Software Engineering: 11th Joint Conference, JCKBSE 2014* (pp. 311-320). Springer International Publishing. https://doi.org/10.1007/978-3-319-11854-3_26

Yolchuyeva, S., Németh, G., & Gyires-Tóth, B. (2019). Grapheme-to-phoneme conversion with convolutional neural networks. *Applied Sciences*, *9*(6), 1-17. https://doi.org/10.3390/app9061143

Young, S. R. (1994, April). Detecting misrecognitions and out-of-vocabulary words. In *Proceedings of ICASSP'94. IEEE International Conference on Acoustics, Speech and Signal Processing* (Vol. 2, pp. II-21). IEEE Publishing. https://doi.org/10.1109/ICASSP.1994.389728

Yu, M., Nguyen, H. D., Sokolov, A., Lepird, J., Sathyendra, K. M., Choudhary, S., Mouchtaris, A., & Kunzmann, S. (2020). Multilingual grapheme-to-phoneme conversion with byte representation. In *ICASSP 2020-2020 IEEE International Conference on Acoustics, Speech and Signal Processing (ICASSP)* (pp. 8234-8238). IEEE Publishing. https://doi.org/10.1109/ICASSP40776.2020.9054696

Zoubir, A. M., & Iskander, D. R. (2007). Bootstrap methods and applications : A tutorial for the signal processing practitioner. *IEEE Signal Processing Magazine*, *24*(4), 10-19. https://doi.org/10.1109/MSP.2007.4286560

Zweig, G., & Nguyen, P. (2009). Maximum mutual information multi-phone units in direct modeling. In *Tenth Annual Conference of the International Speech Communication Association* (pp. 1919-1922). ISCA Publishing.

Pertanika J. Sci. & Technol. 31 (3): 1313 - 1324 (2023)

PERTANIKA JOURNALS

SCIENCE & TECHNOLOGY

Journal homepage: http://www.pertanika.upm.edu.my/

Correlation Between Clinical Features of Type 2 Diabetes Mellitus with CT Findings of Fatty Liver Patients

Hanady Elyas Osman[1]*, Huda Osama[2], Mohamed Yousef[1], Amal Alsalamah[1], Lubna Bushara[3] and Ikhlas Abdalaziz[3]

[1]Radiologic Sciences Program, Batterjee Medical College, Jeddah, Jeddah 23819-6700, Saudi Arabia
[2]Medical Imaging Technology Department, Al-Ghad International College for Applied Medical Science, Jeddah, Riyadh 12751 – 4270, Saudi Arabia
[3]Department of Medical Imaging and Radiation Sciences, College of Applied Medical Sciences, University of Jeddah, Jeddah, Makkah 21589, Saudi Arabia

ABSTRACT

People with fatty liver disease are at major risk of liver cirrhosis and malignancies. This study aims to evaluate the correlation between fatty liver and diabetes features on computed tomography (CT) using Hounsfield units for the liver and spleen. The research was conducted in Jeddah Hospital's Medical Imaging Department and CT scan department from March 2018 until March 2020. A total of 50 patients with diabetes were chosen randomly, with males (26) and females (24) ranging in age from 31 to 80 years old. Descriptive statistics of body mass index were recorded for the liver and the spleen; the main liver enzymes were Alanine aminotransferase (ALT), Gamma-glutamyltransferase (GGT), albumin, total bilirubin, and direct bilirubin, which were measured and analyzed using the Statistical Package for the Social Sciences program, version 23. We found a significant correlation of ALT and direct bilirubin with liver and spleen HU at p value < 0.017 and < 0.073, respectively; the mean and standard deviation for the other liver enzymes GGT, albumin, and total bilirubin in segment 3 of the left liver were 45.48 ± 7.077 HU, 45.00 ± 7.797 HU, 36.67 ± 5.776 HU, and 37.23 ± 4.885 HU, respectively. We concluded that fatty liver is associated with type 2 diabetes mellitus symptoms such as high ALT and direct bilirubin, with no significant association between GGT, albumin, total bilirubin, and liver and spleen HU.

Keywords: Computed tomography, diabetes mellitus (DM), fatty liver, hounsfield units, liver enzyme

ARTICLE INFO

Article history:
Received: 24 April 2022
Accepted: 07 September 2022
Published: 31 March 2023

DOI: https://doi.org/10.47836/pjst.31.3.11

E-mail addresses:
hanadyelyas86@gmail.com (Hanady Elyas Osman)
yaqin_18@hotmail.com (Huda Osama)
mohamed.yousef@bmc.edu.sa (Mohamed Yousef)
amal.alsalamah@bmc.edu.sa (Amal Alsalamah)
Arwa6067@gmail.com (Lubna Bushara)
ikhlasabdelaziz888@gmail.com (Ikhlas Abdalaziz)
*Corresponding author

ISSN: 0128-7680
e-ISSN: 2231-8526

© Universiti Putra Malaysia Press

INTRODUCTION

Type 2 diabetes mellitus (T2DM) is becoming more prevalent worldwide. Globally, 366 million people were diagnosed with diabetes mellitus in 2011, which is anticipated to rise to 552 million by 2030 (Whiting et al., 2011).

Furthermore, there is substantial evidence that patients with T2DM have a high prevalence of fatty liver (Nakahara et al., 2013). As a result, fatty liver disease may pose a significant mortality risk for people with diabetes who also have liver disorders (i.e., cardiovascular disease, cirrhosis, hepatocellular carcinoma, non-liver cancer, and diabetes mellitus). Nonalcoholic fatty liver disease (NAFLD) is when the liver accumulates excessive fat even though the person drinks little or no alcohol. This problem affects at least half of T2DM patients. As a result, assessing fatty liver and related variables in individuals with diabetes mellitus, particularly T2DM, is crucial (Lonardo et al., 2015).

A liver biopsy is a gold standard for diagnosing fatty liver. However, a liver biopsy is not a reliable tool for detecting and assessing fatty liver in a screening assessment because of the procedure's invasiveness, methods, and sampling variability (Ballestri et al., 2012).

The use of abdominal echo examination as a screening and diagnostic test to detect the presence of fatty liver and determine the severity of the condition has long been common; however, researchers have lately reported on the utility and benefits of this test for patients with fatty liver and T2DM, as CT is used to estimate the liver-to-spleen (L/S) Hounsfield unit (HU) ratio (Nagata et al., 2014).

The liver attenuation measured by CT imaging for an average person is around 55 HU, around 10 HU more than that of an average spleen. Because fat has a low attenuation (less than 100 HU), increasing fat accumulation in the liver results in a corresponding decrease in density. To minimize variances across different CT scanner modalities, as reference values, a liver-to-spleen ratio of less than 0.8–1.1 and a liver minus spleen attenuation of less than 9 HU for that spleen are used. However, a simple assessment of liver attenuation using an unenhanced CT image is the best approach for predicting abnormal liver fat content in diabetic-specific T2DM patients. As a result, the spleen's attenuation measurement has no bearing on predicting hepatic fat content. We can avoid invasive biopsy procedures for the liver using these criteria (Osama et al., 2020).

CT imaging determines the L/S ratio, which has recently been found to be beneficial for diabetes mellitus patients (Osama et al., 2020). For example, serum adiponectin 1209 levels have been associated with the L/S ratio (Yoneda et al., 2007). In liver illnesses, CT scans of visceral adipose tissue (VAT) are considered a useful measure of precancerous lesions such as hepatocellular carcinoma. However, the relationship between the L/S ratio and diabetes mellitus clinical markers such as VAT, subcutaneous adipose tissue (SAT), body mass index (BMI), alcohol intake, and various liver enzymes is yet unknown (Yoneda et al., 2007).

For assessing and analyzing fatty liver, CT imaging is regarded as a valid approach. The L/S ratio, the ratio of the liver parenchyma and splenic texture intensities, can be calculated using CT (Matteoni et al., 1999; Osawa & Mori, 1996).

For those at risk of developing metabolic disorders, such as T2DM, CT is a good modality for fat measures in the liver. Thus, the purpose of this research is to determine whether there is a correlation between fatty liver and diabetes features according to CT using HU for the liver and spleen by assessing and characterizing the most common liver enzymes (Alanine aminotransferase [ALT], Gamma-glutamyltransferase [GGT], albumin, total bilirubin, and direct bilirubin) using L/S HU.

MATERIALS AND METHODS

The research was carried out at Jeddah hospital's Medical Imaging Department and CT scan department. Sudan University of Science and Technology in Khartoum and the Department of Radiological Sciences are conducting research and have been accepted by the ethical approval board in Sudan.

Cases were analyzed retrospectively from a database of patients who underwent abdomen CT scans between March 2018 and March 2020. A straightforward sampling procedure was used to choose 50 patients at random. Liver function tests were performed to analyze the morphology and function of the liver, spleen, and pancreas for all patients with T2DM. All individuals studied had non-enhanced CT scans of the liver.

Inclusion Criteria

Patients with diabetes mellitus, either confirmed or newly diagnosed, who had a fasting plasma venous glucose level less than 7 mmol/l (126 mg/dl) or a random or two-hour postprandial plasma venous glucose level less than 11.1 mmol/l (200 mg/dl) according to the World Health Organization's (1999) criteria were included.

Exclusion Criteria

Patients with normal results were non-diabetic, and patients aged < 18 years were excluded.

CT Liver Protocol and Attenuation Measurements

However, the best method for predicting the pathological fat content of the liver for a person with T2DM using CT is the simple measurement of liver attenuation on unenhanced CT scans. The abdominal CT scans were performed on a (TOSHIBA) CT machine at 120 kV, 50-100 mA (AP&LAT), and a 5 mm slice thickness (1 mm for the Axial plane, −1 mm for the Coronal plane) automatically. With a pitch of 0.8 mm, collimation was 0.5 × 80 mm. Every patient was scanned from above the diaphragm to the level of the iliac crests supine,

usually feet first on the scanner. The patients were instructed to hold their breath at the end of inspiration. We measured five regions of interest within the liver on the CT scans of each patient: the left liver lobe (segment 3), right liver lobe (segments 5 and 6), middle of the spleen, and body of the pancreas. Attenuation measurements were obtained for each region of interest, including larger liver and spleen areas. Regions excluded were of non-uniform parenchymal attenuation, including apparent hepatic vessels. Additionally, two-dimensional axial and coronal measurements of the liver and spleen sizes were obtained.

When using computed tomography (CT) imaging to measure liver attenuation, an average liver CT density (attenuation) measures approximately 55 HU, about 10 HU higher than the average spleen. Fat has low attenuation (−100 HU), so a proportionate decrease in density is seen with increasing fat accumulation in the liver. A liver-to-spleen ratio less than 0.8–1.1 and a liver minus spleen attenuation less than −9 HU for that spleen is used as a reference value to minimize variations across different CT scanner modalities.

Blood Sample for Liver Function Test

A disposable plastic syringe drew 5 mL of venous blood from each patient. The pathology department used an automatic 550 Express Plus Chemistry Analyzer to test serum bilirubin, ALT, aspartate aminotransferase (AST), alkaline phosphatase (ALP), GGT, albumin, total bilirubin, direct bilirubin, and prothrombin time (PT). ALT (10–45) U/L, GGT (8–61) U/L, albumin (32–48) g/L, total bilirubin (0–26) umol/L, and direct bilirubin (0-5) umol/L were all within the average range.

Statistical Analysis

Statistical Package for the Social Sciences, version 23, a statistical software package, was used to analyze the data (SPSS Inc, Chicago, IL). Both frequency and percentage are used. The descriptive analysis results are presented as the standard deviation of the mean to describe the qualitative data. Different populations were sampled to compare the means of two continuous, normally distributed variables; the student's t-test was utilized. All patients' CT attenuation values of the liver, spleen, and pancreas were compared using an independent sample t-test. The duration of T2DM and the CT mean attenuation values for the liver, spleen, and pancreas were correlated using the Pearson correlation coefficient. If the *P* value was less than 0.05, it was considered significant.

RESULTS

A total of 50 people with T2DM were included in this study. Table 1 presents the gender distribution of the participants, with 48% female and 52% male.

Table 2 shows the descriptive statistics of age, BMI, duration, and liver spleen HU (min, max, mean ± standard deviation). The mean and standard deviation for age was 57.52 ± 11.755, while BMI was 31.21±6.800, the duration of T2DM was 13.56 ± 6.80, liver HU (left liver lobe, segment 3) was 44.62±7.340, and spleen HU was 52.48 ± 8.057. Table 3 compares the mean ALT and the mean HU for the liver and the spleen.

Segment 3 of the left liver lobe had a mean and standard deviation of 51.00 ± 2.608; the mean HU for the spleen was slightly higher than that of the liver and measured 59.20 ± 1.059 compared with normal ALT levels for liver HU. The mean and standard deviation for segment 3 of the left liver lobe was 43.20 ± 6.888, and average spleen HU ALT levels were 51.10 ± 7.715. The *P* value was 0.017 indicating a significant correlation of ALT for the liver HU, and the *P* value for the spleen HU was 0.044.

Table 4 compares the mean GGT levels for the liver and the spleen. GGT levels were high for segment 3 of the left liver lobe with a mean and standard deviation of 45.48 ± 7.077. The spleen HU mean was slightly higher than the liver's, measuring 54.92 ± 6.097; the average GGT levels for segment 3 of the left liver lobe were 44.14 ± 7.446 HU, and the average levels of GGT for the spleen were 51.47±8.654 HU. There was a *P* value of 0.724 for the HU of the left liver lobe, segment 3, and a *P* value of 0.368 for the spleen HU.

Table 5 compares the mean albumin levels for the liver and the spleen. Albumin levels were low for segment 3 of the left liver lobe, with a mean and standard deviation of 45.00 ± 7.797. The mean HU for the spleen was slightly higher than that of the liver, measuring 53.67 ± 8.335; the average albumin levels for segment 3 of the left liver lobe were 44.57 ± 7.369 HU, and the average levels of albumin for the spleen were 52.32 ± 8.103 HU. There was a *p* value of 0.894 for the HU of the left liver lobe, segment 3, and a *p* value of 0.705 for the spleen HU.

Table 6 compares the mean total bilirubin levels for the liver and the spleen. Total bilirubin levels were high for segment 3 of the left liver lobe, with a mean and standard deviation of 46.67 ± 5.776. The mean HU for the spleen was slightly higher than that of the liver, measuring 54.33 ± 8.145; the average total bilirubin levels for segment 3 of the left liver lobe were 44.49 ± 7.460 HU, and the average levels of total bilirubin for the spleen were 52.36 ± 8.125 HU. There was a *P* value of 0.623 for the HU of the left liver lobe, segment 3, and a *p* value of 0.685 for the spleen HU.

Table 7 compares the mean direct bilirubin levels for the liver and the spleen. Direct bilirubin levels were high for segment 3 of the left liver lobe, with a mean and standard deviation of 47.23 ± 4.885. The mean HU for the spleen was slightly higher than that of the liver, measuring 55.92 ± 6.304; the average direct bilirubin levels for segment 3 of the left liver lobe were 43.70 ± 7.877 HU, and the average levels of direct bilirubin for the spleen were 51.27 ± 8.325 HU. There was a *p* value of 0.138 for the HU of the left liver lobe, segment 3, and a significant correlation with a *p* value of 0.073 for the spleen HU.

Table 1

Frequency distribution of gender

Gender	Frequency	Percent
Female	24	48.0
Male	26	52.0
Total	50	100.0

Table 2

Descriptive statistical analysis of age, BMI, duration, liver spleen, and pancreas HU (min, max, mean ± Std. Deviation)

	N	Minimum	Maximum	Mean	Std. Deviation
Age	50	31	80	57.52	11.755
Body mass index	50	20	48	31.21	6.800
Duration of diabetes/years	50	4	35	13.56	6.923
Liver CT number HU (LT segment 3)	50	28	60	44.62	7.340
Liver CT number (RT Segment 5)	50	31	56	43.30	7.183
Liver CT number (RT Segment 6)	50	28	54	41.14	6.993
Spleen CT number (middle only)	50	30	71	52.48	8.057
Valid N (listwise)	50				

HU: Hounsfield unit, CT: computed tomography, RT: Right, LT: Left, N: Number

Table 3

Comparison means ALT and means HU for liver and spleen

ALT (10–45) U/L		Report			
		Liver CT number HU (LT segment 3)	Liver CT number (RT Segment 5)	Liver CT number (RT Segment 6)	Spleen CT number (middle only)
High	Mean	51.60	49.80	49.20	59.20
	Std. Deviation	2.608	3.033	3.633	1.095
Low	Mean	49.00	45.80	44.00	56.80
	Std. Deviation	9.247	9.418	9.165	10.710
Normal	Mean	43.20	42.18	39.78	51.10
	Std. Deviation	6.888	6.876	6.339	7.715
Total	Mean	44.62	43.30	41.14	52.48
	Std. Deviation	7.340	7.183	6.993	8.057
P value		0.017	0.055	0.008	0.044

Table 4

Correlation of the means GGT and means HU for liver and spleen

GGT (8–61) U/L		Liver CT number HU (LT segment 3)	Liver CT number (RT Segment 5)	Liver CT number (RT Segment 6)	Spleen CT number (middle only)
High	Mean	45.58	43.58	42.50	54.92
	Std. Deviation	7.077	8.096	6.626	6.097
Low	Mean	47.50	47.50	45.00	56.00
	Std. Deviation	10.607	7.778	8.485	4.243
Normal	Mean	44.14	42.97	40.47	51.47
	Std. Deviation	7.446	6.984	7.117	8.654
Total	Mean	44.62	43.30	41.14	52.48
	Std. Deviation	7.340	7.183	6.993	8.057
P value		0.724	0.687	0.508	0.368

Table 5

Compare mean Albumin and means HU for liver and spleen

Albumin (32– 48) g/L	Liver CT number HU (LT segment 3)	Liver CT number (RT Segment 5)	Liver CT number (RT Segment 6)	Spleen CT number (middle only)
Mean	45.00	43.67	41.17	53.67
Std. Deviation	7.797	8.524	8.377	8.335
Mean	44.57	43.25	41.14	52.32
Std. Deviation	7.369	7.094	6.897	8.103
Mean	44.62	43.30	41.14	52.48
Std. Deviation	7.340	7.183	6.993	8.057
P value	0.894	0.896	0.992	0.705

Table 6

Correlation of the mean Bilirubin total and mean HU for liver and spleen

Bilirubin TOTAL (0–26) umol/l		Liver CT number HU (LT segment 3)	Liver CT number (RT Segment 5)	Liver CT number (RT Segment 6)	Spleen CT number (middle only)
High	Mean	46.67	44.33	42.33	54.33
	Std. Deviation	5.774	6.351	6.351	8.145
Normal	Mean	44.49	43.23	41.06	52.36
	Std. Deviation	7.460	7.290	7.088	8.125
Total	Mean	44.62	43.30	41.14	52.48
	Std. Deviation	7.340	7.183	6.993	8.057
P value		0.623	0.800	0.764	0.685

Table 7

Compares mean Bilirubin direct and means HU for liver and spleen

Bilirubin direct (0–5) mol/l		Liver CT number HU (LT segment 3)	Liver CT number (RT Segment 5)	Liver CT number (RT Segment 6)	Spleen CT number (middle only)
High	Mean	47.23	44.46	41.62	55.92
	Std. Deviation	4.885	5.190	5.440	6.304
Normal	Mean	43.70	42.89	40.97	51.27
	Std. Deviation	7.877	7.785	7.522	8.325
Total	Mean	44.62	43.30	41.14	52.48
	Std. Deviation	7.340	7.183	6.993	8.057
P value		0.138	0.504	0.779	0.073

DISCUSSION

Fatty liver may pose a significant mortality risk due to liver damage for people with diabetes. Worldwide, hepatocellular carcinoma is associated with obesity, and type 2 diabetes mellitus (T2DM) is rising. As a result, assessing and diagnosing fatty liver and related variables in diabetic patients is crucial (Manaviat et al., 2008).

Our research aims to determine whether there was a correlation between fatty liver detected by CT and the clinical features of T2DM. We studied 50 patients with abdominal CT scans (for clinical indications such as abdominal discomfort and abnormal ultrasonography results) from March 2018 to March 2020. Patients who met the following criteria were not eligible to participate in the study: (1) patients with normal liver tests but no T2DM, (2) children, and (3) patients with a splenectomy history.

T2DM was found to be substantially linked with fatty liver in the current investigation. Fatty liver is more common in those with metabolic problems, including obesity and T2DM. Osama et al. observed in their research on T2DM patients that fatty liver is highly linked with T2DM features, especially at younger ages (Osama et al., 2020).

This study included 50 T2DM patients. Table 1 presents the sample's distribution of gender: 48% were female, and 52% were male.

Table 2 presents the descriptive statistics (min, max, mean ± standard deviation) of age, BMI, duration, L/S, and pancreas HU: age was 57.52 ± 11.755, and BMI was 31.21 ± 6.800. The probability of increased ALT levels was considerably lower for longer durations of diabetes (Manaviat et al., 2008). Males were more likely than females to have increased ALT levels.

Table 1 presents the mean and standard deviation of HU for segment 3 of the left liver lobe. The mean and standard deviation for the left liver lobe, segment 3, was 44.62 ± 7.340, while the mean and standard deviation for the right liver lobe, segment 5, was

43.30 ± 7.183; these measurements are less than that of the HU for the spleen, which was 52.48 ± 8.057. The HU of the pancreas was lower than that of the liver and the spleen for people with diabetes, with values of 36.08 ± 9.041. These statistical measurements agree with the findings reported by Osama et al. (2020), who evaluated the HU attenuation of the liver and spleen for people with and without diabetes and found that the liver attenuation for people with diabetes was significantly lower than for people without diabetes. People with T2DM had considerably lower CT attenuation for segment 3 of the left liver lobe than those without diabetes (56.2 ± 10.69 HU vs. 44.62 ± 9.93 HU, $p<0.01$). For people with T2DM and people without diabetes, the CT attenuation of the right lower lobe (segment 5) was 43.46 ± 9.77 HU and 56.02 ± 10.65 HU, respectively ($p<0.01$) and 44.62 ± 9.93 HU and 56.2 ± 10.69 HU, respectively ($p<0.01$), for segment 6.

Table 3 presents the relation between the mean ALT levels and the mean HU for the liver, spleen, and pancreas at a p value < 0.01. This study found a correlation between ALT levels and liver HU for the left liver lobe, segment 3, with a p value of 0.01. There was also a significant correlation for the right liver lobe, segment 6, with a p value < 0.008, and there was a significant correlation between the ALT levels and the HU of the spleen, with a p value < 0.044. ALT levels were elevated for people with T2DM, with high levels in segment 3 of the left liver lobe, with a mean and standard deviation of 51.00 ± 2.608. The mean spleen HU was slightly higher than the liver and measured 59.20 ± 1.059. Typical ALT levels for the left liver lobe, segment 3, were 43.20 ± 6.888 HU, and typical ALT levels for the spleen were 51.10 ± 7.715.

Average GGT levels in the liver and spleen were (8–61)U/L, and GGT levels were high in segment 3 of the left liver lobe with a mean and standard deviation of 45.48 ± 7.077. The mean spleen HU was slightly higher than that of the liver and measured 54.92 ± 6.097, and GGT levels were low in segment 3 of the left liver lobe with a mean and standard deviation of 47.50 ± 10.607. The spleen HU had low GGT levels measuring 56.00 ± 4.243; average GGT levels for segment 3 of the left liver lobe HU were 44.14 ± 7.446, and typical GGT levels for the spleen HU were 51.47 ± 8.654. There was a p value of 0.724 for the HU of segment 3 of the left liver lobe and a p value of 0.368 for the HU of the spleen. These findings show no correlation between GGT levels and HU attenuation in the liver and the spleen (Table 4).

Compare Tables 3 and 4 with the results reported by Sakitani et al. (2017), who discuss elevated levels of liver enzymes with HU L/S and the clinical characteristics of T2DM. Their findings indicate that male fatty liver patients had significantly higher albumin, bilirubin, GGT, ALT, and triglyceride levels than female patients with fatty liver ($p<0.0001$).

Typical albumin levels in the liver and spleen were 32–48 g/L, and albumin levels were low for the left liver lobe, segment 3, with a mean and standard deviation of 45.00 ± 7.797. The mean spleen HU was slightly higher than that of the liver and measured 53.67 ±

8.335, while typical albumin levels for segment 3 of the left liver lobe were 44.57 ± 7.369 and typical levels of albumin for the spleen HU were 52.32 ± 8.103. There was a *P* value of 0.894 for the left liver lobe, segment 3, and a *p* value of 0.705 for the spleen HU with no significant correlation between albumin levels and L/S HU attenuation in CT (Table 5).

The average limit for total bilirubin levels in the liver and the spleen was 0–26 mol/l; in our study, total bilirubin levels were high for segment 3 of the left liver lobe with a mean and standard deviation of 46.67 ± 5.776. The mean spleen HU was slightly higher than the liver's and measured 54.33 ± 8.145 compared with typical total bilirubin levels for segment 3 of the left liver lobe 44.49 ± 7.460 while typical levels of total bilirubin for the spleen HU were 52.36±8.125. There was a *p* value of 0.623 for the HU of the left liver lobe, segment 3, and a *p* value of 0.685 for the spleen HU (Table 6).

Comparing Tables 6 and 7, which indicate that the average direct bilirubin level is 0–5 mol\l, there was a high direct bilirubin level in the liver and spleen for people with T2DM. The direct bilirubin level was high in segment 3 of the left liver lobe, with a mean and standard deviation of 47.23 ± 4.885. The mean spleen HU was slightly higher than that of the liver and measured 55.92 ± 6.304 compared with typical levels of direct bilirubin for the left liver lobe, segment 3, which was 43.70 ± 7.877, while typical levels of direct bilirubin for the spleen HU were 51.27 ± 8.325. There was a *P* value of 0.138 for the HU of the left liver lobe, segment 3, and a significant correlation with a *P* value of 0.073 for the spleen HU. Thus, we found no significant relationship between high levels of direct bilirubin for the HU of the left liver lobe, segment 3, and a slight correlation of spleen HU with direct bilirubin enzyme levels with a *P* value ≥ 0.073.

There are limitations to our study. First, the sample size of patients was small, and a large sample of random patients is recommended to give more accurate results. Second, these results should be compared against people without diabetes, or another control group, using CT scans and laboratory testing. Third, the same patients should be investigated using another imaging modality to eliminate radiation hazards for patients that would otherwise result from CT scans. Our study is beneficial because although computerized tomography is an invasive technique, it gives accurate and reliable measurements to assess and characterize the liver and spleen to study fatty liver for people with T2DM.

CONCLUSION

This study found that fatty liver was associated with clinical characteristics of T2DM. Individuals with T2DM had higher incidences of abnormalities for the liver enzymes evaluated. Fatty liver was associated with features of T2DM, including elevated ALT and direct bilirubin levels with a significant correlation with L/S HU and no significant correlation of GGT, albumin, and total bilirubin with L/S HU.

ACKNOWLEDGMENTS

We appreciate the assistance with data collecting provided by the Radiology Department of Jeddah Hospital, Saudi Arabia.

REFERENCES

Ballestri, S., Lonardo, A., Romagnoli, D., Carulli, L., Losi, L., Day, C. P., & Loria, P. (2012). Ultrasonographic fatty liver indicator, a novel score which rules out Nash and is correlated with metabolic parameters in NAFLD. *Liver International*, *32*(8), 1242-1252. https://doi.org/10.1111/j.1478-3231.2012.02804.x

Lonardo, A., Bellentani, S., Argo, C. K., Ballestri, S., Byrne, C. D., Caldwell, S. H., Cortez-Pinto, H., Grieco, A., Machado, M. V., Miele, L., & Targher, G. (2015). Epidemiological modifiers of non-alcoholic fatty liver disease: Focus on high-risk groups. *Digestive and Liver Disease*, *47*(12), 997-1006. https://doi.org/10.1016/j.dld.2015.08.004

Manaviat, M. R., Rashidi, M., Afkhami-Ardekani, M., & Shoja, M. R. (2008). Prevalence of dry eye syndrome and diabetic retinopathy in type 2 diabetic patients. *BMC Ophthalmology*, *8*(1), Article 10. https://doi.org/10.1186/1471-2415-8-10

Matteoni, C., Younossi, Z., Gramlich, T., Boparai, N., Liu, Y., & Mccullough, A. (1999). Nonalcoholic fatty liver disease: A spectrum of clinical and pathological severity. *Gastroenterology*, *116*(6), 1413-1419. https://doi.org/10.1016/s0016-5085(99)70506-8

Nagata, N., Sakamoto, K., Arai, T., Niikura, R., Shimbo, T., Shinozaki, M., Aoki, T., Kishida, Y., Sekine, K., Tanaka, S., Okubo, H., Watanabe, K., Sakurai, T., Yokoi, C., Akiyama, J., Yanase, M., Noda, M., Itoh, T., Mizokami, M., & Uemura, N. (2014). Visceral abdominal fat measured by computed tomography is associated with an increased risk of colorectal adenoma. *International Journal of Cancer*, *135*(10), 2273-2281. https://doi.org/10.1002/ijc.28872

Nakahara, T., Hyogo, H., Yoneda, M., Sumida, Y., Eguchi, Y., Fujii, H., Ono, M., Kawaguchi, T., Imajo, K., Aikata, H., Tanaka, S., Kanemasa, K., Fujimoto, K., Anzai, K., Saibara, T., Sata, M., Nakajima, A., Itoh, Y., Chayama, K., & Okanoue, T. (2013). Type 2 diabetes mellitus is associated with the fibrosis severity in patients with nonalcoholic fatty liver disease in a large retrospective cohort of Japanese patients. *Journal of Gastroenterology*, *49*(11), 1477-1484. https://doi.org/10.1007/s00535-013-0911-1

Osama, H., Siddig, A., Gareeballah, A., Gameraddin, M., & Osman, H. E. (2020). Evaluation of liver in type 2 diabetes mellitus using unenhanced computed tomography. *International Journal of Biomedicine*, *10*(4), 402-406. https://doi.org/10.21103/article10(4)_oa14

Osawa, H., & Mori, Y. (1996). Sonographic diagnosis of fatty liver using a histogram technique that compares liver and renal cortical echo amplitudes. *Journal of Clinical Ultrasound*, *24*(1), 25-29. https://doi.org/10.1002/(sici)1097-0096(199601)24:1<25::aid-jcu4>3.0.co;2-n

Sakitani, K., Enooku, K., Kubo, H., Tanaka, A., Arai, H., Kawazu, S., & Koike, K. (2017). Clinical characteristics of patients with diabetes mellitus and fatty liver diagnosed by liver/spleen Hounsfield units on CT Scan. *Journal of International Medical Research*, *45*(3), 1208-1220. https://doi.org/10.1177/0300060517707672

Whiting, D. R., Guariguata, L., Weil, C., & Shaw, J. (2011). IDF diabetes atlas: Global estimates of the prevalence of diabetes for 2011 and 2030. *Diabetes Research and Clinical Practice*, *94*(3), 311-321. https://doi.org/10.1016/j.diabres.2011.10.029

World Health Organization. (1999). *Definition, diagnosis and classification of diabetes mellitus and its complications: Report of a who consultation. Part 1, diagnosis and classification of diabetes mellitus*. World Health Organization. https://apps.who.int/iris/handle/10665/66040

Yoneda, M., Iwasaki, T., Fujita, K., Kirikoshi, H., Inamori, M., Nozaki, Y., Maeyama, S., Wada, K., Saito, S., Terauchi, Y., & Nakajima, A. (2007). Hypoadiponectinemia plays a crucial role in the development of nonalcoholic fatty liver disease in patients with type 2 diabetes mellitus independent of visceral adipose tissue. *Alcoholism: Clinical and Experimental Research*, *31*(s1), S15-S21. https://doi.org/10.1111/j.1530-0277.2006.00281.x

Pertanika J. Sci. & Technol. 31 (3): 1325 - 1333 (2023)

PERTANIKA JOURNALS

SCIENCE & TECHNOLOGY

Journal homepage: http://www.pertanika.upm.edu.my/

Highly Conductive Graphenated-Carbon Nanotubes Sheet with Graphene Foliates for Counter Electrode Application in Dye-Sensitized Solar Cells

Yusnita Yusuf[1], Suhaidi Shafie[1,2]*, Ismayadi Ismail[1], Fauzan Ahmad[3], Mohd Nizar Hamidon[1,2], Pandey Shyam Sudhir[4] and Lei Wei[5]

[1]Institute of Nanoscience and Nanotechnology, Universiti Putra Malaysia, 43400 UPM, Serdang, Selangor, Malaysia
[2]Department of Electrical and Electronic Engineering, Faculty of Engineering, Universiti Putra Malaysia, 43400 UPM, Serdang, Selangor, Malaysia
[3]Malaysian-Japan International Institute of Technology, Universiti Teknologi Malaysia, 57000 UTM, Kuala Lumpur, Malaysia
[4]Graduate School of Life Science and System Engineering, Kyushu Institute of Technology, 2-4 Hibikino, Wakamatsu, Kitakyushu, Fukuoka 808-0196, Japan
[5]School of Electronic Science and Engineering, Southeast University, Sipailou, Jinling Yuan 109, Nanjing 210096, China

ABSTRACT

This work enlightened the synthesis of graphenated-carbon nanotubes sheet (g-CNT) using the floating-catalyst chemical vapor deposition method (FCCVD) for dye-sensitized solar cell (DSSC) application. The carbon injection flow rate in the experiment was varied to 6, 8, and 10 ml/h. The morphological findings revealed that the g-CNT formed a highly conductive network. Excellent conductivity was obtained for the sample g-CNT8 (34.5 S/cm) compared to the sample g-CNT6 (11.2S/cm) and CNT10 (4.76 S/cm). This excellent feature is due to the hybrid structure of the g-CNT8, which creates efficient electron transfer in the materials resulting in higher conductivity. The hybrid structure provides a high surface area that improves conductivity. Therefore, the g-CNT sheet is an excellent candidate to replace the conventional platinum used as a counter electrode (CE) in DSSC.

Keywords: Carbon-based counter electrode, DSSC, g-CNT sheet

ARTICLE INFO

Article history:
Received: 01 April 2022
Accepted: 07 September 2022
Published: 31 March 2023

DOI: https://doi.org/10.47836/pjst.31.3.12

E-mail addresess:
yusnita5890@gmail.com (Yusnita Yusuf)
suhaidi@upm.edu.my (Suhaidi Shafie)
ismayadi@upm.edu.my (Ismayadi Ismail)
mnh@upm.edu.my (Mohd Nizar Hamidon)
fauzan.kl@utm.my (Fauzan Ahmad)
shyam@life.kyutech.ac.jp (Pandey Shyam Sudhir)
lw@seu.edu.cn (Lei Wei)
*Corresponding author

ISSN: 0128-7680
e-ISSN: 2231-8526

© Universiti Putra Malaysia Press

INTRODUCTION

Brian O'Regan and Micheal Grätzel founded the dye-sensitized solar cells (DSSC) in 1991 (Andualem & Demiss, 2018) due to the advantages of DSSC, including easy fabrication, low-cost, light, and affordable sources of renewable energy (Muhammad et al., 2020; Lokman et al., 2021; Sharif et al., 2022). The main components of the DSSC structure are a photoanode, sensitizer, redox-mediator, and counter electrode (CE). The CE accumulates the electrons from the external circuit connected to the cell and reduces the redox pair reaction in the mediator. The oxidized redox pair is reduced by adding electrons from the CE surface. A large surface area at the interface region is required to provide more active reaction sites for this mechanism to work. Conventional platinum (Pt) CE is extensively used due to its outstanding conductivity and electrocatalytic ability (Hagfeldt et al., 2010). However, Pt-based CE is very expensive and highly resistant when corroded in an iodine electrolyte, which decomposes the Pt into PtI_4 (Olsen et al., 2000). These led many researchers to explore other low-cost materials with low resistance and excellent electrocatalytic ability. Nevertheless, many electrode materials with good catalytic properties do not have the competence for electron transfer.

Recently, extensive studies have investigated carbon-based CE materials, such as carbon nanotubes (CNT), carbon fibers, carbon black, graphene, and graphite (Yella et al., 2011) (Devadiga et al., 2021). Carbon materials are attractive as CE materials in DSSC due to their low-cost, impressive electrocatalytic activity, high corrosion resistance, and superior conductivity (Wu et al., 2017). Biswas et al. (2019) reported graphene/CNT-based CE and observed an efficiency of 4.66 % of that using Pt-based CE of 5.66 %. The hybrid carbon exhibits a promising potential to replace Pt-based CE in DSSC (Samantaray et al., 2020). Therefore, initiating the hybrid carbonaceous materials will effectively improve the charge transfer of conducting electrons (Chang et al., 2013; Yu et al., 2019).

Previously, our group has reported on the synthesis and characterization of a novel three-dimensional (3D) graphenated-carbon nanotube cotton (g-CNT) hybrid (Ismail et al., 2019). The g-CNT was synthesized without substrate using a single-step floating-catalyst chemical vapor deposition (FCCVD). The report showed a direct growth of hybrid g-CNT cotton and its injection flow rate on the g-CNT cotton development for applying gas sensors. The outcome revealed that the synthesized g-CNT hybrid could be applied as an electrode in electronic devices. Similar research on the g-CNT hybrid has been presented, including bilayer graphene/multiwalled-CNT(MWCNT) (Wahyuono et al., 2019) and graphene nanosheet/MWCNT (Ratul et al., 2019). However, studies on g-CNT sheet material for DSSC applications are scarce.

We predicted that the hybrid properties of the g-CNT sheet structure would provide a way to optimize the hybrid structure. It facilitates the charge transport for excellent conductivity than any of the two materials could achieve independently. Wan et al. (2013)

fabricated G/CNT nanowires via in situ joule heating and found an approximate resistance of 104 kΩ. (Wahyuono et al., 2019) demonstrated bilayer graphene/MWCNT and found that the electrode conductivity and the catalytic activity of graphene/MWCNT reduced the redox species within the electrolyte of the DSSC. Biswas et al. (2019) fabricated graphene nanosheet/MWCNT and found a sheet resistance of 123 Ω/sq, in which the graphene-MWCNT hybrid increased the conductivity. This work investigated the effect of g-CNT sheet morphology on its electrical conductivity. In the experiment, we synthesized the g-CNT sheet via a single-step process of the FCCVD method. The injection rate of the carbon source is expected to be a parameter in the synthesis that influences the materials' morphology. For comparison, a standard CNT sheet was used to prove our hypothesis.

MATERIALS AND METHODS

Synthesis of the g-CNT Sheet by FCCVD

This experiment synthesized g-CNT and CNT sheets via the FCCVD method. A similar synthesis of our CNT was also reported in the literature (Yusuf et al., 2021; Ismail et al., 2019; Ibrahim et al., 2019; Ismail et al., 2018; Adnan et al., 2015). We introduced mix gases of argon, Ar (200 sccm) and hydrogen, H_2 (100 sccm) as the carrier gas, thiophene as the promoter, ferrocene as the catalyst (2.4 wt %), and ethanol as the carbon feedstock. Firstly, the promoter was mixed in ethanol and sonicated for dispersion. The synthesis was started with argon flow at 200 sccm to eliminate the oxygen from the furnace reactor at 600°C until it reached 1150°C and then changed to H_2 gas flow at 100 sccm. The synthesis was then carried out using an electronic syringe pump to inject the carbon feedstock for 2 hours. Other synthesis parameters were fixed, such as temperature, catalyst, and gas flow rate. The carbon injection flow rate was varied; 6 and 8, and 10 ml/h. H_2 gas was stopped during the cooling process, and argon gas flow was used. The samples were produced in cotton bulk form during the synthesis. After the synthesis, it was compressed into a sheet form, as shown in Figure 1. The g-CNT and CNT sheets were then cut into the dimension of 1 cm^2 for characterization. The samples were nominated as follows; g-CNT 6 ml/hr as g-CNT6, g-CNT 8 ml/hr as g-CNT8, and CNT 10ml/hr as CNT10.

Material Characterizations

The morphology of the samples was studied by FESEM (FEI NovaNanoSem 230) and HRTEM (Jeol JEM-2100F). The graphitized samples were characterized by Raman spectroscopy (WITec model Alpha 300R) at 532 nm excitation wavelength. The electrical conductivity was measured using a four-point probe (Loresta-GX MCP-T700, Mitsubishi Chemical Analytech). The thermal stability was measured by thermogravimetric analysis (TGA) (Mettler Toledo) at a heating rate of 20°C/min and temperature of 1000°C under oxygen conditions.

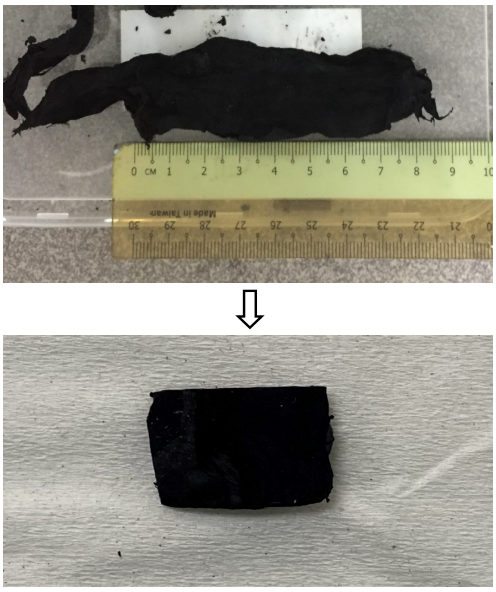

Figure 1. Synthesized g-CNT cotton was pressed into the g-CNT cotton sheet

RESULTS AND DISCUSSION

Morphological Study of g-CNT Sheet Analysis

The FESEM images of g-CNT6 and g-CNT8 in Figures 2a and 2b display a similar structure. They formed a long, thread-like structure and twisted with one another to form the cotton structure of the samples. The respective average diameter (obtained from Image J software) of 0.04 µm and 0.65 µm for samples g-CNT6 and g-CNT8 consists of g-CNT foliates growing from the sidewalls of multi-wall CNTs. Figure 2a shows the density of foliates with some clusters of nanotubes, while Figure 2b shows packed foliates and nanotubes clusters. The structure difference is attributed to the different injection rates during synthesis. The morphology of CNT10 obtained an average diameter of 0.34 µm and non-uniform nanotube growth owing to inadequate sulfur during the reaction (Ismail et al., 2019).

The morphology was observed to form an excellent conductive network of g-CNT. The networks provide a shorter route for electron transfer to increase conductivity. The fundamental advantage of the hybrid g-CNT structure is the high surface area of the three-dimensional framework of the CNTs (Parker et al., 2012). The high edge density of graphene can significantly increase the total charge capacity per unit of nominal area compared to other carbon nanostructures (Parker et al., 2012). The HRTEM image in Figures 2d and 2e showed the graphene foliates with both edges and basal planes of the CNT having an average foliate size of 137.88 nm.

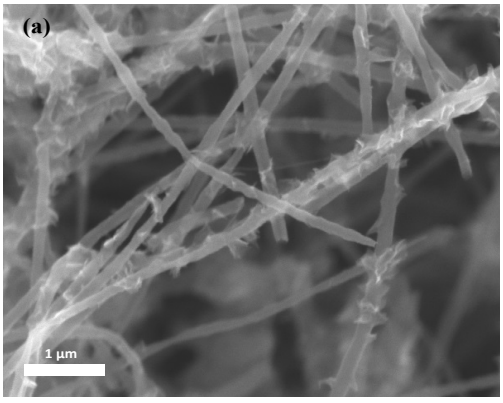

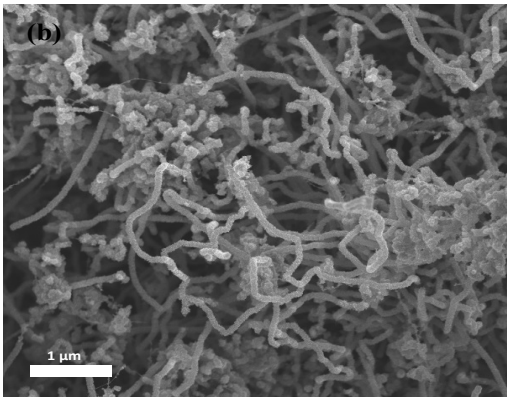

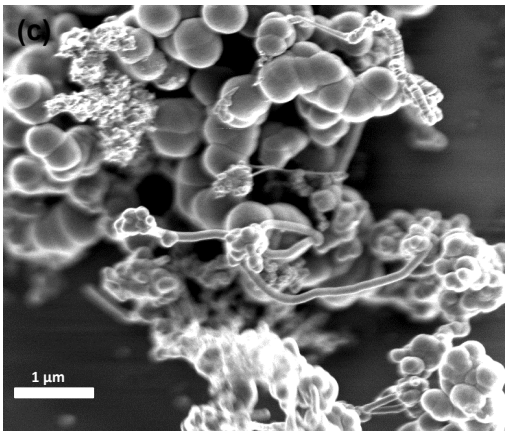

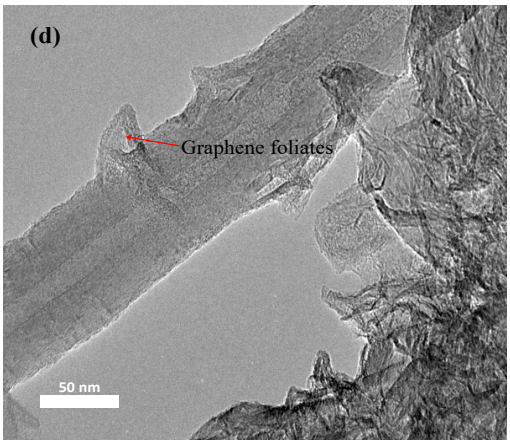

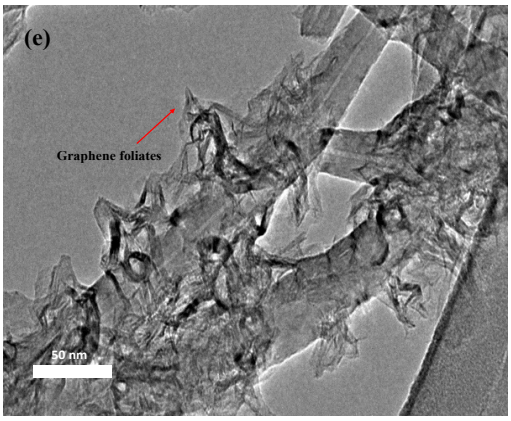

Figure 2. FESEM images of (a) g-CNT6, (b) g-CNT8, (c) CNT10, and HRTEM images of (d) g-CNT6, (e) g-CNT8.

Raman Spectra Analysis

The Raman spectra show the dominant peak at 2673 cm^{-1} (2D band), D and G bands at 1325 cm^{-1} and 1572 cm^{-1}, respectively, in Figure 3. An increase in the G band peak at 1572 cm^{-1} is due to the foliate structures present at the sidewalls of CNT. The high D peak intensity in graphitic materials was reported in the literature (Ni et al., 2006). Meanwhile, the 2D band peak of sample g-CNT8 was increased due to single-layer graphene.

The I_D/I_G ratio for synthesized nanomaterial was 1.06 (g-CNT8, 0.98 (g-CNT6), and 0.99 (CNT10) (Ismail et al., 2019; Abdullah et al., 2021). The intensities of I_D/I_G indicated the lower quality of sp^2 carbon structures when the ratio of I_D/I_G is high (Wepasnick et al., 2010). The higher ratio of defects can improve the exchange current density and electrical conductivity at the interface to improve the catalytic activity of redox reaction according to the catalytic function of CE in DSSC (Chang et al., 2013; Yu et al., 2019). The high ratio is attributed to the growth of graphene foliates at the CNT sidewalls, as agreed in Figure 2. It was also due to graphene structures being higher than the defect. These would help electron mobility move easily through the graphitic interfacial layer because of lower barrier resistance (Ismail et al., 2019).

The absence of radial breathing modes (RBM) peaks at lower wavenumber, suggesting that the samples are multi-walled CNT (Adnan et al., 2015; Ibrahim et al., 2019). It is agreed from the microstructural analysis.

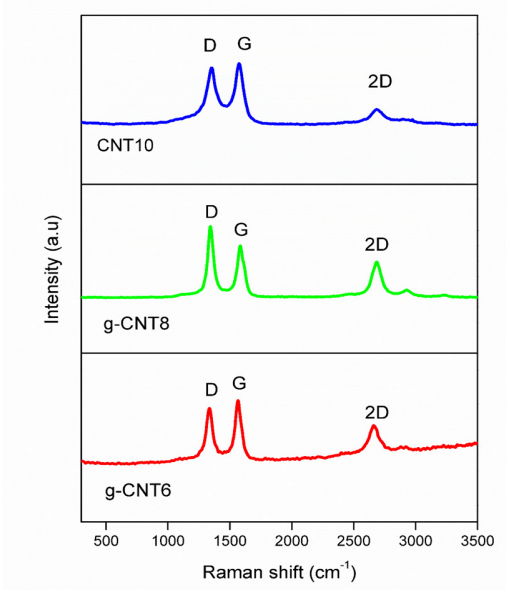

Figure 3. Raman spectra of g-CNT6, g-CNT8, and CNT10.

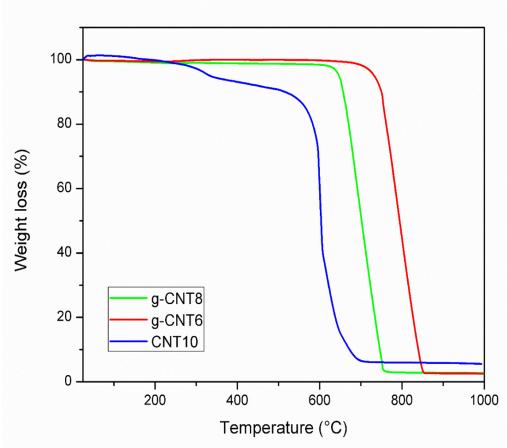

Figure 4. TGA results for g-CNT6, g-CNT8, and CNT10.

Thermogravimetric Analysis

The TGA shown in Figure 4 provides the details of the decomposition temperature of the samples. The TGA analysis can help find the optimal firing temperature for the preparation of the counter electrode. The initial weight begins to lose approximately 400°C because of the elimination of absorbed water and the oxidation of volatile carbon content (Adnan et al., 2015). The rapid weight loss between the temperature of 620 to 860°C was caused by the oxidation of the amorphous carbon. The decomposition seem comparable with result obtained from the previous work (Ismail et al., 2019). In the sample g-CNT6, the thermal stability was observed from 30°C up to 700°C, and after 710°C, weight loss started to decrease significantly. The thermal stability for sample g-CNT8 begins from 30°C up to 610°C, and beyond this temperature, it begins to lose weight. However, for CNT10, the thermal stability decreased at 500°C. These decomposition was similar as reported by (Ibrahim et al., 2019) which indicated that CNT10 are stable up to ~500 °C. We observed that the CNT sheets possess high thermal stability, with g-CNT6 being the most thermally stable. The remaining weight after being sintered at 1000°C was approximately 2.54 wt%, while the g-CNT8 displays 2.71 wt% and CNT10 5.58 wt%.

Electrical Conductivity Analysis

The electrical properties shown in Table 1 provide information regarding the samples' electrical conductivity, resistivity, and sheet resistance. The measurement was conducted using rectangular probes, and the samples were cut into a dimension of 1 cm^2. The results showed that g-CNT8 possessed higher electrical conductivity (34.5 S/cm) than g-CNT6

Table 1
Electrical conductivity analysis

	Sheet resistance (Ω/sq)	Resistivity (Ω.cm)	Conductivity (S/cm)
g-CNT6	3.00	8.93×10^{-2}	11.2
g-CNT8	0.90	2.90×10^{-2}	34.5
CNT10	6.78	0.21	4.76

(11.2 S/cm) and CNT10 (4.76 S/cm). The lower sheet resistance obtained from sample g-CNT8 (0.9 Ω/sq) compared with g-CNT6 (3.0 Ω/sq) and CNT10 (6.78 Ω/sq) resulted in higher conductivity. The existing literature reported that the increase in diameter would decrease the resistivity (Collins et al., 1997). These agree with our FESEM images from Figure 2, in which g-CNT6 and g-CNT8 samples have increased diameters of the g-CNT sheets.

Furthermore, due to the growth of graphene foliates at the sidewalls of CNT, the chemical bond of these materials creates a more charge transfer resulting in higher conductivity (Parker et al., 2012). In DSSC applications, such excellent electrical conductivity performance can promote faster redox reactions and efficiently regenerate the electrons to supply back into the cell. From this measurement, the sample g-CNT8 can be a potential material to substitute platinum as the conventional CE for DSSC.

CONCLUSION

In conclusion, g-CNT and CNT sheets were successfully synthesized via the FCCVD method. The morphology structure of the g-CNT sheet revealed foliates growing out from the sidewalls of multi-walled CNT. The g-CNT6 showed more stability than the g-CNT8 and CNT10. High conductivity was obtained for the sample g-CNT8 (34.5 S/cm) compared to the sample g-CNT6 (11.2 S/cm) and CNT10 (4.76 S/cm). The hybrid structure of the g-CNT sheet creates efficient charge transfer in the materials resulting in higher conductivity. Thus, the g-CNT sheet, especially g-CNT8, can potentially substitute platinum as the conventional CE in DSSC.

ACKNOWLEDGMENT

The authors thank the Institute of Nanoscience and Nanotechnology (ION2), Universiti Putra Malaysia (UPM), for providing the experimental facilities and services. This study was funded by the UniPutra Berimpak grant (Vot: 9689000) and Universiti Putra Malaysia (UPM), and Kyushu Institute of Technology Japan (Kyutech) through (UPM-Kyutech/2019/9300465) grant.

REFERENCES

Abdullah, H. B., Irmawati, R., Ismail, I., Zaidi, M. A., & Abdullah, A. A. A. (2021). Synthesis and morphological study of graphenated carbon nanotube aerogel from grapeseed oil. *Journal of Nanoparticle Research*, *23*(11), Article 244. https://doi.org/10.1007/s11051-021-05363-6

Adnan, N. L., Ismail, I., & Hashim, M. (2015). Effect of ferrocene concentration on the carbon nanotube cotton synthesized via floating catalyst CVD method. *Australian Journal of Basic and Applied Sciences*, *9*(12), 109-113.

Andualem, A., & Demiss, S. (2018). Review on dye-sensitized solar cells (DSSCs). *Edelweiss Applied Science and Technology*, *2*(1), 145-150. https://doi.org/10.33805/2639-6734.103

Biswas, R. K., Nemala, S. S., & Mallick, S. (2019). Platinum and transparent conducting oxide free graphene-CNT composite based counter-electrodes for dye-sensitized solar cells. *Surface Engineering and Applied Electrochemistry*, *55*(4), 472-480. https://doi.org/10.3103/S1068375519040021

Chang, L. H., Hsieh, C. K., Hsiao, M. C., Chiang, J. C., Liu, P. I., & Ho, K. K. (2013). A graphene-multi-walled carbon nanotube hybrid supported on fluorinated tin oxide as a counter electrode of dye-sensitized solar cells. *Journal of Power Sources*, *222*, 518-525. https://doi.org/10.1016/j.jpowsour.2012.08.058

Collins, P. G., Zettl, A., Bando, H., Thess, A., & Smalley, R. E. (1997). Nanotube nanodevice. *Science*, *278*(5335), 100-103. https://doi.org/10.1126/science.278.5335.100

Devadiga, D., Selvakumar, M., Shetty, P., & Santosh, M. S. (2021). Dye-sensitized solar cell for indoor applications: A mini-review. *Journal of Electronic Materials*, *50*(6), 3187-3206. https://doi.org/10.1007/s11664-021-08854-3

Hagfeldt, A., Boschloo, G., Sun, L., Kloo, L., & Pettersson, H. (2010). Dye-sensitized solar cells. *Chemical Reviews*, *110*(11), 6595-6663. https://doi.org/10.1021/cr900356p

Ibrahim, N. I., Ismail, I., Mamat, S. M., & Adnan, N. L. (2019). Effect of carbon source injection rate on CNT film via floating catalyst CVD method. *Solid State Phenomena*, *290*, 113-121. https://doi.org/10.4028/www.scientific.net/ssp.290.113

Ismail, I., Yusof, J. M., Nong, M. A. M., & Adnan, N. L. (2018). Synthesis of carbon nanotube-cotton superfiber materials. In *Synthesis, Technology and Applications of Carbon Nanomaterials* (pp. 61-76). Elsevier. https://doi.org/10.1016/b978-0-12-815757-2.00003-6

Ismail, I., Mamat, S., Adnan, N. L., Yunusa, Z., & Hasan, I. H. (2019). Novel 3-dimensional cotton-like graphenated-carbon nanotubes synthesized via floating catalyst chemical vapour deposition method for potential gas-sensing applications. *Journals of Nanomaterials*, *2019*, 1-10. https://doi.org/10.1155/2019/5717180

Lokman, M. Q., Shaban, S., Shafie, S., Ahmad, F., Yahaya, H., Mohd Rosnan, R., & Ibrahim, M. A. (2021). Improving Ag-TiO_2 nanocomposites' current density by $TiCl_4$ pretreated on FTO glass for dye-sensitised solar cells. *Micro & Nano Letters, 16*(7), 381-386. https://doi.org/10.1049/mna2.12061

Muhammad, N. Y., Mohtar, M. N., Ramli, M. M., Shafie, S., Shaban, S., & Yusuf, Y. (2020). *Enhancement of dye sensitized solar cell by adsorption of graphene quantum dots*. *International Journal of Materials, Mechanics and Manufacturing, 8*(3), 126-130. https://doi.org/10.18178/ijmmm.2020.8.3.494

Ni, Z. H., Fan, H. M., Feng, Y. P., Shen, Z. X., Yang, B. J., & Wu, Y. H. (2006). Raman spectroscopic investigation of carbon nanowalls. *The Journal of Chemical Physics, 124*(20), Article 204703. https://doi:10.1063/1.2200353

Olsen, E., Hagen, G., & Lindquist, S. E. (2000). Dissolution of platinum in methoxy propionitrile containing LiI/I_2. *Solar Energy Materials and Solar Cells*, *63*(3), 267-273. https://doi.org/10.1016/S0927-0248(00)00033-7

Parker, C. B., Raut, A. S., Brown, B., Stoner, B. R., & Glass, J. T. (2012). Three-dimensional arrays of graphenated carbon nanotubes. *Journal of Materials Research*, *27*(7), 1046-1053. https://doi.org/10.1557/jmr.2012.43

Samantaray, M. R., Mondal, A. K., Murugadoss, G., Pitchaimuthu, S., Das, S., Bahru, R., & Mohamed, M. A. (2020). Synergetic effects of hybrid carbon nanostructured counter electrodes for dye-sensitized solar cells : A review. *Materials*, *13*(12), Article 2779. https://doi.org/10.3390/ma13122779

Sharif, N. F. M., Kadir, M. Z. A. A., Shafie, S., Din, M. F., Yusuf, Y., & Samaila, B. (2022). Light absorption enhancement using graphene quantum dots and the effect of N-719 dye loading on the photoelectrode of dye-sensitized solar cell (DSSC). *Key Engineering Materials*, *908*, 259-264. https://doi.org/10.4028/p-0cm1r4

Wahyuono, R. A., Jia, G., Plentz, J., Dellith, A., Dellith, J., Herrmann-Westendorf, F., Dietzek, B. (2019). Self-assembled graphene/MWCNT bilayers as platinum-free counter electrode in dye-sensitized solar cells. *ChemPhysChem*, *20*(24), 3336-3345. https://doi.org/10.1002/cphc.201900714

Wan, N., Sun, L. T., Ding, S. N., Xu, T., Hu, X. H., Sun, J., & Bi, H. C. (2013). Synthesis of graphene-CNT hybrids via joule heating: Structural characterization and electrical transport. *Carbon*, *53*, 260-268. https://doi.org/10.1016/j.carbon.2012.10.057

Wepasnick, K. A., Smith, B. A., Bitter, J. L., & Fairbrother, D. H. (2010). Chemical and structural characterization of carbon nanotube surfaces. *Analytical and Bioanalytical Chemistry*, *396*(3), 1003-1014. https://doi.org/10.1007/s00216-009-3332-5

Wu, J., Lan, Z., Lin, J., Huang, M., Huang, Y., Fan, L., Wei, Y. (2017). Counter electrodes in dye-sensitized solar cells. *Chemical Society Reviews*, *46*(19), 5975-6023. https://doi.org/10.1039/c6cs00752j

Yella, A., Lee, H. W., Tsao, H. N., Yi, C., Chandiran, A. K., Nazeeruddin, M. K., Grätzel, M. (2011). Porphyrin-sensitized solar cells with cobalt (II/III)–based redox electrolyte exceed 12 percent efficiency. *Science*, *334*, 629-633. https://doi.org/10.1126/science.1209688

Yu, F., Shi, Y., Yao, W., Han, S., & Ma, J. (2019). A new breakthrough for graphene/carbon nanotubes as counter electrodes of dye-sensitized solar cells with up to a 10.69% power conversion efficiency. *Journal of Power Sources*, *412*, 366-373. https://doi.org/10.1016/j.jpowsour.2018.11.066

Yusuf, Y., Shafie, S., Ismail, I., Ahmad, F., Hamidon, M. N., Pandey, S. S., Lei, W. (2021). A comparative study of graphenated-carbon nanotubes cotton and carbon nanotubes as catalyst for counter electrode in dye-sensitized solar cells. *Malaysian Journal of Microscopy*, *17*(2), 162-174. https://malaysianjournalofmicroscopy.org/ojs/index.php/mjm/article/view/543

Pertanika J. Sci. & Technol. 31 (3): 1335 - 1351 (2023)

PERTANIKA JOURNALS

SCIENCE & TECHNOLOGY

Journal homepage: http://www.pertanika.upm.edu.my/

Evaluation of Digital's Role in Sustainable Built Environment

Theodore Wayne[1], Chang Saar Chai[1]*, Shirly Siew Ling Wong[2], Fang Lee Lim[3], Kai Chen Goh[4] and Nur IzieAdiana Abidin[5]

[1]Faculty of Engineering, Computing and Science, Swinburne University of Technology Sarawak Campus, 93350 Sarawak, Malaysia
[2]Faculty of Economics and Business, Universiti Malaysia Sarawak, 94300 Kota Samarahan, Sarawak, Malaysia
[3]Department of Environmental Engineering, Faculty of Engineering and Green Technology, Universiti Tunku Abdul Rahmanm, 31900 Perak, Malaysia
[4]Faculty of Technology Management and Business, Universiti Tun Hussien Onn Malaysia, 86400 Johor, Malaysia
[5]Department of Structure and Materials, School of Civil Engineering, Faculty of Engineering, 81310 Johor, Malaysia

ABSTRACT

The construction industry has been evolving, embracing the delicate balance between the Fourth Industry Revolution and sustainable construction to create a sustainable and resilient built environment. Integrating digital tools and technologies in a renowned conventional construction industry is challenging, mainly due to the complex interaction between heterogeneous but heuristic construction processes, building systems, and workflows in achieving a common goal. This study took the initiative to review digital tool adoption and its role in the sustainable built environment by examining the impact of digital adoption in a sustainable built environment in terms of societal and industry impacts. A quantitative analysis is conducted, collecting 63 industry practitioners analysed through regression analysis. The result reveals that energy conservation is the most significant element in the sustainable built environment, which brought the greatest impact on both society and industry in Malaysia. Based on the results, it is found that the digital adoption level in the Malaysian construction industry is still at a minimal level. Through the introduction of Indutry4wrd, National 4IR and Construction 4.0 Strategic Plan (2021–2025), the importance of digital tools and technologies is slowly being acknowledged. The result of the study is significant to benchmark the current digital tools adoption in the Malaysian sustainable built environment. Moreover,

ARTICLE INFO

Article history:
Received: 27 January 2022
Accepted: 30 August 2022
Published: 31 March 2023

DOI: https://doi.org/10.47836/pjst.31.3.13

E-mail addresses:
101213621@students.swinburne.edu.my (Theodore Wayne)
cschai@swinburne.edu.my (Chang Saar Chai)
wslshirly@unimas.my (Shirly Siew Ling Wong)
limfl@utar.edu.my (Fang Lee Lim)
kaichen@uthm.edu.my (Kai Chen Goh)
izieadiana@utm.my (Nur IzieAdiana Abidin)
*Corresponding author

ISSN: 0128-7680
e-ISSN: 2231-8526

© Universiti Putra Malaysia Press

the contribution could be made in terms of better understanding and facilitating, where relevant, greater usage of digital tools in the construction industry to promote efficiency.

Keywords: Digital role, evaluation, quantitative research, sustainable built environment

INTRODUCTION

Visions for cities are more important than ever. It is expected that the migration trend will never stop any time soon, leading to an increase in population. More than half of the world's population lives in cities and urban areas, and this figure will likely increase to 70% by the year 2050 (Daniel, 2020). Thus, sustainable development practices help countries grow in ways that adapt to the challenges posed by climate change, which will help protect important natural resources for ours and future generations. Generally, the backbone of sustainable development is the interplay of three main pillars: economy, society, and environment. Daniel (2020) implied that the three main pillars enhancing the welfare of the entire society force us to reconsider the current urban practices to make sustainable city planning a dominant principle.

One of the key aspects is the necessity of sustainable development in the sphere of society's life to ensure that future generations' needs are not compromised. Establishing the Sustainable Development Goals (SDGs) plays a vital role in sustainability issues as the aim of the SDGs are to end poverty, protect the planet and ensure prosperity for all. Sustainability is a visionary objective that the construction industry and many individuals are gradually working towards. The construction sustainability objectives in the construction industry are always within the building design and construction materials. The shift to sustainability can be seen as a new paradigm where the sustainable objective lies in digital transformation.

Recently, the way humans live their lives and working environment has been transformed digitally. Digital technologies in any industrial process are directly concerned with the quality and productivity of the systems. Among the various fields within the industry, the construction industry has struggled the most with digital adoption and twining (Ahuja et al., 2009). The construction industry is difficult, with legacy processes that span architects, contractors, regulators, and building owners. Bridging different elements of every participant's field and their relationship is necessary for digital transformation (Ubarte & Kaplinski, 2016).

Most past studies in digital construction are focused on infrastructure development which can be seen in areas such as structural, material, and environmental disciplines and the use of design or planning software for the earlier stages of construction. By contrast, relatively little attention has been given to investigating the factors affecting these technologies' infiltration into the construction and project management lifecycle, even

less in building sustainability (Rohana, 2008). This study primarily relies on literature from previous researchers. Thereby, it is hard to disentangle the essential elements of a sustainable built environment and how digital tools can help facilitate a sustainable built environment. There is little evidence from previous research to determine the digital's role in a sustainable built environment. Accordingly, to bridge the knowledge gap of this issue, this study aims at enhancing the built environment through digital adoption by examining the sustainable built environment elements and their adoption impact in the Malaysian construction industry.

LITERATURE REVIEW

Sustainable Development and Built Environment

The general definition of sustainable development is the current generation's use of resources not to jeopardise future generations' ability to meet their needs. Curwell and Cooper (1998) suggested three additional terms for sustainable development which current researchers widely use: 'environment' refers to the protection of local and global ecosystems to support all life; 'public participation' recognizes the need for all people to engage in positive change; and 'equity' refers to an equal distribution of global wealth for human and non-human life. Besides, Sustainable Development Goal 11-Sustainable cities and communities did highlight the necessity of sustainable development- aiming to offer the opportunity to all human settlements by providing transportation, green public places, and affordable housing (UN News Centre, 2015). Therefore, it is important to address the importance of balancing human socio-economic activities and the environment's ability to absorb global waste and provide natural resources.

Over the years, there has been a greater awareness of the importance of sustainable construction because it represents the extensive promise to promote sustainable development globally and locally by preserving the natural environment while improving the built environment. It is the method for establishing a long-term coexistence balance between nature and humans (Jenkin & Zari, 2009). Sustainable development and buildings of the built environment have become dominant principles for sustainability (Conte, 2018). Three factors are emphasised: the consolidation of activities such as construction and manufacturing are responsible for sustainable development, creating a sustainable built environment is the main goal, and nature preservation serves as the starting point for those activities. Holden et al. (2017) suggested that the environment acts as the basis for achieving a sustainable environment through economic activities in the construction sector. As a result, construction became a unique field for testing sustainable practices through the sustainable development of the built environment.

"Sustainability" has a very broad meaning because it encompasses all aspects of development that go beyond the 1987 Brultand report on sustainable development, which

focused on the environment, economy, and society (Holden et al., 2017). As various types of scholars have published to propose and explicate sustainable development, this vague concept has caught the interest of a wide range of disciplines. According to Conte (2018), sustainability has become a popular issue in various industries because it is the latest trend and initiative to reduce environmental impacts in terms of resource waste and energy use. Hence, these indicators assess an organization's ability to meet sustainability goals in the built environment.

Digital Role in Facilitating Sustainable Built Environment

Manyika et al. (2016) define that digitalisation in business covers creating value at new frontiers, creating value in core businesses, and building foundational digital capabilities. Digitalisation allows stakeholders to make informed decisions, reduce decision-making speed and minimise errors. Besides, digitalisation refers to transforming systems and data architecture from siloed legacy systems to support connecting devices, objects, and people (Dörner & Edelman, 2015). Digital approaches in the construction industry allow an integrated approach to development that extends beyond the design profession to include project stakeholders, professional institutions, and governing bodies. By doing so, such approaches become a means of bridging the gap between current working methods and the desired outcomes of a sustainable built environment (Yang et al., 2005).

Digital has multiple roles in facilitating a sustainable built environment, for instance, catalysing enhanced health and the prosperity of humans and the environment and establishing mutually beneficial interactions that self-replicate to generate inclusive resilience (Jenkin & Zari, 2009; Changsaar et al., 2022). To ensure the viability and acceptance of technological advancements in the construction industry, they must respect and have a profound regard for local settings, whether cultural, economic, or ecological, for development to be appropriately tailored to local culture, ecosystems, and economic situations and ensure development that meets the needs of the present without compromising the ability of future generations to meet their own needs.

By recognising the great power of technology, it is possible to shift the solution to an operational level. Tools such as Building Information Modelling (BIM), which are data-related, high-fidelity modelling, or model-based simulation, are employed in digital twin applications and are beneficial to the industry. It can enhance building sustainability, manage different stages of construction processes, allow users to visualise design efficiently, and identify the optimum design and unforeseeable efficiencies of a project (Bratuškins et al., 2020). Therefore, a project can stray away from flaws. Hence, it is clear that digital tools are important in facilitating a sustainable built environment. However, digitalisation is a technological process that is able to integrate into any of the application, defined as neither

good nor bad, viewed as neither desirable nor to be prevented; digitalisation is simply a tool used to achieve a wide range of different objectives (Eling & Lehmann, 2018; Jiancheng et al., 2021). Therefore, there is a need to examine the impact of digitalisation towards the construction industry, especially in terms of the sustainability concept.

Elements of a Sustainable Built Environment

The urban design aims mainly to counter the sprawl of urbanisation, thus channelling it into sustainable design. Akadiri et al. (2012) implied that populations that live in sustainable development would not disperse in different territories as the city is compactly designed. Mondejar et al. (2021) further supported it, highlighting five categories of the sustainable built environment: (1) agricultural and food production, (2) clean water for all, (3) energy challenges, (4) industry and social well-being, and (5) climate research. However, the sustainably built environment should consider the land, natural resources, and adverse environmental conditions when expanding the settlement. Asif et al. (2007) proposed a multi-disciplinary approach to create a sustainable future in the construction sector, including energy conservation, better material utilisation, material waste reduction, pollution, and emissions control. Therefore, this study adopted Asif et al. (2007) due to its wider coverage of the elements of the sustainable built environment in evaluating energy conservation (EC), water management (WM), innovation (IN), indoor environmental quality (IE), sustainable materials (SM) and land use (LU) as shown in Figure 1.

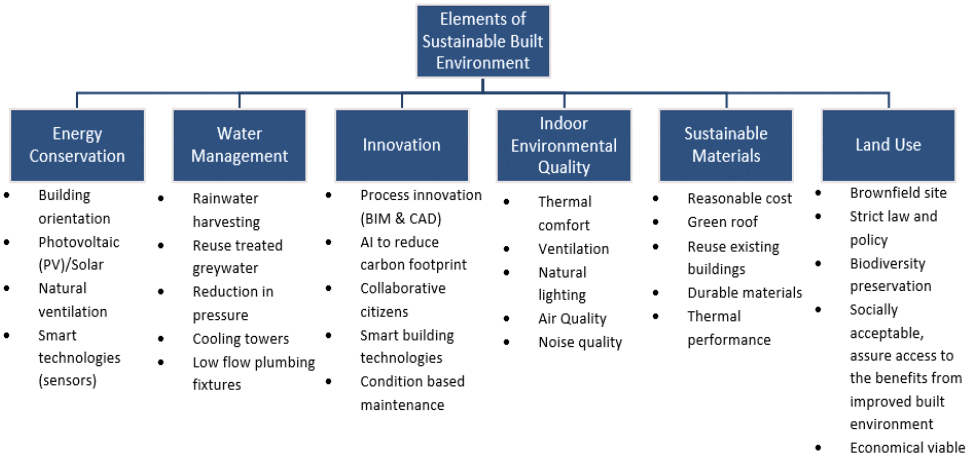

Figure 1. Six elements of a sustainable built environment (Asif et al., 2007)

Impediments and Challenges of Implementing Digital Innovations

Digitalisation brought a new set of tools and technologies which need to be carefully balanced to ensure a smart adoption in the sustainability context. The capability of using the

tools and technologies to make a well-informed decision by using more efficient resources and services has a significant impact on sustainability (Appio et al., 2021; Elshafey et al., 2020; Ardito et al., 2018), but several challenges cannot be neglected to ensure achievement of these targets.

The configuration and organisation of the digital innovation process significantly affect delivery, leading to organisational challenges due to process or performance management becoming an issue (Whyte & Levitt, 2011). Widespread organisational changes across company boundaries have occurred due to utilising new digital tools and processes. Several challenges hinder the adoption of digital approaches in the construction industry (Table 1).

Table 1
Challenges of digital adoption

Challenges	Description
Slow in Generating 3D Information	Some computer operating systems are unable to process much information at once.
High Cost of Investment	Lack of financial resources and support in an organisation
Psychological Barriers	Employees or managers fear failure, work change, and process change with digital adoption.
Technological Barriers	Lack of skill, lack of training, unavailability of new digital tools
Inability to Achieve Unified Goals	Project stakeholders have different perspectives on digital technologies.

Note. Adopted from Whyte and Levitt (2011), Bratuškins et al. (2020), Ramilo and Embi (2014), Rusu et al. (2020), Elmustapha et al. (2018) and Linderoth et al. (2018).

Recently, there has been an ongoing discussion on the qualitative treatment of the power of digital technology development on SDGs. Some scholars highlighted the impact of digital technologies in sustainable construction, considering the high initial cost and ecological cost of economic growth threaten digital change negatively. Digital technologies have been one of the main vectors of economic growth in recent years and will retain this role in the long term, up to 2030 and, according to specific estimates, even up to 2050 (Popkova et al., 2022).

Impact of Digital Innovations in Sustainable Built Environment

Digital approaches allow an integrated approach to development that extends beyond the design profession to include project stakeholders, professional institutions, and governing bodies. By doing so, such approaches become a means of bridging the gap between current

ways of working and the desired outcomes of a sustainable built environment (Yang et al., 2005).

Over the years, there have been limitless discussions over the impacts of digital adoption or innovations in a sustainable built environment. For example, Keeys and Huemann (2017) acknowledged the benefits of digital adoption through innovation, change and value creation; meanwhile, Kempt et al. (2007) and Roome (2013) highlighted the value of integrative collaboration in supporting sustainable pillars (economic, environmental, and social). On the other hand, this study suggested looking into the impact of digital adoption from societal and industry perspectives. The impacts of digital innovation in the sustainable built environment are tabulated in Figure 2.

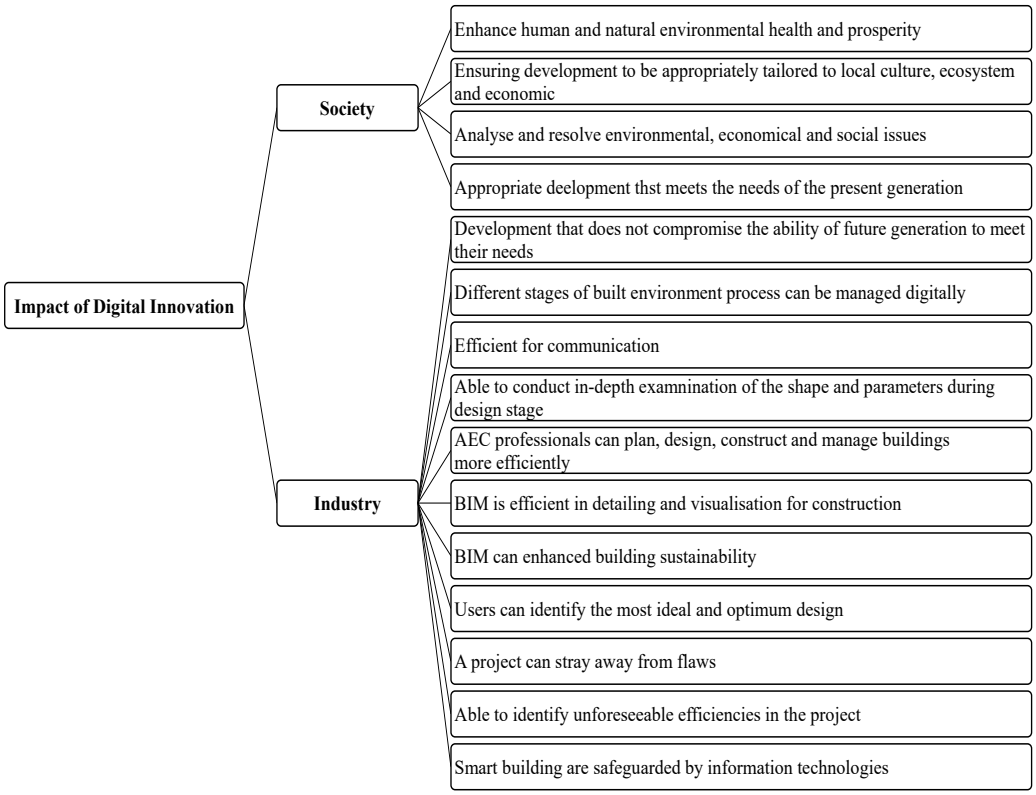

Figure 2. Impacts of digital innovation on the sustainable built environment
Sources. Adopted from Kempt et al. (2007), Juujärvi and Pesso (2013), Aleta et al. (2017), Keeys and Huemann (2017) and Downey (2020).

This study evaluates the digital's role in a sustainable built environment. A quantitative approach will be conducted to examine the causal relationship among the elements of a sustainable built

RESEARCH METHODOLOGY

This study adopted a quantitative approach mainly due to the explorative character of the study. A questionnaire survey with Likert Scale and purposive sampling method is selected to collect the data. Purposive sampling is a non-probability method where the samples are selected based on the researcher's judgement (Etikan et al., 2016). In this study, the samples are selected by screening the LinkedIn profile, where civil and non-civil engineers (construction professionals) were selected as targeted respondents. There were two criteria in selecting the samples: (1) experience in digital construction and (2) experience in sustainable construction. However, the limitation of purposive sampling is prone to researcher bias because the sampling judgement might be too subjective. In order to reduce procedural bias, a thorough research plan was created before the study was conducted. Besides, the questionnaire questions were designed in separate sections, giving clear instructions to the respondents. Moreover, internal reliability and validity were tested before detailed analysis.

There were 200 sets of questionnaire surveys distributed on LinkedIn, received 86 with 63 valid responses contributing to a 31.5% response rate. From the collected data, it is discovered that 65% of the respondents are from Peninsular Malaysia. Kuala Lumpur, Sarawak and Selangor recorded the highest response rate, contributing 28.6%, 27.0% and 17.5% to the sample, respectively.

The preliminary analysis of the reliability and validity tests shows significant internal consistency. Cronbach's Alpha is recorded at 0.929, indicating the presence of a high internal correlation between the items or items based on the same principle. This finding revealed that the questions were appropriately connected, and the factors created the ground for the very reliable outcomes of the following analyses. On the other hand, the Kaiser-Meyer-Olkin (KMO) value of 0.828 implied that factor analysis of variables was feasible for this data. Furthermore, Bartlett's test of sphericity was found to be statistically significant, suggesting that the null hypothesis of the correlation matrix is an identity matrix that can be rejected. On the whole, findings from Cronbach's Alpha and KMO were found to be in the highly acceptable range (Pallant, 2000; Hair et al., 2010), and Bartlett's Test of Sphericity was statistically significant, inferring that sampling adequacy was meritorious and variables were related and therefore ideal for structure detection in factor analysis. Next, we tabulate the demographic profile of the respondents by cross-tabulating the profession category by age, and the finding is illustrated in Table 2.

The respondents are classified into civil engineers and non-civil engineers. The category of non-civil engineers includes architects, quantity surveyors, mechanical and electrical engineers, and project management consultants. This study examines the digital's role in a sustainable built environment, which in many studies identified the important role of civil engineers in sustainable areas. It is further emphasised in the American Society of

Table 2
Demographic profile of respondents

		Age						Total
		< 25	25 - 30	30 - 35	35 - 40	40 - 45	> 45	
Profession	Civil engineers	11	12	9	4	2	1	39
	Non-civil engineers	3	4	7	3	3	4	24
Total		14	16	16	7	5	5	63

Civil Engineers (ASCE) Policy Statement 418 highlights the role of civil engineers in sustainable development (ASCE, 2021). Although this study emphasises the role of civil engineers in sustainable development, the opinions of other construction professionals are relatively important. Thus, a comparison of the civil engineers and non-civil engineers in the sustainable development concept will be made in the next section.

Besides, a three-way cross-tabulation (contingency table analysis) was conducted to demonstrate the relationships within company size, digital tools, and managerial level of the respondents. The cross-tabulation result (Table 3) shows that small enterprises ($5 < 75$ employees) recorded 30 respondents. Meanwhile, medium enterprises ($75 \leq 200$ employees) consist of 33 respondents. There are no micro and large enterprise respondents in this study. Table 3 reveals that junior executives in the small enterprise are keen on digital tools compared to middle and senior executives, especially in using BIM, GPS, QR code, GIS, and AI. The three-way contingency table analysis result allowed multiple options to infer that the young generation in the small enterprise has more exposure to the latest digital tools. Many studies revealed that Generation Z is tech savvy, prefers visual form, fast acquisition of knowledge and is used to social media (Wahab et al., 2018). Digital tools are, to a certain extent, drawn the attention of this generation, leading to such results.

However, the situation is different in the medium enterprise, where senior executives are more informed about digital tools than middle and junior executives. It is mostly because the senior executives in the medium enterprise have a bigger picture in company development and extensive growth strategy. Besides, medium enterprise has recorded higher exposure to digital tools than small enterprise. It can be seen from the medium enterprise BIM (total entry) 31 compared to 28 (small enterprise), GIS 23:20, and GPS 27:23, among others. In most cases, the medium enterprise construction company in Malaysia are CIDB G6 and G7, where the project amount is at least RM5 mil and above. Digital tools have become a strategic tool to improve competitiveness in the construction market. As such, digital tools are not limited to enhancing the sustainable built environment, but they also play an important role in ensuring project productivity and efficiency, which are essential for a company's development.

Table 3

Results of three-way cross-tabulation between company size, digital tools and managerial level

Category of Company Size			Managerial level			Total
			Senior executive	Middle executive	Junior executive	
Small enterprise: 5 < 75 employees	Digital tools	Building Information Modelling (BIM)	6	7	15	28
		Geographic Information Systems (GIS)	4	6	10	20
		Augmented Reality (AR)	3	0	7	10
		Virtual Reality (VR)	5	4	7	16
		3D Laser Scanning	3	2	6	11
		Global Positioning Systems (GPS)	7	4	12	23
		Radio Frequency Identification Devices (RFID)	3	2	8	13
		Photogrammetry	1	1	2	4
		Quick Response Code (QR)	4	3	11	18
		Robotics	2	1	6	9
		Artificial Intelligence (AI)	4	3	10	17
		Onsite mobile devices	1	3	4	8
		Wearable safety devices	2	3	2	7
	Total within group		8	7	15	30
Medium enterprise: 75 ≤ 200 employees	Digital tools	Building Information Modelling (BIM)	13	11	7	31
		Geographic Information Systems (GIS)	10	8	5	23
		Augmented Reality (AR)	7	7	2	16
		Virtual Reality (VR)	10	7	3	20
		3D Laser Scanning	7	7	1	15
		Global Positioning Systems (GPS)	10	10	7	27
		Radio Frequency Identification Devices (RFID)	7	7	4	18
		Photogrammetry	4	2	1	7
		Quick Response Code (QR)	8	8	5	21
		Robotics	7	2	3	12
		Artificial Intelligence (AI)	9	5	4	18
		Onsite mobile devices	3	5	3	11
		Wearable safety devices	5	6	2	13
	Total within group		13	12	8	33

RESULTS AND DISCUSSION

Comparison of Civil Engineers and Non-Civil Engineers in Digital Adoption Impacts

As discussed in the previous section, the respondents in the study are divided into civil engineers and non-civil engineers due to several studies highlighting the importance of civil engineers in a sustainable built environment. An independent sample *t*-test is conducted to examine the significant differences between civil and non-civil engineers in digital adoption. The results of *t*he t-test for equality means and the Levene's homogeneity assumption test are reported in Table 4.

Table 4

Results of independent sample t-test for impacts of digital adoption by category of a profession

		Levene's Test for Equality of Variances		*t*-test for Equality of Means	
		F	*p* value	*t*	*p* value
Impact towards the industry	Equal variances assumed	0.18	0.673	0.922	0.361
	Equal variances not assumed			0.973	0.335
Impact towards the society	Equal variances assumed	0.017	0.896	0.019	0.985
	Equal variances not assumed			0.019	0.985

Table 4 illustrates that there is no significant difference between civil and non-civil engineers in terms of digital adoption impacts on the industry and society. With the outcome of Levene's homogeneity assumption test suggesting non-rejection of the null hypothesis of equal variances, we proceed to compare the means of two independent groups (civil engineers and non-civil engineers) under the condition of "equal variances assumed", both *p* values of the *t*-test for equality of means recorded for impact towards industry (0.361) and impact towards society (0.985) are exceeding the conventional levels of significance ($p < 0.10$). This result indicated that both respondent groups (civil and non-civil engineers) have similar opinions towards digital adoptions in the sustainable built environment. It is probably due to the respondents being recruited from the same industry (construction). The intention to examine the differences among both respondent groups is due to the digital adoption agenda being significantly different. Based on the ASCE Policy Statement 418 highlights, civil engineers' role in life cycle assessments, use resources wisely and plan for resilience and validation through rating tools. Meanwhile, an architect's agenda

in a sustainable built environment aims to transform architecture practice holistically, firm-wide, project-based, and data-driven (American Institute of Architects, 2022). By prioritising energy performance, AIA is mandating that highly inefficient existing buildings undergo detailed audits and upgrades to reduce their energy use, moving towards an energy transparency protocol. Civil engineers and architects focus on different agendas but ultimately work towards embracing a sustainable built environment.

Effects of Sustainable Built Environment on the Impact of Digital Tools Adoption

As suggested in the literature, the adoption of digital tools brought two important impacts: impact to the industry and society. Hence, we examine how the elements of a sustainable built environment shape the impact of digital tools adoption towards the industry and society via the multiple regression analysis. Table 5 reported the multiple regression analysis result for the impact towards the industry, while Table 6 depicted the outcome of the impact towards society. As shown in Table 5, energy conservation (EC) is the only significant sustainable element that impacted the industry. The EC element is statistically significant at a 1% level, indicating the presence of a positive relationship between energy conservation and the impact of digital tools adoption towards the industry. In addition, the *F*-test of overall significance (*F*-statistic=6.728) is statistical significance at a 1% level (*p* value = 0.000), whereas the R^2 is recorded at 0.473, suggesting that 47.3% of the variance found in the dependent variable (impact of digital tools adoption towards industry) is explained by the elements of the sustainable built environment. Therefore, measures of goodness-of-fit for the regression model reported in Panel B of Table 5 revealed that the regression model has a significant predictive capability, implying the existence of a relationship between the dependent variable (impact of digital tools adoption towards industry) and predictors (elements of the sustainable built environment).

In this respect, the importance of renewable energy and its promotion to access the research, technology and investment in clean energy has been well underlined in Sustainable Development Goal 7 (SDG7). Over the years, sustainable policies have been drafted according to UN SDGs, especially SDG7 (affordable and clean energy) and SDG9 (industry, innovation, and infrastructure), embedded into Industry 4.0-related policies. Taking Malaysian's Industry4WRD and National 4IR policies as examples, SDG7 became the foundation of the Industry4WRD policy; meanwhile, the National 4IR policy emphasises ecological integrity. Although most IR4.0 policies highlight the importance of digital adoption in the new era, the sustainable future remains the main agenda in all the policies.

Table 5

Results of multiple regression analysis for the effect of the sustainable built environment on the impact of digital adoption towards industry

Panel A: Parameter estimates			
Independent variables	Coefficients	*t*-statistics	*p*-values
Energy conservation (EC)	0.565	3.681***	0.001
Waste management (WM)	-0.152	-0.986	0.329
Innovation (IN)	0.124	0.523	0.603
Indoor environmental quality (IE)	0.087	0.548	0.586
Sustainable materials (SM)	0.138	0.815	0.419
Land use (LU)	-0.045	-0.217	0.829
Panel B: Measures of goodness-of-fit for the model			
R^2: 0.473			
F-statistic: 6.728*** (0.000)			

Note. Figure in parenthesis is p-value whereas asterisk (***) indicates statistically significant at 1% level.

From a boarder perspective, the sustainable built environment even shapes some larger effect on society when we look at the adoption of digital tools. Two important elements of a sustainable built environment were found to play significant roles in fostering the impact of digital tool adoption in society. These elements are energy conservation (EC) and waste management (WM). The EC element is statistically significant at a 1% level, whereas the WM element is statistically significant at a 5% level, suggesting that energy conservation and waste management are crucial elements of the sustainable built environment that potentially predict the impact of digital tools adoption towards society. Besides, the *F*-test of overall significance (*F*-statistic=9.292) is statistical significance at a 1% level (*p* value = 0.000), whereas the R^2 is recorded at 0.543, signifying that 54.3% of the variance found in the dependent variable (impact of digital tools adoption towards the society) is explained by the elements of the sustainable built environment. Hence, goodness-of-fit measures for the regression model reported in Panel B of Table 6 revealed that the predictors (elements of the sustainable built environment) have significant predictive capability over the impact of digital tools adoption in society.

Furthermore, the multiple regression results reported in Table 6 also showed that energy conservation brought a higher impact on society compared to waste management. It is further justified by Kumar (2020) highlights the important role of energy conservation in society. Meanwhile, Abdel-Shafy et al. (2018) explained the importance of waste management to society, especially solid waste management. Although the other elements are not significant in this study, the sustainable elements might differ in other industries.

Table 6

Results of multiple regression analysis for the effect of the sustainable built environment on the impact of digital adoption towards society

Panel A: Parameter estimates			
Independent variables	Coefficients	*t*-statistics	*p*-values
Energy conservation (EC)	0.656	4.684***	0.000
Waste management (WM)	-0.319	-2.325**	0.024
Innovation (IN)	0.298	1.374	0.176
Indoor environmental quality (IE)	-0.222	-1.542	0.130
Sustainable materials (SM)	0.209	1.364	0.179
Land use (LU)	0.004	0.019	0.985
Panel B: Measures of goodness-of-fit for the model			
R^2: 0.543			
F-statistic: 9.292*** (0.000)			

Note. Figure in parenthesis is p-value whereas asterisks (***) and (**) indicate statistically significant at 1% level and 5%, respectively.

CONCLUSION

This study intended to examine the digital's role in the sustainable built environment by investigating the relationship between elements of a sustainable built environment and its impact on society and industry. Besides, this study has taken additional steps to look into the construction professional's role, i.e. civil and non-civil engineers, in relation to the digital adoption impacts. There is evidence that both civil and non-civil engineers have a similar perspective on the impact of digital adoption.

This study reveals that energy conservation is the most important element in the sustainable built environment, which impacts society and industry. The analysis result is supported by the highly significant regression model, and the result is tallied with some precedent studies. The study's outcome is important to assist industry practitioners in facilitating sustainable development by formulating new working culture. Besides, based on the digital tools adopted in small and medium enterprises helps the authorities to embrace Construction 4.0 Strategic Plan (2021–2025) implementation more strategically.

ACKNOWLEDGEMENT

Authors would like to express their gratitude to the contribution of the Swinburne University of Technology Sarawak Campus (2-5548), Malaysia to support this project.

REFERENCES

Abdel-Shafy, H. I., & Mansour, M. S. M. (2018). Solid waste issue: Sources, composition, disposal, recycling, and valorization. *Egyptian Journal of Petroleum*, *27*(4), 1275-1290. https://doi.org/10.1016/j.ejpe.2018.07.003

Ahuja, V., Yang, J., & Shankar, R. (2009). Study of ICT adoption for building project management in the Indian construction industry. *Automation in Construction*, *18*(4), 415-423. https://doi.org/10.1016/j.autcon.2008.10.009

Akadiri, P. O., Chinyio, E. A., & Olomolaiye, P. O. (2012). Design of a sustainable building: A conceptual framework for implementing sustainability in the building sector. *Buildings*, *2*(2), 126-152. https://doi.org/10.3390/buildings2020126

Aleta, A., Meloni, S., & Moreno, Y. (2017). A multilayer perspective for the analysis of urban transportation systems. *Scientific Reports*, *7*, Article 44359. https://doi.org/10.1038/srep44359

American Institute of Architects. (2022). *The AIA 2030 commitment*. American Institute of Architects. https://www.aia.org/pages/6464938-the-aia-2030-commitment

American Society of Civil Engineers (2021). *Policy statement 418 - The role of the civil engineer in sustainable development*. American Institute of Architects. https://www.asce.org/advocacy/policy-statements/ps418---the-role-of-the-civil-engineer-in-sustainable-development

Appio, F. P., Frattini, F., Petruzzelli, A. M., & Neirotti, P. (2021). Digital transformation and innovation management: A synthesis of existing research and an agenda for future studies. *The Journal of Product Innovation Management*, *38*(1), 4-20. https://doi.org/10.1111/jpim.12562

Ardito, L., D'Adda, D., & Petruzzelli, A. M. (2018). Mapping innovation dynamics in the internet of things domain: Evidence from patent analysis. *Technological Forecasting and Social Change*, *136*, 317-330. https://doi.org/10.1016/j.techfore.2017.04.022

Asif, M., Muneer, T., & Kelley, R. (2007). Life cycle assessment: A case study of a dwelling home in Scotland. *Building and Environment*, *42*(3), 1391-1394. https://doi.org/10.1016/j.buildenv.2005.11.023

Bratuškins, U., Zaleckis, K., Treija, S., Koroļova, A., & Kamičaitytė, J. (2020). Digital information tools for urban regeneration: Capital's approach in theory and practice. *Sustainability*, *12*(19), Article 8082. https://doi.org/10.3390/su12198082

Changsaar, C., Abidin, N. I., Khoso, A. R., Luenhui, L., Yaoli, X., & Hunchuen, G. (2022). Optimising energy performance of an eco-home using building information modelling (BIM). *Innovative Infrastructure Solution*, *7*, Article 140. https://doi.org/10.1007/s41062-022-00747-6

Conte, E. (2018). The era of sustainability: Promises, pitfalls and prospects for sustainable buildings and the built environment. *Sustainability*, *10*(6), Article 2092. https://doi.org/10.3390/su10062092

Curwell, S., & Cooper, I. (1998). The implications of urban sustainability. *Building Research and Information*, *26*(1), 17-28. https://doi.org/10.1080/096132198370074

Daniel, K. (2020). *Goal 11—cities will play an important role in achieving the SDGs.* United Nations. https://www.un.org/en/chronicle/article/goal-11-cities-will-play-important-role-achieving-sdgs

Dörner, K., & Edelman, D. (2015). *What 'Digital' Really Means*. McKinsey & Company.

Downey, J. (2020). *What is digital twin technology and how it benefits manufacturing in the industry 4.0 era?* SL Controls. https://slcontrols.com/what-is-digital-twin-technology-and-how-can-it-benefit-manufacturing/

Eling, M., & Lehmann, M. (2018). The impact of digitalization on the insurance value chain and the insurability of risks. *The Geneva Papers on Risk and Insurance Issues and Practice*, *43*, 359-396. https://doi.org/10.1057/s41288-017-0073-0

Elmustapha, H., Hoppe, T., & Bressers, H. (2018). Understanding stakeholders' views and the influence of the socio-cultural dimension on the adoption of solar energy technology in Lebanon. *Sustainability*, *10*(2), Article 364. https://doi.org/10.3390/su10020364

Elshafey, A., Chai, C. S., Aminudin, E. B., Gheisari, M., & Usmani, A. (2020). Technology acceptance model for augmented reality and building information modeling integration in the construction industry. *Journal of Information Technology in Construction, 25*, 161-172. https://doi.org/10.36680/j.itcon.2020.010

Etikan, I., Musa, S. A., & Alkassim, R. S. (2016). Comparing of convenience sampling and purposive sampling. *American Journal of Theoretical and Applied Statics, 5*(1), 1-4. https://doi.org/10.11648/j.ajtas.20160501.11

Hair, J. F., Anderson, R. E., Black, W. C., & Babin, B. J. (2010). *Multivariate data analysis: A global perspective*. Pearson Education.

Holden, E., Linnerud, K., & Banister, D. (2017). The imperatives of sustainable development. *Sustainable Development*, *25*(3), 213-226. https://doi.org/10.1002/sd.1647

Jenkin, S., & Zari, M. P. (2009). *Rethinking our built environments: Towards a sustainable future*. Ministry for the Environment, New Zealand.

Juujärvi, S., & Pesso, K. (2013). Actor roles in an urban living lab: What can we learn from suurpelto, Finland? *Technology Innovation Management Review*, *3*(11), 22-27. https://doi.org/10.22215/timreview/742

Keeys, L. A., & Huemann, M. (2017). Project benefits co-creation: Shaping sustainable development benefits. *International Journal of Project Management*, *35*(6), 1196-1212. https://doi.org/10.1016/j.ijproman.2017.02.008

Kemp, R., & Martens, P. (2007). Sustainable development: How to manage something that is subjective and never can be achieved? *Sustainability: Science Practice and Policy*, *3*(2), 5-14. https://doi.org/10.1080/15487733.2007.11907997

Kumar, M. (2020). Social, economic, and environmental impacts of renewable energy resources. In K. E. Okedu, A. Tahour & A. G. Aissaou (Eds.), *Wind Solar Hybrid Renewable Energy System* (pp. 1-11). IntechOpen. https://doi.org/10.5772/intechopen.89494

Linderoth, H. C. J., Jacobsson, M., & Elbanna, A (2018, December 3-5). Barriers for digital transformation: The role of industry [Paper presentation]. *Australasian Conference on Information Systems 2018*. University of Technology, Sydney, Australia.

Manyika, J., Lund, S., Bughin, J., Woetzel, J., Stamenov, K., & Dhingra, D. (2016). *Digital globalization: The new era of global flows*. McKinsey Global Institute. https://www.mckinsey.com/business-functions/mckinsey-digital/our-insights/digital globalization-the-new-era-of-global-flows

Mondejar, M. E., Avtar, R., Diaz, H. L. B., Dubey, R. K., Esteban, J., Gómez-Morales, A., Hallam, B., Mbungu, N. T., Okolo, C. C., Prasad, K. A., She, Q., & Garcia-Segura, S. (2021). Digitalization to achieve sustainable development goals: Steps towards a Smart Green Planet. *The Science of the Total Environment*, *794*, Article 148539. https://doi.org/10.1016/j.scitotenv.2021.148539

Pallant, J. F. (2000). Development and validation of a scale to measure perceived control of internal states. *Journal of Personality Assessment*, *75*(2), 308-337. https://doi.org/10.1207/S15327752JPA7502_10

Popkova, E. G., De Bernardi, P., Tyurina, Y. G., & Sergi, B. S. (2022). A theory of digital technology advancement to address the grand challenges of sustainable development. *Technology in Society*, *68*(101831), Article 101831. https://doi.org/10.1016/j.techsoc.2021.101831

Ramilo, R., & Embi, M. R. B. (2014). Critical analysis of key determinants and barriers to digital innovation adoption among architectural organizations. *Frontiers of Architectural Research*, *3*(4), 431-451. https://doi.org/10.1016/j.foar.2014.06.005

Rohana, M. (2008). *An investigation into the barriers to the implementation of automation and robotics technologies in the construction industry* [Doctoral dissertation] Queensland University of Technology, Australia. https://eprints.qut.edu.au/26377/1/Rohana_Mahbub_Thesis.pdf

Roome, N. J. (2013). Sustainable development: Social innovation at the interface of business, society and ecology. In T. Osburg & R. Schmidpeter (Eds.), *Social Innovation. SCR, Sustainability, Ethics & Governance* (pp. 299-308). Springer. https://doi.org/10.1007/978-3-642-36540-9_27

Rusu, L., Balasuriya, B. L., & Bah, O. (2020). Cultural barriers in digital transformation in a public organization: A case study of a Sri-Lankan organization. In M. Themistocleous, M. Papadaki, & M. M. Kamal (Eds.), *Information Systems. EMCIS 2020. Lecture Notes in Business Information Processing* (Vol 402, pp. 640-656). Springer. https://doi.org/10.1007/978-3-030-63396-7_43.

Jiancheng, S., Changsaar, C., Hunchuen, G., & Yaoli, X. (2021). Enhancing project integration using cloud-based Building Information Modelling: A conceptual model. *International Journal of Advanced Research in Technology and Innovation*, *3*(3), 12-25.

Ubarte, I., & Kaplinski, O. (2016). Review of the sustainable built environment in 1998–2015. *Engineering Structures and Technologies*, *8*(2), 41-51. https://doi.org/10.3846/2029882x.2016.1189363

UN News Centre (2015). *Sustainable development goals kick off with start of new year*. United Nations. https://www.un.org/sustainabledevelopment/blog/2015/12/sustainable-development-goals-kick-off-with-start-of-new-year/

Wahab, A., Ang, M. C., Jenal, R., Mukhtar, M. B., Elias, N. F., Arshad, H., Sahari, N. A., & Shukor, S. A. (2018). MOOC implementation in addressing the needs of generation z towards discrete mathematics learning. *Journal of Theoretical and Applied Information Technology, 96*, 7030-7040.

Whyte, J., & Levitt, R. (2011). *Information Management and the Management of Projects*. Oxford University Press.

Yang, J., Brandon, P. S., & Sidwell, A. C. (2005). Introduction - Bridging the gap in smart and sustainable built environments. In J. Yang, P. S. Brandon, & A. C. Sidwell (Eds.), *Smart and Sustainable Built Environments (pp. ix-xviii).* Blackwell Publishing Ltd. https://doi.org/10.1002/9780470759493.fmatter

Pertanika J. Sci. & Technol. 31 (3): 1353 - 1377 (2023)

PERTANIKA JOURNALS

SCIENCE & TECHNOLOGY

Journal homepage: http://www.pertanika.upm.edu.my/

Server-Side Cross-Site Scripting Detection Powered by HTML Semantic Parsing Inspired by XSS Auditor

Chrisando Ryan Pardomuan[1,2]*, Aditya Kurniawan[1], Mohamad Yusof Darus[3], Muhammad Azizi Mohd Ariffin[3] and Yohan Muliono[1]

[1]School of Computer Science, Bina Nusantara University, Kota Jakarta Barat, Daerah Khusus Ibukota, Jakarta, 11530, Indonesia
[2]Computer Science Department, Bina Nusantara University, Jakarta, 11530, Indonesia
[3]Faculty of Computer and Mathematical Sciences, UiTM, Shah Alam, 40450, Malaysia

ABSTRACT

Cross-site Scripting attacks have been a perennial threat to web applications for many years. Conventional practices to prevent cross-site scripting attacks revolve around secure programming and client-side prevention techniques. However, client-side preventions are still prone to bypasses as the inspection is done on the user's browser, so an adversary can alter the inspection algorithm to come up with the bypasses or even manipulate the victim to turn off the security measures. This decreases the effectiveness of the protection and leads to many web applications are still vulnerable to cross-site scripting attacks. We believe that XSS Auditor, which was pre-installed in Google Chrome browser for more than 9 years, is a great approach in combating and preventing XSS attacks. Hence, in this paper, we proposed a novel approach to thoroughly identify two types of cross-site scripting attacks through server-side filter implementation. Our proposed approach follows the original XSS Auditor mechanism implemented in Google Chrome. However, instead of placing the detection system on the client side, we design a detection mechanism that checks HTTP requests and responses as well as database responses for possible XSS attacks from the server side. From 500 payloads used to evaluate the proposed method, 442 payloads were classified correctly, thus showing that the proposed method was able to reach 88.4% accuracy. This work showed that the proposed approach is very promising in protecting users from devastating Cross-site Scripting attacks.

Keywords: Cross-site scripting, injection attack, server-side detection, web application security

ARTICLE INFO

Article history:
Received: 08 February 2022
Accepted: 24 May 2022
Published: 31 March 2023

DOI: https://doi.org/10.47836/pjst.31.3.14

E-mail addresses:
chrisando.pardomuan@binus.edu (Chrisando Ryan Pardomuan)
adkurniawan@binus.edu (Aditya Kurniawan)
yusof@tmsk.uitm.edu.my (Mohamad Yusof Darus)
mazizi@fskm.uitm.edu.my (Muhammad Azizi Mohd Ariffin)
ymuliono@binus.edu (Yohan Muliono)
*Corresponding author

ISSN: 0128-7680
e-ISSN: 2231-8526

© Universiti Putra Malaysia Press

INTRODUCTION

Cross-site Scripting (XSS) is one of the only vulnerabilities in OWASP Top 10 (Wichers & William, 2017) four times in a row—2007, 2010, 2013, and 2017. Moreover, Cross-site Scripting could lead to a more devastating impact, such as obtaining personal information or stealing user cookies to hijack their identity in a fraudulent session, allowing attackers to steal sensitive data or even take control of certain devices (Takahashi et al., 2013). As the adoption of JavaScript spreads through the Internet and more UI libraries (e.g., React, Vue, Angular, among others) are developed and experienced significant growth, the stake and devastating impact that an adversary can execute malicious JavaScript on a user's browser environment is exponentially increasing to the degree that has not been seen before. Although some preventive action has been taken, fixing all vulnerabilities and eradicating Cross-site Scripting attacks by implementing defensive coding techniques on every website is undeniably difficult.

Some research has been proposed to detect Cross-site Scripting attacks occurring in a browser by placing the filtering engine on the browser to search through the HTML string for any occurrence of the input, such as the IE8 Filter implemented in Internet Explorer (Swiat, 2008) that unfortunately achieves low reliability due to its inability to detect partial scripting detection and has no context-aware sanitation (Sarmah et al., 2018). There is also a method called NoScript (https://noscript.net/) filter that analyzes outgoing requests from the browser for potentially malicious XSS payload occurrences; it often leads to high *false positive* rates because there is no way to verify whether the suspicious scripts appear in the HTML document response (Sarmah et al., 2018). With the intention to solve the issues, a more sophisticated method has also been proposed by Bates et al. (2010). Instead, they placed the filtering engine just after the browser's HTML parser to reduce false positivity in the detection result. In their research, Bates et al. (2010) argue that placing the filter after the browser's HTML parser is considered to have a complete interposition in the browser with great performance and high fidelity. Their research shows that by examining the response just after parsing, the filter can examine the semantics of the response, as interpreted by the browser, with more efficiency and error-prone processing.

Furthermore, the proposed method has been implemented first in WebKit and later in Google Chrome, publicly known as the XSS Auditor (The Chromium Projects, 2019) for almost 10 years. Although Google eventually decided to remove XSS Auditor from their Google Chrome browser by late 2020, we believe the originally proposed method is still quite effective in combating Cross-site Scripting attacks. The only caveat we think can be improved is that XSS Auditor, among many other common XSS detection approaches, is designed to be a broad-spectrum detection system that focuses on detecting probable attacks across almost every website opened by the browser. It eliminates the capability of the detection system to protect the user from Stored XSS attacks, only the Reflected and

DOM-based XSS. In Stored XSS attacks, the malicious payload comes inside the database instead of directly from the user's HTTP request. Nevertheless, as the client-side detection system is always placed on the users' browsers, XSS payloads stored inside the database will already be inserted into the HTML document when the browser receives and renders it. Hence the attack cannot be detected by client-side approaches. Moreover, Stored XSS attacks can lead to more devastating damage because while Reflected XSS attacks often limit the scope of the attack to the attacker (i.e., the outcome of the attack is *reflected* by whoever injected the payload), Stored XSS attacks allow the payload injected by an attacker to be executed multiple times and even affecting on the unsuspicious user's browser context because of its nature the payload is *persistently* stored inside the application's database (Cui et al., 2020).

Hence, we propose a detection mechanism by adopting the original XSS Auditor mechanism to detect Cross-site Scripting attempts on the server side, not just Reflected Cross-site Scripting attacks but Stored Cross-site Scripting. Instead of examining an HTTP request and its related HTTP response, we propose that the third element should include the database result when a certain request is processed on the server. Examining the database's response in the same way the XSS Auditor examines the HTTP request makes the proposed method detect most of the Stored Cross-site Scripting attacks. The remainder of this paper is organized as follows. First, we will briefly review three types of Cross-site Scripting (XSS) attacks and the original concept of XSS Auditor proposed by Bates, Barth & Jackson (2010). Then, we will proceed by elaborating an in-depth explanation of our proposed method: the alternative to detect two of the three types of XSS attacks through server-side filtering based on the XSS Auditor mechanism. Finally, the evaluation process and the result will be presented to measure the performance of the proposed method in detecting Cross-site Scripting (XSS) attacks.

MATERIAL

Related Works

Cross-Site Scripting. Cross-site Scripting (XSS) exploits are like most code-based injection attacks, similar to SQL Injection, which injects an arbitrary code into an application so that the application executes the arbitrary code on behalf of the attacker (Rodriguez et al., 2020). In this context, the injected code on XSS attacks usually is JavaScript code or HTML tags that contain JavaScript code.This attack exploits output functions (e.g., browser render process) in an application that references or processes incorrectly sanitized user input results. An XSS attack's basic idea is to use special characters that cause the browser to change the browser's interpretation of a document or input from context as data into context as program code (Liu et al., 2019).For example, when an HTML page references user input as data, an attacker can include an HTML <script> tag that can activate the

JavaScript interpreter in the browser and execute the arbitrary JavaScript code put by the attacker inside the tag. When an attacker manages to do that, and the injected code is executed in the client browser, it can result in more nefarious activities such as stealing cookies, defacing the interface of the website, or even unauthorized request being sent from the victim's browser by unbeknown to the victim (Liu et al., 2019). XSS attacks can be divided into Reflected XSS, Stored XSS, and DOM-based XSS. The characteristics of each attack are the following:

1. Reflected cross-site scripting
   This type of XSS occurs when a dangerous string that causes XSS comes from inputting user data on HTTP requests. This type of XSS is usually found in a web application's error messages and search results (Shar & Tan, 2011). In addition, this type of attack can generally occur due to input sanitation errors on users on the server side (server-side fault). In some cases, interaction by the victim is required for the arbitrary JavaScript code to be executed, for example, through a spoofing attack. In a spoofing attack, the attacker must trick the victim into clicking somewhere on the website to trigger the JavaScript code execution (Rodriguez et al., 2020).
2. Stored cross-site scripting
   This type of XSS occurs when a web application stores a dangerous string from user input on the database, and then the target application's HTML web document references the harmful input. Attacks on social networking sites are generally this type of XSS attack (Shar & Tan, 2011). As Reflected in XSS, this type of attack also occurs due to input sanitation errors on the server side (server-side flaws).
3. DOM-based cross-site scripting
   This type of XSS attack focuses on manipulating the environment and JavaScript program code (Gan et al., 2020), the HTTP response from the original website to the victim does not change, but the client-side script runs unlike it should because the DOM environment of the page has been manipulated by the attacker (Shar & Tan, 2011). This type does not exploit web application server vulnerabilities.

XSS Auditor. XSS Auditor is a rather novel XSS detection method that Bates et al. (2010) proposed. It has been implemented in Google Chrome (and another Chromium-based browser) since 2010 with the release of Google Chrome v4 (The Chromium Projects, 2019). Unfortunately, Google decided to disable and remove XSS Auditor from their browser in 2019. Before the method is proposed, most XSS detection engine relies on examining payload occurrences inside an HTTP response *before* the browser processes the response. According to Bates et al. (2010), those method leads to lower filter precision as it processes the syntax of the response, not its semantics. Also, searching for malicious

payload occurrences inside the HTML response with regular expressions tends to produce un- necessary false positives. In Chrome's XSS Auditor, however, the filter is placed strategically between the HTML parser and the JavaScript engine. Placing the filter in such a position has at least three advantages (Bates et al., 2010):

1. High performance

   As the filter simply receives the HTML response already parsed (or interpreted) by the browser intoa DOM-tree, it does not need the extra time to performa time-consuming, error-prone simulation that usually occurs when a filter performs the parsing itself. Also,the filter can block the execution of the XSS payloads safely instead of forcefully modifying the pre-parsed stream to mangle the injected payload, which reduces the resources and processes taken to mitigate the attack.

2. High precision

   Moreover, since the DOM-tree to be examined by the filter is coming from the browser itself, false positives that usually occur because of a different DOM-tree interpretation between the client's browser and the XSS filter of the same HTML response can be greatly reduced or eliminated.

3. Complete interposition

   Additionally, placing the filter in front of the JavaScript engine lets the filter completely interpose all elements and tags that will be treated as JavaScript instructions by the browser. If the filter detects a malicious payload and wants to block it, it can simply withhold the payload from the JavaScript engine, and the malicious payload will not be executed.

In the actual implementation in WebKit, the filter mediates between the HTML parser engine inside the WebCore component and the JavaScript engine inside the JavaScriptCore component. To perform the inspection, the filter intercepts and examines every attempt to run inline scripts, inline event handlers, and JavaScript URLs. In addition, the filter also intercepts and examines the loading of external scripts and plugins, such as using document. write to write arbitrary script tags to the HTML document itself (which we believe also works as a bypass trick for other XSS filters).

Before searching for malicious payloads in the HTTP request sent by the browser on behalf of the user, it must transform the URL request and any POST data to mimic how the browser sees them (Satish & Chavan, 2017). The transformation includes URL decode, Character set decode, and HTML entity decode. Although the transformation process is involved, the filter does not have to simulate the complex, resource-expensive process of the parser, such as tokenization and element re-parenting. Instead, after the transformation has been done, the filter merely performs a matching algorithm between what can be found

in the transformed HTTP request (including the POST data) and the HTML elements that are to be passed to the JavaScript engine that is intercepted from the parsing engine. If the filter found any match, it means that some (or all) part of the user input is reflected on the element that will be executed by the JavaScript engine, thus indicating a Cross-site Scripting attack. When that happens, the filter refuses to deliver the element to the JavaScript engine.

Server-Side XSS Detection System. Many other proposed methods have put the XSS detection system on the server side instead of the client-side (i.e., browser). For example, Kazal and Hussain (2021) designed a server-side detection and prevention system specifically for Stored (persistent) XSS attacks. The proposed method works by checking and sanitizing the user's input before storing it in the database, preventing the XSS payload from the very beginning of the attack. The input sanitation is conducted using *harmlist*, a list of dangerous keywords and substrings that can be used for XSS attacks and configured by the system's administrators. Their evaluation process was measured on Damn Vulnerable Web Application (DVWA) application, and the proposed method could detect the attempted attacks with staggering accuracy.

Meanwhile, Abaimov and Bianchi (2019) proposed a deep-learning (CNN) model to detect malicious code-injection queries such as SQL Injection and XSS attacks. The dataset used to train and evaluate the model is taken from an online publicly available common code-injection payload list. One of the proposed approach's main novelties lies in the pre-processing module, which the authors argue helps improve the detection rate and accelerate the training process by enriching the dataset with semantic labels and filtering out *noisy* and ambiguous information from the payloads. The detection system is installed on the server-side, but instead of capturing and processing raw data directly from HTTP request, the system converts the payload into an encoded pattern to remove the randomness of the payload and help the model identify the significance of each symbol found on the payload. The model's performance was measured using a *confusion matrix* (Accuracy, Precision, and Recall) and reported achieving 94% accuracy, 99% precision, and 93% recall value in detecting SQL Injection and XSS attack payloads.

Both methods propose a rather sophisticated detection system that prevents the attack, including Stored XSS attacks before the attack even begins (i.e., when the moment the user's payload is to be received and processed) by sanitizing or analyzing the inputs received. However, most of the existing web applications might already have suffered the attack prior to installing the detection system, and the XSS payloads might already be inside their database. Hence, even if the detection system is placed on the server-side to enable Stored XSS detection capability, they will have difficulty detecting and removing threats from XSS payloads already stored inside the database because the content of the database is not inspected or analyzed by the proposed systems.

METHODOLOGY

This section describes the design and implementation of a server-side XSS detection system based on Google Chrome's original XSS Auditor algorithm (Figure 1). The system is designed to perform pattern-matching analysis of HTML responses in the form of an HTML document tree (DOM-tree) instead of analyzing raw string representation of HTML responses that the server received; it aims so that the proposed method checks on the HTML elements that are similar to what the browser sees and render, right before the JavaScript code run by the JavaScript engine. By examining the response after HTML parsing, the detection system can easily identify which part of the response is being treated as a JavaScript instruction. Instead of running regular expressions over the bytes that comprise the response, the detection system examines the DOM-tree created by the parser, making the semantics of those bytes clear similar to how Google Chrome's XSS Auditor works.

Pre-Processing

Before the system looks for signs of malicious JavaScript in both the HTTP request and the Database response and compares them with the content of the HTTP response, the input data (HTTP request or Database response) needs to be transformed as follows:

1. URL Decode
   The input from HTTP requests is often encoded; hence we need to decode them to avoid misinterpretation of the data and detect bypass attempts.
   For example, %41 will be changed to the character 'A'.
2. Character-set Decode
   Should the input is encoded using the uncommon encoding (e.g., UTF-7, among others.), we convert the input to Unicode encoding to ensure that the user's browser and our detection system see the input in the same format.
   For example, UTF-7 encoding is transformed into Uni-code characters.
3. HTML Entity Decode
   The input from HTTP requests is also often encoded into HTML entities (e.g., & < &gt, among others.). Therefore, we also need to decode them to avoid misinterpretation of the data and detect bypass attempts.
   For example: & is transformed into '&'.

The transformation is necessary because the server-side detection system must mimic what the browser does (Satish & Chavan, 2017) to reduce and even prevent the different interpretations between them (the client's browser and the server). We did not design the pre-processing step to be run during the development of the system, but instead is embedded in the system and runs imminently every time an HTTP request or data from

the database is about to be put into the HTML document inside the HTTP response. Table 1 describes every attribute and data source we considered a probable place for the XSS payload that is the subject of this pre-processing step.

Table 1

Attributes for pre-processing

No	Attribute	Source	Example
1	Query Param	HTTP Request (URL)	?search=<script>alert(1)</script>
2	HTTP Body	HTTP Request (Body)	username=<script>alert(1)</script>
3	Cookie	HTTP Request (Header)	SESSION=<script>alert(1)</script>
4	User Agent	HTTP Request (Header)	User-Agent: <script>alert(1)</script>
5	Values from Database	Database	note_name: "<script>alert(1)</script>"

After the inputs are pre-processing, the HTTP response is passed into the system's HTML parser to be converted into an HTMLDOM-tree for XSS checking before it is sent back to the client.

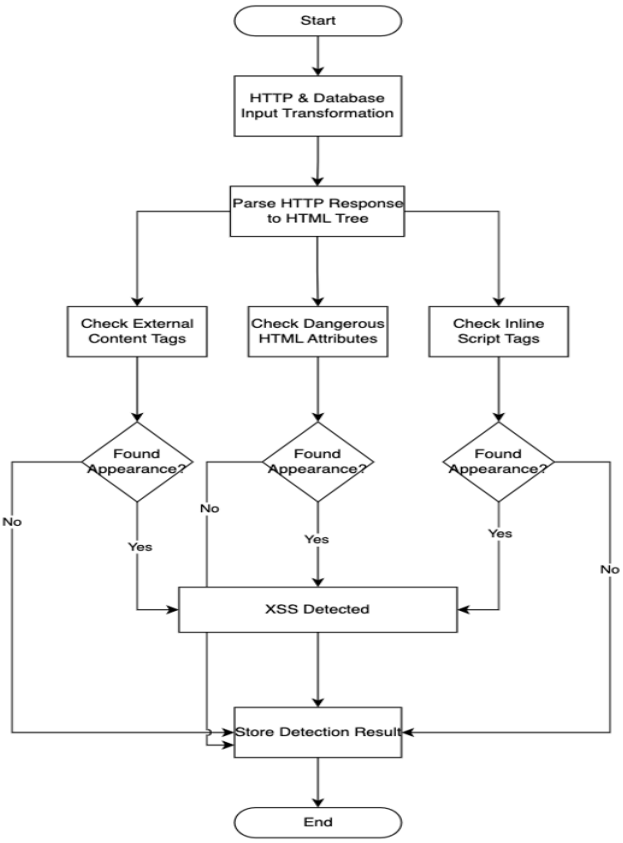

Figure 1. Cross-site scripting detection methodology

Detection Algorithm

According to Stock et al. (2014), the detection process in the original XSS Auditor (from Google Chrome) is designed to analyze every single tag from the HTML DOM-tree and check whether the tag or some of its attributes are also contained in the HTTP request. Our detection system does the same, only it checks and compares the tag with the database response. If the detection system finds a tag (or its attributes) from the HTML DOM-tree contained inthe HTTP request or the Database response, it will consider the tag malicious, and the HTTP request will be marked as a malicious request. In this proposed approach, the detection system assumes every data from the HTTP request (*direct* from user input) and the Database response (*indirect* from user input) as the same input source. Thus, no specific differentiation is applied between the two sources. The examined tag criteria are as follows:

1. Inline script tags
   As the major injection point for most cross-site scriptingattacks, the detection system examines every inline script tag from the document tree.
   For example, <**script**>**alert(1)**</**script**>
2. Dangerous HTML attributes
   The detection system checks for attributes in every HTML tag that are known can be used for JavaScript execution, as can be seen in Table 1.
   For example, <**img src=”profile.jpg” onload=’javascript:alert(1)’**> that allows the attacker to execute JavaScript by injectingthe payload inside an *onload* attribute.
3. External content tags
   The detection system also checks the possibility of the attacker trying to smuggle malicious JavaScript code from external content (e.g., malicious payload placed on arbitrary websites). Thus, the auditor also checks for every script tag that contains *the src* attribute.
   For example, <**script foo=bar src=”http://hacker.com/evil.js”**\>

Figure 2 illustrates how our detection system examines HTTP packets to find any occurrences of arbitrary XSS payload.

When the server receives an HTTP request packet, our detection system inspects the packet and extracts user-inputted values in the request. As we can see in the above picture (right-side), inside the query parameters alone, there are two pieces of information supplied by the user: the username and the search parameters. Furthermore, the arbitrary XSS payload is located inside the search parameter. Comparing the data with the HTTP response (left-side), we can see that the input (<script>alert(1)<script>) is reflected on the HTML response from the server. It is a Reflected Cross-site Scripting attack. In general, for

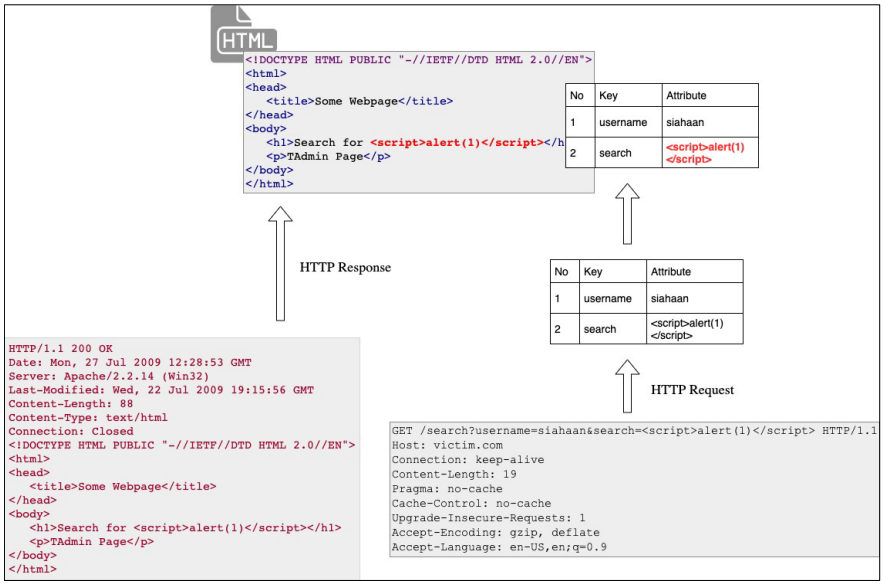

Figure 2. Payload inspection illustration

our detection system to detect the attack, first, it examines the HTTP request and extracts every possible user input from the request (request body, query parameters, among others). Then, when the web server is about to respond to the request with an HTTP response containing the HTML string, our detection system will intercept the response and parse the HTML string into the HTML DOM tree. After that, for all elements and tags that satisfy the examination criteria above, our detection system will check whether the element and/or its content can be found inside the collected user inputs. If so, the detection system will mark the request as a request with a potential Cross-site Scripting attack and either halt the server's response or simply log the event for further examination.

Table 2

HTML attributes that are considered dangerous

No	HTML Attribute	Description	Example
1	href	Specifies the URL of a page the link goes to	<... href="http://web.com/" />
2	src	Specifies the URL of an external (or internal) resource	<... src="run.js" />
3	content	Store the value associated with the http-equiv or name attribute	<... content="some value" />

Table 2 (Continue)

No	HTML Attribute	Description	Example
4	Data Attributes (data-*)	Store an arbitrary data private to the page on all HTML elements	<... data-price=”2000” />
5	Event Attributes (on*)	Let an event triggers action in a browser	<... onerror=someFunctionName />

The detection system utilizes the *source-destination* information of the network packet. For example, when an HTTP request arrives at the server, it contains information about where it came from (called *source*) and where the packet should be delivered to (called *destination*). Later, when the server had finished processing the request, an HTTP response packet was sent back to the client. The packet also contains information about where it came from (*source*) and where it will be delivered to (*destination*), but the *source* and *destination* are inverted compared to the *source* and *destination* in the request package. Thus, if the *source-destination* combination in the HTTP requests is 1234-5678, the HTTP response will have 5678-1234 as the *source-destination* combination.

The detection system also considers the database response so that the detection system can detect more than just a Reflected Cross-site Scripting attack, as designed in the original XSS Auditor paper (Bates et al., 2010), but a Stored Cross-site Scripting attack as well. A Stored Cross-site Scripting attack indicates that the payload will not just reflect on the response of the HTTP request but also be stored persistently on the server (e.g., in the database). Hence, to examine the HTTP response where the user input is not from the HTTP request but from the Database response, our detection system needs to identify which Database response is an HTTP response. It is impossible to use the source-destination combination like in the previous because although almost every database could communicate via TPC/IP protocol, we would need to put two separate listeners: one between the network and the web server and the other between the web server and the Database. That way, we discover that it is not possible to correlate the source-destination combination of the HTTP request to the web server and the source-destination combination of the web server to the database. Therefore, using a timestamp the detection system is designed to correlate the HTTP request and the database response.

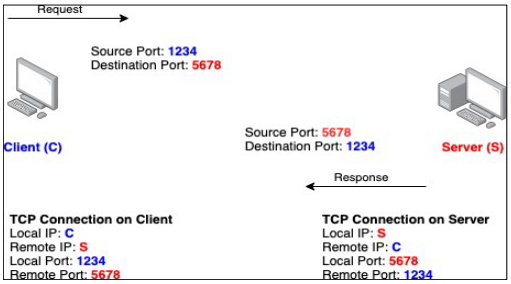

Figure 3. HTTP request and response matching

Nevertheless, we encounter that the implementation of such a method could lead to at least two problems, mainly because the time taken to fetch the data from the database between each HTTP request varies; it can be 0 ms to a few seconds, depending on how big the data and the load of the database server itself.

First problem: we designed the system to record the timestamp of both events, the arrival of either the HTTP request or the Database response, and the completion of the request after being processed by the web server that ends with an HTTP response being sent back to the client. The timestamps of the two events can differ by a few milliseconds, so our detection system needs to ensure that both are synchronized. Timestamp synchronization is important for two reasons: the atomicity of the report and the effectiveness of the correlation process.

Second problem: there may be several (if not many) HTTP request or Database response that arrives at the very same moment, which leads to many request-response elements having the same timestamp record. It can confuse the examination process. The detection system might be unable to differentiate one HTTP response that belongs to an HTTP request from the other responses if the timestamp is similar; hence, the detection system yields low performance and low detection accuracy.

The detection system calculates the average time between the arrival of the HTTP request in the server and the arrival of the Database response to solve both problems, as seen in Equation 1.

$$\bar{T} = \frac{1}{n}\sum_{T=0}^{n} T \tag{1}$$

The detection system calculates the delay between the server receiving an HTTP request until the HTTP response is ready to be sent back to the client after being processed by the server and stored along with the HTTP request data into a structured dataset. Then, when the detection system detects a Database response being sent back to the web server, it calculates the average delay time (Equation 1) and takes every HTTP request that arrived T time before and after the timestamp of the Database response from the structured dataset, where T is the calculated average time. Finally, the detection system retrieves every HTTP request within the scope of the average timestamp constraint and looks for any partial or full occurrences from both input sources (HTTP request or Database response) in the HTTP response. It will take more computing power, but the detection accuracy will be significantly higher.

Implementation

The system needs to intercept traffic from HTTP and the database to ensure the detection system can retrieve data from the user's input and the database. Hence, the implementation

of server-side XSS Auditor in this research consists of two modules: the HTTP Sniffer module and the server-side XSS Auditor itself. HTTP Sniffer module intercepts every HTTP network packet, both Request and Response after it arrives at the server and before it is sent back to the client. The intercepted packet is stored in Redis in-memory storage to support seamless data retrieval. When an HTTP response is ready to be sent back to the client, XSS Auditor takes the HTTP request data from Redis and performs the XSS detection process. If the attack indication is found, the HTTP response packet willbe tainted, or the detection system will generate log information about the attack. Figure 4 illustrates the design of the system proposedin this paper. Both modules are developed using Python, and the HTTP interception capability is possible using the Scapy library. Meanwhile, the database interception capability is made possible with the help of Packetbeat by Elasticsearch[1]. When the server's database sends a query result back to the web application, Packetbeat will intercept them and forward the resulting rows to the HTTP Sniffer module for malicious payload checking. Communication between HTTP Sniffer and Packetbeat is done through a socket-based connection so that they do not occupy any network port while at the same time protecting the confidentiality and integrity of the database by making it harder for perpetrators to intercept and peek at the transferred information.

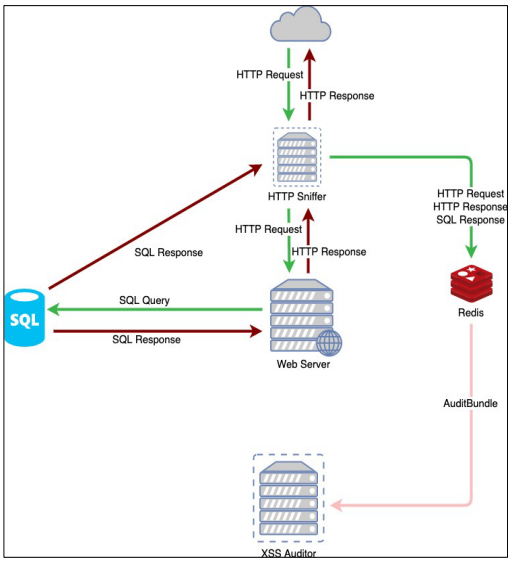

Figure 4. Server-side cross-site scripting detection architecture

HTTP Sniffer

This module is responsible for capturing HTTP packet traffic in the server. The module parses and extracts various attributes from the HTTP packet relevant to Cross-site Scripting detection (Table 2). There are two types of HTTP packets, the HTTP request packet and the HTTP response packet. When the captured packet is an HTTP request packet, the module takes note of the timestamp and stores the data in Redis along with the timestamp information. In addition to the request packet, when the module receives a Database response packet from the database server through Packetbeat, the module will try to correlate the packet with a single HTTP request that is already stored in Redis according to their timestamp difference; by retrieving the HTTP request from Redis, combined it with the Database

1 https://www.elastic.co/beats/packetbeat

response, and then stored it back to the Redis (Figure 6). List of data and information captured from the HTTP can be seen on Table 3. Then, both data are combined and stored in Redis. Finally, when the module captures an HTTP response packet, it retrieves the HTTP request packets and (if any) the Database response from Redis and sends the combined data to the XSS Auditor module for inspection. Also, both storing and retrieving operation inside Redis is done using RedisTimeSeries (https://oss.redislabs.com/redistimeseries/) data structure available on Redis as a third-party module. RedisTimeSeries are used for two reasons: to preserve efficiency and speed when computing and retrieving time data and to make Redis able to store time data effectively.

Table 3
Obtained information from HTTP request packet

No	Attribute	Location	Purpose
1	Cookie	HTTP Header	Potential XSS payload location
2	Host	HTTP Header	Information about the attack
3	Request Body	HTTP Body	Potential XSS payload location
4	Query Param	HTTP Header	Potential XSS payload location
5	Content-type	HTTP Header	Limit checking to text/html content only
6	Request Method	HTTP Header	Information about the attack

Every data collected by the HTTP Sniffer module: the HTTP request, Database response (if any), and the HTTP response, as we called it AuditBundle data to be short, has a unique identifier when stored in Redis. This unique identifier, generated based on the timestamp of arrival as a UUID string, helps this module and every other module find the connection between an HTTP request, a Database response, and an HTTP response. While the raw data is stored inside Redis, the detection system also stores a combination of the uniquely generated packet identifier (named BundleID) and its timestamp of arrival (T) in the form of time series data inside RedisTimeSeries (Figure 5).

Algorithm 1: *AuditBundle* Data Storing in Redis

$httpPacket \longleftarrow$ The Captured Packet;
$T \longleftarrow CurrentTimestamp$;
$BundleID \longleftarrow uuid()$;
$storeIndexToTimeSeries(BundleID, T)$;
$storeAuditBundle(httpPacket, BundleID)$;

Figure 5. Storing AuditBundle to Redis and RedisTimeSeries

A similar concept also applies to data retrieval. When this module needs to retrieve the previously stored data from Redis, it performs a TimeSeries query and retrieves every BundleID that has a timestamp between $\bar{T}$ time before and after the current timestamp (the time when the detection system captures the HTTP response) (Figure 6), where $\bar{T}$ is the calculated average response time of the web server (1). It is

important to know that the TimeSeries query might return more than one BundleID at that time range, depending on how much the traffic load is experienced by the server. After that, for every retrieved BundleID from the query, the module will retrieve the AuditBundle accordingly. Every AuditBundle retrieved will be passed into the XSS Auditor module for a thorough inspection. In the optimal condition, an AuditBundle will contains an HTTP request, a database response, and an HTTP response (Table 3).

Algorithm 2: *AuditBundle* Data Retrieval from Redis

$T \longleftarrow CurrentTimestamp$;
$\Delta T \longleftarrow getAverageResponseTime()$;
for $t \in \{T - \bar{T}, \ldots, T + \bar{T}\}$ **do**
  $BundleID \leftarrow getIndicesFromTimeSeries(t)$;
  $httpPacket \leftarrow getAuditBundle(BundleID)$;
  $performXSSDetection(httpPacket)$;
end for

Figure 6. Retrieving AuditBundle from Redis

Table 3

Obtained information from HTTP request packet

No	Attribute	Location	Purpose
1	Cookie	HTTP Header	Potential XSS payload location
2	Host	HTTP Header	Information about the attack
3	Request Body	HTTP Body	Potential XSS payload location
4	Query Param	HTTP Header	Potential XSS payload location
5	Content-type	HTTP Header	Limit checking to text/html content only
6	Request Method	HTTP Header	Information about the attack

XSS Auditor

This module has two main responsibilities: to manage the data (AuditBundle data) required for the XSS inspection from the HTTP Sniffer module and to perform the inspection itself. Therefore, we designed this module to have two inspection types: Light and Deep Inspections.

Light Inspection is designed so that the XSS Auditor module does not have to wait for a Database response to perform an XSS detection since some requests do not require database interaction (e.g., a simple visit GET request). Light Inspection occurs the moment the HTTP Sniffer module captures an HTTP response. This module then receives an AuditBundle that contains the related HTTP request packet and HTTP response packet from the HTTP Sniffer module and performs Reflected Cross-site Scripting detection. Since Light Inspection does not wait for the Database response, only user input in the HTTP request (e.g., Query Parameter on POST Body) will be checked. On the other side, the Deep Inspection is designed to run the XSS inspection only after the HTTP Sniffer module intercepts a database response. When performing Deep Inspection, this module receives the HTTP request, the Database response information, and the HTTP response, all compiled into an AuditBundle data from the HTTP Sniffer module. With these data, the XSS Auditor module performs Stored and

Reflected Cross-site Scripting detection using the algorithm comprehensively described in the previous section (see Detection Algorithm section).

Finally, suppose the detection system found any occurrences of the evaluated HTML component (see Detection Algorithm section) on the input (HTTP request, Database response, or both). In that case, the detection system taints the response by injecting a custom HTTP header X-XSS-Detected to the HTTP response so that the client-side code or the browser can invalidate the response and prevent the payload from being rendered. In this version of the research, we designed the detection system only to detect attacks, not to prevent attacks. Therefore, when the detection system detects an attack, it logs all information about the request and stores it in a centralized log database for human verification.

RESULT AND DISCUSSION

In this section, we evaluate the accuracy of our server-side Cross-site Scripting detection engine. The accuracy will be measured using a confusion matrix because the reliability of our detection system depends on how many payloads the detection system can detect, shown by the rate of false positives and false negatives (Bates et al., 2010). The evaluation was carried out on two Cross-site Scripting attacks: Reflected Cross-site Scripting and Stored Cross-site Scripting. An attack condition will be made by simulating an HTTP request to the server where our detection system is installed and active. The application that becomes the target of exploitation is Damn Vulnerable Web Application (DVWA), a vulnerable-by-design web application developed for security testing and experiments. The attack simulation consists of 499 HTTP requests, divided into 239 malicious payloads taken from XSS Payload List in GitHub (https://github.com/pgaijin66/XSS-Payloads) and 261 benign payloads taken from HTTP CSIC Dataset 2010 (Giménez et al., 2010). An example of the evaluation data can be seen in Table 4. Note that for the malicious payloads, since some of the payloads listed on the XSS Payload List might not be working on Google Chrome due to some circumstances (e.g., the payload is specific for another browser), we filtered and curated the payload into 239 payloads that can be verified are working in Google Chrome browser.

Table 4

Example of evaluation dataset

Nature	Payload	Source
Benign	maria-terzon@lingotes.com.org	HTTP CSIC Dataset
Benign	<x src=”alert(1)”>IMPORTANT<x>	Custom List
Malicious	<meta http-equiv="refresh" content="0;url=javascript:confirm(1)">	XSS Payload List
Malicious	<script>alert(“XSS”);</script>	XSS Payload List
Malicious	<form><isindex formaction="javascript:confirm(1)"	XSS Payload List

The reason behind the use of those data sources is that HTTP CSIC Dataset 2010 is widely used for training models that can identify dangerous payloads (Yavanoglu & Aydos, 2017; Vartouni et al., 2018); while XSS Payload list provides various types of payloads with encoding, obfuscation, and detection evasion properties that are similar to actual conditions. Furthermore, there are two types of attack scenarios that we set up for the evaluation:

1. Direct-input attack
   In this scenario, the source of the attack comes directly from the user's input (i.e., HTTP request), both on Stored XSS and Reflected XSS attack attempts. Thus, no information from the database is involved in analyzing and detecting the attack. This scenario evaluates our detection system's capability of Light Inspection (see Detection Algorithm section).

2. Persisted attack
   In this scenario, the attack's source originates from data already stored inside the database. That means we first make sure that the XSS payloads are inputted and stored with no alert or prevention from every detection system intentionally, but when those payloads are retrieved from the database into the DVWA page, the detection systems will try to detect the attack. This scenario evaluates our detection system's Deep Inspection (see Detection Algorithm section) capability, where information from the database is analyzed to detect potential attacks.

As a benchmark, we compare the performance of our detection system with a server-side wide-range attack detection system named PHPIDS and the XSS Auditor itself, a client-side XSS attack detection system. Table 5 shows the comparison between our proposed method and the benchmark methods. Both attack scenario above is also performed on the PHPIDS and the XSS Auditor, and the confusion matrix will be measured accordingly. Since XSS Auditor is unavailable on the more recent version of Google Chrome, the evaluation process will use Google Chrome version 70.0.3538.77. Because XSS Auditor is a client-side system, to determine whether it detects the attempted XSS attack, we set up a reporting URL endpoint and tell the XSS Auditor to report the detected attack into the reporting URL using "X-XSS-Protection header=1; report=http://ourservice.com/report". Any attempted attack detected by the XSS Auditor can be collected and verified. As for PHPIDS and our detection method, we rely on the detection result to consider if the attacks have been detected. Should the detection methods classify the payload as malicious, since we have verified that every payload inside the malicious list is working on the Google Chrome browser, the detection result can be considered reliable, and the payload is truly malicious.

Table 5

Comparison between ours and benchmark methods

Comparisons	Our Proposed Method	PHPIDS	XSS Auditor
Location	Server-side	Server-side	Client-side
Scope of Scanning	Database Data, HTTP Request, HTTP Response	HTTP Request, HTTP Response	HTTP Request, HTTP Response
Supported Web	Any web application	PHP-based Web Application	Any web application that a browser can render
Type of XSS attack detected	Stored XSS, Reflected XSS	Reflected XSS	Reflected XSS

Attack Result Comparison

The results obtained by each detection system after the attack simulation can be found in Tables 6 and 7.

Table 6

Attack simulation result

Metrics	Our Detection System		PHPIDS		XSS Auditor	
Scenario	Direct-input	**Persisted Attack**	Direct-input	Persisted Attack	**Direct-input**	Persisted Attack
TP	180	**192**	225	0	**239**	0
FP	0	**0**	0	0	**0**	0
TN	261	**261**	261	261	**261**	261
FN	59	**47**	14	239	**0**	239

For the Direct-input scenario, our analysis of the result is as follows. From 239 malicious payloads, our detection system detected 180 as potential Cross-site Scripting payloads (*true positive*), while 59 failed to be identified (*false negative*). Meanwhile, from 261 benign payloads, our detection system successfully identified 261 requests, or all requests, as harmless (*true negative*), leaving 0 payloads misclassified (*false positive*). On the other hand, the same attack payload is replayed to the DVWA application on different servers with two security countermeasures: (1) PHPIDS and (2) XSS Auditor, as previously mentioned. PHPIDS correctly identified 225 malicious payloads (*true positive*), leaving 14 payloads classified falsely (*false negative*). For the benign samples, PHPIDS could correctly identify all requests as not malicious (*true negative*), also leaving zero payloads

misclassified. Furthermore, XSS Auditor on Google Chrome could correctly detect 239 malicious XSS payloads, leaving 0 payloads that failed to be identified. Furthermore, for benign samples, XSS

Auditor was performing similarly in identifying all requests as not malicious correctly. With that, it can be concluded that XSS Auditor outperforms the other detection mechanisms when detecting XSS attacks through mere HTTP requests. The confusion matrix of the results can be seen in Figure 7.

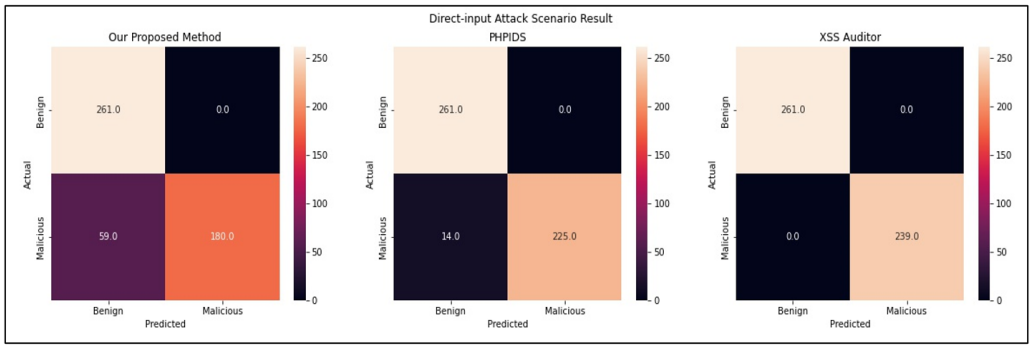

Figure 7. Cross-site scripting detection confusion matrix on direct-input scenario

Meanwhile, our analysis of the result for the Persisted Attack scenario is as follows. From 239 malicious payloads, our detection system detected 192 as potential Cross-site Scripting payloads (*true positive*), while 47 failed to be identified (*false negative*). From 261 benign payloads, our detection system successfully identified all the requests as harmless (*true negative*), leaving zero payload misclassified (*false positive*). On the other hand, neither PHPIDS nor XSS Auditor could correctly identify any malicious XSS payloads that originated inside the database, resulting in 239 *false negatives*. Though, for the benign samples, PHPIDS and XSS Auditor could still correctly identify all requests as not malicious (*true negative*), leaving 0 payloads misclassified. With that, it can be concluded that our proposed method outperforms the other detection mechanisms when detecting XSS attacks that originate from inside the database. The confusion matrix of the results can be seen in Figure 8.

We also calculated 4 basic evaluation metrics from the confusion matrix: *accuracy*, *precision* and *recall*, and the F1-score. The *precision* and *recall* metrics specifically are calculated because in designing such an attack detection system, the risk of having a malicious payload detected as a benign payload (*false negative*) could result in a devastating effect, more than the risk of having a benign payload falsely identified as malicious payload. Therefore, the *precision* and *recall* metrics allow us to capture that characteristic. However, achieving low *false positives* and *falseFeatures negatives* is the grand objective. Finally,

the calculation result of our proposed method, PHPIDS, and XSS Auditor can be seen in Table 7.

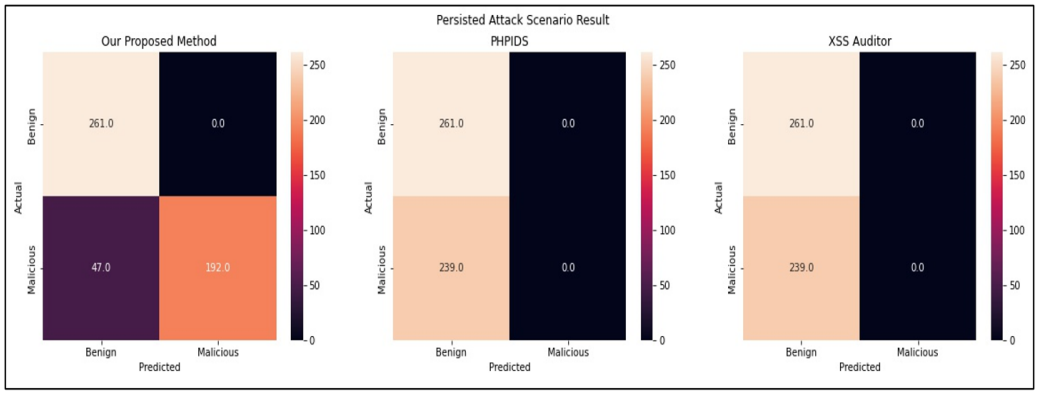

Figure 8. Cross-site scripting detection confusion matrix on persisted scenario

Table 7

Accuracy, precision, recall, and F1 of the evaluation process

Metrics	Our Detection System		PHPIDS		XSS Auditor	
Scenario	Direct-input	**Persisted Attack**	Direct-input	Persisted Attack	**Direct-input**	Persisted Attack
Accuracy	0.88	**0.91**	0.97	0.52	1.00	0.52
Precision	1.00	**1.00**	1.00	0.26	**1.00**	0.26
Recall	0.76	**0.80**	0.94	0.50	**1.00**	0.50
F1-score	0.86	**0.89**	0.97	0.34	**1.00**	0.34

Moreover, our analysis of the result obtained by our proposed method is described as Equation 2:

$$Accuracy = \frac{180 + 261}{180 + 261 + 0 + 58} = 0.88 \quad (2)$$

As an overall performance, the detection system achieves an accuracy of 0.88 means it was able to identify correctly 88% of the payloads (both benign and malicious) that were sent to the server. We believe this number is promising, although there is still much space for further improvement, especially in reducing the false negative rate (Equation 3).

$$Precision = \frac{180}{180+0} = 1 \quad (3)$$

The precision calculation reaching 1.0 point indicates that the detection mechanism has identified all the received attack payloads accordingly or with no false positives. The achieved result must be maintained because any *false positive* will directly reduce the system's effectiveness and inhibit the response to an attack due to additional checks that must be carried out on incoming warnings.

$$Recall = \frac{180}{180+58} = 0.76 \quad (4)$$

While precision measurement reaches a very high score, recall measurement indicates the opposite. As the score only reaches 0.76 points, this reflects that the detection mechanism still results in a high number of false negatives (Equation 4). It will have a side effect on the overall system's reliability since there are possibilities that an attack will go through undetected.

$$F1 = \frac{1\times 0.76}{1+0.76} = 0.86 \quad (5)$$

Finally, the F1-score measurement to calculate the harmonic mean between precision and recall that reaches 0.86 shows that the values of precision and recall are quite balanced but not perfect (Equation 5). As explained before, the high number of *false negative*s or low *recall* values is the main cause.

Result Analysis

From the above results, on the Persisted Attack scenario, our proposed method outperforms the other detection mechanisms in detecting Stored XSS attacks, in which the payload is already stored inside the database. This capability can be impactful, especially when implemented on an existing web application that might (or might not) have suffered an XSS attack because of recent attacks that can be detected and attacks that are prior to the installation of the detection mechanism. PHPIDS, although it is placed on the server-side, does not achieve the same result, mainly due to its inability to examine payloads from the database. Because PHPIDS's checking mechanism relies on the input from HTTP request alone, should an adversary find a way to trigger an XSS attack without having to put the payload on the HTTP request (e.g., through SQL Injection, HTTP request smuggling (Jabiyev et al., 2021), or Stored XSS attack performed before the PHPIDS is installed), the XSS payload cannot be detected.

Moreover, Chrome's XSS Auditor was also unable to detect Stored XSS attack attempts because PHPIDS cannot. Being a client-side detection mechanism, the source of information used by XSS Auditor to determine whether an XSS injection has occurred is only the information that the browser sends (i.e., HTTP request) and receives (i.e., HTTP response). Hence, every bit of data (including the malicious XSS payload) that might

originate from other locations, especially from the database, would already have been inserted into the HTTP response document when it arrived on the user's browser. As no part of the HTTP request is dangerously reflected in the HTTP response received by the auditor, no alert will be triggered. Figure 9 illustrates the gaps in our proposed detection system covered by both approaches.

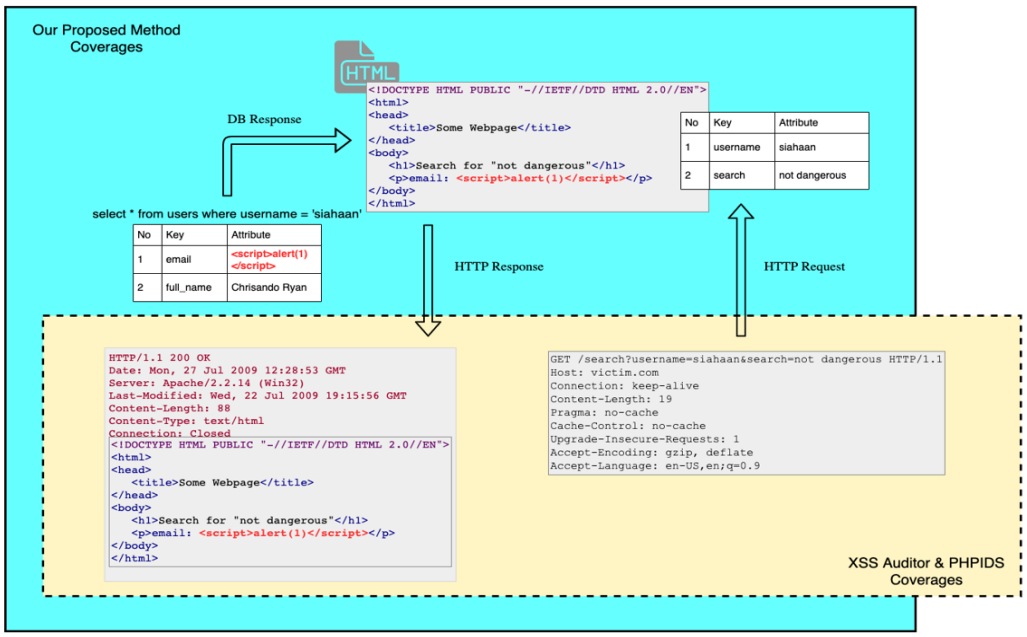

Figure 9. Different detection approaches between ours and other methods

However, another conclusion is that despite the good performance, our proposed method still had a noticeable number of *false negatives*. Our post-simulation analysis discovered that a high rate of a false negatives is majorly caused by the following:

1. Encoding

   As we used the XSS Payload List as the primary malicious data source, we found that many payloads use a non-standard encoding such as UCS-4BE and Windows-1251 to avoid detection of Web Application Firewall (WAF). Although the detection system is designed to mimic the browser's interpretation as closely as possible, these non-standard encoding differences were still causing an unhandled interpretation difference between the detection system with the web server and the browser. Table 8 illustrates the different interpretation that occurs in the simulation.

Table 8

Mismatch encoding interpretation on our detection algorithm

No	Payload	Browser Interpretation	Detection system Interpretation
1	<IMG SRC=”jav◆ascript:alert(’XSS’);”>		\t
2	<body background=javascript:alert(◆XSS◆);>	“	“
3	<iframe/◆/ src=javaSCRIPT:alert(1)	null	%00

◆ indicates the position of encoding mismatch

2. The flaw in the detection algorithm

In our post-simulation analysis, we recorded every payload sent to the server, its kind (benign or malicious), and the detection system’s response to the payload. From the failed detected payload list, we found that some HTML tags apparently can also be used to perform a Cross-site Scripting attack but are not included in the list of elements that must be checked by the detection system, as can be seen in Table 9.

Table 9

Mischecked element on the detection algorithm

No	Payload	Element
1	<svg><style> font-style:’<iframe/onload=alert(1)>’	<style>
2	<div/style=”width:expression(confirm(1))”>X	<div/style=…>
3	<iframe %00 src=” javascript:prompt(1) ”%00>	<iframe>
4	<iframe srcdoc=’<body onload=prompt(1)>’>	Srcdoc=…

CONCLUSION

Our proposed approach, a modified design for a server-side XSS detection system based on Google Chrome’s XSS Auditor, was able to maintain high fidelity characteristics by keeping interposition on the interface for the HTML parser and achieve a good result in detecting XSS payloads from both HTTP request input and inputs that are already stored inside the database. We believe that the original design of XSS Auditor can be more impactful in protecting users from XSS attacks by examining the Database response instead of only the user’s direct input, as can be observed on many client-side XSS detection systems. Compared to other detection approaches, our proposed methods have a strategic advantage in detecting Stored and Reflected XSS attacks with their ability to intercept and analyze user input already stored inside the database. The evaluation result shows that our approach achieves 88% accuracy, a considerably high number in identifying and

detecting malicious XSS payloads, although there is still room for further improvements. In the future, our detection algorithm can be extensively improved by considering more HTML elements to be checked and tweaking and matching the encoding process between the proposed detection system and the browser in general to minimize the false negative rate. A more comprehensive evaluation can also be conducted to measure the performance of the proposed method in terms of speed and memory consumption. Finally, while most browsers have their XSS protection, having more layers of security on the server side to guard the users might not be bad.

ACKNOWLEDGEMENT

We thank everybody involved in this research for their breakthroughs, guidances, and supports, including Universitas Bina Nusantara, Universiti Teknologi MARA (UiTM) Shah Alam, and the entire world's cybersecurity industry.

REFERENCES

Abaimov, S., & Bianchi, G. (2019). CODDLE: Code-injection detection with deep learning. *IEEE Access*, 7, 128617-128627. https://doi.org/10.1109/ACCESS.2019.2939870

Bates, D., Barth, A., & Jackson, C. (2010). Regular expressions considered harmful in client-side XSS filters. In *Proceedings of the 19th International Conference on World Wide Web* (pp. 91-100). ACM Publishing. https://doi.org/10.1145/1772690.1772701

Cui, Y., Cui, J., & Hu, J. (2020). A survey on XSS attack detection and prevention in web applications. In *Proceedings of the 2020 12th International Conference on Machine Learning and Computing* (pp. 443-449). ACM Publishing. https://doi.org/10.1145/3383972.3384027

Gan, J. M., Ling, H. Y., & Leau, Y. B. (2020). A Review on detection of cross-site scripting attacks (XSS) in web security. In M. Anbar, N. Abdullah, & S. Manickam (Eds.), *International Conference on Advances in Cyber Security* (Vol. 1347, pp. 685-709). Springer. https://doi.org/10.1007/978-981-33-6835-4_45

Giménez, C. T., Villegas, A. P., & Marañón, G. Á. (2010). *HTTP data set CSIC 2010*. Information Security Institute of CSIC (Spanish Research National Council). https://www.tic.itefi.csic.es/dataset/

Jabiyev, B., Sprecher, S., Onarlioglu, K., & Kirda, E. (2021). T-Reqs: HTTP request smuggling with differential fuzzing. In *Proceedings of the 2021 ACM SIGSAC Conference on Computer and Communications Security* (pp. 1805-1820). ACM Publishing. https://doi.org/10.1145/3460120.3485384

Khazal, I. F., & Hussain, M. A. (2021). Server side method to detect and prevent stored XSS attack. *Iraqi Journal for Electrical & Electronic Engineering*, *17*(2), 58-65. https://doi.org/10.37917/ijeee.17.2.8

Liu, M., Zhang, B., Chen, W., & Zhang, X. (2019). A survey of exploitation and detection methods of XSS vulnerabilities. *IEEE Access*, *7*, 182004-182016. https://doi.org/10.1109/ACCESS.2019.2960449

Rodríguez, G. E., Torres, J. G., Flores, P., & Benavides, D. E. (2020). Cross-site scripting (XSS) attacks and mitigation: A survey. *Computer Networks*, *166*, Article 106960. https://doi.org/10.1016/j.comnet.2019.106960

Swiat. (2008). *IE 8 XSS filter architecture/implementation*. Microsoft. https://msrc.microsoft.com/blog/2008/08/ie-8-xss-filter-architecture-implementation/

Sarmah, U., Bhattacharyya, D. K., & Kalita, J. K. (2018). A survey of detection methods for XSS attacks. *Journal of Network and Computer Applications*, *118*, 113-143. https://doi.org/10.1016/j.jnca.2018.06.004

Satish, P. S., & Chavan, R. K. (2017). Web browser security: Different attacks detection and prevention techniques. *International Journal of Computer Applications*, *170*(9), 35-41.

Shar, L. K., & Tan, H. B. K. (2011). Defending against cross-site scripting attacks. *Computer*, *45*(3), 55-62. https://doi.org/10.1109/MC.2011.261

Stock, B., Lekies, S., Mueller, T., Spiegel, P., & Johns, M. (2014). Precise client-side protection against DOM-based cross-site scripting. In *23rd USENIX Security Symposium* (pp. 655-670). USENIX Association.

Takahashi, H., Yasunaga, K., Mambo, M., Kim, K., & Youm, H. Y. (2013). Preventing abuse of cookies stolen by XSS. In *2013 Eighth Asia Joint Conference on Information Security* (pp. 85-89). IEEE Publishing. https://doi.ieeecomputersociety.org/10.1109/ASIAJCIS.2013.20

Vartouni, A. M., Kashi, S. S., & Teshnehlab, M. (2018). An anomaly detection method to detect web attacks using stacked auto-encoder. In *2018 6th Iranian Joint Congress on Fuzzy and Intelligent Systems (CFIS)* (pp. 131-134). IEEE Publishing. https://doi.org/10.1109/CFIS.2018.8336654

Wichers, D., & Williams, J. (2017). *OWASP top 10 - 2017.* OWASP Foundation. https://owasp.org/www-pdf-archive/OWASP_Top_10-2017_%28en%29.pdf.pdf

The Chromium Projects. (2019). *XXX Auditor*. https://www.chromium.org/developers/design-documents/xss-auditor

Yavanoglu, O., & Aydos, M. (2017). A review on cyber security datasets for machine learning algorithms. In *2017 IEEE International Conference on Big Data (Big Data)* (pp. 2186-2193). IEEE Publishing. https://doi.org/10.1109/BigData.2017.8258167

Pertanika J. Sci. & Technol. 31 (3): 1379 - 1411 (2023)

PERTANIKA JOURNALS

SCIENCE & TECHNOLOGY

Journal homepage: http://www.pertanika.upm.edu.my/

Influence of Carrier Agents Concentrations and Inlet Temperature on the Physical Quality of Tomato Powder Produced by Spray Drying

S. M. Anisuzzaman[1, 2]*, Collin G. Joseph[3] and Fatin Nadiah Ismail[2]

[1]Energy Research Unit (ERU), Universiti Malaysia Sabah, 88400 Kota Kinabalu, Sabah, Malaysia
[2]Chemical Engineering Program, Faculty of Engineering, Universiti Malaysia Sabah, 88400 Kota Kinabalu, Sabah, Malaysia
[3]Industrial Chemistry Program, Faculty of Science and Natural Resources, Universiti Malaysia Sabah, 88400 Kota Kinabalu, Sabah, Malaysia

ABSTRACT

The study aims to obtain spray-dried tomato powders with a high and effective product yield and enhanced powder quality. The experiment for this investigation entailed the use of several carrier agents, which were maltodextrin (MD) of 4-7 dextrose equivalents (DE), MD of 10-12 DE, and gum Arabic (GA), each in varied concentrations of 5% and 10% with spray drying inlet temperatures of 140°C, 150°C, and 160°C. Powder yield, bulk density, hygroscopicity, moisture content, water solubility, water absorption, color properties, particle size, and powder morphology were all evaluated in spray-dried tomato powders. The results revealed that the stability of the tomato powder is considerably better at high temperatures and concentrations (at 10%, 160°C), with MD 4-7 DE being the best carrier agent among the three tested carrier agents. According to the powder analysis, the product has a moisture content of 3.17 ± 0.29%, the highest yield percentage of 32.1%, a low bulk density of 0.2943 ± 0.01 g/cm^3, the lowest hygroscopicity at 5.67 ± 0.58 %, a high water solubility index (WSI) at 89.98 ± 1.25%, a low water absorption index (WAI) at 6.22 ± 0.22%, an intermediate particle size of 24.73 µm, and color L*, a*,b* values at 31.59 ± 0.03, 11.62 ± 0.08 and 13.32 ± 0.12. The result showed that at higher temperatures and higher concentrations, the powder characteristics are more likely to have a higher yield, WSI, and larger particle size, as well as lower bulk density, hygroscopicity, moisture content, WAI, and color index.

ARTICLE INFO

Article history:
Received: 11 March 2022
Accepted: 01 August 2022
Published: 31 March 2023

DOI: https://doi.org/10.47836/pjst.31.3.15

E-mail addresess:
collin@ums.edu.my (Collin G. Joseph)
dr.anis.ums@gmail.com (S. M. Anisuzzaman)
anis_zaman@ums.edu.my (Fatin Nadiah Ismail)
*Corresponding author

Keywords: Carrier agents, gum Arabic, hygroscopicity, maltodextrin, spray drying

ISSN: 0128-7680
e-ISSN: 2231-8526

© Universiti Putra Malaysia Press

INTRODUCTION

Tomatoes are readily integrated as a healthier part of a balanced diet as they contain good amounts of healthy dietary components, including carotenoids, especially lycopene, water-soluble vitamins, and phenoliccompounds (Li et al., 2018; Martínez-Huélamo et al., 2016; Raiola et al., 2014). However, its high-water content may hinder the conservation of tomato products and post-harvest losses. High moisture level results in higher water activity that promotes quality degradation as the enzymatic activity increases and microbial development (Aderibigbe et al., 2018). Due to this, drying is commonly done to preserve food products. Several drying methods have been used for the convenience of the large food industry, and such fundamental drying methods include conventional hot air drying, solar drying, spray drying, freeze drying, contact drying, infrared, and dielectric drying, as well as reaction engineering approach (REA) (Compaore et al., 2017; Hii et al., 2021; Ismail et al., 2020; Uyar et al., 2015; Ziaforoughi & Esfahani, 2016). Although conventional hot air drying has great availability, the process is time-consuming and an energy-intensive food preservation method.

Solar drying is a very inexpensive drying method, but it has numerous shortcomings since the food has been exposed to a source of contamination (Adak et al., 2017). As for freeze drying, it is much slower and more costly since it includes very complicated and multi-step processes like freezing, primary drying, and secondary drying. This technique is typically used to transform materials sensitive to heat into powder form since it preserves their natural conformations better. Another drying method is contact drying, which includes drying a product by exposing it to heated walls. This method is extensively utilized in heavy industry drying operations and is demonstrated through drum and vacuum drying (Haque & Adhikari, 2014). Infrared drying involves exposing solid food to an infrared heating source, which raises the temperature of the food surface (Ziaforoughi & Esfahani, 2016). In dielectric drying, heat is transferred directly to the product, and faster heating up is observed inside the product than on the surface. However, the drawback of this technique is that it will cause runaway heating that leads to non-uniform heating (Uyar et al., 2015). The REA may identify the product quality and functioning variables by calculating heat and mass balances at the individual droplet level (Patel & Chen, 2008).

Spray drying is one of the processes utilized to create dried food powder and can assist in reducing post-harvest losses while adding value to the raw product. The conversion process comprises the liquid feed atomization, which is then heat treated to lower its moisture content to the desired level (Lee et al., 2018). The benefit of spray drying lies in its ability to manufacture high-nutrient products with flavor retention and rapid moisture evaporation throughout the conversion of liquid feed material to dry powdery form, resulting in higher powder stability and resistance to oxidative and microbiological degradation. Powders formed by spray drying may also be kept at room temperature for extended periods without impacting their stability. Although spray drying is a potential preservation technology,

converting high-value food components into particle form is challenging because of the high amount of low relative molecular weight sugars in their composition, which causes stickiness. As a result, product output will be decreased, and operational difficulties may arise. The low glass transition temperature (T_g) of the low-molecular-weight sugars prevalent in such products, notably fructose, sucrose, and glucose, is mainly accountable for powder stickiness (Bhandari & Howes, 2005; Muzaffar et al., 2015). Because of the low T_g of the tomato's low-molecular-weightsugars, tomato pulp is an excellent sample of a product that is tough to spray dry. Severalsolutes, such as maltodextrins (MD) of 4-7 dextrose equivalents (DE), MD of 10-12 DE, and gum Arabic (GA), were employed as carrier or coating agents during the spray drying process to decrease stickiness.

Measuring the T_g of the food product may not be enough to solve the problem, even though this may be the best instrument for predicting the structural behavior of the product after drying. A more realistic strategy is required to deal with sugary raw materials. Adding carrier agents has been the most utilized strategy for dealing with drying. Even though using a high quantity of carrier agents has become the most frequent way to dry such products, there is no defined strategy for optimizing carrier agent utilization. It is one of the topics that have to be addressed more thoroughly. Aside from the stickiness issue, lycopene, which is important for the red color of tomatoes, can be damaged by spray drying heat processing (Goula & Adamopoulos, 2005). Due to this, the inlet and exit air temperatures, together with the concentration of the feed, in a spray drying process are critical parameters that must be controlled. Table 1 summarizes different drying methods used in the food industry.

Table 1

Summary of different drying methods used in the food industry

Drying method	Advantages	Disadvantages	Reference
Solar drying	Inexpensive drying method	Exposed to a source of contaminations. Very vulnerable to weather conditions. Slow drying process. Also, molding of food may occur due to slow drying.	Adak et al. (2017); Ziaforoughi and Esfahani (2016)
Hot air convective drying	Great availability and moisture saturation capability.	Considered a highly destructive operation, particularly problematic for thermally sensitive materials, it consumes much time and energy.	Szadzińska et al. (2017)

Table 1 *(Continue)*

Drying method	Advantages	Disadvantages	Reference
Freeze drying	Keep most of their taste, shape, and nutritional value. It does not need to be kept cold and can be used for month's even years. Foods that have been dehydrated cannot be rehydrated as quickly as freeze-dried foods.	Expensive. Freeze-dried foods also take up almost as much space as fresh foods.	Ciurzyńska and Lenart (2011); Nowak and Jakubczyk (2020); Haque and Adhikari (2014)
Infrared drying	Short drying time, energy saving. The air is not stirred, unlike conventional convectors. The ambient humidity is pushed out without drying the ambient air.	Heat transmission to food is extremely slow. No heat retaining. The body can suffer from water loss with infrared heaters. It only provides targeted heating.	Adak et al. (2017); Ziaforoughi and Esfahani (2016)
Microwave drying	Because of technological advancement, additional parameters such as time efficiency, low energy usage, and excellent product quality may be monitored.	Heating runaway, high cost. May result in particle overheating and unfavorable degradation of bioactive constituents.	Pu et al. (2016); Zielinska and Michalska (2016); Szadzińska et al. (2017)
Radiofrequency drying	It takes less time, uses less energy, and produces better product quality	Causes runaway heating which often leads to non-uniform heating	Uyar et al. (2015)
Osmotic drying	Preserve color, fragrance, nutritional compounds, and flavor	The final moisture content is unstable. Take days until water loss reaches equilibrium	Eren and Kaymak-Ertekin (2007); da Costa Ribeiro et al. (2016)
Lyophilization	Generally preferred for converting heat-sensitive material to powder since it preserves their natural structures better.	Consume much time and has a high drying cost. Low product yield, not steady production, and the possibility of chill injury.	Wang et al. (2017); Haque and Adhikari (2014)

Table 1 *(Continue)*

Drying method	Advantages	Disadvantages	Reference
Spray drying	A common method for microencapsulation, suitable for heat-sensitive material, effective technology in protecting probiotic and bioactive compounds, and lower time consumed. Fully automated and continuous. Short residence times and suitability for both heat-sensitive and heat-resistant foods.	Low product yield due to dry particle losses. The spray dryer is bulky and also expensive to install. It has a low thermal efficiency which is much heat is wasted during operation.	Chegini and Ghobadian, (2007); Goula and Adamopoulos (2008); Souza et al. (2018); Zhu et al. (2014)

Several studies have been conducted on the effects of different carrier agents on process parameters and the qualities of spray-dried products (Souza et al., 2018; Shishir et al., 2017; Goula & Adamopoulos, 2008). However, there is a scarcity of studies that provide in-depth insight into the effects of different carrier agents on the varied characterization of powders. This study focuses on practical knowledge about additives in spray drying performance and the effects of temperature and concentration. Therefore, the main objective of this study was to study the different effects of carrier agents and examine the impact of different inputs of inlet air temperature and carrier agent concentrations on the powder properties to obtain spray-dried tomato powders with an effective product yield and an improved powder quality. The experiments of this study have used different carrier agents such as MD of 4-7 DE, MD of 10-12 DE, and GA, each in different concentrations of 5% and 10% and different spray drying inlet temperatures 140°C, 150°C, and 160°C. Based on the study, results were tested using analysis of variance (ANOVA) to relate and understand the significance of the variables towards powder characteristics.

METHODOLOGY

Materials

The materials used to produce tomato powder with carrier agents include the tomato fruit, MD of 4-7 DE, MD of 10-12 DE, and GA. The MD of 4-7 DE and 10-12 DE was purchased from Sigma-Aldrich, Munich, Germany The physical appearance of MD was found as a

white hygroscopic powder produced from vegetable starch. The GA used for this study was in powder form and was sourced from A&T Ingredients Sdn. Bhd., Malaysia.

Preparation of Tomato Juice

For the preparation of tomato juice, firstly, the tomato fruit was washed with lukewarm water to get rid of unwanted impurities on the surface of the tomato, and then it was cut into smaller pieces before blanching it for about 2 min in boiling water. Blanching helped to ease the peeling of the tomato skin, and then the tomato fruit was crushed by a blender to obtain the tomato juice. The obtained tomato juice was filtered using a cloth filter.

Preparation of Tomato Juice with Carrier Agents

As for preparing tomato juice with carrier agents, firstly, 1.5 L of tomato juice was weighed in a water jug, and the carrier agents were added. Tomato-MD 4-7 DE, tomato- MD 10-12 DE, and tomato-GA juices were prepared in different concentrations of 5% and 10% of tomato juice to carrier agents. The carrier agent solutions of 5% and 10% were prepared by dissolving the carrier agents in hot water until they carrier agents were submerged enough. The tomato juice was blended with the carrier agents using the blender. Then, the mixture was constantly stirred and heated at 30 to 50°C on a stove. 1.5 L of tomato juice with 5% concentration and another 1.5 L with 10% concentration for each carrier agent were obtained. Prior to drying, the color of the samples was recorded using a Hunter Lab color spectrophotometer. The obtained findings were stated as Hunter color values L*, a*, and b*, where L* stands for brightness and darkness, a* stands for redness and greenness, and b* stands for yellowness and blueness (Caparino et al., 2012).

Preparation of Tomato Powder

The main equipment for the experiment was a pilot-scale spray dryer used to spray dried tomato juices. Figure 1 shows a schematic representation of the spray dryer.

Table 2 shows the formulation to prepare 18 different samples. The samples were fed through a pilot scale spray dryer (Mobile Minor™, GEA, USA). The height of the drying chamber cylinder is 0.62 m, with a diameter of 0.80 m and a conical base of 60^{o} angles. The spray dryer includes a peristaltic pump and a spraying mechanism that comprises a rotating atomizer or two-fluid spray nozzles with a diameter of 1.0 mm. A start-up procedure was done on the spray dryer for the spray drying process to ensure that the atomizer could function well. The start-up procedure was done by referring to the equipment manual. For each 1.5 L of juices, 500 ml was fed into the spray dryer at different inlet temperatures. The operational conditions of the drying process were carried out with the inlet temperature of the spray dryer set at the desired temperature of 140°C, 150°C, and 160°C with a fixed

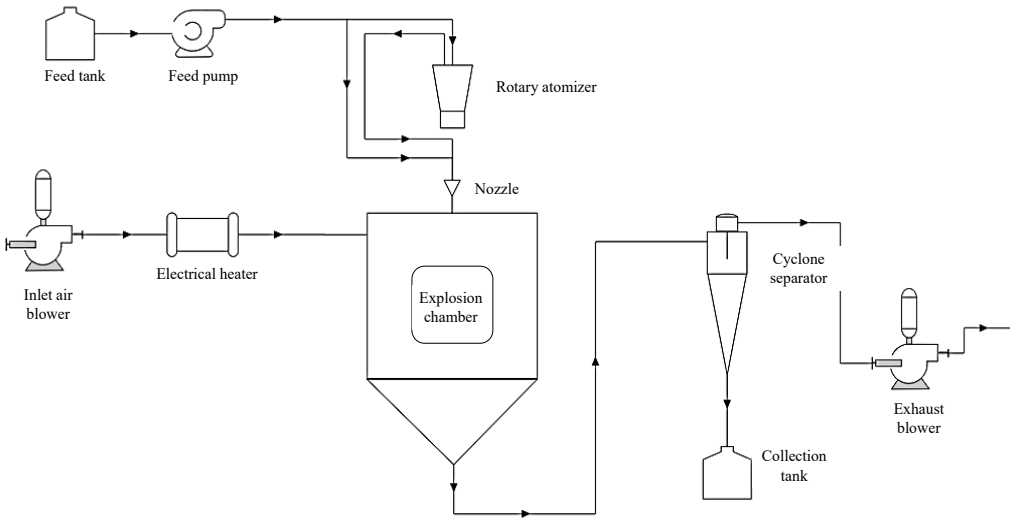

Figure 1. A schematic representation of a spray dryer

outlet temperature of 85°C. The output temperature was kept at 85°C by modulating the flow rate via the peristaltic pump. Atomization was done in co-current and fountain mode with atomizer pressure set at 5 bar. Samples were fed into the spray dryer using a peristaltic pump which controls the feed flow rate set at 18 rpm. The temperature of the outlet powder was regulated and monitored via two temperature sensors positioned in the fluid bed. After spray drying, the powdered sample was retrieved, collected from the cyclone's base, and kept in a sealable zip lock bag. The collected powdered samples were weighed and stored in an airtight container with silica gel at room temperature of 25–27°C. Samples were kept for 3–5 days weeks for further analysis. As for analyzing tomato powder, each analytical work was done in triplicate.

Table 2
Formulation of the samples

Samples	Carrier agent used	Volume of tomato juice, ml	Carrier agent concentration, %	Weight of carrier agent used, g	Inlet temperature, °C
TP1	GA	1500	5	75	140
TP2					150
TP3					160
TP4			10	150	140
TP5					150
TP6					160

Table 2 *(Continue)*

Samples	Carrier agent used	Volume of tomato juice, ml	Carrier agent concentration, %	Weight of carrier agent used, g	Inlet temperature, °C
TP7	MD 4-7 DE	1500	5	75	140
TP8					150
TP9					160
TP10			10	150	140
TP11					150
TP12					160
TP13	MD 10-12 DE	1500	5	75	140
TP14					150
TP15					160
TP16			10	150	140
TP17					150
TP18					160

*TP = Tomato powder

Analysis of Tomato Powder

Powder Yield. Based on dry matter measurements, the process yield of powder was calculated by Equation 1 (Garofulić et al., 2016).

$$Powder\ yield, \% = \frac{a,\ \ g}{(b+c),\ \ g} x\ 100 \quad (1)$$

where a = weight of obtained powder, g; b = dry matter content, g of juice; c = mass, g of the carrier agents used.

Bulk Density. For bulk density, 5.0 ± 0.01 g of tomato powder was filled slowly into a 20 mL dry cylinder. The cylinder was tapped 3 times, and the apparent volume of the powder was recorded. The method is described by Caparino et al. (2012), in which the bulk density of the spray-dried powder was calculated using Equation 2.

$$Bulk\ density, \frac{g}{cm^3} = \frac{Weight\ of\ powder, g}{Volume\ of\ powder, cm^3} \quad (2)$$

Hygroscopicity. The analysis was performed using powder exposure to air relative humidity (RH) of 79.5% and checking of weight increase every 10 min until the maximum weight was reached. Approximately 0.5 g of the sample was weighed and evenly spread on a plate,

then placed in the apparatus, and the analysis started. The calculation of hygroscopicity is given by Equation 3 (Oliveira et al., 2012).

$$\%\ Hygroscopicity = \frac{(\%WI+\%FW)\times 100}{100+\%WI} \quad (3)$$

where %*FW* = % free water; %*WI*= ((*c*-*b*) / (*b* - *a*)) ×100; *a* = weight of plate (g); *b* = weight of plate + powder (g); *c* = weight of plate + powder in equilibrium (g)

Moisture Content. The AOAC method was utilized (AOAC, 2012) to determine powder sample moisture content. The equipment needed was an oven, crucible, and analytical balance. The crucible and lid were dried in a laboratory oven (Binder, Germany) and then cooled in a desiccator. The empty crucible with a lid was measured, and a powder sample of approximately 2 g was placed into a crucible. The weight of the crucible with 2 g of sample was recorded. The crucible was placed inside the oven without the lids. The sample was dried at 105°C in the laboratory oven (Binder, Germany) for 24 h or until a uniform weight was reached. After that, the sample was taken out from the oven, and the samples were cooled in a desiccator prior to weighing. The samples were weighed after 15 min of cooling. The samples were evaluated three times, and the mean value was recorded. The moisture content of the powder samples was calculated by Equation 4.

$$Moisture\ content, \% = \frac{(b-c),\ g}{(b-a),\ g} x100 \quad (4)$$

where *a* = weight of crucible + lid, *b* = weight of sample + crucible + lid before drying process, *c* = weight of sample + crucible + lid after drying process.

Water Solubility Index (WSI). The WSI of tomato powder was measured using the approach outlined by Sabhadinde 2014, in which distilled water of 20 ml was vigorously combined with the spray-dried tomato powder of 2.5 g weight in a 100 ml centrifuge tube and incubated at 37°C for 30 min in a water bath. It was then centrifuged at 10,000 rpm for 20 min. The supernatant was collected carefully into a pre-weighed beaker before being oven-dried at 103 ± 2°C. The WSI (%) was calculated as a percentage of the dried supernatant in proportion to the sample quantity (Equation 5).

$$WSI, \% = \frac{Weight\ of\ supernatant,\ g}{Weight\ of\ sample,\ g} x100 \quad (5)$$

Water Absorption Index (WAI). The WAI of tomato powder was determined by using Sabhadinde's method (2014). 2.5 g tomatopowder suspension in 20 ml distilled water was stirred for 1 h before being centrifuged at 3000 rpm for 10 min. The supernatant is discarded for the removal of free water and to obtain the wet residue only. The wet residue was then weighed. The calculation of WAI is given by Equation 6.

$$WAI, \% = \frac{Weight\ of\ residual, g}{Weight\ of\ sample, g} x100 \quad (6)$$

Color Analysis. A color spectrophotometer (Colorflex D65/10O, Hunterlab, USA) was used to study the color properties of the tomato powder. The obtained data were represented per the Hunterlab scale values of the samples. The color properties were calculated using the total color difference equation. Then, the tomato powder was dissolved in distilled water to prepare a resampling of the obtained tomato powder; for the resampling procedure of the tomato powder, Equation 7 was used so that the color comparison of the tomato powder would be fair to the feed sample in the preliminary stages of conducting the spray drying of tomato juice (Jittanit et al., 2010).

$$WDWR, g = \frac{(WFM - WDP), g}{WDP, g} x\ WPR \quad (7)$$

where *WDWR* = weight of distilled water for resampling, *WFM* = weight of feed material, *WDP* = weight of dried powder obtained, and *WPR* = weight of powder for resampling

This analysis was done in triplicates to take reading for the L*, a*, and b* values, and the mean values were taken. Prior to the sample analysis, the colorimeter was calibrated using a black tile, a white plate with L^*, a*, and b* values of L=93.87, a=-0.73, b=+2.06 and a green plate with L*, a*, and b* values of L=51.23, a=-25.32, b=15.14. For color analysis, control tomato (CT) samples prior to drying were included, in which there are 6 control samples for each carrier agent of different concentrations: CT1 for tomato juice with 5% GA, CT2 for tomato juice with 10% GA, CT3 for tomato juice with 5% MD 4-7DE, CT4 for tomato juice with 10% MD 4-7 DE, CT5 for tomato juice with 5% MD 10-12 DE and CT6 for tomato juice with 10% MD 10-12 DE. These control samples were prepared to study the color difference in the L^*, a*, and b* values before and after drying the juice at three different temperatures. All the initial values were classified as control values stated as *CT1*, CT2, CT3, CT4, CT5, and CT6 and shown in Table 3.

Table 3
Initial values of color properties of the CT samples

Control tomato (CT) samples	Color properties			Control tomato (CT) samples	Color properties		
	L^*	a*	b*		L^*	a*	b*
CT1	33.53	16.99	14.31	CT4	37.01	19.67	18.24
CT2	31.59	15.37	15.40	CT5	33.52	18.96	15.17
CT3	36.15	19.30	15.70	CT6	30.97	17.19	13.93

Particle Size. A particle size analyzer (Malvern Zetasizer, Nano Z, UK) was used to assess the particle size of tomato powder in a liquid medium. The equipment was set at an operating temperature of 25°C, and size measurement was taken in triplicate with 13 runs each. For the preparation of the analysis, 1 g of tomato powder was mixed with 10 ml of distilled water to prepare the aqueous suspensions (Tonon et al., 2011). After thorough stirring, the suspension was put into a disposable cuvette and placed in the instrument for measurement. The particle size was given in micrometers (μm), and each sample was measured in triplicate, with the mean z-average for each sample taken as the size comparisons.

Particle Morphology. A scanning electron microscope (SEM) (Carl Zeiss MA 10, Germany) was used to examine the morphological structure of tomato powders. A few samples were chosen for SEM images: the samples with 140°C and 160°C of the same concentration at 10% and another with a 5% concentration at 160°C for each powder sample of a different carrier agent. The samples were chosen likewise to compare the differences in particle morphology of the resulting tomato powder based on the concentration, inlet temperature, and type of carrier agents. Prior to SEM imaging, samples were coated using a sputter coater (EMITECH, K550X, UK) with a fine coating of gold platinum to make them conductive for SEM imaging and to obtain a much clearer image. The samples were analyzed in the SEM instrument at an accelerating 10–15 kV. Three magnifications were used to observe the sample at an objective magnification of 500x, 1000x, and 2000x magnification (Jafari et al., 2017).

Statistical Analysis. Obtained experimental data were analyzed using repeated measures ANOVA with the alpha set 0.05 to identify the significant difference and the mean scores between the samples. The statistical analysis used IBM statistical product and service solutions (SPSS) software version 28.0. All experiments were carried out in triplicate (n=3), and the data were presented as mean ± standard deviations.

RESULTS AND DISCUSSION

Powder Yield

In this study, all the powder samples were collected at the cyclone, and the hard rubber hammer periodically knocked the drying chamber during the experiment to keep the remaining powder on the drying chamber surface and its accessories as minimal as possible. The production yields of tomato powder were 17.40–32.10%, similar to the data reported by Chegini and Ghobadian (2007), with a production yield of 18–35% in the study on orange juice powder. Compared to their findings, the product yields obtained from the study are accepted as the range obtained is close to the reported product yield. Figure 2 represents the production yield of samples at varied conditions.

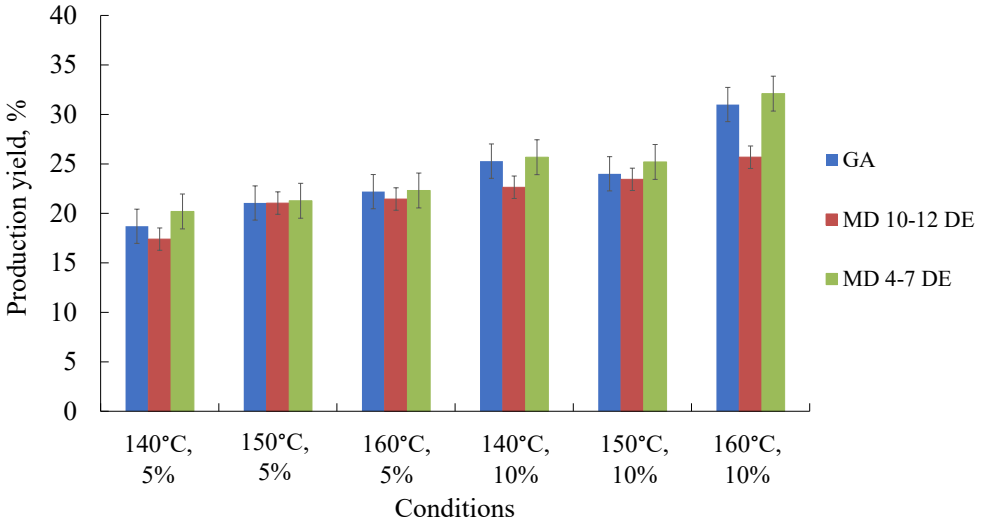

Figure 2. Production yield of samples at varied conditions (different temperatures and concentrations) with different carrier agents

The result shows that the production yield increases with the increase of carrier agents. The concentration of the carrier agents affected the powder properties. A low concentration of carrier agent may obtain the stickiness powder. The addition of carrier agents could increase the total solid content in the feed and increase the number of solid particles available in the drying system while decreasing water evaporation, thus, reducing the moisture content of the product (Tonon et al., 2008). According to Jittanit et al. (2010), a rise in MD concentration decreased the moisture content of pineapple juice powder. It was suggested that carrier agents such as MD and GA could alter the surface stickiness of low molecular weight sugars such as glucose, sucrose, fructose, and organic acids, facilitating drying and reducing the stickiness of the spray-dried product (Bhandari et al., 2005). As the inlet temperature increased, production yield increased. The increase in inlet temperatures has given the higher process yield, and it was due to the greater efficiency of heat and mass transfer processes occurring when the higher inlet air temperature was used (Phisut, 2012; Cai & Corke, 2000). As the inlet temperature increases, the moisture content of the powder produced decreases, resulting in less accumulation of wet powder on the chamber wall of the spray dryer, thus an increase in powder yield.

Characterization of Tomato Powder

All subsequently produced tomato powders were analyzed to determine the features of the physicochemical properties found in the powder. The physical properties to be determined against the resulting tomato powder include bulk density, hygroscopicity, moisture content, WSI, WAI color, particle size, and particle morphology. Table 4 shows the physical

properties of the produced tomato powder. The mean scores were obtained from SPSS based on the data for the following characteristics taken in triplicates.

Table 4

Mean scores on the characteristics of tomato samples

Samples	Bulk density, g/cm^3	Hygroscopicity, %	Moisture content, %	WSI, %	WAI, %	Particle size, µm
TP1	0.3387 ± 0.01	12.00 ± 0.00	7.50 ± 0.50	87.76 ± 2.72	12.44 ± 0.23	14.577 ± 5.17
TP2	0.2943 ± 0.01	11.67 ± 0.58	7.00 ± 1.00	88.39 ± 1.35	12.00 ± 0.22	21.943 ± 1.97
TP3	0.2780 ± 0.01	11.33 ± 0.58	6.17 ± 0.29	89.37 ± 0.87	11.56 ± 0.23	26.937 ± 2.75
TP4	0.2943 ± 0.01	10.67 ± 0.58	5.50 ± 0.50	86.57 ± 1.30	12.44 ± 0.23	18.143 ± 8.09
TP5	0.2860 ± 0.01	9.67 ± 0.58	5.00 ± 0.50	89.43 ± 0.83	11.55 ± 0.24	25.053 ± 1.91
TP 6	0.2630 ± 0.01	10.00 ± 1.00	3.83 ± 0.76	88.17 ± 1.22	12.00 ± 0.22	30.273 ± 2.86
TP 7	0.3753 ± 0.01	9.33 ± 0.58	5.67 ± 1.04	87.50 ± 1.74	9.33 ± 0.23	7.352 ± 0.79
TP 8	0.3573 ± 0.01	8.00 ± 1.00	4.83 ± 2.02	88.11 ± 1.17	8.44 ± 0.23	11.367 ± 3.31
TP 9	0.3327 ± 0.01	7.33 ± 0.58	5.33 ± 1.61	89.56 ± 1.25	7.56 ± 0.23	11.880 ± 0.54
TP 10	0.3334 ± 0.01	6.67 ± 0.58	4.83 ± 0.76	88.11 ± 1.77	7.10 ± 0.23	10.352 ± 0.90
TP 11	0.3230 ± 0.01	6.33 ± 0.58	3.83 ± 1.44	89.56 ± 1.25	6.67 ± 0.23	18.843 ± 6.52
TP 12	0.2943 ± 0.01	5.67 ± 0.58	3.17 ± 0.29	89.98 ± 1.25	6.22 ± 0.22	24.733 ± 0.89
TP 13	0.4007 ± 0.02	14.00 ± 1.00	8.00 ± 0.50	86.02 ± 1.25	11.11 ± 0.22	6.884 ± 0.51
TP 14	0.3890 ± 0.01	13.67 ± 0.58	7.00 ± 1.00	88.64 ± 1.25	10.67 ± 0.23	7.044 ± 1.04
TP 15	0.3573 ± 0.01	13.33 ± 0.58	6.33 ± 0.76	89.12 ± 1.20	8.87 ± 0.22	7.460 ± 0.77
TP 16	0.3450 ± 0.01	13.33 ± 0.58	6.33 ± 0.76	88.91 ± 1.25	7.99 ± 0.23	7.961 ± 0.29
TP 17	0.3230 ± 0.01	12.33 ± 0.58	5.33 ± 1.53	88.91 ± 1.26	7.55 ± 0.22	10.697 ± 0.37
TP 18	0.3130 ± 0.01	12.00 ± 1.00	4.50 ± 0.50	89.12 ± 1.20	7.12 ± 0.22	14.337 ± 1.16

Bulk Density

According to the results of the mean scores in Table 4, the processing of tomato powder has produced a powder with a bulk density range between 0.2630 g/cm^3-0.4007 g/cm^3. Bulk density is one of the very important features for the packaging design and the calculation of transportation volume (Jittanit et al., 2011). High bulk density in the sample resulted in the tendency of powder particles to be stuck to one another (Goula & Adamopoulos, 2008). The study discovered a significant difference (p<0.05) in the effect of temperature and concentration of carrier agents on the bulk density of the spray-dried powder with the increment of the two factors. The result shows a decrease in the bulk density as the temperature and concentration of carrier agents were increased. The results of this study are supported by statements from other studies conducted by Chegini and Ghobadian (2007), which show that orange powder dried at the inlet temperature of the dryer at 130°C had a bulk density as low as 0.42 g/ml and the bulk density of orange powder dropped to as low as 0.21 g/ml when the inlet temperature was increased to 150°C. Results showed that with an increase in inlet temperature, bulk density would decrease as there is an increase in the insoluble solid content (Chegini & Ghobadian, 2007). Bulk density decreases as the apparent volume of the powdered samples obtained is higher for samples with increasing inlet temperature.

At higher temperatures, an increase in the input air temperature frequently results in the quick production of a dry layer on the droplet surface and particle size and skinning over or case hardening on the droplets. It causes the droplet surface to produce vapor-impermeable coatings, followed by the production of vapor bubbles and, as a result, droplet enlargement (Chegini & Ghobadian, 2007). Bulk density will increase when there is a decrease in the inlet temperature (Goula & Adomopoulos, 2005).

Figure 3 illustrates that the bulk density lowers as temperature increases and that there is a significant difference (p<0.05) for both concentrations. Figure 4 also shows the same trend as bulk density decreases with the increase of temperature and increasing concentration of GA, resulting in the lower bulk density followed by MD 4-7 DE. MD 10-12 DE shows a higher bulk density. However, few samples show no significant difference (p>0.05), such as MD 4-7 DE and MD 10-12 DE at all conditions except at 5%, 150°C. GA and MD 4-7 DE also shows no significant difference (p>0.05) at 5%, 140°C. It might be because of the particle size, as most of the samples obtained have no significant difference in their particle size. Smaller particles migrate downward, filling the gaps left by larger particles. The bulk density of a material with many smaller particles is greater than that of a material with a few smaller particulates.

The addition of carrier agents to feed material also has a variable influence on bulk density. Adding MD has a carrier agent's influence on the bulk density of the powdered particles. It is demonstrated by the fact that MD's skin-forming tendency increases the

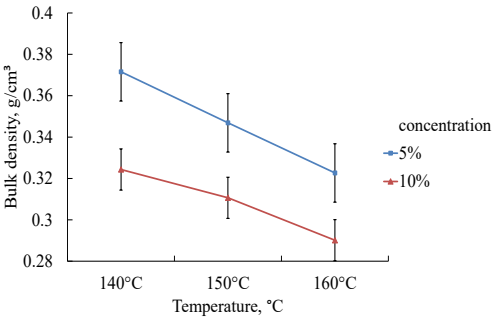

Figure 3. Effect of inlet temperature at different concentrations against estimated marginal means for bulk density

amount of air trapped in the particle and reduces thermoplasticity. According to Kwapinska and Zbicinski (2005), carrier agents with skin-forming qualities, such as MD, frequently include air bubbles, and the greater the usage of comparable carrier agents, the lower the bulk density of powders. The use of acacia GA in spray drying shows roughly equivalent observations since it has a higher T_g point due to its big molecular size. Additionally, with increasing concentrations of carrier agents, the bulk density of orange juice powder has decreased (Shrestha et al., 2007). The heavier the material, the more easily it fits into the gaps between the particles, taking up minimal space and contributing to increased bulk density values. Chegini and Ghobadian (2007) discovered that spray-dried powders with greater moisture levels had a larger bulking weight owing to the existence of water, which is much denser than the dry solid. This characteristic is consistent with the results, as tomato powders made with MD, especially MD 10-12 DE, exhibited higher moisture content and bulk density.

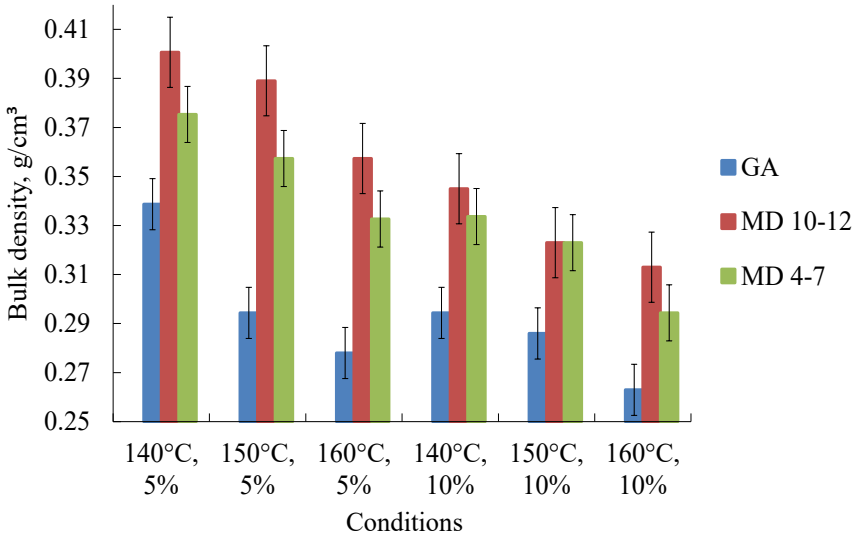

Figure 4. Effect of the conditions (different temperatures and different concentrations) with different types of carrier agents against estimated marginal means for bulk density

Hygroscopicity

As for the hygroscopicity, the result in Table 4 shows that range was at 5.67–13.67%, with TP 12 having the lowest hygroscopicity and TP 14 having the highest hygroscopicity. The results showed that the concentration and inlet temperature have significant differences (p<0.05) to the hygroscopicity of the tomato powder except for formulations of 5% at 140°C and 150°C; 5% at 150°C and 160°C. At 10%, the temperatures 150°C and 160°C also show no significant difference (p>0.05). Figure 5 illustrates that the increasing temperature reduces hygroscopicity and difference in concentration in affecting the powder's hygroscopicity, in which the higher concentration, 10%, resulted in a much lower hygroscopicity compared to the 5% and that the hygroscopicity decreases with an increase in temperature. By comparing the carrier agents, as shown in Figure 6, it is found that adding MD 4-7 DE produced powders with the lowest hygroscopicity, followed by GA and MD 10-12 DE. Carrier agents also showed a significant difference from one another except for sample TP6 with sample TP18 and sample TP2 with sample TP14 (p>0.05). The hygroscopicity decreased as the concentration of the carrier agent increased. The greater the input air temperature difference, the greater impact on the hygroscopicity of the powders, as increasing temperatures yields lower hygroscopicity values. Samples adding GA to MD 10-12 DE show no significant difference when treated, even under the same conditions. It could be due to the agent chemical structure of the carrier agent that explains the differences in water adsorption. The phenomena of adsorption of water by a carbohydrate were ascribed to the connections of the hydrogen contained in water molecules with the hydroxyl groups accessible in the amorphous and surface crystalline areas of the substrate. GA and MD of higher DE have many interactions with hydrophilic groups. As a result, it quickly absorbed moisture from the surrounding air (Tonon et al., 2011). The MD degree of polymerization also impacts the powder's hygroscopicity. The study is in accordance with Tonon et al. (2011) findings, in which the samples made with MD 10 DE had the lowest rate of moisture adsorption, but the samples made with MD 20 DE and GA were found to be much more hygroscopic, had greater adsorption of water and had lower moisture content in the powders.

The powder's hygroscopicity increased considerably when MD 10-12 DE was utilized as a carrier. This study found that the lower the air inlet temperature, the higher the hygroscopicity of the tomato powder. The powders generated with a high air inlet temperature had low moisture content and greater potential to absorb ambient moisture. The high drying air temperature resulted in a considerable temperature gradient at the feed drop surface. It instantly accelerated the heat transmission rate and moisture evaporation from the liquid (Muzaffar et al., 2016). Caparino et al. (2012) state that tiny particle sizes have a considerable surface area for absorbing environmental moisture. Particle size is a key component in determining particle surface area. Smaller particles will increase

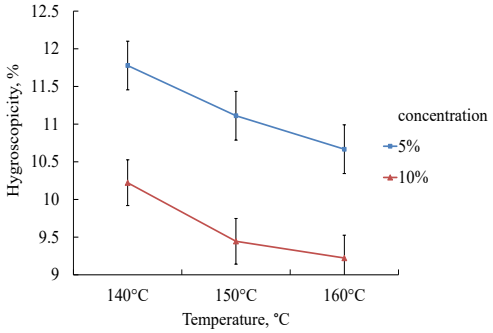

Figure 5. Effect of inlet temperature at different concentrations against estimated marginal means for hygroscopicity

the surface area, while larger particles will reduce it. Depending on the active spots in the dry matrix adsorption force, this results in greater water adsorption from the environment (Sudeep et al., 2010). This condition may result in product aggregation during storage. Food powder particles with a high hygroscopicity could exhibit a process known as caking, which causes the powder to agglomerate. This phenomenon is linked to water absorption on the particle's surface, which forms a saturated solution and makes the particles adhesive and capable of establishing hydrogen bonds, resulting in caking (Goula & Adamopoulos, 2008). Fruit products often have high sugar content, resulting in a hydrophilic nature and sticky powders that tend to agglomerate.

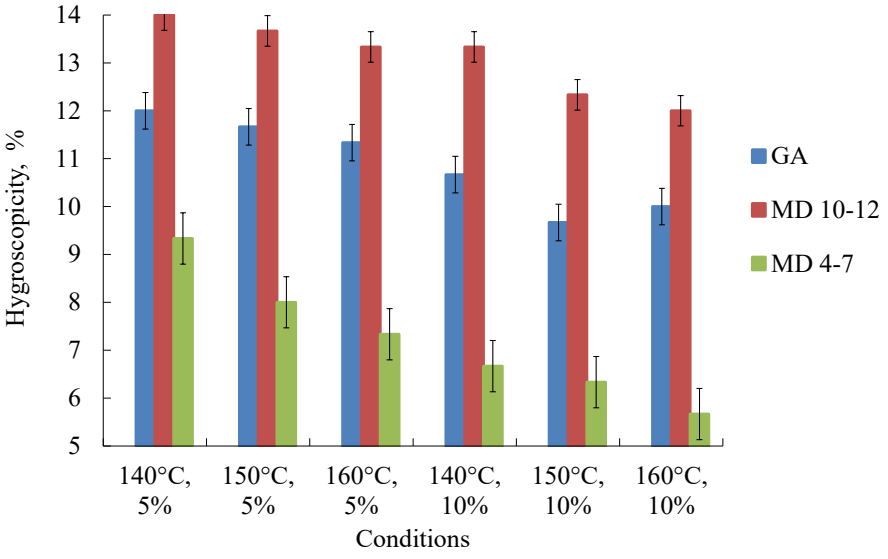

Figure 6. Effect of the conditions (different temperatures and different concentrations) with different types of carrier agents against estimated marginal means for hygroscopicity

Moisture Content

According to the result in Table 4, the percentage range of moisture content found in the resulting tomato powder is 3.17–8.00%, with TP12 having the lowest moisture content

and TP13 having the highest moisture content. Variations in these results are referred to as parameters to measure the quality of a powder labeled as a dry product and similar to that reported for other food powders (Bhandari et al., 2005). The main factor affecting the stability of the powder is the moisture content since a small amount of water can press enough temperature to increase the mobility of the matrix during storage (Bhandari et al., 2005; Osman & Endut, 2009).

Based on Figure 7, increasing the concentration of carrier agents and inlet temperature on the tomato juice resulted in powder with a much lower moisture content. The concentration has no significant difference as the temperature is increased (p>0.05) except for samples prepared at 10%, 140°C, and 10%, 160°C (p<0.05). It is because, compared to 5%, the greater concentration of the carrier agent, the greater the capacity to overcome the sugars present in fruit powder, which have an extremely hygroscopic nature and absorb humidity from the adjacent air (Shrestha et al., 2007). It is also in accordance with Jittanit et al. (2010) increasing the MD content caused pineapple juice powder moisture content to decrease. The greater inlet temperature difference between 140°C and 160°C is significant because the moisture content decreases at higher temperatures.

However, the temperature significantly differs as concentration increases (p<0.05). Figure 8 illustrates the moisture content of the samples prepared with different carrier agents as temperature and concentration increase. The result shows no significant difference between the samples except for samples prepared at 5%, 140°C for GA and MD 10-12 DE, which are sample TP7 and sample TP13. The study found that an increase in the percentage of carrier agents used significantly impacted the moisture content of tomato powder. By increasing the carrier agent concentration, there is more potential to lower the percentage of moisture contained in the tomato powder. For example, spray drying of tomato powder with MD 4-7 DE at a drying temperature of 150°C decreased the moisture content from 4.83 to 3.38% when MD was increased from 5 to 10%. The results of this study agreed with the roselle-pineapple powder studied by Osman et al. (2009), which discovered that the increased MD content reduced the moisture content in the powder. The moisture content in tuna powder decreased from 7.47–4.63% when the MD percentage increased to 26% (Caparino et al., 2012). In addition, Jittanit et al. (2010) also supported this fact through their study of pineapple juice spray drying. The results showed that the moisture content of pineapple powder was 4–5.8% and that the increase in MD content had caused the product's moisture content to be lower. It may be due to increased solid content in food and reduced free water content for evaporation, resulting in reduced moisture content in the produced powders (Osman et al., 2009). Moreover, MD has properties to prevent sugar in powders from absorbing moisture from the surrounding air (Jittanit et al., 2010). It means that powders with lower moisture content can be obtained by increasing the percentage of MD added. An increase in the inlet temperature of the spray dryer equipment affects an insignificant difference in the percentage of moisture content in the resulting tomato powder.

With an increase in the inlet temperature, the moisture content found in the tomatoes is lower. It was supported by Osman et al. (2009) in their study of roselle-pineapple powder, in which the moisture content in the sprayed powder decreased with an increase in inlet temperature. Jittanit et al. (2011) also stated the same statement after conducting their study of tamarind powder. In addition, through studies of pineapple powder, Jittanit et al. (2010) also proved that high temperatures would reduce the humid content in the powder. His study showed that the inert content of pineapple powder decreased from 5.8 to 4.8% when the temperature increased from 130 to 170°C.

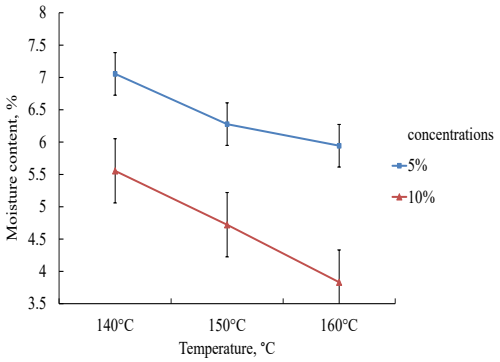

Figure 7. Effect of inlet temperature at different concentrations against estimated marginal means for moisture content

Moisture content is an important powder parameter that is linked to drying efficiency. Because it influences glass transition and crystallization characteristics, the moisture content of a microencapsulated product plays an essential role in determining its flow properties, adhesion, and storage stability (Phisut, 2012). According to the findings, an increase in the inlet air temperature decreased the moisture content of spray-dried powders, consistent with previous research. MD powders had proportionally higher moisture content as temperature

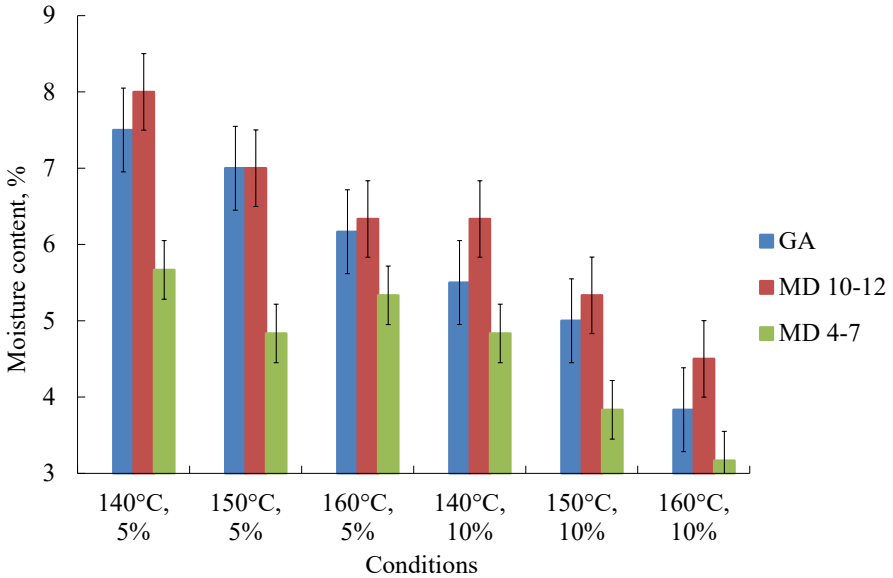

Figure 8. Effect of the conditions (different temperatures and different concentrations) with different types of carrier agents against estimated marginal means for moisture content

increased than GA results. MD's chemical structure can explain this tendency since lower molecular weight MD (20-25 DE) has shorter chains and a much more hydrophilic nature (Cai & Corke, 2000).

Water Solubility Index (WSI)

The reconstitution property WSI was used to investigate the influence of process factors. Based on Table 4, the WSI% ranged from 86.02–89.97% for the spray-dried tomato powder. The results in Figure 9 show a significant difference (p<0.05) as the temperature and concentration increased except for the conditions of 10% at 150°C and 160°C. The solubility index of spray-dried powder is affected by the properties of the powder, which are the moisture content and the size of particles (Lee et al., 2018). From the study, the moisture content decreases at increasing temperatures, and the particle size increases at increasing temperatures. The lower the particle size, the lower the solubility and flow ability of powder (Phisut, 2012).

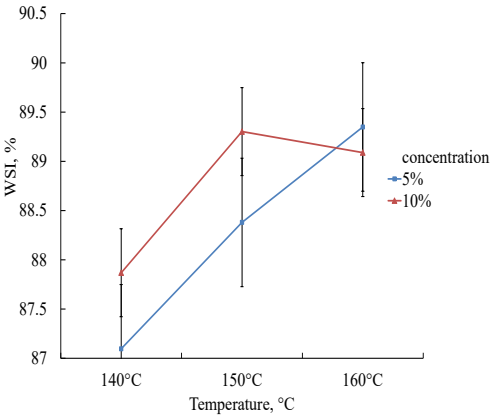

Figure 9. Effect of inlet temperature at different concentrations against estimated marginal means for WSI%

The statistical analysis also shows that there is no significant difference (p>0.05) between the carrier agents even though the data obtained shows that there is a slight increment between WSI% for the carrier agents, with GA giving most of the lower WSI% and MD 4-7 DE giving most of the higher WSI%, and MD 10-12 DE was somewhere in between as shown in Figure 10. The highest mean score for WSI is 89.97% (TP12), and the lowest mean score recorded was 86.02 (TP13). Phoungchandang and Sertwasana (2010) observed a similar pattern while spray-drying ginger juice. The solubility index of spray-dried powder is influenced by the underlying materials and carrier agents employed and the powder's properties (Goula & Adamopoulos, 2008; Grabowski et al., 2006).

Water Absorption Index (WAI)

As for the WAI of the powdered samples, the result shows that the concentration has a significant difference as temperature increases (p<0.05) and that temperature also has a significant difference as concentration increases (p<0.05). Figure 11 explains the two factors that are affecting the WAI of the powdered tomato samples. Figure 12 shows the

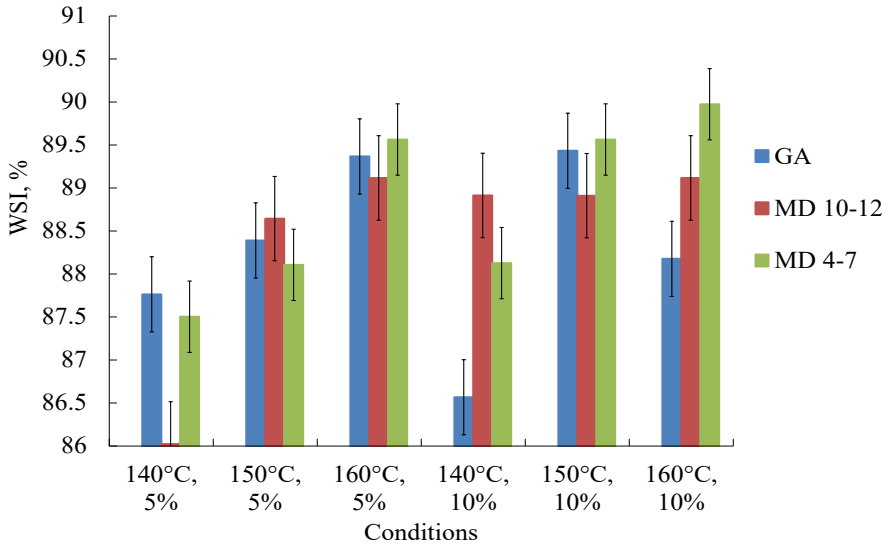

Figure 10. Effect of the conditions (different temperatures and different concentrations) with different types of carrier agents against estimated marginal means for WSI%

effect of carrier agents at varied concentrations and inlet temperatures. The figure shows that increasing the inlet temperature and concentration of carrier agents will result in lower WAI. WAI decreases gradually with the increase of the two factors. Whereas the WAI for MD 10-12 DE also decreases gradually except at 5%, 150°C to 5%, and 160°C, which decreases substantially. For GA, the WAI gradually decreases as temperature increases for the 5% samples. However, for the 10% samples, the WAI increases from 150 to 160°C. Figure 12 also shows that GA carrier agents and MD 4-7 DE have the highest significant difference (p<0.05).

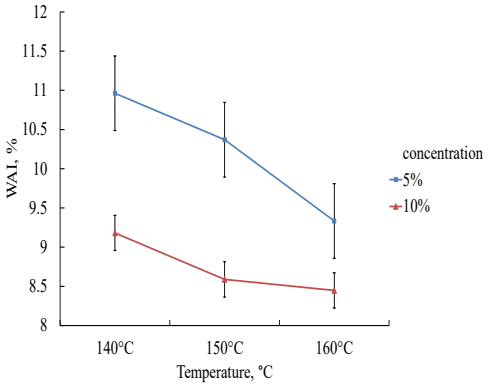

Figure 11. Effect of inlet temperature at different concentrations against estimated marginal means for WAI%

The amount of water that remains bound after applying an external force, such as centrifugation, is called the WAI. WAI is one of the immediate properties of a powder that represents a sample's ability to reassociate with water under constrained water conditions. A good rehydration powder would moisten rapidly and fully, sinking rather than floating. WAI percent results showed significant differences as the inlet temperature and carrier agent amount increased. It could be due to the samples' low hygroscopicity. The low WAI values of

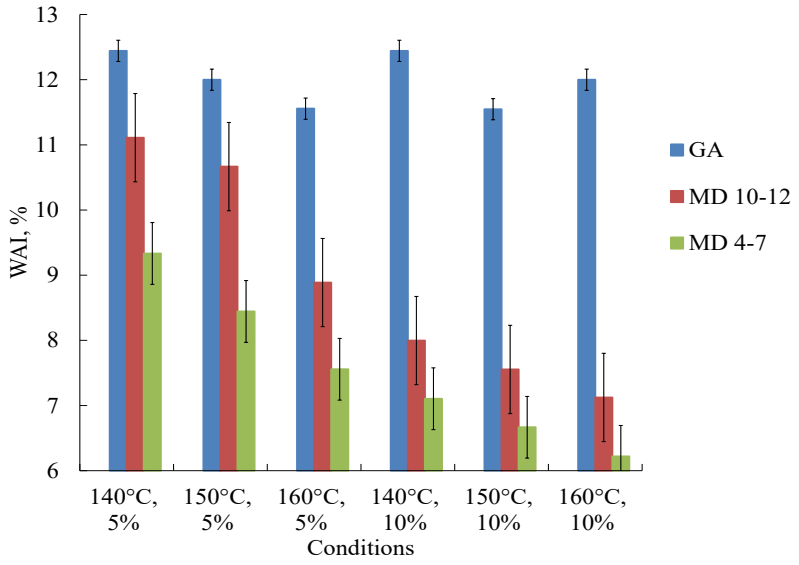

Figure 12. Effect of the conditions (different temperatures and different concentrations) with different types of carrier agents against estimated marginal means for WAI%

the WAI percent could also be attributed to the high WSI values. Based on the data obtained in Table 4, the WAI was lower in TP12 with a mean score of 6.22%, while the highest WAI mean scores were found in TP1 and TP4, both at 12.44%. The results revealed that when concentration increases, the WAI drops. As the concentration of carrier agents increases, the WAI decreases. Grabowski et al. (2006) obtained similar findings with spray-dried yellow sweet potato flour. MD can develop outer layers on the droplet surface, affecting particle surface stickiness due to the transition into a glassy state. Changes in surface stickiness diminish particle cohesion, resulting in less agglomeration and, as a result, lesser water-holding capacity of the powder.

Color Analysis

Figure 13 represents the effect of the varied conditions for the color analysis of the tomato powder. The a^* value for the control sample CT1 was 16.99. The results showed that the range of a* values for the redissolved samples were 11.93–13.16, which has a significant difference ($p<0.05$) from the a^* value of the control sample, CT1. The results also showed that the obtained a^* values of the redissolved samples were between 10.01–10.42, 13.31–13.81, 11.62–16.10, 13.10–14.98, and 10.83–12.04 for the other control samples of CT2, CT3, CT4, CT5, and CT6, respectively. All of which has a significant difference ($p<0.05$) as the concentration of the carrier agents increases and as the temperature increases. The obtained b^* values of the redissolved samples were between 17.24–18.51, 14.84–15.78,

20.34–20.80, 13.32–22.61; 19.43–21.16 and 16.72–16.98 for the control samples of CT1, CT2, CT3, CT4, CT5, and CT6, respectively (Figure 13). As for the b* values, the result also showed a significant difference (p<0.05) between the redissolved samples and the control samples. The results show a decrease in a* and b* values for each sample with different carrier agents as the concentration and inlet temperature increase. It is due to the increasing inlet temperature that causes loss of pigment and results in tomato powder products with lower a* and b* values. The decreasing a* and b* values were also caused by the increasing concentration of the carrier agents as both MD, and GA are white, while tomato juice is red; as a result, all the powder produced had a lighter color. Grabowski et al. (2006) found that a reduction in redness and yellowness was also observed when MD concentrations were raised in the manufacturing of sweet potato powders. The primary changes in the color of powders were caused by variations in the inlet temperature, which indicates that increasing the inlet temperature causes a commensurate drop in the red color. It might be because lycopene degrades significantly at higher temperatures. a* and b* values indicated that increasing inlet temperature causes loss of pigment and results in tomato powder products with lower a* and b* values. The decreasing a* and b* values are also caused by the increasing concentration of the carrier agents as both MD, and GA are white, while tomato juice is red; as a result, all the powder produced had a lighter color.

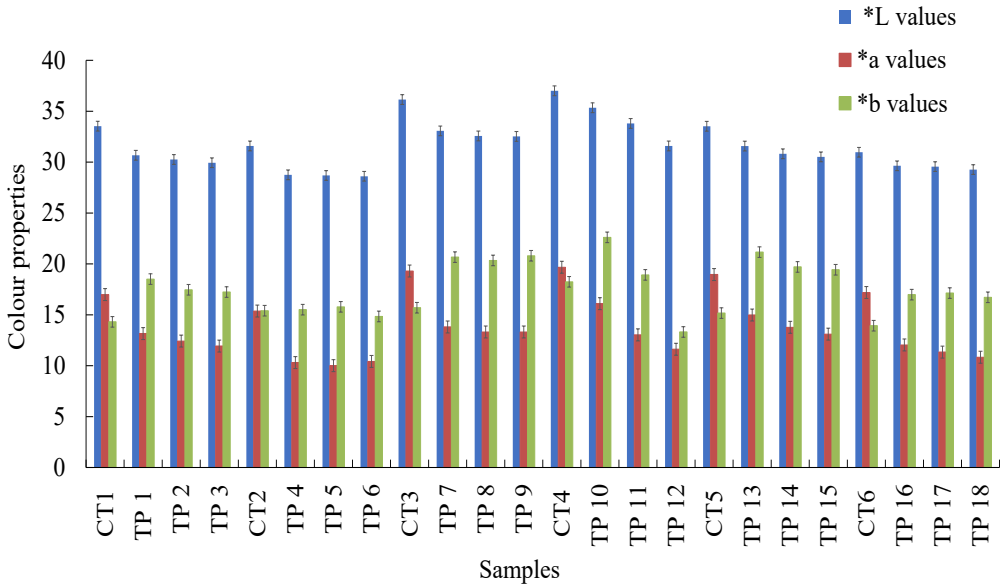

Figure 13. Effect of the conditions (different temperatures and concentrations) with different types of carrier agents against estimated marginal means for color analysis

The obtained L^* values of redissolved samples were between 29.94–30.67, 28.61–28.75, 32.53–33.07, 31.59–35.34, 30.52–31.58, and 29.27–29.64 for the control samples of CT1, CT2, CT3, CT4, CT5, and CT6, respectively (Figure 13). The average L^* value for the tomato sample solution is lower than that of the control sample, and there is a significant difference ($p<0.05$) between the L^* value in the tomato powder re-solution and the increase of carrier agent concentration across the same temperature. The reduced brightness in the solution of the tomato powder sample may be due to the reasons stated by Jittanit et al. (2010), in his note that the lower brightness is due to a small portion of the powder not being dissolved completely in the solution. In addition, the concentration of the carrier agent may also cause the color difference between the control tomato sample and the solution of the tomato powder sample. Among other reasons that affect brightness for reduction is the reaction of non-enzyme browning that occurs when the drying process is carried out. Therefore, the brightness in the solution of the tomato powder sample is lower than the brightness of the control sample. Readings of redness and higher yellowness levels in the sample can also result from non-enzymatic reactions such as the caramelization process and Maillard reaction during the drying process. These reactions can occur due to heat supplied to the samples in the drying chamber (Jittanit et al., 2010).

Particle Size

The mean particle size for tomato powder samples produced at different inlet temperatures and concentrations with different carrier agents ranged from 6.884 μm to 30.273 μm (Table 4). The results show no significant difference ($p>0.05$) at 140°C temperature for both concentrations. However, there is a significant difference at higher temperatures (150°C and 160°C) for both concentrations ($p<0.05$). At 5% concentration, the temperatures of 140 to 150°C and 150 to 160°C have no significant difference ($p>0.05$). Meanwhile, temperature 140 to 160°C significantly differs ($p<0.05$). For the 10% concentration, there is no significant difference in temperatures from 140 to 150°C, but at 140 to 160°C and at 150 to 160°C, it shows a significant difference ($p<0.05$). As for the formulations, all have significant differences ($p<0.05$) from one another except for the following pairs: T7 and T13, T8 and T14, T4 and T10, and T5 and T11. Based on Table 4, the mean score of the particle size shows that the particle size increases as the concentration and the temperature increase, and the higher score is at 10%, 160°C formulations (highest is TP6 with a mean score of 30.273 μm) and the lower score is at 5%, 140°C formulations (lowest is TP13 with a mean score of 6.884 μm). Figure 14 shows a line plot for the interaction of concentration, the temperature that shows the increase in the particle size with the increase in temperature, and the significant differences between the two concentrations.

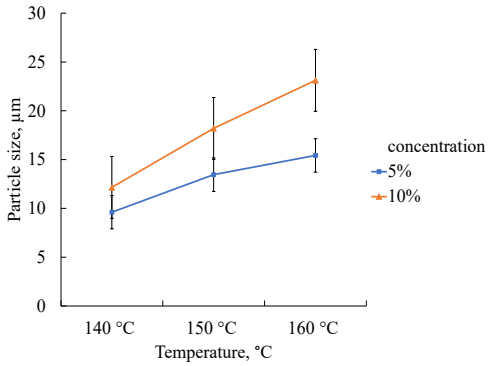

Figure 14. Effect of inlet temperature at different concentrations against estimated marginal means for particle size

Higher inlet temperatures produced bigger particles, which can be attributed to the increased swelling as the drying temperature was raised. When a particle is exposed to greater drying rates, moisture evaporation is fast, promoting the production of a hard crust that prevents particle shrinkage during spray drying. If the inlet temperature is lower, the particle remains wet for longer and contracts, reducing particle size (Gouaou et al., 2019). Tonon et al. (2008) discovered comparable properties in spray-dried acai powders. The

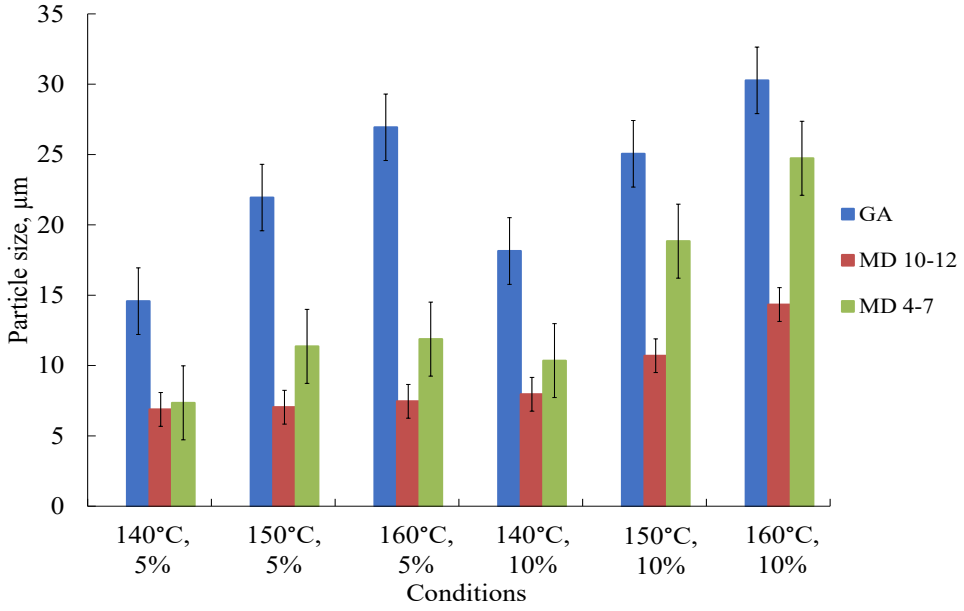

Figure 15. Effect of the conditions (different temperatures and different concentrations) with different types of carrier agents against estimated marginal means for particle size

use of carrier agents, particularly a higher MD content, has been shown to enhance the particle size of the spray-dried powder.

The type of carrier agent also plays a role in affecting particle size. The size of the particles in the feed suspension likely affects spray-dried particle size and encapsulation efficiency. This quality is also significantly connected to suspension stability which is essential to feed successive steps uniformly. The latter had a larger mean diameter based on the findings of Tonon et al. (2011) when comparing MD 20 DE to the powder generated

with MD 10 DE. However, it was found that the larger particle size was obtained with the addition of GA, followed by the addition of MD 4-7 DE, and the smaller particle size was obtained with the addition of MD 10-12 DE (Table 3). The findings agree with Tonon et al. (2011) for the MD 4-7 DE and MD 10-12 DE. The difference in the study is that GA produces a much larger particle size than MD. Figure 15 shows the effect of conditions (different temperatures and different concentrations) with different types of carrier agents against estimated marginal means for particle size.

Powder Morphology

The morphology of spray-dried tomato powder produced with different conditions is shown in Figures 16, 17, and 18. As stated in the methodology, only a few samples were chosen for SEM imaging: the samples with 140°C at 10%, 160°C at 10%, and 160°C at 5%. The samples were chosen likewise to compare the differences in particle morphology of the resulting tomato powder at different inlet temperatures (140°C and 160°C) and differences in powder morphology at different concentrations (5% and 10%) with different types of carrier agents (MD 4-7 DE, MD 10-12 DE, GA). For the spray drying of the tomato powder, the inlet temperature and the concentration of the carrier agents were shown to be the key factors influencing the morphology of the powder. The particle size has been varied, in which GA has formed the largest particle out of the other two carrier agents, and MD 10-12 formed the smallest particle. The particles formed were mostly wrinkled, irregular, and possessed pockmark surfaces and had some agglomeration between the samples' materials, these being the typical morphologies of spray-dried powders (Tonon et al., 2011). Comparing the morphology based on the type of carrier agents, the spray-dried powder with 10% GA at 160°C is considerably large, with many folds of wrinkled surfaces, larger pockmarks, and smaller particles attached to the surface. The 10% GA at 140 °C also shows the same property with a lesser wrinkled surface the 5% GA at 160°C is found to be smaller than the other two and has a smoother surface. The morphology of powders produced with MD 4-7 DE appeared to be the same as those produced with GA and only differed in size. However, smooth spherical shapes were found for the tomato powder with 5% MD 4-7 DE at 160°C. As for the powders produced with MD 10-12 DE, the morphology also follows suit to those produced with GA and differs in size. However, globular and agglomerating shapes are observed on the 5% MD 4-7 DE tomato powder at 160°C. From the observation, it was found that the higher inlet temperature led to more wrinkled particles and that the lower concentration led to some smoother particles. Lower temperature drying makes the particle wetter and much more flexible, and it collapses (Jafari et al., 2017). There was no effect of carrier type on the particle shape, as it appears that carrier agents are more likely to affect the particle size and that the concentration of carrier agents and inlet temperature is deemed to be the key factors affecting the morphology

of the spray-dried powders. Nonetheless, Jafari et al. (2017) concluded from a study of pomegranate juice that a higher content of MD as a carrier produces more particle ridging due to its propensity to migrate in the outer zones of particles, limiting its endurance, which is verified by Tonon et al. (2008). Preceding research has found that wrinkles are caused by mechanical stress caused by uneven drying at various sections of liquid droplets during the initial drying step (Pourashouri et al., 2014).

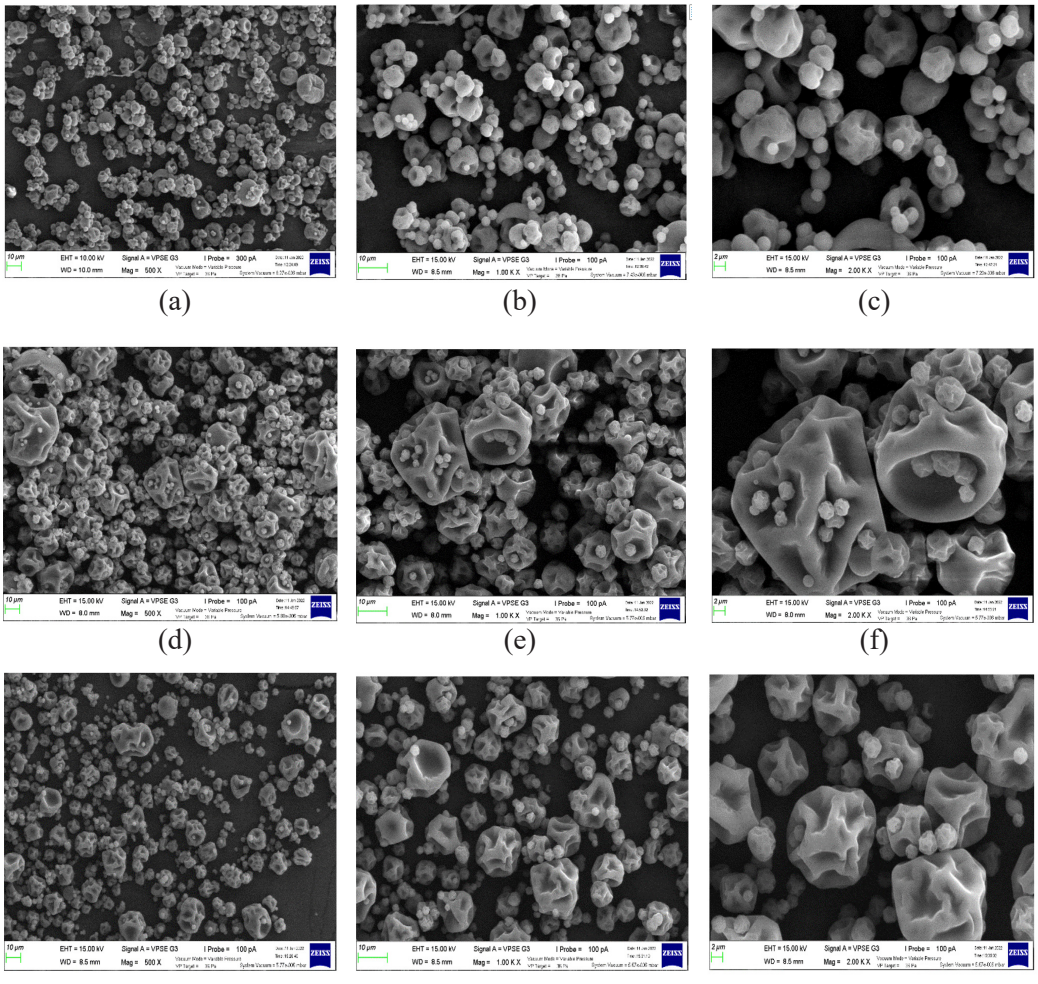

Figure 16. SEM images of tomato powder with the addition of GA at (a) – (c) 160°C, 5%; (d) – (f) 160°C, 10%; (g) – (i) 140°C, 10% with 500x, 1000x, 2000x magnification

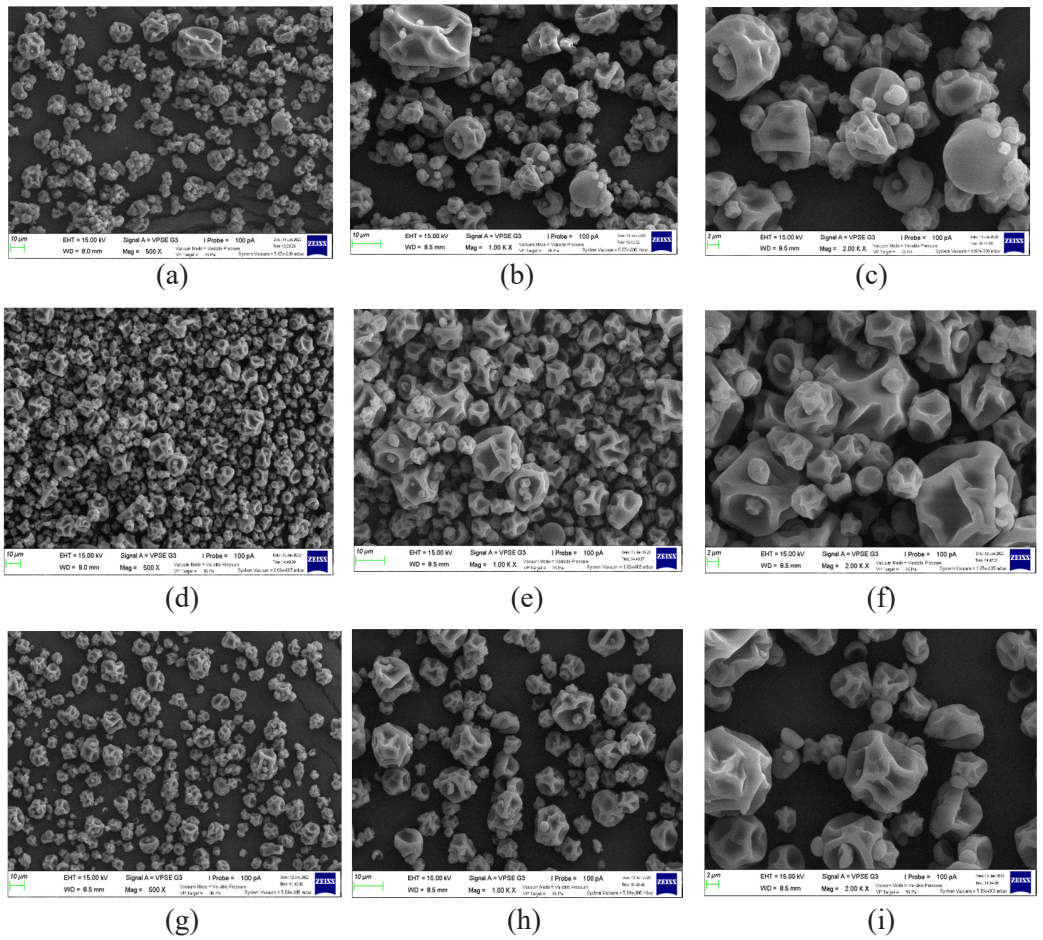

Figure 17. SEM images of tomato powder with the addition of MD 4-7 at: (a) – (c) 160°C, 5%; (d) – (f) 160°C, 10%; (g) – (i) 140°C, 10% with 500x, 1000x, 2000x magnification

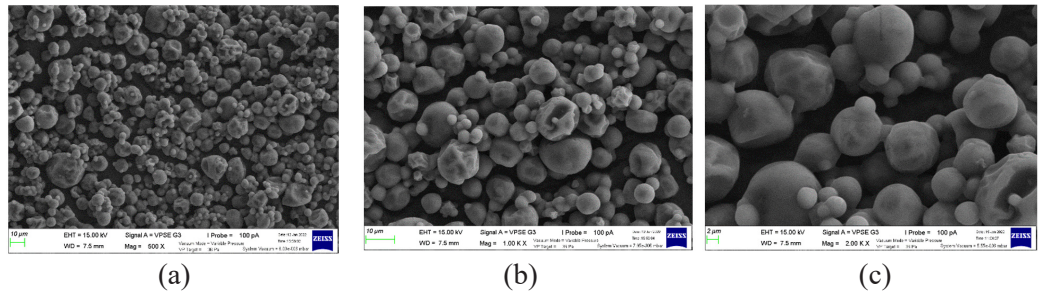

Figure 18. SEM images of tomato powder with the addition of MD 10-12 at: (a) – (c) 160°C, 5%

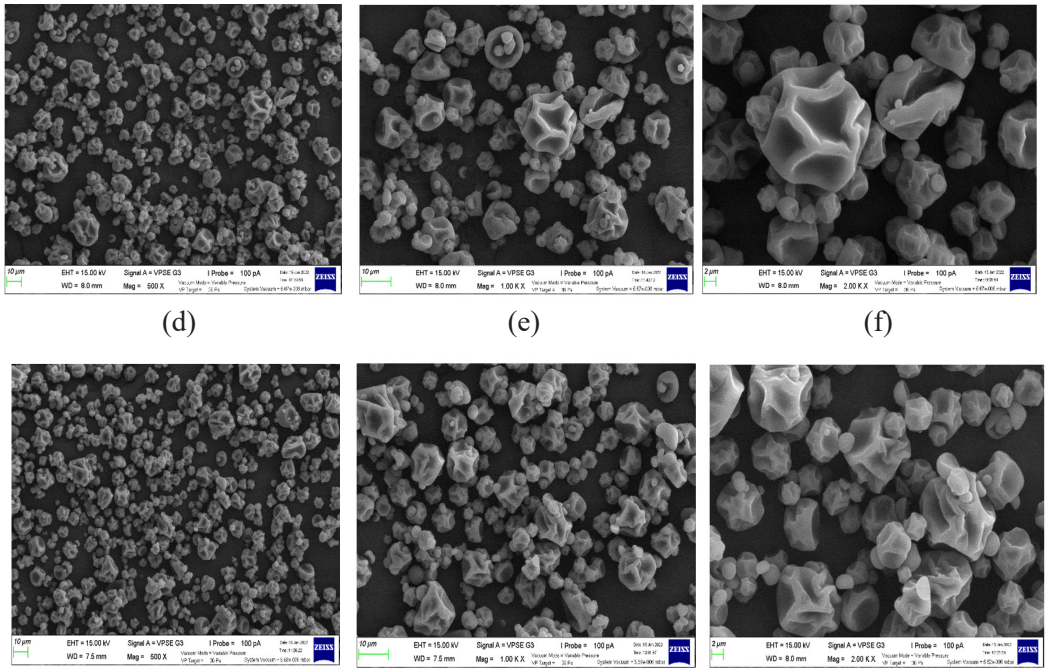

(d) (e) (f)

(g) (h) (i)

Figure 18 (Continue). SEM images of tomato powder with the addition of MD 10-12 at: (d) – (f) 160°C, 10%; (g) – (i) 140°C, 10% with 500x, 1000x, 2000x magnification

CONCLUSION

Spray-dried tomato powder was successfully produced and prepared at different concentrations of various carrier agents at different inlet temperatures. Each spray-dried powder resulted in a satisfactory result on the physical properties. Based on the experiment, the inlet temperature and carrier agent concentration profoundly influence the powder properties. The data obtained shows that the stability of the tomato powder is much better at higher temperatures and higher concentrations, with MD 4-7 DE being the best carrier agent among the three experimented carrier agents. The result showed that at higher temperatures and higher concentrations, the powder characteristics are more likely to have a higher yield, WSI, and larger particle size, as well as lower bulk density, hygroscopicity, moisture content, WAI, and color index. The findings also showed that the type of carrier agents have significantly improved powder characteristics, with MD 4-7 DE that gives better overall performance on powder quality. The powder analysis shows that the product has a moisture content of 3.17 ± 0.29%, the highest yield percentage at 32.1%, a low bulk density of 0.2943 ± 0.01 g/cm^3, the lowest hygroscopicity at 5.67 ± 0.58%, a high WSI at 89.98 ± 1.25%, a low WAI at 6.22 ± 0.22%, an intermediate particle size of 24.73 µm, and color L*, a*, b* values at 31.59 ± 0.03, 11.62 ± 0.08 and 13.32 ±

0.12. As for powder morphology, the product shows wrinkled surfaces, larger pockmarks, and smaller particles attached to the surface. As for the recommendation, it is signified that the effect of additives, their concentration, and inlet temperature on the properties of the powder has shown distinctive characteristics under the influence of these parameters. However, the main function of higher-intensity additives can be emphasized as additives improve product yield by manipulating transition temperature.

ACKNOWLEDGEMENT

This research was supported by the Research Management Center of Universiti Malaysia Sabah (Grant No. DN21100 - Phase 1/2021). These contributions are gratefully acknowledged.

REFERENCES

Adak, N., Heybeli, N., & Ertekin, C. (2017). Infrared drying of strawberry. *Food Chemistry*, *219,* 109-116. https://doi.org/10.1016/j.foodchem.2016.09.103

Aderibigbe, O. R., Owolade, O. S., Egbekunle, K. O., Popoola, F. O., & Jiboku, O. O. (2018). Quality attributes of tomato powder as affected by different pre-drying treatments. *International Food Research Journal*, *25*(3), 1126-1132.

AOAC. (2012). *Official Methods of Analysis: Association of Official Analytical Chemists* (19th ed.). https://www.scirp.org/(S(351jmbntvnsjt1aadkposzje))/reference/ReferencesPapers.aspx?ReferenceID=1819676

Bhandari, B., & Howes, T. (2005). Relating the stickiness property of foods undergoing drying and dried products to their surface energetics. *Drying Technology*, *23*(4), 781-797. https://doi.org/10.1081/DRT-200054194

Cai, Y. Z., & Corke, H. (2000). Production and properties of spray-dried amaranthus betacyanon pigments. *Journal of Food Science*, *65*(7), 1248-1252. https://doi.org/10.1111/j.1365-2621.2000.tb10273.x

Ciurzyńska, A., & Lenart, A. (2011). Freeze-drying - Application in food processing and biotechnology - A review. *Polish Journal of Food and Nutrition Sciences*, *61*(3), 165-171. https://doi.org/10.2478/v10222-011-0017-5

Compaore, A., Dissa, A. O., Rogaume, Y., Putranto, A., Chen, X. D., Mangindaan, D., Zoulalian, A, Rémond, R., & Tiendrebeogo, E. (2017). Application of the reaction engineering approach (REA) for modeling of the convective drying of onion. *Drying Technology*, *35*(4), 500-508. https://doi.org/10.1080/07373937.2016.1192189

Caparino, O. A., Tang, J., Nindo, C. I., Sablani, S. S., Powers, J. R., & Fellman, J. K. (2012). Effect of drying methods on the physical properties and microstructures of mango (Philippine 'Carabao' var.) powder. *Journal of Food Engineering*, *111*(1), 135-148. https://doi.org/10.1016/j.jfoodeng.2012.01.010

Chegini, R. G., & Ghobadian, B. (2007). Spray dryer parameters for fruit juice drying. *World Journal of Agricultural Sciences*, *3*(2), 230-236.

da Costa Ribeiro, A. S., Aguiar-Oliveira, E., & Maldonado, R. R. (2016). Optimization of osmoticdehydration of pear followed by conventional drying and their sensory quality. *LWT - Food Science and Technology*, *72*, 407-415. https://doi.org/10.1016/j.lwt.2016.04.062

Eren, I., & Kaymak-Ertekin, F. (2007). Optimization of osmotic dehydration of potato using response surface methodology. *Journal of Food Engineering*, *79*(1), 344-352. https://doi.org/10.1016/j.jfoodeng.2006.01.069

Garofulić, I. E., Zorić, Z., Pedisić, S., & Dragović-Uzelac, V. (2016). Optimization of sour cherry juice spray drying as affected by carrier material and temperature. *Food Technology & Biotechnology*, *54*(4), 441-449. https://doi.org/10.17113/ftb.54.04.16.4601

Gouaou, I., Shamaei, S., Koutchoukali, M.S., Bouhelassa, M., Tsotsas, E., & Kharaghani, A. (2019). Impact of operating conditions on a single droplet and spray drying of hydroxypropylated pea starch: Process performance and final powder properties. *Asia-Pacific Journal of Chemical Engineering*, *14*(1), Article e2268. https://doi.org/10.1002/apj.2268

Goula, A. M., & Adamopoulos, K. G. (2005). Stability of lycopene during spray drying of tomato pulp. *LWT - Food Science and Technology*, *38*(5), 479-487. https://doi.org/10.1016/j.lwt.2004.07.020

Goula, A. M., & Adamopoulos, K. G. (2008). Effect of maltodextrin addition during spray drying of tomato pulp in dehumidified air: I. Drying kinetics and product recovery. *Drying Technology*, *26*(6), 714-725. https://doi.org/10.1080/07373930802046369

Grabowski, J. A., Truong, V. D., & Daubert, C. R. (2006). Spray drying of amylase hydrolyzed sweet potato puree and physicochemical properties of powder. *Journal of Food Science*, *71*(5), E209-E217. http://dx.doi.org/10.1111/j.1750-3841.2006.00036.x

Haque, M., & Adhikari, B. (2014). Drying and denaturation of proteins in spray drying process. In A. S. Mujumdar (Ed.), *Handbook of Industrial Drying* (pp. 971-983). CRC Press.

Hii C. L., Ong S. P., Yap J. Y., Putranto A., & Mangindaan, D. (2021). Hybrid drying of food and bioproducts: A review. *Drying Technology*, *39*(11), 1554-1576. https://doi.org/10.1080/07373937.2021.1914078

Ismail, M. H., Khan, K. A., Ngadisih, N., Irie M, Ong S. P, Hii, C. L., & Law, C. L. (2020). Two-step falling rate in the drying kinetics of rice noodle subjected to pre-treatment and temperature. *Journal of Food Processing and Preservation*, *44*(11), Article e14849. https://doi.org/10.1111/jfpp.14849

Jafari, S., Ghalenoei, M., & Dehnad, D. (2017). Influence of spray drying on water solubility index, apparent density, and anthocyanin content of pomegranate juice powder. *Powder Technology*, *311*, 59-65. https://doi.org/10.1016/j.powtec.2017.01.070

Jittanit, W., Niti-Att, S., & Techanuntachikul, O. (2010). Study of spray drying of pineapple juice using maltodextrin as an adjunct. *Chiang Mai Journal of Science*, *36(3),* 498-506.

Jittanit, W., Chantara-In, M., Deying, T., & Ratanavong, W. (2011). Production of tamarind powder by drum dryer using maltodextrin and Arabic gum as adjuncts. *Songklanakarin Journal of Science and Technology*, *33*(1), 33-41.

Kwapinska, M., & Zbicinski, I. (2005). Prediction of final product properties after cocurrent spray drying. *Drying Technology*, *23*(8), 1653-1665. https://doi.org/10.1081/DRT-200065075

Lee, J. K. M., Taip, F. S., & Abdullah, Z. (2018). Effectiveness of additives in spray drying performance: A review. *Food Research*, *2*(6), 486-499. https://doi.org/10.26656/FR.2017.2(6).134

Li, T., Yang, X., Yu, Y., Si, X., Zhai, X., Zhang, H., Dong, W., Gao, C., & Xu, C. (2018). Domestication of wild tomato is accelerated by genome editing. *Nature Biotechnology*, *36*, 1160-1163. https://doi.org/10.1038/nbt.4273

Martínez-Huélamo, M., Vallverdú-Queralt, A., Di Lecce, G., Valderas-Martínez, P., Tulipani, S., Jáuregui, O., Escribano-Ferrer, E., Estruch, R, Illan, M., & Lamuela-Raventós, R. M. (2016). Bioavailability of tomato polyphenols is enhanced by processing and fat addition: Evidence from a randomized feeding trial. *Molecular Nutrition & Food Research*, *60*(7), 1578-1589. https:// doi.org/10.1002/mnfr.201500820

Muzaffar, K., Dinkarrao B. V., & Kumar, P. (2016) Optimization of spray drying conditions for production of quality pomegranate juice powder. *Cogent Food & Agriculture*, *2,* 1-9. https://doi.org/10.1080/2331 1932.2015.1127583

Muzaffar, K., Nayik, G. A., & Kumar, P. (2015). Stickiness problem associated with spray drying of sugar and acid rich foods: A mini review. *Journal of Nutrition & Food Sciences*, *S12:003,* 1-3. https://doi.org/10.4172/2155-9600.1000S12003

Nowak, D., & Jakubczyk, E. (2020). The freeze-drying of foods - The characteristic of the process course and the effect of its parameters on the physical properties of food materials. *Foods*, *9*(10), Article 1488. https://doi.org/10.3390/foods9101488

Oliveira, D. M., Clemente, E., & da Costa, J. M. (2012). Hygroscopic behavior and degree of caking of Grugru palm (*Acrocomia aculeata*) powder. *Journal of Food Science and Technology*, *51*(10), 2783-2789. https://doi.org/10.1007/s13197-012-0814-9

Osman, A. F. A., & Endut, N. (2009). Spray drying of roselle-pineapple juice effects of inlet temperature and maltodextrin on the physical properties. In *Second International Conference on Environmental and Computer Science* (pp. 267-270). IEEE Publishing. https://doi.org/10.1109/ICECS.2009.91

Patel, K. C., & Chen, X. D. (2008). Sensitivity analysis of the reaction engineering approach to modeling spray drying of whey proteins concentrate. *Drying Technology*, *26*(11), 1334-1343. https://doi.org/10.1080/07373930802331019

Phisut, N. (2012). Spray drying technique of fruit juice powder: Some factors influencing properties of product. *International Food Research Journal*, *19*(4), 1297-1306.

Phoungchandang, S., & Sertwasana, A. (2010). Spray-drying of ginger juice and physicochemical properties of ginger powders. *ScienceAsia*, *36,* 40-45. http://dx.doi.org/10.2306/scienceasia1513-1874.2010.36.040

Pourashouri, P., Shabanpour, B., Razavi, S., Jafari, S., Shabani, A., & Aubourg, S. (2014). Impact of wall materials on physicochemical properties of microencapsulated fish oil by spray drying. *Food and Bioprocess Technology*, *7,* 2354-2365. https://doi/10.1007/s11947-013-1241-2

Pu, H., Li, Z., Hui, J., & Raghavan, G. S. V. (2016). Effect of relative humidity on microwave drying of carrot. *Journal of Food Engineering*, *190*, 167-175. https://doi.org/10.1016/j.jfoodeng.2016.06.027

Raiola, A., Rigano, M. M., Calafiore, R., Frusciante, L., & Barone, A. (2014). Enhancing the health-promoting effects of tomato fruit for biofortified food. *Mediators of Inflammation*, *2014*, Article 139873. https://doi.org/10.1155/2014/139873

Sabhadinde, V. N. (2014). The physicochemical and storage properties of spray dried orange juice powder. *Indian Journal of Fundamental and Applied Life Sciences*, *4*(4), 153-159.

Shishir, M. R. I., & Chen, W. (2017). Trends of spray drying: A critical review on drying of fruit and vegetable juices. *Trends in Food Science and Technology*, *65*, 49-67. https://doi.org/10.1016/j.tifs.2017.05.006

Shrestha, A. K., Ua-arak, T., Adhikari, B. R., Howes, T., & Bhandari, B. R. (2007). Glass transition behavior of spray dried orange juice powder measures by differential scanning calorimetry (DSC) and thermal mechanical compression test (TMCT). *International Journal of Food Properties*, *10*(3), 661-673. https://doi.org/10.1080/10942910601109218

Souza, A. L. R., Hidalgo-Chávez, D. W., Pontes, S. M., Gomes, F. S., Cabral, L. M. C., & Tonon, R.V. (2018). Microencapsulation by spray drying of a lycopene-rich tomato concentrate: Characterization and stability. *LWT - Food Science and Technology*, *91*, 286-292. https://doi.org/10.1016/j.lwt.2018.01.053

Sudeep, G., Indira T. N., & Bhattacharya, S. (2010). Agglomeration of a model food powder: Effect of maltodextrin and gum Arabic dispersions on flow behavior and compacted mass. *Journal of Food Engineering*, *96*(2), 222-228. https://doi.org/10.1016/j.jfoodeng.2009.07.016

Szadzińska, J., Łechtańska, J., Kowalski, S. J., & Stasiak, M. (2017). The effect of high power airborne ultrasound and microwaves on convective drying effectiveness and quality of green pepper. *Ultrasonics Sonochemistry*, *34*, 531-539. https://doi.org/10.1016/j.ultsonch.2016.06.030

Tonon, V. R., Brabet, C., & Hubinger, M. (2008). Influence of process conditions on the physicochemical properties of acai powder produced by spray drying. *Journal of Food Engineering*, *88*(3), 411-418. http://dx.doi.org/10.1016/j.jfoodeng.2008.02.029

Tonon, V. R., Brabet, C., & Hubinger, M. (2011). Spray drying of acai juice: Effect of inlet temperature and type of carrier agent. *Journal of Food Processing and Preservation*, *35*(5), 691-700. http://dx.doi.org/10.1111/j.1745-4549.2011.00518.x

Uyar, R., Bedane, T. F., Erdogdu, F., Palazoglu, T. K., Farag, K. W., & Marra, F. (2015). Radio-frequency thawing of food products - A computational study. *Journal of Food Engineering*, *146*, 163-171. https://doi.org/10.1016/j.jfoodeng.2014.08.018

Wang, B., Timilsena, Y. P., Blanch, E., & Adhikari, B. (2017). Characteristics of bovine lactoferrin powders produced through spray and freeze-drying processes. *International Journal of Biological Macromolecules*, *95*, 985-994. https://doi.org/10.1016/j.ijbiomac.2016.10.087

Ziaforoughi, A., & Esfahani, J. A. (2016). A salient reduction of energy consumption and drying time in a novel PV-solar collector-assisted intermittent infrared dryer. *Solar Energy*, *136*, 428-436. https://doi.org/10.1016/j.solener.2016.07.025

Zielinska, M., & Michalska, A. (2016). Microwave-assisted drying of blueberry (*Vaccinium corymbosum* L.) fruits: Drying kinetics, polyphenols, anthocyanins, antioxidant capacity, colour and texture. *Food Chemistry*, *212*, 671-680. https://doi.org/10.1016/j.foodchem.2016.06.003

Zhu, C., Shoji, Y., McCray, S., Burke M, Hartman, C. E., Chichester, J. A., Breit, J., Yusibov, V., Chen, D., & Lal, M. (2014). Stabilization of HAC1 influenza vaccine by spray drying: Formulation development and process scale-up. *Pharmaceutical Research*, *31*, 3006-3018. https://doi.org/10.1007/s11095-014-1394-3

Pertanika J. Sci. & Technol. 31 (3): 1413 - 1437 (2023)

PERTANIKA JOURNALS

SCIENCE & TECHNOLOGY

Journal homepage: http://www.pertanika.upm.edu.my/

Review Article

Geochemistry of Foraminifera in the Marginal Seas of the Sunda Shelf: A Review

Aqilah Nur Shahruddin and Che Abd Rahim Mohamed*

Department of Earth Sciences and Environment, Faculty of Science and Technology, Universiti Kebangsaan Malaysia, 43600 UKM, Bangi, Malaysia

ABSTRACT

Foraminiferal geochemistry applies geochemical elements embedded in foraminiferal calcites through bioaccumulation to interpret and reconstruct past oceanic climate histories. Due to its extensive variability and abundance, foraminifera is the easiest to retrieve and the best indicator of marine productivity and ocean temporal changes. In this review, we discuss the development of foraminiferal geochemistry studies in Southeast Asia, analyzing its current status and potential areas to be developed, namely, the Sunda Shelf. The Sunda Shelf is one of the world's largest low-latitude shelves, bordered by marginal seas and sensitive to sea-level changes. The shelf response towards changes in ocean salinity affected the isotopic signals in foraminiferal calcites, which can indicate sea-level changes ideally. The Sunda Shelf has the potential to be developed as a study area for eustatic sea-level changes as it is located far from major glaciation centers; hence through this review, we aim to highlight the potential of exploring the application of geochemical elements in foraminifera as an indicator for sea-level changes. To date, literature on foraminiferal geochemistry in this region is very limited, thus inhibiting progress in such studies. A comprehensive summary of past studies in this region is provided to give a general overview of the direction of foraminiferal geochemistry studies and serve as guidelines for future research.

Keywords: *F*oraminifera, geochemical element, sea-level changes, Southeast Asia, Sunda Shelf

ARTICLE INFO

Article history:
Received: 29 April 2022
Accepted: 05 October 2022
Published: 31 March 2023

DOI: https://doi.org/10.47836/pjst.31.3.16

E-mail addresses:
aqilahnur@live.com (Aqilah Nur Shahruddin)
carmohd@ukm.edu.my (Che Abd Rahim Mohamed)
*Corresponding author

ISSN: 0128-7680
e-ISSN: 2231-8526

© Universiti Putra Malaysia Press

INTRODUCTION

Foraminifera is a member of a large phylum of amoeboid protists that can be found abundantly in marine sediments and usually produce tests or shells made up of calcium carbonate-shaped chambers. In micropalaeontology studies, foraminifera is often used to reconstruct past climate histories. Due to their extensive variability, abundance, and ability to evolve rapidly, foraminifera can also be considered the best indicator for biostratigraphy (Boltovskoy & Wright, 2013). According to the crystal latticework of foraminiferal calcites, almost 99% are composed of pure calcite, while minor and trace elements are accumulated as a substitute for calcium (Ca) or carbonate ions (CO_3^{2-}) to make up for the remaining 1% of the foraminiferal calcites (Lea, 1999). By accumulating trace elements onto the foraminifera calcites, scientists have been able to extract information on past climate histories based on geochemical proxy applications on foraminifera.

The earliest studies on geochemical proxy applications in foraminifera (e.g., Emiliani, 1955; Epstein et al., 1951, 1953; Shackleton, 1967; Urey, 1947) were mostly conducted on the stable carbon and oxygen isotope signatures of foraminifera, commonly expressed as $\delta^{18}O$ and $\delta^{13}C$. The findings from these studies established the utilization of carbon and oxygen isotopic records retrieved from measurements of fossil foraminifera calcites in response to inquiries regarding the evolution and history of ocean climates (Ravelo & Hillaire-Marcel, 2007). The stable isotopic values in foraminiferal calcites are usually influenced primarily by ocean processes such as water mass transport and mixing and secondarily by environmental effects such as microhabitats and carbonate ions (Rohling & Cooke, 1999). More geochemical proxies were developed to complement the stable isotopic analysis data, such as alkenone UK'_{37}, TEX 86, and trace element/calcium ratios of foraminiferal calcites to increase the accuracy of the data obtained from the stable isotopic analyses, more (Schmiedl, 2019). Recent studies have found that paired stable isotopic analyses and trace element/calcium ratio analyses could aid in monitoring sea-level changes, but this only applies to deep-sea dwelling foraminifera (Gupta, 2003). Paired Mg/Ca – $\delta^{18}O$ palaeothermometry of foraminifera, particularly on benthic species, enables the $\delta^{18}O$ paleotemperature equation to be solved for seawater $\delta^{18}O$ ($\delta^{18}O_{sw}$) as it may be related to global ice volume that can be associated with sea-level changes and Mg/Ca ratios acts as independent temperature proxy to estimate $\delta^{18}O_{sw}$ changes caused by ice-volume variations (Evans et al., 2016; Miller et al., 2020). Emiliani (1955) elucidated that the $\delta^{18}O_{sw}$ is greatly influenced by the global ice volume in which glacial ice has a large amount of ^{16}O stored in it while simultaneously the content of ^{18}O in oceanic water will be high. The waxing and waning of the ice will influence the oxygen isotopes, and the isotopic ratio changes indicating the foraminifera will record the sea level. Mg/Ca ratios will then discriminate the local freshwater effect from the global ice volume signal (Felder et al., 2022).

During the Paleogene period, short-term but dramatic environmental changes were detected through the utilization of high-resolution foraminifera isotopic analysis, $\delta^{13}C$, and $\delta^{18}O$, in which the former was used to detect variations in carbon contents and distributions while the latter is used to constrain the timing and scale of temperature and ice volume changes. The study evaluated the abrupt climatic transitions and found evidence from geochemical and sedimentological analyses suggesting two cases of climate extremes during the Paleogene and early Oligocene, accompanied by reorganizations in ocean circulation and major perturbations in marine productivity and the global carbon cycle (Zachos et al., 1993). This study provides an example of utilizing foraminiferal geochemistry to investigate past ocean climate histories.

In comparison, foraminiferal geochemistry in Southeast Asia has yet to be developed into an impactful research area. Regionally, publications in foraminiferal geochemistry were driven by their proximity to the Indo-Pacific Warm Pool (IPWP) and Intertropical Convergence Zone (ITCZ) and how these phenomena influenced foraminiferal geochemistry have only been based in Indonesia and the Philippines. The impact of these phenomena on the global climate could be reflected through data from the Mg/Ca ratio analyses that reported sea surface temperature (SST) variability during the early Holocene period (Haberle et al., 2004; Lo Giudice Cappelli et al., 2016). Other countries such as Thailand, Singapore, and Malaysia have limited contributions to foraminiferal geochemistry research, as most publications on foraminifera focus on foraminiferal ecology and distribution.

In this review, we discuss the development of foraminiferal geochemistry studies in Southeast Asia to provide a general outlook on this area of research. Furthermore, this review highlights the potential of exploring the application of foraminiferal geochemistry as an indicator for sea-level changes, particularly on the Sunda Shelf, due to its high sensitivity to variations in sea-level changes. Based on this gap in the scientific understanding of this area of study, this review is expected to create new ideas and opportunities for the future progress of foraminiferal geochemistry studies in this region.

STATUS OF FORAMINIFERAL STUDIES IN THE SOUTHEAST ASIA REGION

Western Southeast Asia (SEA) is situated on a pre-Mesozoic continental crust called the Sunda Shelf, consisting of a geologically stable continental crust. While, eastern SEA is situated on an oceanic crust. The Sunda Shelf consists of an area between the southern part of the Indo-China Peninsula, the Malay Peninsula, and the large islands of Sumatra, Borneo, and Java forming the south-western part of the semi-enclosed marginal South China Sea (SCS) basin and serving as a connection between the SCS and the Indian Ocean through the Malacca Straits (Szarek, 2001). Sea-level changes in the region have occurred on different magnitudes over thousand to a hundred million-year timescales and have

been categorized according to orders; the first-order represents the highest magnitude of sea-level changes at one hundred million-year timescales, and the fifth-order defines the lowest magnitude changes on ten thousand-year timescales. Tectonic activity in SEA occurs during temporal intervals that are too short and, therefore, cannot be considered as global third-order sequences, which usually correspond to rifting, thermal subsidence, and global eustatic sea-level changes (Gold, 2021). However, if simultaneous sea-level occurrences or trends are found in multiple basins, they will likely hold regional or global significance.

Additionally, the carbonate system in SEA is generally influenced by terrestrial runoff, monsoonal effects, and the Indonesian Throughflow Current (ITFC) in western SEA seas, while eastern SEA seas are commonly impacted by major nutrient upwelling and the El Niño-Southern Oscillation (ENSO) (Wilson, 2011). The changes in the carbonate chemistry of seawater could affect its carbon and oxygen isotopic values, as well as the trace element/calcium ratios, which can signal past changes in oceanic climate (Gray et al., 2018; Spero, 1998).

As mentioned earlier, the numbers of publications considering foraminiferal studies in Malaysia are scarce. Over the past 20 years, most publications have focused on foraminiferal distribution and ecology (Minhat et al., 2018; Parham et al., 2014). The reasons behind the low numbers of foraminiferal studies in Malaysia include the microscopic size of foraminifera, which makes their study difficult, a lack of knowledge of regional taxonomies, and financial constraints to sampling beyond the intertidal zone (Parham et al., 2014). Currently, references on regional taxonomies are incomplete and do not include several genera endemic to the region (Minhat et al., 2018). One of the earliest research attempts in Malaysia that applied foraminiferal geochemistry proxies successfully established a new SST record for the last 7200 years using sediment cores recovered off Sarawak waters (Woodson et al., 2017). The study by Woodson et al. (2017) can serve as evidence that foraminiferal studies can divert their focus from species distribution and ecology to foraminiferal geochemistry and initiate the generation of a new dataset of Malaysia's climate history. In our opinion, past studies have covered almost every aspect of the marine environment of the coastal waters of Malaysia, for instance, intertidal zones (Culver et al., 2015; Minhat et al., 2019; Satyanarayana et al., 2014; Suriadi et al., 2013) and coastal waters (Yahya et al., 2014). Therefore, a new shift in foraminifera studies could open up/initiate new research interests. Table 1 summarizes the foraminiferal studies conducted in Malaysia, which consists of 1 geochemistry study, 2 sea-level reconstruction studies, and 8 distribution studies detailing the locations, geographic or hydrographic characteristics, and methodologies used.

Similar to Malaysia, other countries like Thailand and Singapore have also had a common approach to foraminiferal research and have limited publications on the topic. It can be explained by Singapore's location, namely the Strait of Singapore, the second most

dense navigational traffic globally, where most foraminifera species do not prefer coastal water turbidity. It was reported that in the Strait of Singapore, the complicated geometry and varying bathymetry depth could cause higher tidal amplitude and currents, and turbidity at the straits would increase as an effect of the tidal current (Rusli, 2012). A recent publication by Martin et al. (2022) observed that the monsoon-driven currents impacted the pH in the strait caused by the remineralization of terrestrial dissolved organic carbon (DOC), which would have affected calcifying organisms, especially foraminifera. The study areas are classified into two colors according to their field of study to illustrate the discrepancy between foraminiferal ecology and geochemistry studies in the SEA region (Figure 1). It can be concluded that foraminiferal geochemistry is understudied in the region. Based on Figure 1, 31 study areas were recorded for foraminiferal ecology studies, while 17 were recorded for foraminiferal geochemistry. Most of the studies were conducted in areas that have prominent hydrographic characteristics. In contrast, foraminiferal ecological studies were more widespread comparatively, covering many ecosystems such as mangroves and open oceans.

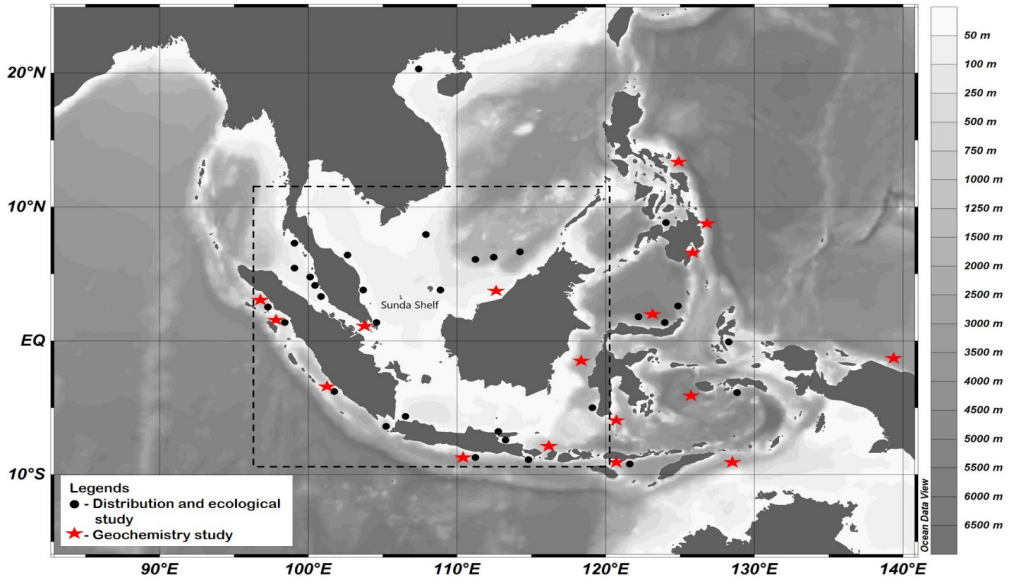

Figure 1. Visual representation of discrepancy between foraminiferal ecology and geochemistry studies in Southeast Asia. Sunda Shelf is located within the illustrated dashed-line box. Black circles represent distribution and ecological studies, while red stars represent geochemistry studies.

Contrary to its neighboring countries, studies in Indonesia and the Philippines have been conducted since the late 1990s. The findings could serve as guidelines for developing foraminiferal geochemistry studies in SEA. Indonesia has published the most articles regionally on foraminiferal research, comprising work on species' distribution or ecology and the application of geochemical proxies. The Philippines have also contributed

several publications on geochemical proxy research. Indonesia and the Philippines are geographically strategic for foraminiferal research due to their proximity to the IPWP and ITCZ. As the regional and monsoonal circulations (e.g., Indonesian Throughflow and Mindanao Current) surrounding the Indonesia and Philippines waters could affect the biogeochemical cycle of the study area, the foraminifera sensitivity to hydrological parameter changes is utilized by analyzing the stable calcite isotopes and trace elemental ratios.

Table 1
Summary of the foraminiferal studies conducted in Malaysia

Aspect of foraminiferal studies	Author(s)	Location	Geographic/ hydrographic characteristics	Methodology used
Geochemistry	Woodson et al. (2017)	Off Bintulu, Sarawak	East Asian Monsoonal influences Shallow continental shelf settings (Sunda Shelf)	Mg/Ca ratios on *Globigerinoides ruber* and *Globigerinoides sacculifer*
Sea-level constructions based on a foraminiferal assemblages transfer function	Minhat et al. (2016)	East coast Johor	Centre of the Sunda Shelf Monsoonal influences (Northeast and Southwest Monsoon)	Transfer function based on foraminiferal assemblages' data
Sea-level constructions based on a foraminiferal assemblages transfer function	Culver et al. (2015)	Setiu Wetland, Terengganu	El Nino-related changes affected coastal evolution Located on the inner part of Sundaland, a tectonically stable region	Transfer function based on foraminiferal assemblages' data
Distribution	Razak et al. (2022)	Sungai Kilim, Langkawi	Combination of several ecosystems such as mangrove swamps, limestone caves, lagoons, and estuaries	Species distribution using foraminiferal diversity indices (e.g., Shannon-Wiener and Fisher's alpha) Statistical correlation between a distribution and environmental parameters

Table 1 *(Continue)*

Aspect of foraminiferal studies	Author(s)	Location	Geographic/ hydrographic characteristics	Methodology used
Distribution	Minhat et al. (2021)	Northern Malacca Strait	Multiple ecosystems Monsoonal influences	Species distribution using foraminiferal diversity indices (e.g., Shannon-Wiener and Fisher's alpha) Cluster analysis on biozonation of foraminiferal assemblages Statistical correlation between a distribution and environmental parameters
Distribution and ecological indicator	Minhat et al. (2020)	Northern Malacca Strait	Study areas are subjected to river discharges	Species distribution using foraminiferal diversity indices (e.g., Shannon-Wiener and Fisher's alpha) Statistical correlation between a distribution and environmental parameters Foraminifera Stress Index
Distribution and composition	Minhat et al. (2019)	Northern Malacca Strait	3.9 m sediment core providing species composition and distribution data during Early Holocene	Raw foraminiferal count data Sediment grain analysis.

Table 1 *(Continue)*

Aspect of foraminiferal studies	Author(s)	Location	Geographic/ hydrographic characteristics	Methodology used
Distribution and abundance	Minhat et al. (2014)	Penang National Park, Penang	Monsoonal influences Sampling sites were based on anthropogenic activities in the area	Species distribution using foraminiferal diversity indices (e.g., Shannon-Wiener and Fisher's alpha) Cluster analysis Nutrient and grain-size analysis
Distribution	Yahya et al. (2014)	Penang National Park, Pemamg	Monsoonal influences Sampling sites were based on anthropogenic activities in the area	Species distribution using foraminiferal diversity indices (e.g., Shannon-Wiener and Fisher's alpha)
Distribution	Satyanarayana et al. (2014)	Kapar and Matang Mangrove Area	Mangrove areas that are strongly influenced by their location in the tropics	Faunal abundance using Bray-Curtis similarity Statistical correlation between a distribution and environmental parameters
Distribution and abundance	Suriadi et al. (2009)	Kelantan Delta	Exposed to strong northeasterly waves from the South China Sea during Northeast Monsoon.	Species distribution using foraminiferal diversity indices (e.g., Shannon-Wiener and Fisher's alpha) Faunal abundance using cluster analysis and non-metric Multi-Dimensional Scaling (nMDS)

Earlier studies by Ahmad et al. (1995) and Spooner et al. (2005) had noted monsoonal influence on foraminiferal $\delta^{18}O$ and implicated that the Banda Sea had undergone numerous changes in water stratigraphy and hydrographical parameters such as salinity through the past ~ 80 000 years. Other than that, the foraminiferal stable isotopic interpretations of the Southwest and West Indonesia had revealed that $\delta^{18}O$ corresponds well to SST during Southeast and Northwest Monsoon (SEM and NWM) and interspecies $\delta^{13}C$ values differences could potentially be used as a productivity proxy as $\delta^{13}C$ and productivity are inversely related (Mohtadi et al., 2007). The water mass mixing from upwelling and freshwater advection as reflected from trace elemental ratios Ba/Ca (Setiawan et al., 2017) are seen to affect the depth of deep chlorophyll maximum, which in turn influenced foraminiferal calcification depth and Mg/Ca-based temperature (Hollstein et al., 2018). In most literature reporting findings from study areas in Indonesia and the Philippines, regional and monsoonal circulations are often considered in analyzing the factors influencing foraminiferal geochemistry; hence the foraminiferal studies are often narrowed to only exploring these aspects, although foraminiferal geochemistry has the potential to elucidate regional sea-level changes.

The status of foraminiferal studies in SEA can be described as underdeveloped since not much information can be gathered from current publications on foraminiferal geochemistry. The factors mentioned above that have contributed to the scarcity of foraminiferal research in Malaysia could also affect other countries in the SEA region, resulting in the stagnant state of foraminiferal geochemistry studies.

FORAMINIFERA AS GEOCHEMICAL TOOLS

The increasing use of isotope and trace element geochemical proxies has contributed to enhancing the use of foraminifera in understanding oceanic climate histories. Over the past decades, there has been great progress in using geochemical proxies in foraminifera especially trace elemental and isotopic proxies. Among them is the application of coupled Mg/Ca palaeothermometry with $\delta^{18}O$ that can yield high-accuracy SST readings compared to other SST reading proxies (Katz et al., 2010; Lea, 2013) and to date, the development of geochemical proxies applied in foraminiferal carbonate tests have enabled us to reconstruct various parameters of past ocean climates (Table 2). Early publications in the SEA region focused on traditional proxies such as stable oxygen and carbon isotope analyses. However, for the past ten years, there has been a slow emergence of publications that have utilized trace elemental proxies (Figure 2).

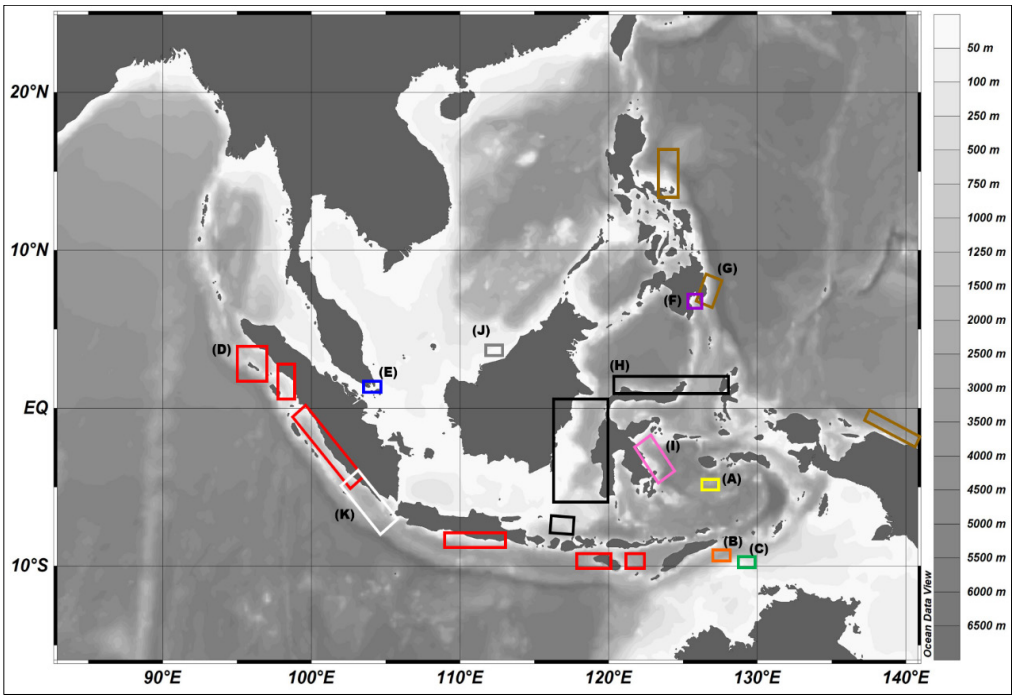

Figure 2. Map of Southeast Asia with bathymetry. The map is produced using Ocean Data View software (ODV). Bathymetry data was obtained from World Ocean Atlas 2018 from NOAA. Previously studied areas are denoted using alphabets with colored boxes for easier identification; note that multiple same-colored boxes represent studies that covered many areas. (A, yellow) Ahmad et al. (1995), (B, orange) Spooner et al. (2005), (C, green) Lo Giudice Cappelli et al. (2016), (D, red) Mohtadi et al. (2007), (E, blue) Michael I Bird et al. (2010), (F, purple) Fraser et al. (2015); (G, brown) Hollstein et al. (2017), (H, black) Zhang et al. (2016, 2019), (I, pink) Rosenthal et al. (2006), (J, grey) Woodson et al. (2017) and (K, white) Setiawan et al. (2017).

Before geochemical proxies were widely used for ocean climate reconstructions, transfer functions based on foraminiferal assemblages were commonly applied since the method does not require complicated procedures and can produce quantitative estimations that can be applied to reconstruct paleoenvironments (Jorissen et al., 2007). An attempt to estimate SST using FP-12E and SIMMAX was unsuccessful as the methods could not reflect true SST variations for the glacial southern SCS due to the amplification of glacial SST from the abnormally high abundance of *Pulleniatina Obliquiloculata* (Li et al., 2010). Infaunal foraminifera and water depth-related faunal shifts in foraminiferal assemblages could also affect paleoenvironmental interpretations (Minhat et al., 2016; Suriadi et al., 2009). Due to a large degree of uncertainty in the assemblage-based proxy, as previously reported, the methods have become less popular. Due to their accuracy, geochemical proxies such as stable isotopic and trace element/calcium ratio analyses have become a better option for past ocean climate reconstructions.

Table 2

Geochemical proxies used frequently in foraminiferal carbonate tests

Geochemical proxies	Measured parameters or uses	Reference
Stable isotopes		
$\delta^{18}O$	Ice volume Temperature reconstructions	Rohling et al. (2017) Salgueiro et al. (2020)
$\delta^{13}C$	Water mass circulation Marine productivity Chemostratigraphy	Mohtadi et al. (2007) Peeters et al. (2002)
Physical proxy		
Mg/Ca	Temperature reconstructions	Rosenthal and Linsley (2013)
Nutrient proxy		
Ba/Ca	Water mass circulation Distribution reflects biogeochemical cycling	Setiawan et al. (2017)
Cd/Ca	Water mass circulation Behavior mimics phosphate distribution	Ripperger et al. (2008)
Zn/Ca	Water mass circulation Carbonate saturation Behavior mimics silica distribution	Marr et al. (2013)

Isotopic Proxies

The use of stable isotopic proxies such as oxygen and carbon isotopes began in the mid-20th century and has played an important role in the development of paleoceanography. The geochemical composition of foraminiferal test calcite reflects numerous environmental variables that occur during calcification (Schmiedl, 2019), where simultaneous kinetic oxygen isotope fractionation is also occurring. While certain foraminifera species are in oxygen isotopic equilibrium with seawater when producing shells, some other species are in disequilibrium due to biological 'vital' effects. These effects do not imply the kinetic fractionation of carbon isotopes because the "equilibrating" pools of oxygen from seawater are far bigger than those of carbon (Ravelo & Hillaire-Marcel, 2007). Common strategies used while analyzing isotopic proxies are limited to only one species used to generate records to minimize the variability caused by specific biological effects. The studied species are selected from established ecological preferences and are generally predictable across locations with varying oceanographic conditions (Table 3). The strategy to pre-select the studied species based on ecological preferences is a good approach since the tested geochemical proxies established in other regions may not apply to a specific region, for example, the Sunda Shelf (Zhang et al., 2019).

Table 3

Foraminifera species used for stable isotopic proxies across Southeast Asia

Author(s)	Location	Isotopes	Foraminifera Species
Ahmad et al. (1995)	Banda Sea, Indonesia (Figure 2A)	$\delta^{18}O$	Planktonic*: Globigerinoides Ruber* Benthic*:* Uvigerina spp. & Cibicides spp.
Spooner et al. (2005)	Banda Sea, Indonesia (Figure 2B)	$\delta^{18}O$, $\delta^{13}C$	Planktonic: Globigerinoides Ruber
Mohtadi et al. (2007)	West and Southwest Indonesia (Figure 2C)	$\delta^{18}O$, $\delta^{13}C$	Planktonic: *Globigerinoides Ruber, Neogloboquadrina Dutertrei*
Bird et al. (2010)	Singapore (Figure 2D)	$\delta^{18}O$, $\delta^{13}C$	Benthic: Ammonia spp. & Elphidium spp.
Fraser et al. (2015)	Davao Gulf, Philippines (Figure 2E)	$\delta^{18}O$ coupled with $U_{37}^{K\prime}$ - temperature	Planktonic: Globigerinoides Ruber
Lo Giudice Cappelli et al. (2016)	Southern Timor Strait (Figure 2F)	$\delta^{18}O$ coupled with Mg/Ca ratio	Planktonic: *Globigerinoides Ruber* Benthic: Hoeglundina Elegans
Zhang et al. (2016)	Indonesia Throughflow (ITF) Region: Sulawesi Sea, Maluku Sea, Bali Sea, Flores Sea, and Timor Sea (Figure 2G)	$\delta^{18}O$, $\delta^{13}C$	Planktonic: *Globigerinoides ruber, Globigerinoides sacculifer, Pulleniatina obliquilocata, Neogloboquadrina dutertrei*
Hollstein et al. (2017)	Offshore Philippines and Papua New Guinea (Figure 2I)	$\delta^{18}O$ coupled with Mg/Ca ratio	Planktonic: *Globigerinoides ruber, Globigerinoides sacculifer, Globigerinoides elongatus, Pulleniatina Obliquilocata, Neogloboquadrina dutertrei, Globorotalia tumida*
Zhang et al. (2019)	Indonesia Throughflow (ITF) Region: Sulawesi Sea, Maluku Sea, Bali Sea, Flores Sea, and Timor Sea (Fig 2G)	$\delta^{18}O$ coupled with Mg/Ca ratio	Planktonic: *Globigerinoides ruber, Globigerinoides sacculifer, Pulleniatina obliquilocata, Neogloboquadrina dutertei*

Referring to the strategies and the table above, we can conclude that *Globigerinoides ruber* is the most preferred species for stable isotopic studies, given that it is a stress-tolerant species and has a cosmopolitan distribution across warm water regions, usually dwelling in the top ~30 m of the water column (Mulitza et al., 1997). The oxygen isotopic composition indicates that the species' life cycle is completed within the top surface layer of the water column (Anand et al., 2003; Richey et al., 2019; Venancio et al., 2017). Other species, such as *Globigerinoides sacculifer, Pulleniatina obliquilocata*, and *Neogloboquadrina dutertrei,* are often selected as studied species as most can be found in warm water regions. *G. sacculifer* is the most abundant species in tropical waters. However, it is sometimes replaced by *G. ruber,* which is more abundant in the sub-tropics and does not prefer higher salinity water than *G. sacculifer* (Haynes, 1981). Based on the calcification depth, *G. ruber* is classified as a mixed layer dweller, while both *P. obliquilocata* and *N. dutertrei* are thermocline dwellers; for *G. sacculifer,* it was recently reported that the species could usually be found dwelling at a depth ranging from the mixed layer to the upper thermocline (Zhang et al., 2019).

Considering past works in the literature on stable isotopic proxies in SEA, it can be concluded that other areas apart from Indonesia and the Philippines have been significantly understudied. The hydrological system in a marginal sea, for example, the SCS, is highly sensitive to changes on both continents and in oceans because it is at the intersection of river runoff and oceanic currents (Wang et al., 2014). Any slight changes in the water carbonate system would affect the isotopic composition of the foraminiferal calcites and would thus also affect the reliability of regional calibrations established from isotopic calibration studies (Hollstein et al., 2017; Dang et al., 2018).

Trace Elemental Proxies

The study of trace elemental proxies started late compared to isotopic proxies, with the earliest research dated around the 1960s. During shell precipitation, trace elements are integrated into the calcites with an abundance of 0.25% or less to make up the remaining 1% of the foraminiferal calcite composition (Lea, 1999). The application of trace elemental proxies can be classified into four main groups, namely, nutrient proxies (e.g., Cd and Ba), physical proxies (e.g., Mg, Sr, and F), chemical proxies (e.g., Sr and Nd isotopes), and diagenetic proxies (e.g., Mn). The seawater composition and environmental conditions control the trace elements in the foraminifera shells during calcification. The trace element compositions are then interpreted to determine the relationship between the concentration and physical conditions at the time of calcification.

Elemental ratios are reported relative to calcium to reduce any uncertainties associated with using multiple proxies since they are usually measured on the same phase with $\delta^{18}O$ and $\delta^{13}C$. We may thus use the strategy mentioned in the earlier sections to select a foraminifera

species as the study subject (Katz et al., 2010). Many earlier studies have applied the paired Mg/Ca, and $\delta^{18}O$ methods to reconstruct water temperatures and estimate relative changes in seawater. There is a good agreement between the three calibration methods, suggesting a similar temperature sensitivity for all planktic species. For benthic foraminifera, on the other hand, the paired Mg/Ca and $\delta^{18}O$ method can be utilized to study changes in bottom water temperature and $\delta^{18}O$ compositions in the seawater of the global ocean. The use of trace elements (e.g., Cd, Zn, and Ba) as nutrient proxies is most suitable because they have a much shorter residence time in seawater than physical proxies. Also, the oceanic behavior of the trace elements closely imitates that of the nutrients in the seawater, which can then be used to study nutrient paleaochemistry (Lea, 1999).

In the SEA region, the application of trace elements in foraminifera is currently understudied and, to date, only. The earliest work from this region (Figure 2I) was published around 15 years ago, studying the potential application of Mg/Ca and Sr/Ca ratios in benthic foraminifera *Hoeglundina elegans* to reconstruct bottom water temperatures (BWT), which discovered that aragonite saturation could influence the applicability of trace elemental ratios to reconstruct BWT or changes in carbonate ions (Rosenthal et al., 2006). Other than benthic and planktonic foraminifera, researchers have also tested the applicability of trace elemental proxies on reef foraminifera. Reef foraminifera *Operculina ammonoid*s could provide a more accurate foraminifera-based Mg/Ca_{sw} reconstruction and seawater Sr/Ca estimation (Evans et al., 2013). In recent years, more studies on trace elemental proxies in planktonic foraminifera have been conducted in Malaysia (Woodson et al., 2017) and Indonesia (Setiawan et al., 2017), and findings from these studies show promising outcomes for the use of trace elemental proxies in foraminifera (Figures 2K and 2J).

Overall, more study is needed to comprehensively assess this region's foraminiferal geochemistry and how it may be utilized to comprehend how the ocean evolves through time. It is critical to enhancing the understanding of oceanic temporal variations to grasp better the biogeochemical cycles influencing foraminiferal geochemistry. It will thus give us updated data on marine geochemical parameters at the microscale. The knowledge expansion on foraminiferal geochemistry would increase the comprehension of biogeochemical cycles and could potentially indicate sea-level changes that occurred on the studied timescale.

FORAMINIFERA AS AN INDICATOR OF SEA-LEVEL CHANGES

The Sunda Shelf is one of the world's largest low-latitude shelves. As marginal seas surround it, it is highly sensitive to sea-level changes (Wang et al., 2014). The shelf is also located in a far-field site, distant from major ice sheets and, theoretically, less affected by isostatic deformation (Clark & Mix, 2002). The total ice-sheet to-sea-level interaction can

thus be represented and provides a potential record of eustatic function (Lambeck et al., 2014; Stanford et al., 2011). Indeed, this region can be considered an ideal location for eustatic sea-level change studies. In a marginal basin such as the Sunda Shelf, responses to sea-level changes from the reduced exchange with the open ocean through narrow gateways lead to amplified changes in surface water salinity. It affects foraminiferal $\delta^{18}O$ values as these are dominated by sea-level changes, especially in a semi-isolated basin such as the southwestern SCS (Lea, 2013; Rohling et al., 2004; Schmiedl, 2019; Siddall et al., 2003).

Eustatic sea-level changes can be defined as a uniform shift in the height of the ocean surface that happens because of the input of meltwater into the ocean without gravitational and rotational effects, ocean dynamics, and solid Earth deformation (Farrell & Clark, 1976). Different opinions on the Holocene sea-level high stand in areas surrounding the southern SCS, particularly in the Sunda Shelf, have created debates mainly due to its complicated topography and lack of high-quality dating results (Wang et al., 2014). Investigating eustatic sea-level changes can be deemed important as it provides an independent method for calibrating the marine oxygen isotope record obtained from foraminifera calcites and the total volume of continental ice during the Last Glacial Maximum (LGM) (Whitehouse & Bradley, 2013). The current proposed sea-level high stand of +2.0 to +3.0 m from 6 to 4 kyr BP on the Sunda Shelf is questionable since the effects of differential crustal movements evident from Malaysian sea-level records (Hassan, 2002; Parham, 2016) suggest that the generalized sea-level curve (Figure 3) could be affected by palaeofluvial systems (Sathiamurthy & Rahman, 2017). It could influence the composition of stable isotopes in foraminiferal calcites.

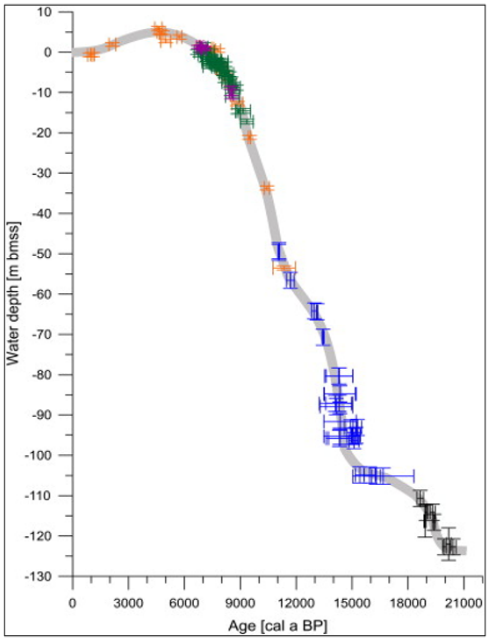

Figure 3. Temporal sea-level changes on the Sunda Shelf constructed from previously studied Sunda core regions (orange: Strait of Malacca; purple: Sungei Nipah and Pulau Semakau, Singapore; blue: Sunda Shelf; green: Singapore; black: Sunda Shelf). Graph illustrated based on a compilation of data from multiple sources (Geyh et al., 1979; Hanebuth et al., 2000; Hanebuth et al., 2009; Hawkes et al., 2007; Hesp et al., 1998). The figure is from Hanebuth et al. (2011).

While using corals as a proxy to reconstruct the sea-level changes is common in far-field study sites, it becomes problematic when interpreting glacio- and hydro-isostatic effects expressed by locally differential vertical movements of the Earth's crust (Lambeck et al., 2002) and dating precisions (Hanebuth et al., 2009). In

addition, caution needs to be exercised when using corals as a proxy due to the difficulty of verifying whether coral growth depth remains constant during all rates of sea-level rise. It can only provide discrete data rather than continuous estimations of sea-level changes (Rohling et al., 2017; Whitehouse & Bradley, 2013).

Previous studies have dismissed the potential of stable oxygen isotopes as a proxy to reconstruct sea-level curves due to their lower resolution over the past 30 cal kyr BP (Hanebuth et al., 2009). However, as the study of foraminiferal geochemistry advanced, Schmiedl (2019) reported that at present, quantitative reconstructions of past global sea-level changes had been refined by utilizing not only stable oxygen isotopic records of deep-sea benthic foraminifera from the open ocean (Waelbroeck et al., 2002) but also stable oxygen isotopic records of planktonic foraminifera from marginal basins (Grant et al., 2014; Rohling et al., 2014; Siddall et al., 2003). Additionally, it has been suggested that eustatic sea-level curves that reflect oxygen isotope trends are more reliable than relying solely on coastal onlaps. Continuing research into the oxygen isotopes of foraminifera deposited over geological time can provide high-resolution data on variations in past climate and global sea-level changes (Gold, 2021). These recent findings emphasize the potential suitability of foraminiferal geochemistry in sea-level studies, as it can provide more extensive data due to its variability.

Locally, Minhat et al. (2016) attempted to evaluate the potential of subtidal foraminifera on the east coast of peninsular Malaysia to reconstruct Holocene sea-level changes using a weighted-average (WA) transfer function. They determined that the WA transfer function resulted in a less robust prediction ($r^2_{jack} = 0.40$) with lower precision ($RMSEP_{jack} = \pm 5$ m), possibly affected by salinity and wave transport factors which were not included in the investigation. However, the findings suggest that subtidal foraminifera can be used to detect sea-level changes. The WA transfer function approach to reconstructing sea-level changes was also utilized by Culver et al. (2015) in their study in the Setiu Wetlands, Terengganu. In addition, another study employed a multi-proxy approach in the same study area to refine and extend the sea-level curves constructed by Bird et al. (2007). The study successfully linked sea-level records with benthic foraminifera's isotopic values, which suggested a period of no or minimal eustatic sea-level rise between 7800 to 7400 cal yr BP, separated by intervals of more rapid rise before and after. It thus provides crucial information that explains the hiatus in the rate of sea-level rise during 7.7 ka BP (Bird et al., 2010). The discovery was made possible as a result of the multi-proxy approach, including benthic foraminiferal isotopic analysis, demonstrating the need to develop similar studies for meaningful comparisons with existing data. It will subsequently facilitate a deeper understanding of eustatic sea-level changes in this region.

Due to the limited availability of publications on how foraminiferal geochemistry enables the reconstruction of eustatic sea-level changes in the SEA region, we are unable

to provide more sample studies as a reference. However, other far-field sites, such as the Japan Sea, have records of 20 planktonic foraminifera-derived $\delta^{18}O$ curves, of which almost all demonstrated extremely light $\delta^{18}O_{Planktonic\ Foraminifera}$ peaks during the LGM. In their study, Oba and Irino (2012) compared data from all 20 oxygen isotopic curves (e.g., Oba et al., 1980, 1991; Kido et al., 2007) and picked three to represent the Japan Sea $\delta^{18}O_{PF}$ curves. The representative curves were later compared to a standard oxygen isotopic curve obtained from a stacked $\delta^{18}O_{BF}$ curve of benthic foraminifera in 57 sediment cores collected from globally distributed sites (Lisiecki & Raymo, 2005). As a result, the eustatic sea level calculated for the LGM is 120 ±7 m below the present level based on a proportionate connection between the standard $\delta^{18}O$ curve in deep-sea cores and globally averaged sea-level changes. It suggests that the Japan Sea, although located far from the continental ice sheets, could provide essential insights into estimating eustatic sea levels. A comparison between the circumstances in the Japan Sea and the Sunda Shelf will therefore allow deductions on the use of isotopic proxies for sea-level determination to be made, with the availability of appropriate data. Further investigations are needed to provide new perspectives on the comprehension of eustatic sea-level change mechanisms in this region, as currently available data is still inadequate to understand the mechanisms at work fully.

CONCLUSION

As geologically advantaged countries, Indonesia and the Philippines lead the research on foraminiferal geochemistry in SEA. A few selected publications are highlighted in this paper. However, there is still a lack of information on the response of foraminifera toward the geochemical cycles in this region and how they can help reconstruct paleoenvironmental parameters. Most studies on foraminifera have focused on ecology and used foraminifera assemblage-based transfer functions to reconstruct sea-level changes and other oceanic parameters. Although this method is widely used, it can be affected by a large degree of uncertainty, hence defining the use of foraminiferal geochemical proxies as a better method for dealing with paleoenvironmental parameter reconstructions.

The Sunda Shelf provides an ideal site for reconstructing sea-level history. It is in a far-field site and has preserved a near-complete early history of sea-level changes during the last glaciation. Despite this, the oceanic climate histories of the Sunda Shelf are still relatively poorly understood. Hence, the research on foraminiferal geochemistry would contribute not only to the understanding of its climate history but also to the biogeochemical cycles that have occurred within it. Attempts to utilize geochemical proxies in foraminifera should be encouraged since the data obtained will help to combat coastal environmental issues in Southeast Asian countries and coastal cities that are surrounded by marginal seas and plagued with the risk of sea-level rise. Also, foraminifera-based climate research could complement the gaps in inter-disciplinary research, such as combining proxy

studies with numerical model simulations to create temperature projections based on the response of foraminifera toward rising SST. The strategic geographical location should be taken advantage of to explore more climate histories through accumulated records of foraminiferal calcites.

ACKNOWLEDGEMENTS

The authors would like to express their sincere gratitude to the members of the Marine Chemistry laboratory at the Faculty of Science and Technology, Universiti Kebangsaan Malaysia (UKM), for their assistance and support in ensuring this review's completion.

REFERENCES

Ahmad, S. M., Guichard, F., Hardjawidjaksana, K., Adisaputra, M. K., & Labeyrie, L. D. (1995). Late quaternary paleoceanography of the Banda Sea. *Marine Geology*, *122*(4), 385-397. https://doi.org/10.1016/0025-3227(94)00116-3

Anand, P., Elderfield, H., & Conte, M. H. (2003). Calibration of Mg/Ca thermometry in planktonic foraminifera from a sediment trap time series. *Paleoceanography*, *18*(2), Article 1050. https://doi.org/10.1029/2002pa000846

Bird, M. I., Fifield, L. K., Teh, T. S., Chang, C. H., Shirlaw, N., & Lambeck, K. (2007). An inflection in the rate of early mid-Holocene eustatic sea-level rise: A new sea-level curve from Singapore. *Estuarine, Coastal and Shelf Science*, *71*(3-4), 523-536. https://doi.org/10.1016/j.ecss.2006.07.004

Bird, M. I., Austin, W. E. N., Wurster, C. M., Fifield, L. K., Mojtahid, M., & Sargeant, C. (2010). Punctuated eustatic sea-level rise in the early mid-Holocene. *Geology*, *38*(9), 803-806. https://doi.org/10.1130/G31066.1

Boltovskoy, E., & Wright, R. C. (Eds.). (2013). *Recent Foraminifera*. Springer Science & Business Media. https://doi.org/https://doi.org/10.1007/978-94-017-2860-7

Clark, P. U., & Mix, A. C. (2002). Ice sheets and sea level of the last glacial maximum. *Quaternary Science Reviews*, *21*(1-3), 1-7. https://doi.org/10.1016/S0277-3791(01)00118-4

Culver, S. J., Leorri, E., Mallinson, D. J., Corbett, D. R., & Shazili, N. A. M. (2015). Recent coastal evolution and sea-level rise, Setiu Wetland, Peninsular Malaysia. *Palaeogeography, Palaeoclimatology, Palaeoecology*, *417*, 406-421.

Dang, H., Jian, Z., Wu, J., Bassinot, F., Wang, T., & Kissel, C. (2018). The calcification depth and Mg/Ca thermometry of *Pulleniatina obliquiloculata* in the tropical Indo-Pacific: A core-top study. *Marine Micropaleontology*, *145*, 28-40. https://doi.org/10.1016/j.marmicro.2018.11.001

Emiliani, C. (1955). Pleistocene temperatures. *The Journal of Geology*, *63*(6), 538-578. https://doi.org/10.1086/626295

Epstein, S., Buchsbaum, R., Lowenstam, H. A., & Urey, H. C. (1953). Revised carbonate-water isotopic temperature scale. *Bulletin of the Geological Society of America*, *64*(11), 1315-1326. https://doi.org/10.1130/0016-7606(1953)64[1315:RCITS]2.0.CO;2

Epstein, S., Buchsbaum, R., Lowenstam, H., & Urey, H. C. (1951). Carbonate-water isotopic temperature scale. *Bulletin of the Geological Society of America*, *62*(4), 417-426. https://doi.org/10.1130/0016-7606(1951)62[417:CITS]2.0.CO;2

Evans, D., Brierley, C., Raymo, M. E., Erez, J., & Müller, W. (2016). Planktic foraminifera shell chemistry response to seawater chemistry: Pliocene–Pleistocene seawater Mg/Ca, temperature and sea level change. *Earth and Planetary Science Letters*, *438*, 139-148. https://doi.org/https://doi.org/10.1016/j.epsl.2016.01.013

Evans, D., Müller, W., Oron, S., & Renema, W. (2013). Eocene seasonality and seawater alkaline earth reconstruction using shallow-dwelling large benthic foraminifera. *Earth and Planetary Science Letters*, *381*, 104-115. https://doi.org/10.1016/j.epsl.2013.08.035

Farrell, W. E., & Clark, J. A. (1976). On postglacial sea level. *Geophysical Journal of the Royal Astronomical Society*, *46*(3), 647-667. https://doi.org/10.1111/J.1365-246X.1976.TB01252.X

Felder, S., Sagawa, T., Greaves, M., Leng, M. J., Ikehara, K., Kimoto, K., Hasegawa, S., Wagner, T., & Henderson, A. C. G. (2022). Palaeoceanography of the Japan Sea across the Mid-Pleistocene transition: Insights from IODP exp. 346, site U1427. *Paleoceanography and Paleoclimatology*, *37*(1), Article e2021PA004236. https://doi.org/10.1029/2021PA004236

Fraser, N., Kuhnt, W., Holbourn, A., Bolliet, T., Andersen, N., Blanz, T., & Beaufort, L. (2015). Precipitation variability within the West Pacific Warm Pool over the past 120 ka: Evidence from the Davao Gulf, southern Philippines. *Paleoceanography*, *29*(11), 1094-1110. https://doi.org/10.1002/2013PA002599

Geyh, M. A., Kudrass, H. R., & Streif, H. (1979). Sea-level changes during the late Pleistocene and Holocene in the Strait of Malacca. In *Nature* (Vol. 278, Issue 5703, pp. 441-443). Nature Publishing Group. https://doi.org/10.1038/278441a0

Gold, D. P. (2021). Sea-level change in geological time. In D. Alderton & S. Elias (Eds.), *Encyclopedia of Geology* (2nd ed., pp. 412-434). Elsevier. https://doi.org/10.1016/b978-0-12-409548-9.11899-8

Grant, K. M., Rohling, E. J., Bronk Ramsey, C., Cheng, H., Edwards, R. L., Florindo, F., Heslop, D., Marra, F., Roberts, A. P., Tamisiea, M. E., & Williams, F. (2014). Sea-level variability over five glacial cycles. *Nature Communications*, *5*(1), 1-9. https://doi.org/10.1038/ncomms6076

Gray, W. R., Weldeab, S., Lea, D. W., Rosenthal, Y., Gruber, N., Donner, B., & Fischer, G. (2018). The effects of temperature, salinity, and the carbonate system on Mg/Ca in Globigerinoides ruber (white): A global sediment trap calibration. *Earth and Planetary Science Letters*, *482*, 607-620. https://doi.org/10.1016/j.epsl.2017.11.026

Gupta, B. K. S. (Ed.). (2003). *Modern Foraminifera*. Springer. https://doi.org/10.1007/0-306-48104-9

Haberle, S., Gagan, M. K., Hendy, E. J., Haberle, S. G., & Hantoro, W. S. (2004). Post-glacial evolution of the Indo-Pacific warm pool and El Nino-Southern oscillation. *Quaternary International*, *118-119*, 127-143. https://doi.org/10.1016/S1040-6182(03)00134-4

Hanebuth, T. J. J., Stattegger, K., & Bojanowski, A. (2009). Termination of the last glacial maximum sea-level lowstand: The Sunda-Shelf data revisited. *Global and Planetary Change*, *66*(1–2), 76-84. https://doi.org/10.1016/j.gloplacha.2008.03.011

Hanebuth, T., Stattegger, K., & Grootes, P. M. (2000). Rapid flooding of the Sunda Shelf: A late-glacial sea-level record. *Science*, *288*(5468), 1033-1035. https://doi.org/10.1126/science.288.5468.1033

Hanebuth, T. J.J., Voris, H. K., Yokoyama, Y., Saito, Y., & Okuno, J. (2011). Formation and fate of sedimentary depocentres on Southeast Asia's Sunda Shelf over the past sea-level cycle and biogeographic implications. *Earth-Science Reviews*, *104*(1-3), 92-110. https://doi.org/10.1016/J.EARSCIREV.2010.09.006

Hassan, K. (2002). Holocene sea level changes in Peninsular Malaysia. *Bulletin of the Geological Society of Malaysia*, *45*, 301-308. https://doi.org/10.7186/BGSM45200246

Hawkes, A. D., Bird, M., Cowie, S., Grundy-Warr, C., Horton, B. P., Shau Hwai, A. T., Law, L., Macgregor, C., Nott, J., Ong, J. E., Rigg, J., Robinson, R., Tan-Mullins, M., Sa, T. T., Yasin, Z., & Aik, L. W. (2007). Sediments deposited by the 2004 Indian Ocean Tsunami along the Malaysia-Thailand Peninsula. *Marine Geology*, *242*(1-3), 169-190. https://doi.org/10.1016/j.margeo.2007.02.017

Haynes, J. R. (Ed.). (1981). *Foraminifera*. Palgrave Macmillan UK. https://doi.org/10.1007/978-1-349-05397-1

Hesp, P. A., Hung, C. C., Hilton, M., Ming, C. L., & Turner, I. M. (1998). A first tentative Holocene sea-level curve for Singapore. *Journal of Coastal Research*, *14*(1), 308-314. https://www.jstor.org/stable/4298779

Hollstein, M., Mohtadi, M., Rosenthal, Y., Moffa Sanchez, P., Oppo, D., Martínez Méndez, G., Steinke, S., & Hebbeln, D. (2017). Stable oxygen isotopes and Mg/Ca in planktic foraminifera from modern surface sediments of the Western Pacific Warm Pool: Implications for thermocline reconstructions. *Paleoceanography*, *32*(11), 1174-1194. https://doi.org/10.1002/2017PA003122

Hollstein, M., Mohtadi, M., Rosenthal, Y., Prange, M., Oppo, D. W., Martínez Méndez, G., Tachikawa, K., Moffa Sanchez, P., Steinke, S., & Hebbeln, D. (2018). Variations in Western Pacific Warm Pool surface and thermocline conditions over the past 110,000 years: Forcing mechanisms and implications for the glacial Walker circulation. *Quaternary Science Reviews*, *201*, 429-445. https://doi.org/10.1016/j.quascirev.2018.10.030

Jorissen, F. J., Fontanier, C., & Thomas, E. (2007). Chapter seven paleoceanographical proxies based on deep-sea benthic foraminiferal assemblage characteristics. *Developments in Marine Geology, 1*, 263-325. https://doi.org/10.1016/S1572-5480(07)01012-3

Katz, M. E., Cramer, B. S., Franzese, A., Hönisch, B., Miller, K. G., Rosenthal, Y., & Wright, J. D. (2010). Traditional and emerging geochemical proxies in foraminifera. *Journal of Foraminiferal Research*, *40*(2), 165-192. https://doi.org/10.2113/gsjfr.40.2.165

Kido, Y., Minami, I., Tada, R., Fujine, K., Irino, T., Ikehara, K., & Chun, J. H. (2007). Orbital-scale stratigraphy and high-resolution analysis of biogenic components and deep-water oxygenation conditions in the Japan Sea during the last 640 kyr. *Palaeogeography, Palaeoclimatology, Palaeoecology*, *247*(1-2), 32-49. https://doi.org/10.1016/j.palaeo.2006.11.020

Lambeck, K., Rouby, H., Purcell, A., Sun, Y., & Sambridge, M. (2014). Sea level and global ice volumes from the last glacial maximum to the Holocene. *Proceedings of the National Academy of Sciences, 111*(43), 15296-15303. https://doi.org/10.1073/pnas.1411762111

Lambeck, K., Yokoyama, Y., & Purcell, T. (2002). Into and out of the last glacial maximum: Sea-level change during oxygen isotope stages 3 and 2. *Quaternary Science Reviews*, *21*(1-3), 343-360. https://doi.org/10.1016/S0277-3791(01)00071-3

Lea, D. W. (2013). Elemental and isotopic proxies of past ocean temperatures. In H. D. Holland & K. K. Turekian (Eds.), *Treatise on Geochemistry: Second Edition* (Vol. 8, pp. 373-397). Elsevier. https://doi.org/10.1016/B978-0-08-095975-7.00614-8

Lea, D. W. (1999). Trace elements in foraminiferal calcite. In B. K. S. Gupta (Ed.), *Modern Foraminifera* (pp. 259-277). Springer Science & Business Media. https://doi.org/10.1007/0-306-48104-9_15

Li, Q., Zheng, F., Chen, M., Xiang, R., Qiao, P., Shao, L., & Cheng, X. (2010). Glacial paleoceanography off the mouth of the Mekong River, southern South China Sea, during the last 500ka. *Quaternary Research*, *73*(3), 563-572. https://doi.org/10.1016/j.yqres.2010.03.003

Lisiecki, L. E., & Raymo, M. E. (2005). A Pliocene-Pleistocene stack of 57 globally distributed benthic δ 18O records. *Paleoceanography*, *20*(1), 1-17. https://doi.org/10.1029/2004PA001071

Lo Giudice Cappelli, E., Holbourn, A., Kuhnt, W., & Regenberg, M. (2016). Changes in Timor Strait hydrology and thermocline structure during the past 130 ka. *Palaeogeography, Palaeoclimatology, Palaeoecology*, *462*, 112-124. https://doi.org/10.1016/j.palaeo.2016.09.010

Marr, J. P., Carter, L., Bostock, H. C., Bolton, A., Smith, E., Marr, C., Carter, L., Bostock, H. C., Bolton, A., & Smith, E. (2013). Southwest Pacific Ocean response to a warming world: Using Mg/Ca, Zn/Ca, and Mn/Ca in foraminifera to track surface ocean water masses during the last deglaciation. *Paleoceanography*, *28*(2), 347-362. https://doi.org/10.1002/PALO.20032

Martin, P., Moynihan, M. A., Chen, S., Woo, O. Y., Zhou, Y., Nichols, R. S., Chang, K. Y. W., Tan, A. S. Y., Chen, Y. H., Ren, H., & Chen, M. (2022). Monsoon-driven biogeochemical dynamics in an equatorial shelf sea: Time-series observations in the Singapore Strait. *Estuarine, Coastal and Shelf Science*, *270*, Article 107855. https://doi.org/https://doi.org/10.1016/j.ecss.2022.107855

Miller, K. G., Browning, J. V., John Schmelz, W., Kopp, R. E., Mountain, G. S., & Wright, J. D. (2020). Cenozoic sea-level and cryospheric evolution from deep-sea geochemical and continental margin records. *Science Advances*, *6*(20), Article eaaz1346.

Minhat, F. I., Yahya, K., Talib, A., & Ahmad, O. (2014). Benthic foraminiferal distributions as bioindicators in coastal waters of Penang National Park, Malaysia. *Journal of Foraminiferal Research*, *44*(2), 143-150. https://doi.org/10.2113/GSJFR.44.2.143

Minhat, F. I., Ghandhi, S. M., Ahzan, N. S. M., Haq, N. A., Manaf, O. A. R. A., Sabohi, S. M., Lee, L. H., Akhir, M. F., & Abdullah, M. M. (2021). The occurrence and distribution of benthic foraminifera in tropical waters along the Strait of Malacca. *Frontiers in Marine Science*, *8*, Article 647531. https://doi.org/10.3389/FMARS.2021.647531

Minhat, F. I., Husain, M. L., Satyanarayana, B., Sulaiman, A., & Hasan, S. S. (2018). Current status of modern foraminiferal research in Peninsular and East Malaysia. *Journal of Sustainability Science and Management*, *13*(5), 75-84.

Minhat, F. I., Husain, M. L., & Sulaiman, A. (2019). Species composition and distribution data of benthic foraminifera from the Straits of Malacca during the early Holocene. *Data in Brief*, *25*, Article 104214.

Minhat, F. I., Satyanarayana, B., Husain, M. L., & Rajan, V. V. V. (2016). Modern benthic foraminifera in subtidal waters of Johor: Implications for holocene sea-level change on the east coast of Peninsular Malaysia. *Journal of Foraminiferal Research*, *46*(4), 347-357. https://doi.org/10.2113/gsjfr.46.4.347

Minhat, F. I., Shaari, H., Razak, N. S. A., Satyanarayana, B., Saelan, W. N. W., Yusoff, N. M., & Husain, M. L. (2020). Evaluating performance of foraminifera stress index as tropical-water monitoring tool in Strait of Malacca. *Ecological Indicators*, *111*, Article 106032. https://doi.org/10.1016/j.ecolind.2019.106032

Mohtadi, M., Max, L., Hebbeln, D., Baumgart, A., Krück, N., & Jennerjahn, T. (2007). Modern environmental conditions recorded in surface sediment samples off W and SW Indonesia: Planktonic foraminifera and biogenic compounds analyses. *Marine Micropaleontology*, *65*(1-2), 96-112. https://doi.org/10.1016/j.marmicro.2007.06.004

Mulitza, S., Dürkoop, A., Hale, W., Wefer, G., & Niebler, H. S. (1997). Planktonic foraminifera as recorders of past surface-water stratification. *Geology*, *25*(4), 335-338. https://doi.org/10.1130/0091-7613(1997)025<0335:PFAROP>2.3.CO;2

Oba, T., Kato, M., Kitazato, H., Koizumi, I., Omura, A., Sakai, T., & Takayama, T. (1991). Paleoenvironmental Changes in the Japan Sea During the Last 85,000 Years. *Paleoceanography*, *6*(4), 499-518. https://doi.org/10.1029/91PA00560

Oba, T., Horibe, Y., & Kitazato, H. (1980). Analysis of the palaeoenvironment since the last glacial age based on the two cores from the Japan Sea. *Kokogaku to Shizen Kagaku*, *13*, 31-49.

Oba, T., & Irino, T. (2012). Sea level at the last glacial maximum, constrained by oxygen isotopic curves of planktonic foraminifera in the Japan Sea. *Journal of Quaternary Science*, *27*(9), 941-947. https://doi.org/10.1002/jqs.2585

Parham, P. R. (2016). Late cenozoic relative sea-level highstand record from peninsular malaysia and Malaysian borneo: Implications for vertical crustal movements. *Bulletin of the Geological Society of Malaysia*, *62*, 91-115. https://doi.org/10.7186/BGSM62201612

Parham, P. R., Minhat, F. I., Husain, M. L., & Satyanarayana, B. (2014). *Review of foraminiferal studies in Nearshore Areas, Peninsular Malaysia*. ResearchGate. https://www.researchgate.net/publication/280690887

Peeters, F. J. C., Brummer, G. J. A., & Ganssen, G. (2002). The effect of upwelling on the distribution and stable isotope composition of Globigerina bulloides and Globigerinoides ruber (*Planktic foraminifera*) in modern surface waters of the NW Arabian Sea. *Global and Planetary Change*, *34*(3-4), 269-291. https://doi.org/10.1016/S0921-8181(02)00120-0

Ravelo, A. C., & Hillaire-Marcel, C. (2007). The use of oxygen and carbon isotopes of foraminifera in paleoceanography. *Developments in Marine Geology*, *1*, 735-764. https://doi.org/10.1016/S1572-5480(07)01023-8

Razak, N., Shaari, H., Minhat, F., Ariffin, E., & Shariful, F. (2022). *Benthic foraminifera as environmental indicators in the lagoon and mangrove environments of Langkawi, Malaysia*. Research Square. https://doi.org/10.21203/rs.3.rs-1484518/v1

Richey, J. N., Thirumalai, K., Khider, D., Reynolds, C. E., Partin, J. W., & Quinn, T. M. (2019). Considerations for globigerinoides ruber (white and pink) paleoceanography: Comprehensive insights from a long-running sediment trap. *Paleoceanography and Paleoclimatology*, *34*(3), 353-373. https://doi.org/10.1029/2018PA003417

Ripperger, S., Schiebel, R., Rehkämper, M., & Halliday, A. N. (2008). Cd/Ca ratios of in situ collected planktonic foraminiferal tests. *Paleoceanography*, *23*, Article 3209. https://doi.org/10.1029/2007PA001524ï

Rohling, E. J., Foster, G. L., Grant, K. M., Marino, G., Roberts, A. P., Tamisiea, M. E., & Williams, F. (2014). Sea-level and deep-sea-temperature variability over the past 5.3 million years. *Nature*, *508*(7497), 477-482. https://doi.org/10.1038/nature13230

Rohling, E J, Sprovieri, M., Cane, T., Casford, J. S. L., Cooke, S., Bouloubassi, I., Emeis, K. C., Schiebel, R., Rogerson, M., Hayes, A., Jorissen, F. J., & Kroon, D. (2004). Reconstructing past planktic foraminiferal habitats using stable isotope data: A case history for Mediterranean sapropel S5. *Marine Micropaleontology*, *50*(1-2), 89-123. https://doi.org/10.1016/S0377-8398(03)00068-9

Rohling, E. J., & Cooke, S. (1999). Stable oxygen and carbon isotopes in foraminiferal carbonate shells. In B. K. S. Gupta (Ed.), *Modern Foraminifera* (pp. 239-258). Kluwer Academic Publishers. https://doi.org/10.1007/0-306-48104-9_14

Rohling, E. J., Hibbert, F. D., Williams, F. H., Grant, K. M., Marino, G., Foster, G. L., Hennekam, R., de Lange, G. J., Roberts, A. P., Yu, J., Webster, J. M., & Yokoyama, Y. (2017). Differences between the last two glacial maxima and implications for ice-sheet, δ18O, and sea-level reconstructions. *Quaternary Science Reviews*, *176*, 1-28. https://doi.org/10.1016/J.QUASCIREV.2017.09.009

Rosenthal, Y., Lear, C. H., Oppo, D. W., & Linsley, B. K. (2006). Temperature and carbonate ion effects on Mg/Ca and Sr/Ca ratios in benthic foraminifera: Aragonitic species Hoeglundina elegans. *Paleoceanography*, *21*(1), 1-14. https://doi.org/10.1029/2005PA001158

Rosenthal, Y., & Linsley, B. (2013). Mg/Ca and Sr/Ca Paleothermometry from Calcareous Marine Fossils. In S. A. Elias & C. J. Mock (Eds.), *Encyclopedia of Quaternary Science: Second Edition* (pp. 871-883). Elsevier. https://doi.org/10.1016/B978-0-444-53643-3.00290-9

Rusli, M. H. B. M. (2012). Protecting vital sea lines of communication: A study of the proposed designation of the Straits of Malacca and Singapore as a particularly sensitive sea area. *Ocean & Coastal Management*, *57*, 79-94. https://doi.org/https://doi.org/10.1016/j.ocecoaman.2011.12.003

Salgueiro, E., Voelker, A. H. L., Martin, P. A., Rodrigues, T., Zúñiga, D., Froján, M., de la Granda, F., Villacieros-Robineau, N., Alonso-Pérez, F., Alberto, A., Rebotim, A., González-Álvarez, R., Castro, C. G., & Abrantes, F. (2020). δ18O and Mg/Ca Thermometry in Planktonic Foraminifera: A Multiproxy Approach Toward Tracing Coastal Upwelling Dynamics. *Paleoceanography and Paleoclimatology*, *35*(2), Article e2019PA003726. https://doi.org/10.1029/2019PA003726

Sathiamurthy, E., & Rahman, M. (2017). Late Quaternary paleo fluvial system research of Sunda Shelf: A review. *Bulletin of the Geological Society of Malaysia*, *64*, 81-92.

Satyanarayana, B., Husain, M. L., Ibrahim, R., Ibrahim, S., & Dahdouh-Guebas, F. (2014). Foraminiferal distribution and association patterns in the mangrove sediments of Kapar and Matang, West Peninsular Malaysia. *Journal of Sustainability Science and Management*, *9*, 32-48.

Schmiedl, G. (2019). *Use of Foraminifera in Climate Science*. Oxford University Press. https://doi.org/10.1093/acrefore/9780190228620.013.735

Setiawan, R. Y., Wirasatriya, A., Shaari, H., Setyobudi, E., & Rachman, F. (2017). Assessing the Reliability of planktic foraminifera Ba/Ca as a proxy for salinity off the Sunda Strait. *Ilmu Kelautan: Indonesian Journal of Marine Sciences*, *22*(4), 201-212. https://doi.org/10.14710/ik.ijms.22.4.201-212

Shackleton, N. (1967). Oxygen isotope analyses and pleistocene temperatures re-assessed. *Nature*, *215*(5096), 15-17. https://doi.org/10.1038/215015a0

Siddall, M., Rohling, E. J., Almogi-Labin, A., Hemleben, C., Meischner, D., Schmelzer, I., & Smeed, D. A. (2003). Sea-level fluctuations during the last glacial cycle. *Nature*, *423*(6942), 853-858. https://doi.org/10.1038/nature01690

Spero, H. J. (1998). Life history and stable isotope geochemistry of planktonic foraminifera. *The Paleontological Society Papers*, *4*, 7-36. https://doi.org/10.1017/s1089332600000383

Spooner, M. I., Barrows, T. T., De Deckker, P., & Paterne, M. (2005). Palaeoceanography of the Banda Sea, and Late Pleistocene initiation of the Northwest Monsoon. *Global and Planetary Change*, *49*(1-2), 28-46. https://doi.org/10.1016/j.gloplacha.2005.05.002

Stanford, J. D., Hemingway, R., Rohling, E. J., Challenor, P. G., Medina-Elizalde, M., & Lester, A. J. (2011). Sea-level probability for the last deglaciation: A statistical analysis of far-field records. *Global and Planetary Change*, *79*(3-4), 193-203. https://doi.org/10.1016/j.gloplacha.2010.11.002

Suriadi, R., Parham, P. R., Sapon, N., Satyanarayana, B., & Husain, M. L. (2013, June 8-9). Sub-surface and infaunal foraminifera of Kelantan Delta, east coast of Peninsular Malaysia: Their potential for interpretation of sea level change. In *National Geoscience Conference* (pp. 1-17). Ipoh, Malaysia.

Szarek, R. (2001). *Biodiversity and Biogeography of Recent Benthic Foraminiferal Assemblages in the South-Western South China Sea (Sunda Shelf)*. Christian-Albrechts Universität Kiel.

Urey, H. C. (1947). The thermodynamic properties of isotopic substances. *Journal of the Chemical Society (Resumed)*, *0*, 562-581. https://doi.org/10.1039/jr9470000562

Venancio, I. M., Belem, A. L., Santos, T. P., Lessa, D. O., Albuquerque, A. L. S., Mulitza, S., Schulz, M., & Kucera, M. (2017). Calcification depths of planktonic foraminifera from the southwestern Atlantic derived from oxygen isotope analyses of sediment trap material. *Marine Micropaleontology*, *136*, 37-50. https://doi.org/10.1016/J.MARMICRO.2017.08.006

Waelbroeck, C., Labeyrie, L., Michel, E., Duplessy, J. C., McManus, J. F., Lambeck, K., Balbon, E., & Labracherie, M. (2002). Sea-level and deep water temperature changes derived from benthic foraminifera isotopic records. *Quaternary Science Reviews*, *21*(1-3), 295-305. https://doi.org/10.1016/S0277-3791(01)00101-9

Wang, P., Li, Q., & Li, C. F. (2014). Paleoceanography and sea-level changes. In P. Wang, Q. Li, & C. F. Li (Eds.), *Developments in Marine Geology* (Vol. 6, pp. 469-570). Elsevier. https://doi.org/10.1016/B978-0-444-59388-7.00006-8

Whitehouse, P. L., & Bradley, S. L. (2013). Eustatic sea-level changes since the last glacial maximum. In S. Elias & C. Mock (Eds.), *Encyclopedia of Quaternary Science: Second Edition* (pp. 439-451). Elsevier. https://doi.org/10.1016/B978-0-444-53643-3.00131-X

Wilson, M. E. J. (2011). SE Asian carbonates: Tools for evaluating environmental and climatic change in equatorial tropics over the last 50 million years. *Geological Society Special Publication*, *355*(1), 347-372. https://doi.org/10.1144/SP355.18

Woodson, A. L., Leorri, E., Culver, S. J., Mallinson, D. J., Parham, P. R., Thunell, R. C., Vijayan, V. R., & Curtis, S. (2017). Sea-surface temperatures for the last 7200 years from the eastern Sunda Shelf, South China Sea: Climatic inferences from planktonic foraminiferal Mg/Ca ratios. *Quaternary Science Reviews*, *165*, 13-24.

Yahya, K., Shuib, S., Minhat, F. I., Ahmad, O., & Talib, A. (2014). The distribution of benthic foraminiferal assemblages in the north-west coastal region of Malacca Straits, Malaysia. *Journal of Coastal Life Medicine*, *2*(10), 784-790. https://doi.org/10.12980/jclm.2.2014jclm-2014-0061

Zachos, J. C., Lohmann, K. C., Walker, J. C. G., & Wise, S. W. (1993). Abrupt climate change and transient climates during the Paleogene: A marine perspective. *Journal of Geology*, *101*(2), 191-213. https://doi.org/10.1086/648216

Zhang, P., Zuraida, R., Rosenthal, Y., Holbourn, A., Kuhnt, W., & Xu, J. (2019). Geochemical characteristics from tests of four modern planktonic foraminiferal species in the Indonesian Throughflow region and their implications. *Geoscience Frontiers*, *10*(2), 505-516. https://doi.org/https://doi.org/10.1016/j.gsf.2018.01.011

Zhang, P., Zuraida, R., Xu, J., & Yang, C. (2016). Stable carbon and oxygen isotopes of four planktonic foraminiferal species from core-top sediments of the Indonesian throughflow region and their significance. *Acta Oceanologica Sinica*, *35*(10), 63-75. https://doi.org/10.1007/s13131-016-0890-1

Pertanika J. Sci. & Technol. 31 (3): 1439 - 1451 (2023)

SCIENCE & TECHNOLOGY

Journal homepage: http://www.pertanika.upm.edu.my/

Railway Urbanozems: Interrelation of Physicochemical and Integral Environmental Indicators

Tatyana Anatolyevna Adamovich and Anna Sergeyevna Olkova*

Vyatka State University, 36 Moskovskaya St, Kirov, 610000, Russian Federation

ABSTRACT

Urbanozems with typical pollution are formed along railways: heavy metals (HM), oil products, anthropogenic organic matter. Depending on the natural zone and intensity of the leaching regime, the accumulated pollution can have a different effect on the integral environmental indicators of soils – the toxicity and enzymatic activity. The aim of the work was to determine the influence of the railway on the physicochemical characteristics of adjacent urbanozems that are formed in the southern taiga zone and to find out the interrelation of these indicators with the toxicity and catalase activity of the soil. Samples of urbanozems were taken from the surface layer of 0-10 cm at the distance of 50 m west and east of the railway and at the distance of 100, 500, 1000 m of it (east). The pH, content of organic matter, humus, ammonium nitrogen, mobile forms of HM, mortality for *Daphnia magna* Straus, influence on bioluminescence of *Escherichia coli* Migula, and the catalase activity were determined in the samples. It was shown that the levels of toxicity and the activity of catalase are strongly related to the distance from the railway: Pearson's coefficients (r) were -0.53 (*D. magna*), -0.69 (*E. coli*), 0.95 (catalase). However, the interrelation between the total pollution index (TPI) of metals and integral indicators is lower: r=0.50 for the pair "*D. magna* – TPI", r=0.42 for "*E. coli* – TPI", r=0.19 for "catalase – TPI". Consequently, the reactions of living organisms and the activity of catalase were formed in response to a combination of pollutants, not to one group of compounds.

Keywords: Bioassay, catalase, *Daphnia magna*, *Escherichia coli,* heavy metals, railways, soil pollution, urbanozems

ARTICLE INFO

Article history:
Received: 06 May 2022
Accepted: 07 September 2022
Published: 31 March 2023

DOI: https://doi.org/10.47836/pjst.31.3.17

E-mail addresses:
morgan-abend@mail.ru (Anna Sergeyevna Olkova)
usr08612@vyatsu.ru (Tatyana Anatolyevna Adamovich)
* Corresponding author

ISSN: 0128-7680
e-ISSN: 2231-8526

© Universiti Putra Malaysia Press

INTRODUCTION

At present railway transport is of great importance, its economic and social role increases. Development of the network of railways and stations improves the quality of physical and social spaces and increases the economic viability of space (Banerjee & Saha, 2022).

Despite high importance of rail transport, the operation of railways is associated with some environmental problems. The problem of an increased level of acoustic noise near the railway is known. More people are exposed to railway noise at night (>50dB) than during the whole day (>60dB), which is related to higher volumes of freight rail transport at night. Loud noise can lead to irritability and aggression, hypertension (increased blood pressure), tinnitus, and even hearing loss (Wrotny & Bohatkiewicz, 2021).

Long lines of railways significantly affect representatives of the natural biota. For example, railroad lines can create obstacles for the movement of animals, separate populations or restrict their access to resources. This way the barrier effect is formed. Barrier effects, landscape fragmentation, increased accidental mortality lead to the risk of extinction of wild animal populations (Balkenhol & Waits, 2009). Scientists draw attention to the impact of roads on birds and mammals. Thus, the negative impact of the railway on the wealth and animal number was shown (Li, 2012). Causes of negative impacts on flora and fauna include chemical air and soil pollution, soil erosion (Balkenhol & Waits, 2009).

One of the main environmental problems associated with rail transport is the linear pollution of environmental components along the railroads. A number of studies report increased air pollution near railways. In particular, in the immediate vicinity of railway stops there is a violation of air quality and an excess of environmental standards for a number of volatile compounds, which is associated with the migration of pollutants from the surface of fuel tanks into the air (Zvyagintseva et al., 2020).

Soils experience the maximum load near railways. Thus, the study of Szmaglinski et al. (2021) shows that Cr is a specific chemical trace that appears along railways due to the use of chromium compounds to resist increased rail wear. The work of Radziemska et al. (2021) showed that the accumulation of Cd, Cr, Cu, Ni, Pb in soils along railways and biological tissues correlated with each other.

Soils near railroads accumulate other pollutants: polyaromatic hydrocarbons, polychlorinated biphenyls, oil products and pesticide residues. Usually the content of these pollutants does not exceed the established standards. However, the toxic effect of railway urbanozems on numerous test organisms of different trophic levels was shown (Wierzbicka et. al., 2015; Zhang et al., 2012). The authors attribute this to the synergistic effect of low concentrations of several pollutants.

Thus, complex studies of soils associated with railways remain relevant. The degree of anthropogenic transformation of the environment significantly depends on a set of environmental factors. The aim of the work was to determine the influence of the railway

on physicochemical characteristics of adjacent urban soils formed in the southern taiga zone and to find out the interrelation of these indicators with the toxicity and catalase activity of the soil.

MATERIALS AND METHODS

Sampling Sites

We assessed the impact of rail transport on urbanozems formed during planning and construction work related to the laying train tracks and organization of land plots adjacent to the railroad tracks. The study sites were located far from large settlements and industrial enterprises, which made it possible to achieve the purpose of the work without imposing additional technogenic factors.

The study area is located in the northeast of the European part of Russia, on the Russian Plain, latitude: 59.363129° N, longitude: 49.0466079° E (Kirov region, the Russian Federation). The climate of this area is similar to the climatic features of the Northern regions of Europe, the northern states of America, most of Canada and other countries of the Northern Hemisphere. The average temperature is 3.5℃, the average winter air temperature is -9.5℃, the average summer temperature is 16.7℃.

The railway in the selected area belongs to the omnibus circuit for passenger and cargo trains. The traffic density of this section of the railway is from 15 to 30 million tons/km. The railway consists of two tracks in opposite directions. The cross-sleepers are made of reinforced concrete. The ballast bearing layer of the railway track consists of gravel, the slopes of the embankment are small - less than 30 m, there is soil covering behind the slopes. The sloping terrain is 7% to the east within 10 km. The area was chosen as the most typical; it represents the longest non-loco shed railway section in the world.

As the distance from the railway increases, the soil cover changes from urbansems to natural soil types. The predominant natural soils are soddy-podzolic, the granulometric composition is sandy and sandy loam, the humus supply is low, the pH reaction of the soil extract is strongly acidic and acidic. The prevailing winds are southern (21.6%), western (17.6%) and northern (15.1%), and the railroad runs in a north-south direction, so the maximum air spread of pollution presumably occurs in the direction of the railway and from west to east. Based on these conditions and the slope of the terrain to the east, the sampling sites were determined.

The samples were taken from the surface layer of 0-10 cm at a distance of 50 m from the western and eastern sides of the railway and at the distance of 100, 500, 1000 m from it (on the eastern side). The background site was located at the distance of 3000 m to the east from the railway to demonstrate a decrease in pollution when moving to distances from a linear anthropogenic object. Sampling was carried out annually at the end of the growing season (at the end of August), since the planned indicators required sufficient development of the

soil biocenosis. All plots were covered with natural herbaceous vegetation, gramineous and other weedy plant species (couch grass, quarry and shepherd's purse). After sampling the soil was freed from plant roots and contaminating impurities, dried to an air-dry state, homogenized, and analyzed according to the research plan.

The observation program was carried out for three years to obtain data on the fluctuations of the selected indicators of the state of the soil.

Complex of Research Methods

The pH value was measured by the potentiometric method on the MI-150 pH meter (Environmental Regulation, 2016). The content of organic matter was determined spectrophotometrically according to the Tyurin method (State Standard, 1992). Determination of ammonium nitrogen in the soil samples was carried out spectrophotometrically (State Standard, 1985). The catalase activity of the soil was determined using the gasometric method (Inisheva et al., 2003). The mass fractions of mobile forms of metals (copper, cadmium, lead, and zinc) were determined by the atomic absorption method (Federal Register, 2012). The toxicity of the samples was determined by the mortality of *Daphnia magna* Straus (Federal Register, 2007) and the change in the bioluminescence of *Escherichia coli* Migula bacteria (Environmental Regulatory Document, 2010).

Results Processing Methods

The level of soil contamination with mobile forms of HM was assessed by the concentration coefficient, defined as the ratio of the content of the element in the studied area to its content in the background area. Next, the total pollution index (TPI) was calculated as the sum of HM concentration factors (Saet et al., 1990; Korelskaya & Popova, 2012). The resulting TPIs characterized the degree of soil pollution are: more than 128 – extreme pollution, 32–128 – dangerous, 16–32 –moderately dangerous, less than 16 – permissible pollution (Ministry of Health of the USSR, 1987).

The physicochemical and integral environmental characteristics of urbanisms were determined three times (2017-2019). The annual processing of the results was carried out according to the recommendations of the methods of analysis used. The summary data in Table 1 is presented as a three-year average with a standard deviation and range of three-year values. The figures show the average values obtained over three years of research.

RESULTS

General Characteristics of the Soil Cover Near the Railway Track

The soil in the background plot corresponded to typical soddy-podzolic soils of treeless territories in the southern and middle taiga climatic natural zones (Eremchenko et al., 2016).

The medium acid pH level and high content of organic matter (up to 13.9 mg/kg of dry soil mass) were found out. The activity of catalase in the soil of the background plot also corresponded to the average data for the soils of the so-called "middle latitudes" (Mitrakova, 2018; Wu et al., 2012). When approaching the railway, some indicators changed (Table 1).

The pH level of the soil solution near the railway changes significantly becoming more alkaline. The shift was about 2 pH units in all experimental sites compared to the average background values. Moreover, the maximum pH levels were recorded at the site 1000 m away from the object of influence. An increase in the pH level in soils near railways is obviously associated with emissions of soot and other alkaline products of coal combustion, since diesel locomotives are operated on this part of the railway. The results show that soils that are not adjacent to the railway, but located at a distance from it (1000 m), experience the maximum impact of alkaline emissions.

The content of organic matter in the soils of most sites did not differ significantly from each other ($p>0.05$). Only in the area, situated at the distance of 500 m, increased concentrations of organic matter compared to the background were revealed ($p<0.05$). The relative remoteness of the site and the fact that most trains in Russia are equipped with dry

Table 1
Characteristics of urbanozems adjacent to railways and soils of the background site (2017-2019 years)

Sampling site/ distance from the railway	pH (units pH)	Organic matter (%)*	Ammonium nitrogen (mg/kg)*	Catalase activity (cm^3 O_2 per 1g of soil for 1 min)*
Background site / 3000 м	4.9±0.1 4.8-5.1 medium acid	3.2±0.4 2.6-4.2 low content	4.8±0.2 4.3-5.7	4.0±0.3 3.6-4.3 weak
Site №1 / 50 m west	7,1±0,1 7,0-7,3 close to neutral, alkaline	3,7±0,6 2.4-4.5 low content	2.0±0.4 1.28-3.21	2.0±0.4 1.6-2.7 weak
Site №2 / 50 m east	7.2±0.1 7.1-7.3 close to neutral, alkaline	2.9±0.4 2.8-3.1 low content	5.65±0.02 5.63-5.68	2.6±1.0 1.1-3.6 weak
Site №3 / 100 m east	6.8±0.1 6.7-6.8 close to neutral, alkaline	3.2±0.5 2.6-4.2 low content	6.92±0.12 6.89-6.97	2.53±0.17 2.3-2.7 weak
Site №4 / 500 m east	6.8±0.1 6.7-6.9 close to neutral, alkaline	5.2±0.5 4.8-5.6 average content	4.4±0.4 4.27-4.47	2.70±0.17 2.4-2.9 weak
Site №5 / 1000 m east	7.5±0.1 6.8-7.9 close to neutral, alkaline	2.9±0.4 2.8-3.1 low content	3.18±0.11 3.14-3.21	3.0±0.2 2.7-3.1 weak

Note. The numerator of the conditional fraction shows the average values of the indicator calculated of the results of 2017-2019 years, the denominator indicates the range of values; * – calculation for the dry weight of the soil.

closets suggest that this local increase in the concentration of organic matter in the soil is not related to the influence of the railway. The trend was confirmed during three years of observations, so we also exclude random errors. It is most likely that this is due to the heterogeneity of the soil and its composition.

The content of ammonium nitrogen in all sites, including the background plot, is rather low (from 2.0±0.4 to 6.92±0.12 mg/kg dry weight). There are reports in the literature about the content of ammonium nitrogen in the soil at the level of 20–30 mg/kg (Masclaux-Daubresse et al., 2010). The lowest accumulation of ammonium nitrogen was found for the plot No. 1 closest to the railway (2.0±0.4 mg/kg). This is probably due to the fact that the areas closest to the road are covered with urbanozems - an artificially formed soil layer characterized by a high degree of compaction and a low projective cover of herbaceous vegetation (30% or less). In such soils all natural cycles are slowed down, including the mineralization of organic matter with the initial release of nitrogen in the form of NH_4^+.

This hypothesis is confirmed by a weak positive correlation between the content of ammonium forms of nitrogen and the activity of soil catalase (r=0.21). Both indicators depend on the saturation of the soil with microorganisms. The connection of a low level is explained by the fact that ammonifying microorganisms are only part of the pool of microorganisms that serve as suppliers of catalase to the soil. In general, the catalase activity naturally decreases when approaching the railway (r=0.95). Average levels of the catalase supply were observed only in the background site, and in the experimental sites the activity of the enzyme was weak.

Thus, the pH level and the catalase activity were most associated with the influence of the railway.

The Content of Mobile Forms of Heavy Metals in Urbanosems Adjacent to Railway

Rail transport is one of the most significant HM suppliers to the environment (Abbasi et al., 2013). In this work we determined the content of mobile forms of metals in the soil, since they are available to soil biota, accumulated by living organisms and affect the integral toxicity of soils. In the Russian Federation the content of mobile forms of HM in the soil is standardized (Federal Law of the Russian Federation, 1999). The admissible concentration limit (ACL) for Pb is 6 mg/kg, for Cu – 3 mg/kg, for Cd – 1 mg/kg, Zn – 23 mg/kg of dry soil mass. Exceeding the standard for Zn by 2.9 times was found one time in 2019 for the site located 1000 m from the railway. In other studied areas no excesses of the standards were found. ACL multiples for Pb and Cd were recorded at the level of 0.53 in the site closest to the road (50 m east). However, the analysis of HM concentration coefficients compared with the background area (Figure 1) and the total pollution index (Figure 2) indicates the accumulation of HM.

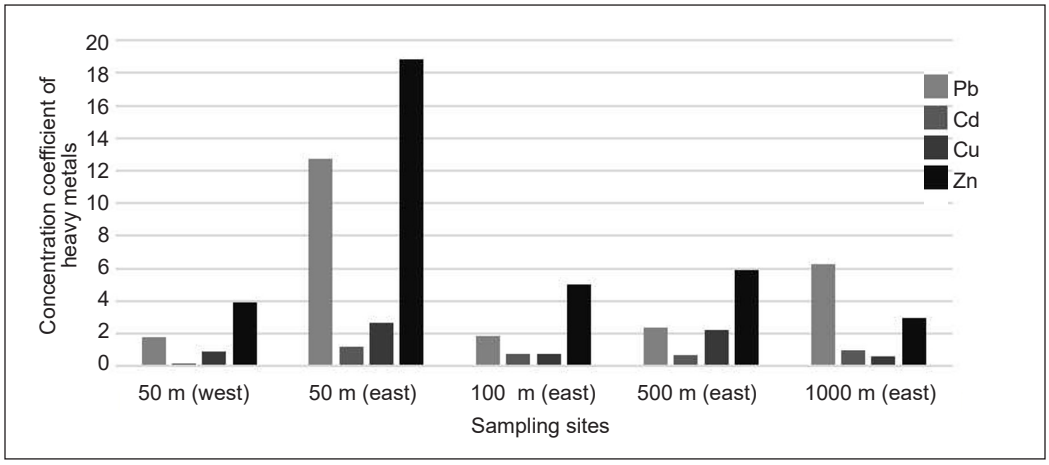

Figure 1. The concentration coefficients of mobile HM forms at different distances from the railway

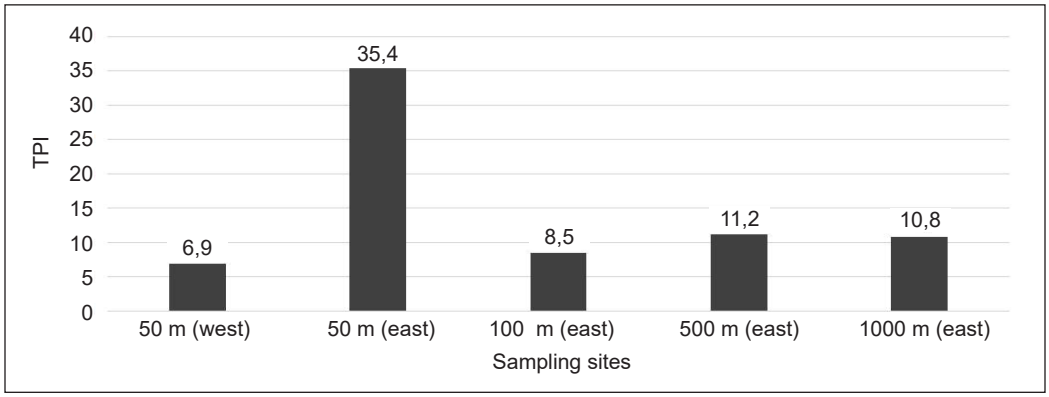

Figure 2. Total indicators of pollution of urbanozems located at different distances from the railway

Zn and Pb take leading positions in terms of concentration coefficients. On average within three years of observations the excess of the Zn content in the soils of railways ranged from 3 to 18.8 times in comparison with the indicator in the background site. A similar comparison is in the range of 1.8-12.7 times for Pb. The maximum concentration coefficients of the mobile forms of Pb, Cd, Cu, Zn were observed in the sites closest to the railway (50 m east), which was also reflected in the highest ACL. It should be noted that to the right of the railway (50 m west) the total pollution indicator was not so high. This is due to the fact that, according to long-term meteorological observations, one of the prevailing wind directions is from west to east.

The accumulation of mobile forms of Cd was comparable to the background area. When calculating the average data within three years, the concentration coefficient of Cd varied from 0.7 to 1.2. The results obtained for mobile forms of Cu are similar: only in two sites the accumulation of copper was 2 or more times compared to the background.

Thus, it is shown that in the site near the railway, the content of mobile HM forms is most often within the established standards, but in comparison with the background territories the accumulation of mobile forms of Zn and Pb is observed. According to the total pollution index, most sites within 50-1000 m from the railway are characterized by an acceptable level of pollution. However, pollution can reach dangerous levels.

Responses of Living Organisms to Soil Pollution Near Railways

Chemical characteristics, which were considered separately, cannot show the consequences of anthropogenic pollution in a certain area. Chemical studies should be combined with environmental quality biodiagnostics. In this work we used two methods of bioassay. Firstly, the lethal effects of water extracts from soils (1:4) for *D. magna* were evaluated within 96 hours. Secondly, we evaluated the prelethal effects of water extracts from soils (1:5) for *E. coli* by changing their bioluminescence (Figure 3).

In the sites closest to the railway the maximum toxicity of soil samples was found. Mortality of *D. magna* in the samples "50 m l west" and "50 m east" was above 50%, that is, the samples had an acute toxic effect on the test organism. Toxicity indices for *E. coli*, taking into account the scatter of results in parallel determinations, indicate a strong toxicity of the samples.

The toxicity indicators expectedly decrease further from the railway. The relationship between the distance from the object of influence and the mortality of *D. magna* is characterized by Pearson's coefficients equal to -0.53. The correlation coefficient for the relationship "distance - toxicity index for *E. coli*" is -0.69. When taking into account the results of the *E. coli* bioassay, a more strict dependence is associated with the assessment of the pre-lethal reaction of the organism, which can manifest itself at fairly low doses of toxic substances (Olkova & Ashikhmina, 2021).

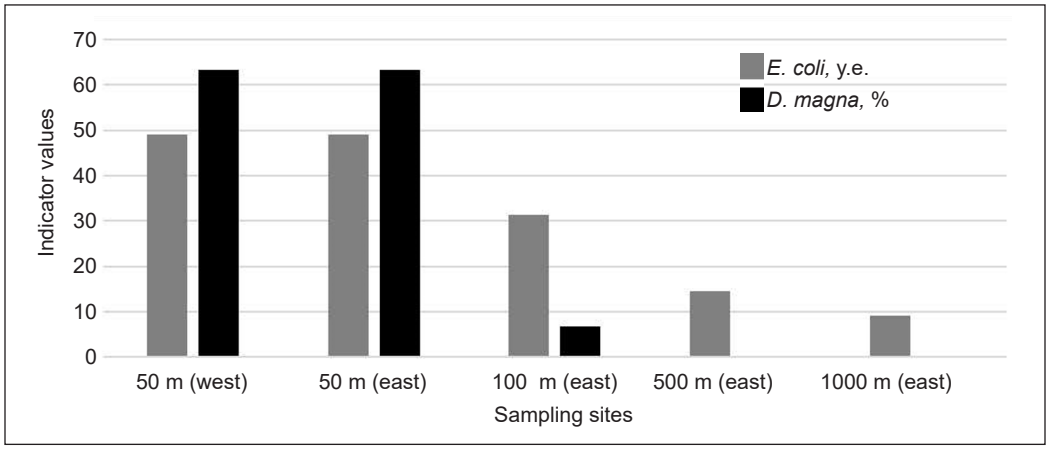

Figure 3. Results of bioassay of water extracts from urbanozems in response to *D. magna* (mortality) and *E. coli* (decrease in bioluminescence)

When analyzing the relationship between the results of bioassay and other characteristics of the studied soils, it was revealed that the highest degree of inverse relationship is observed between the toxicity of the soil and the activity of catalase in it: r=-0.61 for "catalase – *D. magna*" and r=-0.74 for "catalase – *E. coli*". This result is quite natural and is explained by the fact that the levels of toxicity and enzymatic activity are integral indicators that respond to the whole complex of chemicals present in the sample.

The correlation between toxicity and other soil characteristics was much weaker. Thus, even for the pair "total indicator of HM contamination – toxicity for *E. coli*", the Pearson's coefficient was equal to 0.42. This confirms that the detected levels of toxicity were formed in response to a combination of pollutants, and not to one group of compounds.

DISCUSSION

In the first part of the work it was shown that the catalase activity was most associated with the influence of the railway. It is known that the catalase activity is an integral indicator of the state of the soil, which responds both to natural factors (Olkova & Tovstik, 2022) and anthropogenic pollution (Hinojosa et al., 2004; Utobo & Tewari, 2015). In the case of the influence of railways on the soil it can be argued that the catalase activity was inhibited by a complex of pollutants, since a strong dependence of the catalase activity on the distance from the site to the railway was revealed (r = 0.95). In the literature there are data on the relationship between the activity of soil enzymes and chemical pollution. Thus, in Baran et al. (2004), a relationship was established between the content of polycyclic aromatic hydrocarbons (PAH) and the enzymatic activity of soils. It was concluded that the effect of PAH on the enzymatic activity largely depends on such soil properties as the content of total organic carbon and pH. The work Baikhamurova et al. (2020) showed that near the railway the urease activity was reduced by 2 times and the invertase activity was reduced by 3 times compared to the background areas.

It turned out that the soil pH level is associated with the influence of the railway. An increase in pH by 2 units within 3 km without a change in phytocenosis indicates the entry of alkaline products into the soil. In this case soot and other combustion products of coal and diesel fuel, used in diesel locomotives - locomotives with an internal combustion engine, are found on the soil. It should be noted that among the main modes of transport with internal combustion engines (roads, aviation, navigation, and railway) rail transport has the least environmental impact (Paschalidou et al., 2022).

In the second part of the work accumulation of mobile forms of Zn and Pb was shown in the territories adjacent to railways. It was found that an increased content of heavy metals is characteristic of soils directly adjacent to railways. The most likely source of zinc is brass alloys. Bearings, water and steam fittings are made of brass for railway transport. Radiators and heat exchangers are made of sheet brass. In addition, zinc is used in electrical

equipment as part of electrically conductive elements. Lead is released into the soil when coal and other biogenic fuels are burned.

The studied HM can be ranked according to the level of accumulation in railway urban soils as follows: Zn > Pb > Cu=Cd. The study in Poland showed a similar pattern: the maximum values for Cr, Cu, Pb and Zn were 31.1, 145, 80.5 and 115 mg/kg soil mass, respectively (Szmaglinski et al., 2021). In the same work, using isotope analysis methods, it was shown that metals are of anthropogenic origin (coal combustion, road vehicles and railroad transport coal combustion, road vehicles, and railroad transport). The latest studies report that metal contamination of railway urbanozems is not limited to "classical" anthropogenic HM (Pb, Zn, Cu, Cr, Cd). Thus, the authors (Stancic et al., 2022) showed that in soils along railways pronounced enrichment of Sb and Sn is found, it is 87 and 33 times higher than the median value for European soils, respectively.

When further determining the toxicity of the studied soils, it was shown that the responses of test organisms increase when approaching the railway, and they are also most closely related to the activity of catalase and the relation to the concentration of mobile HM forms is average. These patterns are consistent with findings of other scientists. Thus, it is proposed to evaluate the activity of catalase and other enzymes to indicate heavy metal contamination of soils near the railway (Xiaoyi et al., 2018).

CONCLUSION

Railways are a source of pollution of adjacent urbanozems. However, the zone of maximum contamination is 50 m. At a greater distance from the railroad track there are higher levels of mobile forms of Zn, Cu, and Pb compared to the background area. Pollution by anthropogenic organic matter and the content of ammonium nitrogen associated with it, apparently, is of a situational local nature. In general, from the economic and environmental point of view the rail transport is more preferable than road transport.

A limitation of this study is that not the full range of pollutants that are markers of the impact of the rail transport on the environment was identified. However, due to the integral characteristics of the soil a negative interrelation between toxicity levels and the distance to the railway and a positive relationship between the catalase activity and this distance were shown. The confirmation that the soil microbiota and test organisms are affected not only by heavy metals is the high level of correlation "pH - distance to the railway" in combination with the average degree of correlation between the total indicator of Cd, Zn, Cu and Pb pollution with the integral environmental indicators of soils. As it was mentioned above the soil near railways can be characterized by high oil pollution. Also scientists began to pay closer attention to the contribution of rare earth elements and platinum group metals to the overall "metal" pollution.

The presented work complements the available scientific information on the influence of the railway transport on the soil pollution (urbanozems) and contains new data on the interrelation of existing pollution with lethal and pre-lethal reactions of test organisms and soil microbiota (through the index of the soil catalase activity).

ACKNOWLEDGEMENT

The authors want to acknowledge Doctor of Technical Sciences, Professor at Vyatka State University, Russia, Tamara Yakovlevna Ashikhmina, for the long learning process and support.

REFERENCES

Abbasi, S., Jansson, A., Sellgren, U., & Olofsson, U. (2013). Particle emissions from rail traffic: A literature review. *Critical Reviews in Environmental Science and Technology, 43*(23), 2511-2544. https://doi.org/10.1080/10643389.2012.685348

Baikhamurova, M. O., Yuldashbek, D. H., Sainova, G. A., & Anarbekova, G. D. (2020). Change of catalase and urease activity at high content of heavy metals (Pb, Zn, Cd) in serozem. *European Journal of Natural History, 3*, 70-73.

Balkenhol, N., & Waits, L. P. (2009). Molecular road ecology: Exploring the potential of genetics for investigating transportation impacts on wildlife. *Molecular Ecology, 18*(20), 4151-4164. https://doi.org/10.1111/j.1365-294X.2009.04322.x

Banerjee, I., & Saha, A. (2022). Mobility centre-oriented urban regeneration: Examining place value of railway stations. *Geojournal, 87*, 567-581. https://doi.org/10.1007/s10708-022-10582-y

Baran, S., Ebielińska, J., & Oleszczuk, P. (2004). Enzymatic activity in an airfield soil polluted with polycyclic aromatic hydrocarbons. *Geoderma, 118*(3-4), 221-232. https://doi.org/10.1016/S0016-7061(03)00205-2

Environmental Regulation. (2016). *Guidelines for the Application of the Methodology for Performing pH Measurements in Waters by the Potentiometric Method*. https://docs.cntd.ru/document/1200056733

Environmental Regulatory Document. (2010). *Method for Determining the Toxicity of Water and Water Extracts from Soils, Sewage Sludge and Waste by Changing the Intensity of Bacterial Bioluminescence using the Ecolum Test-System.* https://ohranatruda.ru/upload/iblock/99f/4293837368.pdf

Eremchenko, O. Z., Shestakov, I. E., & Moskvina, N. V. (2016). *Soils and Technogenic Surface Formations of Urbanized Territories of the Perm Kama region*. National Research University Russian Federation.

Federal Law of the Russian Federation. (1999). *On the Sanitary and Epidemiological well-being of the Population* (No. 52-FZ). https://duma.consultant.ru/documents/1062895?items=10

Federal Register. (2007). *Biological Control Methods: Method for Determining the Toxicity of Water and Water Extracts from Soils, Sewage Sludge, Waste by Mortality and Changes in Fertility of Daphnia*. https://meganorm.ru/Index2/1/4293842/4293842234.htm

Federal Register. (2012). *Method for Measuring the Mass Concentrations of Elements in Samples of Natural, Drinking and Waste Waters by the Atomic Absorption Method*. https://docs.cntd.ru/document/437193797

Hinojosa, M. B., Carreira J. A., García-Ruíz, R., & Dick R. P. (2004). Soil moisture pre-treatment effects on enzyme activities as indicators of heavy metal-contaminated and reclaimed soils. *Soil Biology and Biochemistry, 36*(10), 1559-1568. https://doi.org/10.1016/j.soilbio.2004.07.003

Inisheva, L. I., Ivleva, S. N., & Shcherbakova, T. A. (2003). *Guidelines for Determining the Enzymatic Activity of Peat Soils and Peat*. Publishing House of Tomsk University.

Korelskaya, T. A., & Popova, L. F. (2012). Heavy metals in the soil and vegetation cover of the city of Arkhangelsk. *Arktika i Sever*, *7*, 1-17.

Li, Z. (2012). Effects of Qinghai-Tibet railway and highway on plateau picas. In *International Conference on Biomedical Engineering and Biotechnology* (pp. 224-227). IEEE Publishing. https://doi.org/10.1109/iCBEB.2012.189

Masclaux-Daubresse, C., Françoise, D. V., Dechorgnat, J., & Chardon, F. (2010). Nitrogen uptake, assimilation and remobilization in plants: Challenges for sustainable and productive agriculture. *Annals of Botany, 105*(7), 1141-1157. https://doi.org/10.1093/aob/mcq028

Ministry of Health of the USSR. (1987). *Methodological Instructions for Assessing the Degree of Danger of Soil Pollution by Chemicals*. https://ohranatruda.ru/upload/iblock/172/4293852444.pdf

Mitrakova, N. V. (2018). *Assessment of the Biological Activity and Toxicity of Soils and Technogenic Surface Formations in the Perm Kama region* (Degree dissertation). National Research University, Russian Federation. https://www.dissercat.com/content/otsenka-biologicheskoi-aktivnosti-i-toksichnosti-pochv-i-tekhnogennykh-poverkhnostnykh-obraz

Olkova, A. S., & Ashikhmina, T. Y. (2021). Factors of obtaining representative results of bioassay of aquatic environments. *Theoretical and Applied Ecology, 2*, 22-30. https://doi.org/10.25750/1995-4301-2021-2-022-030

Olkova, A. S., & Tovstik, E. V. (2022). Comparison of natural abiotic factors and pollution influence on the soil enzymative activity. *Ecological Engineering and Environmental Technology, 23*(1), 42-48. https://doi.org/10.12912/27197050/143003

Paschalidou, A. K., Petrou, I., Fytianos, G., & Kassomenos, P. (2022). Anatomy of the atmospheric emissions from the transport sector in Greece: Trends and challenges. *Environmental Science and Pollution Research, 29*, 34670-34684. https://doi.org/10.1007/s11356-021-18062-5

Radziemska, M., Gusiatin, Z. M., Kowal, P., Bęś, A., Majewski, G., & Jeznach-Steinhagen, A. (2021). Environmental impact assessment of risk elements from railway transport with the use of pollution indices, a biotest and bioindicators. *Human and Ecological Risk Assessment: An International Journal, 27*, 517-540. https://doi.org/10.1080/10807039.2020.1736984

Saet, Y. E., Revich, B. A., Yanin, E. P., & Smirnova, R. S. (1990). *Geochemistry of the Environment.* Nedra Publishing House.

Stancic, Z., Fiket, A., & Vuger, A. (2022). Tin and antimony as soil pollutants along railway lines - A case study from North-Western Croatia. *Environments, 9*(1), Article 10. https://doi.org/10.3390/environments9010010

State Standard. (1985). *Soils: Determination of Exchangeable Ammonium by the TsINAO Method*. Publishing House of Standards.

State Standard. (1992). *Soils: Methods for Determination of Organic Matter Number by the Method of Tyurin in the Modification of TsINAO*. Publishing House of Standards.

Szmaglinski, J., Nawrot, N., Pazdro, K., Walkusz-Miotk, J., & Wojciechowska, E. (2021). The fate and contamination of trace metals in soils exposed to a railroad used by Diesel Multiple Units: Assessment of the railroad contribution with multi-tool source tracking. *Science of the Total Environment, 798*, Article 149300. https://doi.org/10.1016/j.scitotenv.2021.149300

Utobo, E. B., & Tewari, I. L. (2015). Soil enzymes as bioindicators of soil ecosystem status. *Applied Ecology and Environmental Research, 13*(1), 147-169. https://doi.org/10.15666/aeer/1301_147169

Wierzbicka, M., Bemowska-Kałabun, O., & Gworek, B. (2015). Multidimensional evaluation of soil pollution from railway tracks. *Ecotoxicology, 24*, 805-822 https://doi.org/10.1007/s10646-015-1426-8

Wrotny, M., & Bohatkiewicz, J. (2021). Traffic noise and inhabitant health - A comparison of road and rail noise. *Sustainability, 13*, Article 7340. https://doi.org/10.3390/su13137340

Wu, X. D., Zhao, L., Fang, H. B., Chen, J., Pang, Q. Q., Wang, Z. W., Chen, M. J., & Ding, Y.J. (2012). Soil enzyme activities in Permafrost Regions of the Western Qinghai-Tibetan Plateau. *Soil Science Society of America Journal, 76*(4), Article 1280. https://doi.org/10.2136/sssaj2011.0400

Xiaoyi, M., Ai, Y., Li, R., & Zhang, W. (2018). Effects of heavy metal pollution on enzyme activities in railway cut slope soils. *Environmental Monitoring and Assessment, 190*(4), Article 197. https://doi.org/10.1007/s10661-018-6567-9

Zhang, H., Wang, Z., Zhang, Y., & Hu, Z. (2012). The effects of the Qinghai-Tibet railway on heavy metals enrichment in soils. *The Science of the Total Environment, 439*, 240-248. https://doi.org/10.1016/j.scitotenv.2012.09.027

Zvyagintseva A. V., Samofalova A. S., Sazonova S. A., & Kulneva V. V. (2020). Air pollution with oil products in the area of railway tank stops. *Journal of Physics: Conference Series, 1679*, Article 022076. https://doi.org/10.1088/1742-6596/1679/2/022076

Pertanika J. Sci. & Technol. 31 (3): 1453 - 1474 (2023)

PERTANIKA JOURNALS

SCIENCE & TECHNOLOGY

Journal homepage: http://www.pertanika.upm.edu.my/

Heat Rate Deviation Analysis of a Coal-Fired Power Plant (CFPP) with the Influence of Applicable Coal Prices (ACP)

Manmit Singh Jasbeer Singh[1]*, Nawal Aswan Abdul Jalil[1], Sharafiz Abdul Rahim[1], Zamir Aimaduddin Zulkefli[1] and Hasril Hasini[2]

[1]*Department of Mechanical and Manufacturing Engineering, Universiti Putra Malaysia, 43400 UPM, Serdang, Selangor, Malaysia*

[2]*Department of Mechanical Engineering, College of Engineering, Universiti Tenaga Nasional, 43000, Kajang, Selangor, Malaysia*

ABSTRACT

The assessment of a Coal-Fired Power Plant (CFPP) performance is an intricate process that involves the determination of Heat Rate (HR) deviations of current operational parameters from baseline or target values. This study focuses on HR deviations of a CFPP based on the Applicable Coal Price (ACP), and the influence of the ACP price on daily losses or gains are thoroughly analyzed for key performance parameters for three fixed ACP of RM12, 18, and 24 per GJ. This paper mainly investigates key parameters and related equipment that significantly affect the HR of the CFPP and ranks the parameters affecting HR from most significant to least significant. The baseline or target values are obtained from the plant commissioning manuals and the Performance Guarantee Test (PGT). Actual real-life operational data from a 700MWn CFPP is utilized to improve the accuracy and confidence levels of the results obtained. It was found that at the nominal operating baseload, the most significant negative HR deviation is for the Rotary Air Heater (RAH) gas exit temperature with a negative HR deviation of -137.9 kJ/kWh leading to an annual loss of RM17.6 million at ACP of RM24/GJ while the superheater and reheater spray flows are contributing least to the HR deviation. This analysis highlighting the impact of key parameters affecting the performance enables plant operations and maintenance teams to focus on such parameters to mitigate losses.

Keywords: Applicable coal price, coal-fired power plant performance, heat rate deviation analysis, heat rate

ARTICLE INFO

Article history:
Received: 26 May 2022
Accepted: 16 August 2022
Published: 31 March 2023

DOI: https://doi.org/10.47836/pjst.31.3.18

E-mail addresses:
manmitsingh35@gmail.com (Manmit Singh Jasbeer Singh)
nawalaswan@upm.edu.my (Nawal Aswan Abdul Jalil)
sharafiz@upm.edu.my (Shafariz Abdul Rahim)
zamirdin@upm.edu.my (Zamir Aimaduddin Zulkefli)
hasril@uniten.edu.my (Hasril Hasini)
* Corresponding author

ISSN: 0128-7680
e-ISSN: 2231-8526

© Universiti Putra Malaysia Press

INTRODUCTION

Coal Fired Power Plants (CFPP) are the key pillar of support for Malaysia's power generation sector, providing close to 40% of the national energy demand up to 2030 (Energy Commission of Malaysia, 2020). In a rapidly growing economy for a developing country, CFPPs are operated on baseload mode, which means the plant produces power at almost full capacity throughout the day to meet the country's energy demands. Any negative deviation in the Heat Rate (HR) for base loads plants will significantly affect the plant performance. The HR of a CFPP is defined as the amount of energy consumed by an electrical generator to produce one unit of electricity in Kilowatt Hours (kWh), and the HR deviation refers to a positive or negative change in the HR against a baseline value. As such, CFPP needs to operate at its optimum efficiency to reduce the cost of fuel used, which will translate into a lower cost of producing energy to maintain the plant's sustainability and profitability for the country's well-being (Zhang et al., 2018).

Plant personnel and managers must be aware of the HR deviation of the plant to ensure the plant is operating at its optimum performance. The main focus of this investigation is to conduct an HR deviation analysis which can assist plant operators in better understanding the effect of parameter deviations on the HR of the plant and thus take the appropriate action to improve the performance of the plant. The HR deviations analysis can provide key indicators of how well the plant is performing daily or where the operations and maintenance personnel need to work on improving the plant's performance. Actual real-life operational data from a 700 MW CFPP is utilized in this study. The plant has been operating for almost 20 years, so relevant data from the commissioning and Performance Guarantee Test (PGT) are available. Moreover, there are three identical units of 700MW; therefore, the analysis applies to all three units.

Scholars in several previous studies have investigated the performance of CFPP. However, most past research work has only focused on obtaining the overall heat rate of CFPP without focusing on key operational performance indicators of the plant, while this study focuses on the key operational performance indicators of the CFPP. Furthermore, most previous studies have not conducted a financial analysis of the plant, which is vital for plant operators to determine the profitability of the plant based on the current operating regime, while this study correlates key plant performance indicators with economic analysis (Ahmadi & Toghraie, 2016; Elhelw et al., 2019; Sabzpooshani et al., 2019). Moreover, the impact of the Applicable Coal Price (ACP) on the HR deviation of the plant has not been investigated in previous research work, whereas this investigation focuses on the impact of ACP on key plant performance parameters (Devandrin et al., 2016; Almedilla et al., 2018; Oyedepo et al., 2020). In addition, most previously investigated units have a design capacity below 500MWn, while the present study focuses on 700MWn units (Neshumayev et al., 2018; Wijaya & Widodo, 2018).

With the increasing prices of ACP, and the price of coal, the primary fuel source for a CFPP, it is of utmost importance to consider the effect of coal prices and their effect on plant performance. While several studies have investigated certain parameters of the boiler operations, in terms of daily operations, there is nothing much which can be done to monitor and mitigate the issues as the recommendations require the unit to be on outage for maintenance (Gupta & Kumar, 2015; Pachaiyappan & Prakash, 2015). In addition, while there have been previous studies on intelligent boiler maintenance techniques in boiler trips, such studies did not focus on the performance of CFPP (Nistah et al., 2014). Therefore, the present study analyses key areas of CFPP performance where the operations team can address the gaps or negative deviations of plant HR as the analysis can highlight key areas of concern that significantly affect plant performance. Furthermore, it is not feasible to focus on certain areas of CFPP performance that require unit outage as there will be monetary losses when the unit is not producing load; therefore, the present study focuses on areas such as the feedwater heaters, condenser, and overall key parameters which may be addressed operationally without the need of waiting for outage (Braun, 2021).

The main objective of this paper is to investigate HR deviations of a CFPP based on the ACP, and the impact of ACP prices on the daily losses or gains to the plants are thoroughly analyzed for key performance indicators. There are three ACP prices considered in this study, which are RM12, 18, and 24 per GJ, and these three ACP prices reflect the transition of ACP from RM12 from the past five years to the higher ACP of RM24 due to increasing global coal prices (Energy Commission of Malaysia, 2022). Currently, the coal price, or ACP, is Ringgit Malaysia (RM) 24/GJ, equivalent to RM482 per ton for coal with a gross calorific value of 4800 kcal/kg. Therefore, plant personnel needs to understand the more significant impact on gains or losses based on ACP so that more attention may be given to key parameters that might adversely affect the plant HR causing monetary losses. The process of monitoring HR deviation involves utilizing several rules of thumb and key information from the plant commissioning manuals. Several intricate details may also be obtained from the commissioning test runs and the Performance Guarantee Test (PGT), which contains crucial operating parameters of the plant at 100% Turbine Maximum Continuous Rating (TMCR). The parameters obtained from the PGT form the guiding principles of having a robust monitoring regime of the plant as the plant is considered to be operating at its best during the Performance Guarantee Test. Furthermore, several correction curves for key operational parameters are also provided in the PGT, which may be incorporated into the HR deviation monitoring. The CFPP operational data is obtained from the Plant Information (PI) Data Link, which enables the extraction of data from the PI Server linked to the Distributed Control System (DCS), a platform for controlling the plant operations and storing operational data of the CFPP. The usage of actual plant data increases the confidence levels in the outcomes of the study.

It is vital to monitor which parameters are most influential towards the performance of the plant. Thus, such parameters would be categorized as high-priority parameters to be monitored by the operations teams. The constant monitoring and tracking of key parameters would ensure the plant operates optimally. Although the other parameters may be less influential towards plant performance, it is still important to monitor parameters such as the feedwater heaters' Terminal Temperature Difference (TTD) and Drain Cooler Approach (DCA) which are able to provide insights on the correct operating regime of the feedwater heaters, for instance, any abnormalities in the heater level may be obtained from the TTD and DCA results. Such abnormal levels of FWH may lead to overfiring in the boiler and damage the boiler and FWH tubes. Furthermore, incorrect valve lineups around the FWH, such as vent valves, may also be detected through FWH performance monitoring. The health status of the Low-Pressure Heaters (LPH) and High-Pressure Heaters (HPH) feedwaters are vital for maintenance teams, especially before an upcoming outage. This valuable information ensures that the heaters not performing as per the PGT targets may be rectified during the outage. The overall HR deviation due to deviation in TTD is also highlighted and discussed in the proceeding sections.

The condenser TTD and a few other key parameters deviations are able to provide valuable information such as the cleanliness of the water box, the heat load to the condenser by means of cooling water temperature rise, and also the possibility of air ingress due to increases in dissolved oxygen at the Condensate Extraction Pump (CEP) which requires valve line up. The HR deviation caused by variation of backpressure due to cooling water flow is also discussed in the proceeding sections.

The HR deviation can also provide vital information for the maintenance teams to prioritize maintenance activities affecting the plant's performance. Once an HR deviation has been detected by operations personnel, the issue is rectified based on the operations manuals, and if the issue is not resolved, only then the maintenance teams are involved. Such information is valuable in the ever-changing power generation sector, where plants cannot go for regular shutdowns due to the unavailability of planned outages or grid constraints. Longer downtimes are undesirable as the plants' availability factor and finances are adversely affected. Therefore, by early detection and identification of parameters and equipment that adversely affect plant performance, the maintenance team can rectify the issues quickly with proper planning due to early detection based on continuous HR deviation monitoring.

The magnitude of HR deviation changes with the coal prices, known as Applicable Coal Price (ACP), which is quoted in RM/GJ and changes quarterly. In Malaysia, the ACP is regulated by the Energy Commission (EC), and the power plant management is informed of the upcoming new ACP (Energy Commission of Malaysia, 2022). The ACP is affected by changes in coal pricing due to market demand and supply factors. However,

it should be noted that the plant management has no authority to influence the ACP other than buying coal when the coal price is low and delaying coal shipments when the coal pricing is higher, although the storage yard and ship handling capabilities may hinder such a move. Thus, during the higher ACP periods, it is even more crucial for plant operators to focus more on managing the plant at optimum efficiency by frequently monitoring the HR deviation to minimize any potential losses caused by operational parameter deviations.

Background and CFPP Operations

The CFPP under investigation operates at baseload, where the plant produces maximum power output continuously based on the Contractual Available Capacity (CAC), which is the maximum power the plant produces based on the contractual agreement. Therefore, deviations in key parameters cause significant HR deviations leading to greater monetary losses during higher ACP periods. The overall CFPP prosses are illustrated in Figure 1, and Table 1 contains the necessary nomenclature. The cycle begins from the condenser, where demineralized water, which is raw water treated to meet plant requirements, is pumped by the Condensate Extraction Pump (CEP) through the LPHs before reaching the deaerator and the LPH is responsible for preheating the condensate before it enters the deaerator (Bisercic & Bugaric, 2021).

From the deaerator, the operating fluid, now called feedwater, is pumped through the series of HPH by the Boiler Feed Pumps (BFP) before entering the economizer inlet of the boiler. Similar to the LPH, the function of the HPH is to preheat the feedwater using

Table 1
Nomenclature for CFPP process flow as shown in Figure 1

Item	Description
HP Turbine	High-pressure turbine
IP Turbine	Intermediate pressure turbine
IP Exhaust	Exhaust flow from IP turbine to LP turbine
LP1/LP2 Turbine	Low pressure 1,2 turbine
LP Exhaust	Exhaust flow from LP turbine to condenser
CEP	Condensate extraction pump
LPH3,4	Low-pressure heater 3,4
BFP	Boiler feed pump
HPH6,7,8	High-pressure heater 6,7,8
$T_{FurnOut}$	Furnace outlet temperature
T_{RAHOut}	Rotary air heater gas outlet temperature
m_{RHS}	Mass flow of reheater spray flow
m_{SHS}	Mass flow of superheater (attemperator) spray flow
m_{excLPH}	Excess flow of water in the LPH (cycle in dotted lines)
m_{excHPH}	Excess flow of water in the LPH (cycle in dotted lines)

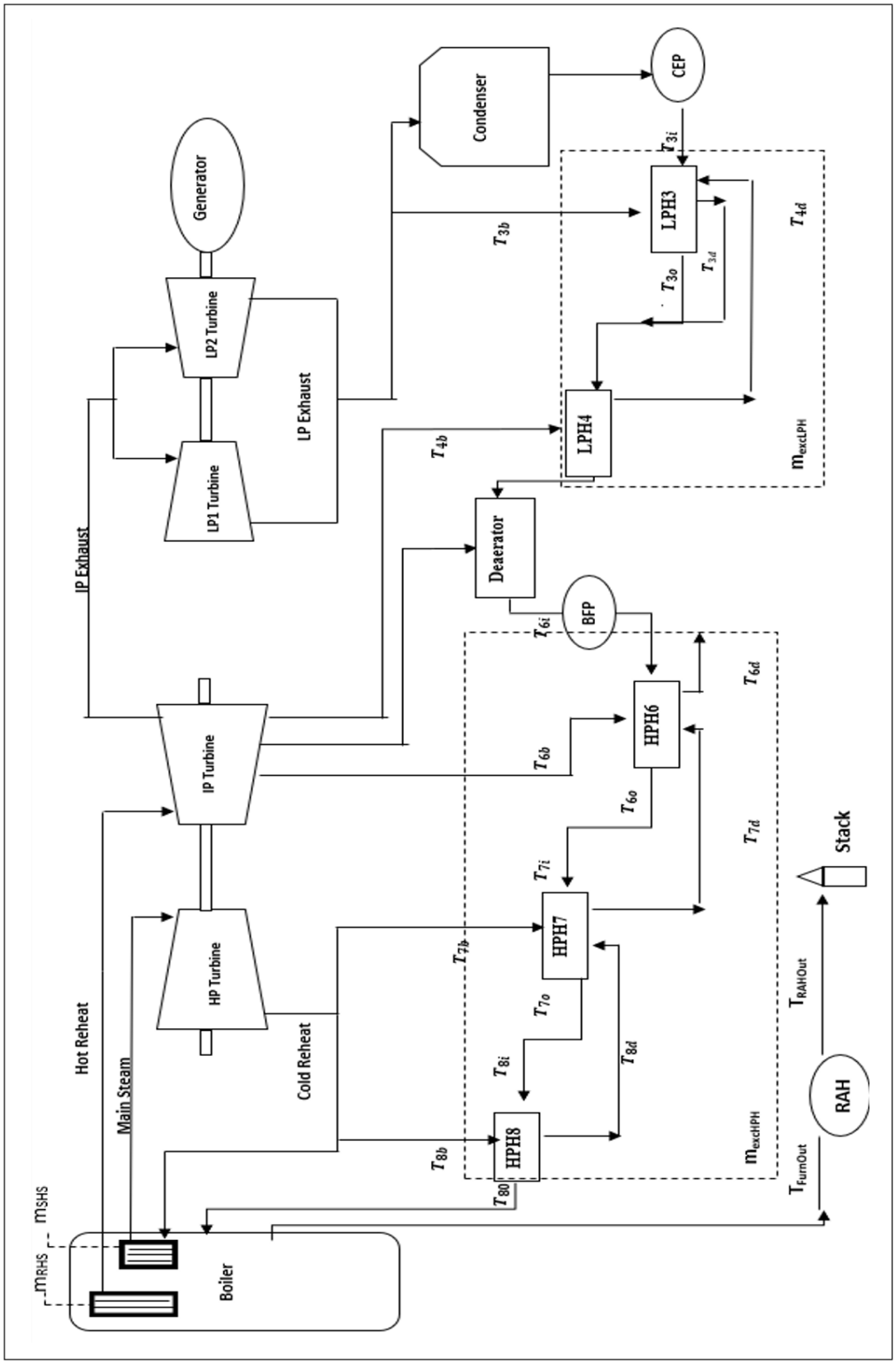

Figure 1. CFPP process flow

extraction steam from various stages of the turbine (Buckshumiyanm & Sabarish, 2017). From the economizer inlet, the operating fluid circulates to the boiler drum and through the downcomers before rising through the water walls of the boiler before re-entering the boiler drum, and a portion of the operating fluid is converted into vapor in this process (Mohammed et al., 2020). The boiler drum separates vapor from the liquid, which is then channeled to the superheaters, after which the superheater steam enters the HP Turbine, rotating the shaft coupled to the electrical generator where conversion of mechanical rotational energy to electrical energy takes place, producing energy (Tian et al., 2017). After expansion in the high-pressure turbine, the exhaust steam renters the boiler before being reheated in the reheater before entering the intermediate pressure turbine as hot reheat steam. The exhaust steam from the intermediate-pressure turbine enters the lower-pressure turbine, and the exhaust of the low-pressure turbine is condensed in the condenser while the cycle is completed when the condensate is circulated through the CEP (Behbahaninia et al., 2017; Wang et al., 2019).

METHODOLOGY

In order to determine the impact of various aspects influencing the HR of the CFPP, it is crucial to determine the HR deviation of the plant. Various parameters may influence the plant's performance, such as main steam temperature, hot reheat temperature, main steam pressure, feed water temperature, and Rotary Air Heater (RAH) outlet temperature. The deviation of the parameter is calculated by obtaining the difference between the present value from the baseline value, which is usually the operational design value or a value based on the present load of the plant.

Therefore, it is possible to obtain both positive and negative HR deviations. The focus is on negative HR deviation, which leads to operational losses, as positive HR deviation indicates gains in operational performance. It is important to note that while positive HR deviation is beneficial, there may be other restraints, for instance, the maximum allowable temperature of the piping in which the medium, such as main steam, flows. Thus, it is desirable to operate at the optimum temperature and pressure. The quantification of the HR deviation is beneficial to identify the key areas contributing to plant losses.

Several factors can influence the significance of HR deviation financially, such as the Fuel Cost (FC) in RM/GJ, the price of coal, the unit's Capacity Factor (CF), and the load generated. In general, the HR deviation for each operational parameter may be determined based on the average figure for several hours, usually by the notation of shifts, which refers to the block of time where one team of operators manage the plant before handing it over to the next team of operators in the following shift. Therefore, monitoring the HR deviation on a shift-per-shift basis is advisable for easy tracking and monitoring. At the same time, this can instill a spirit of responsibility among plant operators to ensure they always operate

the plant at optimum efficiency and report any major deviations to the senior operations personnel and maintenance teams.

Parameter deviation is the difference between the actual value of the parameter and the reference or baseline value of the parameter, as illustrated in Equation 1:

$$\text{Parameter Deviation} = \text{Parameter}_{\text{Actual}} - \text{Parameter}_{\text{Reference}} \quad [1]$$

The heat rate deviation is evaluated using the following relationship as shown in Equation 2, where the HR factor is defined as the fixed change in HR for the parameter, and the HR Factor change refers to the fixed change in the parameter's value:

$$\text{Heat Rate Deviation} = \frac{\text{Parameter Deviation x HR Factor}}{\text{HR Factor change}} \quad [2]$$

The total losses or gain in a day in Ringgit Malaysia (RM) are determined using Equation 3, where the HR deviation is obtained using Equation 2, the Net Energy Output (NEO) is the total net power generated per day while the ACP is the applicable coal price utilized:

$$\text{Losses or Gain in RM per day} = \frac{\text{HR Deviation } (\frac{\text{kJ}}{\text{kWh}}) \text{ x NEO (MWh) x ACP } (\frac{\text{RM}}{\text{GJ}})}{1000} \quad [3]$$

The available data from the plant Distributed Control System (DCS), which is linked to the Plant Information (PI) server, is extracted and shown in a simplified form in Table 2**,** and this input data is utilized to analyze the HR deviation. The measuring points or locations of the items listed in Table 2 are included in Figure 1.

Table 2
Pressures and temperatures of key parameters at load 729 MWg, including nomenclature

Item	Nomenclature	Unit	Parameter
Main steam temperature	T_{MS}	°C	532
Main steam pressure	P_{MS}	bar	530
Hot reheat steam temperature	T_{HRH}	°C	166
Superheater attemperator spray flow	$\dot{m}_{SHS}$	t/h	3.5
Reheater attemperator spray flow	$\dot{m}_{RHS}$	t/h	0.90
Rotary air heater outlet gas temp	T_{RAHOut}	°C	190
Furnace outlet gas temp	$T_{FurnOut}$	°C	382
Excess water flows through LP heaters	$\dot{m}_{excLPH}$	%	2.55
Excess water flows through HP heaters	$\dot{m}_{excHPH}$	%	2.28
Economizer inlet temp	T_{EcoIn}	°C	265
Condenser vacuum	$P_{condvac}$	mbar-A	92

Feedwater Heaters

There are several specific performance indicators for Feedwater Heaters (FWH), such as the Terminal Temperature Difference (TTD), Drain Cooler Approach (DCA), and Temperature Rise (TR) of LPH and HPH, which may be monitored regularly. During normal operations, the TTD and TR can provide quick guidelines on whether the heater is operating at a normal level or otherwise for operators to respond swiftly to mitigate any changes in the FWH operating parameters. It is especially important to monitor the deviations of these parameters before the unit goes for planned maintenance work to ensure the defects may be rectified. The necessary cleaning works of the feedwater heaters using appropriate chemicals may also be done during an outage. The baseline values of the TTD, DCA, and TR, obtained from the Performance Guarantee Test (PGT) and Heat Balance Diagram (HBD), are shown in Table 3, and a general outline of an FWH is illustrated in Figure 2.

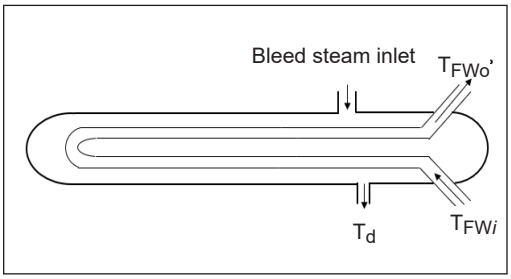

Figure 2. Feedwater heater arrangement

Table 3
FWH TTD, DCA and TR baseline target values

LPH/HPH	Baseline Target Values		
	Terminal Temperature Difference (TTD)	Drain Cooler Approach (DCA)	**Temperature Rise (TR)**
LPH3	3.00	-	**17.8**
LPH4	3.00	-	**37.2**
HPH6	-2.00	3	**30.9**
HPH7	-1.00	3	**37.7**
HPH8	-1.50	3	**18.8**

The terminal temperature difference is the difference between the feedwater outlet temperature and the saturated temperature at the shell pressure as illustrated in Equation 4 and Equations 4 to 6 have been adapted from Devandrin et al. (2016):

$$\text{Terminal Temperature Difference(TTD)} = \text{Feedwater Temperature Out(To)} - T_{\text{Sat@Shell Pressure}} \quad [4]$$

The drain cooler approach is the difference between the drain temperature of the feedwater heater and the feedwater inlet temperature, as shown in Equation 5:

$$\text{Drain Cooler Approach (DCA)} = \text{Drain Temperature}(T_d) - \text{Feedwater Temperature In}(T_i) \quad [5]$$

The temperature rise (TR) is the difference between the feedwater outlet temperature and inlet temperature, as shown in Equation 6:

$$\text{Temperature Rise (TR)} = \text{Feedwater Temperature Out } (T_o) - \text{Feedwater Temperature In}(T_i) \quad [6]$$

The available data from the plant DCS, which is linked to the PI server, is extracted and shown in a simplified form in Table 4**,** and this input data is utilized to analyze the HR deviation.

Table 4
FWH parameters temperature at load 729 MWg, including nomenclature

Item	Nomenclature	Parameter (°C)
A) Feed water		
HPH6 Inlet	T_{6i}	188.4
HPH6 Outlet	T_{6o}	216.2
HPH7 Inlet	T_{7i}	216.2
HPH7 Outlet	T_{7o}	249.6
HP8 Inlet	T_{8i}	246.5
HPH8 Outlet	T_{8o}	266.9
B) Drains		
HPH6	T_{6d}	190.6
HPH 7	T_{7d}	214.7
HPH 8	T_{8d}	250.5
C) Saturated temperature		
HPH8	T_{HP8sat}	265.5
HPH 7	T_{HP7sat}	244.1
HPH 6	T_{HP6sat}	209.1
LPH 4	T_{HP4sat}	140.29
LPH 3	T_{HP3sat}	109.46
D) Condensate		
LPH3 Inlet	T_{3i}	86.3
LPH3 Outlet	T_{3o}	104.2
LPH4 Inlet	T_{4i}	104.3
LPH4 Outlet	T_{4o}	145.7

Condenser

The main function of the condenser is to convert exhaust steam from the LPT to liquid water, which can be pumped back to the boiler. It is vital to monitor the key parameters affecting the condenser's performance. Furthermore, several underlying issues, such as condenser water box cleanliness, may be obtained from the condenser performance monitoring regime. The general outline of a condenser is shown in Figure 3.

The terminal Temperature Difference (TTD) is the difference between saturated temperature obtained at condenser pressure and the cooling water outlet temperature, as shown in Equation 7 and Equations 7 to 10 have been adapted from Sikarwar et al. (2013):

$$\text{Terminal Temperature Difference (TTD)} = T_{\text{Sat@Condenser Pressure}} - \text{CWOutletTemp} \quad [7]$$

The variation due to Cooling Water (CW) flow is the difference between backpressure due to CW flow and target backpressure at the cooling water inlet, as illustrated in Equation 8:

$$\text{Variation due to CW Flow} = \text{Back Pressure due to CW Flow} - \text{Target back pressure at CW inlet} \quad [8]$$

The variation due to air ingress or dirty tubes is the difference between actual condenser pressure and backpressure due to Cooling Water (CW) flow, as illustrated in Equation 9:

$$\text{Variation due to air ingress or dirty tubes} = \text{Actual Condeser pres} - \text{Backpres due to CW Flow} \quad [9]$$

The variation from the target is the difference between actual condenser pressure and target backpressure due to Cooling Water (CW) inlet temperature, as shown in Equation 10:

$$\text{Variation from target} = \text{Actual condenser pres} - \text{Target back pres at CW Inlet temp} \quad [10]$$

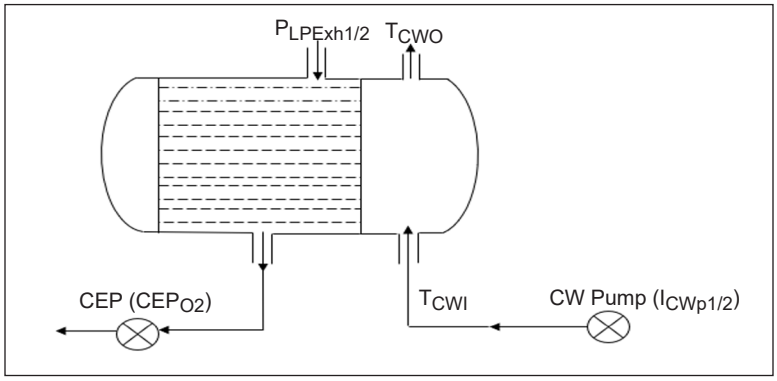

Figure 3. Condenser arrangement

The available data from the plant DCS, which is linked to the PI server, is extracted and shown in a simplified form in Table 5**,** and this input data is utilized to analyze the HR deviation. The measuring points or locations of items listed in Table 5 are included in Figure 3.

Table 5
Condenser parameters pressures, temperature and enthalpy at load 729 MWg including nomenclature

Item	Nomenclature	Unit	Parameter
CW inlet temperature	T_{CWi}	°C	29.96
CW outlet temperature	T_{CWo}	°C	38.22
CW Temperature rise	T_{CWTR}	°C	8.26
CEP discharge oxygen	CEP_{02}	%	4.47
CW Pump1 Motor current	I_{CWP1}	A	183.39
CW Pump2 Motor current	I_{CWP2}	A	179.50
LP1 Exhaust pressure	P_{LPExh1}	mbar-A	86.22
LP2 Exhaust pressure	P_{LPExh2}	mbar-A	79.43
Condenser pressure	$P_{Condpres}$	mbar-A	74.57
Saturated Temperature at Condenser Pressure	$T_{SatCond}$	°C	40.18
Condenser vacuum	$P_{Condvac}$	mbar-A	79.15

RESULTS AND DISCUSSION

Monitoring and analyzing deviations in key parameters affecting the HR deviation is vital for plant operators to ensure the unit is operating at optimal performance. From the HR deviation results, the operators can identify areas requiring intervention, thus mitigating the negative HR parameters. The HR deviation is also able to provide an indicator of underlying issues in the unit. The increase in the ACP causes an increase in the daily loss; thus, with the rising price of coal, it is of utmost importance for the plant operators to ensure the unit operates with minimal negative HR deviation.

The heat rate of CFPP is significantly affected by several key parameters, as shown in Table 6. The main steam temperature, which is the temperature at which the steam leaves the final superheater outlet and enters the High-Pressure Turbine (HPT), is one of the key indicators of the plant's performance. A drop in the main steam temperature will negatively impact the HR. This study shows that an 8^{o}C drop in the main steam temperature from the baseline target temperature leads to an HR increase of 24.3 kJ/kWh, which causes a monetary loss of RM 8,504 per day at the current ACP of RM 24/GJ. The drop in the main steam temperature suggests possible issues with the combustion, such as inadequate firing, which does not supply enough heat to the superheaters to achieve the main steam temperature, or poor cleanliness of the superheater due to slagging, which causes the inability of steam to absorb heat from the flue gas path. One of the possible remedies is conducting selective soot blowing at the superheater area or changing to a different type of coal to address the issue.

The Hot Reheat temperature, the steam flow from the HPT exhaust that has gone through a reheating process in the boiler's reheater section, is also an important indicator of plant performance. A drop in the hot reheat steam temperature will negatively affect the HR of the plant, such as the 10^{o}C drop in hot reheater steam temperature in this study leads to an increase in the HR by 24.5 kJ/kWh leading to a daily monetary loss of RM 8,587 per day. As previously discussed in the context of the main steam temperature, there are many possible reasons, such as poor cleanliness of the reheater surface, which causes poor heat absorption and, thus, the inability of steam to absorb heat. The possible remedies for lower hot reheat steam include conducting selective soot blowing at the rear pass of the boiler and increasing the gas recirculation damper opening if the plant is equipped with the gas recirculation system to enable more heat to be recirculated to the furnace from the tapping after the rotary air heater.

The superheater and reheater attemperator spray flows serve as a control measure to ensure the main steam and hot reheat temperatures do not exceed the setpoint temperature, as higher temperatures can damage boiler tubes and turbine blades while initiating the Boiler Protection system to trip the boiler if the main steam and hot reheat temperatures are too high. Typically, there is an expected superheater spray flow value of 2.68% of the

main steam flow to maintain the nominal main steam temperature. Suppose the superheater spray flow increases above the expected flow. In that case, there is a negative effect on the HR, such as the increase in superheater spray by 0.82% from the baseline value of 2.68% leads to an increase in HR by 2.6 kJ/kWh, causing a daily monetary loss of RM 820 at an ACP of RM 24/GJ as illustrated in Table 6. Furthermore, this indicates the possibility of overfiring in the boiler as more heat is absorbed in the superheater; thus, the main steam requires cooling to protect the tubes obtained from the superheater spray. The typically expected flow for the reheater spray is 0%, and an increase in reheater spray indicates a negative effect on the HR. In this typical scenario, as shown in Table 6, the reheater outlet steam temperature is lower than the reference value; thus, logically, there should be no spray flow to cool down the reheater outlet steam, but since there is a spray flow of 0.9%, which leads to increase of HR by 15.8 kJ/kWh causing daily monetary losses of RM 5,527 at an ACP of RM 24/GJ, this suggests the reheater spray flow valve is passing, or there are issues in the control logic.

The furnace flue gas outlet temperature and the rotary air heater outlet temperature are major indicators of boiler performance, cleanliness, and air heater performance. Generally, an increase in the furnace flue gas outlet temperature indicates poor heat absorption from the flue gas to the boiler water walls, superheater, and reheater elements. An increase in the furnace flue gas outlet temperature negatively affects the HR, such as the increase of furnace outlet flue gas temperature of 32^{o}C which leads to an increase in HR by 80.9 kJ/kWh, causing a daily monetary loss of RM 28,344 at an ACP of RM 24/GJ since there is a wastage of heat which is not absorbed in the furnace water walls or elements. The rotary air heater outlet temperature is a significant indicator of the rotary air heater's performance. An increase in the rotary air heater outlet temperature also negatively affects the HR, such as the increase in rotary air heater outlet temperature of 30^{o}C causing an increase in HR of 137.9 kJ/kWh, which leads to a daily monetary loss of RM 48,314 at an ACP of RM 24/GJ, while this condition indicates there is possible chock age in the air heater elements which is causing poorer heat transfer from the hot end to the cold end of the air heater. Furthermore, a chock age in the air heater would cause a buildup of hot flue gas in the furnace outlet, as seen in this scenario. It reduces the velocity of the flue gas exiting the furnace, thus increasing the chances of the formation of fouling on the rear pass of the boiler, causing poorer heat absorption. The remedy to this situation is to improve the performance of the air heater by clearing the chock age, which may be done by performing high-pressure water washing during a unit outage or conducting soot blowing at lower operating loads as the enthalpy of the steam is higher thus dry steam is utilized to clean the air heater elements. If soot blowing is conducted at higher loads, the air heater soot blower will have lower enthalpy steam which means there will be wet steam; thus, the chock age in the elements will become worse instead of improving. In short, as highlighted by (Sundaravinayaka & Jayapaul, 2017), while several RAH improvements may be achieved by offline cleaning,

several actions may be taken by the operator to mitigate the issue as discussed, such as effective soot blowing and other operational adjustments, such as air-fuel ratio, changing of coal type as temporary mitigation if the situation permits and so forth.

The condenser vacuum is another key indicator of plant performance. The condenser is an important element of the turbine cycle which is responsible for fulfilling the heat rejection criteria of the Rankine cycle. The cooling water absorbs the rejected heat, and it is crucial to maintain the condenser vacuum at the nominal value to ensure the plant's performance is not adversely affected. An increase in the condenser vacuum negatively affects the HR of the plant, such as the increase in condenser vacuum of 7 mbar-A, which increases the HR by 38.2 kJ/kWh leading to a daily monetary loss RM 13,391 at an ACP of RM 24/GJ. This trend has also been seen by Gupta and Kumar (2015).

The economizer inlet temperature is an important indicator of the overall feedwater heaters' performance, as the feedwater heaters are responsible for preheating the feedwater before it enters the boiler. A drop in the economizer inlet temperature affects the heat rate negatively, such as the drop in economizer inlet temperature of 6^{o}C causes an increase in the HR by 24.3 kJ/kWh, leading to a daily monetary loss of RM 8,503 at an ACP of RM 24/GJ since the boiler requires more heat input to achieve the desired main steam and reheat steam temperatures. A lower economizer inlet temperature also generally indicates the feedwater heater train's poor performance, as Devandiran et al. (2016) described.

The daily monetary losses or gains are greatly impacted by the change in ACP price, as seen in Table 6. As the ACP increases from RM 12/GJ to RM 18/GJ and subsequently to the present ACP of RM 24/GJ, the magnitude of daily losses increases for all the key parameters for the same HR change. For instance, the daily losses for a drop in main steam temperature by 8^{o}C increase from RM 4,252 to RM 8,504 as the ACP increase from RM 12/GJ to RM 24/GJ. It highlights the significant impact of the ACP prices towards the monetary gains or losses of the CFPP, and in the situation where the coal price, or in other words, the ACP, increases, it is even more vital for plant operators to pay more attention and to remedy such key parameters which are causing negative HR deviation to minimize the monetary losses.

The ranking of key parameters which are causing the most monetary losses to the least monetary losses based on the analysis of which parameter affects the HR deviation negatively the most is shown in Figure 4. The RAH Outlet temperature has the highest contribution to the HR deviation of the CFPP. The monetary losses of RM 17.6 million per year are for the increase of the RAH outlet temperature alone. The second parameter which affects the HR deviation the most is the furnace outlet temperature, which is closely related to the RAH outlet temperature, as previously discussed. Thus, if the RAH chock age may be improved, the potential for improvement in plant performance is very significant as it will address losses due to RAH outlet temperature and furnace outlet temperature. The other

Table 6
CFPP heat rate impact factor based on parameter

No	Parameter	Nomenclature	Reference value	Actual	Deviation	Heat Rate Factor		Losses/Gain (RM/day)			
						Change in parameter	HR (kJ/ kWh)	HR change (kJ/kWh)	ACP: RM12/ GJ	ACP: RM18/ GJ	ACP: RM24/ GJ
1	Main steam temperature	T_{MS}	540.00	532	-8	10.00	-30.34	24.3	-4252	-6378	-8504
2	Hot reheat steam temperature	T_{HRH}	540.00	530	-10	10.00	-25.28	24.5	-4294	-6441	-8587
3	Main steam pressure	P_{MS}	170.00	166	-4	0.70	-4.05	23.1	-4054	-6082	-8109
4	Superheater spray	$\dot{m}_{SHS}$	2.68	3.5	0.82	0.82	2.63	2.6	-460	-690	-920
5	Reheater spray	$\dot{m}_{RHS}$	0.00	0.9	0.9	1.50	26.29	15.8	-2763	-4145	-5527
6	Rotary air heater outlet temperature	T_{RAHOut}	160.00	190	30	5.50	25.28	137.9	-24157	-36235	-48314
7	Furnace outlet temperature	$T_{FurnOut}$	350.00	382	32	10.00	25.28	80.9	-14172	-21258	-28344
8	Excess water flows through LPH	$\dot{m}_{excLPH}$	0.00	2.55	2.55	5.00	101.12	51.6	-9042	-13563	-18084
9	Excess water flows through HPH	$\dot{m}_{excHPH}$	0.00	2.28	2.28	5.50	101.12	41.9	-7345	-11018	-14690
10	Economizer inlet temperature	T_{EcoIn}	271.00	265	-6	2.50	-10.11	24.3	-4252	-6377	-8503
11	Condenser vacuum	$P_{condvac}$	85.00	92	7	10.00	54.60	38.2	-6696	-10044	-13391

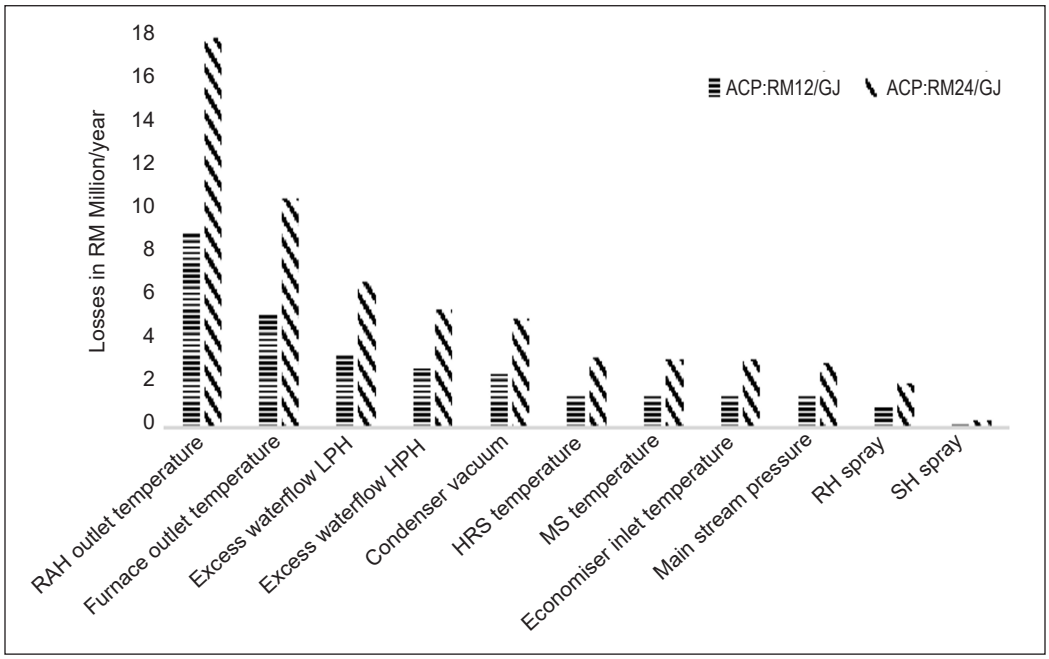

Figure 4. HR deviation losses for key parameters

significant cause for losses due to the excess water flow in the LPH is caused by the higher make of the flow. Thus, the losses due to excess water flow through LPH may be reduced by attending to passing valves, such as drain valves, to reduce the makeup flow. The excess flow of HPH is due to the feedwater flow being higher than the main steam flow, and this also contributed to passing drain and vent valves along the feedwater lines, which must be rectified to reduce this loss. The condenser vacuum is also a significant contributor to the losses, and the performance of the condenser may be improved by addressing potential air ingress and blockage in the cooling water inlet at the water box. The superheater and reheater spray flow contribute the least to the HR deviation.

Feedwater Heaters

The performance of the feedwater heaters is an important aspect of the turbine cycle of a CFPP, which serves the purpose of preheating condensate in the case of LPH and preheating feedwater in the case of HPH preheating feedwater. The extraction steam from various stages of the High Pressure, Intermediate Pressure, and Low-Pressure Turbines is used to preheat the fluid medium passing through the feedwater heater to a higher temperature so that the boiler has to consume less heat energy in the form of coal to achieve the main steam and reheat steam temperatures.

Thus, it is vital to ensure that the FWHs are consistently performing at the optimum performance. The three key performance parameters associated with FWH performance

are the Terminal Temperature Difference (TTD), Temperature Rise (TR), and Drain Cooler Approach (DCA). The nominal values of these key parameters are readily available in the plant Heat Balance Diagram (HBD) or may be taken from the Performance Guarantee Test (PGT).

Based on Table 7, the current values of the TTD are compared with the baseline or reference values obtained from the HBD or PGT. The TTD is an indicator of the FWH's performance in terms of heat transfer. An increase in the TTD value indicates an increase in heat transfer. The TTD for HPH8, 7, and 6 are negative 4.21°C, 5.40°C, and 6.97°C, respectively, while the TTD for LPH 4 and 3 are positive 3.49°C and 5.30°C, respectively. However, it is crucial to ensure the TTD is maintained at the nominal range and does not decrease too much, as it can negatively affect the overall performance of the Turbine Cycles.

The HPH8 has the highest deviation from the design value and combined with a significant HR factor, the daily monetary losses for HPH8 causes are the most significant, RM3,844 per day compared to HPH7 and HPH6, which are contributing to daily monetary losses of RM1,869 and RM2,110 respectively for an ACP of RM 24/GJ. As previously discussed, the daily monetary losses increase as the ACP increases from RM 12/GJ to RM 24/GJ. For instance, for HPH8, the daily losses increase from RM1,922 to RM3,844 as the ACP increases from RM12/GJ to RM 24/GJ. The TTD for the LPH is around the nominal range; thus, the HR deviation may be considered insignificant, although continuous monitoring is necessary to detect any changes in the LPH performance over time. In terms

Table 7
FWH performance parameters

No	Parameter	Reference value (°C)	Actual (°C)	Deviation (°C)	Heat Rate Factor		Daily Gain/Losses (RM/day)		
					Change	HR (kJ/kWh)	ACP: RM12/GJ	ACP: RM18/GJ	ACP: RM24/GJ
1	HPH8 TTD	-1.5°C	-4.21	2.71	2.50	10.1	-1922	-2883	-3844
2	HPH7 TTD	-1.0°C	-5.40	4.40	2.50	3.03	-935	-1402	-1869
3	HPH6 TTD	-2.0°C	-6.97	4.97	2.50	3.03	-1055	-1583	-2110
4	LPH4 TTD	3.0°C	3.49	0.49	2.50	3.03	-104	-155	-207
5	LPH3 TTD	3.0°C	5.30	2.30	2.50	3.03	-489	-733	-977
6	HPH8 TR	18.8	20.34	1.54	-	-	-	-	-
7	HPH7 TR	37.7	33.46	-4.24	-	-	-	-	-
8	HPH6 TR	30.9	27.76	-3.14	-	-	-	-	-
9	LPH4 TR	37.2	41.64	4.44	-	-	-	-	-
10	LPH3 TR	17.8	17.31	-0.49	-	-	-	-	-
11	HPH8 DCA	3	3.96	0.96	-	-	-	-	-
12	HPH7 DCA	3	-1.52	-4.52	-	-	-	-	-
13	HPH6 DCA	3	2.17	-0.83	-	-	-	-	-

of the DCA, the DCA may only be calculated for HPH 6,7 and 8 as the measurements needed to evaluate the DCA are available for these heaters since the heater drain temperature instrument is not installed in the LPHs. The DCA needs to be maintained around the nominal range to prevent flashing in the drain cooler section, which may cause damage to the heater tubes. It is observed that the DCA for HPH 6 and HPH8, 2.17^{o}C and 3.96^{o}C, respectively, are within normal range while the DCA for HP7, -1.52^{o}C, is negative instead of positive, which indicates possible issues with the level control of the heater as the heater level may have increased causing the decrease of DCA. A decrease in DCA alongside a decrease in the TR indicates the heater level increase, as seen in HPH7. An increase in the FWH level causes overfiring in the boiler, which increases fuel consumption and causes other associated issues, such as an increase in furnace outlet temperature, an increase in superheater and reheater spray flows, and damage to boiler tubes and FWH tubes. Although (Almedilla et al., 2018) have investigated the procedure of determining the TTD of FWH, there is no correlation between the deviation of TTD with financial analysis and data utilized from smaller 135 MWn CFPP.

Condenser

The condenser performance monitoring is carried out by monitoring several key parameters around the condenser. The input parameters from the DCS are illustrated in Table 4, and the output of the analysis conducted is summarized in Table 8. There are three data sets that refer to the data taken from the DCS for three days at similar unit loads and at the same time to ensure fair comparison at similar sea tide levels. In general, the first parameter which is observed is the Cooling Water (CW) temperature rise. The actual CW temperature rise is compared with the expected CW temperature rise at design condition, and it is seen that the CW temperature rise has increased by approximately 1^{o}C, which suggests the amount of rejected heat into the condenser has increased and thus, the condenser duty has increased, causing poor condenser performance. The actual condenser TTD is much lower than the expected TTD at design conditions, which suggests the condenser has better heat transfer than expected. The CEP discharge oxygen levels indicate any possible air ingress in the condenser. The increasing trend indicates possible air ingress, which requires the operation teams to perform a valve lineup around the condenser and observe for improvements. Suppose there are passing or leaking valves detected during the valve line. In that case, the maintenance teams can prepare for corrective maintenance in the upcoming outage, as air ingress negatively affects the condenser performance. If there is an increase in the cooling water pump motor currents, as seen in the case of CW Pump 1, where the current increases from 183.39 Amp to 190.95 Amp, there is a possibility of barnacles obstructing the CW intake into the condenser, which requires cleaning works in the condenser box to be carried out. The plant commissioning data manual obtains the target backpressure

at CW inlet temperature and backpressure due to CW flow. The variation was due to CW flow increasing as the actual CW temperature rises increases. Although studies have been related to predictive condenser maintenance and methodologies (Jianlan et al., 2016; Matthews et al., 2020), no correlation exists between condenser performance and financial analysis. Overall, there is negative HR deviation for all three data sets causing daily losses of RM4,858, RM7,051, and RM8,968, respectively, at an ACP of RM24/GJ, and it is evident that the daily monetary losses increase as the ACP increases from RM 12/GJ to RM 24/GJ as illustrated in the last rows of Table 8.

Table 8
Condenser performance parameters

No.	Parameters		Unit	Data Set I	Data Set II	Data set III
1	Unit load		MWg	732.66	730.55	732.31
2	CW inlet temperature		°C	29.96	29.62	29.56
3	CW outlet temperature		°C	38.22	38.51	39.08
4	Actual CW temperature rise		°C	8.26	8.89	9.52
5	CW temperature rise at design conditions			7.46	7.44	7.45
6	Actual condenser TTD		°C	1.97	2.06	1.89
7	Optimum condenser TTD at design conditions			2.92	2.92	2.92
8	CEP discharge oxygen		%	4.47	4.50	4.48
9	CW pump 1 motor current		A	183.39	189.85	190.95
10	CW pump 2 motor current		A	179.50	179.13	179.06
11	LP1 exhaust pressure		mbar-A	86.22	85.74	88.08
12	LP2 exhaust pressure		mbar-A	79.43	81.65	84.84
13	Condenser vacuum		mbar-A	79.15	85.06	86.31
14	Condenser pressure		mbar-A	74.57	76.11	77.75
15	Target back pressure at CW inlet temperature		mbar-A	70.79	70.62	70.76
16	Back pressure due to CW flow		mbar-A	78.34	79.54	81.98
17	Variation due to CW flow			7.55	8.92	11.22
18	Variation due to air ingress /dirty tubes			-3.77	-3.43	-4.24
19	Total variation from the target			3.78	5.49	6.98
20	Daily gains/ losses (RM/day)	ACP:RM12/GJ	RM	-2,429	-3,525	-4,484
		ACP:RM18/GJ	RM	-3,644	-5,288	-6,726
		ACP:RM24/GJ	RM	-4,858	-7,051	-8,968

CONCLUSION

An analysis to evaluate the impact of various aspects influencing the HR of the CFPP by means of HR deviation has been carried out. The analysis incorporates financial analysis

with the influence of ACP included in the study, which is of great benefit as not much importance has been given to the financial analysis of CFPP in previous studies. The HR deviation analysis utilizes real-life plant data, improving the accuracy of the results and outcome as commissioning and PGT data have also been considered. The results obtained in this study apply to other subcritical CFPPs provided the baseline figures for the CFPP are available. It was found that the most significant negative HR deviation is for the RAH flue gas exit temperature with a negative HR deviation of 137.9 kJ/kWh leading to an annual monetary loss of RM17.6 million at an ACP of RM24/GJ and the superheater contributes the least negative HR, and reheater spray flows with HR deviation of 2.63 kJ/kWh and 15.77 kJ/kWh, respectively causing annual monetary losses of RM0.34 million and RM2.02 million respectively at an ACP of RM24/GJ. This trend of gains or losses will also be similar for other CFPPs as the effect of deviation in key parameters will be the same such as monetary losses due to lower main steam temperature and so forth for the other parameters. The monitoring of HR deviation can also provide an indicator of underlying issues in the unit. The ranking of which parameters affecting HR the most are also highlighted so that operation and maintenance personnel can focus more on significant parameters.

ACKNOWLEDGEMENT

The authors thank Universiti Putra Malaysia for the support in completing the manuscript and Yayasan Khazanah, Malaysia, for providing the prestigious Khazanah Watan Scholarship to the corresponding author.

REFERENCES

Ahmadi, G. R., & Toghraie, D. (2016). Energy and exergy analysis of Montazeri steam power plant in Iran. *Renewable and Sustainable Energy Reviews, 56*, 454-463. https://doi.org/10.1016/j.rser.2015.11.074

Almedilla, J. R., Pabilona, L. L., & Villanueva, E. P. (2018). Performance evaluation and off design analysis of the HP and LP feed water heaters on a 3 × 135 MW coal fired power plant. *Journal of Applied Mechanical Engineering, 7*(3), 1-14. https://doi.org/10.4172/2168-9873.1000308

Behbahaninia, A., Ramezani, S., & Hejrandoost, M. L. (2017). A loss method for exergy auditing of steam boilers. *Energy, 140*, 253-260. https://doi.org/10.1016/j.energy.2017.08.090

Bisercic, A. Z., & Bugaric, U. S. (2021). Reliability of baseload electricity generation from fossil and renewable energy sources. *Energy and Power Engineering, 13*, 190-206. https://doi.org/10.4236/epe.2021.135013

Braun, S. (2021). Improving flexibility of fossil fired power plants. *Encyclopedia of Energy Storage Elsevier, 2*, 133-140 https://doi.org/10.1016/B978-0-12-819723-3.00085-8

Buckshumiyanm, A., & Sabarish, R. (2017). Performance analysis of regenerative feedwater heaters in 210 MW thermal power plant. *International Journal of Mechanical Engineering and Technology, 8*(8), 1490-1495.

Devandiran, E., Shaisundaram, V. S., Ganesh, P. B., & Vivek, S. (2016). Influence of feedwater heaters on the performance of coal fired power plants. *International Journal of Latest Technology in Engineering, Management & Applied Science, 5*(3), 115-119.

Elhelwa, M., Dahmaa, K. S. A., & Attiaa, A. E. H. (2019). Utilizing exergy analysis in studying the performance of steam power plant at two different operation mode. *Applied Thermal Engineering, 150*, 285-293. https://doi.org/10.1016/j.applthermaleng.2019.01.003

Energy Commission of Malaysia. (2020). *Peninsular Malaysia Electric Supply Outlook 2020*. https://www.ketsa.gov.my/msmy/pustakamedia/Penerbitan/Report%20on%20Peninsular%20Malaysia%20Generation%20Development%20Plan%202020%20(2021-2039).pdf

Energy Commission of Malaysia. (2022). *Trend of Fuel Prices*. https://www.st.gov.my/contents/2022/Fuel%20Prices/8-%20ACP%20as%20of%20Mac%202022.pdf

Gupta, M., & Kumar, R. (2015). Thermoeconomic optimization of a boiler used in a coal fired thermal power plant based on hot air temperature. *International Journal of Recent Advances in Mechanical Engineering, 4*(2), 39-44. https://doi.org/10.14810/ijmech.2015.4205

Jianlan, L., Zhaoyin, Z., Jizhou, W., & Shuhong, H. (2016). On-line fouling monitoring model of condenser in coal-fired power plants. *Applied Thermal Engineering, 104*, 628-635. 10.1016/j.applthermaleng.2016.04.131

Mathews, E. H., van Laar, J. H., Hamer, W., & Kleingeld, M. (2020). A simulation-based prediction model for coal-fired power plant condenser maintenance. *Applied Thermal Engineering, 174*, Article 115294. https://doi.org/10.1016/j.applthermaleng.2020.115294

Mohammed, M. K., Al Doori, W. H., Jassim, A. H., Ibrahim, T. K., & Al-Sammarraie, A. T. (2020). Energy and exergy analysis of the steam power plant based on effect the numbers of feed water heater. *Journal of Advanced Research in Fluid Mechanics and Thermal Sciences, 56*(2), 211-222.

Neshumayev, D., Rummel, L., Konist, A., Ots, A., & Parve, T. (2018). Power plant fuel consumption rate during load cycling. *Applied Energy, 224*(C), 124-135. https://doi.org/10.1016/j.apenergy.2018.04.063

Nistah, N. N. M., Motalebi, F., Samyudia, Y., & Alnaimi, F. B. I. (2014). Intelligent monitoring interfaces for coal fired power plant boiler trips: A review. *Pertanika Journal of Science and Technology, 22*(2), 593-601.

Oyedepo, S. O., Kilanko, O., Waheed, M. A., Fayomi, O. S. I., Ohunakin, O. S., Babalola, P. O., Ongbali, S. O., Nwaokocha, C. N., Mabinuori, B., & Shopeju, O. O. (2020). Dataset on thermodynamics performance analysis and optimization of a reheat-regenerative steam turbine power plant with feed water heaters. *Data in brief, 32*, Article 106086. https://doi.org/10.1016/j.dib.2020.106086

Pachaiyappan, J., & Prakash, D. (2015). Improving the boiler efficiency by optimizing the combustion air. *Applied Mechanics and Materials, 787*, 238-242. https://doi.org/10.4028/www.scientific.net/AMM.787.238

Sabzpooshani, M., Azadehfar, E., & Sardarian, S. (2019). Exergy evaluation and optimization of a new steam power plant configuration in order to use the boiler blowdown water. *Journal of Energy Management and Technology (JEMT), 3*(1), 30-39.

Sikarwar, A. S., Dandotiya, D., & Agrawal, S. K. (2013). Performance analysis of surface condenser under various operating parameters. *International Journal of Engineering Research and Applications, 3*(4), 416-421.

Sundaravinayaka, U., & Jayapaul T. (2017). Optimization of boiler operation in thermal power station. *International Journal of Latest Engineering Research and Applications, 2*(3), 64-68.

Tian, Z., Xu, L., Yuan, J., Zhang, X., & Wang, J. (2017). Online performance monitoring platform based on the whole process models of subcritical coal-fired power plants. *Applied Thermal Engineering, 124*, 1368-1381. https://doi.org/10.1016/j.applthermaleng.2017.06.112

Wang, Y., Cao, L., Hu, P., Li, B., & Li, Y. (2019). Model establishment and performance evaluation of a modified regenerative system for a 660 MW supercritical unit running at the IPT setting mode. *Energy, 179*, 890-915. https://doi.org/10.1016/j.energy.2019.05.026

Wijaya, A. A., & Widodo, B. U. K. (2018). The effect of feedwater heaters operation schemes to a 200 MW steam power plant heat rate using cycle-tempo software. *IPTEK Journal of Engineering, 4*(3), 33-37. https://doi.org/10.12962/joe.v4i3.4995

Zhang, Y., Wang, J., Yang, S., & Gao, W. (2018). An all-condition simulation model of the steam turbine system for a 600 MW generation unit. *Journal of Energy Institute, 91*(2), 279-88. https://doi.org/10.1016/j.joei.2016.11.007

Pertanika J. Sci. & Technol. 31 (3): 1475 - 1491 (2023)

PERTANIKA JOURNALS

SCIENCE & TECHNOLOGY

Journal homepage: http://www.pertanika.upm.edu.my/

Effects of Shooting Angles and Ricochet Angles on Bullet Weight Upon Impact on Three Types of Woods (Balau, Resak, and Seraya)

Mohd Najib Sam[1,2], Glenna Tan Jie Yee[1], Noor Hazfalinda Hamzah[1], Mohd Zulkarnain Embi[2], Ahmad Zamri Md Rejab[2], Gina Francesca Gabriel[1] and Khairul Osman[1]*

[1]*Forensic Science Program, Faculty of Health Science, Universiti Kebangsaan Malaysia (UKM), 43600 UKM Bangi, Selangor, Malaysia*

[2]*Malaysian Maritime Enforcement Agency, Ministry of Home Affairs, One IOI Square, IOI Resort, 62502 Putrajaya, Malaysia*

ABSTRACT

This study aims to determine if the number of shots fired, bullet striation marks, and shooting and ricochet angles could influence bullet weight on three types of woods: Balau, Resak, and Seraya. The weapon and ammunition used in this study were CZ 75 SP-01 Shadow semi-automatic pistol with 9 mm full metal jacketed bullets (7.45 g). A total of 432 shots were fired, and only 114 bullets produced a ricochet effect. The result of objective one showed no significant relationship between the number of shots and the number of bullet striations for all three kinds of wood. Correlation-Regression analysis for the second objective showed a significant relationship between shooting angle and bullet weight when shooting on Balau ($p < 0.01$, $R^2 = 0.065$) and Seraya ($p < 0.01$, $R^2 = 0.199$) but not on Resak. The shooting angle influenced the bullet weight by 6.5 % to 20 % when shooting on Balau and Seraya. Both kinds of wood are closely related and share fibre composition and modulus of elasticity (MOE) characteristics. The result of the third objective showed a relationship between ricochet angle and bullet weight during the shooting on Resak ($p < 0.01$, $R^2 = 0.142$) but not on Balau and Seraya. The ricochet angle on Resak influenced the bullet weight by 14.2 + 9.8 %. It is probably due to Resak having the highest MOE among the three types of woods. This study concludes that bullet weight loss is due to the ricochet effect and the composition of the bullet's target.

Keywords: Balau, Resak, ricochet, Seraya, shooting angle

ARTICLE INFO

Article history:
Received: 29 May 2022
Accepted: 05 October 2022
Published: 31 March 2023

DOI: https://doi.org/10.47836/pjst.31.3.19

E-mail addresses:
najibmmea@gmail.com (Mohd Najib Sam)
glennatan0520@gmail.com (Glenna Tan Jie Yee)
raviera@yahoo.com (Noor Hazfalinda Hamzah)
mohdzulkarnaini@mmea.gov.my (Mohd Zulkarnain Embi)
zamrirejab@mmea.gov.my (Ahmad Zamri Md Rejab)
ginafgabriel@ukm.edu.my (Gina Francesca Gabriel)
khairos@ukm.edu.my (Khairul Osman)
* Corresponding author

ISSN: 0128-7680
e-ISSN: 2231-8526

© Universiti Putra Malaysia Press

INTRODUCTION

A ricochet effect can occur when a bullet hits a hard target surface. The risk of this phenomenon is exceptionally high when Maritime Enforcement officers board a ship and clear off potential suspects in a closed compartment. According to Brian (2008), when a bullet strikes any surface, there is a critical angle at which it will bounce off or ricochet from the surface rather than penetrate it (Maho et al., 2019; Hamzah et al., 2020). A ballistic reconstruction based on the ricochet effect of bullets can help provide insight into whether that particular enforcement officer is legally responsible for the accidental death of the victim (Nishshanka et al., 2020). The reconstruction of a shooting scene can provide helpful information for investigating officers in solving a crime by evaluating the evidence available, thus deducing what had possibly happened during the shooting incident (Mahoney et al., 2019). Crime scene investigation (CSI) experts have reported that when a bullet is fired, a reduction of bullet weight will occur, particularly after the shooting is made at an angle. It is further postulated that weight loss will occur due to the ricochet effect of the bullet (Nichols, 2018). However, previous studies regarding the impact of ricochets on bullet weight are sparse. Furthermore, it is suspected that the loss of bullet weight due to the ricochet effect is influenced by the composition of the bullet's target (Kpenyigba et al., 2015; Koene & Broekhuis, 2017).

In 2017, fishing vessels plying on seas around Southeast Asia were reported to be around 1,270,000. Studies have shown that these boats are built mainly from Balau, Seraya, and Resak woods (Malaysian Timber Council, 2020a, 2020b, 2020c; Wahab & Ramli, 2020). These vessels are small compared to commercial fishing vessels as they usually have a dimension of around 10 to 15 m in length with a beam of approximately 6.1m (Atzampos et al., 2018). Due to their relatively small size, small water displacement, and commonly found around ocean boundaries between countries, their movement on the sea is relatively unhampered by shallow waters or close monitoring by enforcement agencies (Dang et al., 2018).

Most fishermen are law-abiding men, but a few would supplement their meagre income with illegal activities (United Nations Office on Drugs and Crime, 2011; Mackay et al., 2020). Consequently, lately, Malaysian Maritime Enforcement Agencies (MMEA) within the region have started to conduct frequent random boarding to ensure the vessel's cargo is legal. In rare cases, shooting will occur when enforcement officers approach the craft, board the boat, or conduct searches within the boat (Abbo, 2021).

Although the vessels are small, compartments inside the boat are present to provide a watertight space. It is made in such a way as to allow privacy and further strengthen the vessel's structure. Due to this, unethical fishermen will create hidden panelling. In these panels, illegal drugs would be hidden from sight and, if sufficiently large enough – humans. During the search below deck, shooting could occur, and due to the relatively small area

of each compartment, the shooting would be at an angle and a close distance (less than 10 m) (Dang et al., 2018).

Timber refers to the stage where a woodblock is cut from a fallen tree and is ready for further processing. However, there might be a presence of variability in its mechanical properties due to it being a biological material. Thus, strength grouping was proposed for the timbers to standardise their mechanical properties. This standardisation facilitates the selection of suitable timber for structural purposes. The strength grouping of tropical hardwood timber can be classified into strength groups (SG) A to D, based solely on compression strength parallel to the grain. This study's target of interest is the material used to build local fishing vessels: Balau, Resak and Seraya.

Balau (*Shorea* spp.) is a heavy, dense hardwood with the strength properties of Group A (Asyraf et al., 2021). It is a solid timber with a compressive strength of above 55.2 MPa. The wood is also highly durable resulting in relatively high resilience towards heavy impact forces cast by the sea. Hence, it is commonly used in wooden boat construction in Malaysia.

Resak (*Vatica* spp.) is a hard and heavy wood classified under Group B. Timber classified under-strength properties of Group B are very strong woods with a compressive strength mean of 7.52 MPa (Puaad et al., 2020). However, Resak from Strength Group B has lower strength properties when compared to that Balau, which is in Strength Group A.

On the other hand, Seraya (*Shorea* spp.), commonly known as Dark Red Meranti, is a light hardwood that is moderately durable (Widiyono, 2021). The strength properties of Seraya wood fall in Group C. Group C timbers are strong and have a compressive strength of between 27.6- 44.3 MPa. Despite being the lightest hardwood among the three types of wood investigated in this study, the relatively lightweight properties of Seraya enable better buoyancy than the rest (Dewi et al., 2020). Table 1 shows the characteristics of Resak, Balau and Seraya.

Table 1
Characteristic of woods

Wood type	Woods classification	Strength properties group	Compressive strength (MPa)
Balau	Heavy Hardwood	A	55.2
Resak	Heavy Hardwood	B	7.52
Seraya	Light Hardwood	C	27.6–44.3

Based on the Malaysian Timber Council, Balau wood, known by its scientific name *Shorea* spp., is a heavy hardwood with a density of 850-1,155 kg/m^3 air dry (Malaysian Timber Council, 2020a). It has a Janka Hardness of 8,010-9,520 N. Resak wood with the scientific name of *Cotylelobium* spp. and *Vatica* spp. (Dipterocarpaceae) is also a heavy hardwood with a slightly lower density than Balau wood. The density for Resak wood is 655–1,155 kg/m^3 air dry with a Janka Hardness of between 2,570 to 8,990 N. Meanwhile,

Seraya, the scientific name of *Shorea curtisii*, is a light hardwood with a density of around 415 to 885 kg/m^3 air dry. The Janka Hardness for Seraya wood is usually between 1,020 to 4,480 N (Table 2).

Table 2
Properties of woods

Wod	**Balau (*Shorea* spp.)**	**Resak (*Vatica* spp.)**	**Seraya (*Shorea* spp.)**
Type of wood	Heavy hardwood	Heavy hardwood	Light hardwood
Strength properties of Wood	Strength Group A	Strength Group B	Strength Group C
Janka Hardness (N)	8,010-9,520	2,570-8,990	1,020-4,480
Density (kg/m^3 air dry)	850-1,155	655-1,155	415-885
Modulus of Elasticity (MPa)	16,670	19,500	13,020
Wood grain	Deeply interlocked	Straight or shallowly interlocked	Interlocked
Fibre structure (Texture)	Moderately fine to slightly coarse	Fine and even	Moderately coarse and even
Fibre composition (%)	27	No relevant information	25

Numerous previous studies have been performed regarding a bullet's ricochet effect. Koene (2016) demonstrated in their study that there would be at least 70% of energy loss to the projectile due to ricochet. There will be a more significant energy loss when shooting on harder wood types than a softer wood. Kerkhoff et al. (2015) showed that 50% of fired bullets (.32 Auto and 9 mm Luger) would experience a ricochet effect when a critical angle is reached. Further, the effect is influenced by the weapon calibre and composition of the target drywall (Walters & Liscio, 2020). Their study also found a strong linear relationship between the critical angle, wood density and Janka Hardness. It was further noted that to create a ricochet effect, and the critical shooting angle increases in parallel with the value of the wood's Janka Hardness (Wong & Jacobson, 2013). They reported that the correlation coefficients in their study were 0.997 (density, .32 Auto), 0.985 (density, 9 mm Luger), 0.987 (Janka Hardness, .32 Auto) and 0.962 (Janka Hardness, 9 mm Luger) (Table 3).

Table 3
Bullet correlation coefficients

Cartridges with full metal jacket bullets	**.32 Auto**	**9 mm Luger**
Correlation Coefficients	0.997	0.985
	0.987	0.962

It was also noted that the shooting angle for smaller calibre bullets is higher, as seen in the higher correlation coefficient of .32 Auto bullets compared to 9 mm Luger bullets when shooting on wood with the same density and Janka Hardness.

Nordin et al. (2020) reviewed the forensic significance of gunshot impact marks, including the study of bullet striation after a ricochet effect. Their review highlighted the importance of viewing forensic investigation on a case-specific basis due to the unpredictable difference between real-case shooting scenarios versus controlled studies. They also emphasised the lack of synchronisation and comparable data among current researchers, which leads to difficulties in predicting the bullet's behaviour during shooting reconstruction when a different combination of ammunition and target materials is involved.

Relating to that, this study's main focus is the number of shots fired, bullet striation marks, bullet weight, shooting angle and ricochet angle. The weapon and ammunition used in this study are commonly used by the Malaysian Maritime Enforcement Agency (MMEA) officers (Wahid, 2020; Agensi Maritim Luar Negara, 2019).

It is suspected that the ricochet effect of the bullets would differ after hitting different target surfaces (Nishshanka et al., 2021a). This phenomenon is essential in the forensic context as the impact of firing may vary due to the nature of the target surface, different shooting angles, and distances (Liscio & Imran, 2020). Therefore, this research aims to create an equation model that includes all the factors, including bullet striation marks, shooting angles and ricochet angles, allowing maritime CSI to create a near-accurate ballistic reconstruction scene.

MATERIALS AND METHODS

Firearms and Ammunition

A Czech Republic-made CZ 75 SP-01 SHADOW series semi-automatic pistol with 9mm FMJ bullets were selected. They are commonly used by the Malaysian Maritime Enforcement Agency (MMEA) officers (Wahid, 2020; Agensi Maritim Luar Negara, 2019). It is a standard weapon used during ships' boarding and clearing out potential suspects in small compartments. CZ 75 SP-01 semi-automatic pistol is a reliable weapon with a drop-safe feature that prevents accidental discharge.

Wood

Balau, Resak and Seraya wood were selected as the target surface for this study. They are the three common types of wood used to manufacture fishing boats in Southeast Asia (Murdjoko et al., 2016; Cvetković et al., 2019; El-Taguri et al., 2020; Muslich & Sumarni, 2006; Abdullah, 2015).

Shooting/ Firing Protocol

The pistol was placed in a weapon mount with a string attached from the firearm's trigger to the place of release. Each of the three wood selected for the study (Balau, Resak and

Seraya wood) was clamped on an adjustable stand, with a fixed distance and a variable angle of 15°, 30°, 45°, 60°, 75° and 90° from the position of the gun. Next, a 9 mm FMJ bullet was loaded into the pistol. Then, a string connected to the trigger was pulled. The use of the string is to isolate the recoil effect of the weapon and indirectly improve the bullet's momentum. After each shooting, the fired bullet was searched, labelled, and packaged for further examination.

A minimum of 24 replications was conducted for each of the shooting angles. At each of the shooting angles (15°, 30°, 45°, 60°, 75° and 90°), the distance between the pistol and wood was 5 meters from the target. The shooting angles and distance were chosen based on the limited space available in a fishing boat. The main point of this study was to get the weight of the bullet after being fired (ricochet and penetrate). Hence, 144 shots were made on each type of wood.

The first study objective was to determine the relationship between the number of shots fired against bullet striation marks on different types of wood (Balau, Resak and Seraya). It is suspected that during multiple shots, the barrel within the weapon will heat up, making the inner wall of the barrel become soft. It causes striation marks to be easily developed when firing occurs. When the barrel cools down sufficiently enough, these newly created striation marks within the barrel will solidify. The newly created striations will cause the next bullet to have additional striations. Objective 1 examined the relationship between the number of shots and bullet striations. Thirty fired bullets shot at each wood were selected through random sampling. It was possible as each bullet shot was recorded, and shooting was done in batches: Balau, Resak and Seraya. It allowed us to select 30 bullets randomly in every wood group and still determine when the bullet was shot (sequence number) and the number of striations created. Samples were collected randomly. The sample selection was made by a third party to minimise biases. Thirty samples were selected based on statistics' Central Limit Theorem.

The bullets were then placed on a bullet holder, and the striation marks were examined under a LEICA DM2500M Compound Microscope. A Canon EOS 3000D was used in this research to capture the picture of bullets. As the bullet was not discharged previously, no striation marks were present on the bullet. The images of each side of the bullet's striation marks were captured through a camera attached to the compound microscope. The number of striations counted was based on striations visually observed under a compound microscope. The number of striations counted is based on an imaginary horizontal line created at 10% length of the existing bullet starting from the bottom of the bullet (Leon & Beyerer, 1999). The captured images of the bullet's striation marks were then further analysed with the help of ImageJ (Fiji) Windows 64-bit version software to analyse the number of striation marks present. Correlation-regression analysis was performed with a level of the significant set at $p < 0.05$.

The second objective determined the relationship between the shooting angle and the bullet weight when shooting on different types of wood: Balau, Resak and Seraya. In this research, all bullets were from the same manufacturer. Every bullet's weight was around 7.45g. Digital scales were used to determine the weight of the bullet after a shooting. A total of 432 shots were fired. The bullets were then retrieved and weighed. A correlation regression test was carried out for all the data of bullet weight for each type of wood.

The third specific objective was to determine the ricochet angle and the bullet weight during a shooting on different types of wood: Balau, Resak and Seraya. After the shots were fired, the ricochet angle for bullets with a ricochet effect was measured using basic trigonometry (Nishshanka et al., 2021b; Mattijssen et al., 2017). The angle measuring tool used was the Raymay Zero Base Protractor (Raymay Japan). The ricocheted bullets were also weighed using procedures similar to Objective 2. Again, a correlation regression analysis was conducted to analyse the data generated for each type of wood.

RESULTS

Bullet Striation Marks

Correlation analysis was conducted to determine the relationship between the number of striation marks and the sequence of shots fired on different types of wood (Balau, Resak and Seraya). A number system was used for each shot to avoid errors in identifying bullets and wood. The results of the correlation analysis showed that it is statistically insignificant for all three types of wood. The *p*-values for Balau, Resak and Seraya were 0.076, 0.673, and 0.331, respectively. Hence, we concluded no correlation between the striation marks of bullets when fired at different types of wood. The relationship between the number of shots fired and the number of bullet striation marks on Balau, Resak and Seraya is illustrated in Figures 1, 2 and 3.

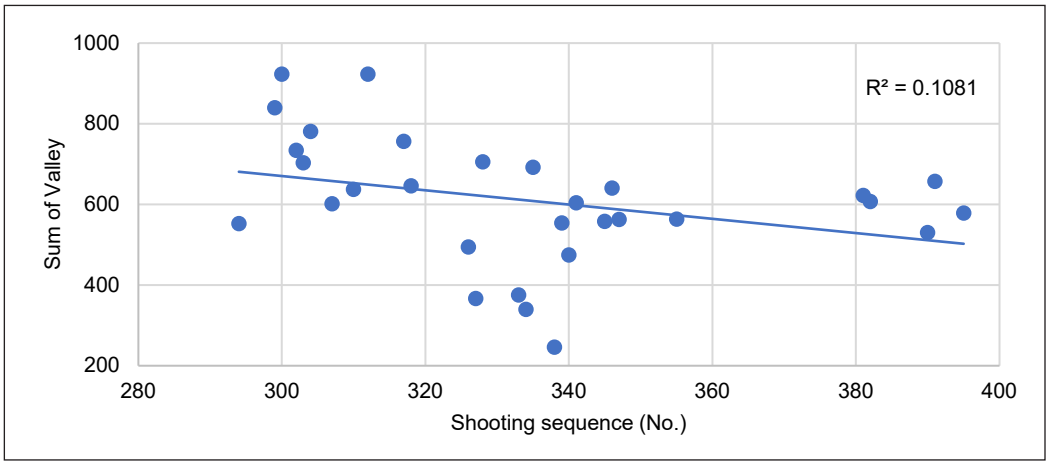

Figure 1. The relationship between the number of shots fired and the number of bullet striation marks on Balau

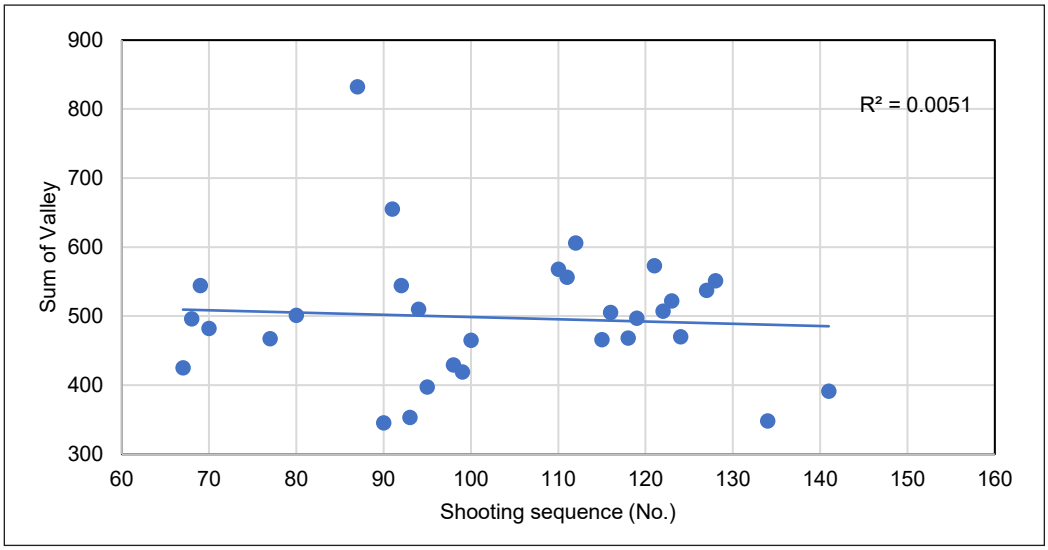

Figure 2. The relationship between the number of shots fired and the number of bullet striation marks on Resak

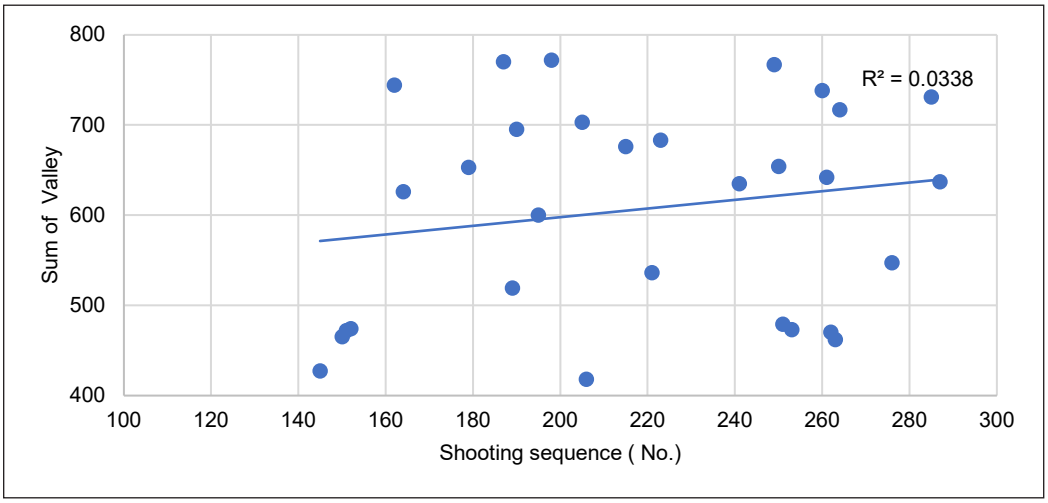

Figure 3. The relationship between the number of shots fired and the number of bullet striation marks on Seraya

Shooting Angle

The results of the Correlation-Regression analysis showed that Balau ($p < 0.01$, $R^2 = 0.065$) and Seraya ($p < 0.01$, $R^2 = 0.199$) have a statistically significant relationship between the shooting angle and bullet weight during shooting, but not for Resak ($p = 0.977$). This factor is related to the strength properties of the wood. Thus, only Balau and Seraya's shooting angle and bullet weight equations were formulated. For Balau, Bullet weight (g) = 0.001 × Shooting angle (SA°) + 7.428; 15° > SA > 90°. Meanwhile for Seraya, Bullet weight (g) = 0.001 × Shooting angle (SA°) + 7.437; 15° > SA > 90°. Although a significant

relationship between shooting angle and bullet weight for Balau and Seraya was observed, shooting angle was only able to influence 14.19% and 19.87% of the outcome of the bullet weight. The weight of a bullet upon impact onto a surface might also be influenced by other possible contributing factors, such as the position of the wood's vein, variation of wood strength and the slight deviation of bullet trajectory immediately after shooting due to the gun recoil effect (Koene & Broekhuis, 2017; Karger et al., 2001; Vermeij et al., 2012). The relationship between the shooting angle and bullet weight when shooting on Balau and Seraya is illustrated in Figures 4 and 5.

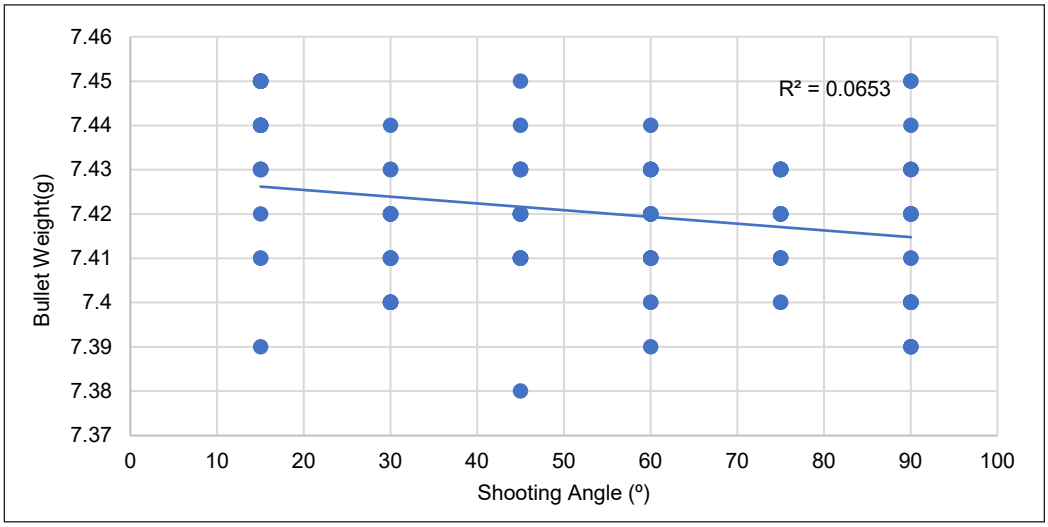

Figure 4. The relationship between the shooting angle and bullet weight when shooting on Balau

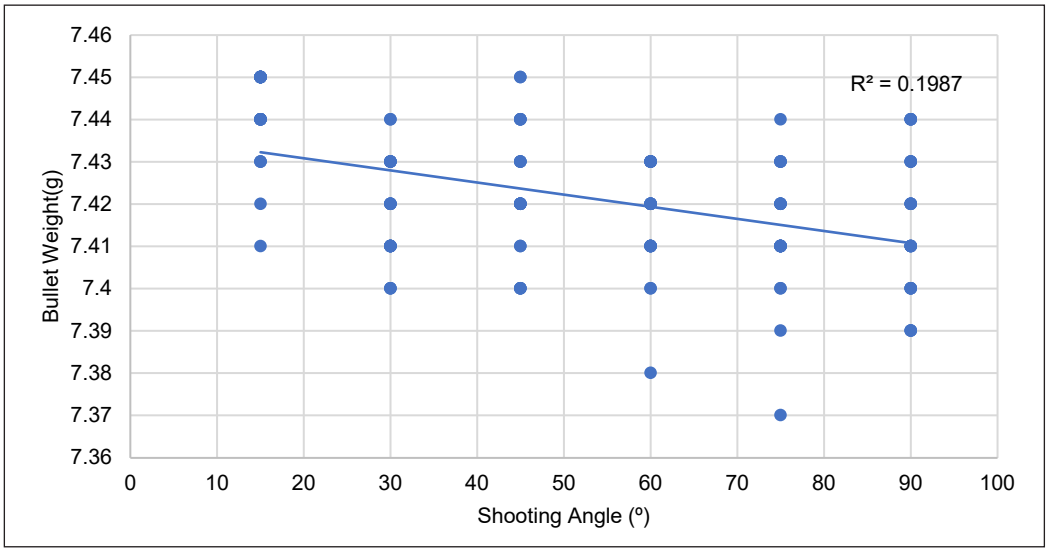

Figure 5. The relationship between the shooting angle and bullet weight when shooting on Seraya

Ricochet Angle

Correlation- Regression analysis showed a significant relationship for Resak between ricochet angle and bullet weight after shooting ($p < 0.05$, $R^2 = 0.1419$) but not for Balau and Seraya ($p = 0.835$ and $p = 0.099$, respectively). The equation of bullet weight generated for Resak is, Bullet weight (g) = -0.001 + Ricochet angle (RA°) + 7.458; 10° > RA > 66°. The relationship between the shooting angle and bullet weight when shooting on Resak is shown in Figure 6.

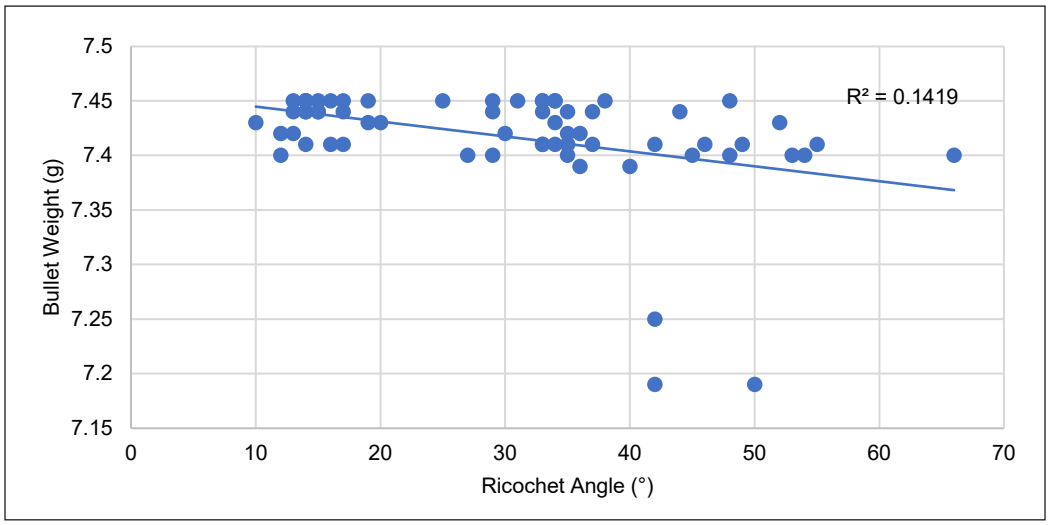

Figure 6. The relationship between the ricochet angle and bullet weight when shooting on Resak

DISCUSSION

Number of Shots Fired vs Bullet Striation Marks

The unique striation marks on the bullets are individual characteristics that can help to link a fired bullet to a specific firearm (Mahanta et al., 2019; Hamzah, 2016). In the past, ballistics experts have postulated that when a gun barrel is used multiple times without cleaning, multiple grooves within the gun barrel will form. There is not much information on how grooves are formed within a gun barrel after manufacturing it. It is suspected that the barrel within the weapon will heat up during multiple shots, making the inner wall of the barrel soft. It causes groove marks to be easily developed when firing occurs. When the barrel cools down sufficiently enough, these newly created groove marks within the barrel will solidify. The newly created groove will cause the next bullet to have additional striations.

When sufficient grooves are in the barrel, experts suspect a bullet passing through the barrel will lose significant weight. In essence, the grooves will shave some metal from the bullet. It will cause the bullet to be much lighter than before it was shot.

This study's outcome showed no significant relationship between the number of shots fired and bullet weight when shooting at Balau, Resak or Seraya targets. It indicates that the difference in the number of striation marks after multiple shots was insufficient to cause significant changes that would lead to the shift in bullet weight and indirectly to the identification of a specific weapon. It was consistent with the study, which reported that although the markings on the bullet continued to change, the 4000th bullet was identifiable as the first bullet (Doelling, 2001).

A similar outcome could be due to the similar composition of barrels used for both studies. The barrel of the CZ 75 SP-01 semi-automatic pistol used in this study and the 9 x18 mm calibre Makarov semi-automatic pistol used were made up of 4150 Carbon Steel bullets (Doelling, 2001). A similar steel composition of molybdenum and chromium had made the barrel much harder than other pistol brands. The "41" in the first two numbers of the barrel steel refers to chromium-molybdenum steels, which contain 0.15-0.25% molybdenum and 0.80-1.10% chromium in their composition. Meanwhile, the "50" on the last two numbers refers to the amount of internal carbon content, which is 0.50%. 4150 Carbon Steel. This steel is generally tougher and more resistant than regular carbon steel (Liscio & Imran, 2020). Hence, this might have likely contributed to the insignificant increase of bullet striation marks as the number of shots fired increased.

Shooting Angle

The original weight of the 9 mm FMJ bullet used in this study was 7.45 g. For each shooting angle of 15°, 30°, 45°, 60°, 75° and 90°, a minimum of six shooting replications were made from four fixed shooting distances (1, 3, 5 and 10 meters). The shooting angle was used to compare whether shooting angles or ricochets affect bullet weight.

According to Kerkhoff et al. (2015), when a bullet hits on wood at various angles, which is softer than itself, it will either penetrate (lodge itself in the object), perforate (penetrate and exit from a surface other than the impact surface), or ricochet (bounce off from the impact surface). Irrespective of the outcome, there will be kinetic energy and deformation loss. Deformation of the bullet will sometimes cause shearing, leading to bullet weight loss.

The outcome of this study supported the study mentioned above. The result showed a significant relationship between shooting angle and bullet weight when shooting on Balau and Seraya. Unfortunately, no significant relationship was seen in Resak. Resak has the lowest wood compressive strength compared to the other two kinds of wood. Referring to Figures 4 and 5, the equation for the weight of bullets generated for Balau is Bullet weight (g) = 0.001 × Shooting angle (°) + 7.428; 15° > SA > 90°, whereas, for Seraya, the equation is Bullet weight (g) = 0.001 × Shooting angle (°) + 7.437; 15° > SA > 90°. These equations represent the Influence of the wood, shooting angle and shooting distance on bullet weight after the shooting. It was further noted that the shooting angle would influence the bullet

weight by 6.5 % ($R^2 = 0.065$) and 4.2 % ($R^2 = 0.142$) when shooting onto Balau and Seraya wood, respectively. However, we would like to highlight that this equation only applies to firing a 9 mm FMJ bullet on the two wood types. It is suspected that a different combination of ammunition and wood type might result in a different result of bullet weight loss. For instance, the combination of .32 Auto bullets and Abachi wood used in the study led to different results in bullet weight loss than in this study (Kerkhoff et al., 2015).

Furthermore, the result variation between the woods could be explained as Balau and Seraya belonging to the same genus (*Shorea* spp) while Resak is from *Vatica spp*. Despite these two kinds of wood (Balau and Seraya) having a hardness at two extreme ends—Balau is a heavy hardwood while Seraya is light hardwood. Balau and Seraya are closely related and share similar characteristics, such as fibre composition and MOE.

In addition, both the woods from *Shorea* spp. have the same type of grain alignment called interlocked grains. Resak, on the other hand, is structured as straight or shallowly interlocked grains. Interlocked grain refers to how the wood grain spirals around the axis of the tree. The spiral reverses its direction for a certain period, resulting in alternating directions of the spiral grain (Slater & Ennos, 2015). Due to these characteristics, Balau and Seraya are the hardest wood to work within the wood-based industry and hence are highly sought after because the interlocking wood grain patterns improve overall wood strength properties (Slater & Ennos, 2015). Concerning the characteristics, the improved strength could have further caused more deformation towards the bullet and resulted in significant bullet weight loss after being shot at the angles.

On the contrary, Resak has a straight grain. The grains run in a single direction parallel to the tree's axis. During shooting, the bullet might have been forced to follow the softer wood cell structures along the direction of the wood grain and hence be deflected from its original trajectory. It, in turn, leads to lesser bullet deformation (Mattijssen et al., 2016).

It is also important to note that the grain alignment will cause the bullet to have a higher tendency to form indentations on the wood. In contrast, the frequency of bullet ricochets is more likely to occur with the increased value of the wood's elasticity. Consequently, bullets will bounce from the wooden surface due to a ricochet effect. The ricochet effect is closely related to wood elasticity. The issue of word elasticity will be discussed further, as the shooting and ricochet angles are closely interconnected.

Ricochet Angle

The Ricochet angle is where the bullet hits the wood and ricochets off the surface. A significant relationship exists between the ricochet angle on the bullet weight when shooting on Resak but not Balau and Seraya. Of 144 shots fired on Resak, 66 bullets had a ricochet effect. Based on Figure 6, the equation generated for bullet weight for Resak (Bullet weight (g) = -0.001 × Ricochet angle (°) + 7.458) is only applicable for ricochet angles of 10°

to 65°. The ricochet angle influenced the bullet weight by 14.2%. The remaining 85.8% indicates that other factors could affect the bullet weight, which is yet to be determined when shooting on Resak.

This finding might be due to the wood elasticity, often referred to as the MOE or Young's modulus. Technically, MOE is the measurement of the ratio of the stress (force applied) over the strain (deformation) on the wood (Meier, 2019). Resak, with an elasticity of 19,500 MPa, has the highest MOE. On the other hand, Balau and Seraya have an elasticity of 16,670 MPa and 13,020 MPa, respectively. The relatively high elasticity of Resak compared to the other two types of wood might result in more bullets experiencing a ricochet effect instead of burying into the wood (Azlan et al., 2018).

Concerning the above, wood is strongest in the direction parallel to the grain (Fu et al., 2021). However, our study had not considered the horizontal and vertical grain of the wood during the shooting process. Shooting on horizontal grain is referred to as parallel to the grain, whereas if on grain that shows vertical direction, it will be referred to as perpendicular to the grain. Therefore, if the bullet hits the wood positioned in the direction with horizontal wood grains, there will likely be more bullet weight loss. Thus, it is essential to note the direction of the wood grain when positioning wood before shooting for future research.

CONCLUSION

The factors influencing the bullet weight during shooting include the shooting angle, ricochet angle and the type of wood used. However, expanding its database using other kinds of weapons, bullets, and words would benefit forensic investigators, particularly when reconstructing a scene involving the discharge of a firearm.

ACKNOWLEDGEMENT

This work was supported by the Universiti Kebangsaan Malaysia under Grant GUP-2020-052; and Destini Shipbuilding and Engineering Sdn Bhd (JPA(I) 800929105545).

REFERENCES

Abbo, D. (2021). The ballistics case study of the Enrica Lexie incident. *International Journal of Mechanical and Industrial Engineering, 15*(5), 237-254.

Abdullah, M. Y. (2015). *Bicara dunia Melayu: Tradisi pelayaran Melayu* [Narration of the Malay world: Malay sailing traditions]. Muzium Negeri Terengganu. http://www.jmm.gov.my/files/ORANG%20MELAYU%20DAN%20ALAM%20KELAUTAN.pdf

Agensi Maritim Luar Negara. (2019). *Latihan menembak senjata kecil pistol maritim negeri Kedah dan Perlis* [Training of arms maritime pistols for the state of Kedah and Perlis]. https://www.mmea.gov.my/index.php/ms/?option=com_content&view=article&id= 144:logo-bendera-apmm& catid =18:mengenai-kami&Itemid=115

Asyraf, M. R. M., Ishak, M. R., Sapuan, S. M., & Yidris, N. (2021). Comparison of static and long-term creep behaviors between balau wood and glass fiber reinforced polymer composite for cross-arm application. *Fibers and Polymers, 22*(3), 793-803. https://doi.org/10.1007/s12221-021-0512-1

Atzampos, G., Paterson, D., Vassalos, D., & Boulougouris, E. (2018). A new era of fishing vessel safety emerges. In *Transport Research Arena (TRA)* (pp. 1-9). https://doi.org/10.5281/zenodo.1486497

Azlan, H. M., Puaad, M. B. F. M., Ahmad, Z., Talip, A. R. A., & Yasin, M. H. (2018). Compressive strength properties of Malaysian tropical timber in structural size: Timber strength grading. In *AIP Conference Proceedings* (Vol. 2020, No. 1, p. 020034). AIP Publishing LLC. https://doi.org/10.1063/1.5062660

Brian, J. H. (2008). Forensic firearms examination. In *Handbook of Firearms and Ballistics: Examining and Interpreting Forensic Evidence* (2nd ed.) (pp. 145-210). Wiley-Blackwell.

Cvetković, T., Hinsinger, D. D., & Strijk, J. S. (2019). Exploring evolution and diversity of Chinese Dipterocarpaceae using next-generation sequencing. *Scientific Reports, 9*(1), 1-11. https://doi.org/10.1038/s41598-019-48240-y

Dang, X. K., Ho, L. A. H., & Do, V. D. (2018). Analyzing the sea weather effects to the ship maneuvering in Vietnam's sea from BinhThuan province to Ca Mau province based on fuzzy control method. *TELKOMNIKA (Telecommunication Computing Electronics and Control), 16*(2), 533-543. http://doi.org/10.12928/telkomnika.v16i2.7753

Dewi, L. M., Damayanti, R., & Muslich, M. (2020). Inventory of wooden ship materials and determination of its alternative materials through wood properties approach: Case studies in the Riau Islands, the Northern and Southern Coast of Java. In *IOP Conference Series: Earth and Environmental Science* (Vol. 415, No. 1, p. 012014). IOP Publishing.

Doelling, B. (2001, February 19-24). Comparison of four thousand consecutively fired, steel jacketed bullets from a 9x18mm makarov pistol. In *Annual Meeting of the American Academy of Forensic Sciences*. Seattle, Washington

El-Taguri, H. A., Omar, N., Al-Hakimi, A. S., & Latiff, A. (2020). A revision of Vatica L. (Dipterocarpaceae) in Peninsular Malaysia. *Malayan Nature Journal, 72*(2), 229-266.

Fu, W. L., Guan, H. Y., & Kei, S. (2021). Effects of moisture content and grain direction on the elastic properties of beech wood based on experiment and finite element method. *Forests, 12*(5), Article 610. https://doi.org/10.3390/f12050610

Hamzah, N. H., Khairul, O., & Gina, F. G. (2020). *Pemilikan Senjata Api di Malaysia* [Firearms Ownership in Malaysia]. UKM Press.

Hamzah, N. H. (2016). Development of an objective method for the comparison of fired projectiles using an air pistol as a template. *Forensic Science International, 264*, 106-112. https://doi.org/10.1016/j.forsciint.2016.03.050

Karger, B., Hoekstra, A., & Schmidt, P. (2001). Trajectory reconstruction from trace evidence on spent bullets. *International Journal of Legal Medicine, 115*(1), 16-22. https://doi.org/10.1007/s004140000202

Kerkhoff, W., Alberink, I., & Mattijssen, E.J.A.T. (2015). An Empirical study on the relation between the critical angle for bullet ricochet and the properties of wood. *Journal of Forensic Sciences, 60*(3), 605-610. https://doi.org/10.1111/1556-4029.12738

Koene, L., & Broekhuis, F. R. (2017, September 11-15). Bullet penetration into wooden targets. In *Proceedings of the 30th International Symposium on Ballistics 2017* (pp. 1905-1916). Long Beach, CA.

Koene, L. (2016, May 9-13). Modelling bullet richochet from wooden targets. In *Proceedings of the 29th International Symposium on Ballistics 2016* (pp. 1952-1963). Edinburgh, Scotland, UK.

Kpenyigba, K.M., Jankowiak, T., Rusinek, A., Pesci, R., & Wang, B. (2015). Effect of projectile nose shape on ballistic resistance of interstitial-free steel sheets. *International Journal of Impact Engineering, 79*, 83-94. https://doi.org/10.1016/j.ijimpeng.2014.10.007

Liscio, E., & Imran, R. (2020). Angle of impact determination from bullet holes in a metal surface. *Forensic Science International, 317*, Article 110504. https://doi.org/10.1016/j.forsciint.2020.110504

Leon, F. P., & Beyerer, J. (1999). Automatic comparison of striation information on firearm bullets. In D. P. Casasent (Ed.), *Intelligent Robots and Computer Vision XVIII: Algorithms, Techniques, and Active Vision* (Vol. 3837, pp. 266-277). SPIE Digital Library. https://doi.org/10.1117/12.360306

Mahanta, L. B., Bora, K., Kumar, R., Purkayastha, S., & Suresh, R. (2019). A pilot study on image processing methods for segmentation of striations in fired bullets. *International Journal of Computer Sciences and Engineering, 7*(3), 449-455.

Maho, B., Sukontasukkul, P., Jamnam, S., Yamaguchi, E., Fujikake, K., & Banthia, N. (2019). Effect of rubber insertion on impact behavior of multilayer steel fiber reinforced concrete bulletproof panel. *Construction and Building Materials, 216*, 476-484. https://doi.org/10.1016/j.conbuildmat.2019.04.243

Mahoney, P., Carr, D., Harrison, K., McGuire, R., Hepper, A., Flynn, D., Delaney, R.J., & Gibb, I. (2019) Forensic reconstruction of two military combat related shooting incidents using an anatomically correct synthetic skull with a surrogate skin/soft tissue layer. *International Journal of Legal Medicine, 133*(1), 151-162. https://doi.org/10.1007/s00414-018-1802-z

Malaysian Timber Council. (2020a). *Technical Information for Balau*. http://mtc.com.my/wizards/mtc_tud/items/report(97).php

Malaysian Timber Council. (2020b). *Technical Information for Dark Red Meranti (Seraya)*. http://mtc.com.my/wizards/mtc_tud/items/report(103).php

Malaysian Timber Council. (2020c). *Technical Information for Resak*. http://mtc.com.my/wizards/mtc_tud/items/report(102).php

Mackay, M., Hardesty, B. D., & Wilcox, C. (2020). The intersection between illegal fishing, crimes at sea, and social well-being. *Frontiers in Marine Science, 7*, Article 589000. https://doi.org/10.3389/fmars.2020.589000

Mattijssen, E. J. A. T., Alberink, I., Brouwer, S. D., & Kerkhoff, W. (2016). The influence of wood grain on the bullet's ricochet behavior. *Journal of Forensic Sciences, 61*(3), 765-772. https://doi.org/10.1111/1556-4029.13023

Mattijssen, E. J. A. T., Kerkhoff, W., & Bestebreurtje, M. E. (2017). Bullet trajectory after impact on laminated particle board. *Journal of Forensic Sciences, 63*(5), 1374-1382. https://doi.org/10.1111/1556-4029.13717

Meier, E. (2019). *Wood! Identifying and using Hundreds of Woods Worldwide*. The Wood Database.

Murdjoko, A., Marsono, D., Sadono, R., & Hadisusanto, S. (2016). Population dynamics of pometia for the period of post-selective logging in tropical rainforest, Southern Papua, Indonesia. *Biosaintifika Journal of Biology & Biology Education, 8*(3), 321-330.

Muslich, M., & Sumarni, G. (2006). Keawetan 25 jenis kayu dipterocarpaceae terhadap penggerek kayu di laut [Durability of 25 types of dipterocarpaceae wood against sea wood borers]. *Jurnal Penelitian Hasil Hutan, 24*(3), 191-200. https://doi.org/10.20886/jphh.2006.24.3.191-200

Nichols, R. (2018). *Firearm and Toolmark Identification: The Scientific Reliability of the Forensic Science Discipline.* Academic Press.

Nishshanka, L. C. B., Shepherd, C., & Paranirubasingam, P. (2020). Forensic based empirical study on ricochet behaviour of Kalashnikov bullets (7.62 mm× 39 mm) on 1 mm sheet metal. *Forensic Science International, 312*, Article 110313. https://doi.org/10.1016/j.forsciint.2020.110313

Nishshanka, L. C. B., Shepherd, C., Punyasena, M. A., & Ariyarathna, M. R. (2021a). Ricochet of AK bullets (7, 62× 39 mm) on concrete and cement surfaces; a forensic-based study. *Science & Justice, 61*(5), 467-476. https://doi.org/10.1016/j.scijus.2021.06.004

Nishshanka, L. C. B., Shepherd, C., & Ariyarathna, R. (2021b). AK bullet (7.62× 39 mm) holes on 1-mm sheet metal: A forensic-related study in aid of bullet trajectory reconstruction. *Journal of Forensic Sciences, 66*(4), 1276-1284. https://doi.org/10.1111/1556-4029.14717

Nordin, F. A. D., Bominathan, U. R., Abdullah, A. F. L., & Chang, K. H. (2020). Forensic significance of gunshot impact marks on inanimate objects: The need for translational research. *Journal of Forensic Sciences, 65*(1), 11-25. https://doi.org/10.1111/1556-4029.14142

Puaad, M. B. F. M., Ahmad, Z., Talip, A. R. A., Salleh, M. Z. M., & MohamÂmad, S. N. (2020). Torsional shear strength properties of malaysian tropical timber in structural size. *Jurnal Teknologi*, *82*(5), 1-10.

Slater, D., & Ennos, R. (2015). Interlocking wood grain patterns provide improved wood strength properties in forks of hazel (*Corylus avellana* L.). *Arboricultural Journal*, *37*(1), 21-32. https://doi.org/10.1080/03071375.2015.1012876

United Nations Office on Drugs and Crime. (2011). *Transnational organised crime in the fishing industry: Focus on: Trafficking in persons smuggling of migrants illicit drugs trafficking*. United Nations. https://www.unodc.org/documents/human-trafficking/Issue_Paper_-_TOC_in_the_Fishing_Industry.pdf

Vermeij, E., Rijnders, M., Pieper, P., & Hermsen, R. (2012). Interaction of bullets with intermediate targets: material transfer and damage. *Forensic Science International, 223*(1-3), 125-135. https://doi.org/10.1016/j.forsciint.2012.08.016

Wahab, M. R. A., & Ramli, Z. (2020). The Malay traditional boat: Defending Malay heritage objects in Kelantan, East Coast of the Malaysian Peninsula. *Journal of Maritime Archaeology, 15*(1), 57-68. https://doi.org/10.1007/s11457-019-09247-8

Wahid, A. S. (2020, August 21). Nelayan tempatan jadi tali barut [Local fishermen become informers]. *Sinarharian.* https://www.sinarharian.com.my/article/97675/ EDISI/Kelantan/Nelayan-tempatan-jadi-tali-barut.

Walters, M., & Liscio, E. (2020). The accuracy and repeatability of reconstructing single bullet impacts using the 2D ellipse method. *Journal of Forensic Sciences, 65*(4), 1120-1127. https://doi.org/10.1111/1556-4029.14309

Widiyono, W. (2021). Biological and economic value of Dipterocarpaceae, the main timber forest product of Indonesia. *Applied Environmental Studies, 2*(2), 104-112.

Wong, K. S., & Jacobson, J. (2013). Angle of impact determination from bullet holes. *Journal of Forensic Identification, 63*(3), 233-246.

Pertanika J. Sci. & Technol. 31 (3): 1493 - 1502 (2023)

PERTANIKA JOURNALS

SCIENCE & TECHNOLOGY

Journal homepage: http://www.pertanika.upm.edu.my/

The Effect of Graphene Nanoplatelets Content on the Hardness of Mg6%Zn0.2%Mn Composites

Abang Mohamad Harith Abang Beniamin*, Noor Hisyam Noor Mohamed and Mahsuri Yusof

Department of Mechanical and Manufacturing Engineering, Faculty of Engineering, Universiti Malaysia Sarawak, 94300 UNIMAS, Kota Samarahan, Sarawak, Malaysia

ABSTRACT

The effect of graphene nanoplatelets (GNPs) content on the hardness of magnesium-based composites was studied. A magnesium-based composite, Mg6%Zn0.2%Mn with graphene nanoplatelets (GNPs), was fabricated via powder metallurgy process at room temperature and compressive pressures of 50kN for 20 minutes, which was then sintered at 500°C for 2 hours. It produced significant grain refinement microstructure. The change in microstructure was examined by 3D microscope analysis, and the hardness value was evaluated using the Vickers microhardness apparatus. This study demonstrated the importance of GNPs reinforcement with zinc and manganese for microhardness analysis in the sintered Mg-based GNPs composites. It also portrayed their influence on grain refinement of the microstructure. The hardness results agreed with the microstructure results, proving that the presence of GNPs increases the hardness of the Mg-based composites.

Keywords: Graphene nanoplatelets, magnesium-based composites, microhardness test, powder metallurgy

ARTICLE INFO

Article history:
Received: 02 July 2022
Accepted: 05 October 2022
Published: 31 March 2023

DOI: https://doi.org/10.47836/pjst.31.3.20

E-mail addresses:
harith110195@gmail.com (Abang Mohamad Harith Abang Beniamin)
nmnhisyam@unimas.my (Noor Hisyam Noor Mohamed)
ymashun@unimas.my (Mahsuri Yusof)
* Corresponding author

INTRODUCTION

Magnesium (Mg) is one of the most abundant metals present in the Earth's crust. Mg is the lightest of all the engineering metals, having a density of 1.74 g/cm^3. It is 35% lighter than aluminium (2.7 g/cm^3), 60% lighter than titanium and over four times lighter than steel (7.86 g/cm^3) (Mordike & Ebert, 2001). Mg has become desirable engineering material in every specific application, especially in automotive industries, with its

ISSN: 0128-7680
e-ISSN: 2231-8526

© Universiti Putra Malaysia Press

low density, specific strength, stiffness, and excellent damping capacity. Mg has been used widely in industrial applications due to its lightweight properties. This lightweight property of Mg in industrial applications, especially the automotive perspective, can increase the power-to-weight ratio, reducing fuel consumption and increasing fuel efficiency. Besides that, Mg is used for medical applications that are less dense for body implants than titanium. Despite having some exclusive mechanical properties, Mg has a critical limitation on its resistance towards corrosion. Mg is identified as one of the metals that is reactive to corrosion. The corrosion of Mg can occur either by generalised corrosion, localised corrosion, galvanic corrosion, or environmental cracking (Prasad et al., 2022). Additionally, Mg is chemically unstable and extremely susceptible to corrosion in a marine environment. It is known that the corrosion is most likely due to impurities in the metal rather than having an inherent characteristic.

Besides using Mg-based alloys as an engineering material, Mg-based composites are one of the interests of researchers for automotive applications up until this date. This development is made to enhance the mechanical properties of Mg apart from utilising alloying and heat treatment processes. One of the latest developments of Mg in engineering applications is fabricating magnesium reinforced with graphene nanoplatelets. Graphene nanoplatelets, also known as GNPs, are a form of graphene made in the large-scale production of the graphene layer. Meanwhile, single graphene is a monolayer of graphite that has a 2-dimensional (2D) geometry structure with a thickness of one atom (0.34 nm) (Cataldi et al., 2018). Graphene possesses a remarkably high elastic modulus of 1 TPa and yield strength (YS) of 130 GPa, which has been considered a promising candidate for enhancing composite materials (Meng et al., 2018). A research study by Rashad et al. (2014) showed that magnesium-reinforced graphene nanoplatelets composite has superior properties to magnesium alloys and other magnesium-based composites. They reported that adding graphene nanoplatelets into magnesium composite helps maintain the lightweight property as the density of magnesium is not influenced. Therefore, the Mg-reinforced GNPs composite gives an identical mass value to Mg.

Another study conducted by Arab and Marashi (2019) stated that GNPs could help to increase the hardness of Mg-based composite. It can be achieved by applying friction stir processing that can increase the hardness up to 14% and further improve the hardness by 41% via adding GNPs. GNPs help with grain refinement, dynamic recrystallisation and pinning effect of AZ31 Mg GNPs composite. Besides that, other mechanical properties such as universal tensile strength, elongation, Vickers hardness, and porosity have enhanced Mg-reinforced GNPs composites fabricated using the thixomoulding process. Chen et al. (2019) reported that GNPs affect mechanical properties significantly, enhancing AZ91D-GNPs composites compared with AZ91D Mg alloy. The thixomoulding process is well known in common industry manufacturing, thus promising the production of Mg-based

composites. It is due to the shortened process time on production that enables large-scale production via this method.

It is known that Mg in its pure form needs to be improved for better performance in various applications. The hardness of Mg must be improvised by selecting the fabrication and choosing the best ways of treatment, such as alloying, heat treatment or fabrication of Mg-based composites. Rotary parts, especially automotive, railway and aerospace parts, need materials with high hardness to withstand plastic deformation over time. Therefore, Mg-reinforced GNPs composites were fabricated using the powder metallurgy method in this study. The powder metallurgy method comprises three primary operations: powder mixing, powder compacting, and sintering. The powder metallurgy method offers a homogeneous and uniform distribution of reinforcement particles in the matrix for composite synthesis (Rashad et al., 2015). Powder metallurgy can also help to control the metal porosity, perform well under stress and increase mechanical properties such as hardness and wear resistance (Boopathy et al., 2011). In another research by Rodzi and Hussain (2018), the powder metallurgy method on Mg-based composites can improve mechanical properties. These results proved that the powder metallurgy technique with ball mill treatment might help increase strength due to the dispersion of the elements of Mg-based composites more evenly. In this research, the presence and increase in the weight percentage of GNPs within Mg-based composites will help refine the Mg matrix's grain boundary and increase the hardness. The increase in hardness is important in Mg-based composites as it enables them to resist deformation, bending, scratching, abrasion or cutting on specific moving parts such as gears and motors.

MATERIALS AND METHODS

Materials

In this research, commercially available Mg powder (>99% purity), Mn powder, Zn powder (−325 mesh, ≥99% trace metals basis) and GNPs powder (5 μm particle size with a surface area of 120-150 m^2/g) were used as starting materials. The Merck Company supplied all these powders. For the fabrication of MgMnZn mixture powder, 93.8wt.% of magnesium powders, 0.2wt.% of manganese and 6wt.% of zinc powders were stirred first, while graphene nanoplatelets were sonicated before being stirred with mixed MgMnZn-based powder.

Methods

Powder Metallurgy. To fabricate a pallet sample of Mg0.2Mn6.0Zn-1% GNPs composite, 0.03 g of GNPs powder was mixed with 40 ml of ethanol in a beaker. The mixture was then sonicated using a bath sonicator for about 1 hour. 2.784 g of Mg powder, 0.18 g of

Zn powder and 0.006 g of Mn powder were added to 40 ml of ethanol in a beaker, and the mixture was stirred on a magnetic stirrer for 2 hours. GNPs and Mg mixture solutions were mixed and stirred for another 1 hour. The mixed and stirred solution was then filtered using filter paper. The filtered mixture was left to dry in an oven at a fixed temperature of 50°C until it was completely dry. 1 g of dried powder mixture was taken and was then compressed by using a hydraulic compressor with a pressure of 50kN for 20 minutes to produce a cylindrical shape from pallet. Then, the obtained cylindrical pallet was sintered using the tube furnace under an inert argon gas environment and was heated at a temperature of 500°C with a heating rate of 10°C/min for 2 hours to enhance the bonding between Mg mixtures and GNPs. As a precautionary step, the sintered pallet would be taken out after the furnace was cooled down completely. This sample fabrication method was repeated similarly for Mg0.2Mn6.0Zn-0.5% GNPs, Mg6%Zn0.2%Mn and high purity (HP) Mg, respectively.

Microstructure Observation. The microstructural observation was conducted to study the characteristic of the grain boundary, interface integrity between matrix and reinforcement, the presence of porosity and the grain size of the composite samples. This characterisation process was conducted under a 3D optical microscope.

After the composite samples were fabricated, all the composites were ground with 1000 to 2000 grit of silicon carbide (SiC) abrasive paper and polished with alumina suspension until mirror-like surfaces were obtained. Then, the polished composites were washed with distilled water and were allowed to dry using high-pressure air. After that, the samples were etched using a 3% nital (nitric acid mixed with ethanol) solution. The composite samples were dipped into the etching solution for only 2 seconds to prevent over-etching on the surface of the samples.

All the composite samples were observed using a 3D optical microscope. A 3D optical microscope was used as it gave higher resolution when the samples were zoomed at 1000x magnification using high brightness light emitting diode (HB-LED) support. Besides that, the image produced would have a significantly high dynamic range (HDR). The observed images and analysis of the microstructure of the composites were obtained and recorded.

Hardness Test. The hardness test is a measurement of the resistance of a material against plastic deformation. The hardness of a metal is measured by forcing an indenter onto the composite surface. In the process of testing hardness, a known load is applied to indent slowly at 90° onto the tested surface of a sample. After the indentation is done, the indenter is withdrawn from the surface. The hardness measurement is then calculated based on the cross-sectional area and depth of indentation, depending on the type of hardness machine used.

In this study, the hardness test of the composite samples was done using the Vickers microhardness test. The fabricated samples were indented with a load of 5 kgf for 10 seconds. The diamond shape indentation on the surface was then measured and recorded. For the Vickers hardness test, the indenter has a pyramidal with a square base shape and a semi-apex angle of 68◦. The corresponding hardness number HV is a calculated function of the contact area, d^2. The test was repeated, with three readings recorded for the samples. Then, the average of the readings was calculated as the hardness of the samples. The indention results were then calculated based on the following equation:

$$Vickers\ Hardness(HV) = \frac{Applied\ Load}{Surface\ Area\ of\ Depression}$$

$$= \frac{2Psin\left(\frac{136°}{2}\right)}{d^2}$$

$$= 1.854\ \frac{P}{d^2}$$

Where,

P = Applied Load (kgf)

d = $\frac{d_1 + d_2}{2}$

RESULTS AND DISCUSSION

Microstructure Observations

Figure 1 shows the microstructure of HP Mg, Mg0.2%Mn6.0%Zn, Mg0.2%Mn6.0%Zn-0.5% GNPs and Mg0.2Mn6.0Zn-1% GNPs sample that was obtained from 3D optical microscope after grinding, polishing, and etching, respectively.

The samples for all the grains of samples were equiaxed and irregular in shape based on Figure 1. The 3D optical microscope images showed that HP Mg in Figure 1a has the largest grain size, followed by Mg0.2%Mn6.0%Zn in Figure 1b, Mg0.2%Mn6.0%Zn-0.5% GNPs in Figure 1c, and Mg0.2%Mn6.0%Zn-1% GNPs in Figure 1d. The addition of Zn in the composite caused the coarsening of the grain size (Budinski & Budinski, 1999). Besides Zn, the addition of Mn helps in reducing grain size. After adding 0.2 wt% of Mn, the grain size was slightly reduced by about 25% to 35% with the sample without adding Mn. Mn's effect on grain refinement is gradually weakened when the Mn content exceeds 1.3 wt% (Zhao et al., 2019). GNPs in the composite successfully suppressed the growth of the grain size. Grain boundaries contribute primarily to the diffusion channels of Mg0.2%Mn6.0%Zn

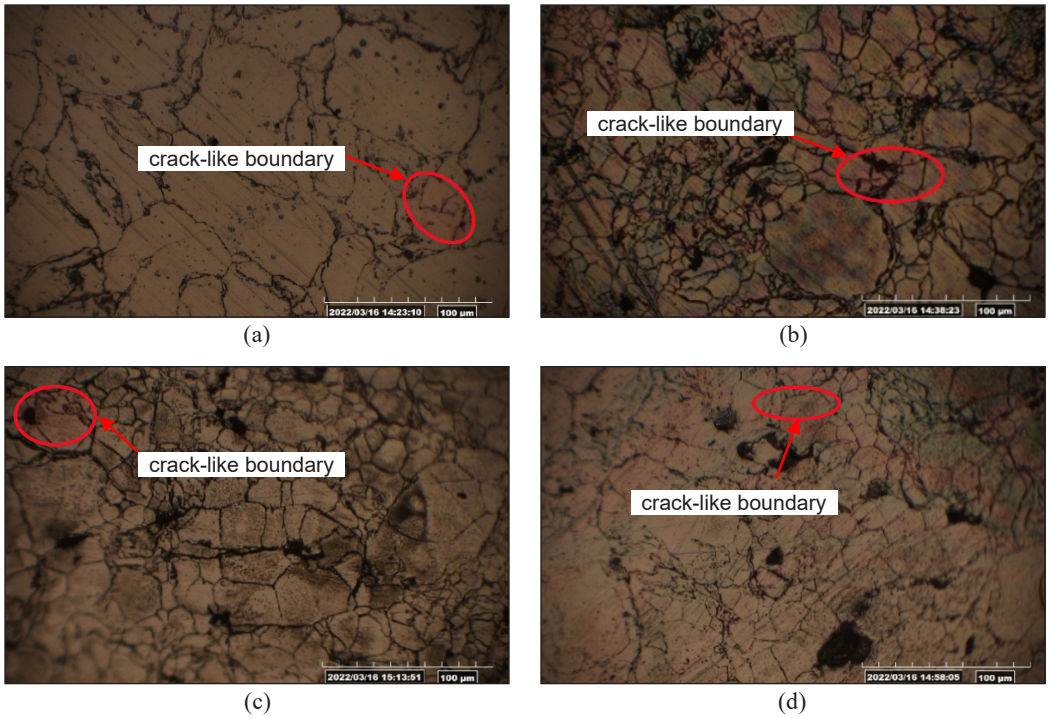

Figure 1. Microstructure of: (a) HP Mg; (b) Mg6%Zn0.2%Mn; (c) Mg6%Zn0.2%Mn-0.5% GNPs composite; (d) Mg-6%Zn0.2%Mn-1% GNPs composite was observed under 3D optical microscope with 1000× magnification

alloy matrix and GNPs in the nucleation sites formation, thus reducing the grain size. The heterogeneous nucleation mode promoted the formation of a tight mechanical interfacial bonding between the GNPs and Mg0.2%Mn6.0%Zn matrix. With the increase in GNPs content, more heterogeneous nucleation substrates were provided, leading to more crystal nuclei of Mg on the GNPs. Hence, the increase in nucleation rate can effectively refine the Mg crystal grains at a given Mg0.2%Mn6.0%Zn matrix (Sun et al., 2020). It implies that GNPs can act as nucleation sites and grain refiners in magnesium-based composites. Besides, it shows further results in more refined grains than Mg0.2%Mn6.0%Zn (Rashad et al., 2016). It was observed that the Mg0.2%Mn6.0%Zn-0.5% GNPs and Mg0.2%Mn6.0%Zn-1% GNPs produced almost equal size of the grains with the help of GNPs that reinforced the Mg alloy matrix.

Many crack-like boundaries were observed in all samples, as highlighted in Figure 1, which differed from the grain boundaries. These crack-like boundaries were formed as transgranular crack boundaries. A more severe transgranular crack happens with the presence of GNPs, especially where the GNPs concentration in the area is high. Due to the residual thermal stress and pressure during compaction, the crack will be pinned down in the grain boundary and defected into the grain. Then, the transgranular crack will occur. It

needs more additional external stress to promote crack propagation. In general, the change in crack fracture mode is also related to the strength of the interface because cracks tend to propagate along with the weaker interfaces (Fan et al., 2019).

Vickers Microhardness Test

The samples were tested using 5kgf of load for 10 seconds in this test. The Vickers hardness for HP Mg, Mg0.2%Mn6.0%Zn, Mg0.2%Mn6.0%Zn-0.5% GNPs and Mg0.2%Mn6.0%Zn-1% GNPs composite were recorded, while the average of Vickers Hardness Number (VHN) and standard deviation were calculated and shown in Table 1.

Table 1
Vickers hardness test

Type of sample	Sample	VHN 1	VHN 2	VHN 3	Average VHN	Standard Deviation
HP Mg	1	34.2	34.4	34.2	34.27	0.094
	2	34.6	34.6	34.3	34.50	0.141
Mg0.2%Mn6.0%Zn	1	44.3	44.5	44.6	44.47	0.125
	2	44.5	44.2	44.3	44.33	0.125
Mg0.2%Mn6.0%Zn-0.5%GNPs	1	45.5	45.4	45.7	45.53	0.126
	2	45.6	45.5	45.3	45.47	0.124
Mg0.2%Mn6.0%Zn-1%GNPs	1	48.6	48.4	48.6	48.53	0.094
	2	48.2	48.2	48.4	48.27	0.095

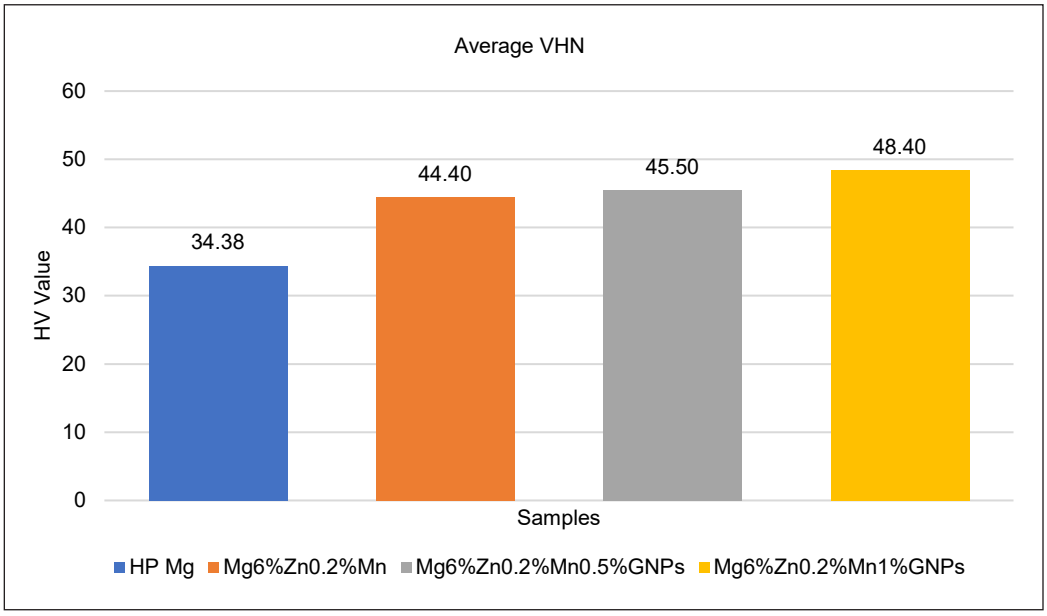

Figure 2. Bar chart of average Vickers hardness of the samples

Three measurements and readings were applied during the test and the average values of each composite were considered. From the result obtained, Mg0.2%Mn6.0%Zn-1% GNPs showed the highest value of VHN, giving it the highest hardness sample among the other samples. For Mg0.2%Mn6.0%Zn-0.5%, GNPs offered higher hardness than Mg0.2%Mn6.0%Zn, and the material that had the least hardness was HP Mg. In comparison, Mg0.2%Mn6.0%Zn-1% GNPs give an increase of hardness by 33.87%, followed by Mg0.2%Mn6.0%Zn-0.5% GNPs hardness with an increase of 27.84% and Mg0.2%Mn6.0%Zn with an increase of 25.55%.

Other than that, the Mg0.2%Mn6.0%Zn-1% GNPs had shown higher hardness than Mg0.2%Mn6.0%Zn without GNPs by 9.52%. From the bar chart shown in Figure 2, the alloying of Mg with Mn and Zn can give better hardness than the HP Mg by 24.54%. These results were supported by previous research with other micro constituents, which mentioned that adding graphene nanoplatelets into the magnesium matrix could increase its hardness. It is confirmed because the GNPs restrict the dislocation movement of the Mg and the constituents present in Zn and Mn as alloying elements. Zn and Mn improve the mechanical properties by reducing the grain size of Mg alloy and introducing dislocations in the microstructure (Shuai et al., 2018; Wang et al., 2019). Due to the hindrance in dislocation movement, the surface hardness increased at a high concentration of reinforcements. Rajaganapathy et al. (2020) also found that adding graphene into AA6082 aluminium-based composites could increase the graphene from 1% to 5%, gained from 86HV to 107HV with an increment of 24.08%. However, the hardness of the composites is improved by the existence of a comparatively more rigid reinforcement. Besides that, Liu et al. (2017) discussed that the mechanical properties of alloys and composites could change due to the high-temperature diffusion rate during the sintering process. Hence, the reinforcement particle of the composite in the matrix can make the distance between particles closer due to thermal diffusion on compacted powdered samples.

CONCLUSION

Overall, Mg0.2%Mn6.0%Zn-based reinforced GNPs composites with the powdered structure were fabricated via a feasible method and showed exceptionally enhanced hardness through powder metallurgy. GNPs were dispersed uniformly on the Mg0.2%Mn6.0%Zn matrix. The following mixing and sintering processes promoted the distribution of GNPs. GNPs reinforcements were well embedded into the Mg matrix and formed good bonding with the Mg0.2%Mn6.0%Zn matrix. The reduced grain size structure that was induced by the introduction of GNPs suppressed the grain localisation movement. It promoted an increase in grain boundary; thus, increasing the hardness of the composite up to 41% is beneficial compared with HP Mg. This research study highlighted the significance of the

distribution design of nanoscale carbon-based reinforcement, such as GNPs reinforcements, in fabricating metal matrix composites in terms of hardness and enhancing other mechanical properties with suitable fabrication methods in the future.

ACKNOWLEDGEMENT

The authors thank the Department of Mechanical and Manufacturing Engineering, Faculty of Engineering Universiti Malaysia Sarawak, for offering a good facility for this research and funding for this project.

REFERENCES

Arab, M., & Marashi, S. P. H. (2019). Effect of graphene nanoplatelets (GNPs) content on improvement of mechanical and tribological properties of AZ31 Mg matrix nanocomposite. *Tribology International*, *132*, 1-10. https://doi.org/10.1016/j.triboint.2018.11.023

Boopathy, J., Pari, R., Kavitha, M., & Angelo, P. C. (2011). Preparation of nano fluids by mechanical method. *AIP Conference Proceedings*, *1461*(1), 218-221. https://doi.org/10.1063/1.4736890

Budinski, K. G., & Budinski, M. K. (1999). *Engineering Materials: Properties and Selection*. Prentice Hall.

Cataldi, P., Athanassiou, A., & Bayer, I. S. (2018). Graphene nanoplatelets-based advanced materials and recent progress in sustainable applications. *Applied Sciences, 8*(9), Article 1438. https://doi.org/10.3390/app8091438

Chen, L., Zhao, Y., Hou, H., Zhang, T., Liang, J., Li, M., & Li, J. (2019). Development of AZ91D magnesium alloy-graphene nanoplatelets composites using thixomolding process. *Journal of Alloys and Compounds*, *778*, 359-374. https://doi.org/10.1016/j.jallcom.2018.11.148

Fan, B., Zhu, S., Ding, H., Bai, Y., Luo, Y., & Di, P. (2019). Influence of MgO whisker addition on microstructures and mechanical properties of WC-MgO composite. *Materials Chemistry and Physics*, *238*, Article 121907. https://doi.org/10.1016/j.matchemphys.2019.121907

Liu, C., Shen, J., Yeung, K. W. K., & Tjong, S. C. (2017). Development and antibacterial performance of novel polylactic acid-graphene oxide-silver nanoparticle hybrid nanocomposite mats prepared by electrospinning. *ACS Biomaterials Science and Engineering*, *3*(3), 471-486. https://doi.org/10.1021/acsbiomaterials.6b00766

Meng, L., Hu, X., Wang, X., Zhang, C., Shi, H., Xiang, Y., Liu, N., & Wu, K. (2018). Graphene nanoplatelets reinforced Mg matrix composite with enhanced mechanical properties by structure construction. *Materials Science and Engineering A*, *733*, 414-418. https://doi.org/10.1016/j.msea.2018.07.056

Mordike, B. L., & Ebert, T. (2001). Magnesium: Properties - applications - potential. *Materials Science and Engineering A*, *302*(1), 37-45. https://doi.org/10.1016/S0921-5093(00)01351-4

Prasad, S. V. S., Prasad, S. B., Verma, K., Mishra, R. K., Kumar, V., & Singh, S. (2022). The role and significance of Magnesium in modern day research-A review. *Journal of Magnesium and Alloys, 10*(1), 1-61. https://doi.org/10.1016/j.jma.2021.05.012

Rajaganapathy, C., Vasudevan, D., & Selvakumar, N. (2020). Investigation on tribological and mechanical behaviour of AA6082 - Graphene based composites with Ti particles. *Materials Research Express*, *7*(7), Article 076514. https://doi.org/10.1088/2053-1591/aba508

Rashad, M., Pan, F., Asif, M., She, J., & Ullah, A. (2015). Improved mechanical proprieties of "magnesium based composites" with titanium-aluminum hybrids. *Journal of Magnesium and Alloys*, *3*(1), 1-9. https://doi.org/10.1016/j.jma.2014.12.010

Rashad, M., Pan, F., Asif, M., & Tang, A. (2014). Powder metallurgy of Mg-1%Al-1%Sn alloy reinforced with low content of graphene nanoplatelets (GNPs). *Journal of Industrial and Engineering Chemistry*, *20*(6), 4250-4255. https://doi.org/10.1016/j.jiec.2014.01.028

Rashad, M., Pan, F., Lin, D., & Asif, M. (2016). High temperature mechanical behavior of AZ61 magnesium alloy reinforced with graphene nanoplatelets. *Materials and Design*, *89*, 1242-1250. https://doi.org/10.1016/j.matdes.2015.10.101

Rodzi, S. N. H. M., & Hussain, Z. (2018). The effect of milling time on properties of magnesium-based composite fabricated via powder metallurgy. *International Journal of Current Research in Science, Engineering & Technology*, *1*(Spl-1), 510-515. https://doi.org/10.30967/ijcrset.1.S1.2018.510-515

Shuai, C., Guo, W., Wu, P., Yang, W., Hu, S., Xia, Y., & Feng, P. (2018). A graphene oxide-Ag co-dispersing nanosystem: Dual synergistic effects on antibacterial activities and mechanical properties of polymer scaffolds. *Chemical Engineering Journal*, *347*, 322-333. https://doi.org/10.1016/j.cej.2018.04.092

Sun, X., Li, C., Dai, X., Zhao, L., Li, B., Wang, H., Liang, C., Li, H., & Fan, J. (2020). Microstructures and properties of graphene-nanoplatelet-reinforced magnesium-matrix composites fabricated by an *in situ* reaction process. *Journal of Alloys and Compounds*, *835*, Article 155125. https://doi.org/10.1016/j.jallcom.2020.155125

Wang, Y., Zhang, F., Wang, Y., Duan, Y., Wang, K., Zhang, W., & Hu, J. (2019). Effect of Zn content on the microstructure and mechanical properties of Mg-Gd-Y-Zr alloys. *Materials Science and Engineering A*, *745*, 149-158. https://doi.org/10.1016/j.msea.2018.12.088

Zhao, T., Hu, Y., He, B., Zhang, C., Zheng, T., & Pan, F. (2019). Effect of manganese on microstructure and properties of Mg-2Gd magnesium alloy. *Materials Science and Engineering A*, *765,* Article 138292. https://doi.org/10.1016/j.msea.2019.138292

Pertanika J. Sci. & Technol. 31 (3): 1503 - 1521 (2023)

PERTANIKA JOURNALS

SCIENCE & TECHNOLOGY

Journal homepage: http://www.pertanika.upm.edu.my/

Discovery of *Mycobacterium tuberculosis* CYP121 New Inhibitor via Structure-Based Drug Repurposing

Tarek El Moudaka[1,2], Priya Murugan[2], Mohd Basyaruddin Abdul Rahman[2] and Bimo Ario Tejo[2]*

[1]*Department of Biotechnology, Faculty of Applied Sciences, UCSI University, No. 1 Jalan Menara Gading, Cheras, Malaysia*
[2]*Department of Chemistry, Faculty of Science, Universiti Putra Malaysia, 43400 UPM, Serdang, Malaysia*

ABSTRACT

Tuberculosis (TB) remains a serious threat to human health with the advent of multi-drug resistant tuberculosis (MDR-TB) and extensively drug-resistant tuberculosis (XDR-TB). The urge to find novel drugs to deal with the appearance of drug-resistant TB and its variants is highly needed. This study aims to find new CYP121 inhibitors by screening 8,773 compounds from the drug repositioning database RepoDB. The selection of CYP121 potential inhibitors was based on two criteria: the new inhibitor should bind to CYP121 with higher affinity than its original ligand and interact with catalytically important residues for the function of CYP121. The ligands were docked onto CYP121 using AutoDock Vina, and the molecular dynamics simulation of the selected ligand was conducted using YASARA Structure. We found that antrafenine, an anti-inflammatory and analgesic agent with high CYP inhibitory promiscuity, was bound to CYP121 with a binding affinity of -12.6 kcal/mol and interacted with important residues at the CYP121 binding site. Molecular dynamics analysis of CYP121 bound to the original ligand and antrafenine showed that both ligands affected the dynamics of residues located distantly from the active site. Antrafenine caused more structural changes to CYP121 than the original ligand, as indicated by a significantly higher number of affected residues and rigid body movements caused by the binding of antrafenine to CYP121.

Keywords: CYP121, drug repositioning, drug resistance, molecular docking, molecular dynamics, tuberculosis, virtual screening

ARTICLE INFO

Article history:
Received: 15 July 2022
Accepted: 05 October 2022
Published: 31 March 2023

DOI: https://doi.org/10.47836/pjst.31.3.21

E-mail addresses:
tareqmedaka@gmail.com (Tarek El Moudaka)
gs60358@student.upm.edu.my (Priya Murugan)
basya@upm.edu.my (Mohd Basyaruddin Abdul Rahman)
bimo.tejo@upm.edu.my (Bimo Ario Tejo)
* Corresponding author

ISSN: 0128-7680
e-ISSN: 2231-8526

© Universiti Putra Malaysia Press

INTRODUCTION

Finding an effective treatment and control of tuberculosis (TB) remains a global challenge due to the emergence of new strains of *Mycobacterium tuberculosis* expressing resistance to the present generation of drugs. TB is an infectious disease that continues to impose risks on public health, as it has infected over ten million of the population globally, of which 1,500,000 cases have resulted in death (WHO, 2019).

In humans, *M. tuberculosis* generally attacks the lungs of the infected, followed by symptoms of persistent cough, fever, hemoptysis, hyperhidrosis, and weight loss (CDC, 2019). *M. tuberculosis* from TB patients can infect a healthy person via airborne. When a person with TB coughs or sneezes, the disease can spread through the air, as *M. tuberculosis* is contained in aerosols (Saleem & Azher, 2013). Ultimately, a single patient suffering from TB may infect up to 15 healthy people upon being continuously in direct contact for a year (Kanabus, 2020).

Every year, approximately ten million people are infected with TB worldwide. People from middle and low-income countries such as India, Bangladesh, Indonesia, China, Nigeria, Philippines, Pakistan, and South Africa were mostly affected by TB infection in 2019 (WHO, 2020). Meanwhile, TB made a comeback in Europe recently when there was an increase in the number of cases. In Paris, for example, the numbers rose from 14.6 per 100,000 inhabitants in 2016 to 15.8 per 100,000 in 2017 due to many migrants from countries with high incidences and increased TB cases in Eastern Europe (Silue et al., 2019).

There has been a rising demand for renewed efforts in researching this devastating disease as the world is confronting a new crisis due to multidrug-resistant (MDR) and extensively drug-resistant (XDR) strains of *M. tuberculosis*. The standard treatment options for TB are no longer effective, mainly contributing to the growing spread of these MDR and XDR bacteria. The *M. tuberculosis* pathogens that have developed resistance can adapt to the TB drugs by altering their cell structures, thereby rendering the effectiveness of these drugs useless (Singh et al., 2020).

One of the emerging targets for anti-tuberculosis drugs is CYP121, a member of the cytochrome P450 family that is only found in *M. tuberculosis* (de Montellano, 2018). This enzyme is considered the most promising anti-TB drug target among other *M. tuberculosis* CYPs due to its prominent substrate specificity. CYP121 significantly binds only cyclodityrosine (cYY) with a conserved 2,5-diketopiperazine (DKP) ring carrying two aryl side chains in l-configuration. CYP121 does not efficiently or selectively transform other cYY analogs, indicating a high specificity for cYY (Fonvielle et al., 2013). Phylogenetic analysis shows that CYP121 is unique to *M. tuberculosis* with limited similarity (≤34% protein sequence identity) to other *M. tuberculosis* P450s (Belin et al., 2009), which could be attributed to the role of this enzyme in catalyzing the C–C bond-forming reaction that is not required by other bacteria (Hudson et al., 2012).

This study aims to identify new CYP121 inhibitors by virtual screening of repurposed drugs. Over eight thousand compounds from a repurposed drug database, RepoDB, were virtually screened to discover the most potential antituberculosis inhibitors. We found that antrafenine, a piperazine derivative and an analgesic anti-inflammatory drug with high CYP inhibitory promiscuity, binds to CYP121 stronger than its respective original inhibitor. Further study using molecular dynamics simulation showed that antrafenine changes the dynamics of residues located distantly from the active site of CYP121. Antrafenine can be further tested to confirm its inhibitory activity against *M. tuberculosis*.

METHODOLOGY

Software

BIOVIA Discovery Studio Visualizer (Dassault Systèmes Biovia) was utilized to visualize and modify the receptor and ligand structure and post-docking interaction analysis. Molecular format conversion was done using OpenBabel (O'Boyle et al., 2011). Molecular docking was conducted using AutoDock Vina (Trott & Olson, 2010). AutoDock Tools (Morris et al., 2009) was used to prepare the *pdbqt* files of protein and ligands. YASARA Structure software (Krieger et al., 2002) was used for molecular dynamics simulation.

CYP121 Structure Preparation

The CYP121 structure in complex with ligand 69M was downloaded from the RCSB Protein Data Bank (PDB ID: 5IBE) (http://www.rcsb.org/). The crystal structure was set up for molecular docking by eliminating all water molecules and sulfate ions using BIOVIA Discovery Studio Visualizer. Ligand 69M was separated from the protein structure and saved as a *.pdbqt* file.

Preparation of Ligand Structures

The three-dimensional structures of 8,773 drug molecules were downloaded from the RepoDB database (http://apps.chiragjpgroup.org/repoDB/) in *.sdf* format (Brown & Patel, 2017). All the drug molecules in the RepoDB database were linked to the DrugBank database (https://go.drugbank.com/) (Wishart et al., 2018). A specific ID number was used to identify the molecular compounds used in this work. All 8,773 ligands were converted to *.pdbqt* file format for molecular docking.

Molecular Docking

Molecular docking was performed using AutoDock Vina. AutoDock Tools was used to create the *.pdbqt* input file for CYP121 and set the size and center of the grid box. Polar hydrogen atoms and Kollman charges were set for CYP121. The validation step

to determine the docking parameters was conducted by re-docking the original ligand of CYP121 (69M) into its respective binding site. The ligand 69M was removed from the CYP121 crystal structure and prepared for re-docking by adding polar hydrogen and partial charges, then saved as a *.pdbqt* file. The center of the grid box and box size was varied until the re-docked conformation of ligand 69M matched its crystal structure. Based on the validation step result, the grid box's center was set to -7.612 × 18.984 × 4.466 (x, y, z) using 1.000 Å spacing and a box size of 40 × 40 × 40. The predicted binding affinity (kcal/mol) was calculated using the AutoDock Vina scoring function. BIOVIA Discovery Studio Visualizer was used to analyze the docking results.

ADMET Prediction

Toxtree (http://toxtree.sourceforge.net/predict/) and SWISSADME (http://swissadme.ch/) were employed to determine the toxicological and pharmacological properties of the ligands. The analyzed properties were carcinogenicity, mutagenicity, AMES test, Lipinski's rule of five for drug-likeness, and corrosive properties. The CYP450 inhibitory promiscuity of each ligand was determined using admetSAR as implemented in the DrugBank database (http://lmmd.ecust.edu.cn/admetsar2/) (Cheng et al., 2012).

Molecular Dynamics

Molecular dynamics simulations were conducted using YASARA Structure on a Windows 10 computer. The AMBER03 force field implemented in YASARA Structure was used in the simulation. The Ewald particle algorithm was used to calculate the long-distance Coulomb interactions. The van der Waals force was set to 8 Å. A hexahedral box of 50 x 50 x 50 Å size was placed around the protein. The water density was fixed to 1 g / mL at a temperature of 298 K. The periodic boundary condition (PBC) was set for the simulated box. The simulation was conducted for 50 ns with trajectories saved every 100 ps. Molecular dynamics outputs were analyzed using *md_analyze.mcr* and *md_analyzeres.mcr* macros implemented in YASARA Structure. The protein domain movement was analyzed using the DynDom program (http://dyndom.cmp.uea.ac.uk/dyndom/ runDyndom.jsp) (Hayward & Berendsen, 1998).

RESULTS AND DISCUSSION

Tuberculosis (TB) has emerged as a significant health issue, and a concern in many nations due to the existence of multidrug-resistant (MDR) and, more recently, extensively drug-resistant (XDR) strains of *M. tuberculosis* (Ouellet et al., 2010). The extensive spread of drug-resistant TB creates a threatening scenario with only a 30% success rate in the treatment (Bhat et al., 2018). Current treatments are becoming complicated by the increasing

number of resistant strains of *M. tuberculosis*, which has led to the urgency to discover new drugs to treat TB disease (Lockart et al., 2020).

The latest recommended treatment available for TB includes isoniazid, rifampicin, pyrazinamide, and ethambutol for the first two months. For the next four months, isoniazid and rifampicin drugs are needed for treatment. MDR-TB is resistant to first-line TB drugs such as isoniazid and rifampicin, whereas XDR-TB is highly resistant to second-line TB drugs. Meanwhile, drug-resistant tuberculosis (TDR-TB) is resistant to a wide range of first-line and second-line drugs (Reddyrajula et al., 2019).

The resistance of bacterial strains to the first-line and second-line drugs and antibiotics is mainly due to the thick, hydrophobic cell envelope and the presence of enzymes that deteriorate and alter the drugs (Gygli et al., 2017). The treatment given to the drug-resistant bacterial strain is strenuous and requires at least 6−9 months of constant therapy in ideal circumstances (Hoagland et al., 2016). Besides that, the treatment is considered more expensive, highly toxic, and requires sophisticated facilities and equipment for drug-resistant testing (Hoagland et al., 2016).

Several potential TB drugs have been approved and tested in clinical trials (Reddyrajula et al., 2019). Bedaquiline and diaryl quinoline-based molecules were approved by the US Food and Drug Agency (FDA) and the European Medicines Agency (EMA) to treat adult MDR-TB. Bedaquiline causes side effects such as cardiac arrhythmias (Reddyrajula et al., 2019). Therefore, there is an urgent need to discover new drugs targeting new receptors to combat MDR-TB and XDR-TB.

The cytochrome P450 is a superfamily of the monooxygenase enzymes having the β-heme and protoforfirin IX groups as the heme cofactor (Leys et al., 2003). In bacteria, cytochrome P450 functions in xenobiotic degradation, nitric oxide reduction, antibiotic synthesis, and fatty acid metabolism (Bogaert et al., 2010), whereas in humans, the cytochrome P450 functions in the metabolism of various drugs (Nerbert et al., 2013). Cytochrome P450 CYP121 is essential for the viability of *M. tuberculosis*, as it catalyzes the formation of mycocyclosin by forming a C-C bond between the two tyrosyl side chains of the cyclodityrosine (cYY, cyclo-L-Tyr-L-Tyr) (Ugalde et al., 2020).

The emphasis on CYP121's importance is due to its strong affinity for azole molecules and its analogs used as very effective antimycobacterial compounds for *M. tuberculosis* growth inhibition (Ahmad et al., 2005). Most azole antifungals, however, are incompatible as scaffolds for front-line oral anti-TB drug candidates due to their poor bioavailability and non-specific affinity for human CYPs, resulting in severe systemic toxicology and induced drug-drug interaction. Furthermore, azole-resistant *M. tuberculosis* mutants with up-regulation of a transmembrane transporter protein thought to function as an azole efflux pump have been isolated. (Hudson et al., 2012), which highlights the need for finding molecules other than azole drugs to bind to CYP121.

This work discovered potential inhibitors against the *M. tuberculosis* CYP121 drug target by docking a large database of molecules from the RepoDB database. The molecule compounds in the repositioning drug database (RepoDB) have been approved to treat various diseases. More than 8,000 molecules were docked into the binding site of the CYP121 crystal structure using the AutoDock Vina program. The binding affinity calculation for all 8,773 molecular compounds was determined by AutoDock Vina using a specific implemented algorithm and scoring function in the program. This study used CYP121's original ligand (69M) as a control ligand in molecular docking.

Validation of Docking Parameters

A validation step was conducted to ensure that the docking parameters allowed ligands to adopt correct conformations in the binding pocket. The original ligand (69M) was re-docked into the CYP121 crystal structure for validation docking. Our result shows that the re-docked 69M inhibitor adopted a similar conformation with its crystal structure with a binding affinity of -11.7 kcal/mol (Figure 1).

Ligand 69M was stabilized by three hydrogen bonds, i.e., between Ser237 and N25 nitrogen atoms of the ligand, between Val228 and O1 oxygen atom of the ligand, and another hydrogen bond between Thr77 and N11 nitrogen atom of the ligand. The heme group formed a pi-pi interaction with the aromatic ring of the ligand. A pi-pi stacking interaction was formed between Trp182 and Phe168 with the aryl alcohol ring of the ligand. Ala167 and Ala233 formed a pi-alkyl interaction with two aromatic ligand rings. A pi-sigma interaction was observed between Val78 and the imidazole ring of the ligand. It is interesting to note that the residues interacting with ligand 69M involve the same residues anchoring cyclodipeptide cYY ligand to CYP121, i.e., Met62, Val78, Val83, Asn85, Phe168, Trp182, Ala233, Ser237, Phe280, Gln385, Arg386, and heme group (Belin et al., 2009).

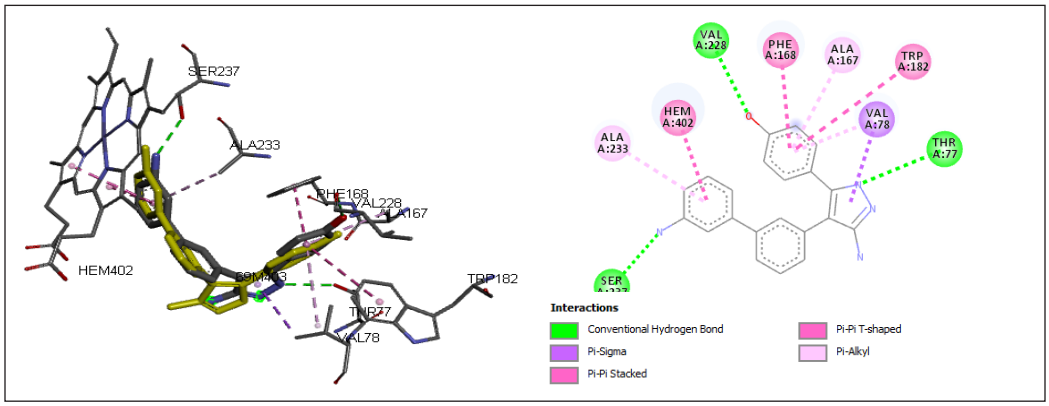

Figure 1. The redocked ligand 69M (grey) in comparison to its original position and conformation (yellow). A two-dimensional interaction map shows the types of interaction between ligand 69M and its surrounding residues.

Molecular Docking of Drug Compounds

The molecular docking of 8,773 drug compounds from the RepoDB database was carried out using the AutoDock Vina program. In order to find the potential inhibitors for *M. tuberculosis* CYP121, the compounds should have a higher binding affinity to CYP121 than that of the original ligand 69M, i.e., -11.7 kcal/mol. The top 10 docked compounds with higher binding affinity values than ligand 69M were displayed (Table 1).

Table 1
Top 10 drugs with the highest docking binding affinity to CYP121

Compound ID	Drug name	Affinity (kcal/mol)	CYP inhibitory promiscuity	Molecular structure
DB04098	Balanol	-13.0	Low	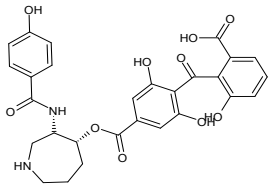
DB03992	3-(Benzoylamino)-L-alanine	-13.0	Low	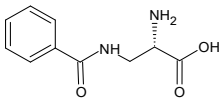
DB01419	Antrafenine	-12.6	High	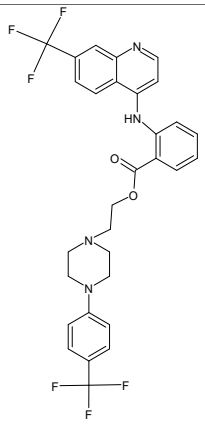
DB01891	Tl-3-093	-12.5	Low	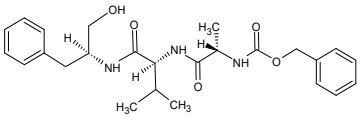
DB05861	Tasquinimod	-12.5	Low	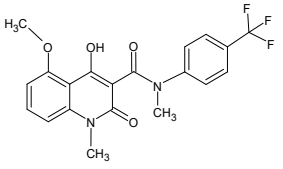

Table 1 *(continue)*

Compound ID	Drug name	Affinity (kcal/mol)	CYP inhibitory promiscuity	Molecular structure
DB05855	Rivanicline	-12.4	Low	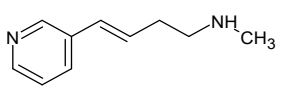
DB01459	Bezitramide	-12.3	Low	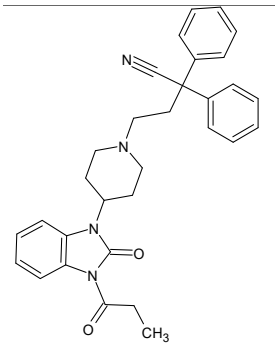
DB01876	Bis(5-amidino-2-benzimidazolyl) methanone	-12.2	High	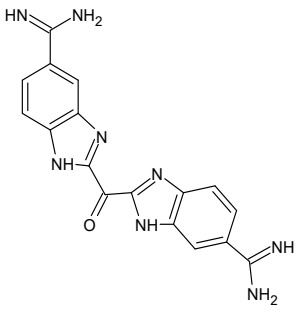
DB01902	1-Ethyl-pyrrolidine-2,5-dione	-12.1	Low	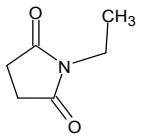
DB02327	Triethylene glycol	-11.9	Low	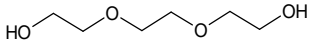

The toxicological and pharmacological properties of the top ten drugs were determined using Toxtree and SWISSADME (Table 2). All drugs used in this work were taken from RepoDB, a repurposed drug database. Therefore, we did not expect the compounds used in this work to be toxic or pharmacologically unfavorable. Toxtree and SWISSADME analysis showed that the top ten compounds were noncarcinogenic and nonmutagenic. All compounds passed the ADME test and were non-corrosive to skin, except triethylene glycol. Five compounds violated Lipinski's rule of five; however, these compounds could be formulated to improve their absorption and permeation in the later stages of drug development.

Table 2
Toxicological and pharmacological properties of the top 10 drugs with the highest docking binding affinity to CYP121

	Benigni/Bossa rules		Lipinski's rule of five			
Ligand	Carcinogenicity	Mutagenicity	AMES test	Violation	Druglikeness	Skin corrosive
Balanol	Noncarcinogenic	Nonmutagenic	Pass	3	Yes	No
3-(Benzoylamino)-L-alanine	Noncarcinogenic	Nonmutagenic	Pass	3	Yes	No
Antrafenine	Noncarcinogenic	Nonmutagenic	Pass	2	No	No
T1-3-093	Noncarcinogenic	Nonmutagenic	Pass	0	Yes	No
Tasquinimod	Noncarcinogenic	Nonmutagenic	Pass	0	Yes	No
Rivanicline	Noncarcinogenic	Nonmutagenic	Pass	0	Yes	No
Bezitramide	Noncarcinogenic	Nonmutagenic	Pass	1	Yes	No
Bis(5-amidino-2-benzimidazolyl) methanone	Noncarcinogenic	Nonmutagenic	Pass	1	Yes	No
1-ethyl-pyrrolidine-2,5-dione	Noncarcinogenic	Nonmutagenic	Pass	0	Yes	Unknown
Triethylene glycol	Noncarcinogenic	Nonmutagenic	Pass	0	Yes	Yes

Balanol (DB04098) and 3-(benzoylamino)-L-alanine (DB03992) were the highest-ranked compounds with a binding affinity of -13.0 kcal/mol. However, both compounds had low promiscuity in inhibiting cytochrome P450. Interestingly, the second-ranked compound, i.e., antrafenine (DB01419) with a binding affinity of -12.6 kcal/mol, was predicted to have high cytochrome P450 inhibitory promiscuity. The fluorine atoms attached to C25 and C42 carbon atoms of antrafenine formed hydrogen bonds with Arg386, which plays an important role in CYP121 catalytic activity (Belin et al., 2009). Furthermore, two hydrogen bonds were formed between Gln385 and Thr77 with an O8 oxygen atom of antrafenine. The aromatic ring next to the O8 oxygen atom interacted with three different residues as it formed a pi-sigma interaction with Val78, a pi-pi stacked interaction with Phe168, and a pi-alkyl bonding with Ala167.

It is important to note that antrafenine formed four interactions with the heme group, in which pi-alkyl and pi-pi interactions occurred between the heme group and quinoline ring antrafenine, also pi-alkyl and halogen interactions between fluorine of antrafenine and the heme group (Figure 2). Of 12 CYP121 residues interacting with antrafenine, six (Val78, Phe168, Phe280, Gln385, Arg386, and heme) are involved in the binding of cyclodipeptide cYY and CYP121 (Belin et al., 2009).

Antrafenine formed multiple non-covalent interactions with the heme functional group, which is important in the CYP121 catalytic activity (McLean et al., 2008; Belin et al., 2009). Among these interactions are pi-pi stacking, which stabilizes the non-covalent

contact between the aromatic rings of the heme group and antrafenine via London dispersion forces and electrostatics (Brylinski, 2018), pi-alkyl interaction, which is weaker than pi-pi stacking and dominated by London dispersion forces (Ribas et al., 2002), as well as halogen bonding which is essential for an accurate molecular interaction prediction (Li et al., 2016) and stabilizes the non-covalent interaction between a protein and a ligand (Suárez-Castro et al., 2018).

Antrafenine is a piperazine derivative and acts as an anti-inflammatory drug with high CYP inhibitory promiscuity, specifically for CYP1A2, CYP2C9, CYP2C19, and CYP3A4. Antrafenine is an analgesic agent for the relief of mild to moderate pain (Lv et al., 2020). Antrafenine targets the prostaglandin G/H synthase-1 (COX-1) and prostaglandin G/H synthase-2 (COX-2) in the cyclooxygenase pathway. The inhibition of COX-2 by antrafenine is presumably responsible for its anti-inflammatory activity. However, inhibition of COX-1 by antrafenine may be responsible for its toxicity. Further use of antrafenine as a repurposed anti-TB drug requires its dose to be adjusted to balance the risks and benefits.

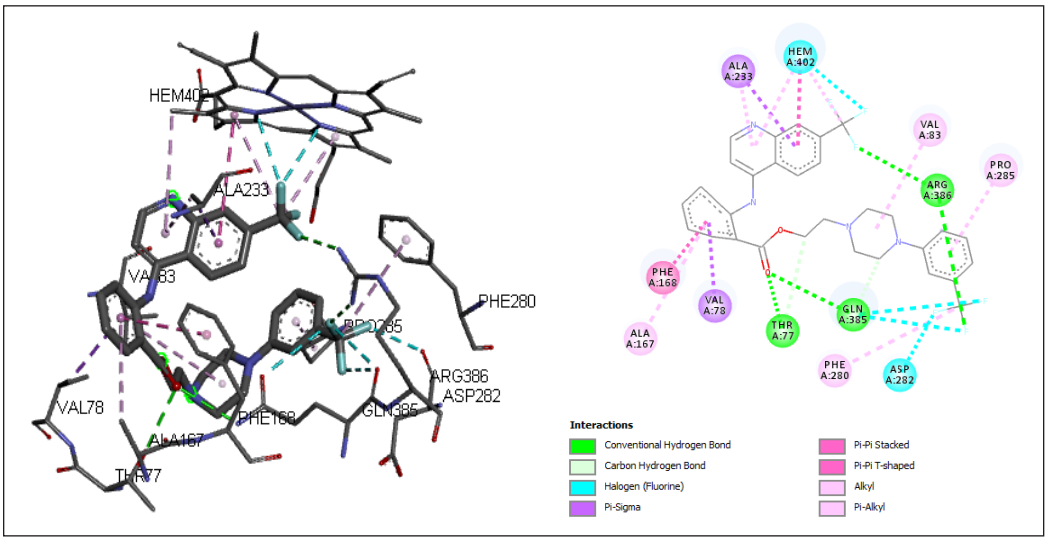

Figure 2. Antrafenine and its interactions with the surrounding amino acid residues

Molecular Dynamics

Molecular dynamics simulations were conducted to study the effect of ligands on the structure and dynamics of protein receptors. Molecular docking is typically performed on the rigid structure of the protein receptor, which does not represent a realistic condition. Molecular dynamics simulation provides a more realistic picture, where the interactions between ligand and protein receptor are optimized through conformational adjustment of the ligand and receptor after docking. Therefore, the combination of molecular docking and molecular dynamics simulation is appropriate for studying the ligand-receptor binding

mechanism and the impact of ligand binding on the structure and dynamics of receptors (Santos et al., 2019). This research used YASARA Structure to simulate the molecular dynamics of three different systems. i.e., CYP121 with no ligand (code: CYP), CYP121 in complex with ligand 69M (code: 69M), and CYP121 in complex with antrafenine (code: ANT).

The deviation of the simulated trajectory from the crystallographic structure was monitored by calculating the root-mean-square deviation (RMSD) as a function of time. RMSD compares the conformation of the protein system at a certain time to the conformation of the protein at the initial time (t = 0). Analysis of molecular dynamics trajectories is usually conducted when the system has reached equilibrium, i.e., when the RMSD plot has plateaued. RMSD also provides information on how far the conformational changes of the protein with the presence of the ligand are compared to those without the presence of the ligand.

The RMSD plot of the CYP system (protein without ligand) achieved a plateau earlier than that of protein with ligands, i.e., at 10 ns. The RMSD plot of the 69M system (protein with ligand 69M) reached a plateau at 20 ns. Meanwhile, the RMSD plot of the ANT system (protein with antrafenine) reached a plateau at 25 ns (Figure 3). In the CYP system, the RMSD at the equilibrium ranged between 1.4–1.7 Å. In the 69M system, the RMSD at the equilibrium ranged between 1.5–1.9 Å. Meanwhile, in the ANT system, the RMSD at the equilibrium ranged between 2.0–2.5 Å. Interestingly, the presence of antrafenine caused the CYP121 protein to have a higher deviation from its crystal structure, as indicated by the higher RMSD of ANT systems than that of the CYP and 69M systems. The difference was prominent beyond 25 ns of simulation time, where the protein in the ANT system was 2.0–2.5 Å away from its initial structure.

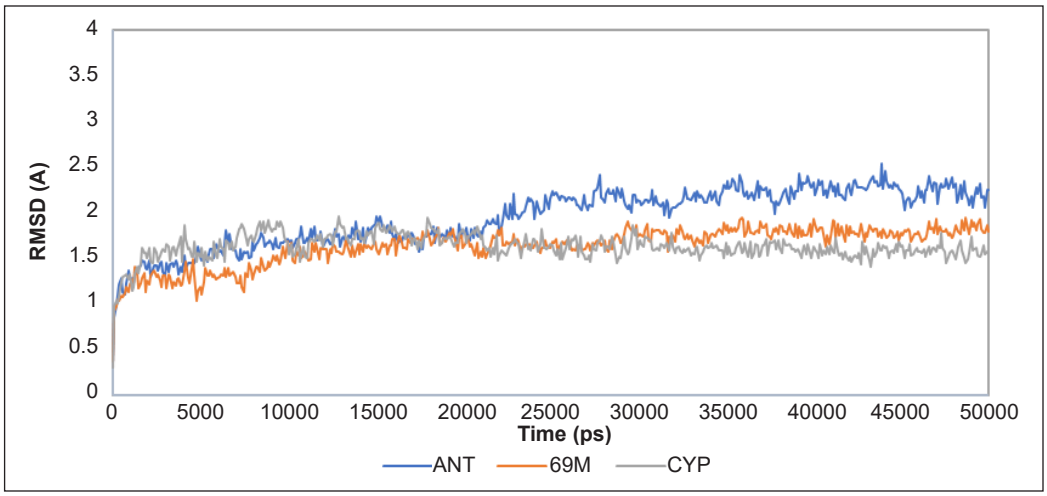

Figure 3. Root mean square deviation (RMSD) of three simulation systems (CYP, 69M, and ANT) over 50 ns of MD simulation

Analysis of CYP121 fluctuations was done by calculating the root-mean-square fluctuations (RMSF) of each residue. The RMSF values of the protein backbone in the presence of ligands, i.e., 69M and ANT systems, were compared to the RMSF values of protein without ligands, i.e., CYP system. A comparison of the RMSF values between the three systems was conducted to see the impact of ligands on the dynamics of residues in proteins. A ligand at the protein binding site impacts the dynamics of nearby residues and residues far from the binding site.

The comparison of the RMSF of the 69M and CYP systems shows that there were 17 residues in the 69M system whose RMSF were at least 50% higher than those of their values in the CYP system (Table 3 and Figure 4a). The largest change in the RMSF of the 69M system was observed at residue Phe280 with an increase of more than 100% than its value in the CYP system. On the other hand, Ala92 showed significantly lower RMSF in the 69M system, with a more than 50% drop compared to its value in the CYP system. The location of residues whose RMSF was increased by more than 50% due to the presence of ligand 69M are shown in red (Figure 4b). Interestingly, of 17 amino acid residues whose RMSF values were increased upon binding to ligand 69M, only three residues, i.e., Arg72, Ile102, and Phe230, had direct contact with ligand 69M. Fourteen residues did not interact directly with ligand 69M, indicating the long-range effect of ligand binding.

The comparison of the RMSF of the ANT and CYP systems shows that there were 61 residues in the ANT system whose RMSF were at least 50% higher than those of their values in the CYP system (Table 3 and Figure 5a). Of these 61 residues, 20 residues had

Table 3
List of residues in the 69M and ANT systems whose RMSF values are greater than 50% of their values in the CYP system

System	Residues	RMSF value
69M	Arg72, Ile102, Pro104, Arg134, Phe137, Glu155, Gly157, Pro158, Ala178, Asn181, Phe230, Ser240, Thr243, Phe280, Asp282, Leu308, Leu306	≥ 50% of their values in the CYP system
	Phe280	≥ 100% of their values in the CYP system
ANT	Arg72, Ala75, Leu76, Val82, Ala101, Pro104, Cys147, Ile152, Pro153, Gln154, Glu155, Pro158, Lys159, Leu160, Phe161, Arg162, Ser163, Leu164, Ser165, Ile166, Phe168, Ser170, Ser171, Ala172, Pro174, Pro176, Ala177, Ala178, Ile180, Asn181, Trp182, Asp183, Arg184, Asp185, Ile186, Glu187, Tyr188, Met189, Ala190, Gly191, Ile192, Leu193, Asn195, Met203, Leu206, Gly227, Val228, Phe231, Gly232, Ala233, Gly234, Ser237, Ser240, Phe280, Gln323, His354, Gln356, Gln385	≥ 50% of their values in the CYP system
	Arg28, Gly151 and Arg353	≥ 100% of their values in the CYP system

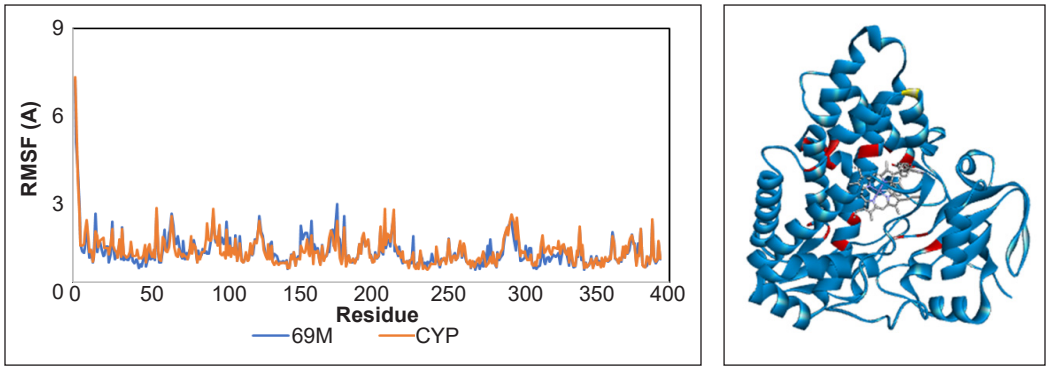

(a) (b)

Figure 4. (a) Root mean square fluctuation (RMSF) of CYP (blue) and 69M (red) systems; and (b) Residues in the 69M system, whose RMSF values were increased by 50% and more, are shown in red.

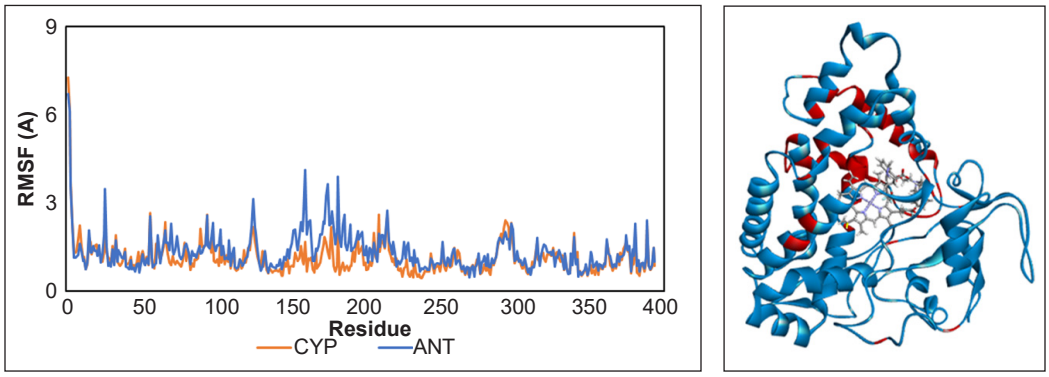

(a) (b)

Figure 5. (a) Root mean square fluctuation (RMSF) of CYP (blue) and ANT (red) systems; and (b) Residues in the ANT system, whose RMSF values were increased by 50 % and more, are shown in red.

their RMSF increase more than 100% compared to their values in the CYP system, i.e., Arg72, Gln154, Phe161, Arg162, Ser163, Leu164, Ser165, Asn181, Trp182, Asp183, Asp185, Glu187, Tyr188, Gly191, Ile192, Met203, Gly227, Val228, Gly232 and Ser 237. The location of residues whose RMSF was increased by more than 50% due to the presence of ligand ANT is shown in red (Figure 5b). Interestingly, of 61 amino acid residues whose RMSF was increased upon binding to ANT ligand, only 10 residues, i.e., Arg72, Val82, Leu164, Phe168, Trp182, Gly232, Ala233, Ser237, Phe280, and Gln385 had direct contacts with ligand ANT. Fifty-one residues did not interact directly with ligand ANT, indicating the long-range effect of ligand binding.

Analysis of protein domain movement was carried out using DynDom, which uses the K-means clustering algorithm to find clusters of rotation vectors. DynDom analysis on the CYP system trajectory (simulated CYP121 protein without ligand) showed no rigid body movement during 50 ns of MD simulation. Similarly, for the 69M system, which was a

simulation that included the 69M ligand at the binding site of the CYP121 protein, no rigid body movement was observed during 50 ns of MD simulation. Interestingly, for the ANT system, which simulated ANT ligand with CYP121 protein, rigid body movements were observed in four segments, i.e., residues 77−80, 85−95, 164−196, and 209−228. The rigid movements of the four segments were assisted by six "hinges" (Figure 6 and Table 4). In these four moving segments, there were 12 residues whose RMSF values were more than 100% higher than their RMSF in the absence of ligand, i.e., Leu164, Ser165, Asn181, Trp182, Asp183, Asp185, Glu187, Tyr188, Gly191, Ile19, Gly227 and Val228.

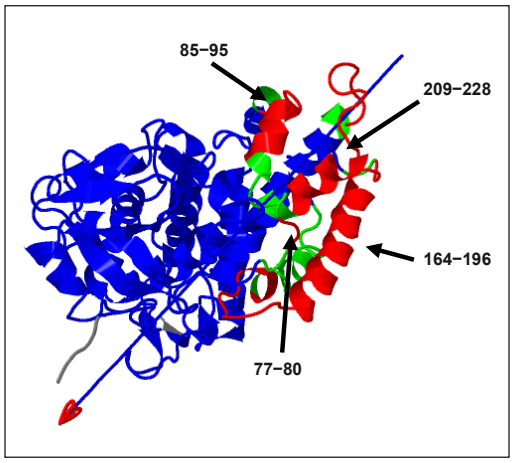

Figure 6. DynDom domain movement analysis of CYP121 in complex with ligand ANT. The fixed domains are colored blue, the moving domains are red, and the hinge domains are green. The locations of four moving domains are labeled. The arrow indicates the hinge axis. The figure was taken from DynDom output.

Table 4
List of residues that are classified as fixed (blue), moving (red), and hinge (green) in Figure 6

Domain	Residues
Fixed (blue)	6–76, 81–84, 96–163, 197–208, 229–394
Moving (red)	77–80, 85–95, 164–196, 209–228
Hinge (green)	76–77, 80–85, 95–96, 152–164, 196–197, 207–209, 228–229

Based on the DynDom dynamic contact analysis, there are four modes of domain movements in the structure of CYP121 in complex with ligand ANT, i.e., "maintained," "exchanged-partner," "exchanged-pair," and "new" (Figure 7a) (Taylor et al., 2013). The dynamic contact graph or DCG (Figure 7b) showed there were seven "maintained" (anchored) domain movements that happened between residues Thr38 → Ala172, Ala75 → Ser171, Ala75 → Pro174, Ala75 → Ile175, Ile192 → Met203, Asn195 → Ile198, and Met189 → Met203. Six "new" (open-closed) domain movements happened between residues Met86 → Val98, Met86 → Met99, Met86 → His343, Met86 → Pro346, and Lys63 → Gly87. There were two "exchanged-partner" (sliding-twist) domain movements that happened between residues Ala75 → Asp173 → Arg72 and Ala75 → Asp173 → Thr38. There were four "exchanged-pair" (see-saw) domain movements that happened between residues Ala75 → Asp173 and Pro174 → Ala75, Ala75 → Pro174 and Ser171 → Ala75, Ala75 → Ser171 and Ile175 → Ala75, Ile198 → Ile192 and Asn195 → Ile198 (Figure 7b). The four domain movements occurred only at residue segments 85−95 and 164−196,

which indicated the higher complexity of movements in these two segments. Meanwhile, the other two residue segments (77−80 and 209−228) moved freely by not following any of the four modes of domain movements.

Our results show that ligands 69M and ANT binding cause dynamic structural changes in the CYP121 protein. Most residues affected by ligands are far from the protein binding site. The long-range effect, which refers to changes in the dynamics of residues far from the binding site, is presumably caused by a "domino effect" (Oelschlaeger et al., 2003). Perturbations cause the domino effect in the residues around the ligand, which are transferred to the adjacent residues and then forwarded to the next residues. One example of a domino effect mechanism is elaborated by Stahl and Sieber (2017) using protease caseinolytic peptidase P (ClpP) as a model. The structural analysis of crystal structures of LmClpP isoforms (LmClpP1 and LmClp2) shows alterations in the amino acid arrangement within the active site and ring-ring interface. The presence of substrate in the active site seems important for the activated state. Structural x-ray analysis reveals that the domino effect resulting in an active ClpP is caused by the transfer of binding information from the apical surface into the ClpP core. The interaction of ClpX leads to changes in the conformation of Tyr63, which seems to start at the adjacent residue Met31. It would cause Asn42 to move flexibly, exchanging its hydrogen interaction from Tyr21 to Gly33 and Asn65 and eventually resulting in conformational changes in the receptor.

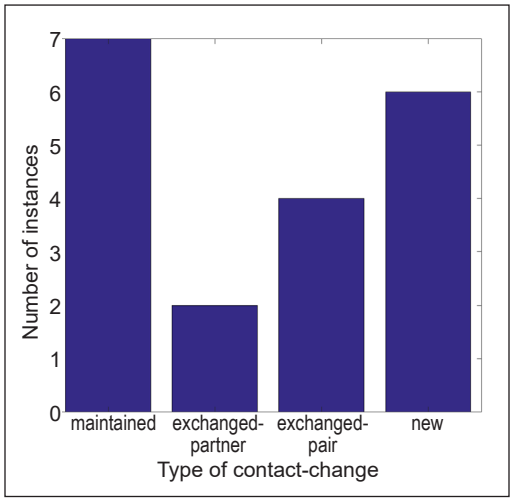

(a)

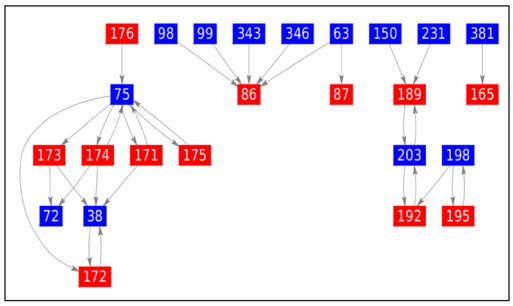

(b)

Figure 7. Dynamic contact analysis of CYP121 in complex with ligand ANT: (a) Types of domain movement and their number of instances; and (b) Dynamic contact graph (DCG) between residues in the fixed domain (blue) and moving domain (red) of CYP121. The definitions of each domain movement and elemental dynamic contact graphs (DCGs) are described in Taylor et al. (2013).

Prasasty et al. (2020) recently reported the prediction of inhibitory activity of natural compounds isolated from Rhoeo spatheca and Pluchea indica against M. tuberculosis CYP121. They observed that the original ligand GGJ caused changes in the flexibility of residues at the binding site and distant residues. However, the natural compound (KAE)

and its derivative (KAE3) did not cause any changes in the flexibility of distant residues. Our results show that the original ligand 69M changed the flexibility of distant residues, which concurs with the finding by Prasasty et al. (2020) that the long-range effect seems to play a major role in the binding mechanism of CYP121 inhibitors.

CONCLUSION

We have found antrafenine, an anti-inflammatory drug with high promiscuity to inhibit cytochrome P450, as a potential inhibitor for *M. tuberculosis* CYP121. Antrafenine, which emerged as the top CYP121 binder after docking 8,773 compounds from the RepoDB drug repositioning database, is bound to CYP121 with a binding affinity of -12.6 kcal/mol and interacts with important residues at the CYP121 binding site. Upon binding to CYP121, antrafenine affects the dynamics of residues located distantly from the active site. Our finding warrants further investigation by testing the inhibitory activity of antrafenine against *M. tuberculosis* CYP121.

ACKNOWLEDGEMENTS

The authors thank the Malaysian Ministry of Higher Education for funding (FRGS/1/2020/STG01/UPM/02/24).

REFERENCES

Ahmad, Z., Sharma, S., & Khuller, G.K. (2005). In vitro and ex vivo antimycobacterial potential of azole drugs against Mycobacterium tuberculosis H37Rv. *Federation of European Microbiological Societies Microbiology Letters, 251*(1), 19-22. https://doi.org/10.1016/j.femsle.2005.07.022

Belin, P., Le Du, M., Fielding, A., Lequin, O., Jacquet, M., Charbonnier, J., Lecoq, A., Thai, R., Courçon, M., Masson, C., Dugave, C., Genet, R., Pernodet, J., & Gondry, M. (2009). Identification and structural basis of the reaction catalyzed by CYP121, an essential cytochrome P450 in *Mycobacterium tuberculosis*. *Proceedings of the National Academy of Sciences, 106*(18), 7426-7431. https://doi.org/10.1073/pnas.0812191106

Bhat, Z. S., Rather, M. A., Maqbool, M., & Ahmad, Z. (2018). Drug targets exploited in Mycobacterium tuberculosis: Pitfalls and promises on the horizon. *Biomedicine and Pharmacotherapy, 103*, 1733-1747. https://doi.org/10.1016/j.biopha.2018.04.176

Bogaert, I. N., Groeneboer, A. V., Saerens, S. K., & Soetaert, W. (2010). The role of cytochrome P450 monooxygenases in microbial fatty acid metabolism. *The Federation of European Biochemical Societies Frequency Journal*, *278*(2), 206-221. https://doi.org/10.1111/j.1742-4658.2010.07949.x

Brown, A. S., & Patel, C. J. (2017). A standard database for drug repositioning. *Scientific Data, 4*(1), Article 170029. https://doi.org/10.1038/sdata.2017.29

Brylinski, M. (2018). Aromatic interactions at the ligand–protein interface: Implications for the development of docking scoring functions. *Chemical Biology and Drug Design*, *91*(2), 380-390. https://doi.org/10.1111/cbdd.13084

CDC. (2019). *Infectious Disease Related to Travel*. CDC. https://wwwnc.cdc.gov/travel/yellowbook/2020/travel-related-infectious-diseases/tuberculosis

Cheng, F., Li, W., Zhou, Y., Shen, J., Wu, Z., Liu, G., Lee, P. W., & Tang, Y. (2012). admetSAR: A comprehensive source and free tool for evaluating chemical ADMET properties. *Journal of Chemical Information and Modeling, 52*(11), 3099-3105. https://doi.org/10.1021/ci300367a

de Montellano, P. R. O. (2018). Potential drug targets in the Mycobacterium tuberculosis cytochrome P450 system. *Journal of Inorganic Biochemistry*, *180*, 235-245. https://doi.org/10.1016/j.jinorgbio.2018.01.010

Fonvielle, M., Le Du, M. H., Lequin, O., Lecoq, A., Jacquet, M., Thai, R., Dubois, S., Grach, G., Gondry, M., & Belin, P. (2013). Substrate and reaction specificity of Mycobacterium tuberculosis cytochrome P450 CYP121: Insights from biochemical studies and crystal structures. *Journal of Biological Chemistry*, *288*(24), 17347-17359. https://doi.org/10.1074/jbc.M112.443853

Gygli, S. M., Borrell, S., Trauner, A., & Gagneux, S. (2017). Antimicrobial resistance in Mycobacterium tuberculosis: Mechanistic and evolutionary perspectives. *Federation of European Microbiological Societies Microbiology Reviews*, *41*(30, 354-373. https://doi.org/10.1093/femsre/fux011

Hayward, S., & Berendsen, H. J. C. (1998). Systematic analysis of domain motions in proteins from conformational change: New results on citrate synthase and T4 lysozyme. *Proteins*, *30*(2), 144-154. https://doi.org/10.1002/(SICI)1097-0134(19980201)30:2%3C144::AID-PROT4%3E3.0.CO;2-N

Hoagland, D. T., Liu, J., Lee, R. B., & Lee, R. E. (2016). New agents for the treatment of drug-resistant Mycobacterium tuberculosis. *Advanced Drug Delivery Reviews*, *102,* 55-72. https://doi.org/10.1016/j.addr.2016.04.026

Hudson, S. A., McLean, K. J., Munro, A. W., & Abell, C. (2012). Mycobacterium tuberculosis cytochrome P450 enzymes: A cohort of novel TB drug targets. *Biochemical Society Transactions, 40*(3), 573-579. https://doi.org/10.1042/BST20120062

Kanabus, A. (2020). *Information about Tuberculosis*. Tbfact.org. http://www.tbfacts.org/tb/

Krieger, E., Koraimann, G., & Vriend, G. (2002). Increasing the precision of comparative models with YASARA NOVA- A self-parameterizing force field. *Proteins: Structure, Function, and Genetics*, *47*(3), 393-402. https://doi.org/10.1002/prot.10104

Leys, D., Mowat, C. G., McLean, K. J., Richmond, A., Chapman, S. K., Walkinshaw, M. D., & Munro, A. W. (2003). Atomic structure of Mycobacterium tuberculosis CYP121 to 1.06 Å reveals novel features of cytochrome P450. *Journal of Biological Chemistry*, *278*(7), 5141-5147. https://doi.org/10.1074/jbc.M2099282200

Li, Y., Guo, B., Xu, Z., Li, B., Cai, T., Zhang, X., Yu, Y., Wang, H., Shi, J., & Zhu, W. (2016). Repositioning organohalogen drugs: A case study for identification of potent B-Raf V600E inhibitors via docking and bioassay. *Scientific Reports*, *6*(1), Article 31074. https://doi.org/10.1038/srep31074

Lockart, M. M., Butler, J. T., Mize, C .J., Fair, M. N., Cruce, A. A., Conner, K. P., Atkins, W. M., & Bowman, M. K. (2020). Multiple drug binding modes in *Mycobacterium tuberculosis* CYP51B1. *Journal of Inorganic Biochemistry*, *205,* Article 110994. https://doi.org/10.1016/j.jinorgbio.2020.110994

Lv, Y., Wang, Y., Zheng, X., & Liang, G. (2020). Reveal the interaction mechanism of five old drugs targeting VEGFR2 through computational simulations. *Journal of Molecular Graphics and Modelling*, *96*, Article 107538. https://doi.org/10.1016/j.jmgm.2020.107538

McLean, K. J., Carroll P., Lewis D., Dunford A. J., Seward H. E., Neeli R., Cheesman M. R., Marsollier L., Douglas P., Smith W. E., Rosenkrands I., Cole S. T., Leys D., Parish T., & Munro A. W. (2008). Characterization of active site structure in CYP121-A cytochrome P450 essential for viability of Mycobacterium tuberculosis H37rv. *Journal of Biological Chemistry*, *283*(48), 33406-33416. https://doi.org/10.1074/jbc.M802115200

Morris, G. M., Huey, R., Lindstrom, W., Sanner, M. F., Belew, R. K., Goodsell, D. S., & Olson, A. J. (2009). AutoDock4 and AutoDockTools4: Automated docking with selective receptor flexibility. *Journal of Computational Chemistry*, *30*(16), 2785-2791. https://doi.org/10.1002/jcc.21256

Nerbert, D. W., Wikvall, K., & Miller, W. L. (2013). Human cytochromes P450 in health and disease. *Philosophical Transactions of the Royal Society of London B: Biological Sciences*, *368*(1612), Article 20120431. https://doi.org/10.1098/rstb.2012.0431

O'Boyle, N. M., Banck, M., James, C. A., Morley, C., Vandermeersch, T., & Hutchison, G. R. (2011). Open babel: An open chemical toolbox. *Journal of Cheminformatics, 3*(1), 1-14. https://doi.org/10.1186/1758-2946-3-33

Oelschlaeger, P., Schmid, R. D., & Pleiss, J. (2003). Modeling domino effects in enzymes: Molecular basis of the substrate specificity of the bacterial metallo-β-lactamases IMP-1 and IMP-6. *Biochemistry*, *42*(30), 8945-8956. https://doi.org/10.1021/bi0300332

Ouellet, H., Johnston, J. B., & de Montellano, P. R. O. (2010). The Mycobacterium tuberculosis cytochrome P450 system. *Archives of Biochemistry and Biophysics*, *493*(1), 82-95. https://doi.org/10.1016/j.abb.2009.07.011

Prasasty, V. D., Cindana, S., Ivan, F. X., Zahroh, H., & Sinaga, E. (2020). Structure-based discovery of novel inhibitors of Mycobacterium tuberculosis CYP121 from Indonesian natural products. *Computational Biology and Chemistry, 85*, Article 107205. https://doi.org/10.1016/j.compbiolchem.2020.107205

Reddyrajula, R., Dalimba, U., & Kumar, S. M. (2019). Molecular hybridization approach for phenothiazine incorporated 1,2,3-triazole hybrids as promising antimicrobial agents: Design, synthesis, molecular docking and in silico ADME studies. *European Journal of Medicinal Chemistry*, *168*, 263-282. https://doi.org/10.1016/j.ejmech.2019.02.010

Ribas, J., Cubero, E., Luque, F. J., & Orozco, M. (2002). Theoretical study of alkyl-π and aryl-π interactions. Reconciling theory and experiment. *Journal of Organic Chemistry, 67*(20), 7057-7065. https://doi.org/10.1021/jo0201225

Saleem, A., & Azher, M. (2013). The next pandemic- tuberculosis: The oldest disease of mankind rising one more time. *British Journal of Medical Practitioners*, *6*(2), 21-46.

Suárez-Castro, A., Valle-Sánchez, M., Cortés-García, C. J., & Chacón-García, L. (2018). Molecular docking in halogen bonding. In P. Vlachakis (Ed.), *Molecular Docking* (pp. 99-112). Intechopen. http://dx.doi.org/10.5772/intechopen.72994

Santos, L. H. S., Ferreira, R. S., & Caffarena, E. R. (2019). Integrating molecular docking and molecular dynamics simulations. In W. F. de Azevedo (Ed.), *Methods in Molecular Biology* (pp. 13-34). Humana Press. https://doi.org/ 10.1007/978-1-4939-9752-7_2

Silue, Y., Lepoutre, A., Mounchetrou-Njoya, I., Lapora, S., Calba, C., & Guthmann, J. (2019). Increase of tuberculosis incidence in Ile-de-France region and the role of recent migration. *European Journal of Public Health*, *29*(Supplement_4), Article ckz186-033. https://doi.org/10.1093/eurpub/ckz186.033

Singh, R., Dwivedi, S. P., Gaharwar, U. S., Meena, R., Rajamani, P., & Prasad, T. (2020). Recent updates on drug resistance in Mycobacterium tuberculosis. *Journal of Applied Microbiology*, *128*(6), 1547-1567. https://doi.org/10.1111/jam.14478

Stahl, M., & Sieber, S. A. (2017). An amino acid domino effect orchestrates ClpP's conformational states. *Current Opinion in Chemical Biology*, *40*, 102-110. https://doi.org/10.1016/j.cbpa.2017.08.007

Taylor, D, Cawley, G., & Hayward, S. (2013). Classification of domain movements in proteins using dynamic contact graphs. *PLoS ONE*, *8*(11), Article e81224. https://doi.org/10.1371/journal.pone.0081224

Trott, O., & Olson, A. J. (2010). AutoDock Vina: Improving the speed and accuracy of docking with a new scoring function, efficient optimization and multithreading. *Journal of Computational Chemistry*, *31*(2), 455-461. https://doi.org/10.1002/jcc.21334

Ugalde, S. O., Wallraven, K., Speer, A., Bitter, W., Grossman, T. N., & Commandeur, J. N. M. (2020). Acetylene containing cyclo(L-Tyr-L-Tyr)-analogs as mechanism-based inhibitors of CYP121A1 from Mycobacterium tuberculosis. *Biochemical Pharmacology*, *177*, Article 113938. https://doi.org/10.1016/j.bcp.2020.113938

Wishart, D. S., Feunang, Y. D., Guo, A. C., Lo, E. J., Marcu, A., Grant, J. R., Sajed, T., Johnson, D., Li, C., Sayeeda, Z., Assempour, N., Iynkkaran, I., Liu, Y., Maciejewski, A., Gale, N., Wilson, A., Chin, L., Cummings, R., Le, D., Pon, A., Knox, C., & Wil, M. (2018). DrugBank 5.0: A major update to the DrugBank database for 2018. *Nucleic Acids Research*, *46*(1), 1074-1082. https://doi.org/10.1093/nar/gkx1037

WHO. (2019). *Global Tuberculosis Report 2019*. World Health Organization. https://www.who.int/publications/i/item/9789241565714

WHO. (2020). *Global tuberculosis report 2020*. World Health Organization. https://www.who.int/publications/i/item/9789240013131

Pertanika J. Sci. & Technol. 31 (3): 1523 - 1533 (2023)

PERTANIKA JOURNALS

SCIENCE & TECHNOLOGY

Journal homepage: http://www.pertanika.upm.edu.my/

Study and Simulation of the Electric Field-Induced Spin Switching in PZT/NiFe/CoFe Nanostructured Composites

Minh Hong Thi Nguyen[1], Thanh Tien Pham[1], Nam Van La[1], Soo Kien Chen[2] and Tiep Huy Nguyen[1]*

[1]Faculty of Engineering Physics and Nanotechnology, VNU University of Engineering and Technology, Building E3, 144 Xuan Thuy, Cau Giay, Hanoi, Vietnam
[2]Department of Physics, Faculty of Science, University Putra Malaysia, 43400 UPM, Serdang, Selangor, Malaysia

ABSTRACT

In this work, we have studied the electric field-induced spin switching in the PZT/NiFe/CoFe nanostructured composites by sputtering ferromagnetic layers on a horizontal polarized piezoelectric PZT substrate. The electric field-induced change in the magnetization orientation was investigated systematically using a vibrating sample magnetometer and analytical simulations. The results revealed that electric field applications could indirectly control the magnetic spin orientations. Moreover, the magnetization change depends not only on the electric field but also on the direction of the electric field applying against the magnetic field. The images of magnetic moment orientations under various electric field applications are modeled by the Monte Carlo and NMAG simulations. In particular, a critical electric field of $E_{cr} \approx 300$ kV/cm, which makes a 90^o spin switching, was determined. These results are proposed to offer an opportunity for random access memory applications.

Keywords: Electric field controlled magnetic anisotropy, Monte Carlo and NMAG simulations, nanostructured composites

ARTICLE INFO

Article history:
Received: 04 August 2022
Accepted: 02 November 2022
Published: 31 March 2023

DOI: https://doi.org/10.47836/pjst.31.3.22

E-mail addresses:
hongntm@vnu.edu.vn (Minh Hong Thi Nguyen)
thanhpro13112@gmail.com (Thanh Tien Pham)
lvnambg97@gmail.com (Nam Van La)
chensk@upm.edu.my (Soo Kien Chen)
tiepnh@vnu.edu.vn (Tiep Huy Nguyen)
* Corresponding author

INTRODUCTION

Magnetoelectric (ME) effect-induction of magnetization by an electric field or of electric-polarization by a magnetic field can be realized in multiferroic composites that exhibit a linear coupling between the applied electric voltage and magnetic field (Cheong & Mostovoy, 2007; Liang et al., 2021; Palneedi et al., 2016). A representative

ISSN: 0128-7680
e-ISSN: 2231-8526

© Universiti Putra Malaysia Press

example of this idea is the ME random access memory (MERAM) device which permits an electric field-induced magnetization switching in a ferromagnetic (FM) layer based on the combination of ME coupling and interfacial exchange coupling between ferroelectric (FE) and FM phases. In particular, the electric-field control of spin switching, known as the converse ME effect, has attracted the attention of a large number of scientists from areas such as physics, computer science, and mathematics due to its potential applications in electrically tunable microwave magnetic devices (Eerenstein et al., 2006; Hong, Doan et al., 2013; Lin et al., 2016) and electric-write magnetic memories (Cheng et al., 2018; Kumar et al., 2021; Hu et al., 2010; Liu et al., 2009; Palneedi et al., 2016; Popov et al., 2020).

In the research topic of the electric field-induced spin-switching effect, we have demonstrated the switchability of voltage control to the magnetic anisotropy in PZT/NiFe/CoFe heterostructured nanocomposites (Hong, Doan et al., 2013). In this work, the material characterizations of the nanostructured composites have also been reported. Then, the converse magnetoelectric effect (Hong, Duc, et al., 2013) and the electrical field-induced magnetization switching in the nanocomposites (Hong et al., 2014) were systematically investigated under applied voltages up to ± 700 V and ± 400 V, respectively. Particularly, a change in magnetization up to 245% and above 100%, respectively, at low-bias magnetic fields could be reached thanks to elastic stress transfers from the PZT piezoelectric phase to NiFe/CoFe magnetic phase and/or the changes of NiFe thickness. However, higher bias voltages could not be increased due to the limitation of our experimental instruments. In order to further investigate the electric field-induced spin-switching behavior in the nanostructured composites and find out the critical electric field (E_{cr}), the magnetic characterizations combined with analytical Monte Carlo simulations will be done in this work with inheriting characterized results from our previous studies.

The Monte Carlo simulation has been an effective method to model the magnetic properties of ferromagnetic layers such as antiferromagnetic Fe/Cr layers (Masrour et al., 2014), multilayered magnetic structures with giant magnetoresistance (GMR) effect (Prudnikov et al., 2016), fcc Ni_cFe_{1-c} alloy (Taylor & Gyorffy, 1992), and Layered Ising Nanocube Fe/Co/Fe (Kadiri et al., 2022). The method has also been used for investigating the ferroelectric properties of PZT material (Tamerd et al., 2020; Cornelissen et al., 2019; Wei et al., 2021). However, few reports regarding Monte Carlo simulation for ferromagnetic (FM) and ferroelectric (FE) heterostructured nanocomposites exist. The work of Dung and Long (2016) should be a rare example. We have calculated the critical electric field E_c and determined electric field E_d for different ferromagnetic layers: Fe, Fe_3O_4, and $CoFe_2O_4$ (CFO) grown on ferroelectric PZN-PT substrate and proposed the structures for the MERAM application. Using Monte Carlo simulation to investigate the electric field-induced spin switching effect for PZT/NiFe/CoFe heterostructured nanocomposites, to the best of our knowledge, is the first trial.

Herein, the electric field-induced changes in the magnetization orientation of nanostructured PZT/NiFe/CoFe multiferroics have been investigated to determine the conformable parameters of the external electric field for upcoming experimental research on MERAM (Figure 1). The particular 90° spin switching behavior of the nanostructured composites, which may correspond to the switching between the "0" and "1" bits in MERAM, will be discussed. Furthermore, we observed that the applied electric field could control the spin configuration in the FM layer. Particularly, in the case of isotropic coupling, a small critical electric field (E_{cr}) at which the spin started to rotate has been demonstrated.

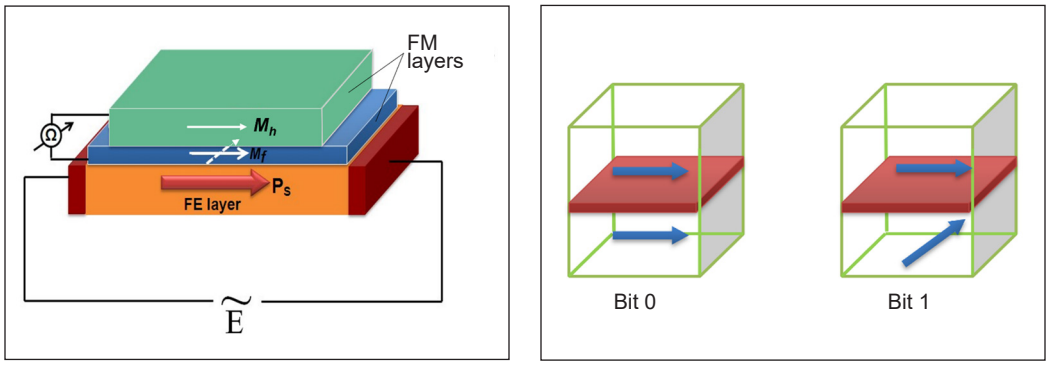

(a) (b)

Figure 1. (a) Schematic of PZT/NiFe/CoFe nanostructured composites with the proposed MERAM element. M_h and M_f are initial orientations of magnetization of the CoFe and NiFe layers, respectively. An electric field E is applied to the FE layer (PZT) to generate a 90° in-plane magnetization switching; and (b) Bits "0" and "1" switching in MERAM

MATERIALS AND METHODS

The FM layers of NiFe and CoFe were deposited in sequence on the horizontal polarized 500 µm thick PZT ⟨100⟩ substrate at room temperature using a radio frequency (RF) magnetron sputtering device (2000-F, AJA International). The polarization of the PZT substrate was aligned along its original ⟨100⟩ plane. During the deposition process, an argon pressure and RF sputtering power of 2.2×10^{-3} Torr and 50 W, respectively, were set in the main deposited chamber. Finally, a thin Ta layer was sputtered onto the film surface to prevent the oxidization of FM layers. All sample areas were similar, but the thickness of the CoFe layer was fixed at 190 nm, while the thicknesses of the FM thin films were 10, 25, 50, and 90 nm for samples N1, N2, N3, and N4, respectively. The area of all samples was fixed at 5 mm × 5 mm. The electric field-induced change in the magnetization orientation was measured using a vibrating sample magnetometer (VSM 7400, Lakeshore). The switching of the magnetization vector driven by an electric field applied to the FE layer was investigated systematically using an analytical approach and Monte Carlo and NMAG simulations.

In this study, we used the parameters of the fabricated material and Monte Carlo simulation for the electrical-induced change in magnetization. In the MERAM structure, the ME effect occurred when an electric field was applied to the PZT substrate. This electric field created mechanical stress/strain on the piezoelectric substrate via ME coupling. Then, the stress was transported to the magnetostrictive phase, creating a strain in film planes x and y (corresponding to stress σ_x and σ_y). The total magnetoelastic energy is as stated in Equation 1:

$$F_{me} = -\frac{3}{2}\lambda\sigma_x \sin^2\theta\cos^2\varphi - \frac{3}{2}\lambda\sigma_y \sin^2\theta\sin^2\varphi \quad [1]$$

where θ is the angle between the magnetization and electrical field directions, φ is the angle between the easy magnetization axis and electrical field direction, and λ is the effective magnetostriction constant in the film plane. This electrical field creates the effective field of $\overrightarrow{H_{eff}} = -\nabla_M \cdot F_{me}$. The total free energy is represented by Equation 2:

$$F_{free} = F_{me} + F_{zeeman} = \frac{-3}{2}\lambda\sigma_x \sin^2\theta\cos^2\varphi \frac{-3}{2}\lambda\sigma_y \sin^2\theta\cos^2\varphi - \overrightarrow{H}\cdot\overrightarrow{M_s} + 2\pi M_s \cos^2\theta \quad [2]$$

The effective anisotropy field in the x, y, and z axes was computed using Equation 3:

$$H_{eff,x} = \frac{3\lambda(\sigma_x - \sigma_y)}{M_s},\ H_{eff,y} = \frac{-3\lambda(\sigma_x - \sigma_y)}{M_s},\ H_{eff,z} = \frac{-3\lambda(\sigma_x + \sigma_y)}{M_s} \quad [3]$$

where σ_x, σ_y is the compressive stress in [100] axis and the tensile stress in [011] axis, respectively. The effective anisotropy field is calculated by the following Equations 4 to 6:

$$H_{eff,x} = \frac{3\lambda Y}{M_s(1+\upsilon)}(d_{31} - d_{32})E \quad [4]$$

$$H_{eff,y} = \frac{-3\lambda Y}{M_s(1+\upsilon)}(d_{31} - d_{32})E \quad [5]$$

$$H_{eff,z} = \frac{-3\lambda Y}{M_s(1+\upsilon)}(d_{31} + d_{32})E \quad [6]$$

where λ is the magnetostriction constant in the film plane, Y is Young's modulus, d_{31}, and d_{32} are the piezoelectric coefficients, E is the electric field, and υ is Poisson's constant. The total magnetoelastic energy is given by the following Equation 7:

$$F_{ME,x} = -H_{eff,x}\cdot\overrightarrow{M_S} \quad F_{ME,y} = -H_{eff,y}\cdot\overrightarrow{M_S} \quad F_{ME,z} = -H_{eff,z}\cdot\overrightarrow{M_S} \quad [7]$$

In the ME material, the rotation process can only occur when the condition $\Delta F_{total} < 0$ is satisfied. The spin switched from the film plane to out of the plane, corresponding to the switching between the "0" and "1" bits in MERAM. For the calculation for $F_{ME,x}$ was determined by using Equation 7, and with the material parameters, we obtained remarkable results that will be discussed in the below section.

RESULTS AND DISCUSSION

PZT/NiFe/CoFe Nanostructure Composites

Magnetic Properties. Figure 2 shows the room temperature M(H) curves of sample N1 under magnetic fields up to 10 kOe at various angles between the film plane and magnetic-field directions of α = 0°, 45°, and 90°. The results indicate that the M(H) curves were easier magnetized along the in-plane direction (i.e., α = 0°) than in 45° and out-of-plane (i.e., α = 90°) directions. The coercivity (H_C) values are 136, 147, 163 Oe; the saturation magnetization (M_S) values are 1074, 1057, 1041 μemu; and the remanence magnetization (M_R) values are 179, 136, 59 μemu, corresponding to the angles of 0°, 45°, and 90°, respectively. The smallest H_C, highest M_S, and highest M_R values belong to the in-plane M(H) curve. A similar tendency was observed for the samples N2, N3, and N4, whose H_C, M_S, and M_R values are listed in Table 1. These results reveal the in-plane magnetic anisotropy and the typical soft magnetic property of the NiFe/CoFe layers that originated from the contribution of the horizontally polarized PZT ⟨100⟩ substrate.

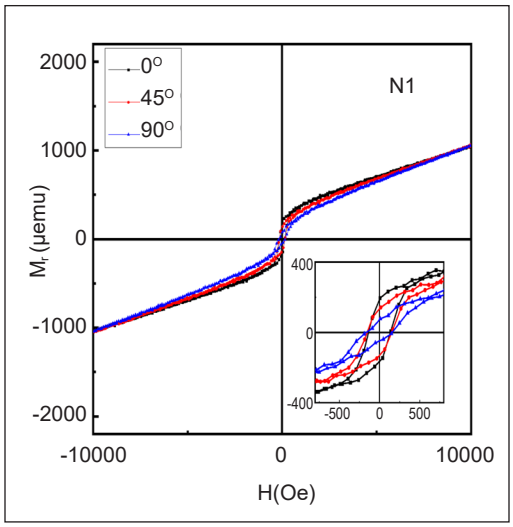

Figure 2. M(H) loops of 240 nm NiFe/CoFe magnetic films on PZT substrate (sample N1) were measured for in-plane, 45°, and out-of-plane configurations. The inset shows zoom in M(H) loops near the coercive field region

Table 1
Coercivity (H_C), saturation magnetization (M_S), and remanence magnetization (M_R) of samples N1, N2, N3, and N4

Sample	H_C (Oe)			M_S (μemu)			M_r (μemu)		
	//	45°	⊥	//	45°	⊥	//	45°	⊥
N1	136	147	163	1074	1057	1041	179	136	**59**
N2	97	102	108	1495	1466	1460	90	69	**35**
N3	91	97	104	1612	1459	1375	225	135	**82**
N4	58	63	75	2004	1805	1718	394	246	**129**

Electrical Field-Induced Magnetization Switching in PZT/NiFe/CoFe Nanostructured Composites. Figure 3 depicts the dependence of the magnetization M on the angle α of sample N1 with zero applied bias voltage under various applied magnetic fields of H_{bias} = 0, ± 50, ± 100, ± 200, ± 500, ± 1000, and ±2000 Oe. The magnetization's changing slope, and phase shift in the sinusoidal form can be observed.

Under zero applied bias voltage, the M(α) curve reaches its maximum absolute magnitude while the magnetic field was applied parallelly to the sample plane at α = 0°, 180°, and 360°. The changing period of M(α) should be T = 180°. The magnetization was the smallest while the magnetic field was applied perpendicularly to the sample plane (α = 90°, 270°). Furthermore, the sinusoidal form of M(α) curves is in the same direction for H_{bias} = -100 to 2000 Oe. The change in the direction of curves appeared when the magnetic field value of H_{bias} = -200, -1000, and -2000 Oe, which exceeded the value of the out-of-plane coercivity field H_C of 163 Oe. This behavior is supposed to be the elastic stress-induced transition from the piezoelectric PZT substrate to the ferromagnetic NiFe/CoFe layers resulting in the electrical field-induced magnetization switching. Particularly, the stress caused by the film-to-substrate mismatch may substantially impact the observed anisotropy. Two couplings are supposed to be responsible for the rotation of magnetization orientation when an electric field is applied: (1) the exchange interaction between NiFe and CoFe layers and (2) the electromagnetic coupling between NiFe/CoFe and PZT phases.

In order to investigate the dependence of the magnetic reversal of sample N1 in bias voltage applications through the PZT substrate, the M(α) curve at H_{bias} = 50 Oe under applied bias voltages of U = 0 V, 100 V, and -200 V were plotted (Figure 4). Under an applied bias voltage of U = 100 V, the maximum absolute magnitude of the M(α) curve increased

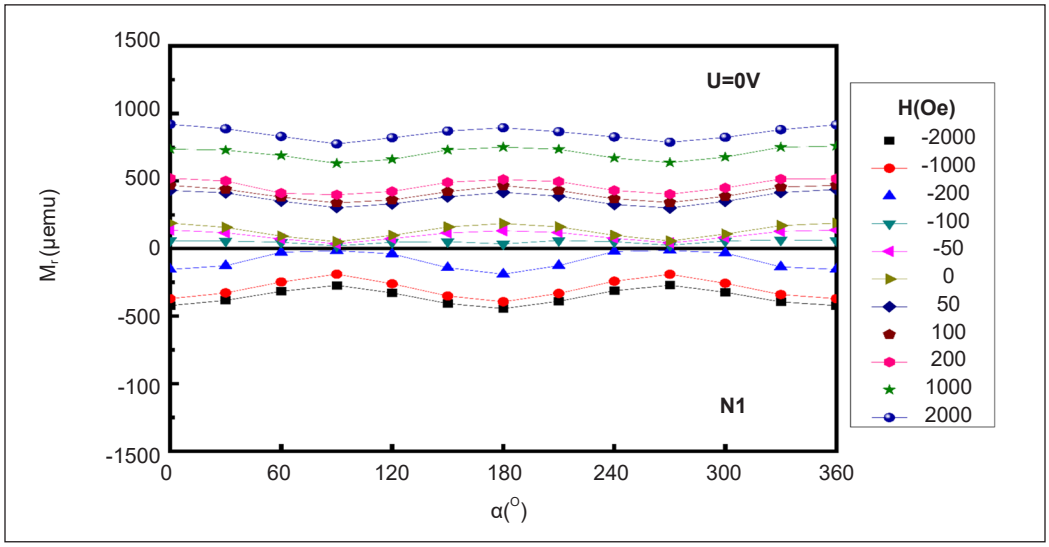

Figure 3. M(α) curve of sample N1 measured at various applied magnetic field H_{bias}

higher than that under zero bias voltage at α = 30°, 150°, and 270°. The changing period of T = 120° is lower than that under zero bias. In particular, a revered sinusoidal M(α) curve was also observed with an applied bias voltage of U = -200 V, similar to the above case of applied magnetic field $H_{bias} > H_C$. This result proposed that the change in the magnetic reversal mechanism under a sufficiently large applied bias voltage is due to the competition between magnetic and electrical energy. Moreover, the magnetization change depends not only on the electric field applying against the PZT substrate but also on the direction of the electric field applying against the magnetic field. When an electric field is present, the competition between the electric and magnetic fields will determine the magnitude and anisotropy of the magnetic layers.

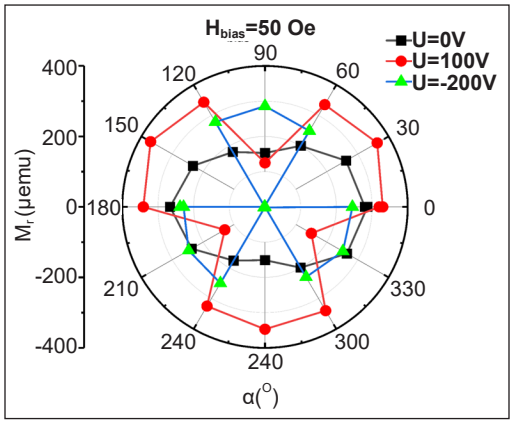

Figure 4. M(α) curves of sample N1 measured at H_{bias} = 50 Oe under bias voltage U = 0 V (black line), U = 100 V (red line), and U = -200 V (blue line)

Table 2 shows the variation of magnetization $\Delta M = M_{max} - M_{min}$ measured at α = 0° under various electric voltages and magnetic fields. At H_{bias} = 50 Oe, the ΔM value is 120 μemu under zero bias voltage and increases to 215 μemu when the bias voltage of U = 100 V, then reaches 230 μemu when the bias voltage up to U = -200 V. Since the NiFe/CoFe films were sputtered directly onto the piezoelectric PZT substrate, and the piezoelectric force will be transferred directly from the substrate to the thin films that make changes in the composite magnetization. Furthermore, the ΔM(α) showed different magnitudes depending on the magnetic field H_{bias} demonstrating the competition of electric and magnetic fields in the process to varying degrees.

Table 2
The change of magnetization ΔM (μemu) measured at α = 0° under various electric voltages and magnetic fields

U (V)	H_{bias} = -2000 Oe	H_{bias} = -50 Oe	H_{bias} = 50 Oe	H_{bias} = 200 Oe
0	160	100	120	140
100	240	220	215	245
-200	270	265	230	240

In this work, the distance between two electrodes was 5 mm due to the sample area was fixed at 5 × 5 mm^2, resulting in electric fields being E = 0, 0.2, and -0.4 kV/cm for bias voltages of U = 0, 100, and -200 V, respectively. Needless to say, the polarization moments in the PZT substrate are hard to reach the saturation states under these small electric field applications. However, higher bias voltages could not be increased due to the limitation

of our experimental instruments. In order to further investigate the electric field-induced spin-switching behavior in PZT/NiFe/CoFe nanostructured composites, the Monte Carlo and NMAG simulations should be an appropriate approach in this situation.

Analytical and Numerical Approach

The Monte Carlo and NMAG simulations were conducted for the PZT/NiFe/CoFe composite, assuming that the isotropic biaxial stress $d_{31} = d_{32}$ (the deformation on the x and y axes is the same) where the effective field generated by the strain on these axes was zero (Hu et al., 2010). In other words, the distortion in the z-axis mainly generated the effective field value. In this work, the values of $d_{31} = d_{32} = -276$ pC/N were used for the composite.

Figure 5 shows the side-view and top-view simulating images of the magnetic moments under various electric field applications for the PZT/NiFe/CoFe composite. Without an external electric field (Figure 5a), the magnetic moments, described by red arrows, were aligned parallel along the polarization moments of the PZT ⟨100⟩ substrate (i.e., the film plane) due to the interactive energy exchanged being ignored in the initial state. With an external electric field of E = 30 kV/cm, the effective field produced a rearrangement in the magnetic moments that deviated from the film plane with an angle of 6.87° and increased to 45° under a higher electric field of E = 190 kV/cm (Figures 5b & 5c). The distribution and direction of the magnetic moments in the FM layer are shown in Figure 5d with the critical electric field $E_{cr} \approx 300$ kV/cm, at which point the angle $\theta = 89.9°$, and the magnetic moments were nearly perpendicular to the film plane. From this point onward, the system reached the saturation state, and the magnetic moments were oriented parallel to each other and perpendicular to the film plane.

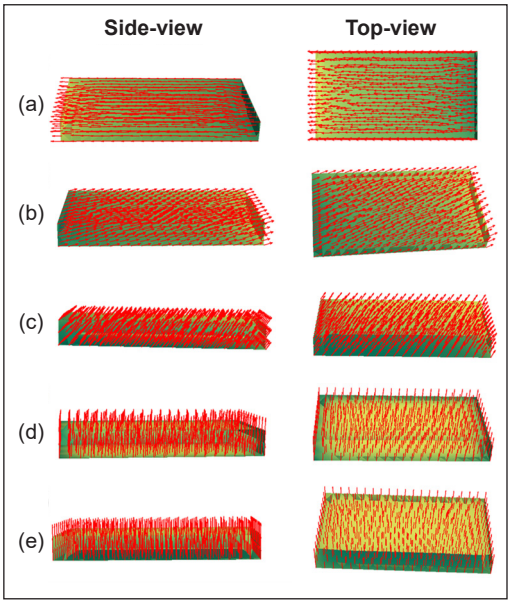

Figure 5. Side-view and top-view images of the magnetic moment orientations under various electric field applications: (a) E = 0 kV/cm; (b) E = 30 kV/cm; (c) E = 190 kV/cm; (d) E = 540 kV/cm; and (e) 1100 kV/cm, respectively

Figures 6a and 6b show the graphs of the changes in the orientations of magnetic moments under various electric fields in $\cos\theta$ and θ, respectively. The change can be explained by the effective field generated when an external electric field is applied, and the magnetic moments are rearranged in the direction of the effective field. The rotation angle of the magnetic moment increased linearly as the electric field

increased and reached the saturation value of θ = 90° under electric fields of $E \geq E_{cr}$, at which the magnetic moment is perpendicular to the film plane. This finding is proposed to offer an opportunity for fabricating the MERAM devices using the PZT/NiFe/CoFe composite based on the magnetic reversal effect in its isotropic structure mode.

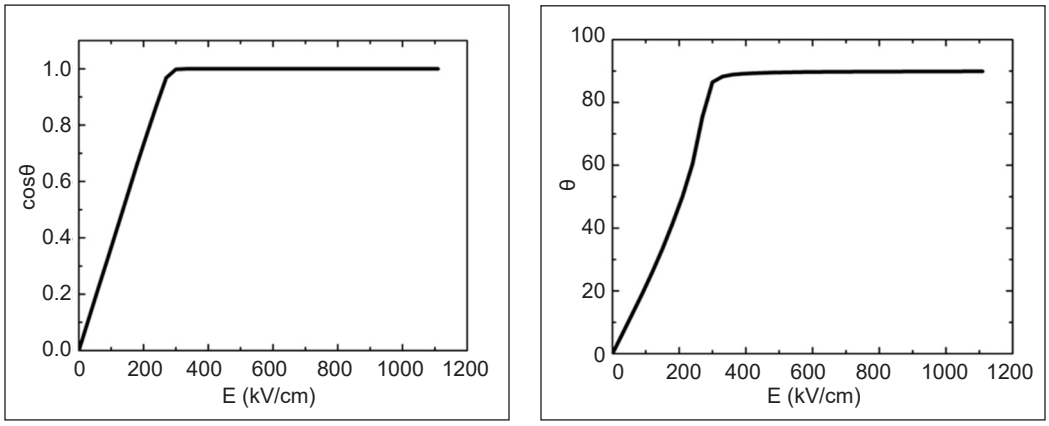

(a) (b)

Figure 6. The changes in orientations of the magnetic moment based on the applied electric field through (a) cosθ and (b) θ in the isotropic biaxial stress mode

CONCLUSION

The electric field-induced spin switching has been studied in the PZT/NiFe/CoFe nanostructured composites. The rotation of magnetization orientation under an electric field application is demonstrated for the exchange interaction between NiFe and CoFe layers and the electromagnetic coupling between NiFe/CoFe and PZT phases. The NMAG simulation has observed the orientation of magnetic moments under various electric field applications. In addition, using the Monte Carlo simulation, a critical electric field of E_{cr} ≈ 300 kV/cm has been determined to make a 90° spin switching. The findings proposed an opportunity to achieve new types of memory devices, such as voltage-tunable field random access memories.

ACKNOWLEDGMENTS

This work has been supported by Vietnam National University, Hanoi (VNU), under Project No. QG.20.58.

REFERENCES

Cheng, Y., Peng, B., Hu, Z., Zhou, Z., & Liu, M. (2018). Recent development and status of magnetoelectric materials and devices. *Physics Letters A*, *382*(41), 3018-3025. https://doi.org/https://doi.org/10.1016/j.physleta.2018.07.014

Cheong, S. W., & Mostovoy, M. (2007). Multiferroics: A magnetic twist for ferroelectricity. *Nature Materials, 6*(1), 13-20. https://doi.org/10.1038/nmat1804

Cornelissen, T. D., Biler, M., Urbanaviciute, I., Norman, P., Linares, M., & Kemerink, M. (2019). Kinetic Monte Carlo simulations of organic ferroelectrics. *Physical Chemistry Chemical Physics*, *21*(3), 1375-1383. https://doi.org/10.1039/C8CP06716C

Dung, T. V., & Long, D. D. (2016). Electric-field control of a spin "bit" configuration in MERAM model: A Monte Carlo study. *VNU Journal of Science: Mathematics - Physics*, *32*(2), 61-68.

Eerenstein, W., Mathur, N. D., & Scott, J. F. (2006). Multiferroic and magnetoelectric materials. *Nature*, *442*(7104), 759-765. https://doi.org/10.1038/nature05023

Hong, N. T. M., Doan, N. B., Tiep, N. H., Cuong, L. V., Trinh, B. N. Q., Thang, P. D., & Kim, D. H. (2013). Switchable voltage control of the magnetic anisotropy in heterostructured nanocomposites of CoFe/NiFe/PZT. *Journal of the Korean Physical Society*, *63*(3), 812-816. https://doi.org/10.3938/jkps.63.812

Hong, N. T. M., Duc, N. H., & Thang, P. D. (2013). Converse magnetoelectric effect in PZT/NiFe/CoFe nanocomposites. *International Journal of Nanotechnology*, *10*(3-4), 206-213. https://doi.org/10.1504/IJNT.2013.053133

Hong, N. T. M., Ha, P. T., Cuong, L. V., Long, P. T., & Thang, P. D. (2014). Electrical field-induced magnetization switching in CoFe/NiFe/PZT multiferroics. *IEEE Transactions on Magnetics*, *50*(6), 1-4. https://doi.org/10.1109/TMAG.2014.2304518

Hu, J. M., Li, Z., Wang, J., & Nan, C. W. (2010). Electric-field control of strain-mediated magnetoelectric random access memory. *Journal of Applied Physics*, *107*(9), Article 093912. https://doi.org/10.1063/1.3373593

Kadiri, A., Tamerd, M. A., Ngantso, G. D., Arejdal, M., Abbassi, A., Amraoui, Y. E., Ez-Zahraouy, H., & Benyoussef, A. (2022). Effect of thickness size on magnetic behavior of layered Ising nanocube Fe/Co/Fe: A Monte Carlo simulation. *Journal of Superconductivity and Novel Magnetism*, *35*(9), 2425-2434. https://doi.org/10.1007/s10948-022-06232-6

Kumar, S. D., Gupta, S., Swain, A. B., Subramanian, V., Padmanabhan, M. K., & Mahajan, R. L. (2021). Large converse magnetoelectric effect in Sm doped $Pb(Mg1/_3Nb_2/_3)$-$PbTiO_3$ and $NiFe_2O_4$ laminate composite. *Journal of Alloys and Compounds*, *858*, Article 157684. https://doi.org/https://doi.org/10.1016/j.jallcom.2020.157684

Liang, X., Chen, H., & Sun, N. X. (2021). Magnetoelectric materials and devices. *APL Materials*, *9*(4), Article 041114. https://doi.org/10.1063/5.0044532

Lin, H., Gao, Y., Wang, X., Nan, T., Liu, M., Lou, J., Yang, G., Zhou, Z., Yang, X., Wu, J., Li, M., Hu, Z., & Sun, N. X. (2016). Integrated magnetics and multiferroics for compact and power-efficient sensing, memory, power, RF, and microwave electronics. *IEEE Transactions on Magnetics*, *52*, 1-8. https://doi.org/10.1109/TMAG.2016.2514982

Liu, M., Obi, O., Lou, J., Chen, Y., Cai, Z., Stoute, S., Espanol, M., Lew, M., Situ, X., Ziemer, K. S., Harris, V. G., & Sun, N. X. (2009). Giant electric field tuning of magnetic properties in multiferroic ferrite/ferroelectric heterostructures. *Advanced Functional Materials*, *19*(11), 1826-1831. https://doi.org/https://doi.org/10.1002/adfm.200801907

Masrour, R., Bahmad, L., Hamedoun, M., Benyoussef, A., & Hlil, E. K. (2014). Magnetic properties of Fe/Cr layers studied by Monte Carlo simulations. *Journal of Superconductivity and Novel Magnetism*, *27*(3), 845-850. https://doi.org/10.1007/s10948-013-2344-8

Palneedi, H., Annapureddy, V., Priya, S., & Ryu, J. (2016). Status and perspectives of multiferroic magnetoelectric composite materials and applications. *Actuators*, *5*(1), Article 9. https://www.mdpi.com/2076-0825/5/1/9

Popov, M., Liu, Y., Safonov, V. L., Zavislyak, I. V., Moiseienko, V., Zhou, P., Fu, J., Zhang, W., Zhang, J., Qi, Y., Zhang, T., Zhou, T., Shah, P. J., McConney, M. E., Page, M. R., & Srinivasan, G. (2020). Strong converse magnetoelectric effect in a composite of weakly ferromagnetic iron borate and ferroelectric lead zirconate titanate. *Physical Review Applied*, *14*(3), Article 034039. https://doi.org/10.1103/PhysRevApplied.14.034039

Prudnikov, V. V., Prudnikov, P. V., & Romanovskiy, D. E. (2016). Monte Carlo simulation of magnetic multilayered structures with giant magnetoresistance effects. *Journal of Physics: Conference Series*, *681*, Article 012016. https://doi.org/10.1088/1742-6596/681/1/012016

Tamerd, M. A., Abraime, B., El Rhazouani, O., Lahmar, A., El Marssi, M., Hamedoun, M., Benyoussef, A., & El Kenz, A. (2020). Modelling of the ferroelectric and energy storage properties of $PbZr_{1-x}Ti_xO_3$ thin films using Monte Carlo simulation. *Materials Research Express*, *6*(12), Article 126429. https://doi.org/10.1088/2053-1591/ab625f

Taylor, M. B., & Gyorffy, B. L. (1992). Monte Carlo simulations of an fcc NicFe1−c alloy with vector magnetic freedom. *Journal of Magnetism and Magnetic Materials*, *104-107*, 877-878. https://doi.org/https://doi.org/10.1016/0304-8853(92)90403-B

Wei, X. K., Prokhorenko, S., Wang, B. X., Liu, Z., Xie, Y. J., Nahas, Y., Jia, C. L., Dunin-Borkowski, R. E., Mayer, J., Bellaiche, L., & Ye, Z. G. (2021). Ferroelectric phase-transition frustration near a tricritical composition point. *Nature Communications*, *12*(1), Article 5322. https://doi.org/10.1038/s41467-021-25543-1

Pertanika J. Sci. & Technol. 31 (3): 1535 - 1554 (2023)

PERTANIKA JOURNALS

SCIENCE & TECHNOLOGY

Journal homepage: http://www.pertanika.upm.edu.my/

The Characteristics of Polymer Concrete Reinforced with Polypropylene Fibres Under Axial and Lateral Compression Loads

Nur Aqilah Azman[1], Agusril Syamsir[1,2], Mohd Supian Abu Bakar[2]*, Muhammad Asyraf Muhammad Rizal[3], Khairul Amri Sanusi[4] and Mohammed Jalal Abdullah[1]

[1]Civil Engineering Department, College of Engineering, Universiti Tenaga Nasional, Jalan IKRAM - UNITEN, 43000 Kajang, Selangor, Malaysia

[2]Institute of Energy Infrastructure, College of Engineering, Universiti Tenaga Nasional, Jalan IKRAM - UNITEN, 43000 Kajang, Selangor, Malaysia

[3]Centre for Advanced Composite Materials (CACM), Universiti Teknologi Malaysia (UTM), Johor Bahru 81310, Johor, Malaysia

[4]TNB Grid Division, Grid Solution Expertise (GSE), Bangunan Dua Sentral, No. 8, Jalan Tun Sambanthan, 50470 Kuala Lumpur, Malaysia

ABSTRACT

The use of cement is expected to increase over the years as the infrastructure continues to develop, and the needs to repair or rehabilitate an old and deteriorated building are necessary. However, many investigations have been conducted to establish promising polymer concrete applications in the last few decades. Meanwhile, using concrete in the construction industry has led to environmental issues. It is because relying on cement production in concrete will contribute to about 7% of the world's carbon dioxide emissions. Therefore, polymer concrete was introduced in this study to minimise the use of cement in the industry. This research investigated the influence of different amounts of polypropylene (PP) fibre content on polymer concrete (PC) properties by determining the compressive strength, flexural strength and indirect tensile strength. Furthermore, the results of PC failure characteristics have been discussed. The polymer concrete specimens in this study have been cast into cylinders and prismatic specimens using PVC pipe and plywood formwork to determine the compressive strength, splitting tensile strength and flexural strength. By reinforcing PP fibre in the polymer concrete with a specific percentage of fibre reinforced, the overall strength of the polymer concrete

ARTICLE INFO

Article history:
Received: 25 April 2022
Accepted: 07 September 2022
Published: 07 April 2023

DOI: https://doi.org/10.47836/pjst.31.3.23

E-mail addresses:
aaqilahazman@yahoo.com (Nur Aqilah Azman)
Agusril@uniten.edu.my (Agusril Syamsir)
mohdsupian7779@gmail.com (Mohd Supian Abu Bakar)
asyrafriz96@gmail.com (Muhammad Asyraf Muhammad Rizal)
khairulams@tnb.com.my (Khairul Amri Sanusi)
Eng.MJ96@hotmail.com (Mohammed Jalal Abdullah)
* Corresponding author

ISSN: 0128-7680
e-ISSN: 2231-8526

© Universiti Putra Malaysia Press

was improved. Based on the compressive, splitting tensile, and flexural test results, it has been hypothesised that the 0.16% PP fibre will considerably improve polymer concrete. Additionally, PP fibre maintains a moisture content of less than 0.5% in the aggregates, resulting in a significant enhancement in the mechanical properties of polymer concrete.

Keywords: Axial and lateral, compression load, material characteristics, polymer concrete, polypropylene fibre

INTRODUCTION

The global population has increased to over 6.3 billion. More than 60% of the world's population will reside in cities by 2030. Population rise is a significant factor in housing demand. Concrete is commonly used in the premises construction field (Liu et al., 2020; Manjunatha et al., 2021). Roads, bridges, buildings, energy, and water management systems all require a great deal of concrete, making it the second most commonly used material worldwide each year after water. The previous 20 years have produced over half of the concrete used throughout history. The global concrete industry roughly consumes 7.5 billion tonnes annually (Arulmoly et al., 2021; Sanjith et al., 2015; Scope et al., 2021). The prime ingredient for making concrete is, of course, cement. However, cement clinker production is a very energy-intensive and polluting process. Figure 1 displays the cement industry's increasing rate of CO_2 emissions and its proportion of total annual emissions (Ghasemi, 2019; Harison et al., 2014; Oey et al., 2017; Teixeira et al., 2022).

In order to reduce the product's carbon footprint and overall cost, it is common to practise using as little cement as possible when proportioning cementitious mixtures. As a result, the methods and actions that reduce the carbon footprint of cement are of extreme relevance to the concrete and cement industries. Over the past century, since the widespread use of coal for power generation began in the 1920s, millions of tonnes of ash and other by-products have been produced. About 500 million tons, or 75 to 80% of the total ash generated, is fly ash. The annual global production of coal ash is estimated at roughly 600 million tons, and the disposal of a large amount of fly ash has become a serious environmental problem. Therefore, in recent years, the use of fly ash as an ordinary Portland cement replacement in concrete mixes has become common. These pozzolanic materials, such as fly ash, can contribute to forming calcium silicate hydrates by reacting with the calcium hydroxide produced during cement hydration, thus having comparable properties to Portland cement. Their use can be a promising way to address concrete sustainability (Abdulrahman et al., 2022; Blazy & Blazy, 2021; McCarthy et al., 2022; Mocharla et al., 2022; Qin et al., 2019).

Concrete is a highly compressive material but around ten times smaller tensile strength. It exhibits brittle behaviour and does not permit stress transfer following cracking. Polypropylene Fibres (PPF) can be added to the concrete mixture to reduce the possibility

of brittle failure and enhance the material's mechanical properties to overcome this problem. Polypropylene fibre (PPF) is one of the most widely used fibres in industrial or daily life. Polypropylene-fibre-reinforced concrete (PPFRC) has been common recently in different applications such as tunnels, ground slab bridge decks, canals, concrete pipe, and pavement construction, which shows a noticeable improvement in mechanical characteristics such as tensile strength, flexural strength, toughness, and energy absorption (Afroughsabet & Ozbakkaloglu, 2015; Akid et al., 2021; Asyraf et al., 2022; Blazy, 2021; Jafari et al., 2018; Supian et al., 2022).

Polymer concrete (PC) is a type of FRC that is strong enough to be used in precast applications. Thus, it is important because the strength will permit the structures to resist higher stresses early due to form-stripping, handling, transportation, and erection operations. Polymer concrete is a form of concrete in which a polymer is used as a binder instead of lime-type cement. The overall performance of polymer concrete depends on the amount and specific types of resin used in the composite material (Mohamad et al., 2019; Ribeiro et al., 2004). Furthermore, the properties of concrete with varying fibre concentrations have been studied in various parameters. Polypropylene fibres have been used in construction because of their availability, high strain, increased cracking resistance, low cost, and superior softening response. Meanwhile, the fly ash-polypropylene-fibre concrete mixture has been used in industrial and civil construction sprayed concrete, tunnels, guard rails, anti-seepage concrete structures, anti-cracking, and waterproof layers. Thus, in the context of the study of the mechanical strength capabilities of polymer concrete, the incorporation of polypropylene fibre and other synthetic fibre content substantially enhanced the tensile and compressive capacity of concrete (Afroughsabet & Ozbakkaloglu, 2015; Agusril et al., 2012; Blazy, 2021; Yin, 2015; Pan et al., 2021; Ramezanianpour et al., 2013).

Researchers are interested in concrete durability due to the long lifespan of the structure. Therefore, the properties of polymer concrete can be affected by many factors for diverse applications. For instance, Supplementary Cementitious Materials (SCM) from other materials can lower the cost of cement while resolving landfill waste disposal. Meanwhile, the study by Akid et al. (2021) has indicated that adding supplementary cementitious materials from the fibres to concrete has been proven to improve the concrete's toughness and toughened qualities of crack propagation characteristics and post-softening residual stress in compression. Besides, Reis's (Fluminense, 2014) experiments have shown that glass fibres and nylon have improved the mechanical characteristics of reinforced polymer concrete. Meanwhile, in the study by Rebeiz (1996) of steel fibres in polymer concrete, it was identified that adding 1.3% of fibre content by volume increases the compressive strength of polymer concrete.

Furthermore, several studies have shown that the mechanical strength of polymer concrete is 4 to 5 times that of cement concrete (Hameed & Hamza, 2019). Likewise, Kayali

et al. (2003) and Song et al. (2005) have stated that polypropylene fibres contribute to the strength of compression, flexure, pressure, under-impact blows, and plastic shrinkage. Furthermore, the advantages of polymer concrete compared to ordinary Portland concrete make PC widely used in many applications, especially in the construction and repair of structures due to the rapid hardening of PC, ability to withstand corrosive elements, higher compressive strength, lower permeability, and many more (Kayali et al., 2003; Song et al., 2005). Polymer waste polypropylene from bottle caps was used in a study by Martínez-López et al. (2021) to enhance compressive strength, compressive deformation, and flexural deflection by 82%. However, recent advancements in polymer concrete have resulted in considerable reductions in the cost of construction materials, indicating that polymer concrete is progressively becoming more common. In addition, because of their physico-chemical characteristics and being inexpensive, they have become an environmental concern due to inadequate ultimate disposal methods (Bedi et al., 2021; Ferdous et al., 2020; Ghasemi, 2019)

The curing conditions influence the ultimate qualities of polymer concrete. Researchers discovered that polymer concrete might be cured in various methods, including at room or high temperatures, underwater, with saline solutions, and more (Guo et al., 2021; Rebeiz, 1995). Allowing the specimens to cure at room temperature is one of the most preferred methods of curing polymer concrete since it is simple to handle and operate. Polymer concrete may obtain a strength of roughly 70% to 75% after one day of curing at room temperature, but typical Portland cement concrete can only achieve a 20% strength growth of its 28-day strength in one day due to its fast-curing characteristic. Although higher temperature curing speeds up the curing of polymer concrete, most research agrees that the optimum curing period for polymer concrete is 7 days since the compressive strength of PC is reported to become consistent after 7 days of curing (Ferdous et al., 2020; Ohama & Demura, 1982). Hsie et al. (2008) found that adding polypropylene hybrid fibre to concrete yielded more strength than using only one fibre. With the addition of hybrid polypropylene fibre, the compressive strength increased by 14.60% to 17.31%, the splitting tensile increased by 8.88 to 13.35 %, and the modulus of rupture increased by 8.99% to 24.60%

The research demonstrated that using polypropylene fibre-reinforced concrete in public areas is viable. The concrete polymer might help greatly for usage in vandalism, surface abrasion, and improved impact damage characteristics since they are subjected to, for example, unfavourable weather conditions. Therefore, this research investigated the effect of polypropylene fibre PPF on the mechanical properties of polymer concrete when in different percentages as reinforcement through compressive strength, indirect split tensile strength, and flexural strength. Polypropylene is added to polymer concrete at 0%, 0.12%, 0.16%, and 0.2% in mixes 1, 2, 3, and 4.

METHODOLOGY

Coarse Aggregates

Aggregates account for 60% to 75% of the total volume of concrete. Coarse aggregates significantly affect polymer concrete's bending and compressive strength. Therefore, the aggregates must be free from dust and undesired contaminants to avoid any interaction with the setting and hardening of resin in polymer concrete. The aggregates used in polymer concrete are often determined by the availability of resources, with the ideal design composition being 50% pebble, 42.5% sand, and 7.5% resin. As a result, the cost of creating composites will be reduced. Crushed coarse limestone aggregates were used to produce polymer concrete. The 5 mm single size was used to ensure that the resin is disseminated and coated uniformly with the aggregate while maintaining the same flow ability; it is possible to utilise less polymer matrix when using smaller aggregates as opposed to larger aggregates with a large surface area.

Furthermore, when single-sized aggregates are employed, the resin and filler used may readily cover the gaps or space between the stones. Aggregates with an angular form and a rough surface roughness were particularly crucial in this study because a stronger bond could be created when the aggregates were combined with the resin, providing the polymer concrete with more strength. Angular aggregates with a rough surface roughness were also important because when they were mixed with the resin, a stronger bond could be formed, providing the polymer concrete more strength.

Fly Ash

Fly ash (FA) is the finely divided residue that results from pulverised coal combustion and is transported from the combustion chamber by exhaust gases. The particle size distribution of CFA is similar to the particle size of cement, with an average diameter of 9 μm. Therefore, fly ash was used as a filler in this study to further improve the performance of polymer concrete since its use in polymer concrete has been documented to give superior mechanical characteristics and lower water absorption. FA was used as a filler in this study to further improve the performance of polymer concrete since its use in polymer concrete has been documented to give superior mechanical characteristics and lower water absorption. As a result, fly ash may be a highly useful substance for increasing the strength of polymer concrete. Based on the most recent research, the best-known PC performance may be obtained at a volume ratio of resin to FA matrix of 60:40 for creating a perfect PC mix.

Polyester Resin

One of the most significant ingredients in the production of polymer concrete is resin, which bonds all the elements together for increased strength. In this study, REVERSOL

P 9509 resin was used. Berjaya Bintang Timur Sdn. Bhd. (Malaysia) provided the resin. Bhd. REVERSOL P 9509 resin was mixed with Methyl Ethyl Ketone Peroxide (MEKP) as a catalyst. REVERSOL P 9509 resin is displayed in Table 1.

Table 1
Property of polyester resin (Parker & Moffett,1954)

Property	Value	Test Method
Specific Gravity	1.12	
Volumetric Shrinkage, %	8	
Tensile Strength, MPa	62	BS2782 – 320C
Elongation at Break, %	2.2	BS2782 – 320C
Water Absorption 24 hr at 25°C, mg	20	BS2782 – 430A
Deflection Temperature (under load 1.80 MPa), °C	55	BS2782 – 121A
Barcol Hardness (Model GYZJ 934-1)	40	BS2782 – 1001

Polypropylene Fibre (PPF)

Polypropylene fibre (PPF) was used in this study as fibre reinforcement to produce fibre-reinforced polymer concrete (Figure 1 and Table 2). Polypropylene fibres have been used for years to reinforce concrete and cement mortar. The fibres limit the spread of cracks and positively impact several concrete properties. Polypropylene fibres that have been geometrically distorted or changed are frequently employed to increase the material's adherence to the cement matrix. The fibres have an impact on the mortars' bending strength. The bending strength of mortars reinforced with fibrillated fibres has been shown to have significantly increased. Aside from that, the effects of polypropylene fibre on the physical and mechanical properties of concrete, such as its workability, compressive strength, stiffness, and flexibility, as well as its resistance to impact and abrasion and its ability to withstand the effects of freezing and thawing, as well as its cost, durability, and friendliness to the environment, need to be studied (Blazy & Blazy, 2021; Broda, 2016).

Figure 1. Polypropylene Fibre (PPF) (Blazy, 2021; Broda, 2016)

Table 2
Physical properties of PP fibre

Property	Value
Specific Gravity	0.91 gr/cm^3
Diameter	22µm
Width crossing	Circular
Melting point	160 - 170^{O}C
Water absorption	0
Torsion resistibility	400 -350 MPa

This present study utilised PPF at relatively low volume fractions to control plastic shrinkage cracking in the polymer concrete. PPF was added to polymer concrete in different percentages of 0.12%, 0.16%, and 0.20% to reveal the strength of polymer concrete reinforced with polypropylene fibres.

Concrete Mixture Properties

Polymer concrete mixtures are prepared at a volume ratio of 60: 40: 1.35 (resin + hardener; fly ash; coarse particles). Polypropylene fibre (PPF) was added (0%, 0.12%, 0.16%, and 0.2%) mixture weight to improve the mechanical qualities of polymer concrete. Furthermore, the polymer concrete PC properties and polypropylene fibre PPF are shown in Tables 3 and 4. respectively. According to Ferdous et al. (2020) study, the ideal resin-to-filler ratio is 60:40 to produce a long-lasting polymer concrete with an even distribution of aggregates, and the ideal matrix-to-aggregate ratio is 1:1.35 to obtain a suitable mix of cost, durability, and mechanical qualities. The polymer concrete mixture ingredients are shown in Figure 2. Polymer concrete was cast in four main stages. The volume required for each mix was modest and easy to handle; therefore, all the specimens were mixed by hand. Because of the rapid hardening, the specimens had to be done and finished one at a time rather than all at once.

Figure 2. Materials used in the preparation of polymer concrete mixture

Table 3
Polymer concrete (PC) mixture properties

Ratio	Resin + Hardener + Filler		Aggregate
	1		
Volume fraction (%)	Resin + Hardener	Filler	1.35
	60	40	
For 1 - cylinder specimen (g)	74.12 g	67.04 g	330.38 g
For 1 - prism specimen (g)	58.98 g	53.35 g	262.91 g

Table 4
Polypropylene fibre (PPF) content on polymer concrete (PC) specimens

Specimens	Polypropylene Fibre		
	0.12%	0.16%	0.20%
For 1 - cylinder specimen	0.57 g	0.75 g	0.94 g
For 1 - prism specimen	0.45 g	0.60 g	0.75 g

The 5 mm single-size aggregates were sieved and washed to remove contaminants that could interfere with the polymer concrete hardening process. The resin and hardener were mixed in a separate bowl at a weight ratio of 100:32 to create a reactive mixture that retains its fluidity, ensuring an ideal connection between the polymer matrix and the aggregates. The resin and hardener were combined for 120 minutes before being completely poly-condensed until a uniform colour was achieved. The fly ash was then added to the resin mixture and mixed until homogenous. The coarse aggregate was then added to the matrix and stirred for around 5 minutes to create a new polymer concrete. After the previous process, the required fibres were added to the polymer concrete. To ensure that the fibres were evenly distributed throughout the concrete, the mixture was stirred for 3 minutes until all the aggregates were coated with a polymer. At that point, the mixtures were put into the moulds. Finally, the mixture was compacted into three equal layers on a compaction machine, as illustrated in Figure 3, to achieve the required density. The specimens were cast and kept at room temperature for 24 hours to harden completely. After 24 hours of harding, all the specimens were cured for 7 days at room temperature (20°C) with 30% relative humidity before being examined. Because of its fast-curing characteristic, polymer concrete can achieve a strength of roughly 70% to 75% after one day of curing at room temperature, whereas typical Portland cement concrete can only achieve a 20% strength growth of its 28-day strength in one day. Although higher temperature curing speeds up the curing of polymer concrete, most research agrees that the optimum curing period for polymer concrete is 7 days since the compressive strength of PC is reported to become consistent after 7 days of curing (Ferdous et al., 2020).

(a) (b) (c)

Figure 3. (a) A uniform colour of resin and hardener was obtained, (b) A fresh polymer concrete mixture with the addition of PP Fibre, and (c) The specimens were compacted using a compaction machine

Mechanical Properties

The effects of polypropylene fibre rates of 0.12 %, 0.16 %, and 0.2 % on the compressive strength, splitting tensile strength, and flexural strength of polymer concrete were examined. The tests were carried out at UNITEN's BD Laboratory using the Universal Testing Machine (UTM) as the testing instrument.

Compressive Strength. The compressive strength test was conducted on specimens of the cylinder (50mm × 100mm). According to ASTM C39 (ASTM, 2001), three specimens were tested for each mixture (Figure 4a). The specimen was weighed, and all the essential data, such as the diameter, length, and weight, was entered into the software. The cylindrical specimen was then vertically positioned in the centre of the UTM machine, as indicated in Figure 4b. The load was then applied to the specimens until they failed to acquire the results. The highest load achieved during the test was divided by the cross-sectional area of the specimen in Equation 1. It determined the specimen's compressive strength. The strength results obtained from the investigation will be influenced mostly by the size and shape of the specimen, the mixing procedure used, and the temperature and moisture conditions during curing.

$$\text{Compressive strength} = \frac{\text{Maximum load applied}}{\text{Cross} - \text{sectional area}} \quad (1)$$

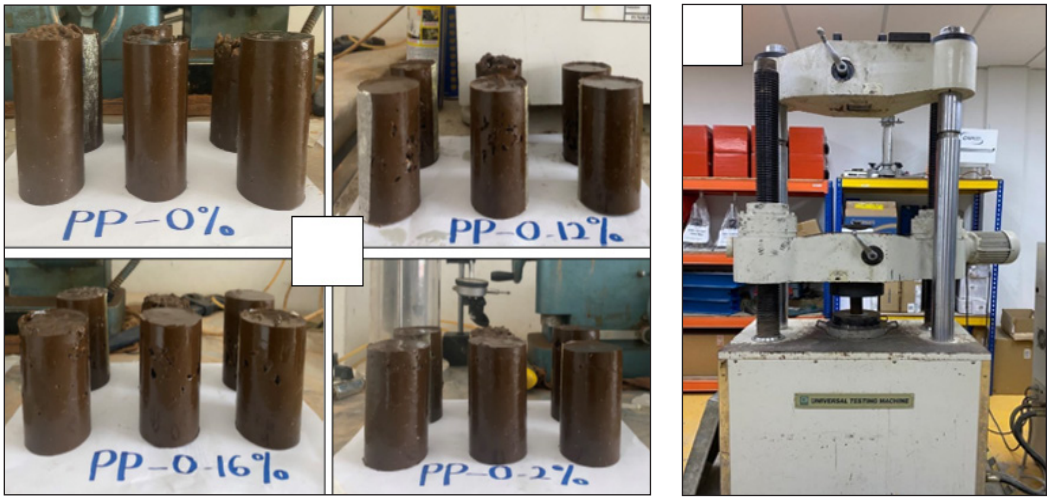

(a) (b)

Figure 4. (a) Polymer concrete with various PP Fibre contains, (b) Compression machine used for axial and lateral compression of polymer concrete

Indirect Tensile Strength. Meanwhile, the indirect tensile strength tests were conducted on 50 mm × 100 mm specimens according to ASTM C496. The specimens are fixed horizontally in the middle of the UTM machine (Figure 5). The forces were constantly delivered at a steady rate until the specimens failed. The indirect tensile strength test procedure includes applying a diametric compressive force along the length of a cylindrical concrete specimen at a rate that matches within a prescribed range until failure occurs. This loading causes tensile stresses in the plane holding the applied load and rather strong compressive stresses in the surrounding area. Because the areas of load application are in a condition of tri-axial

compression, tensile failure occurs rather than compressive failure. It allows them to endure significantly higher compressive loads than would be suggested by a uniaxial compressive strength test result. The tensile strength was calculated using Equation 2.

$$T = \frac{2P}{\pi l d} \quad (2)$$

Figure 5. Lateral compression load of polymer concrete

Where;
T = splitting tensile strength (MPa);
P = maximum applied load indicated by the testing machine (N);
l = length (mm); and
d = diameter (mm).

Flexural Strength Test. Flexural strength, also known as modulus rupture, is one of the most significant criteria when developing polymer concrete. It determines the concrete's capacity to withstand bending stresses caused by the load. The flexural strength test used a beam with 25 mm × 25 mm × 250 mm dimensions (Figure 8). A three-point flexural strength test (Figure 6) was conducted on polymer concrete specimens according to ASTM (2016). Due to the smaller beam size used in this study, the spans and distance between the loading head and the supports of the flexural testing machines were changed to assess the strength of the specimens. It is to confirm that the specimens were positioned correctly to avoid any possible inaccuracies in the results. Furthermore, the surface of the specimens must be free of any impurities for the test result to be of high quality. The load will then be applied perpendicular to the face of the specimen at a constant pace until it reaches the breaking point without shock. The maximum load obtained was then computed as follows (Equation 3):

$$R = 3PL \,/\, 2bd^2 \quad (3)$$

Where;
R = modulus of rupture (MPa),
P = maximum applied load indicated by the testing machine (kN),
L = span length (mm),
b = average width of specimen (mm), and
d = average depth of specimen (mm).

(a)

(c)

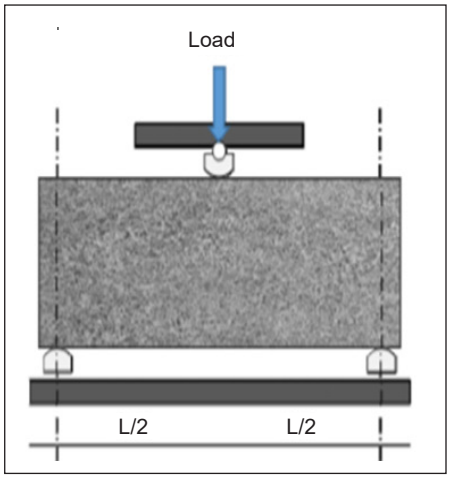

(b)

Figure 6. (a) Beam specimens, (b) ASTM C293–Centre Point Loading (ASTM, 2016), (c) Centre point loading applied on the beam

RESULTS AND DISCUSSION

The results characterise the mechanical properties of polypropylene fibre-reinforced polymer concrete. Due to the different fractions of polypropylene fibre being integrated into the polymer concrete (PC), the behaviour of each amount was monitored to determine the effects on the strength of the polymer concrete (PC) and compared to previous studies. The Compressive Strength Test, Indirect Tensile Strength, and Flexural Strength Test were the three types of tests used to explore the behaviour of PP Fibre in polymer concrete.

Compressive Strength

Figure 7 shows the average compressive strength for each mix. This test determines whether the polypropylene fibre-reinforced polymer concrete is conducted properly. Resin content, fly ash content, polypropylene fibre content, quality of material, and quality control during concrete production are the main factors that affect the compressive strength of concrete. From the results, the polypropylene fine PPF reinforcement significantly affects the compressive strength of polymer concrete. The compressive strength increased with increasing the content of polypropylene fibre PPF. The results showed that adding 0.12%, 0.16%, and 0.2% polypropylene fibre increased the compressive strength of polymer concrete by 27.81%, 31.79%, and 145.03%, respectively. Furthermore, as shown in Table 5, fibre-reinforced polymer concrete has a higher strength than non-fibrous polymer concrete.

Because of the continual compression force exhibited in Figure 7 of the fibre polymer concrete sample, the cracks have begun to distort. As the load increases, more cracks will appear until it reaches a fibre (Figure 7b). The results are consistent with Hsie et al.

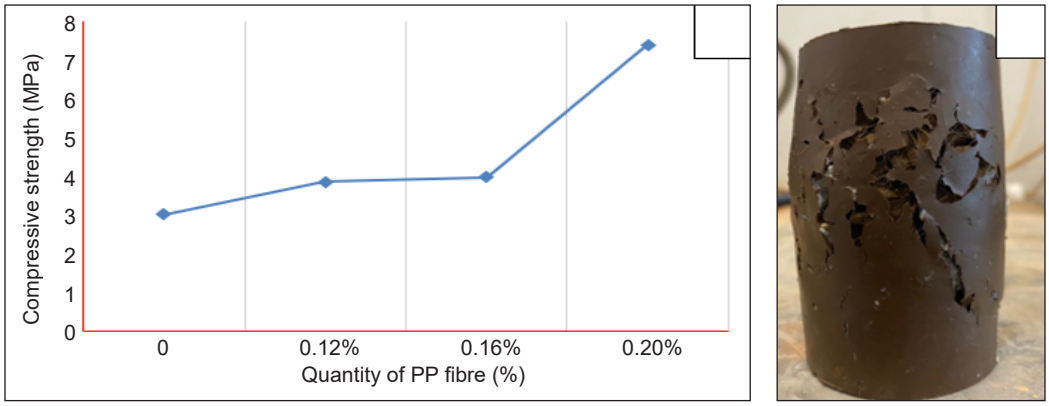

(a) (b)

Figure 7. (a) Compressive strength of polymer concrete containing various percentages of Polypropylene fibre reinforcement, (b) Failure behaviour Polymer concrete with 0.16% of PP Fibre

Table 5
The compressive strength of polypropylene fibre-reinforced concrete

Specimens	Quantity of Fibre (%)	Compressive Strength Average (MPa)	Percentage increment of strength (%)
Mix 1	0	3.02	-
Mix 2	0.12	3.86	27.81
Mix 3	0.16	3.98	31.79
Mix 4	0.20	7.40	145.03

(2008). It was found that adding polypropylene hybrid fibre to concrete resulted in more strength than using only a single fibre. With the addition of hybrid polypropylene fibre, the compressive strength increased by 14.60% to 17.31%, the splitting tensile increased by 8.88% to 13.35%, and the modulus of rupture increased by 8.99% to 24.60%. In a study by Marciano, reinforcing carbon fibre in the PC results in a 16% increase in compressive strength, whereas only an 8.7% increase in compressive strength was recorded when glass fibre reinforcement was used. However, when PP fibre was added to the polymer concrete in this investigation, compressive strength values expanded compared to carbon and glass fibre (Fluminense, 2014). The greater tensile stress in the polymer concrete due to the crack path perpendicular to the fibre matrix surfaces causes de-bonding between the fibre matrix surfaces. Due to the presence of the de-bonding crack earlier, a blunting process happened at the tip of the fracture when it eventually reached the interface. As a result, the crack-tip stress concentration was lowered, creating a diverting path for the crack and even preventing additional cracks. Because the fracture was blunted, stopped, and redirected, the fibrous polymer concrete cylinders could withstand more compressive stress, making them stronger than non-fibrous polymer concrete cylinders (Song et al., 2005).

Indirect Split Tensile Strength

The tensile strength of the concrete generally influences the extent and size of cracking in the structure. However, concrete is fragile in tension because of its brittle nature. Therefore, polypropylene fibre was added to investigate improvement. Figure 8a shows the results of the indirect split tensile strength of polymer concrete with different contents of polypropylene fibre PPF. Increasing the volume of PP fibre in the normal concrete increased the split tensile strength and flexural strength of the concrete mix design. The rupture modulus will be reduced with an additional 0.16% PP Fibre. Unfortunately, even though investigations into reinforcing PP fibre in Portland cement concrete have yielded reasonably large positive results, no polymer concrete experiments have been conducted. The splitting tensile strengths of polypropylene fibre-reinforced polymer concrete increase as the volumetric ratio of PP fibre increases. Non-fibrous polymer concrete has a tensile strength of 0.82 MPa, but adding 0.12%, 0.16%, or 0.2% PP Fibre raises the strength to 1.09 MPa, 1.28 MPa, and 1.57 MPa, respectively (Table 6). Meanwhile, compared to control polymer concrete, polymer concrete containing 0.2% polypropylene fibre PPF increased by 91.46% due to the advantages of PP fibre having high tensile strength properties.

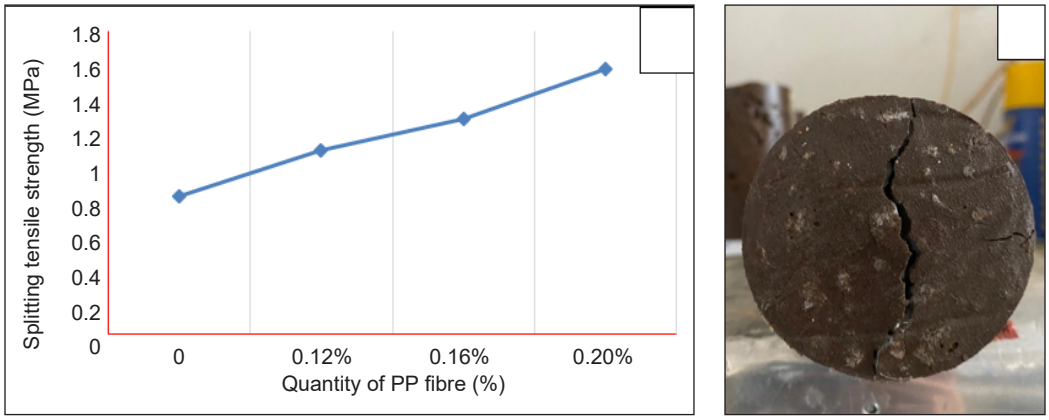

(a) (b)

Figure 8. (a) Splitting Tensile Strength of polymer concrete PC with different polypropylene fibre PPF reinforcement, (b) Splitting of cylinder specimens

Table 6
Indirect tensile strength of polymer concrete with different contain PPF

Specimens	Quantity of Fibre (%)	Splitting Tensile Strength Average (MPa)	Percentage increment of strength (%)
Mix 1	0	0.82	-
Mix 2	0.12	1.09	32.93
Mix 3	0.16	1.28	56.09
Mix 4	0.20	1.57	91.46

When the stress is continuously applied to the cylinder specimens, they split until they fail. The addition of fibres in the PC, on the other hand, aids in support of the full load, hence boosting strength as stress is passed from the matrix to the fibres. As a result, the fibres aid in the strengthening of the matrix's divided parts. When compared to unreinforced control polymer concrete, the stress transferred improved the tensile strain capacity of the polypropylene fibre reinforced polymer concrete, and thus the reinforced polymer concrete's splitting tensile strength increased (Song et al., 2005). Aside from that, due to the huge amount of PP fibre that crossed the split sections, 0.2% fibre inclusion in polymer concrete resulted in higher strength than 0.12% and 0.16%. In general, the number of fibres intersecting the fracture surfaces affects the splitting tensile strength of fibre-reinforced polymer concrete. The cylinder specimens were cut into two halves along their vertical plane at the end of the test, as shown in Figure 8b.

Flexural Strength

Flexural strength, also known as bending strength, or transverse rupture strength, is a material property defined as the maximum stress in a material just before it yields in a bending test. Figure 9 displays the flexural strength of polymer concrete containing 0.12%, 0.16%, and 0.2% PPF, shows that the flexural strength of fibre-reinforced polymer concrete is higher than non-fibrous polymer concrete, with a maximum value strength of 64.42 MPa at 0.16% fibre addition. Increasing the PPF content leads to the flexural strength of fibre-reinforced polymer concrete having the opposite trend to its splitting tensile and compressive strength. Increasing the fibre content from 0% to 12% resulted in a 60.36% increase in flexural strength while increasing the fibre content by 0.16% resulted in a 62.99% increase in strength. The flexural strength of the polymer concrete is reduced from 64.42 MPa to 62.13 MPa when 0.20% PP Fibre is added, as shown in Table 7.

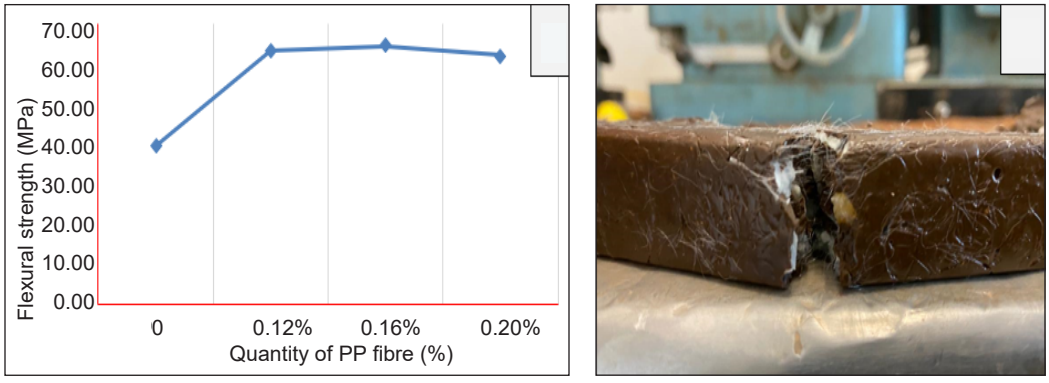

(a) (b)

Figure 9. (a) relationship between flexural strength and against PPF dosage, (b) failure behaviour of polymer concrete containing 16% PPF under flexural strength test

Table 7
Flexural strength of polymer concrete with different percentages of PPF

Specimens	Quantity of Fibre (%)	Flexural Strength Average (MPa)	Percentage increment of strength (%)
Mix 1	0	0.82	-
Mix 2	0.12	1.09	32.93
Mix 3	0.16	1.28	56.09
Mix 4	0.20	1.57	91.46

The fibres intersected the cracks that developed in the tension area of the reinforced beam, increasing flexural strength. By fitting into the crack so that the fibres' rubbery qualities come into place, these fibres mend the separation caused by the facial crack. It will minimise the pressure in the crack-tip surrounding the area formed by micro-cracks and increase the strength of the polymer concrete by giving an additional buffer in terms of energy that can be absorbed (Song et al., 2005). Based on the appearance of the sample, Figure 9b shows that PP Fibre reinforced polymer concrete has the same flexural strength as other types of fibres. Numerous studies demonstrate that when the resin content of polymer concrete increases, the compressive and flexural strengths likewise increase (Gagandeep, 2021; Otoom et al., 2022; Varun & Kumar, 2021).

A study conducted by Saribiyik et al. (2013) showed that compressive strength increases by about 7% when resin dosage is increased, while flexural strength is unaffected. Resin and quartz aggregates were added to the polymer concrete in the following ratios: The workability, compressive strength, and flexural strength of these materials were tested to evaluate the relationship between polyester percentage and strength. Similarly, Jafari et al. (2018) discovered that increasing the epoxy resin dosage and coarse aggregate size boosted the compressive strength of polymer concrete in destructive tests based on their experimental results. For the most part, it is seen that as the resin dosage is increased, the strength of the resin grows as well. However, as the resin dosage increases, the strength diminishes or remains unchanged. As a result, it was determined that a resin dose of 12% to 16% by weight of polymer concrete was the most effective.

Furthermore, the study by Gorninski et al. (2007) found that adding 3.5% steel fibre to a concrete mix increased the strength by 40%. Jo et al. (2008) discovered that adding nanoparticle fibre to polymer concrete increased its strength by approximately 38%. As a consequence, it can be concluded that reinforcing PP fibre in the PC is one of the most suited fibres for use in polymer concrete, as it produces a higher flexural strength of up to 63%, whereas other types of fibre produce a lower flexural strength.

CONCLUSION

This experiment found that polypropylene fibre reinforcement in polymer concrete offers exceptional mechanical performance. Compressive strength studies showed that as the amount of polypropylene (PP) fibres increased, so did the compressive strength of polymer concrete. The amount of PP fibre in polymer concrete makes the splitting tensile strength of the concrete stronger.

The flexural strength of fibre-reinforced polymer concrete, in contrast to the compressive and breaking tensile strengths, has demonstrated a trend opposite to the rise in the fraction of PP fibre employed in the mix. The results imply that fibre reinforcement is a viable option for enhancing the mechanical characteristics of polymer concrete, and polypropylene fibre has demonstrated potential as an additive for polymer concrete. Furthermore, the study discovered that 0.16% PP Fibre was the best fibre percentage to use in polymer concrete. The results showed that adding PP Fibre to the polymer concrete strengthened it in the compressive, splitting tensile, and flexural tests. Each test's results were thoroughly explained, and a graph was created to show the relationship between the strength measured and the fibre intake.

Therefore, these results from experiments have demonstrated that PP Fibre significantly impacts the mechanical characteristics of polymer concrete. The workability of fibre-reinforced concrete must be considered because it can degrade significantly when too many fibres are used in its composition. Additionally, it should be noted that the statement "greater fibre content-better qualities" is not always accurate. In other words, polypropylene fibres enhance the material's qualities, but only up to a specific dosage, which, if surpassed, has adverse effects. When choosing the ideal fibre content, it is crucial to consider the mixture's composition and the characteristics of the fibres (material, form, and dimensions: length, diameter, and slenderness). Sustainable development has benefited from polypropylene fibre-reinforced concrete's ecological and economic advantages. A prospective application for polypropylene fibre-reinforced concrete is in public places. Using concrete with improved qualities will unquestionably be advantageous because they are exposed to unfavourable environmental conditions, impact damage, surface abrasion, and vandalism. Decorative pavements, fountains, sculptures, artificial rocks, beaches, exotic scenery, door surrounds, and skate parks can all be created with polypropylene fibre-reinforced concrete.

ACKNOWLEDGMENTS

The authors express their gratitude to Universiti Tenaga Nasional (UNITEN), Malaysia, for supporting this research under BOLD 2022 through Project No: J510050002/2022004; special thanks to those who contributed to this project directly or indirectly.

REFERENCES

Abdulrahman, H., Muhamad, R., Visintin, P., & Shukri, A. A. (2022). Mechanical properties and bond stress-slip behaviour of fly ash geopolymer concrete. *Construction and Building Materials*, *327*, Article 126909. https://doi.org/10.1016/j.conbuildmat.2022.126909

Afroughsabet, V., & Ozbakkaloglu, T. (2015). Mechanical and durability properties of high-strength concrete containing steel and polypropylene fibers. *Construction and Building Materials, 94*, 73-82. https://doi.org/10.1016/j.conbuildmat.2015.06.051

Agusril, S. T., Nor, N. M., & Zhao, Z. J. (2012). Failure analysis of Carbon Fiber Reinforced Polymer (CFRP) bridge using composite material failure theories. In A*dvanced Materials Research* (Vol. 488, pp. 525-529). Trans Tech Publications Ltd. https://doi.org/10.4028/www.scientific.net/AMR.488-489.525

Akid, A. S. M., Hossain, S., Munshi, M. I. U., Elahi, M. M. A., Sobuz, M. H. R., Tam, V. W. Y., & Islam, M. S. (2021). Assessing the influence of fly ash and polypropylene fiber on fresh, mechanical and durability properties of concrete. *Journal of King Saud University-Engineering Sciences*, 1-11. https://doi.org/10.1016/j.jksues.2021.06.005

Arulmoly, B., Konthesingha, C., & Nanayakkara, A. (2021). Performance evaluation of cement mortar produced with manufactured sand and offshore sand as alternatives for river sand. *Construction and Building Materials*, *297*, Article 123784. https://doi.org/10.1016/j.conbuildmat.2021.123784

ASTM. (2001). Standard Test Method for Compressive Strength of Cylindrical Concrete Specimens 1 - ASTM C39/C39M - Standard. In *Annual Book of ASTM Standards. https://normanray.files.wordpress.com/2010/10/kuliah-7b-beton-segar-astm-c39.pdf*

ASTM. (2016). Standard Test Method for Flexural Strength of Concrete (using Simple Beam with Center-Point Loading)1 - C293/C293M - 16 - Standard. In *Annual Book of ASTM Standards*. https://doi.org/DOI: 10.1520/C0293_C0293M-16

Asyraf, M. R. M., Ishak, M. R., Syamsir, A., Amir, A. L., Nurazzi, N. M., Norrrahim, M. N. F., Asrofi, M., Rafidah, M., Ilyas, R. A., Rashid, M. Z. A., & Razman, M. R. (2022). Filament-wound glass-fibre reinforced polymer composites: Potential applications for cross arm structure in transmission towers. *Polymer Bulletin, 80*, 1059-1084. https://doi.org/10.1007/s00289-022-04114-4

Bedi, R., Chandra, R., Singh, S. P., Martínez-lópez, M., Martínez-barrera, G., Salgado-delgado, R., Gencel, O., Parker, E. E., Moffett, E. W., Ferdous, W., Manalo, A. C., Wong, H. S., Abousnina, R., AlAjarmeh, O. S., Zhuge, Y., Schubel, P., Afroughsabet, V., Ozbakkaloglu, T., Blazy, J., … & Hss, J. (2021). Optimal design for epoxy polymer concrete based on mechanical properties and durability aspects. *Construction and Building Materials*, *167*, 185-196. https://doi.org/10.1016/j.conbuildmat.2019.117229

Blazy, J., & Blazy, R. (2021). Polypropylene fiber reinforced concrete and its application in creating architectural forms of public spaces. *Case Studies in Construction Materials*, *14*, Article e00549. https://doi.org/10.1016/j.cscm.2021.e00549

Broda, J. (2016). Application of polypropylene fibrillated fibres for reinforcement of concrete and cement mortars. In *High Performance Concrete Technology and Applications* (pp. 189-204). IntechOpen Limited. https://doi.org/10.5772/64386

Ferdous, W., Manalo, A., Wong, H. S., Abousnina, R., AlAjarmeh, O. S., Zhuge, Y., & Schubel, P. (2020). Optimal design for epoxy polymer concrete based on mechanical properties and durability aspects. *Construction and Building Materials*, *232*, Article 117229. https://doi.org/10.1016/j.conbuildmat.2019.117229

Fluminense, U. F. (2014). Mechanical characterization of fiber reinforced polymer concrete. *Materials Research, 8*(3), 357-360. https://doi.org/10.1590/S1516-14392005000300023

Gagandeep. (2021). Experimental study on strength characteristics of polymer concrete with epoxy resin. *Materials Today: Proceedings*, *37*, 2886-2889. https://doi.org/10.1016/j.matpr.2020.08.665

Ghasemi, Y. (2019). *Flowability and proportioning of cementitious mixtures* (Master thesis). Lulea University of Technology, Sweden. https://doi.org/10.13140/RG.2.2.32843.23849

Gorninski, J. P., Molin, D. C. D., & Kazmierczak, C. S. (2007). Strength degradation of polymer concrete in acidic environments. *Cement and Concrete Composites*, *29*(8), 637-645. https://doi.org/10.1016/j.cemconcomp.2007.04.001

Guo, L., Zhang, F., Zhong, L., Guo, L., & Wang, L. (2021). Texture analysis of the microstructure of concrete with different concentrations of superabsorbent polymer after internal curing. *Materials Today Communications*, *27*, Article 102361. https://doi.org/10.1016/j.mtcomm.2021.102361

Hameed, A. M., & Hamza, M. T. (2019). Characteristics of polymer concrete produced from wasted construction materials. *Energy Procedia*, *157*(2018), 43-50. https://doi.org/10.1016/j.egypro.2018.11.162

Harison, A., Srivastava, V., & Herbert, A. (2014). Effect of fly ash on compressive strength of Portland pozzolona cement concrete. *Journal of Academia and Industrial Research*, *2*(8), 476-479.

Hsie, M., Tu, C., & Song, P. S. (2008). Mechanical properties of polypropylene hybrid fiber-reinforced concrete. *Materials Science and Engineering A*, *494*(1-2), 153-157. https://doi.org/10.1016/j.msea.2008.05.037

Jafari, K., Tabatabaeian, M., Joshaghani, A., & Ozbakkaloglu, T. (2018). Optimizing the mixture design of polymer concrete: An experimental investigation. *Construction and Building Materials*, *167*, 185-196. https://doi.org/10.1016/j.conbuildmat.2018.01.191

Jo, B., Park, S., & Kim, D. (2008). Mechanical properties of nano-MMT reinforced polymer composite and polymer concrete. *Construction and Building Materials, 22*(1), 14-20. https://doi.org/10.1016/j.conbuildmat.2007.02.009

Kayali, O., Haque, M. N., & Zhu, B. (2003). Some characteristics of high strength fiber reinforced lightweight aggregate concrete. *Cement and Concrete Composites*, *25*(2), 207-213. https://doi.org/10.1016/S0958-9465(02)00016-1

Liu, R., Li, T., & Greene, R. (2020). Migration and inequality in rental housing: Affordability stress in the Chinese cities. *Applied Geography*, *115*, Article 102138. https://doi.org/10.1016/j.apgeog.2019.102138

Manjunatha, M., Preethi, S., Malingaraya, Mounika, H. G., Niveditha, K. N., & Ravi. (2021). Life cycle assessment (LCA) of concrete prepared with sustainable cement-based materials. *Materials Today: Proceedings, 47*(13), 3637-3644. https://doi.org/10.1016/j.matpr.2021.01.248

Martínez-López, M., Martínez-Barrera, G., Salgado-Delgado, R., & Gencel, O. (2021). Recycling polypropylene and polyethylene wastes in production of polyester based polymer mortars. *Construction and Building Materials*, *274*, Article 121487. https://doi.org/10.1016/j.conbuildmat.2020.121487

McCarthy, M. J., Yakub, H. I., & Csetenyi, L. J. (2022). Impact of fly ash production and sourcing changes on chemical and physical aspects of concrete durability. *Construction and Building Materials*, *342*, Article 127313. https://doi.org/10.1016/j.conbuildmat.2022.127313

Mocharla, I. R., Selvam, R., Govindaraj, V., & Muthu, M. (2022). Performance and life-cycle assessment of high-volume fly ash concrete mixes containing steel slag sand. *Construction and Building Materials*, *341*, Article 127814. https://doi.org/10.1016/j.conbuildmat.2022.127814

Mohamad, D., Syamsir, A., Beddu, S., Kamal, N. L. M., Zainoodin, M. M., Razali, M. F., Abas, A., Seman, S. A. H. A., & Ng, F. C. (2019). Effect of laminate properties on the failure of cross arm structure under multi-axial load. *IOP Conference Series: Materials Science and Engineering*, *530*(1), Article 012029. https://doi.org/10.1088/1757-899X/530/1/012029

Oey, T., Timmons, J., Stutzman, P., Bullard, J. W., Balonis, M., Bauchy, M., & Sant, G. (2017). An improved basis for characterizing the suitability of fly ash as a cement replacement agent. *Journal of the American Ceramic Society*, *100*(10), 4785-4800. https://doi.org/10.1111/jace.14974

Ohama, Y., & Demura, K. (1982). Relation between curing conditions and compressive strength of polyester resin concrete. *International Journal of Cement Composites and Lightweight Concrete*, *4*(4), 241-244. https://doi.org/10.1016/0262-5075(82)90028-8

Otoom, O. F., Lokuge, W., Karunasena, W., Manalo, A. C., Ozbakkaloglu, T., & Ehsani, M. R. (2022). Flexural behaviour of circular reinforced concrete columns strengthened by glass fibre reinforced polymer wrapping system. *Structures*, *38*, 1326-1348. https://doi.org/10.1016/j.istruc.2022.02.071

Pan, Y., Zhang, Y., Zhang, D., & Yang, H. (2021). Effect of polymer and conventional molds on the aesthetical surface quality of concretes. *Construction and Building Materials*, *302*, Article 124375. https://doi.org/10.1016/j.conbuildmat.2021.124375

Parker, E. E., & Moffett, E. W. (1954). Physical properties of polyester resin. *Industrial & Engineering Chemistry, 46*(8), 1615-1618. https://doi.org/10.1021/ie50536a031

Qin, Y., Zhang, X., Chai, J., Xu, Z., & Li, S. (2019). Experimental study of compressive behavior of polypropylene-fiber-reinforced and polypropylene-fiber-fabric-reinforced concrete. *Construction and Building Materials*, *194*, 216-225. https://doi.org/10.1016/j.conbuildmat.2018.11.042

Ramezanianpour, A. A., Esmaeili, M., Ghahari, S. A., & Najafi, M. H. (2013). Laboratory study on the effect of polypropylene fiber on durability, and physical and mechanical characteristic of concrete for application in sleepers. *Construction and Building Materials*, *44*, 411-418. https://doi.org/10.1016/j.conbuildmat.2013.02.076

Rebeiz, K. S. (1995). Time-temperature properties of polymer concrete using recycled PET. *Cement and Concrete Composites*, *17*, 119–124. https://doi.org/10.1016/0958-9465(94)00004-I

Rebeiz, K. S. (1996). Precast use of polymer concrete using unsaturated polyester resin based on recycled PET waste. *Construction and Building Materials*, *10*(3), 215-220. https://doi.org/10.1016/0950-0618(95)00088-7

Ribeiro, M. C. S., Nóvoa, P. R., Ferreira, A. J. M., & Marques, A. T. (2004). Flexural performance of polyester and epoxy polymer mortars under severe thermal conditions. *Cement and Concrete Composites*, *26*(7), 803-809. https://doi.org/10.1016/S0958-9465(03)00162-8

Sanjith, J., Kiran, B. M., Chethan, G., & N, M. K. K. (2015). A study on mechanical properties of latex modified high strength concrete using bottom ash as a replacement for fine aggregate. *International Journal, 3*(6), 114-121.

Saribiyik, M., Piskin, A., & Saribiyik, A. (2013). The effects of waste glass powder usage on polymer concrete properties. *Construction and Building Materials*, *47*, 840-844. https://doi.org/10.1016/j.conbuildmat.2013.05.023

Scope, C., Vogel, M., & Guenther, E. (2021). Greener, cheaper, or more sustainable: Reviewing sustainability assessments of maintenance strategies of concrete structures. *Sustainable Production and Consumption*, *26*, 838-858. https://doi.org/10.1016/j.spc.2020.12.022

Song, P. S., Hwang, S., & Sheu, B. C. (2005). Strength properties of nylon- and polypropylene-fiber-reinforced concretes. *Cement and Concrete Research*, *35*(8), 1546-1550. https://doi.org/10.1016/j.cemconres.2004.06.033

Supian, A. B. M., Sapuan, S. M., Jawaid, M., Zuhri, M. Y. M., Ilyas, R. A., & Syamsir, A. (2022). Crashworthiness response of filament wound kenaf/glass fibre-reinforced epoxy composite tubes with influence of stacking sequence under intermediate-velocity impact load. *Fibers and Polymers*, *23*(1), 222-233. https://doi.org/10.1007/s12221-021-0169-9

Teixeira, E. R., Camões, A., & Branco, F. G. (2022). Synergetic effect of biomass fly ash on improvement of high-volume coal fly ash concrete properties. *Construction and Building Materials*, *314*, Article 125680. https://doi.org/10.1016/j.conbuildmat.2021.125680

Varun, B. K., & Kumar, C. A. (2021). Flexural and shear characteristics of polymer modified high volume fly ash concrete. *Materials Today: Proceedings*, *46*, 289-293. https://doi.org/10.1016/j.matpr.2020.08.040

Yin, S. (2015). *Development of Recycled Polypropylene Plastic Fibres to Reinforce Concrete*. Springer.

Pertanika J. Sci. & Technol. 31 (3): 1555 - 1586 (2023)

PERTANIKA JOURNALS

SCIENCE & TECHNOLOGY

Journal homepage: http://www.pertanika.upm.edu.my/

Analysis of Influence of Vertical Vibration on Natural Heat Convection Coefficients from Horizontal Concentric and Eccentric Annulus

Baydaa Khalil Khudhair*, Adel Mahmood Saleh and Ali Laftah Ekaid

University of Technology, Mechanical Engineering Department, Baghdad 00964, Iraq

ABSTRACT

The research looks at how heat transmission is improved when two horizontal cylinders are concentric or vertically eccentric, creating vertical motion. The inner cylinder is uniformly heated, whereas the outer cylinder is isothermal. Apart from Rayleigh's number ($10^2 \geq Ra \geq 10^6$), eccentricity (normalized by the radius difference) at range ($\epsilon = 0, \pm 0.625$ & ± 0.333), and Prandtle number is fixed Pr = 0.7(air), the vibrational frequencies are changed from ($\varpi = 0$, 100, 1000 &10000). The steady-state, two-dimensional Navier-Stokes equations (with Boussineq approximation) are generated using central difference approximation and solved using the successive over-relaxation (LSOR) method line by line. The contour maps of streamlines and heat lines clearly illustrate the annuli's heat and fluid flow patterns. According to the results, it is found that the vibration generally enhanced the heat transfer rate more than the stationary one for all values of frequency and different eccentricities with various rates of enhancement. Vibration thermal convection is prominent at low Rayleigh ($Ra = 10^2, 10^3, 10^4$), and the vibration significantly boosts the heat transfer rate within an annular annulus. In a high Rayleigh number situation, a high Rayleigh number situation ($Ra=10^5$ and 10^6), gravitational thermal convection predominates, and vibration motion does not significantly improve heat transmission. The vibration is a powerful augmentation tool for placing the inner cylinder towards the bottom of the outer cylinder (negative vertical eccentricity ($\epsilon = -0.625$)), the heat rate enhancement more than 3.8-fold at $Ra = 10^3$, $\varpi = 10000$. The Nusselt number has been correlated in a dimensionless form as the Rayleigh number and the vibrational Rayleigh number.

Keywords: Cylindrical annulus, heat convection, numerical validation, Rayleigh number, vertical vibration

ARTICLE INFO

Article history:
Received: 05 June 2022
Accepted: 04 November 2022
Published: 07 April 2023

DOI: https://doi.org/10.47836/pjst.31.3.24

E-mail addresses:
21979@student.uotechnology.edu.iq (Baydaa Khalil Khudhair)
Adel.M.Saleh@uotechnology.edu.iq (Adel Mahmood Saleh)
ali.l.ekaid@uotechnology.edu.iq (Ali Laftah Ekaid)
*Corresponding author

ISSN: 0128-7680
e-ISSN: 2231-8526

© Universiti Putra Malaysia Press

INTRODUCTION

Predicting heat transfer due to natural (convection and conduction) between eccentric cylinders (horizontal annular fluid layers) has gained substantial attention from researchers in recent decades due to its importance in many engineering applications. Because of the intriguing character of the particular heat transport phenomena and its essential relevance in practical applications, convection in the horizontal annular of concentric and eccentric cylindrical systems has gained substantial weight. Examples of application domains using the horizontal coaxial cylinder geometry investigated in this study include concentrating solar collector receiver design, initial melting of phase change material around heating pipes in thermal storage systems, compressed gas insulated high voltage electric transmission cables, and designing nuclear reactors.

Kuehn and Goldstein (1978) performed a rather extended investigation of instance concentric numerically using the finite difference approach and empirically on the concentric and impact of vertical eccentricity (positive and negative) of the inner cylinder on the local and average heat transfer parameters using Mach-Zehnder techniques; by analyzing this influence with a fixed radius ratio of 2.6 in the boundary layer regime ($3 \times 10^4 < Ra < 5 \times 10^5$). The average heat transfer coefficients were all within 10% of concentric geometry at the boundary layer regime for $\epsilon = \frac{1}{3}, \frac{2}{3}$.

Any thermal device (electronic and thermoelectric) depend upon the feasibility of rejecting waste heat by trouble-free economic methods and, during its normal operation, will encounter some degree of vibration. In particular, the most challenging part of any nonexpendable coolant cooling system, which most rejects heat to the atmosphere, is usually the thermal coupling between the solid convective surface and the cooling air. It is well known that the boundary layers provide the primary resistance to heat flow from the solid surface to the fluid. Therefore, it would seem logical that an approach that could remove the boundary layers would substantially affect the heat flow.

The increasing emergence of diverse technologies worldwide has increased global energy consumption exponentially. A large percentage of this energy is in the form of heat, thus enhancing the heat transfer mechanisms at the forefront of energy transfer and storage.

So, the conceptualized mechanism of vibration breaks through the boundary layer limitation and achieves massive heat transport enhancement. Many vibration and oscillation phenomena occur in the industrial field, like the fluid flow in the medium being subjected to pulsation or agitation (fluid-induced vibration) relative to a stationary cylinder or any other container. The other type of vibration in which the heated body or surface is moved relative to the stationary surrounding fluid of vibration of the mechanical devices has been investigated in studies. Engineering applications of natural convection in eccentric annulus have become of great interest to researchers in recent years. Such a claim arises from eccentricity in mechanical equipment, electrical motors, and generators, which often

cause design tolerance and manufacturing limits. Further applications include drilling and completing an oil well, heat exchanger industries, cooling of the nuclear reactor, and the insulation for burned tubes in district heating and cooling underground electric cables.

Fu and Hung (2006) developed a numerical convection study in a vertical channel flow. According to their theory, a vibrational heat plate with a particular frequency and amplitude combination has less natural convection than an equilibrium point. Alawadhi (2008) investigated the influence of transversely oscillating frequency for the inner cylinder enclosed by an annulus enclosure on the flow fields and thermal behavior. It is concluded that the oscillating frequency of the inner cylinder greatly enhances the average heat transfer rate at the inner cylinder.

Hosseinian et al. (2018) searched experimentally for the enhancement of heat transfer in a flexible double-pipe heat exchanger made of PVDF using MWCNT-water nanofluid as a working fluid. The test rig was examined for different mass frictions, and forced vibration was applied to the outer wall of the heat exchanger generated by electric vibrators. The results showed that using vibration increases the heat transfer rate but simultaneously reduces the deposition of nanoparticles. The increase of many parameters, such as the temperature of nanofluid, vibration level, and mass flow rate, enhances heat transfer. The highest increase in heat transfer coefficient was obtained at the most significant level of vibration $(9\,\frac{m}{s})$ and the lowest mass fraction (0.04%).

Nasrat et al. (2019) experimentally studied the effect of transverse vibration on the natural convection heat transfer in a rectangular enclosure with an aspect ratio of 0.5 filled with air as a working fluid aligned horizontally on a mechanical shaker generating a sinusoidal transverse vibrational displacement. Shokouhmand et al. (2011) discovered vortices in test samples' left and right areas due to horizontal vibration, which reduced the heat transmission rate. Furthermore, due to more excellent convective flow crossing cylinders, oscillation had little effect on heat transmission at large Rayleigh numbers. Mahfouz (2012) investigated natural heat convection numerically among two vertical, eccentric, long cylinders inside a circumferential circular pattern. Mahian et al. (2013) conducted a detailed study on a vertical annulus using nanofluids. They demonstrated that frequency magnitude might classify thermal convection into five zones. They also noted that buoyancy-driven thermal convection dominates at a high Rayleigh number ($Ra = 10^6$).

Tayebi et al. (2016) conducted a numerical investigation on natural convection fluid flow and heat transfer in an annulus of two differentially heated eccentric cylindrical ducts filled with the Cu-water nanofluid. A detailed study, including the effects of the mechanical force vibration on the heat transfer characteristics of internal flow in a circular heated tube, has been investigated by Liu et al. (2017). Imtiaz and Mahfouz (2017) used the Fourier Spectral method to examine the impact of thermal boundary conditions on conjugated conduction-free convection heat transfer in an annulus between two concentric cylinders. A

non-Newtonian hybrid nanofluid flowing around a concentric annulus was investigated by Shahsavar et al. (2018) using the Genetic algorithm technique. Using natural convection as a cooling strategy is one of the primary ways to ensure the functional reliability of equipment. The flow characteristics of the annulus are not explored, especially the unsteady flow. It has been investigated theoretically and experimentally how hydrodynamic, and thermal effects interact. Only a handful of studies examined vertical or horizontal eccentricity in their extensive research evaluation (Sarhan et al., 2019).

Ali et al. (2020) presented a 3D simulation of heat transfer (turbulent/laminar) and fluid flow of water through the annulus side of conically tube heat exchangers. Sarhan et al. (2019) proposed a new model to investigate the effect of dynamic response on the thermal stability of a rectangle plate with a constant heating rate. According to test findings, the influence of vibration frequency reached in the horizontal position offered the best performance and maximum heat transfer rate. However, when the plate is vertical, and the vase is flat, the heat transfer rate decreases as the vibration frequency increases. Bouzerzour et al. (2020) achieved a numerical study on natural convection heat transfer and fluid flow in a two-dimensional annulus founded by two differentially heated confocal elliptic cylinders oriented and filled with the water-based silver nanofluid. Wang et al. (2020) presented a numerical and theoretical study of a thermal vibrational turbulence technique that overcomes the constraints of the boundary layer and gains massive heat transport augmentation. Thermal turbulence was a powerful way for the fluid to transport heat through space. However, the presence boundary layer near the surfaces trapped the heat exchanged capacity. As a horizontal vibration was applied to the convection sample, a strong shear was induced to the fluid near the conducting surfaces, destabilizing thermal boundary layers, vigorously triggering thermal plume eruptions, and resulting in augmentation in heat transfer rate to 600%. The natural convective flow mechanism and heat exchange under a magnetic field within a concentric circular annulus between a heat-generating conductive internal cylinder and an isothermally cold external cylinder filled with a CNTswater-based nanoliquid is investigated by Tayebi, Oztop et al. (2021).

Al-Azzawi et al. (2021) examined heat transfer performance in a brass body of a concentric vertical cylinder and the effect of induced vibration on the system. The results indicated that the heat transfer rate was improved and increased, and the thermal boundary layer increased from the bottom to the top surface under vibration. In addition, the Rayleigh number had a negative effect on the heat transfer rate, whereas the vibration Reynolds number positively impacted the heat transfer rate during the vibration. Tayebi and Chamkha (2021) investigated the influences of local thermal non-equilibrium on thermo-natural convection in an elliptical annular space separated by a nanofluid-saturated porous sleeve using the standard SIMPLER algorithm. Tayebi, Chamkha, et al. (2021) explained the effect of a solid conductive partition on the thermal-free convective motion mechanism and heat

transmission process within a concentric circular annulus filled with a water-based hybrid nano liquid containing copper and alumina nanoparticles.

Tayebi et al. (2022) conducted a comprehensive and accurate numerical analysis of the local thermal non-equilibrium effects on the natural convection characteristics in a horizontal elliptical porous annulus saturated with nanofluid using a finite volume technique. In the presence of magnetic fields, Tayebi et al. (2022) performed a numerical analysis of thermo-natural convection and entropy generation in an alumina-water nanofluid enclosed by two circular cylinders.

According to the literature, many experimental and theoretical studies have investigated the influence of vibration on convective heat transfer. Different structures such as flat plates, cylinders, wires, and various shapes of enclosed cavities; for different orientations have been used. The vibration vector was analyzed relative to these surfaces; for other vibration parameters, including amplitude and frequency, based on various heating conditions.

The motivation of this investigation purpose is to scrutinize the influence of vibration frequency, Rayleigh number (Ra= 10^2, 10^3, 10^4,10^5, and 10^6), eccentricity, and vibration Rayleigh number (Rav = 10^2, 10^3, 10^4, and 10^5) on the natural heat transfer rate performance using a horizontal annulus with a vibrating inner cylinder. The emphasis is on the inner vibration cylinder being heated under constant heat flux subjected to vertical sinusoidal vibrations and eccentricity on the temperature and flow fields. The range of vibration frequency (ϖ = 0, 100, 1000 &10000) and the Prandtle number is 0.7. According to changes in vibration frequency from low to high, flows and heat transfer rates were altered from a quasi-static state zone via a resonant region. Furthermore, we also examine the results of two vertical eccentricities of the streamlines, isothermal lines, and the changes in the fluid's Nusselt number and those for concentric arrangement. Meanwhile, the mechanical vertical vibration effects have been successfully used to control heat and mass transfer, such as in heat exchangers, stirrers, mineral separators, nuclear reactors, and crystal growth. Therefore, a good understanding of the fundamental theory of thermal vibrational convection behind those applications and phenomena is necessary. So, this is the motivation, the "innovation", and the main contribution of this paper.

In addition to the results for the concentric configuration, results for two vertical eccentricities of the streamlines, isothermal lines, and variations in the fluid's Nusselt number are presented. The following is the structure of this paper; the mathematical statement of the problem is supplied in the next section. Then there are the governing equations and the numerical approach. Next, changing the cylinder's Rayleigh number, eccentricity, and vibration frequency on the streamlines, isotherms, and temporal average Nusselt number will be illustrated and discussed. Finally, some closing remarks are included.

MATERIALS AND METHOD

A sketch of the physical model for consideration is shown in Figure 1. The annulus is formed by two cylinders: vertically eccentric and horizontally centric. The outer cylinder, with a radius (R_o), is fixed in this model. However, the inner cylinder, with a radius (R_i), may be adjusted vertically to vary the eccentricity and can be vertically vibrated with frequency (Ω).A positive eccentricity (ϵ) between two cylinders is achieved if the inner cylinder's center is higher than the outer cylinder's. In contrast, a negative eccentricity (ϵ) would be achieved if the inner cylinder was oriented vertically in five different ways.

The annulus contains air (as working fluid $Pr = 0.7$), and the inner wall of the annulus is heated at constant heat flux (q_i), while the annulus's outer wall is cooled and kept at a constant temperature (T_o). Initially (t = 0), the inner cylinder is at the center of the annulus, the air in the annulus is stationary, and its temperature and the cylinder's surface are kept at $T_s = T_0$. Afterward ($t > 0$), the inner cylinder is forced to vertical vibration with displacement (-b sin Ωt) parallel to the gravity vector, the inner cylinder's buoyancy and vibration impact heat transfer from the inner cylinder to the outer cylinder.

The following assumptions are made:

1. The fluid is Newtonian (air), and the flow is 2-D space formed between two eccentric horizontal cylinders to make the analysis more accessible.
2. The vibration amplitude (bΩ) is small, and the flow is incompressible and laminar.
3. The Boussinesq assumption is correct; viscous dissipation, heat generation, and the radiation heat transfer impact are disregarded.
4. The characteristics of air are assumed constant, and the density of the fluid is considered constant except for density in buoyancy terms.
5. There is no-slip condition held on the interfaces between the fluid and surface.
6. The induced vibration is in the vertical direction and parallels gravity.
7. The eccentricity, ϵ the two cylinders, is taken positively if the center of the inner cylinder is above the outer cylinder and negative if below it.

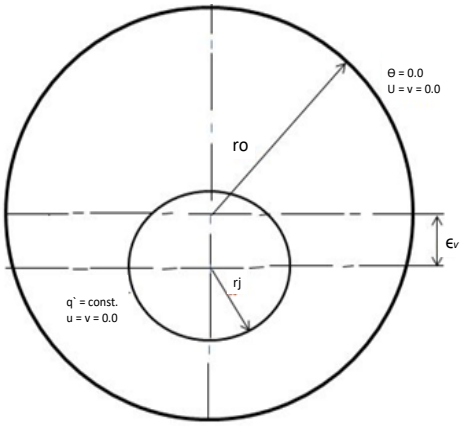

Figure1. Geometry of annulus

a. Physical plane

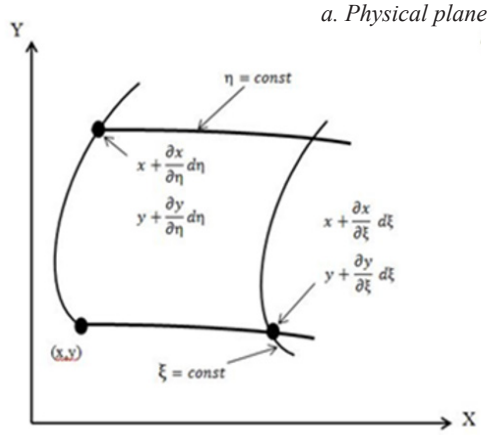

Figure 2. Physical and transformed computational planes

b. Computational plane

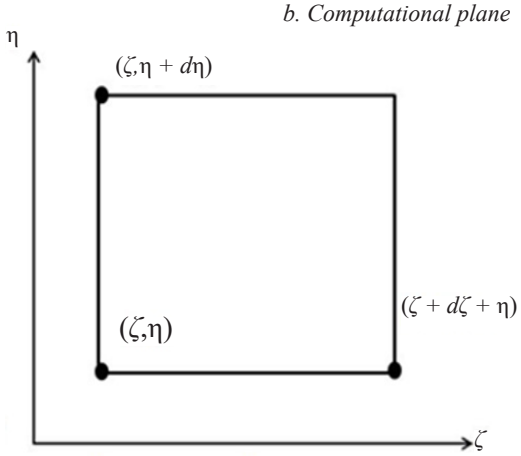

Figure 2. (Continue)

Mathematical Formulation [Coordinate Transformation & Governing Equations] Method

Thompson et al. (1974) proposed a numerical mapping method to generate a body-fitted coordinate system (BFCs) to overcome the problems associated with the complex physical domain. This method enables us to approximate or interpolate at the outside limits of the body. Navier-Stokes equations in the dimensionless form are governing equations for the conservation of mass, momentum, and energy. The energy equation in Cartesian coordinates is written in Table 1, the in-stream function - vorticity formulation.

Table 1

Navier-Stokes equations in dimensionless form, and the energy equation in Cartesian coordinates

$X,Y = \frac{x,y}{L}, L = \frac{D_O - D_i}{2} = R_O - R_i$	$\theta = \frac{(T - T_c)K}{q"L}$
$u_{ref} = \frac{\alpha}{L}$	$\varpi = \frac{\Omega}{\Omega_r} = \frac{\Omega L}{u_{ref}}; \Omega_r = \frac{u_{ref}}{L}$
$\tau = \frac{t}{t_r} = \frac{t\, u_{ref}}{L}; t_r = \frac{L}{u_{ref}}$	$\Psi = \frac{\varphi}{\varphi_r}, \varphi_r = u_{ref} L$
$\rho^* = \frac{\rho}{\rho_{ref}}, \mu^* = \frac{\mu}{\mu_{ref}}$	$\mathrm{W} = \frac{\omega}{\omega_r}, \omega_r = \frac{u_{ref}}{L}$
$Pr = \frac{\nu}{\alpha} = \frac{\mu C_p}{K}$	$Ra = \frac{\rho^2 g_o \beta q" L^4}{K\, \mu^2} Pr$
$Gr_{vib} = \frac{1}{2}\left[\frac{\rho^2 (b\Omega) \beta q" L^2}{K\, \mu^2}\right]^2$	$Ra_{vib} = \frac{1}{2}\left[\frac{\rho^2 (b\Omega) \beta q" L^2}{K\, \mu^2}\right]^2 Pr$

The horizontal and vertical components of velocity can be re-written in the transformed plane as given in Equations 1 and 2:

$$U = \frac{1}{J}(\Psi_\eta \cdot X_\xi - \Psi_\xi . X_\eta) \quad [1]$$

$$V = \frac{1}{J}(\Psi_\eta \cdot Y_\xi - \Psi_\xi . Y_\eta)\ ) \quad [2]$$

The stream function-vorticity formulation in an elliptic partial differential equation can be hung to the following generic form in computational space (ξ, η). A generalized scalar's Laplacian in the converted plane may be given as Equations 3 and 4:

$$\frac{1}{J^2}\left(\lambda . \Psi_\xi + \sigma . \Psi_\eta + \alpha . \Psi_{\xi\xi} - 2\beta . \Psi_{\xi\eta} + \gamma . \Psi_{\eta\eta}\right) = -\mathrm{W} \quad [3]$$

$$\mathrm{W}_\tau + \frac{1}{J}\left(-\Psi_\xi . \mathrm{W}_\eta + \Psi_\eta . \mathrm{W}_\xi\right) = \frac{Pr}{J^2}\left(\lambda . \mathrm{W}_\xi + \sigma . \mathrm{W}_\eta + \alpha . \mathrm{W}_{\xi\xi} - 2\beta . \mathrm{W}_{\xi\eta} + \gamma . \mathrm{W}_{\eta\eta}\right) + \frac{1}{J}\left[\left(y_\eta \frac{\partial\theta}{\partial\xi} - y_\xi \frac{\partial\theta}{\partial\eta}\right)\right]\left[PrRa + \varpi\sqrt{PrRa_{vib}}\, sin\, \varpi\tau\right] \quad [4]$$

And by substituting the parameters of the transformed computational field (ξ, η) in the equation of energy, it becomes Equation 5:

$$\frac{\partial\theta}{\partial\tau} + \frac{1}{J}\left(-\Psi_\xi . \theta_\eta + \Psi_\eta . \theta_\xi\right) = \frac{1}{J^2}\left(\lambda . \theta_\xi + \sigma . \theta_\eta + \alpha . \theta_{\xi\xi} - 2\beta . \theta_{\xi\eta} + \gamma . \theta_{\eta\eta}\right) \quad [5]$$

Hence, introducing the following parameters, where (J) is the (Jacobian of the transformation) defined as Equations 6 to 10:

$$\mathrm{J} = \mathrm{x}_\xi \mathrm{y}_\eta - \mathrm{x}_\eta \mathrm{y}_\xi \quad [6]$$

$$\left\{\begin{array}{c} \alpha = x_\eta^2 + y_\eta^2 \\ \beta = x_\xi x_\eta + y_\xi y_\eta \\ \gamma = x_\xi^2 + y_\xi^2 \end{array}\right\} \quad [7]$$

$$\left\{\begin{array}{l} D_x = \alpha . y_{\xi\xi} - 2\beta . y_{\xi\eta} + \gamma . y_{\eta\eta} \\ D_y = \alpha . x_{\xi\xi} - 2\beta . x_{\xi\eta} + \gamma . x_{\eta\eta} \end{array}\right\} \quad [8]$$

$$\lambda = \frac{1}{J}\left(x_\eta . D_y - y_\eta . D_x\right) \quad [9]$$

$$\sigma = \frac{1}{J}\left(y_\xi . D_x - x_\xi . D_y\right) \quad [10]$$

The non-dimensional initial and BCs can be represented in Equations 11 to 15:

at $\tau = 0$ $\quad w = \psi = U = V = \theta = 0$

1. At the inner cylinder ($\eta=\eta i$) , $\Psi(\xi i,\eta) = U = V = 0$

$$W^{k+1}(i,w) = \frac{-3\gamma_{(i,w)}\cdot(\Psi_{(i,w+1)}-\Psi_{(i,w)})}{\Delta\eta^2\cdot J^2_{(i,w)}} - \frac{W_{(i,w+1)}}{2.0} \quad [11]$$

$$\xi_x\frac{\partial\theta}{\partial\xi} + \eta_x\frac{\partial\theta}{\partial\eta} = \frac{1}{J}\left(y_\eta\frac{\partial\theta}{\partial\xi} - y_\xi\frac{\partial\theta}{\partial\eta}\right) = -1 \quad [12]$$

The above equation can be re-written as

$$\theta(i,j) = \theta(i,j+1) - \frac{\beta(i,j)}{2\gamma(i,j)}.[\theta(i+1,j) - \theta(i-1,j)] + J\sqrt{\gamma}.\frac{\Delta\eta}{\gamma} \quad [13]$$

2. At the outer cylinder ($\eta = \eta_o$), $\Psi(\xi o, \eta) = U = V = 0$

$$W^{k+1}(i,w) = \frac{-3\gamma_{(i,w)}\cdot(\Psi_{(i,w-1)}-\Psi_{(i,w)})}{\Delta\eta^2\cdot J^2_{(i,w)}} - \frac{W_{(i,w-1)}}{2.0} \quad [14]$$

$$\theta(i,j-1) = 0 \quad [15]$$

The stream function is zero because the cylinder is a continuously solid surface, entering or exiting it. The non-dimensional heat transfer coefficient of local Nusselt number Nu can be found in Equations 16 and 17:

$$Nu = -\left(\frac{\partial T}{\partial r}\right)_{y=yi} * \frac{L}{(T_H - T_C)} \quad [16]$$

$$Nu = \frac{1}{\theta} \quad [17]$$

The average Nusselt number may be calculated by integrating the local Nusselt number, which yields the below Equation 18:

$$\overline{Nu} = \frac{\bar{h}\,L}{k} \quad [18]$$

Method of Solution and Numerical Technique

Grid Generation. The numerical method employed in the current study is discussed in this section, grid generation; because of the complexity of the physical shape used, we use the body-fitted coordinate system (BFC) technique first proposed by Thomson et al. (1974). After that, a curvilinear grid was created by solving two elliptic differential equations. Then, it was used to solve vorticity-stream equations in the vicinity of complex bodies (Figure 2) without the need to use approximating or interpolating at the outside limits of the body given as Equations 19 and 20:

$$\xi_{xx} + \xi_{yy} = P(\xi, \eta) \quad [19]$$

$$\eta_{xx} + \eta_{yy} = Q(\xi, \eta) \quad [20]$$

P and Q are coordinate control functions that can focus the coordinate lines on domain areas with high fluctuations of a given characteristic. The physical coordinates can be used as the dependent variable in Equations 21 and 22:

$$\alpha x_{\xi\xi} - 2\beta x_{\xi\eta} + \gamma x_{\eta\eta} + J^2\left(Px_{\xi} + Qx_{\eta}\right) = 0 \quad [21]$$

$$\alpha y_{\xi\xi} - 2\beta y_{\xi\eta} + \gamma y_{\eta\eta} + J^2\left(Py_{\xi} + Qy_{\eta}\right) = 0 \quad [22]$$

The transformation coefficients and Jacobian are defined in Equations 6, 7, 9, and 10.

Discretization Technique and Method of Solution. The numerical solution for the governing equations used general curvilinear coordinates ($x = x(\xi, \eta)$, $y = y((\xi, \eta))$ are solved in the stream function-vorticity formulation (Ψ, W) to avoid enforcing the additional integral demand for the single pressure interpretation. The mesh of the generated model available in the form of the bipolar coordinate system was illustrated in Figure 3, where the (radial-like curves) represent constant angles in angular coordinate (ξ), and the eccentric circles indicate constant lines (η). The eccentricity and azimuthal position of the inner circle were easily obtained by changing the location of the inner cylinder and vibrating it in a direction parallel to gravity acceleration. Equations 3 to 5 are solved by successive line over-relaxation LSOR technique. The partial differential equations use second-order central-difference schemes for all derivatives. Figure 3 depicts the computation mesh with the internal cylindrical part in 5 different vertical locations within the outer cylindrical surface (centric) and for the vertical eccentric annulus configuration (ϵ = -0.625, -0.333, 0, +0.333 & + 0.625).

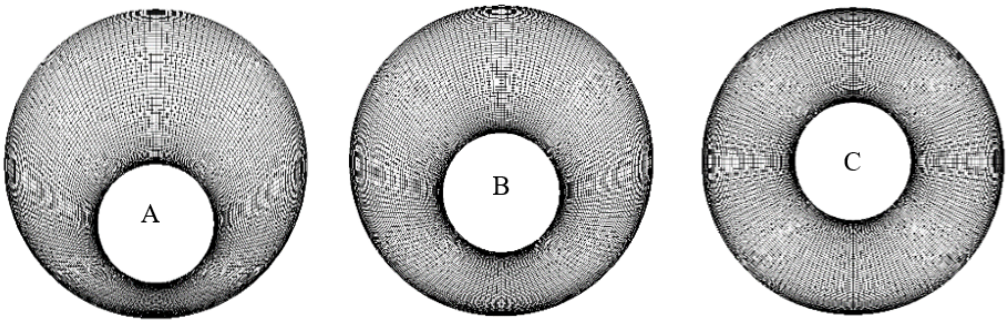

Figure 3. Inner cylinder location and computational mesh for A: ϵ = -0.625; B: ϵ -0.333; C: ϵ = 0

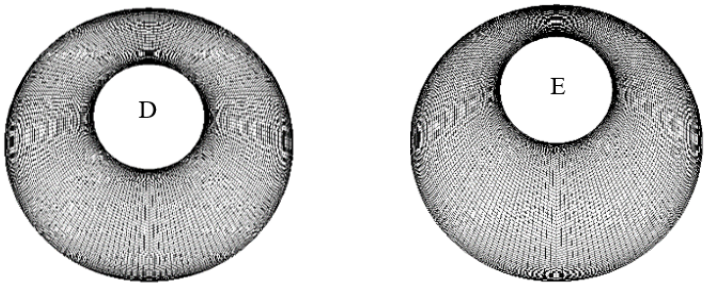

Figure 3 (Continue). Inner cylinder location and computational mesh for D: ϵ = +0.333; E: ϵ = +0.625

Since the domain's boundaries do not lie along natural coordinates, a boundary-fitted nonorthogonal coordinate system is used. The solution procedure involves grid generation, discretization of the governing equations, and an algorithm for solving the equations. The finite difference method in the transformed plane solves the design of governing Equations 3 to 5. In the second-order central difference scheme, except for the convective terms in the two transport equations which utilize the standard major plan, all the spatial discretization is done with them. The stability of the numerical method is investigated for case = 10^6 and all frequencies. The time steps are chosen with values of 0.00001. A nonuniform grid field has been used for the radial direction, which has smoothly varying grid spacing with a denser grid near the inner and outer walls of the annulus to account for the boundary layers formed in these regions. The mesh size 175 × 76 is used for a grid independence study of numerical results for all cases. It is noted that the total number of grid points is 100000. Dirichlet conditions are stated at the boundaries.

NUMERICAL VALIDATION

In this study, the flow field is based on streamlines, and the thermal area uses isotherms for the following parameters (Ra = 10^3, 10^4, and 10^5), (ϵ = ±0.625), radii ratio ($\frac{ro}{ri} = 2.6$), and keeping the ratio of gap width to diameter ($\frac{L}{Di} = 0.8$) for a fluid with (Pr = 0.7). Figures 4 and 5 show comparisons (in the absence of vibration and constant temperature boundary conditions) between the flow pattern of the streamlines and isotherms of numerical results, which contain 0.5 of the isotherms and 0.5 of the respective streamlines**.** Figures 4 and 5 show reasonable matching with eccentric inner cylinder configurations beyond a simple qualitative interpretation.

Kuehn and Goldsten (1976) conducted extensive computational and experimental research on concentric annuli; a test run was carried out for (Ra = 5 *x* 10^4). Figure 6 explains the results of the Local equivalent thermal conductivity (k_{eq}). A strong consensus can be seen with the tests and validated by Kuehn and Goldstein (1976; 1978) for outer and inner cylinders. Furthermore, the maximum surface temperature (MST) results on the inner

cylinder and the average Nusselt number are compared with the data found by Ho et al. (1989) using the same characteristics and without vibration. Another practical parameter is the size of the MST on the inner surface of the homogeneous Heat flow, shown in Tables 2 and 3, which appears to be consistent with those predicted in the current study.

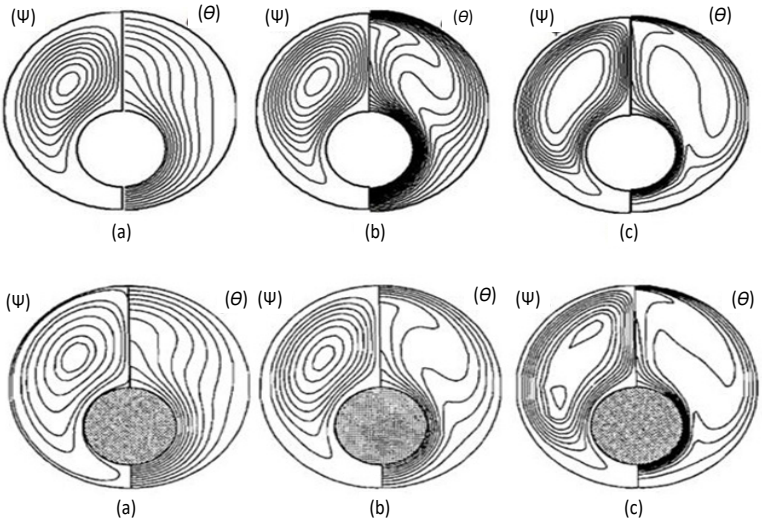

Figure 4. Comparison streamlines (left half), and isotherms (right half), Pr = 0.7; ϵ = -0.625; $(\frac{L}{Di}) = 0.8$: upper, present. method; lower, from (Projahn et al., 1981). (a) *Ra* = 10^3; (b) *Ra* = 10^4; (a) *Ra* = 10^5

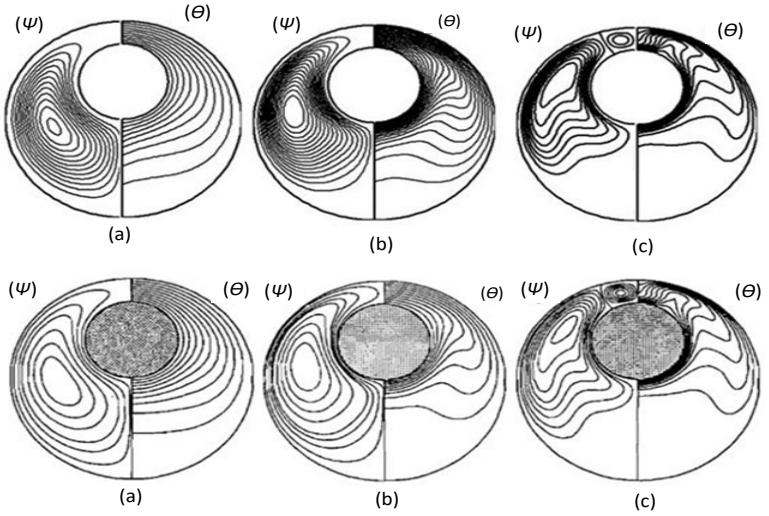

Figure 5. Comparison streamlines (left half), and isotherms (right half) *Pr* = 0.7, ϵ = +0.625; $(\frac{L}{Di}) = 0.8$: upper, present method; lower, from (Projahn et al., 1981). (a) *Ra* = 10^3 ; (b) *Ra* = 10^4, (c) *Ra* = 10^5

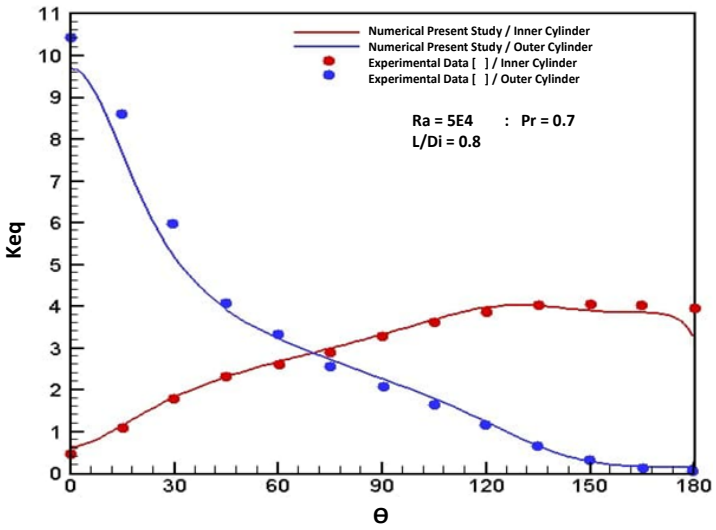

Figure 6. Validation of Concentric local heat transfer coefficients at $Ra = 10^5$, $Pr = 0.7$, $\epsilon = 0$, $\left(\frac{L}{Di}\right) = 0.8$, from (Kuehn & Goldstein, 1976).

Table 2

MST on the inner cylinder of the uniform heat flux at Ra

ϵ	P_r	10^3	10^4	10^5	10^6
0.625 (present study)	0.700	0.550	0.451	0.400	0.201
+ 0.625 (Ho et al., 1989)	0.700	0.562	0.468	0.445	0.358
0 (present study)	0.700	0.651	0.530	0.36	0.240
0 (Ho et al., 1989)	0.700	0.696	0.525	0.347	0.229
- 0.625 (present study)	0.700	0.641	0.432	0.33	0.221
- 0.625 (Ho et al., 1989)	0.700	0.648	0.444	0.331	0.227

Table 3

Average Nusselt number

ϵ	P_r	10^3	10^4	10^5	10^6
0.625 (present study)	0.700	2.137	2.515	3.785	6.622
+ 0.625 (Ho et al., 1989)	0.700	2.272	3.207	4.482	6.894
0 (present study)	0.700	1.705	2.667	4.310	6.588
0 (Ho et al., 1989)	0.700	1.731	2.763	4.418	6.729
- 0.625 (present study)	0.700	2.394	3.096	4.371	6.806
- 0.625 (Ho et al., 1989)	0.700	2.048	2.610	3.911	6.390

RESULTS AND DISCUSSION

As previously stated, the primary goal of this research is to evaluate fluid flow and heat transfer characteristics at vibrating concentric and eccentric horizontal cylinders. Therefore, all numerical computations were completed for the Rayleigh number ($10^2 \leq Ra \leq 10^6$) based on the radius difference = (L: is the mean gap width = R_o - R_i), vibrational Rayleigh number $0 \leq$ Ravib $\leq 10^5$, non-dimensional vibrational frequencies (ϖ = 0, 100, 1000 &10000), and besides the influence of vibration, eccentricity reveals themselves as local flow and temperature field disturbances. For example, the concentric case with four eccentricities yielded results (ϵ = 0, ±0.625 & ±0.333), radii ratio $(\frac{Ro}{Ri}) = 2.6$ while preserving the gap width/diameter ratio $(\frac{L}{Di} = 0.8)$ for a fluid with (Pr = 0.7).

Flow and Temperature Fields

This section presents fluid and heat transfer properties represented by the streamlines and isotherms. The streamlines and temperature contoured when the inner was changed vertically within the outer cylinder for different Rayleigh numbers and various frequencies shedding on the inner cylinder.

Eccentricity's Influence (Effect of Inner Cylinder Position)

A computation with precise parameters of (Ra = 10^4, Ra_v = 10^5, ϖ = 1000) and contour plots of stream functions and isotherms are shown to visualize the flow evolution in Figures 7a and 7b. When the heated inner cylinder is in the concentric position ϵ = 0, Figure 7a (C), the streamlines and isotherms show that the hot flow tends to move upward due to thermal expansion along the vertical symmetry line. As the air impinges the cold wall of the outer cylinder, it becomes colder and denser; thus, it moves radially away from the cold wall and downward again. Thus, two similar recirculation air pockets are formed on the side of the vertical symmetry line with the center of the cylinders. The effect of the heated inner cylinder moving vertically upward to the center of the outer cylinder ϵ = (+0.625 and + 0.333) Figures 7a (D & E) presses air at the top, and vacant space is induced at the bottom. These two actions force air at the top region to flow to the bottom region. The forced convection due to the inner cylinder vibration affects the natural convection flow and thermal transport in the annulus. The astonishing vortex splitting as the vortex core is halved and bisected (closet position to the upper wall of the inner cylinder), the flow tends to separate by approaching cylinders at ϵ = +0.625 is depicted consecutively in Figure 7a (E). As the heated inner cylinder is moved vertically down to the center of the outer cylinder, the flow does not separate, and a center with large plumes occurs. Hence the pump is hot air toward the upper wall along the vertical symmetry line, as shown for the negative eccentric position (ϵ = -0.625 and -0.333). Figure 7a (A & B) illustrate that the

inner cylinder is located at the bottom region, the air at the bottom is pressed, and vacant space is induced at the top region, reversing the flow direction.

Figure 7(b) shows the isotherms in the annulus during the vibration for different inner cylinder positions at the same vibrational frequency $\varpi = 1000$. The inner cylinder in the concentric position $\epsilon = 0$ in Figure 7b (c) indicates a wide temperature zone at the top region. It is due to the buoyancy effect promoted by the changes in the mass density, and the reverse is noted in the bottom region. As the inner cylinder is on its way to moving upward $\epsilon = (+0.625$ and $+ 0.333)$ Figures 7b (D & E), the heat transfer between the inner and outer cylinder is affected by the movement of the inner cylinder. The isothermal lines are dense at the top region, showing high heat flow in this region. At the bottom region, the heat flow is dominated by conduction, making the heat transfer rate low. When the inner cylinder moves upward $\epsilon = +0.625$, the conduction region expands, reducing heat flow. At this instant, the heat transfer in the annulus is less than that of the concentric annulus case. At the negative eccentricity ($\epsilon = -0.333$) and - 0.625 Figures 7b (A & B), the heat transfer rate at the bottom region is extensively promoted by reducing the thermal boundary layer (thermal resistance). Also, the convection cell at the top region is expanded by strong convection, enhancing the heat flow in this region. When the eccentricity of the inner cylinder is minimal, the heat transfer from the inner cylinder to the outer cylinder reaches its maximum value.

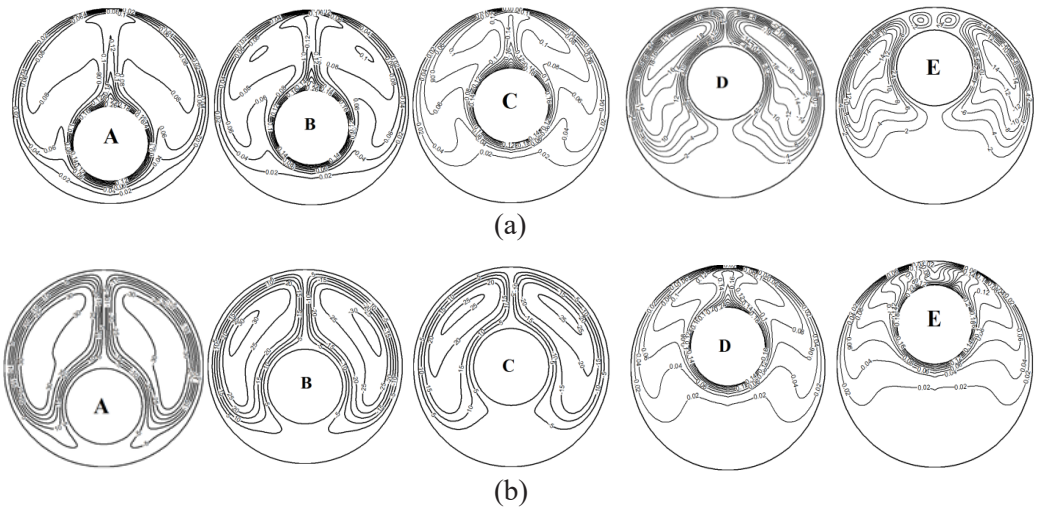

Figure 7. (a). Streamlines, (b). Isotherms; at $RaL = 10^4$, $Ra_v = 10^5$, vibrational frequency $\omega = 1000$, at different eccentricity (A) $\epsilon = -0.625$, (B) -0.333, (c) 0, (D) +0.333, (E) +0.625, respectively.

The Effect of Rayleigh's Number Ra_L. The effect of the Rayleigh number on the kinematic and thermal fields (streamlines and isotherms) are shown in Figures 8 and 9 for ($10^2 \leq Ra \leq 10^6$), $Ra_{vib} = 10^5$, $\varpi = 1000$, and ϵ = (-0.625 and + 0.625) from these results, and it can be seen that the flow is symmetrical concerning the medium vertical axis passing through the center of these cylinders. For each case, the flow over the inner cylinder creates a circulation zone on both sides of the cavity for all values of the Rayleigh number. The flow is organized in two main counter-rotating cells. The flow is organized into two central contour-rotating cells. The cell on the left rotates counterclockwise while the suitable cell rotates clockwise. It is due to the strength of buoyancy produced by the temperature gradient. According to these conditions, the fluid is raised on the side of the inner cylinder, leading to flow becoming fresh and denser in the outer cylinder. At (ϵ = +0.625), show that at low Ra = 10^2, 10^3, 10^4. The remarkable process of outer vortex splitting by increasing the Rayleigh number is sequentially observed in Figures 8a and b (A, B & C). As a result, the laminar convection is weak, and the values of the current function are shallow and almost similar. In these cases, the heat transfer is mainly by conduction. By increasing the Rayleigh number to $Ra = 10^5$ and then to 10^6, with (ϵ = +0.625), we are in a pseudo-conductive regime. The thermal transfers are, therefore, essentially conducive. The values of the current function appearing in Figures 8 and 9 are always small so that the conduction dominating flow region at the narrowest gap of the annuli becomes locally stagnant, continuously splitting the outer vortex core in the constricted region into two sub vortices rotating in the same direction. In the broader part of the eccentric annulus, the vortex current is slowed down, and the location of its core is upper at $Ra = 10^6$, as shown in Figures 8a and 8b (D & E). The convection eddy is relatively vigor and produces a clockwise symmetrical recirculation, unlike positive eccentricity (ϵ = +0.625), so the impact of the secondary flow cell at the top is reflected in the form of the isotherm. Increasing Rayleigh to 10^5 means a higher stream function absolute value causes an intensified internal convection eddy and a more excellent fluid motion; as the Rayleigh further increases to $Ra = 10^6$, the inner vortex grows and becomes more extensive than at $Ra = 10^5$, as shown in Figures 9a (D & E).

The effect of Rayleigh number as the inner cylinder at the bottom region ϵ = -0.625 the reverse demeanor is noticed in the bottom region as shown in Figures 9a and 9b. In the inner cylinder, the global flow joins near the bottom of the inner wall and connects with the inner wall's top, while secondary vortices over the top disappear and diminish. When the inner cylinder moves downward, more spaces between the hot inner cylinder and the top cold wall are secured, enhancing the buoyancy-induced convection. Thus, isotherms move upward, and more enormous plumes exist on the top of the inner cylinder, which increases the thermal gradient on the top of the annulus. As the form of the dominant flow at the upper half of the annulus, the recirculating eddies form there, so Rayleigh increases to 10^5, and the stagnant region under the heated inner cylinder decreases.

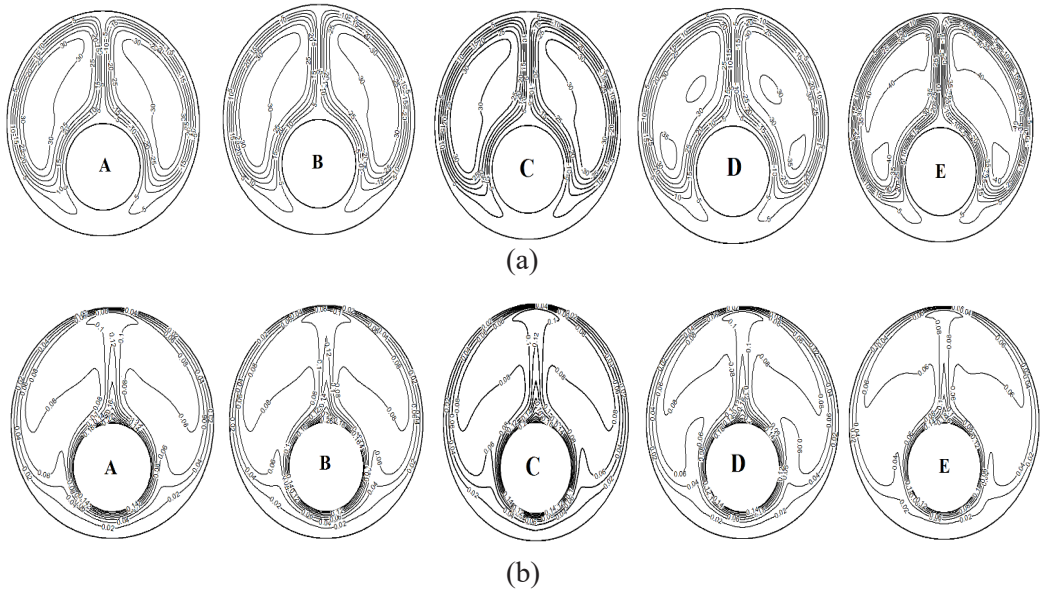

Figure 8. (a) Streamlines and (b) Isotherms of annuli of the eccentricity ϵ = -0.625 and ϵ = +0.625, respectively; vibrational frequency ϖ = 1000, Ra_{vib} = 10^5, $\frac{L}{Di} = 0.8$ at different *Ra* = (A)10^2, (B)10^3, (C)10^4, (D)10^5, (E)10^6.

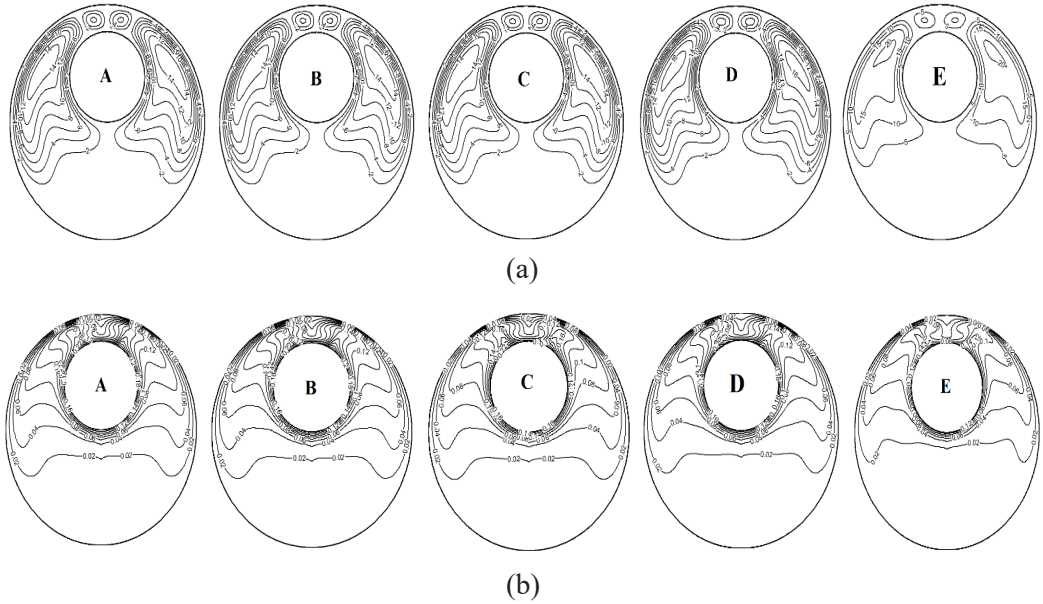

Figure 9. (a) Streamlines and (b) Isotherms of annuli of the eccentricity ϵ = *+0.625*; vibrational frequency, Ra_{vib} = 105, $\omega = 1000$, at different *Ra* = (A)10^2, (B)10^3, (C)10^4, (D)10^5, (E)10^6

Vibration Frequency's Influence

Figures 10 and 11 comparatively present the influence of vibrational frequency on the variations of streamlines and isotherms at $Ra = 10^4$, $Ra = 10^4$, $Ra_{vib} = 10^5$, ϵ = (-0.625, and + 0.625). The vibration frequency changed (ϖ = 0, 100, 1000 and 10000). Initially, the system is at a static case ($\varpi = 0$) without vibration. It is used for analysis and comparisons. In Figures 10a and 11a (B), the inner cylinder commences vibrating vertically, even at a low frequency (ϖ = 100). The influence of dynamic response on the fluid flow is extraordinary, as the thermal vibrational convection is weak at a moderate value $Ra = 10^4$. As the frequency increases to ($\varpi = 1000$) near the resonant frequency, it can be inferred that the fluid movement is becoming more apparent, and the variations in the streamlines and isotherms are quite different from those of static convection and previous circumstances.

Two outer counter-rotating eddies are formed at the vertical position ϵ = +0.625, strongly influencing the heat transfer. The vibration effect is more remarkable than when the vibrational frequency rises (ϖ = 10000). During the vibration of the inner cylinder, as it shifts upward and the fluid near the upper region of the cylinder will be pressed by the cylinder surfaces; on the other hand, the fluid near the lower region of the cylinder simultaneously replenishes the vacant space induced by the cylinder's movement due to the continuity law. A similar phenomenon occurs when the direction of movement of the inner cylinder changes, resulting in refilled empty spaces near the upper regions. As a result of internal cylinder vibration at the vertical position ϵ = +0.625, a tiny vortex appears at the top part of the cylinder. Due to isotherms distortion caused by vibration, some portion of the hot flow will be located inside the hot flow, discovered inside the cold fluid region, and lose their high temperature. As a result, the colder and, thus, denser fluids will descend. The colder fluids meet hot liquid again during their descent due to isotherms` distortion and will be heated again and cause an eddy appearance. As the cylinder oscillates, isotherms become distorted, and new vortices will come into sight. Cylinders` upward and downward movements give vortices appropriate to growth and ascent.

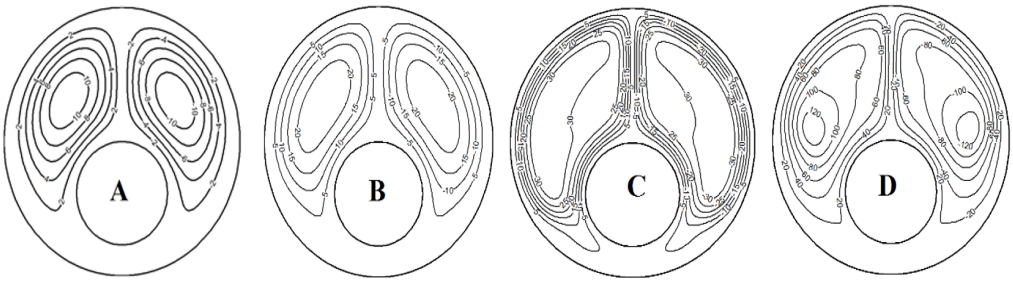

(a)

Figure 10. (a) Streamlines and (b) Isotherms of annuli of the eccentricity ϵ = -0.625; $Ra = 10^4$, $Ra_{vib} = 10^5$, ro/ri = 2.6, and $\frac{L}{Di} = 0.8$ but in different vibrational frequency

(b)

Figure 10. (Continue)

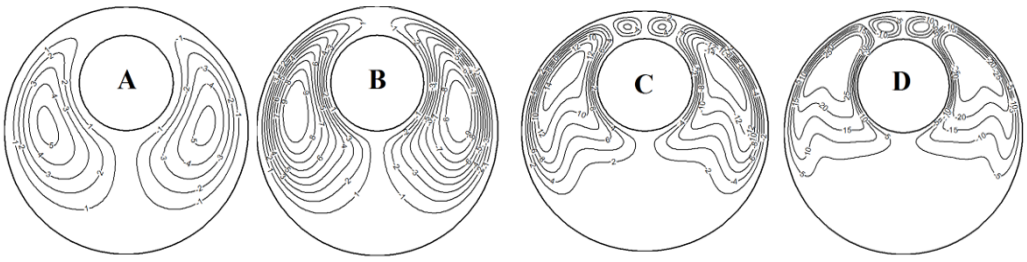

(a)

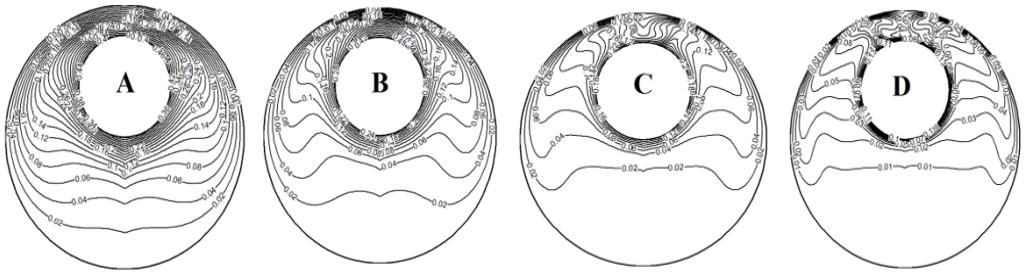

(b)

Figure 11. (a) Streamlines and (b) Isotherms of annuli of the eccentricity $\epsilon = +0.625$; $Ra = 10^4$, $Ra_{vib} = 10^5$, (ro/ri) = 2.6, $\frac{L}{Di} = 0.8$ but in different vibrational frequency (A) $\varpi = 0$, (B) $\varpi = 100$, (C) $\varpi = 1000$, and (D) $\varpi = 10000$.

Local Nusselt Number (Nu)

Effect of Eccentricity (Effect of Inner Cylinder Position). Figures 12a, 12b, and 12c show the distribution of the local Nusselt number at various angles along the circumference of the inner cylinders at $Ra = 10^4$, $0 \leq Ra_{vib} \leq 10^5$, ($\varpi = 1000$) and for different vertical inner cylinder locations with concentric an eccentric ϵ = (-0.625, -0.333, 0, +0.333 and +0.625). Because the stream and temperature patterns are found for cases ϵ = -0.333 almost similar at ϵ = -0.625 and ϵ = +0.333similar to the case at ϵ = +0.625, the results at ϵ = -0.333 and ϵ = +0.333 are not presented here for the sake of brevity. However, if there is any difference between those, it will be mentioned. The results for concentric ϵ = 0 and negative eccentric

ϵ = -0.625 geometry are qualitatively similar and will be discussed. The minimum *Nu* is seen at the top of the cylinder (ϕ = 180°), where the plume occurs and the isotherm contour coarsest. The maximum Nu is shown to be at (ϕ = 0°), where the temperature contours are densest due to the movement of the upward-directed cold fluid. (*Nu*)increases from the bottom of the (ϕ = 0°) to the top (ϕ = 180°) of the inner cylinder.

As Ra_{vib} increases, the angular variation of (*Nu*) becomes more pronounced such that the heat transport is highly concentrated in the upper half of the inner cylinder. The effect of positive eccentricity ϵ = +0.625 on *Nu* is quite different from the two cases described before, as depicted in Figure 12c. At the region from (ϕ = 0° to 120°), (Nu) behaved as two cases for the behavior ϵ = 0, and -0.625 as mentioned above. At (ϕ = 120°), the deflection of the Nusselt number is seen. This peculiar behavior is due to the existence of the secondary flow cell above the inner cylinder, which develops for $Ra_{vib} > 10^4$ convection and has a minor influence at the bottom of the annulus ϕ = 0°, where the boundary layer starts to develop and is still thin. On the contrary, at (ϕ > 150°), the minimum heat transfer rate shifts to the maximum, increasing the vibrational Rayleigh number. The maximum due to convection becomes pronounced when the vibrational Rayleigh number exceeds 10^4.

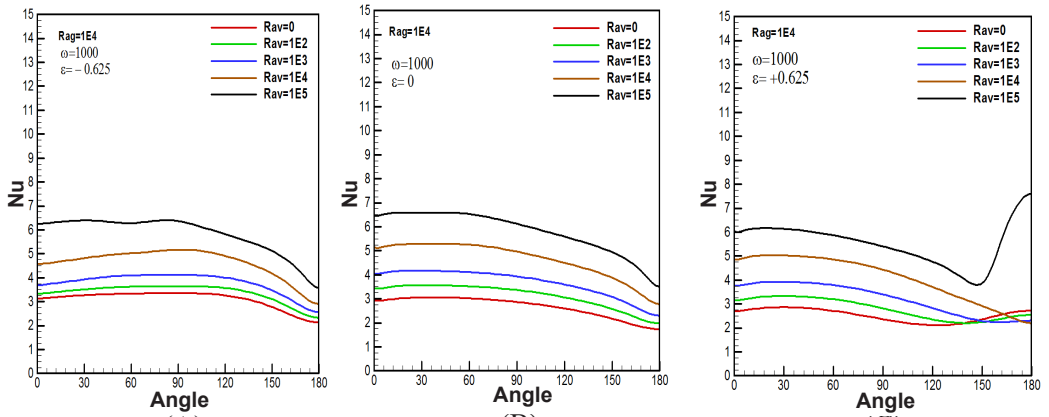

Figure 12. The local Nusselt number along the inner cylinder, $Ra = 10^4$, $Ra_{vib} = 10^5$ vibrational frequency ϖ = 1000, (ro/ri) = 2.6 but in different eccentricities (A) ϵ = -0.625, (B) ϵ = 0, and (D) ϵ = +0.625, respectively.

The Effect of Rayleigh Number *Ra*

The effect of Rayleigh number *Ra* on the local Nusselt number Nu with the circumferential position around the inner cylinder at various angles without and with the vibrational vibrated frequency (ϖ = 1000) at eccentricity ϵ = (-0.625 and +0.625) is plotted at Ra = (10^2, 10^3, 10^4, 10^5, and 10^6) with $0 \leq Ra_{vib} \leq 10^5$ at each value of *Ra* Figures 13 and 14 (A–E). As the inner cylinder at the bottom ϵ = -0.625, the Nu at $Ra = 10^2$, 10^3 and 10^4 does not change significantly and has an almost constant value for $0 \leq Ra_{vib} \leq 10^5$. Figures 13 and 14 show the proportional relation between the local Nusselt number and the vibrational Rayleigh

numbers, which increase as the Ra_{vib} increases at each Ra. It can be inferred that where the boundary layer starts to develop, heat transfer will become approximately without any remarkable variation. With increasing Rayleigh for each vibrational Rayleigh number $0 \leq Ra_{vib} \leq 10^5$, the local Nusselt numbers converge, close with each other, and increase rapidly, particularly at $Ra = 10^5$ and 10^6 — the optimal heat transfer rate at $Ra = 10^6$. The gradient of isotherms on the bottom wall increases rapidly when the inner cylinder keeps moving downward, and the gap between the inner cylinder and the bottom decreases, as shown in Figure 13. It may be ascribed to the secondary flow superimposed, leading to a higher heat transfer coefficient. As explained above from the streamlines and isotherms, at the positive vertical position $\epsilon = +0.625$, the Nu in the region $(0 \leq \phi \geq 90°)$ has a similar distribution to that at the inner cylinder at the bottom of the outer cylinder $\epsilon = -0.625$ is not significant for all different values of Rayleigh number. For all ranges of vibrational Rayleigh number, the symmetry on Nu is broken, and the deflection occurs, which causes a decrease in heat transfer rate at the angular location that deviates ($\phi > 90°$). On the contrary, as Rayleigh increases to $Ra = 10^5$ and 10^6, vibration enhances heat transfer and promotes breaking down the boundary layer. This improvement appears more pronounced at the high Rayleigh number.

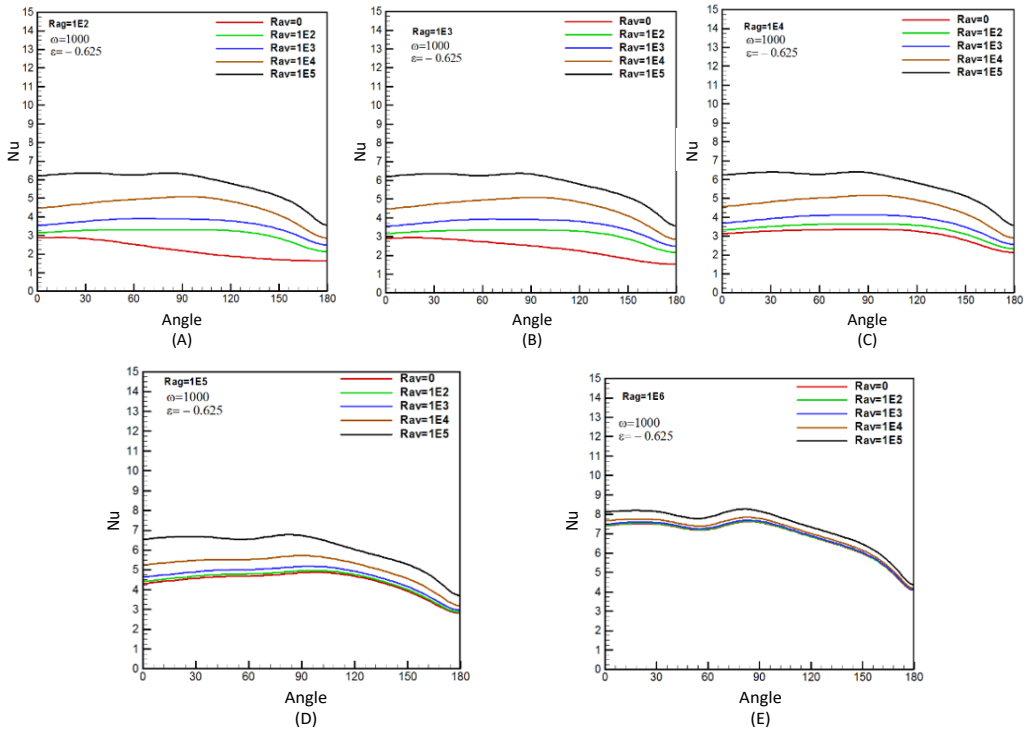

Figure 13. The local Nusselt number along the inner cylinder of annuli for the eccentricity $\epsilon = -0.62$; vibrational frequency $\varpi = 1000$, $0 \leq Ra_{vib} \leq 10^5$,at different Ra = (A)10^2, (B) 10^3, (C)10^4, (D)10^5, (E)10^6, respectively.

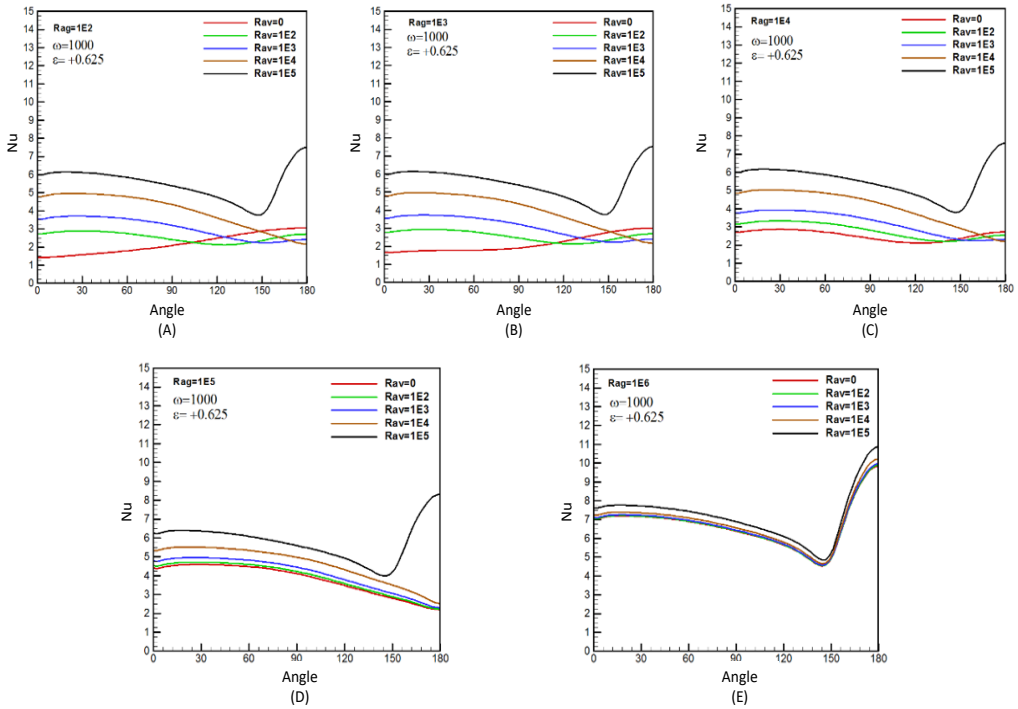

Figure 14. The local Nusselt number along the inner cylinder of annuli for the eccentricity ϵ = +0.625; vibrational frequency ϖ = 1000, $0 \leq Ra_{vib} \leq 105$, Pr = 0.7, $\frac{ro}{ri} = 2.6$ and $\frac{L}{Di} = 0.8$ at different Ra = (A)10^2, (B)10^3, (C)10^4, (D)10^5, (E)10^6, respectively.

The Effect of Vibrational Frequency

Figures 15 and 16 show the effect of vibrational frequency ϖ on the local Nusselt number Nu with the circumferential position around the inner cylinder at various angles without and with the vibration at the vibrational frequency ϖ = (0, 100, 1000, and 10000), eccentricity ϵ = (-0.625 and +0.625) is plotted at $Ra = 10^4$, $Ra_{vib} = 10^5$. As can be seen, a significant effect of the frequency of the inner cylinder. The values of the local Nusselt number increased as ϖ increased very rapidly, especially for high vibrated frequency (ϖ = 10000). The vibration effect appears more pronounced on the positive vertical position at ϵ = +0.625 as it breaks down the boundary layer and enhances the heat transfer rate. Regardless of the status of the vibrated inner cylinder, it was evident that the thermal boundary layer became distorted due to vibration. This disturbance of the thermal boundary layer augments the local Nusselt number and, thus, the average Nusselt number. Consequently, replenishment, caused by vibrations in the inner cylinder, can be explained by comparing it to the separation of boundary layers that reduces local Nusselt numbers. Meanwhile, pressing makes the hot surface contact the fresher and colder fluid. As a result, the local Nusselt number rises.

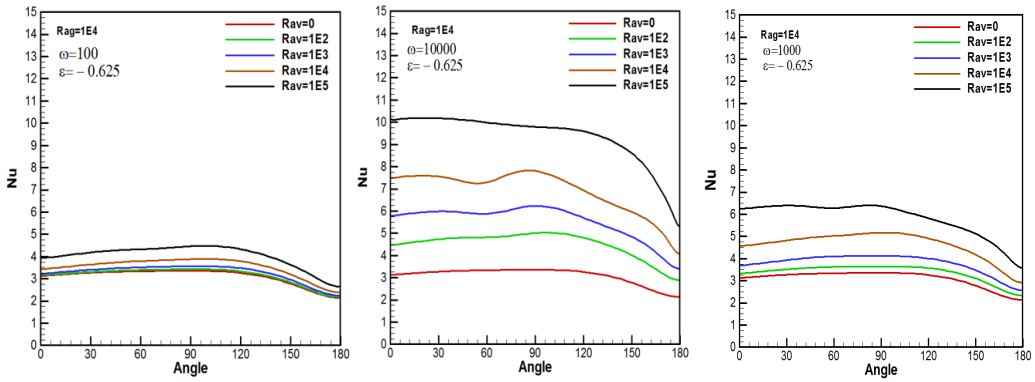

(A) (B) (C)

Figure 15. Local Nusselt number along the inner cylinder of annuli of the eccentricity ϵ = - 0.625, $Ra_L = 10^4$, $Ra_y = 10^5$ but in different vibrational frequencies (A) ϖ = 100, (B) ϖ = 1000, and (C) ϖ = 10000, respectively.

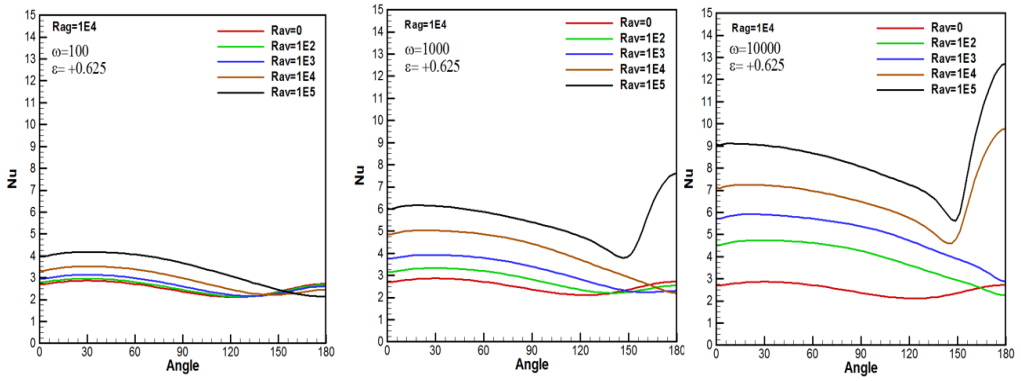

(A) (B) (C)

Figure 16. Local Nusselt numbers along the inner cylinder of annuli of the eccentricity ϵ = +0.625, $Ra_L = 10^4$, $Ra_y = 10^5$ but in different vibrational frequencies (A) ϖ = 100, (B) ϖ = 1000, and (C) ϖ = 10000, respectively.

Average Nusselt Number ($\overline{Nu}$)

The effect of vibrational frequency ϖ = (100, 1000, and 10000) on the eccentric configuration of the inner cylinder ϵ = (-0.625, -0.333, 0 , +0.333 and +0.625) at a range of the Rayleigh number Ra = (10^2, 10^3, 10^4, 10^5, and 10^6) on the average Nusselt number ($\overline{Nu}$) with a logarithmic vibrational Rayleigh number $0 \leq Ra_{vib} \leq 10^5$, is plotted in Figures 17 and 18 (A, B & C), respectively. In general, it is inferred from Figures 17 and 18 the following facts:

1. The average Nusselt number ($\overline{Nu}$) values increase with increasing Ra. Moreover, these values of ($\overline{Nu}$) converge and get closer to each other for all eccentric configurations at $Ra \geq 10^4$. The influence of the vibration reduces as the Rayleigh number increases $Ra \geq 10^5$.

2. The Nusselt number reaches its maximum value when the eccentricity of the inner cylinder is minimal (at a negative vertical position ϵ = -0.625), while the minimum is when the inner cylinder's eccentricity is maximal at (ϵ = +0.625). When the inner cylinder moves upward at (ϵ = +0.625), the conduction mode of the heat transfer zone at the bottom region is expanded, increasing the thermal resistance in the annulus. On the other hand, when the eccentricity of the inner cylinder reaches its minimum value at (ϵ = -0.625), the convection mode of the heat transfer zone at the top region is expanded, and the conduction is dominated mode zone at the bottom area is reduced. The two actions reduce the annulus's heat flow resistance (thermal boundary layer). Figure 19 shows the average Nusselt number **(** $\overline{Nu}$ **)** with a logarithmic vibrational Rayleigh number at different eccentricities.
3. Figures 17 and 18 show the effect of the vibrational frequency of the inner cylinder on the average Nusselt number ($\overline{Nu}$). Figures 17 and 18 show that when the inner cylinder is at the bottom region, the heat flow is greatly increased, but the heat flow is significantly decreased when the inner cylinder is at the top region. A high vibrational frequency of the inner cylinder further decreases the thermal resistance at the top region and increases the resistance at the bottom region even more.

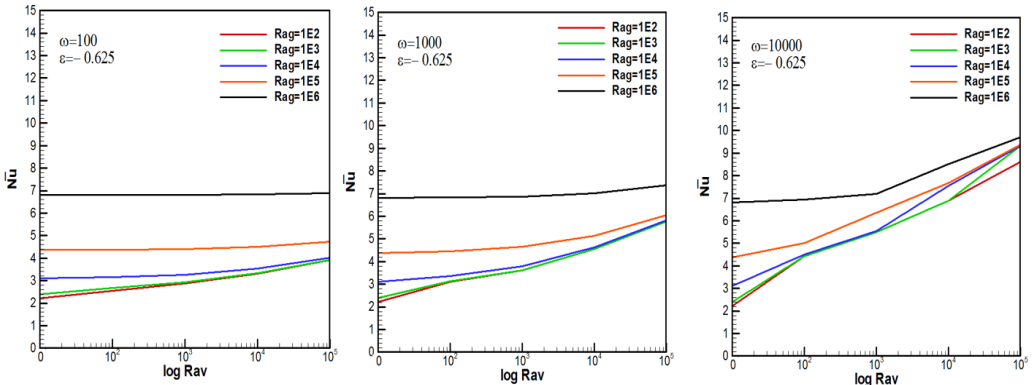

Figure 17. Average Nusselt numbers versus log Ra_v of anuuli of the eccentencity ϵ = -0.625; $10^2 \leq Ra \leq 10^6$, at (A) $\omega = 100$, (B) $\omega = 1000$, and (C) $\omega = 10000$, respectively.

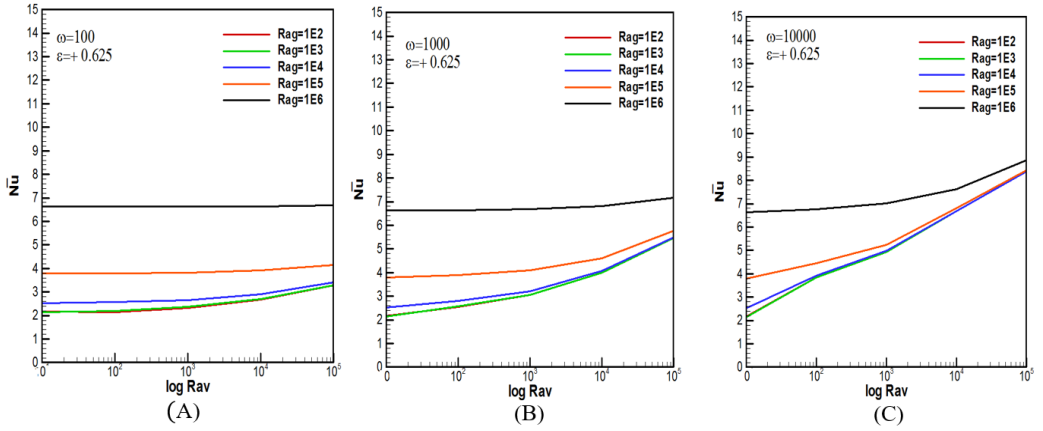

Figure 18. Average Nusselt numbers versus log Ra_v of anuuli of the eccentencity $\epsilon = +0.625$; $10^2 \leq Ra \leq 10^6$, (A) $\omega = 100$, (B) $\omega = 1000$, and (C) $\omega = 10000$, respectively.

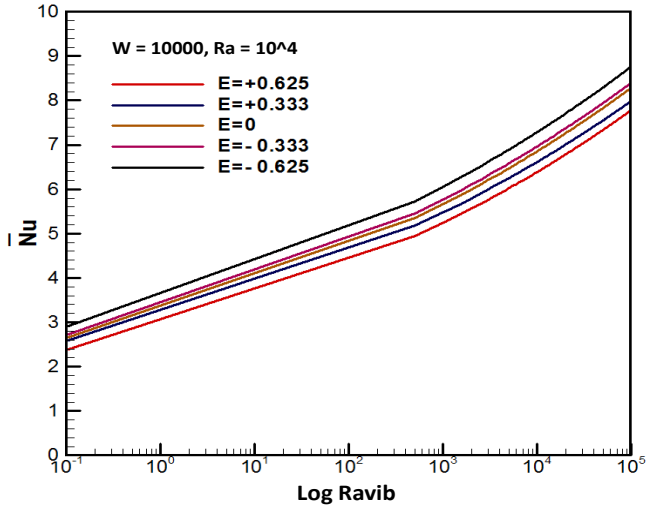

Figure 19. Average Nusselt numbers versus log Ra_v along the inner cylinder at $Ra = 10^4$, $0 \leq Ra_{vib} \leq 10^5$, vibrational frequency $\omega = 1000$, but in different eccentricity.

Table 4

Enhancement factor at $\epsilon = +0.625$

(a) ω=100

Ra_{vib}	$Ra = 10^2$	$Ra = 10^3$	$Ra = 10^4$	$Ra = 10^5$	$Ra = 10^6$
0	1	1	1	1.000	1.000
100	0.986	1.027	1.019	1.003	1.000
1000	1.065	1.103	1.058	1.0111	1.001

Table 4 *(Continue)*

(a) $\omega = 100$

Ra_{vib}	$Ra = 10^2$	$Ra = 10^3$	$Ra = 10^4$	$Ra = 10^5$	$Ra = 10^6$
0	1	1	1	1.000	1.000
100	0.986	1.027	1.019	1.003	1.000
1000	1.065	1.103	1.058	1.0111	1.001
10000	1.233	1.266	1.153	1.034	1.003
100000	1.508	1.541	1.353	1.098	1.010

(b) $\omega = 1000$

Ra_{vib}	$Ra = 10^2$	$Ra = 10^3$	$Ra = 10^4$	$Ra = 10^5$	$Ra = 10^6$
0	1	1	1	1	1
100	1.166	1.200	1.109	1.027	1.002
1000	1.401	1.433	1.272	1.081	1.009
10000	1.833	1.870	1.619	1.213	1.028
100000	2.515	2.561	2.188	1.526	1.081

(c) $\omega = 10000$

Ra_{vib}	$Ra = 10^2$	$Ra = 10^3$	$Ra = 10^4$	$Ra = 10^5$	$Ra = 10^6$
0	1	1	1	1	1
100	1.767	1.802	1.558	1.175	1.020
1000	2.275	2.312	1.980	1.382	1.058
10000	3.068	3.123	2.658	1.795	1.1521
100000	3.855	3.924	3.336	2.229	1.339

Table 5

Enhancement factor at $\epsilon = -0.625$

(a) $\omega = 100$

Ra_{vib}	$Ra = 10^2$	$Ra = 10^3$	$Ra = 10^4$	$Ra = 10^5$	$Ra = 10^6$
0	1	1	1	1	1
100	1.1498	1.114	1.018	1.002	1
1000	1.293	1.222	1.054	1.009	1.001
10000	1.488	1.389	1.138	1.027	1.003
100000	1.763	1.638	1.300	1.080	1.010

(b) $\omega = 1000$

Ra_{vib}	$Ra = 10^2$	$Ra = 10^3$	$Ra = 10^4$	$Ra = 10^5$	$Ra = 10^6$
0	1	1	1	1	1

Table 5 *(Continue)*

(b) ω = 1000					
Ra_{vib}	$Ra = 10^2$	$Ra = 10^3$	$Ra = 10^4$	$Ra = 10^5$	$Ra = 10^6$
0	1	1	1	1	1
100	1.397	1.307	1.089	1.021	1.002
1000	1.626	1.514	1.221	1.064	1.009
10000	2.050	1.903	1.494	1.173	1.028
100000	2.605	2.415	1.876	1.386	1.082
(c) ω= 10000					
Ra_{vib}	$Ra = 10^2$	$Ra = 10^3$	$Ra = 10^4$	$Ra = 10^5$	$Ra = 10^6$
0	1	1	1	1	1
100	1.995	1.851	1.452	1.144	1.019
1000	2.478	2.298	1.786	1.451	1.058
10000	3.103	2.881	2.227	1.755	1.251
100000	3.883	3.894	3.012	2.142	1.424

Enhancement Factor (E)

The enhancement factor for the heat transfer enhancement by an external oscillation is defined as Equation 23 (Kim et al., 2002).

$$E\left(\overline{Nu}\right)=\frac{\left(\overline{Nu}\right)_{p}}{\left(\overline{Nu}\right)_{s}} \quad [23]$$

Enhancement factor (E) is the average Nusselt number with a vibration ratio to the steady-state average Nusselt number. For each Rayleigh number, the percentage of increase in average Nusselt numbers for frequency is tabulated in Tables 3 and 4. It is shown that an increase in vibrational levels increases the enhancement factor but decreases with the fall of vibration levels.

Suggested Correlation

The present study calculates the relationship between the average Nusselt number ($\overline{Nu}$), Rayleigh number, and the vibrational Rayleigh number made using these parameters. Based on that and the inner cylinder position (eccentricity ratio) (ϵ), It was shown that the heat transfer equations for all the parts and vibrating the inner cylinder have the same following form (Equation 24):

$$\overline{Nu} = C * (Ra)^{A} * (Ra_{vib})^{B} \quad [24]$$

As a result, Table 6 lists all the constant values (A, B, and C) that appear in the equation for each position based on the search criteria. Figure 20 shows the relation between the Nusselt number calculated from the suggested equations ($\overline{Nu}\,c$) and the numerical one ($\overline{Nu}$). It is seen from Figure 20 that most of the numerical Nusselt number points fall within ± 13.7% of the predicted Nusselt number.

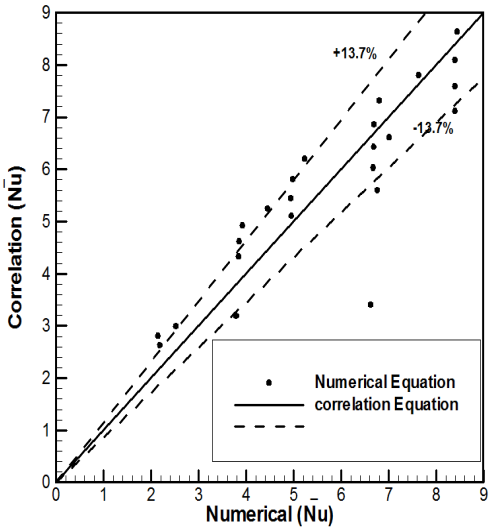

Table 6
Values of constants (A, B, and C)

ϵ	ϖ	A	B	C
	100	1.356	0.107	0.01
- 0.625	1000	2.076	0.067	0.03
	10000	2.076	0.03	0.071
	100	1.017	0.126	0.013
0	1000	1.86	0.069	0.038
	10000	2.959	0.026	0.065
	100	0.914	0.135	0.08
+ 0.625	1000	2.133	0.069	0.016
	10000	2.732	0.028	0.072

Figure 20. The predicted ($\overline{Nu}$) results

CONCLUSION

A study of vibration and natural heat convection in an annular circle was conducted between two horizontally centric and vertically eccentric long cylinders during gravity and vibration. The body-fitted coordinate system (BFCs) transformed the physical field into a rectangular domain. Finite-difference schemes approximate partial differential equations directly using iterative methods. From this study, it is concluded that:

1. It was revealed that vibration boosted the heat transfer rate at which the flow transitioned from laminar to turbulent. This turbulence occurred due to a disruption in the flow produced by the generated vibration. Many factors influence the Nusselt number, including the following:
   a. For each inner cylinder location, the Nusselt number increases as the vibration frequency increases.
   b. The heat transfer rate increased significantly for the negative vertical position at (ϵ = -0.625) for the same frequency and Rayleigh number compared with the positive vertical position (ϵ = +0.625).

c. The heat transfer rate decreased for the same inner cylinder position, and vibrational frequency as the Rayleigh number decreased in the annulus and significantly increased as the Rayleigh number increased.

2. The Rayleigh number, vibrational number, frequency, and inner cylinder locations were all associated with the average Nusselt number.

ACKNOWLEDGEMENT

The authors appreciate the cooperation of the University of Technology/Iraq in completing this work.

NOMENCLATURE

Parameter	Symbol
Di, Do	Inner and outer cylinder diameter (m)
e	Eccentricity(m)
ϵ	Dimensionless eccentricity = $\frac{e}{L}$
g	Gravitational acceleration $\left(\frac{m}{s^2}\right)$
L	The gap width(radius difference) = (Ro-Ri) m
h	Heat transfer coefficient W/m^2.K
k	Thermal conductivity(W/m.°C)
J	Jacobian of coordinate transformation
U, V	Dimensionless horizontal and vertical components of velocity
Nu, Nu	Local and average Nusselt number
Pr	Prandtle number $(\frac{\vartheta}{\alpha})$
q``	Heat flux $\left(\frac{W}{m^2}\right)$
Gr	Grashof number ($g\beta qL^4/K\vartheta^2$)
Ra_L	Rayleigh number ($g\beta qL^4/K\vartheta^2$)Pr
Gr_{vib}	Vibrational Grashof number $= \frac{1}{2}\left[\frac{\rho^2(b\Omega)\beta q" L^2}{K\,\mu^2}\right]^2$
Ra_{vib}	Vibrational Rayleigh number $(\frac{1}{2}[\rho^2(b\Omega)\beta \mathrm{q}" L^2/K\,\mu^2]^2 \mathrm{Pr})$
θ	Dimensionless temperature $(\frac{(T-T_c)K}{\mathrm{q}"L})$ in the case of CHF
(ξ, η)	Bipolar coordinate in the computational domain

REFERENCES

Alawadhi, E. M. (2008). Natural convection flow in a horizontal annulus with an oscillating inner cylinder using Lagrangian–Eulerian kinematics. *Computers & Fluids*, *37*, 1253-1261.

Al-Azzawi, M. M., Abdullah, A. R., Majel, B. M., & Habeeb, L. J. (2021). Experimental investigation of the effect of forced vibration on natural convection heat transfer in a concentric vertical cylinder. *Journal of Mechanical Engineering Research and Developments*, *44*(3), 56-65.

Ali, M., Rad, M. M., Nuhait, A., Almuzaiqer, R., Alimoradi, A., & Tlili, I. (2020). New equations for Nusselt number and friction factor of the annulus side of the conically coiled tubes in tube heat exchangers. *Applied Thermal Engineering*, *164*, Article 114545. https://doi.org/10.1016/j.applthermaleng.2019.114545

Bouzerzour, A., Tayebi, T., Chamkha, A. J., & Djezzar, M. (2020). Numerical investigation of natural convection nanofluid flow in an annular space between confocal elliptic cylinders at various geometrical orientations. *Computational Thermal Sciences: An International Journal*, *12*(2), 99-114. https://doi.org/10.1615/computthermalscien.2020026938

Fu, W. S., & Huang, C. P. (2006). Effects of a vibrational heat surface on natural convection in a vertical channel flow. *International Journal of Heat and Mass Transfer*, *49*(7-8), 1340-1349. https://doi.org/10.1016/j.ijheatmasstransfer.2005.10.028

Ho, C. J., Lin, Y. H., & Chen, T. C., (1989). A numerical study of natural convection in concentric and eccentric horizontal cylindrical annuli with mixed boundary conditions. *International Journal of Heat and Fluid Flow*, *10*(1), 40-47. https://doi.org/10.1016/0142-727X(89)90053-2

Hosseinian, A., Meghdadi I. A. H., & Shirani, E. (2018). Experimental investigation of surface vibration effects on increasing the stability and heat transfer coefficient of MWCNTs-water nanofluid in a flexible double pipe heat exchanger. *Experimental Thermal and Fluid Science*, *90*, 275-285. https://doi.org/10.1016/j.expthermflusci.2017.09.018

Imtiaz, H., & Mahfouz, F. M. (2017). Conjugated conduction-free convection heat transfer in an annulus heated at either constant wall temperature or constant heat flux. *Journal of Engineering and Technology*, *36*(2), 273-288. https://doi.org/10.22581/muet1982.1702.06

Kim, S. K., Kim, S. Y., & Choi, Y. D. (2002). Resonance of natural convection in a side heated enclosure with a mechanically oscillating bottom wall. *International Journal of Heat and Mass Transfer*, *45*(15), 3155-3162. https://doi.org/10.1016/S0017-9310(02)00030-3

Kuehn, T. H., & Coldstein., R. J. (1976). An experimental and theoretical study of natural convection in the annulus between horizontal concentric cylinders. *Journal of Fluid mechanics*, *74*(4), 695-719. https://doi.org/10.1017/S0022112076002012

Kuehn, T. H., & Goldstein, R. J. (1978). An experimental study of natural convection heat transfer in concentric and eccentric horizontal cylindrical annuli. *Journal of Heat and Mass Transfer*, *100*(4), 635-640. https://doi.org/10.1115/1.3450869

Liu, W., Yang, Z., Zhang, B., & Lv, P. (2017). Experimental study on the effects of mechanical vibration on the heat transfer characteristics of tubular laminar flow. *International Journal of Heat and Mass Transfer*, *115*, 169-179. https://doi.org/10.1016/j.ijheatmasstransfer.2017.07.025

Mahfouz, F. M. (2012). Heat convection within an eccentric annulus heated at either constant wall temperature or constant heat flux. *Journal of Heat Transfer*, *134*(8), Article 082502. https://doi.org/10.1115/1.4006170

Mahian, O., Pop, I., Sahin, A. Z., Oztop, H. F., & Wongwises, S. (2013). Irreversibility analysis of a vertical annulus using TiO_2/water nanofluid with MHD flow effects. *International Journal of Heat and Mass Transfer*, *64*, 671-679. https://doi.org/10.1016/j.ijheatmasstransfer.2013.05.001

Nasrat, K. M., Hameed, D. L., & Sadiq, E. A. (2019). The effect of transverse vibration on the natural convection heat transfer in a rectangular enclosure. *International Journal of Mechanical Engineering and Technology, 10*(6), 266-277.

Projahn, U., Rieger, H., & Beer, H. (1981). Numerical analysis of laminar natural convection between concentric and eccentric cylinders. *Numerical Heat Transfer*, *4*(2), 131-146. https://doi.org/10.1080/01495728108961783

Sarhan, A. R., Karim, M. R., Kadhim, Z. K., & Naser, J. (2019). Experimental investigation on the effect of vertical vibration on thermal performances of rectangular flat plate. *Experimental Thermal and Fluid Science, 101*, 231-240. https://doi.org/10.1016/j.expthermflusci.2018.10.024

Shahsavar, A., Moradi, M., & Bahiraei, M. (2018). Heat transfer and entropy generation optimization for flow of a non-Newtonian hybrid nanofluid containing coated CNT/Fe_3O_4 nanoparticles in a concentric annulus. *Journal of the Taiwan Institute of Chemical Engineers*, *84*, 28-40. https://doi.org/10.1016/j.jtice.2017.12.029

Shokouhmand, H., Abadi, S. M. A. N. R., & Jafari, A. (2011). The effect of the horizontal vibrations on natural heat transfer from an isothermal array of cylinders. *International Journal of Mechanics and Materials in Design*, *7*(4), 313-326. https://doi.org/10.1007/s10999-011-9170-6

Tayebi, T., & Chamkha, A. J. (2021). Analysis of the effects of local thermal non-equilibrium (LTNE) on thermo-natural convection in an elliptical annular space separated by a nanofluid-saturated porous sleeve. *International Communications in Heat and Mass Transfer*, *129*, Article 105725. https://doi.org/10.1016/j.icheatmasstransfer.2021.105725

Tayebi, T., Chamkha, A. J., Melaibari, A. A., & Raouache, E. (2021). Effect of internal heat generation or absorption on conjugate thermal-free convection of a suspension of hybrid nanofluid in a partitioned circular annulus. *Communications in Heat and Mass Transfe*r, *126*, Article 105397. https://doi.org/10.1016/j.icheatmasstransfer.2021.105397

Tayebi, T., Chamkha, A. J., Öztop, H. F., & Bouzeroura, L. (2022). Local thermal non-equilibrium (LTNE) effects on thermal-free convection in a nanofluid-saturated horizontal elliptical non-Darcian porous annulus. *Mathematics and Computers in Simulation*, *194*, 124-140. https://doi.org/10.1016/j.matcom.2021.11.011

Tayebi, T., Djezzar, M., Bouzerzour, A., Azzouz, K., & Khan, Z. H. (2016). Numerical Simulation of Natural Convection of Water Based Nanofluids in Horizontal Eccentric Cylindrical Annuli. *Journal of Nanofluids*, *5*(2), 253-263. https://doi.org/10.1166/jon.2016.1211

Tayebi, T., Öztop, H. F., & Chamkha, A. J. (2021). MHD natural convection of a CNT-based nanofluid-filled annular circular enclosure with inner heat-generating solid cylinder. *The European Physical Journal Plus*, *136*(2), Article 150. https://doi.org/10.1140/epjp/s13360-021-01106-7

Thompson, J., F., Thames, F. C., & Mastin, C. W. (1974). Automatic numerical generation of body-fitted curvilinear coordinate system for fields containing any number of arbitrary two-dimensional bodies. *Journal of Computational Physics*, *15*(3), 299-319.

Wang, B. F., Zhou, Q., & Sun, C. (2020). *Vibration-Induced Boundary-Layer Destabilization Achieves Massive Heat-Transport Enhancement*. *Science Advances*, *6*(21). https://doi.org/10.1126/sciadv.aaz8239

Pertanika J. Sci. & Technol. 31 (3): 1587 - 1603 (2023)

PERTANIKA JOURNALS

SCIENCE & TECHNOLOGY

Journal homepage: http://www.pertanika.upm.edu.my/

An Alternative Count Distribution for Modeling Dispersed Observations

Ademola Abiodun Adetunji[1,2] and Shamsul Rijal Muhammad Sabri[1]*

[1]School of Mathematical Sciences, Universiti Sains Malaysia, 11800 USM, Penang, Malaysia
[2]Department of Statistics, Federal Polytechnic, Ile-Oluji, Ondo 351, Nigeria

ABSTRACT

In most cases, count data have higher variances than means; hence using the Poisson distribution to model such observations is misleading because of the equality of the Poisson mean and variance. This study proposes a new two-parameter mixed Poisson distribution for modeling dispersed count observations. The exponential distribution is transmuted to obtain a new mixing distribution for the new proposition. Different moment-based mathematical properties of the new proposition are obtained. Applications using dispersed count observations with excess zero are made. Comparisons with related distributions for modeling dispersed observation reveal that the new distribution performs creditably well.

Keywords: Count observations, cubic rank transmutation, mixed Poisson distribution

INTRODUCTION

The classical Poisson distribution is widely utilized for modeling count data. However, since the distribution assumes equi-dispersion (variance equals mean), its general applicability is limited (Ong et al., 2021). There is model misspecification if the Poisson distribution is assumed for heterogeneous data (Asamoah, 2016) since count observations are often dispersed (Adetunji & Sabri, 2021; Omari et al., 2018). Several techniques have been developed in the literature to model over-dispersed observations (Bhati et al., 2015; Das et al., 2018; Sankaran, 1970; Zakerzadeh & Dolati, 2009). Among these diverse techniques is the mixed Poisson distribution, first proposed in the early 20th century (Greenwood & Yule, 1920). The technique is based on the assumption

ARTICLE INFO

Article history:
Received: 02 July 2022
Accepted: 05 October 2022
Published: 07 April 2023

DOI: https://doi.org/10.47836/pjst.31.3.25

E-mail addresses:
adecap4u@gmail.com (Ademola Abiodun Adetunji)
rijal@usm.my (Shamsul Rijal Muhammad Sabri)
*Corresponding author

ISSN: 0128-7680
e-ISSN: 2231-8526

© Universiti Putra Malaysia Press

that there is an inherent fluctuation in the parameter of the Poisson distribution, and hence a continuous distribution is assumed for the parameter. To this end, several mixing distributions have been introduced to obtain mixed Poisson distributions. In most cases, the mixing distributions arise from the exponential distribution paradigm. Karlis and Xekalaki (2005) provide a detailed survey on the properties of mixed Poisson distribution, while Ong et al. (2021) provide recent research on the distribution.

The classical exponential distribution is suitable when the system for its application assumes a constant failure rate. This limitation has motivated researchers to improve its flexibility to model systems with diverse hazard rates. It is often achieved by adding an extra shape parameter (compounding the classical form) using different generalization techniques (Karina et al., 2019). Applications of compounded exponential distributions in reliability theory pervade almost all works of life, including but not limited to economic, reliability, environmental, industrial, and engineering spaces (Aguilar et al., 2019; Mohammed et al., 2015; Rasekhi et al., 2017).

Mixture distributions offer flexibility in modeling observations (Karlis & Xekalaki, 2005). This study uses the one-parameter cubic rank transmutation map (Al-kadim, 2018) to compound the exponential distribution to obtain a new mixing distribution. The obtained mixing distribution is then used to obtain a new mixed Poisson distribution. Karlis and Xekalaki (2005) provide some properties of mixed Poisson distributions.

MATERIALS AND METHOD

Cubic Rank Transmuted Exponential Distribution

The distribution function of a continuous random variable X that follows an exponential distribution with scale parameter α is given as in Equation 1:

$$G_x = 1 - e^{-\alpha x}, \qquad \alpha > 0 \tag{1}$$

Given G_x as in Equation 1, the distribution function of the Cubic Rank Transmutation (CRT) map due to Al-kadim (2018) with an extra shape parameter β is given as in Equation 2:

$$F(x) = (1+\beta)G_x - 2\beta G_x^2 + \beta G_x^3, \qquad -1 \le \beta \le 1 \tag{2}$$

Hence, the Cubic Rank Transmuted Exponential Distribution (CRTED) is obtained by inserting Equation 1 into Equation 2. Therefore, the CDF and PDF of the CRTED using the transmutation map of Al-kadim (2018) are obtained as in Equations 3 and 4:

$$F_x = 1 - e^{-\alpha x} + \beta e^{-2\alpha x} - \beta e^{-3\alpha x}, \qquad -1 \le \beta \le 1; \alpha > 0 \tag{3}$$

$$f_x = \alpha e^{-\alpha x}(1 - 2\beta e^{-\alpha x} + 3\beta e^{-2\alpha x}), \qquad -1 \leq \beta \leq 1; \alpha > 0 \quad [4]$$

When the extra parameter assumes zero ($\beta = 0$), the CRTED becomes the exponential distribution. The corresponding survival and hazard rate functions (HRF) are obtained as in Equations 5 and 6:

$$S_x = e^{-\alpha x} - \beta e^{-2\alpha x} + \beta e^{-3\alpha x} \quad [5]$$

$$h_x = \frac{\alpha(1 - 2\beta e^{-\alpha x} + 3\beta e^{-2\alpha x})}{1 - \beta e^{-\alpha x} + \beta e^{-2\alpha x}} \quad [6]$$

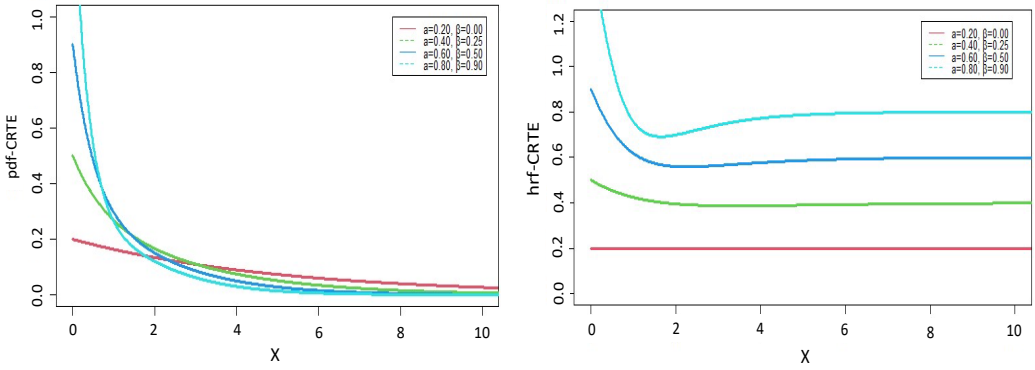

Figure 1. Shapes of the PDF and HRF of the CRTED

Figure 1 shows that the PDF of the CRTED is monotonically decreasing for different parameter combinations. Except when the CRTED becomes the exponential distribution ($\beta = 0$), the HRF plot has an inverted J-shape.

Mathematical Properties of the CTRED

Proposition 1: If a random variable X has a CRTED, the rth moment is defined as in Equation 7:

$$E(x^r) = \left(1 - \frac{\beta}{2^r} + \frac{\beta}{3^r}\right)\frac{r!}{\alpha^r} \quad [7]$$

Proof:

$$E(x^r) = \int_0^\infty x^r f_x \, dx$$

$$= \int_0^{\infty} x^r \left(\alpha e^{-\alpha x} - 2\alpha\beta e^{-2\alpha x} + 3\alpha\beta e^{-3\alpha x}\right) dx$$

$$= \alpha \int_0^{\infty} x^r e^{-\alpha x}\, dx - 2\alpha\beta \int_0^{\infty} x^r e^{-2\alpha x}\, dx + 3\alpha\beta \int_0^{\infty} x^r e^{-3\alpha x}\, dx$$

$$= \frac{r!}{\alpha^r} - \frac{\beta r!}{(2\alpha)^r} + \frac{\beta r!}{(3\alpha)^r}$$

$$= \left(1 - \frac{\beta}{2^r} + \frac{\beta}{3^r}\right)\frac{r!}{\alpha^r}$$

Proposition 2: If a random variable *X* has a CRTED, the Moment Generating Function (MGF) is obtained as in Equation 8:

$$E(e^{tx}) = \frac{\alpha}{\alpha - t} - \frac{2\alpha\beta}{2\alpha - t} + \frac{3\alpha\beta}{3\alpha - t} \quad [8]$$

Proof:

$$E(e^{tx}) = \int_0^{\infty} e^{tx} f_x\, dx$$

$$= \int_0^{\infty} e^{tx} \left(\alpha e^{-\alpha x} - 2\alpha\beta e^{-2\alpha x} + 3\alpha\beta e^{-3\alpha x}\right) dx$$

$$= \int_0^{\infty} \alpha e^{-(\alpha - t)x} - 2\alpha\beta e^{-(2\alpha - t)x} + 3\alpha\beta e^{-(3\alpha - t)x}\, dx$$

$$= \alpha \int_0^{\infty} e^{-(\alpha - t)x}\, dx - 2\alpha\beta \int_0^{\infty} e^{-(2\alpha - t)x}\, dx + 3\alpha\beta \int_0^{\infty} e^{-(3\alpha - t)x}\, dx$$

$$= \frac{\alpha}{\alpha - t} - \frac{2\alpha\beta}{2\alpha - t} + \frac{3\alpha\beta}{3\alpha - t}$$

Hence, the mean and variance of CRTED are as in Equations 9 and 10:

$$E(X) = \frac{6 - \beta}{6\alpha} \quad [9]$$

$$Var(X) = \frac{36 + 2\beta - \beta^2}{36\alpha^2} \quad [10]$$

Mixed Poisson CRTED

Proposition 3: If a conditional random variable $N|X \sim Poisson\ (X)$ is such that X ~ CRTED (α, β), the PMF of the unconditional random variable N has a mixed Poisson-CRTED if its PMF is defined as Equation 11:

$$f_n = \frac{\alpha}{(1+\alpha)^{n+1}} - \frac{2\alpha\beta}{(1+2\alpha)^{n+1}} + \frac{3\alpha\beta}{(1+3\alpha)^{n+1}} \quad [11]$$

Proof:

$$f_n = \int_0^\infty \frac{x^n e^{-x}}{n!} . \alpha e^{-\alpha x}(1 - 2\beta e^{-\alpha x} + 3\beta e^{-2\alpha x})dx$$

$$= \frac{\alpha}{n!}\int_0^\infty x^n e^{-(1+\alpha)x}(1 - 2\beta e^{-\alpha x} + 3\beta e^{-2\alpha x})dx$$

$$= \frac{\alpha}{n!}\int_0^\infty \left(x^n e^{-(1+\alpha)x} - 2\beta x^n e^{-(1+2\alpha)x} + 3\beta x^n e^{-(1+3\alpha)x}\right)dx$$

$$= \frac{\alpha}{n!}\int_0^\infty \left(\frac{1}{(1+\alpha)^{n+1}}u^n e^{-u} - \frac{2\beta}{(1+2\alpha)^{n+1}}u^n e^{-u} + \frac{3\beta}{(1+3\alpha)^{n+1}}u^n e^{-u}\right)du$$

$$= \frac{\alpha}{(1+\alpha)^{n+1}} - \frac{2\alpha\beta}{(1+2\alpha)^{n+1}} + \frac{3\alpha\beta}{(1+3\alpha)^{n+1}}$$

Special Case: Equation 11 becomes the mixed Poisson Exponential Distribution when the shape parameter $\beta = 0$

Generally, mixed Poisson distributions assign more probability to 0 observations (Shaked, 1980). As shown in Figure 2, the shapes of the PMF of the new distribution are unimodal (Holgate, 1970), with the ability to model data with excess zero. The unimodality exhibited by a mixed Poisson distribution is an attribute derived from the mixing distribution (Karlis & Xekalaki, 2005).

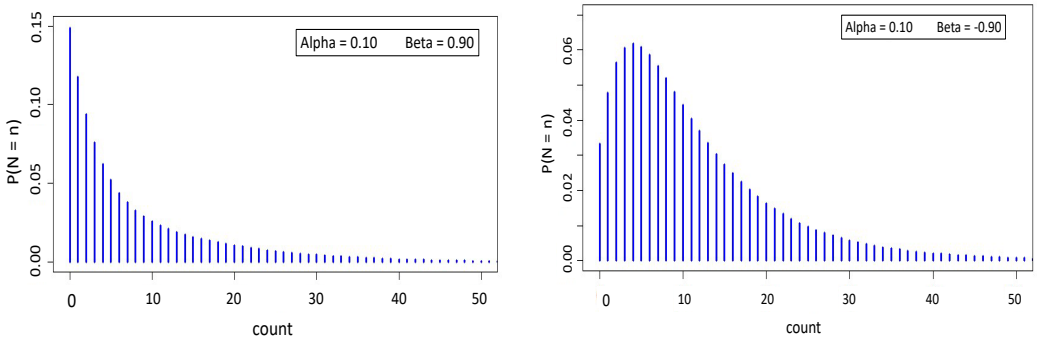

Figure 2. Shapes of the PMF of the mixed Poisson CRTED

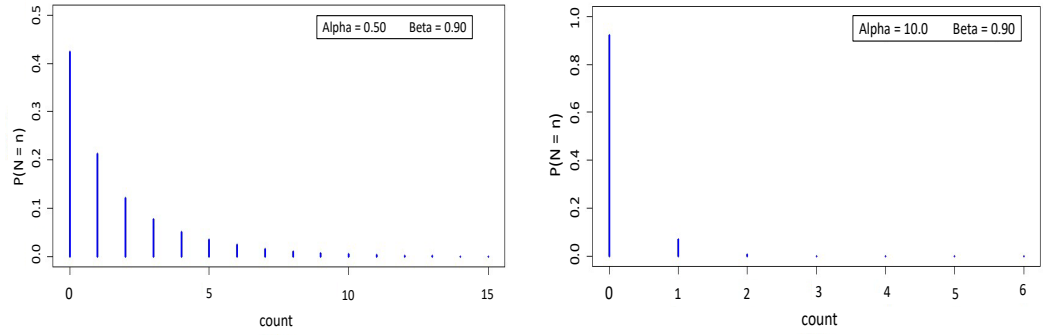

Figure 2. (Continue)

The Proof of Legitimacy of the PMF of Mixed Poisson CRTED

It is shown by proving that sum over f_n is equal to 1, i.e., $\sum_{n=0}^{\infty} f_n = 1$

Therefore,

$$\sum_{n=0}^{\infty}\left(\frac{\alpha}{(1+\alpha)^{n+1}}-\frac{2\alpha\beta}{(1+2\alpha)^{n+1}}+\frac{3\alpha\beta}{(1+3\alpha)^{n+1}}\right)$$

$$=\alpha\sum_{n=0}^{\infty}\frac{1}{(1+\alpha)^{n+1}}-2\alpha\beta\sum_{n=0}^{\infty}\frac{1}{(1+2\alpha)^{n+1}}+3\alpha\beta\sum_{n=0}^{\infty}\frac{1}{(1+3\alpha)^{n+1}}$$

$$=\alpha\left(\frac{1}{(1+\alpha)^1}+\cdots\right)-2\alpha\beta\left(\frac{1}{(1+2\alpha)^1}+\cdots\right)+3\alpha\beta\left(\frac{1}{(1+3\alpha)^1}+\cdots\right)$$

$$=\alpha\left(\frac{1}{\alpha}\right)-2\alpha\beta\left(\frac{1}{2\alpha}\right)+3\alpha\beta\left(\frac{1}{3\alpha}\right)=1-\beta+\beta=1$$

THE CDF OF THE MIXED POISSON CRTED

Proposition 4: If a discrete random variable *N* has the mixed Poisson CRTED, the distribution function is obtained as in Equation 12:

$$F_n=1-\left(\frac{1}{(1+\alpha)^{n+1}}-\frac{\beta}{(1+2\alpha)^{n+1}}+\frac{\beta}{(1+3\alpha)^{n+1}}\right) \quad [12]$$

Proof:

$$F_n=P(N\le n)$$

$$=1-P(N>n)$$

$$=1-\sum_{k=n+1}^{\infty}P_k$$

$$=1-\sum_{k=n+1}^{\infty}\left(\frac{\alpha}{(1+\alpha)^{k+1}}-\frac{2\alpha\beta}{(1+2\alpha)^{k+1}}+\frac{3\alpha\beta}{(1+3\alpha)^{k+1}}\right)$$

$$= 1 - \left(\sum_{k=n+1}^{\infty} \frac{\alpha}{(1+\alpha)^{k+1}} - \sum_{k=n+1}^{\infty} \frac{2\alpha\beta}{(1+2\alpha)^{k+1}} + \sum_{k=n+1}^{\infty} \frac{3\alpha\beta}{(1+3\alpha)^{k+1}} \right)$$

$$= 1 - \left(\frac{1}{(1+\alpha)^{n+1}} - \frac{\beta}{(1+2\alpha)^{n+1}} + \frac{\beta}{(1+3\alpha)^{n+1}} \right)$$

Mathematical Properties of the Mixed Poisson CRTED

1. According to Willmot (1990), if a random variable ***N*** has a mixed Poisson distribution and the distribution function of its mixing distribution is denoted with F_x, the following results hold:

a. $$P(N \leq n) = \int_0^{\infty} \frac{x^n e^{-x}}{n!} F_x \, dx$$

$$= \int_0^{\infty} \frac{x^n e^{-x}}{n!} (1 - e^{-\alpha x} + \beta e^{-2\alpha x} - \beta e^{-3\alpha x}) \, dx$$

$$= \frac{1}{n!} \left(\int_0^{\infty} x^n e^{-x} \, dx - \int_0^{\infty} x^n e^{-(1+\alpha)x} \, dx + \beta \int_0^{\infty} x^n e^{-(1+2\alpha)x} \, dx - \beta \int_0^{\infty} x^n e^{-(1+3\alpha)x} \, dx \right)$$

$$= 1 - \frac{1}{(1+\alpha)^{n+1}} + \frac{\beta}{(1+2\alpha)^{n+1}} - \frac{\beta}{(1+3\alpha)^{n+1}}$$

It is equivalent to the CDF of ***N*** as obtained in Equation 12

b. $$P(N > n) = \int_0^{\infty} \frac{x^n e^{-x}}{n!} [1 - F_x] \, dx$$

$$= \int_0^{\infty} \frac{x^n e^{-x}}{n!} (e^{-\alpha x} - \beta e^{-2\alpha x} + \beta e^{-3\alpha x}) \, dx$$

$$= \frac{1}{n!} \left(\int_0^{\infty} x^n e^{-(1+\alpha)x} \, dx - \int_0^{\infty} \beta x^n e^{-(1+2\alpha)x} \, dx + \int_0^{\infty} \beta x^n e^{-(1+3\alpha)x} \, dx \right)$$

$$= \frac{1}{(1+\alpha)^{n+1}} - \frac{\beta}{(1+2\alpha)^{n+1}} + \frac{\beta}{(1+3\alpha)^{n+1}}$$

2. **Probability Generating Function (PGF)**: Let $\pi(x)$ denotes the PDF of the mixing distribution; Karlis and Xekalaki (2005) defined the PGF of a mixed Poisson random variable N as:

$$P_n(z) = \int_0^{\infty} e^{x(z-1)} \, \pi(x) dx$$

Hence, for the mixed Poisson CRTED, the probability generating function is obtained as:

$$P_n(z) = \int_0^\infty e^{x(z-1)}\alpha(1 - 2\beta e^{-\alpha x} + 3\beta e^{-2\alpha x})dx$$

$$= \alpha \int_0^\infty \left(e^{-(1-z+\alpha)x} - 2\beta e^{-(1-z+2\alpha)x} + 3\beta e^{-(1-z+3\alpha)x}\right)dx$$

Therefore,

$$P_n(z) = \frac{\alpha}{1+\alpha-z} - \frac{2\alpha\beta}{1+2\alpha-z} + \frac{3\alpha\beta}{1+3\alpha-z} \quad [13]$$

Note: Equation 13 can be obtained from Equation 8 (the moment generating function of the mixing distribution, Cubic Rank Transmuted Exponential Distribution) by substituting ***t*** with ***z – 1***. Hence, the moment-generating function of a mixing distribution can uniquely define the PGF of its mixed Poisson version.

3. **Moment Generating Function:** The MGF in Equation 14 is obtained by replacing z with e^t in Equation 13.

$$M_N(t) = \frac{\alpha}{1+\alpha-e^t} - \frac{2\alpha\beta}{1+2\alpha-e^t} + \frac{3\alpha\beta}{1+3\alpha-e^t} \quad [14]$$

Using the relation $E(N^r) = \frac{d^r M_N(t)}{dt^r}|_{t=0};\ r = 1,2,\ldots$ for the central moments, the first four moments about the origin are obtained respectively as in Equations 15 to 18:

$$E(N) = \frac{6-\beta}{6\alpha} \quad [15]$$

$$E(N^2) = \frac{36 - 5\beta + 18\alpha - 3\alpha\beta}{18\alpha^2} \quad [16]$$

$$E(N^3) = \frac{216 - 19\beta + (216 - 30\beta)\alpha + (36 - 6\beta)\alpha^2}{36\alpha^3} \quad [17]$$

$$E(N^4) = \frac{1296 - 65\beta + (54 - 9\beta)\alpha^3 + (756 - 105\beta)\alpha^2 + (1944 - 171\beta)\alpha}{54\alpha^4} \quad [18]$$

4**. Mean and Variance**: The mean and variance of the mixed Poisson CRTED are obtained as in Equation 19:

$$E(N) = E\big(E(N|X)\big) = E(X) = \frac{6-\beta}{6\alpha} \quad [19]$$

Hence, the mean of the mixed Poisson distribution is equal to the mean of its mixing distributions (Equation 20).

$$Var(N) = E\big(Var(N|X)\big) + V\big(E(N|X)\big) = E(X) + V(X) = \frac{36+2\beta-\beta^2-6\alpha\beta+36\alpha}{36\alpha^2} \quad [20]$$

It implies that the variance of mixed Poisson distribution is the sum of the mean of its conditional variance and the variance of its conditional mean (Karlis & Xekalaki, 2005). Hence, the variance of the mixed Poisson distribution always exceeds that of the classical Poisson distribution.

Using the relationships of the moment about the origin (De Jong & Heller, 2008), skewness and kurtosis measures are respectively defined as Equation 21:

$$S_k(N) = \frac{E(N^3) - 3E(N^2)E(N) + 2\big(E(N)\big)^3}{\big(Var(N)\big)^{\frac{3}{2}}}$$

$$Kurt(N) = \frac{E\big(N^4\big)-4E\big(N^3\big)E(N)+6E\big(N^2\big)\big(E(N)\big)^2-3\big(E(N)\big)^4}{\big(Var(N)\big)^2}$$

Therefore, the skewness and kurtosis for the mixed Poisson CRTED are as in Equations 21 and 22:

$$S_k(N) = \frac{2\,(216 + 33\beta + 3\beta^2 - \beta^3 + (324 + 18\beta - 9\beta^2)\alpha + (108 - 18\beta)\alpha^2)}{(36 + 2\beta - \beta^2 + (36 - 6\beta)\alpha)^{\frac{3}{2}}} \quad [21]$$

$$Kurt(N) = \frac{1296(1+\alpha)\big(9+9\alpha+\alpha^2\big)-3\beta^4+12\beta^3(1-3\alpha)+24\beta^2\big(2-3\alpha-6\alpha^2\big)+8\beta\big(201-27\alpha^3-99\alpha^2+189\alpha\big)}{(\beta^2+(6\alpha-2)\beta-36\alpha-36)^2} \quad [22]$$

The Dispersion Index (DI) measures the degree of dispersion in observations. When DI > 1, there is over-dispersion. There is under-dispersion when DI < 1 and equi-dispersion when DI = 1. The measure is given as in Equation 23:

$$DI = \frac{Var(N)}{E(N)}$$

Hence, the Dispersion Index for the mixed Poisson CRTED is:

$$DI(N) = \frac{36+2\beta-\beta^2-6\alpha\beta+36\alpha}{6\alpha(6-\beta)} \quad [23]$$

Table 1 shows simulated Skewness, Kurtosis, and DI for some parameters of the mixed Poisson CRTED.

Table 1

Skewness, kurtosis, and DI for some parameters for mixed Poisson CRTED

	Skewness			Kurtosis			Dispersion Index		
	α = 1.0	α = 2.0	α = 10	α = 0.1	α = 2.0	α = 10	α = 0.1	α = 2.0	α = 10
β = -0.9	1.92	2.06	3.30	8.93	8.91	15.37	9.07	1.40	1.08
β = -0.5	1.94	2.16	3.43	8.88	9.48	16.48	9.91	1.45	1.09
β = 0.0	2.00	2.31	3.62	9.01	10.33	18.09	11.00	1.50	1.10
β = 0.5	2.11	2.48	3.83	9.36	11.39	20.03	12.14	1.56	1.11
β = 0.9	2.22	2.63	4.02	9.81	12.42	21.88	13.09	1.60	1.12

Remarks:

For fixed β, both skewness and kurtosis increase as parameter α increases.

For fixed β, the dispersion index decreases as α increases.

For fixed α, skewness and kurtosis gradually increase as parameter β increases.

For fixed α, the dispersion index slowly increases at β increases.

Maximum Likelihood Estimation

Given a random sample of size k from the mixed Poisson CRTED with PMF, as stated in Equation 11, the log-likelihood function for the distribution is obtained as in Equation 24.

$$f_n = \frac{\alpha}{(1+\alpha)^{n+1}} - \frac{2\alpha\beta}{(1+2\alpha)^{n+1}} + \frac{3\alpha\beta}{(1+3\alpha)^{n+1}}$$

$$\mathcal{L} = \prod_{i=1}^{k} f_{n_i} = \prod_{i=1}^{k}\left(\frac{\alpha}{(1+\alpha)^{n+1}} - \frac{2\alpha\beta}{(1+2\alpha)^{n+1}} + \frac{3\alpha\beta}{(1+3\alpha)^{n+1}}\right) \quad [24]$$

$$\ell = log\,\mathcal{L} = \sum_{i=1}^{k} log\left(\frac{\alpha}{(1+\alpha)^{n+1}} - \frac{2\alpha\beta}{(1+2\alpha)^{n+1}} + \frac{3\alpha\beta}{(1+3\alpha)^{n+1}}\right)$$

The estimators for (α, β) denoted with $(\hat{\alpha}, \hat{\beta})$ are the solutions of Equation 24. These solutions contain non-linear equations, which make analytical solutions quite tedious. Using the *MaxLik* functions in the R language (R-Core Team, 2020), the Newton-Raphson algorithm is used to obtain the estimates.

RESULTS AND DISCUSSION

Competing Distributions

The performances of the new distributions are compared with four related discrete distributions. (1) Poisson distribution, (2) Negative Binomial (NB) distribution, (3) Mixed Poisson Exponential (MPE) distributions, and (4) Mixed Poisson Lindley (MPL) distribution. These distributions are considered because they are all mixed probability

distributions (the Negative Binomial is obtained when the gamma distribution is used as the mixing distribution, see Greenwood & Yule, 1920). In particular, the mixed Poisson Exponential distribution is a special case of the new proposition. Table 2 gives the PMF of the considered related distributions.

Table 2

Some related distributions

Distribution	PMF
Poisson	$\frac{e^{-\alpha}\alpha^{n}}{n!}$
Negative Binomial	$\left(\frac{n+\beta-1}{n}\right)\left(\frac{\alpha}{1+\alpha}\right)^{n}\left(\frac{1}{1+\alpha}\right)^{\beta}$
Mixed Poisson Exponential	$\frac{\alpha}{(1+\alpha)^{n+1}}$
Mixed Poisson Lindley`	$\frac{\alpha^{2}(n+\alpha+2)}{(1+\alpha)^{n+3}}$

Count Data

The performance of the proposed distribution is assessed using six-count observations (Table 3). The first dataset is found in De Jong and Heller (2008). It consists of a one-year insurance policy for third-party claims for Australian vehicle owners. The second data set is the frequency of insurance claims from Belgium in 1993, earlier utilized by Zamani et al. (2014). The third data contains the frequency of claims for automobile injury obtained by the General Insurance Association in Singapore for 1993. The data was earlier used by Frees (2010) and Frees and Valdez (2008). The fourth dataset is the frequency of mistakes in copying groups of random digits first reported by Kemp and Kemp (1965) and in several other propositions (Sah & Mishra, 2019; Samutwachirawong, 2021; Shanker & Mishra, 2014; Shanker & Mishra, 2016) involving new discrete distributions. The fifth dataset (yeast cell counts per square) was used to assess the mixed Poisson Lindley distribution and other related distributions (Shanker & Hagos, 2015). The sixth dataset is the number of epileptic seizures previously used on weighted generalized Poisson distribution (Chakraborty, 2010) and mixed Poisson Transmuted Exponential distribution (Samutwachirawong, 2021).

Table 3

Summary of Count Datasets

Observation	Dataset 1	Dataset 2	Dataset 3	Dataset 4	Dataset 5	Dataset 6
0	63232	57178	6996	35	128	126
1	4333	5617	455	11	37	80
2	271	446	28	8	18	59

Table 3 *(Continue)*

Observation	Dataset 1	Dataset 2	Dataset 3	Dataset 4	Dataset 5	Dataset 6
3	18	50	4	4	3	42
4	2	8		2	1	24
5						8
6						5
7						4
8						3
Percentage of 0	93.19	90.33	93.49	58.33	68.45	35.90
Dispersion Index	1.08	1.08	1.09	1.61	1.32	1.87
Skewness	4.07	3.52	4.27	1.31	1.75	1.31
Kurtosis	18.50	14.59	20.88	0.72	2.80	1.71

Although the negative binomial distribution provides a good fit for the dataset, the proposed distribution best fits dataset 1, as shown in Table 4, with the least – 2 log-likelihood (36099.26) and chi-square statistic (0.85). The mixed Poisson CRTED also best fits dataset 2 with the least – 2 log-likelihood (44127.64) and chi-square value (10.92), as shown in Table 5.

Table 6 shows that the negative binomial distribution better fits the new proposition with the lowest – 2 log-likelihood and chi-square values. The new position competes quite well with very close values to the minimum obtained when a negative binomial is assumed. From Table 7, the mixed Poisson CRTED has the least chi-square value and the joint least – 2 log-likelihood value (along with the mixed Poisson Lindley distribution). The new proposition also performs creditable well for datasets 5 and 6 with relatively lower – 2 log-likelihood and chi-square values.

As shown in Tables 8 and 9, the results of the fifth and sixth datasets reveal that the new proposition provides a relatively better fit with the least chi-square values (2.55 and 5.64) for the fifth and sixth datasets and lower – 2 log-likelihood.

Table 4

Performance of mixed Poisson CRTED using Dataset 1

Obser.	Freq.	Expected Frequency				
		Poisson-CRTED	Poisson	Neg. Bin	MPE	MPL
0	63232	63232.39	63091.61	63230.60	63252.72	63255.08
1	4333	4330.00	4593.07	4330.57	4291.00	4289.95

Table 4 *(Continue)*

Obser.	Freq.	Expected Frequency				
		Poisson-CRTED	Poisson	Neg. Bin	MPE	MPL
2	271	275.15	167.19	276.48	291.10	290.01
3	18	17.29	4.06	17.22	19.75	19.55
4	2	1.09	0.07	1.06	1.34	1.31
ML Estimate		$\hat{\alpha}$ = 14.6190	$\hat{\alpha}$ = 0.0728	$\hat{\alpha}$ =1.1569	$\hat{\alpha}$ = 13.7408	$\hat{\alpha}$ = 14.6315
		$\hat{\beta}$ = -0.3817		$\hat{\beta}$ = 0.9408		
-2 LL		36099.26	36203.00	36099.36	36100.90	36100.76
Chi-Square		0.85	177.66	0.98	2.29	2.17

Table 5

Performance of mixed Poisson CRTED using Dataset 2

Obser.	Freq.	Expected Frequency				
		Poisson-CRTED	Poisson	Neg. Bin	MPE	MPL
0	57178	57203.04	56949.763	57188.34	57247.47	57243.92
1	5167	5569.68	6019.590	5581.31	5472.99	5479.09
2	446	481.59	318.135	485.28	523.23	521.46
3	50	40.88	11.209	40.47	50.02	49.39
4	8	3.49	0.296	3.30	4.78	4.66
ML Estimate		$\hat{\alpha}$ = 10.4502	$\hat{\alpha}$ = 0.1057	$\hat{\alpha}$ = 1.2791	$\hat{\alpha}$ = 9.460	$\hat{\alpha}$ = 10.2973
		$\hat{\beta}$ = -0.6081		$\hat{\beta}$ = 0.9237		
-2 LL		44127.64	44301.08	44128.62	44136.36	44135.66
Chi-Square		10.92	413.84	12.33	17.44	16.87

Table 6

Performance of mixed Poisson CRTED using Dataset 3

Obser.	Freq.	Expected Frequency				
		Poisson-CRTED	Poisson	Neg. Bin	MPE	MPL
0	6996	6996.35	6977.80	6996.71	6994.08	6994.03
1	455	452.97	487.75	452.52	456.97	457.12
2	28	31.33	17.05	31.38	29.86	29.79
3	4	2.19	0.40	2.22	1.95	1.94

Table 6 *(Continue)*

Obser.	Freq.	Expected Frequency				
		Poisson-CRTED	Poisson	Neg. Bin	MPE	MPL
ML Estimate		$\hat{\alpha}$ =13.5556	$\hat{\alpha}$ = 0.0699	$\hat{\alpha}$ = 0.8740	$\hat{\alpha}$ = 14.3052	$\hat{\alpha}$ = 15.1903
		$\hat{\beta}$ = 0.3169		$\hat{\beta}$ = 0.9260		
-2 LL		3864.80	3882.36	3864.76	3864.94	3864.96
Chi-Square		1.86	41.96	1.79	2.28	2.32

Table 7

Performance of mixed Poisson CRTED using Dataset 4

Obser.	Freq.	Expected Frequency				
		Poisson-CRTED	Poisson	Neg. Bin	MPE	MPL
0	35	34.19	27.41	33.95	33.64	33.06
1	11	14.27	21.47	14.49	14.78	15.27
2	8	6.31	8.41	6.39	6.49	6.74
3	4	2.85	2.20	2.85	2.85	2.88
4	2	1.30	0.43	1.28	1.25	1.21
ML Estimate		$\hat{\alpha}$ = 1.2250	$\hat{\alpha}$ = 0.7833	$\hat{\alpha}$ = 0.9381	$\hat{\alpha}$ = 1.2766	$\hat{\alpha}$ = 1.7434
		$\hat{\beta}$ = 0.2544		$\hat{\beta}$ = 0.5449		
-2 LL		146.70	155.10	146.74	146.76	146.70
Chi-Square		2.06	14.44	2.15	2.28	2.50

Table 8

Performance of mixed Poisson CRTED using Dataset 5

Obser.	Freq.	Expected Frequency				
		Poisson-CRTED	Poisson	Neg. Bin	MPE	MPL
0	128	127.26	118.06	126.73	128.09	127.41
1	37	41.43	54.30	42.08	40.35	41.11
2	18	12.76	12.49	12.84	12.71	12.86
3	3	3.87	1.91	3.80	4.00	3.94
4	1	1.17	0.22	1.11	1.26	1.18
ML Estimate		$\hat{\alpha}$ = 2.2633	$\hat{\alpha}$ = 0.4599	$\hat{\alpha}$ = 1.1950	$\hat{\alpha}$ = 2.1744	$\hat{\alpha}$ = 2.7416
		$\hat{\beta}$ = -0.2481		$\hat{\beta}$ = 0.7221		
-2 LL		340.14	347.66	340.05	340.19	339.98
Chi-Square		2.55	12.16	2.88	2.78	2.72

Table 9

Performance of mixed Poisson CRTED using Dataset 6

Obser.	Freq.	Expected Frequency				
		Poisson-CRTED	Poisson	Neg. Bin	MPE	MPL
0	126	122.60	74.93	120.23	137.96	128.68
1	80	92.65	115.71	93.00	83.74	87.13
2	59	57.85	89.34	59.17	50.82	55.27
3	42	33.75	45.99	34.94	30.85	33.64
4	24	19.19	17.75	19.83	18.72	19.90
5	8	10.82	5.48	10.99	11.36	11.53
6	5	6.10	1.41	5.98	6.90	6.58
7	4	3.45	0.31	3.22	4.19	3.70
8	3	1.96	0.06	1.72	2.54	2.06
ML Estimate		$\hat{\alpha}$ = 0.7285	$\hat{\alpha}$ = 1.5442	$\hat{\alpha}$ = 1.5501	$\hat{\alpha}$ = 0.6476	$\hat{\alpha}$ = 0.9734
		$\hat{\beta}$ = -0.7753		$\hat{\beta}$ = 0.5010		
-2 LL		1189.44	1272.09	1189.88	1196.79	1190.36
Chi-Square		5.64	37.20	6.51	9.65	5.72

CONCLUSION

Using cubic rank transmuted exponential distribution as the mixing distribution (a newly introduced continuous distribution), this paper proposed a new two-parameter mixed Poisson distribution. The mixed Poisson exponential distribution, a special form of the geometric distribution, is a special case of the new proposition. Shapes of the new distribution are unimodal, with the ability to model skewed data with excess zero.

Various mathematical properties of the new proposition, like the measures based on the moment (skewness, kurtosis, and dispersion index), are obtained. Parameters of the distribution are obtained using the maximum likelihood estimation. Six moderately dispersed count observations with varying percentages of zero are used to assess the performance of the new proposition along with other related mixed Poisson distributions (Poisson, negative binomial, mixed Poisson exponential, and mixed Poisson Lindley). Using the – 2 log-likelihood and the chi-square goodness of fit to compare performances, the new proposition performs creditably well and can be used as an alternative for the competing distributions. In some cases, the – 2 Log Likelihood values obtained for the proposed distribution are closer to some competing distributions; however, the chi-square goodness of fit test reveals that the new proposition provides the best fit to the assessed datasets.

ACKNOWLEDGMENT

A sincere appreciation goes to the Federal Government of Nigeria through the Tertiary Education Trust Fund (TETFund) for the Doctoral Scholarship. The authors would like to express their sincere appreciation to all staff of the School of Mathematical Sciences, Universiti Sains Malaysia.

REFERENCES

Adetunji, A. A., & Sabri, S. R. M. (2021). Modelling claim frequency in insurance using count models. *Asian Journal of Probability and Statistics*, *14*(4), 14-20. https://doi.org/10.9734/ajpas/2021/v14i430334

Aguilar, G. A. S., Moala, F. A., & Cordeiro, G. M. (2019). Zero-truncated poisson exponentiated gamma distribution : Application and estimation methods. *Journal of Statistical Theory and Practice, 13*(4), 1-20 . https://doi.org/10.1007/s42519-019-0059-2

Al-kadim, K. A. (2018). Proposed generalized formula for transmuted distribution. *Journal of Babylon University, Pure and Applied Sciences*, *26*(4), 66-74.

Asamoah, K. (2016). On the credibility of insurance claim frequency: Generalized count models and parametric estimators. *Insurance: Mathematics and Economics*, *70*, 339-353. https://doi.org/10.1016/j.insmatheco.2016.07.003

Bhati, D., Sastry, D. V. S., & Maha Qadri, P. Z. (2015). A new generalized poisson-lindley distribution: Applications and properties. *Austrian Journal of Statistics*, *44*(4), 35-51. https://doi.org/10.17713/ajs.v44i4.54

Chakraborty, S. (2010). On some distributional properties of the family of weighted generalized poisson distribution. *Communications in Statistics - Theory and Methods*, *39*(15), 2767-2788. https://doi.org/10.1080/03610920903129141

Das, K. K., Ahmed, I., & Bhattacharjee, S. (2018). A new three-parameter poisson-lindley distribution for modelling over-dispersed count data. *International Journal of Applied Engineering Research*, *13*(23), 16468-16477.

De Jong, P., & Heller, G. Z. (2008). *Generalized Linear Models for Insurance Data*. Cambridge University Press.

Frees, E. W. (2010). *Regression Modeling with Actuarial and Financial Applications*. Cambridge University Press. https://doi.org/10.1017/CBO9780511814372

Frees, E. W., & Valdez, E. A. (2008). Hierarchical insurance claims modeling. *Journal of the American Statistical Association*, *103*(484), 1457-1469. https://doi.org/10.1198/016214508000000823

Greenwood, M., & Yule, G. U. (1920). An inquiry into the nature of frequency distributions representative of multiple happenings with particular reference to the occurrence of multiple attacks of disease or of repeated accidents. *Journal of the Royal Statistical Society*, *83*(2), Article 255. https://doi.org/10.2307/2341080

Holgate, P. (1970). The modality of some compound poisson distributions. *Biometrika*, *87*(3), 666-667. https://doi.org/10.1093/biomet/57.3.666

Karina, T. M., Nurrohmah, S., & Fithriani, I. (2019). Heterogeneous Weibull count distribution. *Journal of Physics: Conference Series*, *1218*(1), Article 012020. https://doi.org/10.1088/1742-6596/1218/1/012020

Karlis, D., & Xekalaki, E. (2005). Mixed poisson distributions. *International Statistical Review*, *73*(1), 35-58. https://doi.org/10.1111/j.1751-5823.2005.tb00250.x

Kemp, C. D., & Kemp, A. W. (1965). Some propoerties of the Hermite distribution. *Biometrika*, *52*(3-4), 381-394. https://doi.org/10.1093/biomet/52.3-4.381

Mohammed, Y. A., Yatim, B., & Ismail, S. (2015). Mixture model of the exponential, Gamma and Weibull distributions to analyse heterogeneous survival data. *Journal of Scientific Research and Reports, 5*(2), 132-139. https://doi.org/10.9734/JSRR/2015/15014

Omari, C. O., Nyambura, S. G., & Mwangi, J. M. W. (2018). Modeling the frequency and severity of auto insurance claims using statistical distributions. *Journal of Mathematical Finance*, *8*(1), 137-160. https://doi.org/10.4236/jmf.2018.81012

Ong, S. H., Low, Y. C., & Toh, K. K. (2021). Recent developments in mixed poisson distributions. *ASM Science Journal*, *14*(3), 1-10. https://doi.org/10.32802/asmscj.2020.464

R-Core Team. (2020). *R: A Language and Environment for Statistical Computing.* R Foundation for Statistical Computing. https://www.r-project.org/

Rasekhi, M., Alizadeh, M., Altun, E., Hamedani, G., Afify, A. Z., & Ahmad, M. (2017). The modified exponential distribution with applications. *Pakistan Journal of Statistics*, *33*(5), 383-398.

Sah, B. K., & Mishra, A. (2019). A Generalised Exponential-Lindley Mixture of Poisson Distribution. *Nepalese Journal of Statistics, 3*, 11-20. https://doi.org/10.4135/9781412952644.n350

Samutwachirawong, S. (2021). Poisson-exponential and Gamma distribution: Properties and applications. *Journal of Applied Statistics and Information Technology*, *6*(2), 17-24.

Sankaran, M. (1970). 275. Note: The discrete poisson-lindley distribution. *Biometrics*, *26*(1), 145-149. https://doi.org/10.2307/2529053

Shaked, M. (1980). On mixtures from exponential families. *Journal of Royal Statistical Society. Series B (Methodological)*, *42*(2), 192-198. https://doi.org/10.1111/j.2517-6161.1980.tb01118.x

Shanker, R., & Hagos, F. (2015). On poisson-lindley distribution and its applications to biological sciences. *Biometrics and Biostatistics International Journal*, *2*(5), 1-5.

Shanker, R., & Mishra, A. (2014). A Two-Parameter Poisson-Lindley distribution. *International Journal of Statistics and Systems*, *9*(1), 79-85.

Shanker, R., & Mishra, A. (2016). A Quasi Poisson-Lindley distribution. *Journal of the Indian Statistical Association*, *54*(1), 113-125.

Willmot, G. E. (1990). Asymptotic tail behaviour of poisson mixtures with applications. *Advances in Applied Probability*, *22*(1), 147-159. https://doi.org/10.2307/1427602

Zakerzadeh, H., & Dolati, A. (2009). Generalized Lindley distribution. *Journal of Mathematical Extension*, *3*(2), 1-17.

Zamani, H., Ismail, N., & Faroughi, P. (2014). Poisson-weighted exponential univariate version and regression model with applications. *Journal of Mathematics and Statistics*, *10*(2), 148-154. https://doi.org/10.3844/jmssp.2014.148.154

REFEREES FOR THE PERTANIKA
JOURNAL OF SCIENCE & TECHNOLOGY

Vol. 31 (3) Apr. 2023

The Editorial Board of the Pertanika Journal of Science and Technology wishes to thank the following:

Abam Fidelis
(MOUAU, Nigeria)

Abd Rahman Abdul Rahim
(UTM, Malaysia)

Abdul Naser Abdul Ghani
(USM, Malaysia)

Ahmed Al-Jumaili
(UFL, USA)

Ahmed Kadhim Hussein
(University of Babylon, Iraq)

Aidi Hizami Alias
(UPM, Malaysia)

Amir Hamzah Ahmad Ghazali
(USM, Malaysia)

Arli Aditya Parikesit
(i3L, Indonesia)

Ashwani Kumar
(JUIT, India)

Ayu Haslija Abu Bakar
(UCSI University, Malaysia)

Chang Kah Haw
(USM, Malaysia)

Chukwu Ogbonnaya
(FUTMinna, Nigeria)

Dzulkiflee Ismail
(USM, Malaysia)

Edlic Sathiamurthy
(UMT, Malaysia)

Ekaterina V. Koval
(URGAU, Russian Federation)

Elango Natarajan
(UCSI University, Malaysia)

Faizal Abdul Manaf
(UPNM, Malaysia)

Farah Nora Aznieta Abd. Aziz
(UPM, Malaysia)

Flora Somidin
(UNIMAP, Malaysia)

Juhaida Abu Bakar
(UUM, Malaysia)

Khaled Abbas El-Tarabily
(UAE University, United Arab Emirates)

Khoo Shin Yee
(UM, Malaysia)

Law Ming Chiat
(Curtin University, Malaysia)

Mo Kim Hung
(UM, Malaysia)

Mohammed Alias Yusof
(UPNM, Malaysia)

Mohd. Yusri Abd Rahman
(UKM, Malaysia)

Muhajir Ab Rahim
(UNIMAP, Malaysia)

Muhammad Heikal Ismail
(UPM, Malaysia)

Muhammad Idzdihar Idris
(UTeM, Malaysia)

Muhammad Imran Tariq
(Superior University, Pakistan)

Muhammad Ubaidah Syafiq Mustaffa
(UKM, Malaysia)

Mustafa Z. Mahmoud
(PSAU, Saudi Arabia)

Muzamir Isa
(UNIMAP, Malaysia)

Nasibah Mohamad
(USM, Malaysia)

Noor Azlinda Ahmad
(UTM, Malaysia)

Noor Diyana Osman
(USM, Malaysia)

Nor Nadiah Abdul Karim Shah
(UPM, Malaysia)

Norlaila Mohd Zanuri
(USM, Malaysia)

Nozieana Khairuddin
(UPM, Malaysia)

Nur Hana Samsudin
(USM, Malaysia)

Ong Seng Huat
(UCSI University, Malaysia)

Rohana Hassan
(UiTM, Malaysia)

Roslina Ahmad
(UM, Malaysia)

Sathya Shankara Sharma
(MIT, India)

Sharifah Md. Yasin
(UPM, Malaysia)

Siti Aisyah Razali
(UMT, Malaysia)

Siti Nur Aliaa Roslan
(UPM, Malaysia)

Siti Rohaiza Ahmad
(UBD, Brunei Darussalam)

Soong Ming Foong
(UM, Malaysia)

Syam Krishnan
(Queensland University of Technology, Australia)

Tahar Tayebi
(UNIV-BBA, Algeria)

Yusnita Mohd Ali
(UiTM, Malaysia)

Zaleha Mustafa
(UTeM, Malaysia)

Zalisham Jali
(USIM, Malaysia)

Zamira Hasanah Zamzuri
(UKM, Malaysia)

Zarul Fitri Zaaba
(USM, Malaysia)

Zdzislaw Kaliniewicz
(UWM, Poland)

FUTMinna	*– Federal University of Technology Minna*
i3L	*– Indonesia International Institute for Life Sciences*
JUIT	*– Jaypee University of Information Technology*
MIT	*– Manipal Institute of Technology*
MOUAU	*– Michael Okpara University of Agriculture*
PSAU	*– Prince Sattam bin Abdulaziz University*
UBD	*– Universiti Brunei Darussalam*
UFL	*– University of Florida*
UiTM	*– Universiti Teknologi MARA*
UKM	*– Universiti Kebangsaan Malaysia*
UM	*– Universiti Malaya*
UMT	*– Universiti Malaysia Terengganu*
UNIMAP	*– Universiti Malaysia Perlis*
UNIV-BBA	*– University of Bordj Bou Arreridj*
UPM	*– Universiti Putra Malaysia*
UPNM	*– Universiti Pertahanan Nasional Malaysia*
URGAU	*– State Agrarian University of Northern Trans Urals*
USIM	*– Universiti Sains Islam Malaysia*
USM	*– Universiti Sains Malaysia*
UTeM	*– Universiti Teknikal Malaysia Melaka*
UTM	*– Universiti Teknologi Malaysia*
UUM	*– Universiti Utara Malaysia*
UWM	*– University of Warmia and Mazury*

While every effort has been made to include a complete list of referees for the period stated above, however if any name(s) have been omitted unintentionally or spelt incorrectly, please notify the Chief Executive Editor, *Pertanika* Journals at executive_editor.pertanika@upm.edu.my

Any inclusion or exclusion of name(s) on this page does not commit the *Pertanika* Editorial Office, nor the UPM Press or the university to provide any liability for whatsoever reason.

Heat Rate Deviation Analysis of a Coal-Fired Power Plant (CFPP) with the Influence of Applicable Coal Prices (ACP) 1453
Manmit Singh Jasbeer Singh, Nawal Aswan Abdul Jalil, Sharafiz Abdul Rahim, Zamir Aimaduddin Zulkefli and Hasril Hasini

Effects of Shooting Angles and Ricochet Angles on Bullet Weight Upon Impact on Three Types of Woods (Balau, Resak, and Seraya) 1475
Mohd Najib Sam, Glenna Tan Jie Yee, Noor Hazfalinda Hamzah, Mohd Zulkarnain Embi, Ahmad Zamri Md Rejab, Gina Francesca Gabriel and Khairul Osman

The Effect of Graphene Nanoplatelets Content on the Hardness of Mg6%Zn0.2%Mn Composites 1493
Abang Mohamad Harith Abang Beniamin, Noor Hisyam Noor Mohamed and Mahsuri Yusof

Discovery of *Mycobacterium tuberculosis* CYP121 New Inhibitor via Structure-Based Drug Repurposing 1503
Tarek El Moudaka, Priya Murugan, Mohd Basyaruddin Abdul Rahman and Bimo Ario Tejo

Study and Simulation of the Electric Field-Induced Spin Switching in PZT/NiFe/CoFe Nanostructured Composites 1523
Minh Hong Thi Nguyen, Thanh Tien Pham, Nam Van La, Soo Kien Chen and Tiep Huy Nguyen

The Characteristics of Polymer Concrete Reinforced with Polypropylene Fibres Under Axial and Lateral Compression Loads 1535
Nur Aqilah Azman, Agusril Syamsir, Mohd Supian Abu Bakar, Muhammad Asyraf Muhammad Rizal, Khairul Amri Sanusi and Mohammed Jalal Abdullah

Analysis of Influence of Vertical Vibration on Natural Heat Convection Coefficients from Horizontal Concentric and Eccentric Annulus 1555
Baydaa Khalil Khudhair, Adel Mahmood Saleh and Ali Laftah Ekaid

An Alternative Count Distribution for Modeling Dispersed Observations 1587
Ademola Abiodun Adetunji and Shamsul Rijal Muhammad Sabri

The Effect of Preload, Density and Thickness on Seat Dynamic Stiffness 1267
Azmi Mohammad Hassan, Khairil Anas Md Rezali, Nawal Aswan Abdul Jalil, Azizan As'arry and Mohd Amzar Azizan

Effects of Fibre Length on the Physical Properties of Oil Palm Empty Fruit Bunch Cement Board (OPEFB-CB) 1279
Wenish Anak Maynet, Emedya Murniwaty Samsudin, Nik Mohd Zaini Nik Soh, Lokman Hakim Ismail, Hasniza Abu Bakar and Ahmed Elgadi

Review Article
A Review on Grapheme-to-Phoneme Modelling Techniques to Transcribe Pronunciation Variants for Under-Resourced Language 1291
Emmaryna Irie, Sarah Samson Juan and Suhaila Saee

Correlation Between Clinical Features of Type 2 Diabetes Mellitus with CT Findings of Fatty Liver Patients 1313
Hanady Elyas Osman, Huda Osama, Mohamed Yousef, Amal Alsalamah, Lubna Bushara and Ikhlas Abdalaziz

Highly Conductive Graphenated-Carbon Nanotubes Sheet with Graphene Foliates for Counter Electrode Application in Dye- Sensitized Solar Cells 1325
Yusnita Yusuf, Suhaidi Shafie, Ismayadi Ismail, Fauzan Ahmad, Mohd Nizar Hamidon, Pandey Shyam Sudhir and Lei Wei

Evaluation of Digital's Role in Sustainable Built Environment 1335
Theodore Wayne, Chang Saar Chai, Shirly Siew Ling Wong, Fang Lee Lim, Kai Chen Goh and Nur IzieAdiana Abidin

Server-Side Cross-Site Scripting Detection Powered by HTML Semantic Parsing Inspired by XSS Auditor 1353
Chrisando Ryan Pardomuan, Aditya Kurniawan, Mohamad Yusof Darus, Muhammad Azizi Mohd Ariffin and Yohan Muliono

Influence of Carrier Agents Concentrations and Inlet Temperature on the Physical Quality of Tomato Powder Produced by Spray Drying 1379
S. M. Anisuzzaman, Collin G. Joseph and Fatin Nadiah Ismail

Review Article
Geochemistry of Foraminifera in the Marginal Seas of the Sunda Shelf: A Review 1413
Aqilah Nur Shahruddin and Che Abd Rahim Mohamed

Railway Urbanozems: Interrelation of Physicochemical and Integral Environmental Indicators 1439
Tatyana Anatolyevna Adamovich and Anna Sergeyevna Olkova

Pertanika Journal of Science & Technology
Vol. 31 (3) Apr. 2023

Content

Foreword i
Mohd Sapuan Salit

Humic Acid-Amended Formulation Improves Shelf-Life of Plant Growth-Promoting Rhizobacteria (PGPR) Under Laboratory Conditions 1137
Buraq Musa Sadeq, Ali Tan Kee Zuan, Susilawati Kasim, Wong Mui Yun, Nur Maizatul Idayu Othman, Jawadyn Talib Alkooranee, Sayma Serine Chompa, Amaily Akter and Md Ekhlasur Rahman

Effects of Density Variation on the Physical and Mechanical Properties of Empty Fruit Bunch Cement Board (EFBCB) 1157
Mohammad Nasrullah Ridzuan, Hasniza Abu Bakar, Emedya Murniwaty Samsudin, Nik Mohd Zaini Nik Soh and Lokman Hakim Ismail

Ex-Situ Development and Characterization of Composite Film Based on Bacterial Cellulose Derived from Oil Palm Frond Juice and Chitosan as Food Packaging 1173
Norshafira Syazwani Abu Hasan, Shahril Mohamad, Sharifah Fathiyah Sy Mohamad, Mohd Hafiz Arzmi and Nurul Nadia Izzati Supian

Effect of Moisture Content on Frictional Properties of Some Selected Grains in Indonesia 1189
Nursigit Bintoro, Alya Iqlima Zahra, Azizah Putri Khansa, Muftia Chairin Nissa, Aldhayu Sam Safira and Sastika Nidya Ashari

Examination of the Partial Discharge Behaviour Within a Spherical Cavity in Insulation Paper of Transformer 1209
Muhammad Hakirin Roslan, Norhafiz Azis, Mohd Zainal Abidin Ab Kadir, Jasronita Jasni and Mohd Fairouz Mohd Yousof

Sociodemographic Characteristics, Dietary Intake, and Body Image Dissatisfaction Among Saudi Adolescent Girls 1223
Abeer Ahmad Bahathig, Hazizi Abu Saad, Nor Baizura Md Yusop, Nurul Husna Mohd Sukri and Maha M. Essam El-Din

Automation of Quantifying Security Risk Level on Injection Attacks Based on Common Vulnerability Scoring System Metric 1245
Aditya Kurniawan, Mohamad Yusof Darus, Muhammad Azizi Mohd Ariffin, Yohan Muliono and Chrisando Ryan Pardomuan

Pertanika Editorial Office, Journal Division,
Putra Science Park,
1st Floor, IDEA Tower II,
UPM-MTDC Center,
Universiti Putra Malaysia,
43400 UPM Serdang,
Selangor Darul Ehsan
Malaysia

http://www.pertanika.upm.edu.my
Email: executive_editor.pertanika@upm.edu.my
Tel. No.: +603- 9769 1622

PENERBIT UPM PRESS
http://www.penerbit.upm.edu.my
Email: penerbit@upm.edu.my
Tel. No.: +603- 9769 8851

ISSN 0128-7680
9 770128 768083 04 >